UNIVERSIDADE ESTADUAL PAULISTA
"Júlio de Mesquita Filho"
Instituto de Geociências e Ciências Exatas
Câmpus de Rio Claro

RODRIGO PRUDENTE DE MELO

CARACTERIZAÇÃO DO METAMORFISMO DA FAIXA MÓVEL AGUAPEÍ E SUA RELAÇÃO COM A GÊNESE DOS DEPÓSITOS DE OURO DA REGIÃO DE PONTES E LACERDA - MT

Tese de Doutorado apresentada ao Instituto de Geociências e Ciências Exatas do Câmpus de Rio Claro, da Universidade Estadual Paulista "Júlio de Mesquita Filho", como parte dos requisitos para obtenção do título de Doutor em Geociências e Meio Ambiente

Orientador: Marcos Aurélio Farias de Oliveira

Rio Claro-SP
2016

549
M528c

Melo, Rodrigo Prudente de
Caracterização do metamorfismo da Faixa Móvel Aguapeí e sua relação com a gênese dos depósitos de ouro da região de Pontes e Lacerda - MT / Rodrigo Prudente de Melo. - Rio Claro, 2016
256 f. : il., figs., tabs., fots. + mapa + folder

Tese (doutorado) - Universidade Estadual Paulista, Instituto de Geociências e Ciências Exatas
Orientador: Marcos Aurélio Farias de Oliveira

1. Mineralogia. 2. Ouro orogênico. 3. Depósito Pau-a-Pique. 4. Depósito Ernesto. 5. Província Aurífera Alto Guaporé. 6. Metalogênese. I. Título.

Ficha Catalográfica elaborada pela STATI - Biblioteca da UNESP
Campus de Rio Claro/SP

DOUTORADO

RODRIGO PRUDENTE DE MELO

CARACTERIZAÇÃO DO METAMORFISMO DA FAIXA MÓVEL AGUAPEÍ E SUA RELAÇÃO COM A GÊNESE DOS DEPÓSITOS DE OURO DA REGIÃO DE PONTES E LACERDA - MT

Tese de Doutorado apresentada ao Instituto de Geociências e Ciências Exatas do Câmpus de Rio Claro, da Universidade Estadual Paulista "Júlio de Mesquita Filho", como parte dos requisitos para obtenção do título de Doutor em Geociências e Meio Ambiente

Comissão Examinadora

Prof. Dr. Marcos Aurélio Farias de Oliveira (Orientador) - IGCE/UNESP/Rio Claro (SP)

Prof. Dr. Washington Barbosa Leite Junior - IGCE/UNESP/Rio Claro (SP)

Prof. Dr. Norberto Morales - IGCE/UNESP/Rio Claro (SP)

Dr. Richard J. Goldfarb - USGS/Denver/USA

Prof. Dr. Frederico Meira Faleiros - IG/USP/São Paulo (SP)

Resultado: APROVADO

Rio Claro, SP, 28 de Abril de 2016

AGRADECIMENTOS

Agradeço às instituições que financiaram e deram suporte cientifico e logístico e ao desenvolvimento dessa pesquisa.

À **Fundação de Amparo à Pesquisa do Estado de São Paulo** (FAPESP), que deu apoio financeiro a este projeto por meio de bolsa de doutorado (Processo 2012/17432-8) e por meio de projeto regular de pesquisa (Processo 2013/22082-9).

À **Yamana Gold Inc.** que, atraves de suas subsidiárias **Yamana Desenvolvimento Mineral** e **Serra da Borda Mineração e Metalurgia S/A** (dententoras dos direitos minerários da área estudada durante os anos iniciais dessa pesquisa), foi fundamentais no desenvolvimento desse projeto permitindo o acesso aos depósitos estudados, bem como liberdade na coleta de amostras, além de ter colocado à disposição parte de sua equiope técnica para dar suporte e apoio logístico durante os trabalhos de campo. Agrageço em especial aos membro do time de exploração, geólogos, técnicos, corpo administrativo e estagiários, aqui representados pelo então coordenador de exploração Marcio Coppi, e gerentes André Idalgo de Oliveira e Dr. Jorge L. Feola.

Ao **Serviço Geológico dos Estados Unidos (USGS)** por ter me recebido como pesquisador visitante entre o período de Junho de 2014 a Julho de 2015, durante o qual foi feita grande parte da coleta de dados analíticos. Em especial aos ciêntistas do Laboratório de Análise de Inclusões de Denver (DIAL), Erin Marsh, Dr. Ryan Taylor, Heather Lowers e Alan Koenig, e aos ciêntistas do Laboratório de Isótopos Estávies do Centro Ciêntífico de Geoquímica e Geofísica Crustal (CGGSC), Cayce A. Gulbransen, Dr. Craig A. Jhoson e Richard J. Moscati pela ajuda durante as análises, preparação de amostra e discussão dos dados obtidos.

Ao **Conselho Nacional de Desenvolvimento Ciêntífico e Tecnológico** (CNPq) pela conceção de bolsa de doutorado Sanduíche (Processo 236487/2013-2) através da qual foi possível a execução deste projeto em parceria com o Serviço Geológico dos Estados Unidos.

Agradeço em especial ao Dr. Richard J. Goldfarb por ter compatilhado toda sua experiência e conhecimento durante discuções e conversas no Serviço Geológico dos Estados Unidos. Da mesma forma agradeço ao Prof. Dr. Roberto Perez Xavier e ao Prof. Marcos Aurélio Farias de Oliveira por sua orientação e contribuição ao desenvolvimento dessa pesquisa.

Aos membros da Comissão Examinadora por suas críticas e sugestões que auxiliaram na revisão deste trabalho.

Por fim à minha familia e amigos por todo o apoio, em especial ao amigo Aparecido Buchner por sua preciosa ajuda durante os trabalhos de campo.

RESUMO

A Faixa Móvel Aguapeí compreende uma estreita faixa de dobramentos de aproximadamente 500Km de comprimento, estruturalmente confinada entre a margem leste do Craton Paraguá e o embasamento da província San-Ignacio. A reativação de estruturas de escala crustal tem sido apontado como o principal responsável pela evolução tectônica e metamórfica da faixa, que ocorreu no início do Neoproterozóico (~0.92Ga) e que causou a deformação e o metamorfismo de rochas sedimentares previamente depositadas em um Aulacógeno (Aguapeí Group), bem como seu embasamento Mezoproterozóico. A evolução da Faixa Móvel Aguapeí e sua relação com mineralizações auríferas que ocorrem em sua porção mais setentrional, foi investigado nessa pesquisa através de petrografia auxiliada pelo estudo de inclusões fluidas, geotermobarometria e geoquímica. A área de estudo está localizada a sul da cidade de Pontes e Lacerda (MT), mais ou menos na porção central da Província Aurífera Alto Guaporé que compreende uma série de depósitos de auríferos hospedados ao longo da faixa. Na parte sul da área de estudo, na região do depósito Pau-a-Pique, o arcabouço estrutural é dado por uma série de zonas de cisalhamento transcorrentes, enquanto que a porção norte, região do depósito Ernesto, é caracterizada por dobramentos e cavalgamentos. O padrão estrutural, por sua vez, sugere que a deformação foi contralada principalmente pela ação de zonas de cisalhamento com encurtamento NNE-SSW. Dados de geotermobarometria com base no conteúdo de Si em muscovita, Ti em quartzo e no fracionamento isotópico entre quartzo e magnetita, presente em veios de quartzo e em muscovita xisto ao longo de zonas de cisalhamento, sugerem que as condições metamórficas atingiram a zona de transição entre as fácies xisto verde anfibolito, com temperaturas superiores a 490ºC e pressão acima de 3.2Kbar. Essas condições estão de acordo com feições petrográficas observadas em dioritos e andesitos preservados em núcleos pouco deformados ao longo de zonas de cisalhamento anastomosadas. Também são mais ou menos coerente com presença de migração de bordas de grão (GBM) como principal mecanismo de recristalização de quartzo em zonas de cisalhamento. Dados de geoquímica de rocha total sugerem que fluidos estavam presentes durante a formação de zonas de cisalhamento transcorrente da região do depósito Pau a Pique. A percolação de fluidos associado ao cisalhamento causou importantes modificações químicas e texturais nas rochas e transformou granitóides em mica-xistos pela remobilização de elementos químicos. As condições (PT) encontradas em zonas de cisalhamento contrastam fortemente com as condições encontradas em rochas metassedimentares pouco deformadas, presentes principalmente na porção central e norte da área de estudo. A ausência de biotita em sedimentos pelíticos e a presença de *Bulging* (BLG) como mecanismo de recristalização do quartzo são indicativos de baixa temperatura (abaixo de 400ºC). Ao mesmo tempo o parâmetro *b* da célula unitária de micas brancas (sericita) em rochas metassedimentares indicam baixo conteúdo de fengita nas micas, comum em zonas de metamorfismo de pressão baixa a intermediária. Essas condições são compatíveis com metamorfismo na fácies xisto verde e sugerem que as condições metamórficas não foram uniformes ao longo da área.A percolação de fluidos redutores ricos em CO_2 foram responsáveis pelo evento de mineralização aurífera, como observado nos depósitos Pau-a-Pique e Ernesto (Nível Intermediário). A relação próxima entre clorita, sulfeto e carbonato, que geralmente ocorrem ao longo de fraturas em veios de quartzo-albita foi usado para estimar a temperatura de precipitação do sulfeto através do uso de geotermômetros específicos para clorita. Os resultados sugerem que no depósito Pau-a-Pique, que clorita, carbonato e sulfeto ocorrendo em fraturas de veio de quartzo, se formaram a 325ºC durante a fase de retrometamorfismo. Os aspectos texturais de piritas revelam que se cristalizaram pela alteração de óxidos de Ti e Fe presentes nas encaixantes de veios de quartzo mineralizados do depósito Ernesto e em muscovita xisto do depósito Pau-a-Pique, devido a reação destes fluidos redutores ricos em H_2S. Tal processo foi também responsável pela precipitação do ouro. As características das inclusões fluidas e da alteração hidrotermal dos depósitos estudados são comuns em depósitos do tipo ouro orogênico. Dados de isótopos estáveis (δD e $\delta^{18}O$) indicam fonte metamórfica para fluidos responsáveis pela cristalização dos principais minerais de ganga presente nos depósitos estudados e em outros seis depósitos da área de estudo. Além disso dados de δD em inclusões fluidas são compatíveis com valores encontrados na maioria das províncias de ouro orogênico pelo mundo. Os resultados permitem concluir que os depósitos estudados foram formados tardiamente na evolução metamórfica da Faixa Móvel Aguapeí, após o pico metamórfico da área, a partir de fluidos redutores ricos em CO_2 que transportaram ouro via complexação com H_2S.

Palavras chave: Ouro Orogênico; Depósito Pau-a-Pique; Depósito Ernesto; Província Aurífera Alto Guaporé

ABSTRACT

The Aguapeí belt comprises a narrow and long (~500Km) NNW-SSE zone of deformed and metamorphosed rocks structurally confined between the eastern margin of the Paraguá Craton and the reactivated basement of Rondonian San-Ignacio. Neoproterozoic (~0.92 Ga) reactivation of crustal scale structures has been pointed out as responsible for the tectonic and metamorphic evolution of the belt. It has caused the deformation and metamorphism of previously deposited sedimentary rocks in an aulacogen basin and its Mesoproterozoic basement as well. The metamorphic evolution of Aguapeí belt, and its relationship with gold mineralization occurring on its southernmost portion was investigated in this research through petrography coupled with fluid inclusions studies, geochemistry and geothermobarometry. The studied area is located to the south of Pontes e Lacerda city (MT), more or less on central portion of Alto Guaporé Gold Province (AGGP), which in turn comprises a series of gold deposits hosted along the belt. The structural architecture of the south portion of the studied area (Pau-a-Pique region) is given by a series of strike-slip shear zones, whereas trusting and folding are dominant on central and northern (Ernesto area). The structural pattern suggest that the deformation was controlled by strike-slip shearing due to oblique shortening. Geothermobarometry based on Si content in muscovite, Ti in quartz and oxygen isotopes fractionation between the pair quartz-magnetite occurring in quartz veins and in muscovite schist present in shear zones suggest that the conditions reached the greenschist-amphibolite facies transition with temperature above 490ºC and minimum pressure of 3.2Kbars. These P-T condition are in agreement with the petrographic features found in mafic diorite and andesite preserved in cores of low deformation along anastomosed shear zones in Pau-a-Pique area and are also more or less consistent with the presence GBM quartz recrystallization mechanism occurring within shear zones. Whole rock geochemistry suggest that fluid were present during strike-slip shearing in Pau-a-Pique area. Percolating fluids during shearing has caused major chemical transformation of the mylonite during the prograde conditions. In the extremely modified rocks, metagranitoids were transformed to micas schist due elemental remobilization. The P-T conditions found in shear zones contrast strongly with those recorded in most of low deformed metasedimentary rocks of Aguapeí Group, mainly present on central and northern portion of the studied area. The presence of biotite-absent pelite and bulging recrystallization mechanism of quartz suggest low temperature conditions (below 400ºC). Meanwhile *b*-parameter in white micas of metasedimentary rocks records low content of phengite generally found in low to intermediate pressure regions. These conditions are compatible with greenschist facies metamorphism and suggest that the metamorphic conditions was not uniform through the area. Percolation of reduced aqueous-CO_2 fluids were responsible for gold mineralization as recorded in Pau a Pique and Ernesto (intermediate Level) fluid inclusions. The close relationship between chlorite, sulfide and carbonate occurring along fractures in early formed quartz albite veins in Pau-a-Pique was used to estimate the temperature of sulfide precipitation using chlorite thermometry. The results suggest that chlorite, carbonate and sulfide found in fractures of early formed quartz, has been crystallized at 325ºC at the retrograde path in Pau-a-Pique deposit. The textural aspects of pyrite suggest that previously formed Fe-Ti oxides occurring in the wall rock of mineralized veins in the Ernesto deposit (Intermediate level) and in mica schist in shear zones of the Pau a Pique deposit, were replaced by pyrite due to reaction of Fe-Ti oxides with reducing H_2S rich fluids. Such process was the main mechanism responsible for gold precipitation. The characteristics of fluid inclusions and the hydrothermal alteration of the studied deposits are similar to those found in most of orogenic gold deposit around the world. δD and $\delta^{18}O$ stable isotope geochemistry are in agreement with metamorphic source for the fluid-forming of the main guange phases present in Pau-a-Pique, Ernesto (intermediate level) and other six gold occurrences in the central portion of AGGP. Meanwhile δD signature of fluid inclusions are compatible with those observed in major orogenic gold provinces worldwide. The results allows to conclude that the studied gold deposits were formed latter on metamorphic evolution of Aguapeí belt, during retrograde conditions, and from mixed aqueos-CO_2 fluids that has transported gold by complexation with H_2S.

Key words: Orogenic Gold; Pau-a-Pique deposit; Ernesto deposit; Alto Guaporé Gold Province

Sumário

1. Introdução

Depósitos de ouro podem ser formados em todos os estágios da evolução de um orógeno. Depósitos do tipo pórfiro e epitermal são os exemplos mais comuns de depósitos hidrotermais associado a magmatismo formado durante o processo de espessamento crustal ao longo de margens convergentes. Depósitos de ouro orogênico, ocorrem associados a cinturões metamórficos ao longo de cadeia de montanhas. Nesse tipo de depósito, fluidos mineralizantes circulam por fraturas e descontinuidades na crosta onde precipitam veios de quartzo mineralizados. Dentre as características mais comum desses depósitos estão a presença de fluidos aquosos ricos em CO_2 $\underline{+}$ CH_4 aproximadamente neutro e que transportam ouro através de sua complexação com H_2S (Groves et al., 1998).

Depósitos de ouro orogênico têm sido formado ao longo dos últimos três bilhões de anos, episodicamente desde o Mesoarqueano até final do Pré-cambriano e continuamente durante o Fanerozoico (Goldfarb et al., 2001). Depósitos do início do Pré-cambriano foram protegidos da exumação e erosão por estarem hospedados no centro de regiões cratônicas. Esses, entretanto, são raros entre 1700 e 600 Ma, devido a mudanças para um estilo mais moderno de tectônica de placas, onde a exumação e erosão de cinturões orogênicos mais vulneráveis causou a destruição de depósitos dessa idade (Groves et al., 2005).

A exumação e erosão de cinturões orogênicos formados durante o Mesoproterozóico e final do Neoproterozóico, durante o amalgamento do supercontinente Rodínia, expondo a raiz das cadeias de montanhas, têm sido usado para explicar a falta de depósitos do tipo orogênico associado a esse período, visto que geralmente ocorrem hospedados em zonas da fácies xisto verde, nas porções superiores da crosta. Dessa forma depósitos orogênicos formados entre o Esteniano e o Toniano são raros. Os poucos existentes são reportados na província Greenville na America do Norte, no SW do Craton Amazônico, na America do Sul (Goldfarb et al., 2001) e no Escudo Fenoscadian na Suécia (Alm et al., 2003). Todos esses exemplos têm sido associado a eventos deformacionais associado ao estabelecimento do Supercontinente Rodínia.

Apesar da baixa tonelagem, os exemplares sul-americanos ocorrendo no território brasileiro, mais especificamente na região do Vale do Rio Guaporé (no estado do Mato Grosso), constituem uma importante província aurífera, em termos de produção e importância econômica regional.

Esse depósitos foram descobertos ainda no período colonial, em 1733, por expedições portuguesas chamadas de Monções. Foram importantes para a economia da colônia e fundamentais para a consolidação da expansão do territorial brasileira. Estima-se que entre

1719 e 1822, cerca de 3.2 Moz tenham sido extraídas das minas do território, hoje, mato-grossense que incluíam depósitos na região de Cuiabá e no Vale do Rio Guaporé (Holanda, 2003). Segundo Zanettini et al., (2004), mesmo utilizando práticas rudimentares, que incluía o uso de mão de obra escrava, a produção de ouro das minas do Vale do Guaporé (Fig. 1-1) teriam alcançado seu auge entre 1736 e 1738 onde, juntas, teriam produzido cerca de 48Koz.

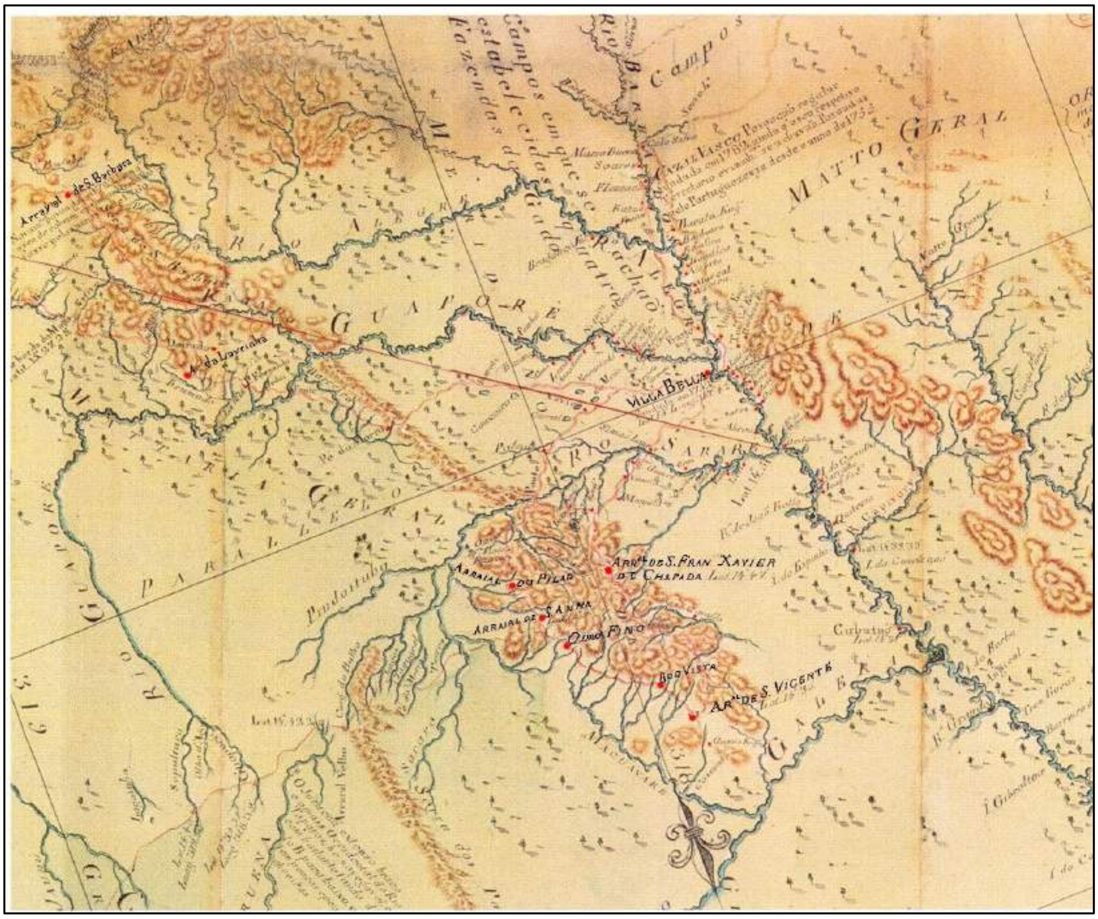

Figura 1-1: Carta geográfica histórica do Vale do Rio Guaporé. O ano de publicação é desconhecido, no entanto, de acordo com Zanettini et al., (2004) a fonte citada é de 1751. Importante notar que o norte no está rotacionado e é indicado como uma lança na porção inferior da figura. Os pontos vermelhos com nomes são núcleos urbanos formados no entorno das minas (arraiais de mineração).

O Vale do Guaporé voltou a ser foco da exploração de ouro em meados da década de 70, após mais de 150 anos desde sua descoberta, com intensa atividade garimpeira na região entre as cidades de Pontes e Lacerda e Nova Lacerda. Mas foi só a partir da década de 80, que a lavra de ouro na região começou a ter importância para a economia formal, com a implantação de instalações da Mineração Santa Elina. Inicialmente focada na lavra de minério em placer, a mineração Santa Elina passou a lavrar minério primário hospedado em metassedimentos do Grupo Aguapeí, na Mina São Vicente (município de Nova Lacerda), a partir da metade da década de 80. A atividade de lavra na Mina São Vicente pela Mineração Santa Elina foi encerrada em 1997, devido à queda nos preço do metal, que inviabilizou a lavra em função dos altos custos.

Em 2002 a região voltou a receber investimentos e assim iniciou-se novo ciclo de exploração. Os investimentos ocorridos nos últimos dez anos resultaram na reativação da Mina de São Vicente, que voltou a lavrar minério primário entre 2009 e 2014, além da instalação da Mina São Francisco, que iniciou as atividades em meados de 2005, e o início da implantação de mais duas minas nos municípios de Pontes e Lacerda e Porto Esperidião, que integradas a uma só planta são denominadas Projeto Ernesto/Pau-a-Pique e apresentam reservas de cerca de 20 toneladas de ouro.

Atualmente são conhecidas mais de 30 ocorrências de ouro na região do Vale do Rio Guaporé. Essas ocorrências, em conjunto com os depósitos e minas, têm sido agrupadas sob o nome de Província Aurífera Alto Guaporé (Fernades et al., 2005a). Se estendem por cerca de 200Km desde o limite com o território boliviano, ao sul, até a parte norte da Serra de São Vicente (Fig. 1.2). A maioria dos depósitos ocorrem encaixados em rochas metassedimentares deformadas (Grupo Aguapeí), ou no contato entre as rochas metassedimentares e seu embasamento.

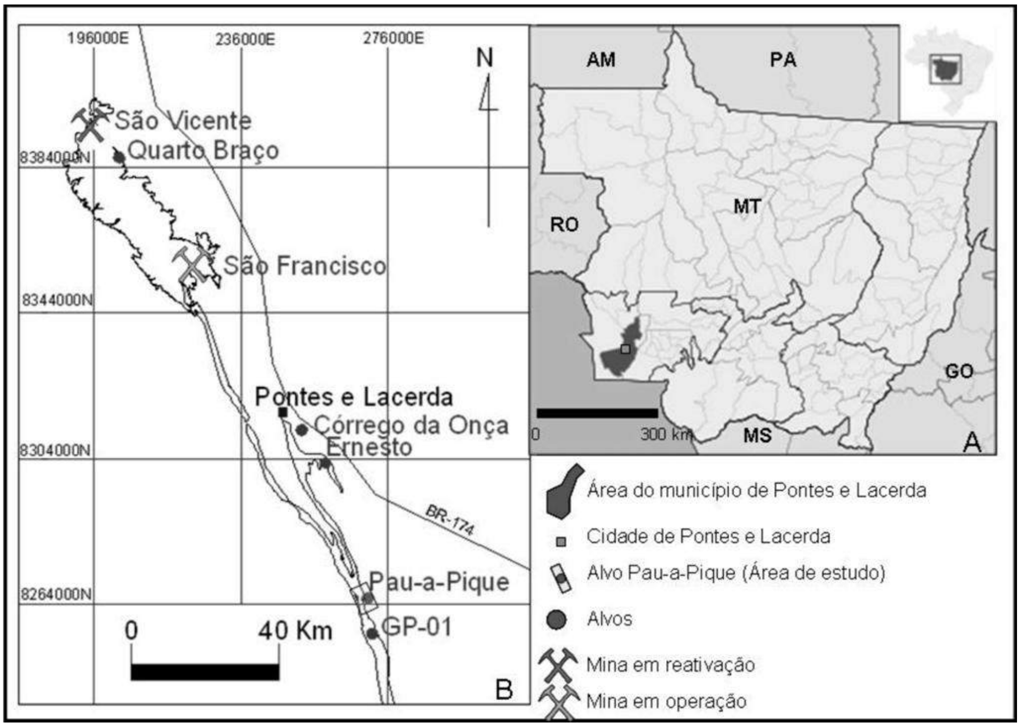

Figura 1.2: Localização geográfica da Província Aurífera Alto Guaporé mostrando alguns dos mais importantes depósitos da área.

2. Objetivo

O metamorfismo regional têm sido aceito como uma das principais fontes de fluido na formação de depósitos do tipo orogênico. Terrenos sedimentares e vulcanossedimentares, colocados em níveis profundos da crosta durante a subducção em margens convergentes, têm sido sugerido por alguns autores como principal fonte de fluido mineralizantes para depósitos desse tipo. Outros defendem uma fonte metamórfica ainda mais profunda, tal como crosta oceânica subductada ou resíduos de sua fusão parcial (Groves et al., 2003). Os principais problemas relacionados à teoria de depósitos de ouro do tipo orogênico incluem: (1) a determinação precisa da idade e do ambiente tectônico em muitas províncias; (2) a fonte de fluidos e metais; (3) a precisa arquitetura do sistema hidrotermal; (4) os mecanismos deposicionais (Groves et al., 2003).

Na área de estudo, os depósitos associados a Província Aurífera Alto Guaporé, estão hospedados ao longo de uma longa e estreita faixa (~500Km) de dobramentos de baixo grau metamórfico de idade Neoproterozóica (~0.92 Ga). O evento tectônico que gerou a Faixa Móvel Aguapeí têm sido interpretado como produto da reativação de estruturas crustais ao longo de uma zona de sutura entre dois blocos cratônicos aglutinados durante o Mezoproterozóico (Rizzoto et al., 2013; Rizzoto et al., 2014). O evento deformacional Neoproterozóico afetou o embasamento Mesoproterozóico bem como rochas sedimentares depositadas em uma bacia aulacógeno (Grupo Aguapeí) entre o final do Mesoproterozóico e início o Neoproterozóico (Teixeira et al., 2010). Essa linha de interpretação sugere que a evolução tectônica da faixa móvel em que os depósitos da área de estudo estão hospedados, se deu pela reativação de estruturas ao longo de uma zona de fraqueza na crosta. Não se trata, portanto, de um típico cinturão metamórfico formado em cadeias de montanhas ao longo de margens continentais ativas.

Trabalhos publicados sobre as características e composição de fluidos e de alguns dos depósitos da porção central da área de estudo reportam a presença de fluidos aquo-carbônicos e sugerem a desvolatilização de rochas vulcanossedimentares, como fonte dos fluidos mineralizantes (Fernandes et al., 2005c; Pulz et al., 2003). As características das inclusões fluidas e da alteração hidrotermal reportadas, se assemelham aquelas tipicamente encontradas em depósitos do tipo orogênico.

A presença de depósitos com características similares a de depósitos orogênicos hospedados ao longo de uma faixa de dobramentos formada pela reativação de estruturas crustais (como têm sido interpretado a evolução da Faixa Móvel Aguapeí), têm implicações diretas para teoria envolvendo a formação de depósitos orogênico, em termos de origem dos fluidos e fonte dos metais.

No entanto, antes de qualquer interpretação sobre a fonte de fluidos e metais, é importante que as características desses depósitos e composição dos fluidos que os formaram esteja bem estabelecida. Da mesma forma, o estudo das condições metamórficas da área e sua relação com o evento de mineralização, de maneira a se estabelecer a relação entre os eventos.

Apesar de longa história de exploração e sua importância econômica, os depósitos da Província Aurífera Alto Guaporé foram pouco estudados. Como consequência, a exata composição e origem dos fluidos mineralizantes ainda permanece mal entendida. Da mesma forma as condições metamórficas ao longo da Faixa Móvel Aguapeí têm sido negligenciadas pela maioria dos trabalhos científicos executados na área.

Nesse sentido essa pesquisa têm como objetivo investigar a formação de dois depósitos da porção central da Província Aurífera Alto Guaporé (depósito Pau-a-Pique e depósito Ernesto - Nível intermediário) e a relação com o metamorfismo de suas encaixantes. A pesquisa foca em dois pontos principais, o primeiro diz respeito ao evento metamórfico, investigado através de petrografia e geotermobarometria. O segundo foca na metalogênese dos depósitos através do estudo de inclusões fluidas, da alteração hidrotermal e de isótopos estáveis a fim de se estabelecer um modelo de evolução entre o metamórfismo e o evento de mineralização da área.

Os capítulos a seguir estão estruturados de forma a apresentar primeiramente um panorama do estado da arte do conhecimento da área de estudo, seguido pelos métodos adotados nessa pesquisa, com ênfase nos parâmetros analíticos utilizados durante as análises, e por fim a apresentação dos resultados, que se inicia com a descrição geológica das unidades que ocorrem na área de estudo, seguido pelo estudo da geologia estrutural e do metamorfismo, e por fim o estudo metalogenético dos depósitos.

Importante destacar que a maioria dos capítulos a seguir estão escritos em língua inglesa que representarão artigos a serem publicados em periódicos científicos.

3. State of Art

3.1. The Southwestern of Amazon Craton

The studied area is located in the Southwestern margin of the Amazon Craton (Fig. 3.1-1), one of the largest cratonic blocks in the world. The Amazon Craton has been matter of recent attention by research geologist but it remained very poorly understood until about two decades ago when the first researches regarding its tectonic architecture and geochronology were published. Since then some models to the architecture and evolution of Amazon Craton has been proposed nevertheless the evolution of such a large area seems to be far from complete understanding and it is still matter of debate within the academic community. The late advance on the knowledge of the Amazon Craton is easily explained by the intrinsic difficulties related to the area such as strongly weathered rocks, poor accessibility and the dense Amazon rain forest that cover great part of its area.

Until 1974 the Amazon Craton was interpreted as composed of two shields, the Guiana Shield on its northern part and the Guaporé Shield on its southern part, separated by Phanerozoic sediments of Amazon Basin (Santos et al., 2008). The pioneer work of Amaral (1974) demonstrated that the major internal limits of Amazon Craton is NNW-SSE instead of E-W as previously supposed, and the western part is younger than the central and eastern part. This model served asbasis for followingresearches that led to delineate the architecture of Amazon Craton and propose models for its evolution based on isotope data (e.g. Cordani et al., 1979; Teixeira et al., 1989; Tassinari et al., 1996; Tassinari and Macambira, 1999;Santos et al., 2000).The one that seems to be the most widely accepted model divides the Amazon Craton into six geochronological provinces based on Sr, Pb and Nd isotopic compositions of igneous and orthogneissic rocks (Tassinari and Macambira, 1999). According to the authors, Archean rocks in the Mideast part of Amazon Craton evolved due to amalgamation of independent micro-continents by paleoproterozoic mobile belts between 2,2 and 1,95 Ga. It was followed by addition of juvenile magmas to the crust between 1,95 and 1.4 Ga and reworking of older continental crust in the younger provinces cropping in the western part of Amazon Craton.A different model based on U/Pb and Sm/Nd isotopes data was proposed by Santos et al. (2000). The model separated the Amazon Craton intoeight major Precambrian tectonic provinces comprising Archean and Paleoproteroic rocks to the east, volcano plutonic belt of Paleoproterozoic age to the Mideast and magmatic rocks formed by recycling of older orogenic belts in the central and western part.In most of proposed models the authors agreed that the youngest stage of evolution of Amazon Craton is recorded in its southwestern portion.

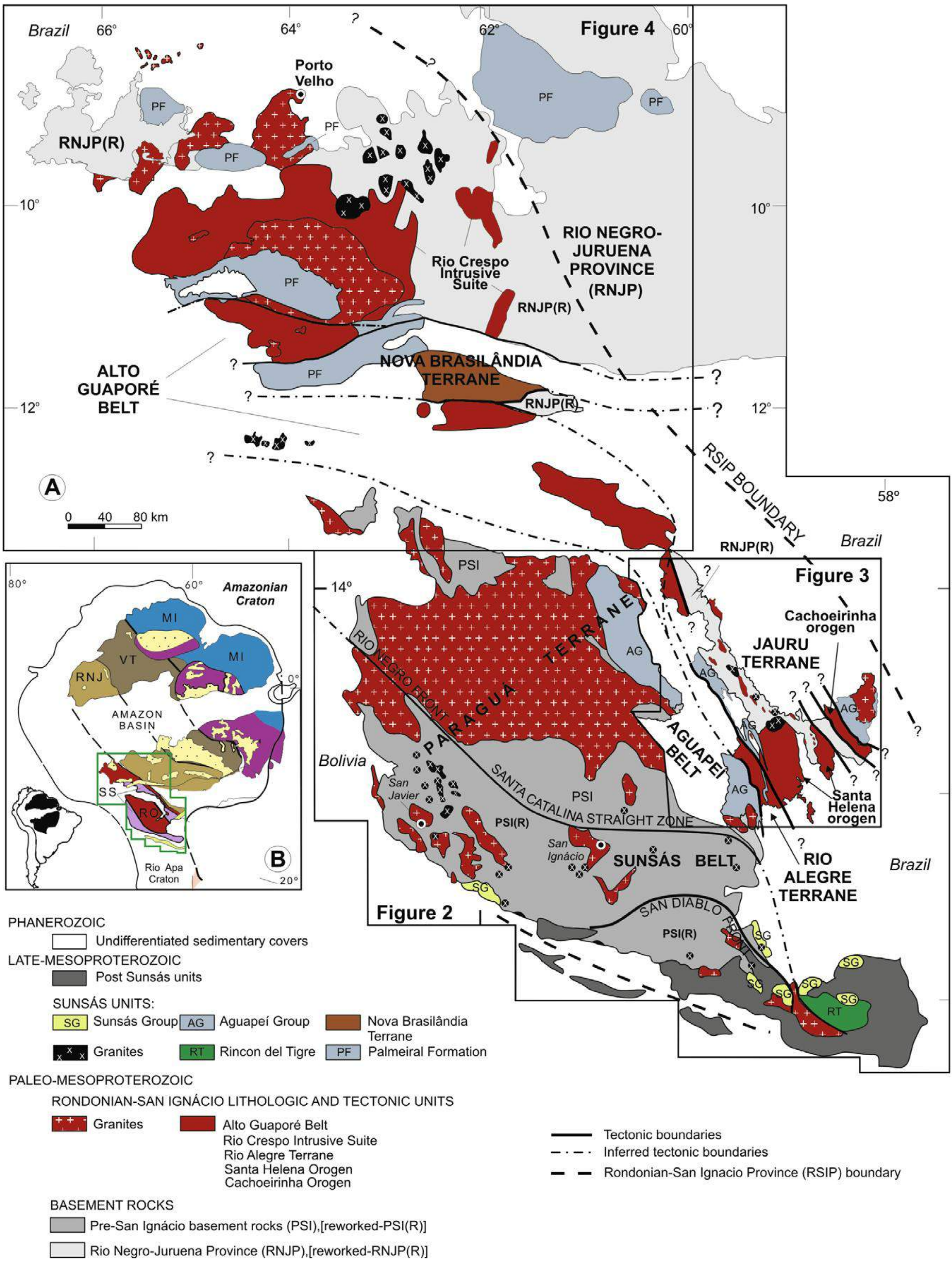

Figure 3.1-1: (A) Simplified map of the SW Amazon Craton showing the approximate boundaries of the main provinces, major orogens, terranes and belts, tectonic elements, and lithologic units. (B) Major geochronological provinces of the Amazon Craton. MI, Maroni- Itacaiunas Province; VT, Venturi-Tapajós Province; RNJ, Rio Negro-Juruena Province; RO, Rondonian-San Ignacio Province; SS, Sunsá-Aguapeí Province. (Extracted from Bettencourt et al., 2010).

According to Tassinari and Macambira (1999), the SW portion of Amazon Craton is represent by four sub parallel Proterozoic Provinces (Fig. 2.1-1): Ventuari-Tapajós (2.00–1.80 Ga), Rio Negro-Juruena (1.78–1.55 Ga), Rondonian-San Ignacio (1.50–1.30 Ga), and Sunsás-Aguapeí (1.25–1.00 Ga).

Most plate reconstruction models for the late Mesoproterozoic place the southwestern margin of Amazon Craton (AC) in proximity to some part of east Laurentia during Rodínia assembly (Tohver et al., 2004; Cordani et al., 2009). Based on geological arguments two landmark papers (Dalziel, 1991 and Hoffman, 1991) proposed the matching of Laurentia and Amazonia during Rodínia evolution. In the first one, the author proposed a northerly position for the Amazonia alongside Newfoundland and Labrador in North America based on the matching of Iapetan rift history of Laurentia with Argentine Pre-cordilleran margin meanwhile Hoffman (1991) proposed the matching of SW of Amazon Craton to the Central province of Ontario and New York, based on rifting of Neoproterozoic on both sides and in peleomagnetic data for Laurentia (Cordani et al., 2009).The Hofman's model has served as basis to latter worksregarding the evolution of Amazon Craton such as Sadowski and Bettencourt (1996) and Bettencourt el al. (1996).

Recent paleogeographic reconstructions based on paleomagnetic data from AmazoniaCratonsuggest a dynamic scenario in which Amazoniacollided with the (present day) south of Laurentia at ca 1.2 Ga (Tohver et al., 2002) and moved northeastward direction along the (present day) southeast coast of Laurentia (D'Agrella-Filho et al., 2008; Elming et al., 2009) (Fig 2.1-3). It has involved a sinistral strike-slip shear in the Amazon Craton in the time interval 1.20-1.10 Gameanwhile clockwise rotation by approximately180^{o}reaching afinal configuration where the northeastern margin of Amazon was facing to the southern margin of Baltica at the end of Grevillian Orogeny (~980Ma) (Elming et al., 2009).

Li et al., 2008 in a review about assembly and break-up of Rodíniaagues in favor of Hofman's rather than the collision of Amazon in the south marginof Laurentia as proposed by Tohver et al. (2002). They argued that such paleomagnetic reconstructions utilizing a single pole from each continent rather than matching relatively long segments of apparent polar wander path have inherent longitudinal uncertainties. Howeverthe contemporary and later works of D'Agrella-Filho et al. (2008) and Elming et al. (2009) has reinforcedthe Tohver's hypothesis.

A recent complimentary configuration was proposed by Teixeira et al. (2014). According to the authors the SW of Amazonia were juxtaposed with the eastern of Laurentia at ca. 1110 Ma and even 1170-1200 Ma prior to the main Grenville (and Sunsas) collision. Their hypothesis is based in similar U-Pb (ID-TIMS) baddeleyite ages (1110 - 1112 Ma) for mafic sills intruded in Aguapeí sediments and layered sill cropping in the southeast of Sunsas belt (Rincon del Tigre complex) which suggest the existence of a Large Igneous Province (LIP) in Amazon Craton that matches with the major Keweenawan LIP of Central Laurentia.

3.2. Aguapeí - Sunsás Province

Evidences of heterogeneous collisional events with Laurentia can be found in the youngest geochronological province of Amazon Craton, the Sunsas-Aguapeí Province (1.20 - 0.95 Ga) (Tohver et al., 2006; Teixeira et al., 2010). Its evolution occurred after a long period of quiescence and erosion of older and cratonized terranes (>1.3 Ga) and deposition of sediments in a passive margin stage (Sunsas and Visbosi groups), meanwhile almost contemporary intra-plate tectonics has caused the reactivation of major shear zones that led formation of a proto-oceanic basin (Nova Brasilândia Group) and a aborted rift system basin (Aguapeí and Huanchaca groups) followed by anorogenic magmatism and later deformation and metamorphism of the sedimentary sequences forming three folded and thrust belts: Sunsas, Aguapeí and Nova Brasilândia belts (Teixeira et al., 2010). This evolutionary model take in account the presence of a cratonic block between the Laurentia margin and Amazon Craton (Paraguá Terrane- see Fig. 3.1-1) suggesting a allochthonous evolution for the Sunsas Belt in Bolivian territory (Litherland et al., 1986, 1989; Boger et al., 2005; Tohver et al., 2006).Another line of thought do not recognize the existence of Paraguá Craton and agues in fovour of an autochthonous evolution for Sunsas Province being it part of an accretionary orogen evolved from 1.45 to 1.00 Ga (Santos et al., 2000; Santos et al., 2008).

Based on U/Pb zircon geochronological data with airborne geophysical survey and field relationship Rizzoto et al. (2014) suggests that the Nova Brasilândia, Sunsas and Aguapeí belts represents a unique geotectonic unit (Western Amazon belt) formed through the reactivation of Guaporé paleosuture Fig. 3.1- (Rizzoto et al., 2013) formed by the docking of Paraguá Craton and the proto-Amazon Craton during the middle-Mesoproterozoic time (1470-1330 Ma). According to the authors the tectonic evolution of Nova Brasilândia, Aguapeí and Sunsás groups may be related with the final break-up of Columbia supercontinent occurred at about 1.3-1.2 Ga marked by a major episode of plate wide extension and rifting.

The Sunsas belt occurs mainly in the eastern of Bolivian territory close to the Brazil-Bolivia boundary. Its evolution starts by deposition of Sunsas and Visbosi Group (alluvial to deltaic sediments) in a passive margin environment (Litherland and Bloomfield, 1981). The orogenic phase was active from 1.08 to 1.05 Ga and is marked by extensive mylonitic shear zones or "tectonic fronts" with sinistral offsets resulted from the direct collision of the belt (under ductile to brittle-ductile conditions) against the Paraguá Microcontinent (Teixeira et al., 2010). The crustal thickening was responsible by regional low grade metamorphism over sedimentary cover of Sunsas and Visbosi groups (Litherland and Bloomfield, 1981) and allowed the emplacement of syn- to late tectonic granites (Litherland et al., 1989).

The Brazilian segments of Sunsas-Aguapeí Province are given by the Aguapeí Mobile Belt (Litherland and Power, 1989; Litherland and Bloomfield, 1981; Fernandes et al., 2005a) in Mato Grosso state and Nova Brasilândia Belt (Tohver et al. 2004a; Rizzoto, 1999; Rizzoto et al., 2014) mainly in Rondonia state. The Nova Brasilândia belt comprises a ~200 km E-W mobile belt located mainly on the Brazilian state of Rondonia. It is composed by deep-water metasedimentary rocks (turbiditic greywackes and marls) and basic metaigneous rocks (Nova Brasilândia Group) and two granite intrusive suites (Tohver et al., 2004; Rizzoto 1999; Teixeira et al., 2010). The evolution of Nova Brasilândia Belt starts with the deposition of sediments in an intra-continental rift that evolves to a proto-oceanic opening (Teixeira et al., 2010; Tohver et al., 2004a) followed by medium to high grade metamorphism caused by crustal thickening in a transpressional zone and the later granite emplacement (Tohver et al., 2004a). The maximum sedimentation age is estimated between 1215 ± 20 Ma (Rizzoto et al., 2001) and 1231 ± 14 Ma (Santos et al., 2000). The metamorphic peak has occurred around 1090 Ma (U/Pb in monazite) and 1060Ma (U/Pb in titanite) and the following cooling between 970 Ma (Ar/Ar in Hornblende) and 910 Ma (Ar/Ar in biotite) (Tohver et al., 2004a).

3.2.1. Evolution of Aguapeí belt

The evolution of Aguapeí belt (Fig. 3.2-1) starts with an extensive stage that led deposition of siliciclastic sediments of Aguapeí group in an aulacogen basin (Saes and Leite, 1993; Saes, 1999;). Reactivation of crustal discontinuities due to intraplate tectonics has been used to explain the presence of a rift basin in an intracontinental environment. Some authors (e.g. Rizzoto etal., 2014; Rizzoto et al., 2013) has argued in favor of existence of a paleosuture (Guaporé paleosututre zone-Fig. 3.2-1) between Paraguá and Amazonia cratons acting as weakness zone in the Amazonian crust during both, extensional (supposedly related to break-up of Columbia) and orogenetic episodes (associated with Rodínia assembly and the collision of Amazonia and Laurentia).

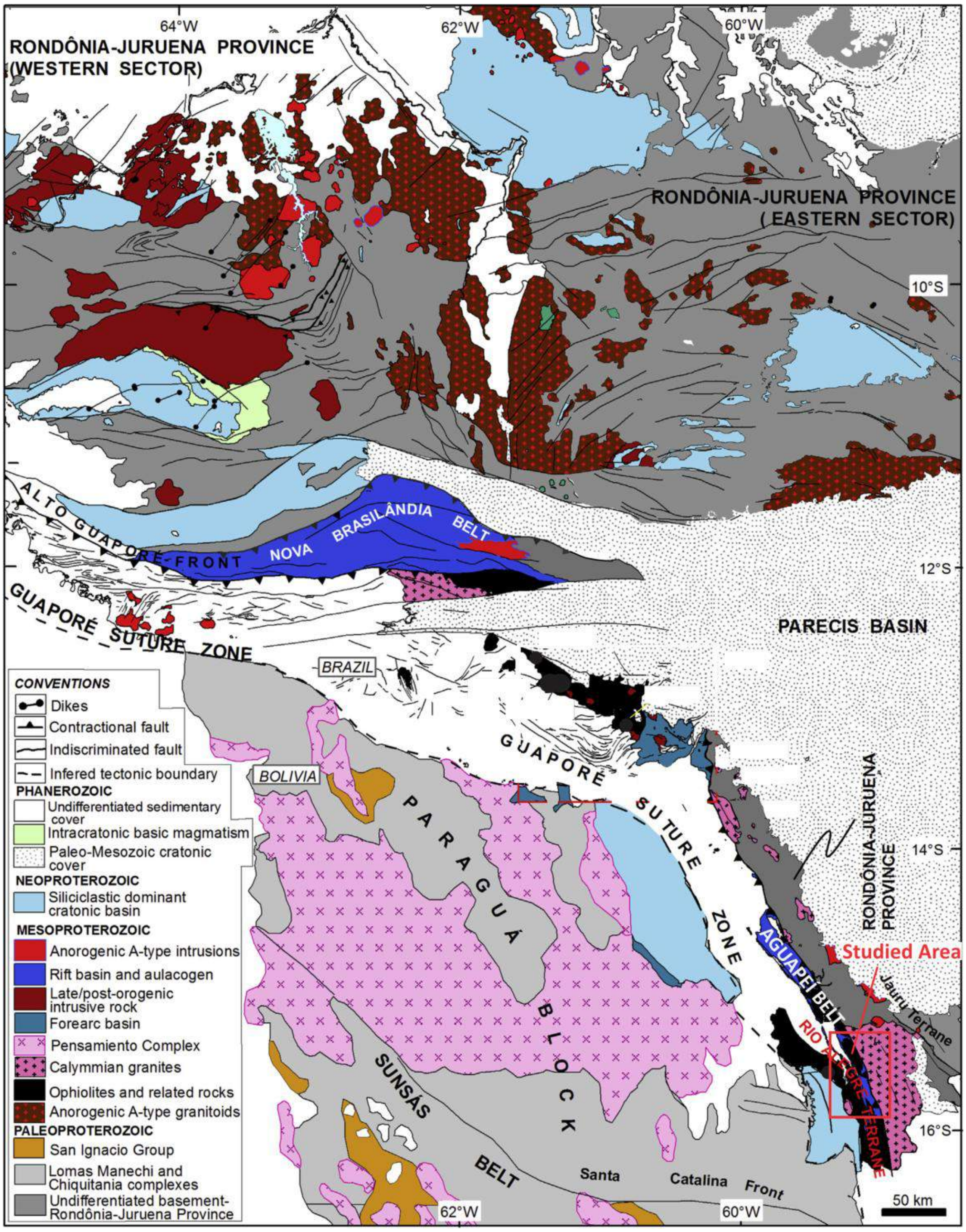

Figure 3.2-1: Geological map of the southwestern Amazon Craton showing the approximate boundaries of the main terranes and belts, and the suture zone proposed by Rizzoto et al., 2013. (Extracted from Rizzotto et al., 2013).

The Aguapeí group comprises non-metamorphosed to low grade siliciclastic sedimentary rocks (Saes and Leite, 1993; Souza and Hildred, 1980; Menezes et al., 1993) and is given by basal sandstone and conglomerate (initial transgressive phase) followed by intermediate psammites (marine progradation phase) and upper fluvial sandstones (ultimate marine regression phase) stratigraphically divided in three formation from top to the base whilst overlay the basement rocks with a well-marked unconformity: the Morro Cristalino, Vale da Promissão and Fortuna formations (Teixeira et al., 2010; Saes & Leite, 1993; Geraldes et al., 1997; Tohver at al., 2004). The sedimentation of Aguapeí group is well constrained and has been estimated between 1167 ± 27 Ma (maximum deposition age according to Santos et al., 2005) or 1265 Ma (the maximum deposition age according to Geraldes et al., 2014) and 1149 ± 7 (the minimum deposition age, estimated from diagenetic xenotime in sedimentary zircon from Fortuna Formation by D'Agrella-Filho et al., 2008).

The rifting episode was followed by an event of tholeitic magmatism represented by sills and dikes of basalt and diabase intrusive to Huanchaca sedimentary rocks. The best known example is the Huanchaca dolerite suite (Litherland and Power, 1986). It comprises dikes and sills of quartz dolerite (tholeitic) composition intruded to non-deformed sediments of Huanchaca group, a flat lying sequence of metassedimentary rocks (occurring mainly in Bolivia territory) correlated with Aguapeí Group (e.g., Litherland and Power, 1989; Teixeira et al., 2010) that was preserved from Sunsás-Aguapeí deformation by being settled over the tectonic stable Paraguá Craton (Litherland and Power, 1989). Other similar occurrence of tholeitic rocks intrusive into Aguapeí sediments are reported near to Rio Branco town where is recordedthe occurrence of basaltic sills and dikes intruded intoflat lying Aguapeí sediments settled over rocks of Jauru Terrane (Elming et al., 2009). As mentioned above the Huanchaca dolerite suitehas closecrystallization agetolayered intrusion of Rincon del Tigre complex occurring in Sunsas belt (in Bolivia territory)andaccording to Teixeira et al., 2014, it shows evidence for the existence of a Large Igneous Province at ca 1110 Ma.

The metamorphic and deformational event that led formation ofthe Aguapeí fold and thrust belt (Aguapeí belt) has been regarded as the last branch of Sunsas Orogeny and was responsible for deformation and low grade metamorphism of the sediments and its older basement (Litherland et al., 1986; Teixeira et al., 2010; Geraldes et al., 2001). The Aguapeí belt is a narrow and long (~500 km) NNW-SSE zone of folded and deformed rocks structurally confined between the eastern margin of the Paraguá Craton and the reactivated basement of Rondonian-San Ignacio Province (Teixeira et al., 2010; Leite and Saes 2000). Some authors (e.g. Tohver et al., 2004) have explained the tectonic and metamorphic evolution of Aguapeí belt as a minor episode of low grade intracratonic deformation occurred towards the end of Greenville interval. Deformation ages have been reported in an interval between 964 ± 40 and

908 ± 0.9 Ma, most of all based on K/Ar and Ar/Ar in micas (Geraldes et al., 1997; Fernades et al., 2006). An event of acid magmatism is associatedwith the evolution of Aguapeí belt. It is by given by series of elliptical to circular plutons of isotropic peraluminous syn- to post-kinematic granites named Guapé intrusive suite (Ruiz et al., 2007; Ruiz 2005). Zircon U/Pb and Rb/Sr age for these rocks yielded 914 ± 15 Ma and 950 ± 40 Ma respectively (Ruiz, 2005; Menezes et al., 1993).

3.3. Pré- Aguapeí Sunsas units

The pre-Sunsas Aguapeí rocks in the southwestern margin of Amazon Craton are given by rocks of Rondonian-San-Ignacio and Rio Negro-Juruena provinces. The rocks of Rondonian-San Ignacio province has been interpreted as a composite orogens created through successive accretion of arcs, ocean basin closure and final oblique microcontinent-continent collision between 1.56 and 1.30 Ga (Bettencourt et al., 2010). The Rondonian - San Ignacio province is divided into three terranes (from west to east): (1) Paraguá terrane, (2) Rio Alegre Terrane and (3) Jauru terrane (e.g. Bettencourt et al., 2010):

3.3.1 Paraguá Terrane

Introduced by Litherland et al., (1986) the term Paraguá Craton represents a tectonically stable region in eastern Bolivia preserved from deformational events occurred during Meso- to Neoproterozoic relative to the evolution of Sunsás -Aguapeí Province (Bettencourt el al., 2010). Boger et al. (2005) proposed that the Paraguá Craton must represent a geologically distinct micro-continent that was accreted to the southern margin of Amazon Craton during the Sunsas Orogeny. Some authors suggest that the accretion of Paraguá Craton to the margin of Amazon Craton has occurred around 1350 Myr ago (e.g. Rizzoto et al., 2014; Bettencourt et al., 2010) being it positioned between Amazonia and Laurentia during the Sunsas Orogeny (see Tohver et al., 2006).

According to Bettencourt et al., 2010 the Paraguá terrane is a composite terrane that comprises Paleoproterozoic basement rocks older than 1640 Myr composed by gneiss, schist and granulites (Chiquitania Gneissic Complex, San Ignacio schist Group, Lomas Manechis Granulitic Complex) and Mesoproterozoic granitoids (Pensamiento Granitoid Complex) amalgamated to the proto-Amazon Craton during the Rondonian-San Ignacio Orogeny. The Pensamiento granitoid complex was formed during the San Ignacio Orogeny and forms much of Paraguá terrane. It is divided into syn- to late kinematic and (1373-1347 Myr) and late- to post-kinematic (1340 Myr) magmatism.

3.3.2. Rio Alegre Terrane

The Rio Alegre Terrane is a relatively narrow belt of Mesoproterozoic volcanosedimentary rocks occurring on the eastern margin of the Paraguá Craton. It was first interpreted as a suture zone by Saes and Fragoso Cesar (1996) being latter classified as Rio Alegre terrane (Saes 1999) and Rio Alegre Orogen (Bettencourt et al., 2010; Matos et al., 2004). The rocks of the Rio Alegre terrane comprises mafic and ultramafic volcanic rocks, chemical and clastic sedimentary rocks, metamorphosed at greenschist to low-amphibolite facies, subdivided into three sub-unit as follows: a basal basic to ultrabasic unit (Minouro Formation); an intermediate and acid pyroclastic unit (Santa Isabel Formation); and a clastic, chemical and volcanoclastic unit (São Fabiano Formation) (Bettencourt et al., 2010; Matos et al., 2004). According to Matos et al., 2004 the volcanic and subvolcanic basic and ultra basic rocks were derived from an oceanic floor formed in a back-arc basin or in a middle ocean ridge environment meanwhile the basic to intermediate rocks were generated in an island arc setting at 1.51-1.50 Ga followed by later intrusions of by basic and felsic rocks (1.48 - 1.46 Ga) in a magmatic arc setting.

Based on U-Pb zircon geochronology, Sr-Nd geochemistry and aeromagnetic data, the latest evolutionary model proposed by Rizzoto el al. (2013) considerthe Rio Alegre terrane as part of the Guaporé suture zone. According to the authors the Guaporé suture zone is an approximately 1000 km long paleosuture structure extending from Southwestern of Mato Grosso to Rondonia states and was formed by the docking of Paraguá Craton to Amazonia at ca 1350 Myr (Rizzoto et al., 2013). According to Rizzoto et al. (2013) the evidence for a suture hypothesis is given by the presence of relicts of oceanic crust marked by presence of mafic-ultramafic ophiolite (Trincheira Complex), minor tonalites (such as Rio Galera, São Felipe and Colorado complexes) and the volcano-sedimentary sequences of Rio Alegre terrane.

3.3.3. Jauru Terrane

The Jauru terranehas been classified as composite terrane formed by basement rocksof Paleoproterozoic Age (Rio Negro-Juruena province)and two Mesoproterozoic Orogens (Bettencourt et al., 2010). The Paleoproterozoic basement (1.78-1.72 Ga) has been divided into four lithoestratigraphic units: (1) the Alto Jauru Group, composed by gneisses, migmatites and volcano-sedimentary sequences interpreted as successive arcs formed in intra-oceanic environment (Pinho et al., 1997; Geraldes et al., 2001) evolved during the evolution of continental margin of Rio Negro-Juruena Province (Bettencourt et al., 2010); (2) the Figueira Branca Intrusive Suite, a group of intrusive metabasic to metaultrabasic plutons intruded in the Alto Jauru group that, together with the Alto Jauru group, seems to represent relicts of a Paleoproterozoic oceanic crust (Ruiz, 2005); (3) the Alto Guaporé metamorphic suíte, composed by intrusive bodies of granodiorite to tonalite orthogneiss occurring in the supracrustal volcano-sedimentary sequences suggesting a large mantle derived magmas with crustal contribution (Pinho et al., 1997; Geraldes et al., 2001); and (4) the Cabaçal tonalite, a metamorphosed tonalite botholith intruded in the volcano-sedimentary sequences of Alto Jauru (Bettencourt et al., 2010).

The Mesoproterozoic history of Jauru terrane comprises intrusive magmatic suites developed duringAndean-type accretionary orogeny (Santa Helena and Cahoeirinha orogeny) (Bettencourt et al., 2010). The term Santa Helena Orogen and Cachoeirinha orogen was coined by Tassinari et al. (2000) and according to the authors they adopted the term orogen to designate a period of metamorphic episodes accompanied by deformation, partial melting and syn-tectonic granitic intrusions rather than in the wider usage of the term a complete orogenic cycle.

According to Bettencourt et al. (2010) the oldestCachoeirinha orogeny is recorded bypresence of tonalite, granodiorite, granite and gneissic migmatite formed during magmatic and metamorphic events occurred between 1.56 and 1.52 Ga. These rocks have evolved through two magmatic stages, a syn- kinematic stage (Santa Cruz intrusive suite) and a late-kinematic stage (Alvorada intrusive suite) (Ruiz, 2005; Araujo, 2008).

The Santa Helena orogen comprises rocks formed in a continental magmatic arc (Bettencourt et al., 2010) and encompasses the syn-kinematic Santa Helena and Água Clara intrusive suites (1.48-1.42 Ga) and Pindaiatuba intrusive suite (1.46-4.42 Ga) as well as the post kinematic anorogenic rapakivi granites and the related mafic rocks included in the Rio Branco intrusive suite (1.42 Ga) (Bettencourt et al., 2010; Geraldes et al., 2001; Ruiz, 2005; Araujo, 2008). The Água Clara intrusive suite is represented by a botholith of medium to coarse grained granodiorite and minor monzogranite of sub-alkaline affinity (Ruiz, 2005), formed at 1.48 Ga (Geraldes et al., 2001). The Pindaiatuba intrusive suite comprises several fault controlled tonalite to sienogranite batholiths intruded in the meta-sedimentary sequence of Alto Jauru Group (Ruiz, 2005).

It was formed between 1.46 and 1.42 Ga from magmas with large juvenile signature (Bettencourt et al., 2010). The rocks of Rio Branco intrusive suite are composed by basic (diabase and gabbro) and acid (riolite, porphyry granite, andesite and dacite) rocks intruded in the volcanic-plutonic rocks of the Alto Jauru Terrane (Leite et al., 1985; Ruiz 2005) and have been considered as part of a bimodal rapakivi igneous association by (Geraldes et al., 2004; 1999; Bettencourt et al., 2010).

The Santa Helena intrusive suite is the most expressive magmatic suite related to Santa Helena Orogeny. It has taken place around 1.46 to 1.42 Ga and is exposed as a large and enlongate batholith extending for a minimum of 35 km in east-west direction and over 75 km in a northerly direction (Geraldes et al., 2001; Saes et al., 1984). The rocks encompass four strongly foliated petrographic facies given mainly by sienogranite and monzogranite in composition (Ruiz, 2005). It has been classified mainly as I-type, peraluminous to metaluminous and sub-alkaline to calc-alkaline magmatism with large juvenile contribution (Geraldes et al., 2001; Bettencourt et al., 2010).

Finally the information about the Mesoproterozoic evolution of SW of Amazon Craton as well as the Sunsas Province is summarized in a figure (Appendix Ix) and takes into account the most recent tectonic interpretations for the SW of Amazon Craton.

3.4 Structural geology of Aguapeí belt

Very few studies were conducted on tectonic and structural geology of Aguapeí belt. The wider overview about the subject was, for example published as conference paper (Ruiz et al., 2007). According to the authors the Aguapeí belt show evidences of two tectonic episodes, a compressive episode responsible for folding, thrusting and related metamorphism and an extensional episode characterized by ductile shear zones with normal kinematic. The compressive episode evolved through three deformational phases: the first deformational phase (F_1) is given by regional scale (gentle to closed) folds with subhorizontal hinge line (~N140/10 or ~N320/10) (eg. Cagado anticline and caldeirão syncline). The axial planar foliation is given by a schistosity or a slaty cleavage ~N20W/80SW; the second phase (F_2) is given by asymmetrical folds of centimetric size. The axial planar foliation is characterized by crenulation clevage in metasiltstones and metarudites plunging at ~30º SW and fold axis dipping at 5º - 10º NNW; in the third phase (F_3) were formed open to gentle folds (D_3) of metric dimension. It has vertical axial plane (S_3) dipping at ~80º to SE or NW. According to the authors most magamatic rocks associated with the evolution of Aguapeí belt (Guapé intrusive suite) show evidence for post to late emplacement except for Banhado batholith, clearly syn-kinematic.

Fernandes et al. (2005a). divided the Aguapeí Belt into four tectonic domains. According to the authors, the following domains occurs from SE to NW: (1) a transcurrent domain (TD) with predominance of strike slip deformation concentrated along shear zones (Corredor shear zone); (2) low angle contractional tectonic domain (LACD) characterized by a series of sinform and antiform formed by thrusting; (3) symmetric folding domain given by closed to open symmetric folds formed by flexural slip and characterized by hinge line plunging to NW; (4) brittle tilting domain characterized joint families best recorded at the non-folded sediments of Santa Barbara and Ricardo Franco hills and at the west portion of São Vicente hill.

Other contributions about the structure of the Aguapeí belt comprises more localized studies executed in some of gold deposits of Alto Guaporé gold province (AGGP).

Fernandes et al., (2005c) have studied the structures of **Lavrinha**, a gold deposit occurring at the central portion of AGGP (close to **Ernesto Mine**). According to the authors two deformational events were recognized; a Dn(pre-Sunsas) event,onlyrecorded in the rocks of the basement characterized by a metamorphic Sn foliation given by a compositional banding andassociated crenulation cleavage and; a D_1 event characterized by thrusting of Aguapeí sediments over the gneissic basement and consequent regional folding of the sedimentary package (eg. Caldeirão syncline, Cágado anticline).According to the authors the thrusting has generated amylonitic shear zones on the contact between the sediments and the basement (Morro Solteiro shear zone), characterized by S_1mylonitic foliation (dipping at ~45º to NE or SW) meanwhile folding in the sedimentary sequence generate a axial plane foliation dipping ~50º to NE or SW.

Scabora and Duarte (1998) has studied the structural geology of **Sao Vicente Mine,** a sediment hosted ore deposit occurring on Northeastern Sao Vicente Hill (on northern AGGP). According to the authors the highly deformed zone where the São Vicente Mine is located is result of compressive oblique movements from east to west, and the proposed evolution starts with shortening characterized by inverse faulting on the weakness zone of thecontact between the Aguapeí basin and its basement and progressively evolves to synistral shear zones preferentially developed on litologic contacts. The major structureis given by a series of regional-scale synforms and antiforms of high amplitude with subvertical axial planes and hinge line dipping at NW. Tight folds of low amplitude occurs at the core of the major antiforms and synforms and are divided into two types: symmetric folds with subvertical axial planes and; asymmetric folds with axial plane plunging to NE. Locally, at the most intensely deformed zones the folded sedimentary strata (S_0) is transposed by S_1 axial plane foliation and inverse faulting evidenced by rupture of fold flanks.

The only structural study at **São Francisco mine** (still in the northern portion of AGGP and one of the most economically important gold deposit of the area) is published as ainternal consulting report requested by Yamana Gold Inc. and elaborated by Dr. Norberto Morales in 2007. According to Morales (2007) the mineralized zone of São Francisco Mine is located in the core of an anticline and is characterized by ore-bearing quartz veins hosted by feldspathic metasandstone. The hundred meter-scale fold where the mineralized zone is hosted is characterized by high angle axial plane and sub-horizontal axis dipping at low angle to NW. Two NW-SE reverse faults (dipping to NE) occurs at the hinge zone of the fold, and are more or less limiting the mineralized zone. The area between the reverse faults is characterized by intense hydrothermal alteration given by quartz veins and alteration minerals. According to the author the structural evolution starts with folding through flexural slip which formed symmetrical folds and a subvertical family of quartz veins in the most competent layers (metaconglomerates and metasandstones). As the deformation progresses a sub horizontal quartz vein family were formed as result of NE-SW pure shear deformation. The progress of NE-SW shortening through folding goes until reaching the rupture point when were formed the reverse faults that acted as conducts for hydrothermal fluids. Since the most external sedimentary layers of the anticline are given by fine grained metassedimetary rocks (metapelite) the zone between the two reverse faults (SW and NE) were enriched in hydrothermal fluids reducing the rupture limit of the rocks and allowing (T) traction fracturing of Riedel´s model, that were filled by quartz, forming then the third family of quartz vein.

Baia (2007) has studied the structure of the **Pau-a-Pique Mine** and describes at least two deformational phases in the area; Dn phase given by folds with Sn foliation parallel to S_0 (dipping at 30º-88º SW) and down dip lineation associated to it; and a Dn+1 phase associated with shear zones (Corredor shear zone) characterized by high angle mylonitic foliation (90º-60º) dipping to SW. Associated to the Dn+1 phase there is an well marked Ln+1 lineation best observed in the metaconglomerates near to Corredor shear zone given by elongated pebbles. according to the author the Ln+1 plunges at 50º-76º NNW and seems to be a major structural control for mineralization, since it is parallel to the axes of gold-bearing quartz boudins.

According to Fernandes et al. (2006) the Pau-a-Piquedeposit is on the northern portion of Corredor shear zone, a NNW/SSE-trending anastomosed subvertical mylonitic belt occurring at the contact between Aguapeí sediments and the gneiss of Santa Helena terrain. According to the author kinematic indicators suggest a general dextral strike-slip component combined with thrusting. The S_1 mylonitic foliation is the most prominent planar structure at the deposit and is represented by a series of SC subverticalplans dipping at 50º - 80º SW. The authors also recognized a well marked stretching lineation in quartz pebbles and mica fish, however according to then it is sub horizontal and is result of the directional component of shearing meanwhile the vertical component of thrusting is recorded as mineral lineation with rake of 76º over the inverse fault surface.

4. Methods

The methods applied to this research can be divided in three main steps: (1) an office step, given by literature review and data collecting; (2) a field work step, which included sampling, regional mapping, drill core logging and face mapping; and (3) a lab step, which consisted of sample preparation, analytical procedures and data interpretation.

4.1- Literature review and data collecting

An extensive literature review regarding the geological settings and evolution of the SW portion of Amazon Craton was followed by compilation and organization of the geological, geophysical and geographical database kindly provided by Yamana Gold Inc. These information was organized in a spatial geodatabase in GIS platform in order to allow the inclusion of new data during field work and sampling campaigns. Thus detailed geologic maps and geologic cross sections of the studied deposits presented as pictures along the text were made by the exploration team of Yamana Gold and was an essential background information for sampling as well as the interpretation about the structural architecture of the studied deposits.

4.2- Field work and sampling

Most of samples were collected during the almost the eighty days of field work executed at the area. In the first year of the doctorate research a phase of regional geological recognition and mapping were executed in order to obtain a reliable structural geological background of the studied area. Subsequent detailed geological works included high resolution geological mapping of some berms in the open pit mine of Ernesto intermediate level and in an estope access to the mineralized body of Pau-a-Pique underground mine and drill core logging of four representative drill-holes of the studied deposits, in order to indentify the geometry and aspects of the hydrothermal alteration and it correlation with the ore grades in each deposit.

4.3 Analytical methods

4.3.1- Petrographic study

Most of analytical procedures were driven by petrographic studies executed prior to any analytical technique.

Petrographic studies were conducted using optical light microscopy, supported by scanning electron microscopy (SEM). SEM imaging (backscattered electron and secondary electron imaging) of polished and double polished thin sections of the studied samples was conducted using a JEOL 5800LV scanning electron microscope at the U.S. Geological Survey Denver Inclusion Analysis Laboratory (DIAL) in Lakewood Colorado. Additionally, three of the studied polished thin sections had its mineralogical composition determined using QEMSCAN, at the Automated Mineralogy Laboratory within the Center for Subsurface Earth Resources from the Department of Geology and Geological Engineering of Colorado School of Mines in Golden, Colorado. Maps of mineral abundance were made through the scanning of the entire thin sections using an electron-beam instrument (QEMSCAN) to perform rapid and accurate mineralogical maps of the thin sections. The maps were made using pixel size of 45 microns and the modal composition (vol. %) was calculated by the QEMSCAN system based on area and shape of mapped phases.

4.3.2- Whole rock Geochemistry

Based on petrographic criteria samples from the mineralized zone of Pau a Pique as well as its host rock were selected to whole rock geochemistry. Uncrushed pieces of samples collected during the field work was selected based on petrographic criteria and were shipped to the Acme Laboratories in Vespaziano, Minas Gerais, Brazil where major, trace and Rare Earth Elements were analyzed by ICP-MS method (LF-200 and AQ200).

4.3.3- Microprobe Analysis

Major element mineral chemistry of biotite, muscovite, chlorite, amphibole and plagioclase as well as trace element composition of pyrite was determined through microprobe analysis using a A JEOL JXA 8900 electron microprobe at the Denver Microbeam Laboratory, USGS Denver office, Colorado. Analysis of silicates was conducted using 15 KeV accelerating potential and 20 nA beam current for a spot size of 3micrometer. Counting times of all major elements were 20 seconds on and off peak except for F (only analyzed in micas) in which counting time was 120 seconds and off peak. The Same equipment was used to analyze trace element composition of pyrites operated using 20 keV accelerating potential, 100 nA beam current, and a spot size of 5µm.

4.3.4- Fluid inclusion Study

Petrographic and micro-thermometric studies of fluid inclusions present in ore-bearing quartz veins from Pau a Pique and Ernesto (Intermediate level) deposits were made in order to identify the composition and physical characteristics of mineralizing fluids at these deposits. Twelve samples of quartz veins (5 from Ernesto and 7 from Pau a Pique) were initially selected for petrographic studies. Reflected and transmitted-light petrography were performed in double polished thin sections (~200μm) in order to identify the different types of fluid inclusions present in each sample and its relationship to the deformation of quartz and to the sulfide phases. Petrography was supported by SEM-cathodoluminescence (CL) imaging in order to obtain the textural aspect of quartz and its relationship with the families of fluid inclusion though the identification of different generations of quartz, and zoning textures. Cathodoluminescence imaging was conducted on the same double polished thin sections used for petrography and in the later microthermometric analysis. It was made using a Cathodoluminescence (CL) attached to a Scanning Electron Microscope (SEM) JEOL JSM-5800LV using a 20 keV accelerating potential, 1-10 nA beam current.

After petrography, 3 quartz samples of Pau-a-Pique and 1 of Ernesto were selected for the micro-thermometric analysis. Temperatures were measured on LINKAM heating and cooling stages (TMS 92) with a working range from –185° to +600°C. Calibrations were made against known melting points of synthetic fluid inclusions. The precisions of the measurements were ±0.1°C for the melting temperatures and within ±3°C for the homogenization temperatures.

In order to obtain the composition of gaseous phases in the fluid inclusions, laser Raman analysis was performed with a Xplora Horiba/Jobin Yvon Raman spectrometer equipped with an 532nm wavelenght (green) line from Hitachi laser as excitation source. The laser beam was focused on the samples with a 100x objective in an optical microscope. The spectra were accumulated in 3 increments using measuring time of 60s each. CO_2 rich inclusions were analyzed for the characteristic peaks of CO_2 (~1388 and ~1285cm^{-1}), CH_4 (~2917 cm^{-1}), N_2 (~2331 cm^{-1}) and H_2S (~2611, ~2590 and ~2580 cm^{-1}) Burke (2001).

Trace elements of fluid inclusions were analyzed using LA-ICP-MS system given by a 193nm (MicroLas-Geolas-Pro) laser ablation coupled to Thermo Scientific XSERIES II Quadrupole Inductively Coupled Plasma Mass Spectrometer (ICP-MS) at the USGS Denver office. The analysis were conducted on pieces of double-polished thin sections using laser energy density of 120mJ, repetition rate of 5Hz and beam size of 32 μm.

4.3.5- Stable isotopes (δ18O, δD e δS)

Oxygen isotope compositions were measured in 26 samples of quartz, 7 samples of muscovite, 2 samples of albite and 3 samples of magnetite from deposits occurring along the central portion of Alto Guaporé Gold Belt. The analyzed quartz samples comprises 16 samples from mineralized and barren quartz veins (12 samples from Pau-a-Pique a 5 samples from Ernesto intermediate level). The other 11 samples comprises mineralized quartz veins collected in 8 other gold occurrence and deposits in the central portion of Alto Guaporé Gold Belt. The muscovite samples were collected from mineralized muscovite schist from Pau-a-Pique (5 samples) in the mineralized wall-rocks of Ernesto Intermediate level (2 samples). Both Albite and magnetite samples were obtained from quartz-albite veins and muscovite schist occurring in the mineralized zone of Pau-a-Pique deposit.

The quartz was crushed and sieved to 250μm, and about 0.1 g of the purest and clearest quartz from each sample was hand-picked under a binocular stereomicroscope. The same amount of muscovite, albite and magnetite was manually separated from the sample using a dental curette and a binocular stereomicroscope. Part of the analysis (samples of magnetite, albite, muscovite and 16 sample of quartz from Pau-a-Pique and Ernesto deposits) were performed at the U.S. Geological Survey stable isotope laboratory in Lakewood, Colorado. The oxygen extraction use the BrF_5 method of Clayton and Mayeda (1963), which involves reacting the quartz at 550ºC overnight in a nickel vessel to produce CO_2 gas that was analyzed in a Isotope Ratio Mass Spectrometer Finnigan MAT 252. The Other 12 samples of quartz was sent to the Stable Isotope Laboratory of Geological Survey of Canada, Ottawa.

D/H ratios were determined for hydrous minerals (chlorite and muscovite) and for fluid inclusion waters extracted from quartz. Chlorite were manually obtained from 4 samples of quartz albite veins from Pau a Pique deposit in which chlorite occurs as almost pure aggregates filling fractures in the veins or associated with carbonate and sulfide. Concentrates of pure muscovite was manually obtained from 23 samples of mica schist occurring in mineralized shear zones of both, Pau a Pique and Ernesto deposits as well as in another 8 gold occurrences also located in the central portion of AGGP. The concentrates of muscovite and chlorite were hand picked and weighted into silver capsules with vanadium pentoxide. Samples of Chlorite and muscovite from Pau -a-Pique and Ernesto intermediate level, were analyzed in an Delta Plus XL IRMS at the U.S. Geological Survey stable isotope laboratory in Lakewood, Colorado. Sample were introduced via Costech blank auto sampler into a high temperature conversion elemental analyzer (TC/EA) coupled to a Conflo II mixing box interface. Other 15 sample of muscovite was analyzed in a IRMS system at the Stable Isotope Laboratory of Geological Survey of Canada, Ottawa.

For δD analysis of fluid inclusions waters, a total of 11 samples of mineralized quartz veins from 8 gold deposits occurring in the central portion of AGGP were caused and washed. Subsequently it was out gassed at 150ºC and then inclusions were decrepitated by heating at 1,050 ºC for one hour. Released waters was converted to hydrogen gas by reduction with zinc and the gas was analyzed in a IRMS at the Stable Isotope Laboratory of Geological Survey of Canada, Ottawa.

For sulfur analysis pyrite were obtained from 15 samples (6 from Ernesto intermediate level and 9 from Pau a Pique) representing the ore zone in the studied deposits. Individual grains were obtained from drill core samples using a dental curette. The grains were subsequently milled to a finer granulometry (<50 um) and about 0.05 grams of pure pyrite was hand picked under a binocular stereomicroscope. The fine-grained crystals were weighed into tin capsules with vanadium pentoxide, and analyses were carried out using an Isotope Ratio Mass spectrometer Delta Plus XP coupled to a Flash 2000 elemental analyzer via a Conflo III mixing box at the U.S. Geological Survey stable isotope laboratory in Lakewood, Colorado.

4.3.6- Laser Ablation ICP-MS in Quartz.

Laser Ablation ICP-MS analysis of quartz were performed in order to obtain the trace elements concentration to apply specific geothermometer based on Ti concentration in quartz. The analysis was carried out in the same LA-ICP-MS system used for fluid inclusion analysis, given by a 193nm (MicroLas-Geolas-Pro) laser ablation coupled to Thermo Scientific XSERIES II Quadrupole Inductively Coupled Plasma Mass Spectrometer (ICP-MS). The analysis were conducted on double-polished thin sections (~200μm in thickness) using laser energy density of 17 J/cm^2. The ablation was made in 200 pulses using repetition rate of 5Hz and beam size of 60μm. The standards for calibration was NIST612 and NIST610 glass reference materials. The flux of He was maintained in ~400 ml/min during the running.

5. Results

5.1. Geological mapping

A1:50 000-scale geological map of the researcharea (Appendix X) was made trough compilation and refinement of previous large scale maps supported by geophysical data and field work. The studied region has an area of about 1300 km^2 extending 42km from Ernesto Mine to the south of Pau-a-Pique Mine The mapped units include: (1) metasedimentary rocks of the Aguapeí group; (2) granite of the Santa Helena intrusive suite (SHIS); Granite, diorite and tonalite related to the Pindaituba intrusive suite (PIS); (3) volcanosedimentary rocks of Alto Jauru Group; and (4) volcanosedimentary sequences of the Rio Alegre Terrain.Detailed description of the rocks cropping at area is presented bellow (***in Portuguese***) and follows stratigraphy from older units to the younger ones.

5.1.1.- Terreno Jauru (Jauru Terrain)

Grupo Alto Jauru (Alto Jauru group):

Na porção norte da área de estudo ocorrem rochas aparentemente associadas a sequências metavulcanossedimentares que, de acordo com Bettencourt et al. (2010) pertenceriam ao Grupo Alto Jauru, correspondendo ao embasamento paleoproterozóico (1.76 - 1.72 Ga) do Terreno Jauru. Segundo Monteiro et al. (1986), essa unidade consiste de gnaisses, migmatitos e três sequências metavulcanossedimentares: Cabaçal, Araputanga e Jauru.

Menezes et al. (1993) denominou essa unidade como Complexo Metavulcanosedimentar Pontes e Lacerda,subdividindo-o em três unidades: Unidade São José, formada por metabasitos e anfibolitos de natureza toleítica associados a rochas metassedimentares químico-exalativas (BIFs e cálcio-silicatadas); Unidade Triângulo, composta por muscovita xistos, biotita muscovita xistos, sendo comum a granada e cianita como acessórios e raras intercalações de anfibolitos; a Unidade Paumar de topo, é composta essencialmente por xistos e quartzitos. Segundo Geraldes et al. (1997) inclui basaltos metamorfisados, tufos ácidos, rochas vulcanoclásticas riodacíticas e rochas sedimentares clásticas e químicas

Durante os trabalhos de campo não foram observados afloramentos de rochas dessa unidade. A área de ocorrência dessas rochas é caracterizada por uma topografia plana dada por uma espessa cobertura de solo laterítico. As raras exposições são de corte de estrada onde que expõem apenas perfis lateríticos exibindo no máximo a zona saprolítica do perfil de alteração. Só foram observadas amostras de rocha fresca dessa unidade em furos de sondagem feitos pela empresa Yamana Gold Inc (Fig.5.1-1).

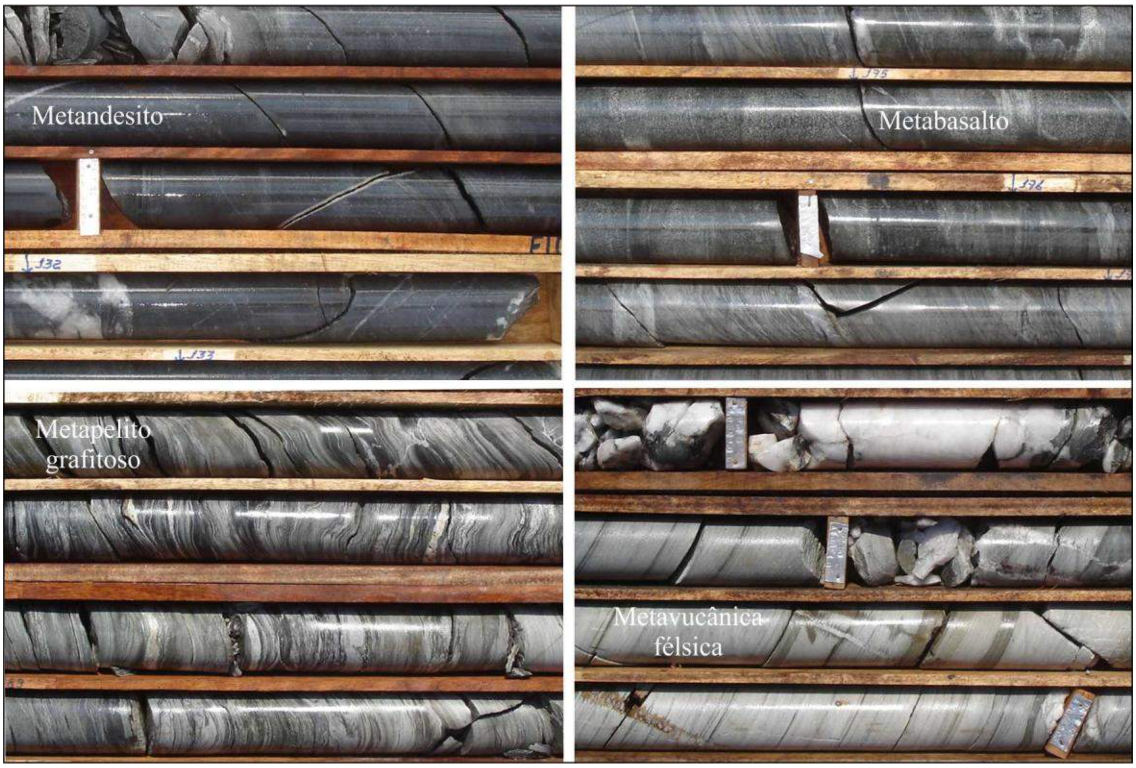

Figura 5.1-1: Fotografias de testemunhos de sondagem de furos do alvo Córrego da Onça, exibindo os diferentes litotipos associados ao Complexo metavulcanosedimentar Pontes e Lacerda.

Os furos de sondagem executados pela empresa apresentam espessa capa de alteração intempérica, podendo chegar a 60 metros de profundidade, abaixo da mesma ocorrem rochas metavulcanicas e metasedimentares foliadas com um forte bandamento composicional. Tratam-se de metapelitos grafitosos a grafita xistos, clorita xistos, metandesitos, metabasaltos e metavulcânicas félsicas (Fig. 5.1-1).

Suíte Intrusiva Santa Helena (SHIS)

Segundo Ruiz (2005), a suíte intrusiva Santa Helena consiste de um corpo ígneo batólítico com aproximadamente 4500 Km^2, cujo eixo maior orienta-se segundo a direção NNW. Segundo Sousa et al(2005), o batólito é constituído por rochas de foliação proeminente, equigranulares, inequigranulares a porfirítica, de granulação preferencialmente grossa até fina, leucocráticas a mesocráticas, com colorações variando entre cinza e rosa avermelhado, tendo biotita como principal máfico e, subordinadamente, hornblenda e granada. Foram divididas, com base na textura e mineralogia quatro principais associações de fácies petrográficas que apresentam estruturas gnáissicas e composição sieno a monzogranitica.

Geraldes et al. (2001) apresentam idades de U/Pb em zircões magmáticos variando entre 1.46 e 1.42 Ga, sendo que as idades modelo TDM estão entre 1.5 e 1.6 Ga. Segundo os autores o magmatismo é do tipo I, calcio-alcalino, sendo que as fácies granitóides menos desenvolvidas são aproximadamente metaluminosas e as mais fracionadas, fracamente peraluminoso indicando contaminação crustal. Idades de Ar/Ar em biotita e sericita variam de 0,91 a 0,89 Ga e são interpretados como reflexo da reativação regional ocorrida durante o evento Sunsás (Tohver et al., 2006; Paulo, 2005).

As rochas associadas à Suíte Intrusiva Santa Helena (SISH) são relativamente homogêneas e compreendem hornblenda biotita granitos foliados.

Hornblenda-biotita granito: É o litotipo predominante na porção leste da área de estudo e trata-se de um granito de cor rósa com granulação média foliado (Fig. 5.1-2 A, B).

Aflora na forma de lajedos e matacões arredondados e o relevo da região onde ocorre é caracterizado por alta rugosidade e alta densidade de drenagem controladas por sistemas de fratura e foliação, contrastando com as áreas adjacentes que geralmente apresentam espessa cobertura de solo laterítico associado a um relevo arrasado. A análise de mapas geofísicos de raios Gama (contagem total), K, Th e U executados pela CPRM (escala 1:100 000) e fornecidos pela empresa Yamana Gold, associados a modelos digitais de elevação, imagens STRM e trabalhos de campo, permitiram delimitar com certa precisão a área de ocorrência dessa fácies granítica que é homogênea por uma grande extensão na porção oriental da área de estudo.

A rocha é caracterizada pela baixa quantidade de máficos (menos de 15%) e, em lâmina, essa rocha apresenta granulação média, estrutura foliada, holocristalina, fanerítica, equigranular, textura granítica em que os grãos de quartzo aparecem preenchendo os interstícios da malha formada pelos cristais de plagioclásio e microclínio. A rocha é composta por feldspato potássico, quartzo, plagioclásio biotita podendo ocorrer hornblenda (Fig. 5.1-3 A, B). Como acessórios observa-se a presença de magnetita, titanita, zircão e apatita. Foi observada também a presença de textura de exsolução no microclinio e plagioclásio com a formação de pertitas e antipertitas respectivamente.

O feldspato potássico é o mineral predominante na rocha e geralmente ocorre com forma anedral e geminação em grade. O plagioclásio é do tipo oligoclásio e ocorre como cristais anedrais com geminação do tipo polissintética.

Dada sua composição modal essa rocha foi classificada como monzogranito.

Suíte Intrusiva Pindaituba (PIS)

Segundo Ruiz (2005), constitui um conjunto de intrusões graníticas alojadas nos terrenos supracrustais e ortognáissicos do Domínio Jauru. Ainda segundo o autor, tratam-se de plutons e batólitos claramente orientados segundo a direção média de N20-40W, apresentando rochas com granulação média a grossa e frequente textura porfirítica. São rochas leucocráticas a mesocráticas e composicionalmente variam desde termos tonalíticos a sienograníticos. Apresentam foliação penetrativa, por vezes milonítica, sendo que alguns corpos apresentam foliação apenas em suas bordas.

Fariam parte da Suíte Pindaituba os granito Maraboa, Guaporé, Santa Elina e Tonalito Lavrinha (Ruiz, 2005; Bettencourt et al., 2010). Trabalhos prévios como o de Geraldes (2000) sugerem que tais granitóides seriam parte da Suíte Santa Helena.

Muscovita-biotita monzogranito porfirítico: Ocorre na porção SSE da área, a leste do depósito Pau-a-Pique. Trata-se de uma rocha de coloração rósea, granulação grossa, porfirítica, composta por microclínio pertítico, quartzo, plagioclásio, biotita e muscovita (Fig. 5.1-2C e 5.1-2 D). Os afloramentos dessa rocha estão restritos a poucos locais onde ocorrem como matacões ou em cortes de estrada recentes, onde ocorre fortemente saprolitizado.Apresenta foliação gnáissica e textura semelhante a "*Augen*", dada pela presença de cristais porfiríticos com forma sigmoidal.

Os cristais de feldspato potássico são róseos e compõe cerca de 30 a 40% da composição modal da rocha e ocorrem tanto na matriz, na forma de cristais anedrais com geminação do tipo grade com tamanho submilimétrico ou como grandes cristais porfiríticos com até 3cm de comprimento onde, geralmente apresenta textura de exsolução do tipo pertítica.

A quantidade de plagioclásio é estimada em torno de 15 a 25% da composição modal da rocha. Geralmente ocorrem como cristais anedrais com geminação do tipo polissintética. A lâmina descrita apresenta uma rocha de composição sienogranítica com uma foliação gnáissica bem marcada dada pela orientação dos cristais de mica em torno dos cristais de feldspato potássico (Fig. 5.1-3 C e 5.1-3 D). Como a rocha apresenta grande quantidade de feldspato alcalino (microclínio e pertitas da albita) sua classificação no QAP cai no campo dos monzogranitos a granodioritos, já que a quantidade de quartzo na rocha está em torno de 20 a 25%.

Granito Maraboa: Na porção Norte da área, à leste do Depósito Ernesto, foi constatada a presença de rochas graníticas associadas a mica xistos. Na área de ocorrência dessa rocha há uma espessa cobertura intempérica dada por um solo argilo-arenoso cor marrom avermelhado ou então exposições da rocha saprolitizada. Amostras frescas foram observadas apenas em furos de sondagem onde observa-se um granito de cor vermelha, granulação grossa, constituído por biotita, quartzo, plagioclásio e feldspato potássico (Fig. 5.1-2 G).

O granito, na maioria das amostras de testemunhos observados e nos afloramentos visitados, apresenta-se cataclasado e é comum observar a presença de afloramentos de mica xisto fortemente alterados de cor vermelha. Entretanto o estado de alteração da rocha nos afloramentos visitados, não permite a identificação do tipo de xisto que está associado ao granito.

Idades U/Pb (1449 ± 07 Ma) e T_{DM} (1.70 Ga) para esse granito são apresentadas por Geraldes et al. (2001). Segundo os autores trata-se de um pluton de rochas graníticas de composição monzosienítica que apresenta contato gradacional com tonalitos foliados, sugerindo fusão parcial localizada, associados com a evolução de rochas do Domínio Rio Alegre.

Devido a espessa cobertura de solo e ao elevado grau de intemperismo dos afloramentos, a delimitação dos limites da unidade foi feita com o auxilio de imagens geofísicas (appendix X). Essa unidade tem formato aproximadamente triangular e é limitada a oeste por rochas do grupo Aguapeí à oeste, por granitos da suíte Santa Helena à leste e por rochas metavulcanossedimentares associadas ao Grupo Alto Jauru à norte, cujo limite é marcado por uma falha dada por forte anomalia magnética.

No contato leste com o hornblenda biotita sienogranito foi mapeada a ocorrência de uma brecha cor branco esverdeada, formada quase que exclusivamente por quartzo. Essa rocha sustenta o topo de um longo de um alinhamento de serra com direção N-S que deve marcar o contato tectônico entre o Granito Maraboa e o Granito Santa Helena.

Metagranitóides (Tonalito Lavrinha e Tonalito Pau-a-Pique): Marcado por espessa coberturar de solo, exposições de rochas frescas na superfície são extremamente raras e só foram observadas em testemunhos de sondagem do Depósito Pau-a-Pique e do nível inferior do Depósito Ernesto. Na literatura esse litotipo é genericamente apresentado como metatonalito ou tonalito Pau-a-Pique e Lavrinha respectivamente (Geraldes, 2000; Geraldes et al., 2001; Ruiz, 2005).

Geraldes et al., (2001) apresenta dados de datação U/Pb para o Tonalito Lavrinha (1465 ± 04 Ma) e Tonalito Pau-a-Pique (1481 ± 07 Ma) e idades Sm/Nd T_{DM} 1.53 Ga e 1.50 Ga respectivamente o que, segundo os autores, sugere que são partes de um terreno juvenil representado por rochas vulcânicas andesíticas associadas ao Domínio Rio Alegre. No entanto Ruiz (2005) e Bettencourt et al. (2010) colocam o Tonalito Lavrinha como parte da Suíte

Intrusiva Pindaituba, associada ao Terreno Jauru. Nesse trabalho optou-se por seguir a classificação adotada por Ruiz (2005) e Bettencourt et al (2010) visto que se trata da abordagem mais recente sobre o assunto.

Dados geocronológicos (SHIRIMP U/Pb em zircão - ver mais adiante) de uma amostra de do Pau-a-Pique mostra idade muito similar à idade U/Pb em zircão para o Tonalito Lavrinha obtidos por Geraldes et al. (2001) que por sua vez são no geral mais velhas que as idades U/Pb em zircão para o Batólito Santa Helena (1456 - 1419 Ma). Dessa forma assume-se que os metagranitóides do Pau-a-Pique são correlatos ao Tonalito Lavrinha sendo dessa forma também interpretados como parte da Suíte Intrusiva Pindaituba.

O perfil de alteração intempérica onde ocorrem essas rochas, é marcado por um solo argiloso vermelho e que comumente chega a mais de 30 metros de profundidade, motivo pelo qual é difícil de encontrar exposições dessas rochas em afloramentos na superfície.

Nos testemunhos observados, nota-se grande variedade textural e composicional, mas geralmente apresenta-se como uma rocha cor verde escura, granulação fina a média, fanerítica, equi a inequigranular porfirítica, com estrutura foliada a milonítica. Em alguns casos é possível observar feições de textura porfirítica dado por fenocristais de plagioclásio.

As amostras analisadas petrograficamente são de testemunhos de sondagem que compõe o embasamento do depósito Pau-a-Pique e portanto estão próximos à zona de alteração hidrotermal. Os minerais presentes são quartzo, actinolita, pargasita, epidoto, clorita, carbonato, plagioclásio, biotita, hornblenda, ilmenita, pirita, titanita. A actinolita e pargasita ocorrem como observada na rocha apresenta-se com cor verde e pleocroismo para verde azulado (Fig. 5.1-3 E). Em uma das lâminas analisadas ocorrem grandes cristais de plagioclásio com geminação do tipo polissintética cobertos por uma massa de cristais de epidoto e carbonato associado. Além disso ocorrem diversas vênulas de quartzo e carbonato.

Análises geoquímicas e petrográficas de algumas amostras mostram que oteor de SiO_2 das rochas do embasamento do depósito Pau-a-Pique geralmente esta entre 47% e abaixo de 65% sendo que a maioria é de composição intemediária. Algumas fácies apresentam textura porfirítica com fenocristais de plagioclásio do tipo oligoclasio com geminação polissintética, que foram fortemente epidotizados. Com base nos estudos petrográficos e geoquímicos acha-se mais conveniente o uso do termo diorito para a composição geral das rochas do embasamento do depósito Pau-a-Piquedada sua composição química intermediária (Figura 5).

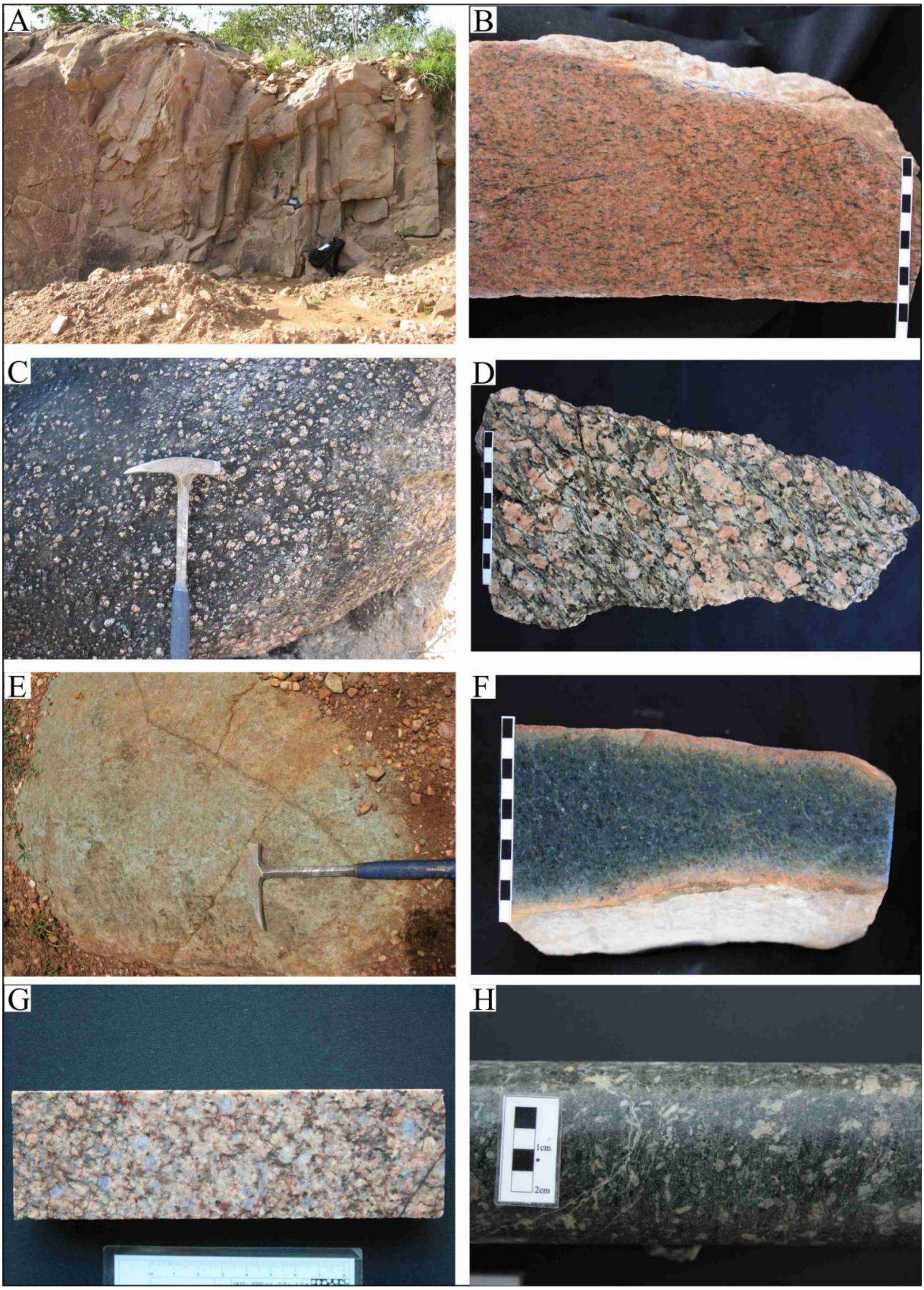

Figura 5.1-2: Granitos e Granitóides associados a SISH e SIP. (A e B): Afloramento e amostra de hornblenda-biotita sieno granito foliado relacionado a SISH respectivamente. (C e D): Afloramento e amostra de biotita Sienogranito porfiritico cor rósea relacionado a SISH respectivamente. (E e F): Afloramento e amostra de metabásica encaixada em biotita sieno granito porfírítico aflorante na região do Pau-a-Pique. (G): Amostra de testemunho de sondagem do Granito Maraboa associado a SIP.(H: Amostra de testemunho de sondagem do Metadiorito que ocorre no embasamento do depósito Pau-a-Pique relacionado a SIP.

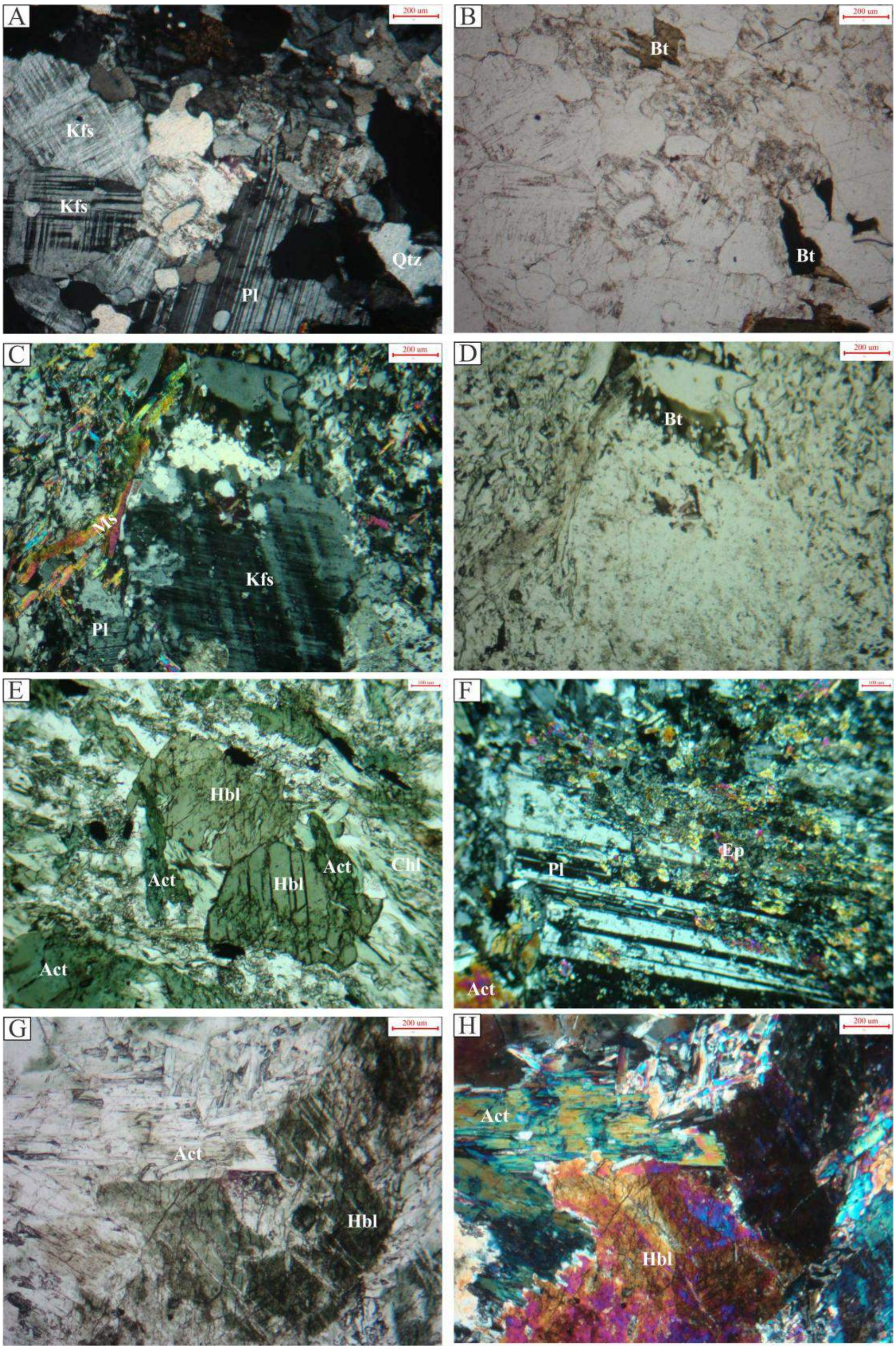

Figura 5.1-3: Prancha de fotomicrografias das diferentes fácies e litotipos associados a SISH e SIP (A e B): biotita sienogranito apresentando feldspato potássico com geminação em grade, biotita, quartzo e plagioclásio como mineralogia. (C e D): Biotita sienogranito porfirítico exibindo grande cristal de feldspato potássico no centro bordejado por muscovita e biotita.(E e F): Aspecto petrografico do metadiorito exibindo em (E) cristais de hornblenda sendo transformados em actinolita e em (F) grande cristal de plagioclásio fortemente epidotizado. (G e H): aspecto petrográfico da metabásica onde observa-se cristais de hornblenda associados a cristais de actinolita.

Metamáficas: Próximo ao depósito Pau-a-Pique ocorrem blocos no chão de uma estrada, de uma rocha máfica de coloração verde, granulação grossa, fracamente foliada (Fig. 5.1-2 E e 5.1-2 F), composta basicamente por hornblenda, muito pouco plagioclásio, actinolita e clorita. Estima-se que a quantidade de plagioclásio na rocha seja inferior a 5% (Fig. 5.1-3 G e 5.1-3H). A análise química de rocha total de uma das amostras desse litotipo mostra que trata-se de uma rocha de composição ultrabásica ($SiO_2<45\%$).

O afloramento dessa rocha ocorre em uma área onde a rocha dominante é o muscovita biotita sienogranito porfirítico. Não é possível precisar a extensão da área de ocorrência dessa rocha tampouco se trata de uma unidade mapéavel na escala de trabalho, porém observa-se no entorno do afloramento desses blocos a presença de um solo vermelho escuro e argiloso que se estende por um raio de mais de 300 metros em torno do afloramento.

Mapas geológicos de detalhe da área da Mina Pau-a-Pique, disponibilizados pela Yamana Gold Inc., mostram que, durante os trabalhos de prospecção da área, foram identificadas mais duas ocorrências de rochas básicas encaixadas nos granitos e dioritos do embasamento, que aparentemente indicam que se trata do mesmo litotipo. A ocorrência dessas rochas é portanto apresentada no mapa geológico da área de estudo como ocorrências de rocha básicas a ultrabásicas.

5.1.2 Terreno Rio Alegre

Na porção SW da área de pesquisa ocorrem rochas associadas à Unidade Vulcanossedimentar Rio Alegre. Segundo Ruiz (2005), essa unidade é a mais antiga do Domínio Rio Alegre ou Terreno Rio Alegre (Bettencourt et al., 2010), dispondo-se ao longo de uma estreita faixa com direção NNW.

A região onde ocorrem essas rochas é caracterizada por topografia extremamente plana e pela ocorrência de espesso perfil de alteração laterítica. Os afloramentos nessa região são muito escassos e durante os trabalhos de campo observou-se que, em grande parte da área, ocorrem extensas porções de crostas lateríticas ferruginosas associadas ao perfil de alteração laterítica. Além disso, a área é cortada pelo rio Alegre, que é meandrante próximo à sua jusante, em grande parte de seu percurso ocorrem extensas áreas de depósitos de sedimentos inconsolidados associados ao depósito fluvial do rio ou áreas alagadas associadas a sua planície de inundação.

Os poucos afloramentos com exposição de rocha fresca foram encontrados próximo ao contato com rochas do Grupo Aguapeí, na forma de blocos no chão de estradas e raramente na porção central da área na forma de blocos em drenagens.

As rochas mapeadas incluem: (1) blocos arredondados de rochas de cor cinza escuro granulação fina a muito fina, composta quase que essencialmente por quartzo, que tem sido interpretada como metachert (Fig. 5.1-4 E); (2) afloramento de metadiabásio, de cor verde escura, granulação fina, estrutura foliada, textura blastointersertal (Fig. 5.1-4 A e 5.1-4B) e; (3) blocos de metagabros de cor verde escura, textura porfirítica (Fig. 5.1-4 C e 5.1-4 D).

Os metagabros exibem textura blastofítica onde cristais ripiformes de plagioclásio que foram quase que totalmente substituídos por epidoto estão englobados por cristais de hornblenda.(Fig. 5.1-4 G e 5.1-4 H)

Essas rochas fazem parte da Formação Minouro, a unidade basal da sequencia Vulcanosedimentar Rio Alegre que, segundo Matos *et al.* (2004), é constituída por metavulcânicas a subvulcânicas básicas, além de metabasaltos e metadiabásios, formações ferríferas bandadas e sedimentos químicos (metacherts).

Na porção oeste da área, próximo a Serra de Santa Bárbara foram observados afloramentos de xistos micáceos extremamente alterados e também a ocorrência de afloramentos de uma rocha cor branca amarelada saprolitizada muito semelhante a um granito gnaissificado (Fig. 5.1-4 F).

5.1.3- Província Sunsás

Grupo Aguapeí

Na área de estudo afloram rochas da Formação Fortuna e Formação Vale da Promissão que correspondem, respectivamente, a Unidade Basal e Intermediária do Grupo Aguapeí.

Na área de estudo a Formação Fortuna ocorre ao longo de alinhamentos de serra com direção NNW-SSE. É caracterizada pela presença de metaconglomerados com intercalações métricas a octamétricas de metarenito fino a grosso e raras lentes de metassiltito e meta-argilito.

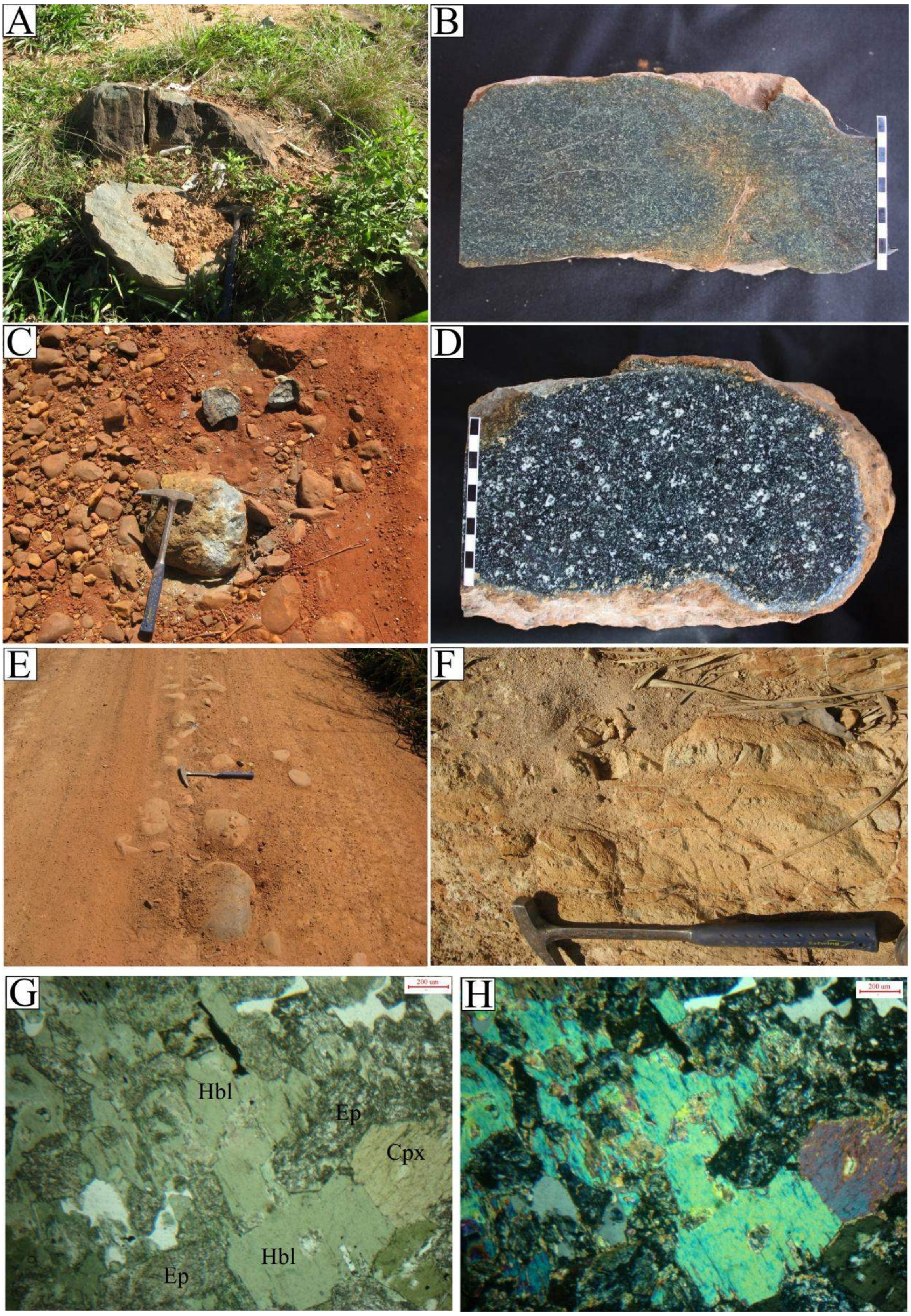

Figura 5.1-4: Aspecto das rochas da Unidade Vulcanossedimentar Rio Alegre. (A e B) afloramento e amostra de metadiabásio respectivamente. (C e D), afloramento e amostra de metandesito com textura porfirítica respectivamente. (E) blocos de metachert aflorantes próximo ao contato com o Grupo Aguapeí. (F): Afloramento de granito gnaissificado fortemente saprolitizado aflorante na porção oeste da área. (G e H): fotomicrografia dos metagabros do Rio Alegre exibindo textura blastofítica. (G): Nicois cruzados e (H): Nicóis descruzados.

São as rochas mais bem preservadas da área e apresentam-se foliadas, muitas vezes dobradas, metamorfizadas em fácies xisto verde. O topo das serras sustentadas pela Formação Fortuna geralmente apresenta rochas silicificadas e é comum a presença de grande quantidade de *float* e veios de quartzo. Essa silicificação generalizada é a principal responsável pela resistência que a rocha apresenta à erosão preservando topos que muitas vezes apresentam diferenças topográficas de mais de 400 metros de amplitude.

É comum a presença de estruturas reliquiares dada por estratificações cruzadas acanaladas e, mais raramente, a presença de bandamentos rítmicos dado pela intercalação milimétrica a centimétrica de metarenito fino e metassiltito a meta-argilito em porções onde predominam rochas de granulometria mais fina. O contato entre domínios com diferente granulometria é geralmente gradacional.

Os metaconglomerados (Fig. 5.1-5 A, B, C e D) apresentam grande variedade de cor e granulometria e geralmente apresentam-se com seixos de quartzo e feldspato com tamanhos variados podendo chegar a 4 cm de comprimento nos metaconglomerados de granulometria mais grossa. Trata-se de uma rocha foliada com textura blastopsefítica onde clastos de quartzo e por vezes, feldspato são mal selecionados, subarredondados a subangulosos e estão sustentados por uma matriz predominantemente quartzo-sericítica com cristais de tamanho submilimétrico. Os cristais de sericita têm cerca de 25 mícron de comprimento e, por vezes, apresentam manchas de oxidação de cor vermelha. No geral o quartzo é o mineral predominante nas lâminas estudadas e geralmente compõe mais de 70% da composição modal da rocha.

Os metarenitos (Fig. 5.1-5 E) apresentam-se na maioria das vezes intercalados com metaconglomerados em contatos graduais com granocrescência ao logo de planos de estratificação (Fig. 5.1-5 F). A mineralogia é praticamente a mesma observada nos metaconglomerados dada por grandes grãos de quartzo ou felsdspato com forma subarredondada, com matrix dada pela presença de micas, grãos de quartzo e por vezes magnetita. Geralmente exibem textura clástica sedimentar preservada, dada por arenitos finos a grossos onde os clastos são subarredondados a subangulosos com alta esfericidade, moderadamente bem a moderadamente selecionados. Em alguns casos observou-se feições de dissolução por pressão.

Os metapelitos (metassititos e metargilitos) (Fig. 5.1-5 G) ocorrem geralmente em camadas de espessura centimétrica, intercalados com metarenitos de granulometria fina a média, formando, por vezes, bandamentos rítmicos (Fig. 5.1-5 H). Com quantidade de quartzo variável, são rochas onde há o predomínio de mica branca sendo que a quantidade de quartzo pode ser inferior a 20%. As lâminas estudadas exibem rocha de granulação muito fina, xistosa textura lepdoblástica, com intercalações de camadas mais ricas em quartzo, e camada compostas basicamente por mica.

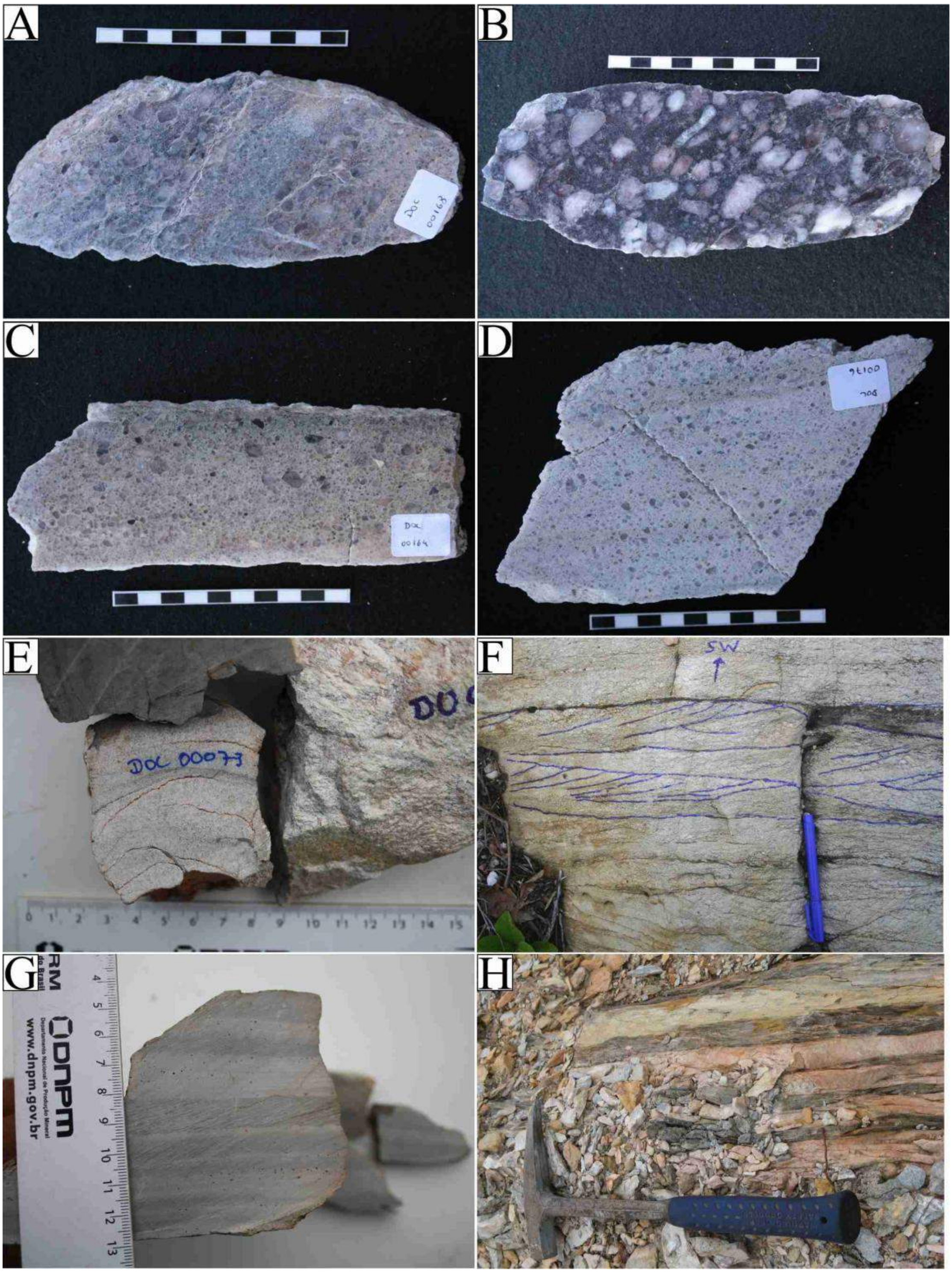

Figura 5.1-5: Aspecto das rochas da Formação Fortuna na área de estudo. (A, B, C e D): Amostras de metaconglomerados exibindo diferentes cores, texturas estruturas e granulometria. (E): amostra de metarenito fino. (F):Afloramento de metaconglomerado intercalado com metarenito exibindo estratificação cruzada; (G):amostra de metassiltito cinza com variações no Bandamento composicional. (H):intercalação rítmica de meta-argilito e metarenito fino.

O tamanho médio dos cristais de sericita é de 25 a 30 mícron. Em porções da rocha onde se tem o predomínio de mica, ocorre foliação do tipo SC associada à foliação principal. A rocha é composta por sericita, quartzo e hematita- magnetita podendo ocorrer traços de turmalina, biotita e zircão.

Formação Vale da Promissão**:** Segundo Leite & Saes (1993), a Formação Vale da Promissão (Souza & Hildred 1980), caracteriza-se por variada associação de fácies. Segundo os autores, nas serras do Aguapeí e Rio Branco, esta unidade apresenta uma sequência de pelitos amarelados e subarcóseos líticos muito finos arranjados em sequências granocrescentes cíclicas com espessura de 10-40 m. Na seção de Santo Corazón, esta unidade atinge espessuras de cerca de l .200 m e, a julgar pelo registro de acamamentos gradacionais (Litherland et al., 1986).

Rochas associadas à Formação Vale da Promissão ocorrem na porção central da área de estudo compondo a porção interna da Sinclinal do Caldeirão. Nessa região ocorrem rochas metassedimentares de granulação fina, incluindo metassiltitos a meta-argilitos com estratificações e marcas de onda (Fig. 5.1-6).

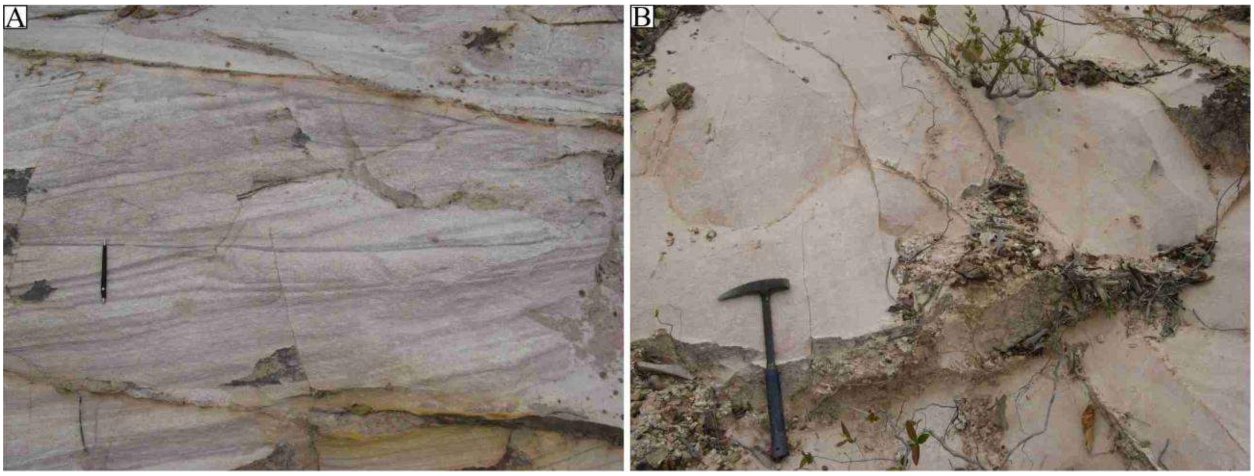

Figura 5.1-6: Afloramentos da Formação Vale da Promissão. (A): metarenito feldspático intercalado com finas camada de meta-argilito com roxa arranjados em estratificação cruzada de baixo angulo.(B) Metarenito fino homogêneo cor creme.

As rochas dessa unidade não apresentam boas exposições e a região onde ocorrem é marcada por um relevo plano muitas vezes com espessa cobertura de solo laterítico. Na área as melhores exposições de rochas da Formação Vale da promissão foram observadas apenas na região do Garimpo do Bananal na Serra do Caldeirão, próximo ao contato com a Formação Fortuna. Nessa região ocorre metarenito feldspático fino a médio, intercalado com metassiltito marrom avermelhado em bandas rítmicas com granodecrescência ascendente ou em estratificações cruzadas de baixo ângulo. O contato com da Formação Vale da Promissão com a Formação fortuna nessa região é marcado por uma zona de brecha.

Devido à forte alteração intempérica, não foram coletadas amostras de rochas da Formação Vale da Promissão.

5.2. Structural geology and tectonic background

Based on scientific literature and supported by field work data of the mapped area, this section makes a review and propose a general structural evolution for Aguapeí belt in the studied area.

Some of the geological units of the studied area has been reworked by successive episodes of magmatism and deformation since the Paleoprotezoic era, and thus record a complex structural history. This section will give attention to the structures associated with the evolution of Aguapeí belt. Structures related to older events, eventually preserved in the basement rocks are not being considered.

5.2.2. Deformation in the Pau-a-Pique area

The southern portion of the mapped area (Pau-a-Pique area), located to the south of Caldeirão syncline, is dominated by strike-slip shearing.

Based on previous structural studies, drill core data and field observation, it is possible to set the structures occurring at Pau-a-Pique Mine area in three deformational phases evolved through a unique evolutionary stage: a (**P_1**) phase which deformed and folded the sedimentary stratification (**S_0**) and is given by tight-isoclinal folds (**F_1**) with axial planar foliation (**S_1**) dipping at high angle to SW. Few measurements of the fold axis (**Fa_1**) has indicated general plunging at low angle to NW, being then classified as plunging inclined folds. The folded S_0 has parallel slaty cleavage and a down-dip stretching lineation (**Ls_1**) associated with it. Such structures, are found on the western and northern portion of the Pau-a-Pique deposit, generally recorded in the layers of fine grained metasandstones and in metapelites.

The (**P_2**) phase is characterized by subvertical mylonitic foliation (**S_2**).It is the most prominent planar structure in the area and is given by subvertical cleavage foliation dipping at high angle to SW (parallel to the axial plane F_1 folds). In the most deformed zones it is characterized by S-C planes. The rocks affected by such deformation show variable level of shearing being it characterized by centimetric to metric scale mylonitic zones displayed in an anastomosed pattern affecting both the metasediments and the basement rocks. The most deformed zone is located along the contact between the basement and the sedimentary rocks.

The effects of shearing over the sedimentary rocks is heterogeneous and is characterized by the presence of meter- to centimetric-scale subvertical mylonitic zones sided by low deformed metasediments in which, within few centimeter, it is possible to observe an abrupt transition from mylonite to low deformed metasediments with preserved primary structures (Fig. 5.2-1). Hydrothermal process during shearing seems to have transformed the mylonite zones into layer of light green muscovite schist (Fig. 5.2-1). Quartz veins hosted at these highly deformed portion are marked by asymmetrical boudinage that formed sigmoidal shape quartz veins, being it the most common kinematic indicator in the area (Fig. 5.2-1).

The effects of shearing at the basement rocks seems to be more homogeneous due the rheological characteristics of these rocks. Cores of low deformed granitoids are surrounded by metric zones of highly deformed rocks (the mylonitic zones). The shear zones, for instance, has been transformed into mica schist (biotite schist with variable amount of muscovite, chlorite and epidote). Aluminum silicate (kyanite) is also reported here, occurring in some of the studied samples. Such Ky-bearing schist, however, has been observed only at highly deformed zones over the basement, located near the contact with the metasedimentary rocks of Aguapeí.

The mineralized zone of Pau a Pique deposit is hosted along one of the vertical contact of the metasedimentary rocks with the basement. Such portion seems to be the center of a major shear zone affecting the area as a whole (Corredor shear zone) and, at roughly, it seems to be followed by sub-parallel minor shear zones affecting both, the sedimentary package and the basement, being it progressively smaller and less frequent towards outside of the mineralized zone.

As observed by Baia (2007), there is a stretching lineation (**Ls$_2$**) occurring in the mylonitic planes. It is better recorded by alignment of conglomerate pebbles occurring near the contact. It is parallel to elongation axis of gold-bearing quartz boudins occurring at the mineralized zone and seems to be an important structural control on Pau-a-Pique mineralization, as confirmed by three dimensional modeling of the mineralized body in which the ore grades roughly follow a structural trend with general attitude of N300º/55º.

The (**P$_3$**) phase is characterized by gentle-open with subvertical axis dipping at SW. Such family of fold show subvertical axial plane characterized by a fracturing system that locally shows evidence for fracturing foliation. The tightness of the folds is variable and depends on the rock's rheology being gentle in the coarser sediments (metaconglomerates and coarse-grained metasandstone) and open in fine-grained ones (metapelites). It is believed to be formed to the end of the shearing process as result of the the last compressive strain.

Most of kynematic indicators observed in the area has pointed out to dextral movements coincident with the regional pattern.

To the west of the Pau-a-Pique mineralized zone occurs a zone of silicified breccias. Drill cores data indicates it can reach 50 meters in width. Its evolution seems to be late on the structural evolution of the area and probably correlates to the last stage of deformation (**P_3**). It has been analyzed for gold by the mining company operating the deposit however there are no positive result for gold associated to it.

The deformational aspects of Pau-a-Pique area is synthesized in Fig. 5.2-2.

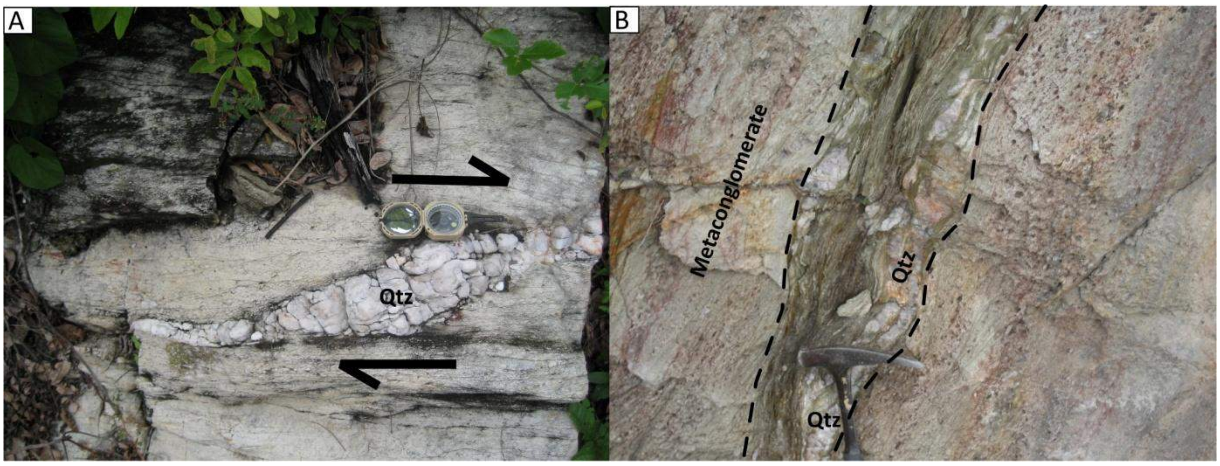

Figure 5.2-1:Structural features associated to shearing, occurring on Pau-a-Pique area. (A): Deformed barren quartz vein showing sigmoidal shape given by differential boudinage, indicative of dextral movement. (B): Centimeter-scale shear zone occurring within metassedimentary rocks near with Pau-a-Pique mineralized zone, showing high deformed shear zone given by light green muscovite schist and boudins of quartz sided by low deformed metaconglomerate.

5.2.3. Deformation on central and northern mapped area

A different deformation stile is found on central and northern portion of the mapped area. It is characterized by the occurrence of thrusting and folding.

Regional-scale folds are recognized at the area (Caldeirão syncline and Cagado anticline). The Caldeirão syncline is an open, NW/SE-trending, regional fold composed by the intermediateAguapeí sedimentary unit (Vale da Promissão formation) in its coreand thebasal Aguapeí unit (Fortuna formation) in its rim (Fig. 5.2.4). The coarse-grained metassedimentary rocks of the Fortuna formation occurringin the fold flanks crops along NW-SE aligned segments of hills contrasting with nearly flat topography where occurs the fine-grained metasedimentary rocks of the Vale da Promissão formation (in the core of the syncline) and the basement in its external portion.

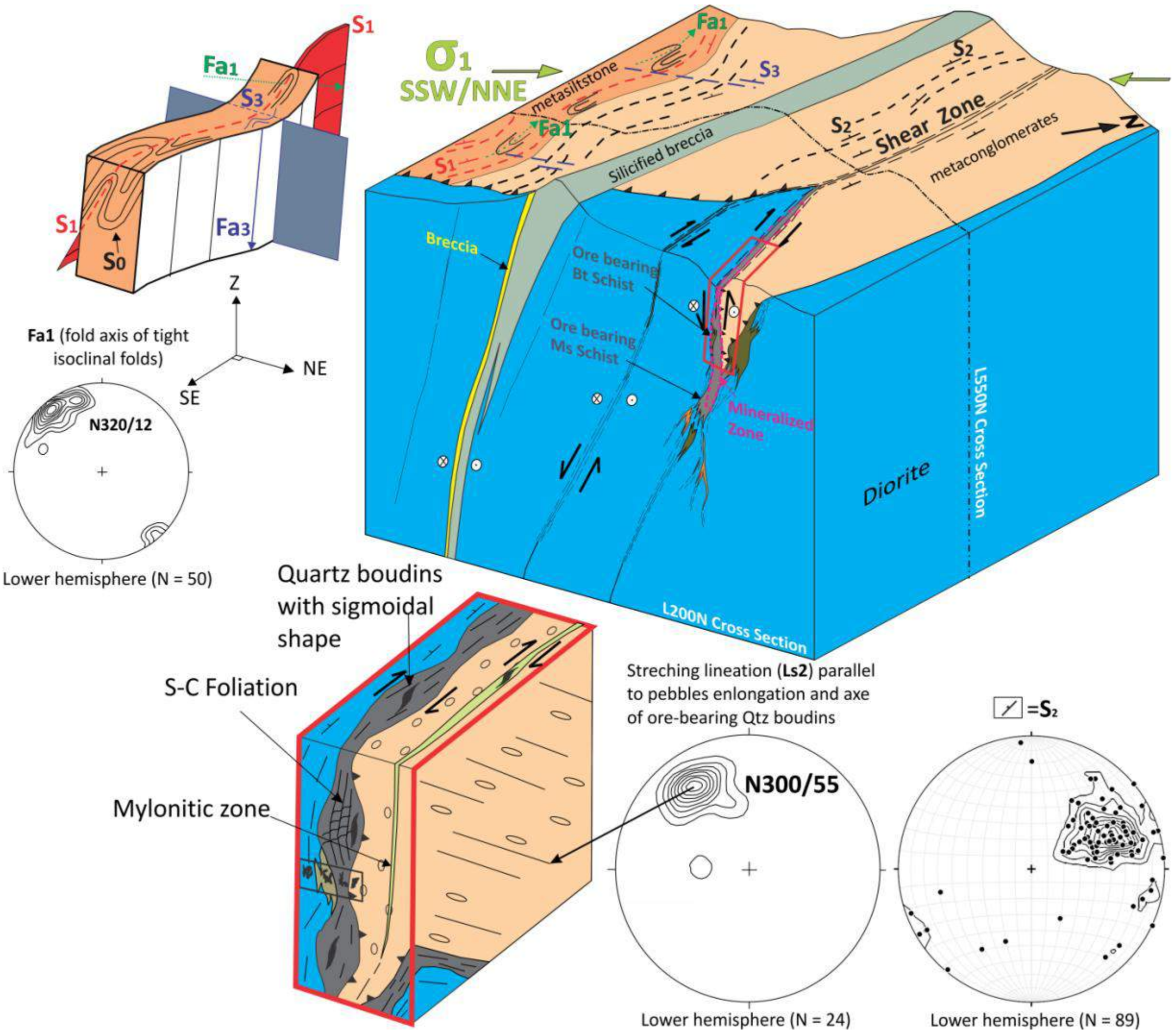

Figure 5.2-2:Schematic geologic and strucutural block diagrams for Pau-a-Pique area. It was created based on drill-hole supported cross sections and field work data executed during the research. Streching lineation and 'fold axis measurements extracted from Baia (2007).

Very few structural informations could be extracted from the internal portion of Caldeirão syncline since fine grained metasedimentary rocks occurring in such portion were subject to strong weathering and are covered by laterites.

Remote sensing interpretation and structural data collected to the north of Pau-a-Pique Mine, where the hinge zone of the Caldeirão syncline is exposed, indicates that the fold axis dip at low angle (~20º) to NW coherent with the plunging proposed by Ruiz et al. (2007), for the axis of the Caldeirão syncline and Cágado anticline.

The most frequent structure occurring in the Caldeirão syncline area, is a **S_1** slaty cleavage parallel to the **S_0**, which in turn, is folded and form meter-scale open-close symmetrical folds with sub-horizontal axis correlative to F1 phase of Ruiz et al. (2007) (Fig. 5.2-3). Pole to plane stereogram for the **S_1**foliation shows girdle like pattern reflecting the regional folding (Fig. 5.2-3). A second pattern of folding is characterized by asymmetrical-monoclinal folds observed only in few outcrops of fine-grained metasedimentary rocks occurring on the eastern flank of the Caldeirão syncline. It is correlated to the folds of **F$_2$** compressive phase described by Ruiz et al. (2007) and as described by the authors it comprises centimetric-scale folds with axial plane foliation dipping at low angle (~30º) to SW (Fig 5.2-3).

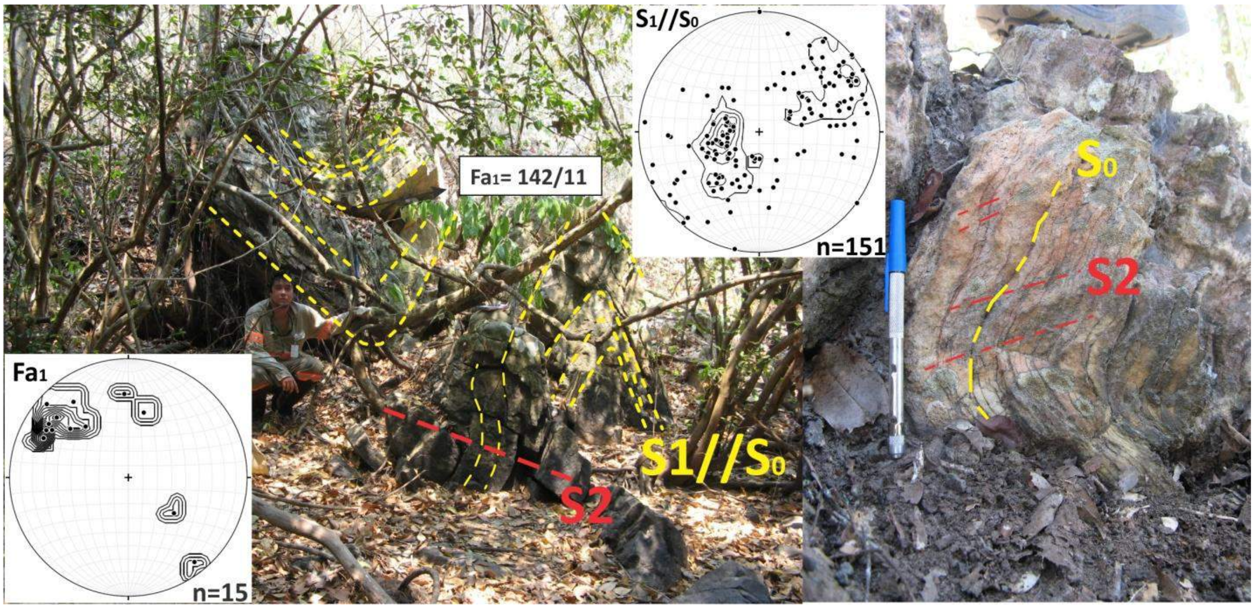

Figure 5.2-3: Structural features occurring on central and northern portion of mapped area: On the left, symmetrical folds of (P1) phase occurring on western flank of Caldeirão syncline. On the right, assymmetrical gentle fold of the (P2) phase occurring on eastern flank of Caldeirão syncline. On the top, pole of plane diagram for S1 foliation showing a girdle like pattern and on the bottom, diagram of fold axis formed during the P1 phase.

The Cágado anticline (Fig. 5.2-4) is the host structure of Ernesto Mine and more than nine other gold deposits. It has been interpreted as a gentle upright dipping fold with axis plunging at low-intermediate angle to NW.

The center of the structure is eroded exposing the basement, composed by tonalite. The contact between the basement and the sedimentary rocks is characterized by 3-10 meter thickness mylonitic zone called Morro Solteiro shear zone (Fernandes et al., 2005c). It was formed by the thrusting of the sedimentary package over the basement and is marked by a mylonitic foliation (**S$_2$**). Despite the nearly regular dip angle of about 45º it has variable atittude depending on which part of the strucutre the foliation is being measured. Some of gold deposits in the area, such as the lower level of Ernesto Mine evolved along the contact and seems to be associated to the evolution of the shear zone and likewise the mineralized zone of Pau-a-Pique, the fine crushed mylonite of the contact was tranformed to muscovite schist that hosts quartz boudins of sigmoidal shape.

Other structural features associated within the Cagado anticline are in many aspects similar to those found in the Caldeirão syncline such as symmetrically folded S_0, best exposed in fine grained metasedimentary rocks.

The third phase (**P_3**), given by gentle folds with subvertical axial plane dipping to SE or NW is not a structural feature easily observable in such portion of the area. However the regional gentle bending of the Caldeirão syncline axis seems to be related the last deformational feature registered in the area.

5.2.4. Disccussion

As mentioned above the structures occurring in the mapped area can be grouped into three deformational phases evolved during a unique compressive event.

In the first phase (**P_1**) were formed symmetrical upright NW plunging folds, observable in different scales (macroscopic and regional scale). As mentioned above such structures are characterized by folding of S_0 through. As the deformation progresses the strain evolved from folding to shearing and thrusting. Such change on deformational pattern configures the **P_2** deformational phase. In areas where strike-slip shearing is predominant (e.g. on southern portion) the deformation is represented by a series of oblique subvertical shear zones. Folds formed in the innitial stages of deformation evolved to subvertical shear zones with oblique strike slip movement responsible for formation of stretching lineation on shear zones. In the portions where thrusting predominate, subhorizontal shear zones occurs on contact between the metasedimentary rocks and the basement rocks. In the metasedimentary package the **P_2** deformational phase is recorded as asymmetrical gentle to open folds with axial planar foliation dipping at low angle to SW. On northern AGGP, in São Vicente Mine the main deformational phase is marked by thrusting of the sediments over the basement and by inverse faulting giver by the rupture of fold flanks as described by Scabora and Duarte (1998). It seems to be correlative to inverse fault zones occurring in the marginal portions of São Francisco mineralized zone as described by Morales (2007).

The third phase (P3) is more evident on southern mapped area. It is characterized by gentle folds occurring along shear zones with subvertical axial plane dipping to SE or NW. On central and northern the gentle bending of Caldeirão syncline is interpreted as evidence for such deformational phase.

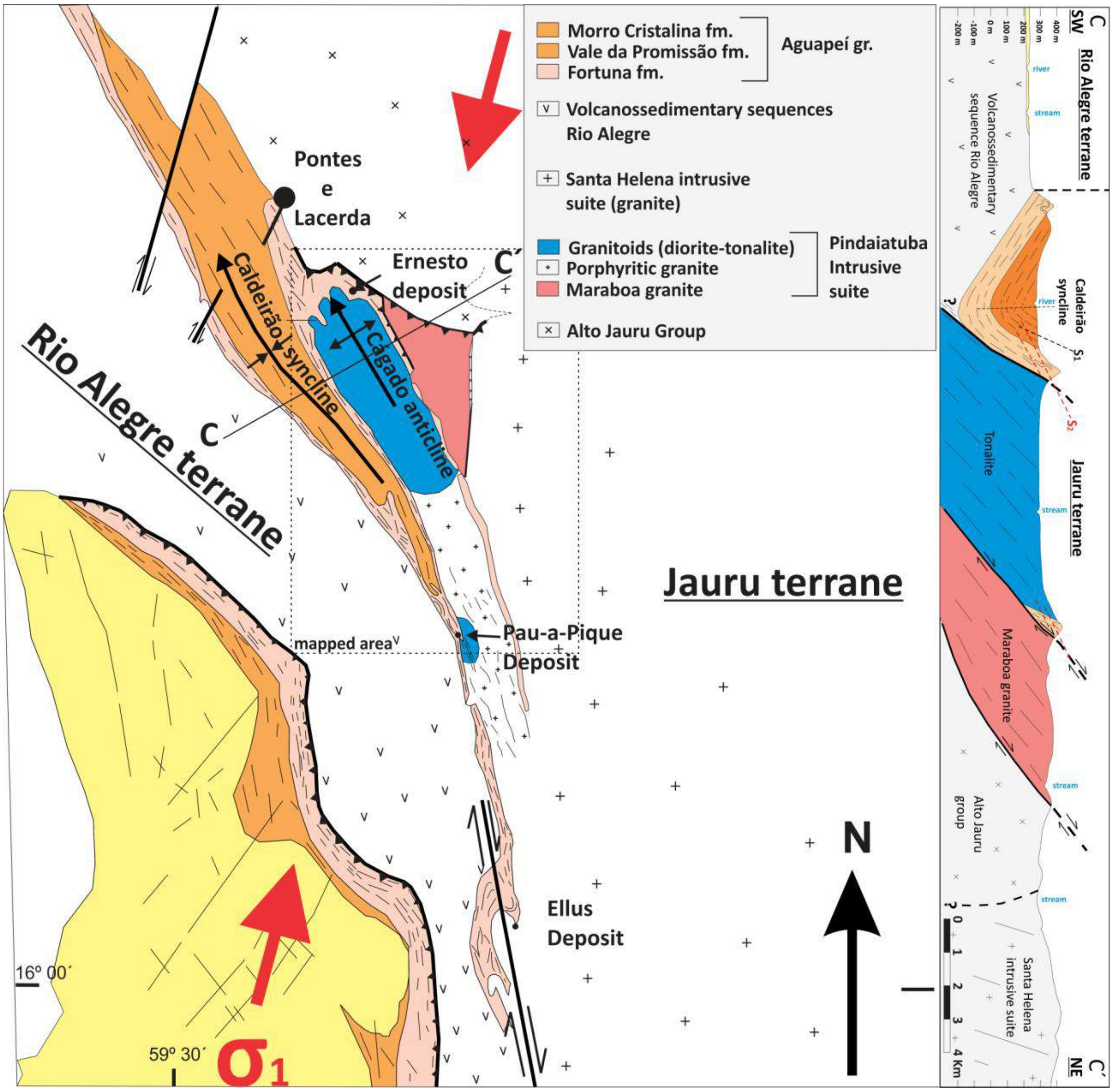

Figure 5.2-4: Schematic geological map and cross-section of the area with the proposed position of shortening direction. Geological map modified from Fernandes et al. (2006).

In short, there is plenty of evidences suggesting that the Aguapeí belt deformation evolved by a system of shear zones formed by reactivation of older strctures as proposed Rizzoto et al. (2013). At the studied area the contact between two major terranes (Rio Alegre and Jauru terranes) are covered by deformed metasedimentary rocks of Aguapeí group and the deformation pattern show evidences of strong shearing on the main control of deformation.

Considering the structural pattern on mapped area the most suitable direction for the shortening seems to be a SSW-NNE direction. The positioning of $\boldsymbol{\sigma_1}$ in a SSW-NNE direction could explain most of structures occurring in the area such as the alloctony of the sedimentary package over the basement in the northen portion of the mapped area, as reported by Fernades et al. (2005c). Such position for shortening direction also find support on general dextral movement recorded by kinematic indicators along the Aguapeí belt and also explain major strike-slip faults such as Ellus fault (Fig. 5.2-4).

5.3. Metamorphism of Aguapei belt

Previous works reported a low-grade regional metamorphism for the Aguapeí belt (Scabora and Duarte, 1998; Leite and Saes, 2000; Fernandes et al., 2005a; Ruiz et al., 2007). It is from general agreement that the evolution of Aguapeí belt has recorded low grade metamophism in the greenschist facies. However none of the previous studies about the Aguapeí belt has foccused on investigation of the metamorphic conditions recorded along the belt.

As the main goal of this research is the study of the relationship between the metamorphism and the hydrothermal process that led the formation of gold deposits of AGGP (Pau-a-Pique and Enesto's intermediate level) we present below the petrographic aspects of the metamorphosed rocks and use some of the geothemobarometry tecniques to estimate the temperature and pressure of the metamorphic peak.

5.3.1 Petrography

The basement rocks

As mentioned before, the basement of Aguapeí groupcomprises a large variety of rocks that include volcanosedimentary sequences and granitic suits of both Jauru and Rio Alegre Terrane. These rocks were partially affected by the deformation and metamorphism resulted from crustal thickening during the Sunsas Orogeny and together with the metasedimentary rocks of Aguapeí group it comprises the Aguapeí belt.

Most of the basement rocks arecovered by thick layer of lateritic soil, specially those of mafic composition, being it a limiting on studding the effects of metamorphism over these rocks as well as the mapping of the lateral extension of the metamorphic effects of Aguapeí belt.

In the studied area, the basement of the Aguapeí group mostly comprises granites and granitoids of the Jauru Terrane on eastern portion of the area and volcanosedimentary sequences of Rio Alegre terrain on western.

It is from general sense that Pau-a-Pique area seems to record the highest metamorphic condition among most of studied portions of Aguapeí belt. It is due to the presence of ductile shear zones affecting both the basement and metassedimentary rocks. The presence of an underground mine in the area and the availability of non-weathered drill core samples makes

Pau-a-Pique a key area to explore the effects of metamorphism over the basement rocks as indicative of the highest metamorphic conditions reported along Aguapeí belt. Most of the basement rocks cropping in the studied area comprises felsic granites that in general are not sensible to metamorphic changes under low grade condition meanwhile mafic diorites are commonly reported on the hangwall of Pau-a-Pique deposit.

The basement of Pau-a-Pique deposit comprises deformed and metamorphosed igneous rocks here interpreted as part of Pindaituba intrusive suite (Ruiz, 2005; Bettencout et al., 2010). It has been generically classified as a tonalite intrusion (e.g. Geraldes et al., 2001; Fernades et al., 2005b; Fernades et al., 2006; Ruiz 2005), however petrographic studies supported byX-ray fluorescence analysis has shown a much larger variety of granitoids. The SiO_2 content in these rocks vary from 46.30 wt% to 67.60%. meanwhile the increase in Na_2O and K_2O grades tend to roughly follow the increase in SiO2 rocks. These rocks chemically range from basic to acid composition (Fig. 5.3-1) and such a chemical trend is suggestive of a single magmatic suite.

Coarse-grained diorite is the most frequent igneous facies, however andesite with porphyritic textures, fine-grained diorite, tonalite and granodiorite are also reported (Fig. 5.3-1). The deformation, given by shearing, has erased most of the igneous texture in many of studied samples, however few examples of well preserved meta-granitoids has been found in drill core samples being preserved from shearing by being set in low deformed zones between the shear zones.

Metadiorite and metandesite

The mineral phases of the metadiorites are amphibole, biotite, plagioclase, chlorite, epidote, quartz and carbonate. Rutile, titanite and zircon are frequent accessory minerals. The composition ofplagioclase vary from albite to oligoclase (An 9-20). It occurs in two forms, as small anhedral crystal or as medium to large porphyry crystals with albite twining (Fig.5.3-2d). The largest crystals are often covered bysmall crystals of epidote and biotite.Biotite has brown to light-brown pleochroism, and is often associated with chlorite amphibole in the matrix or with epidote when it occurs over plagioclase crystals.

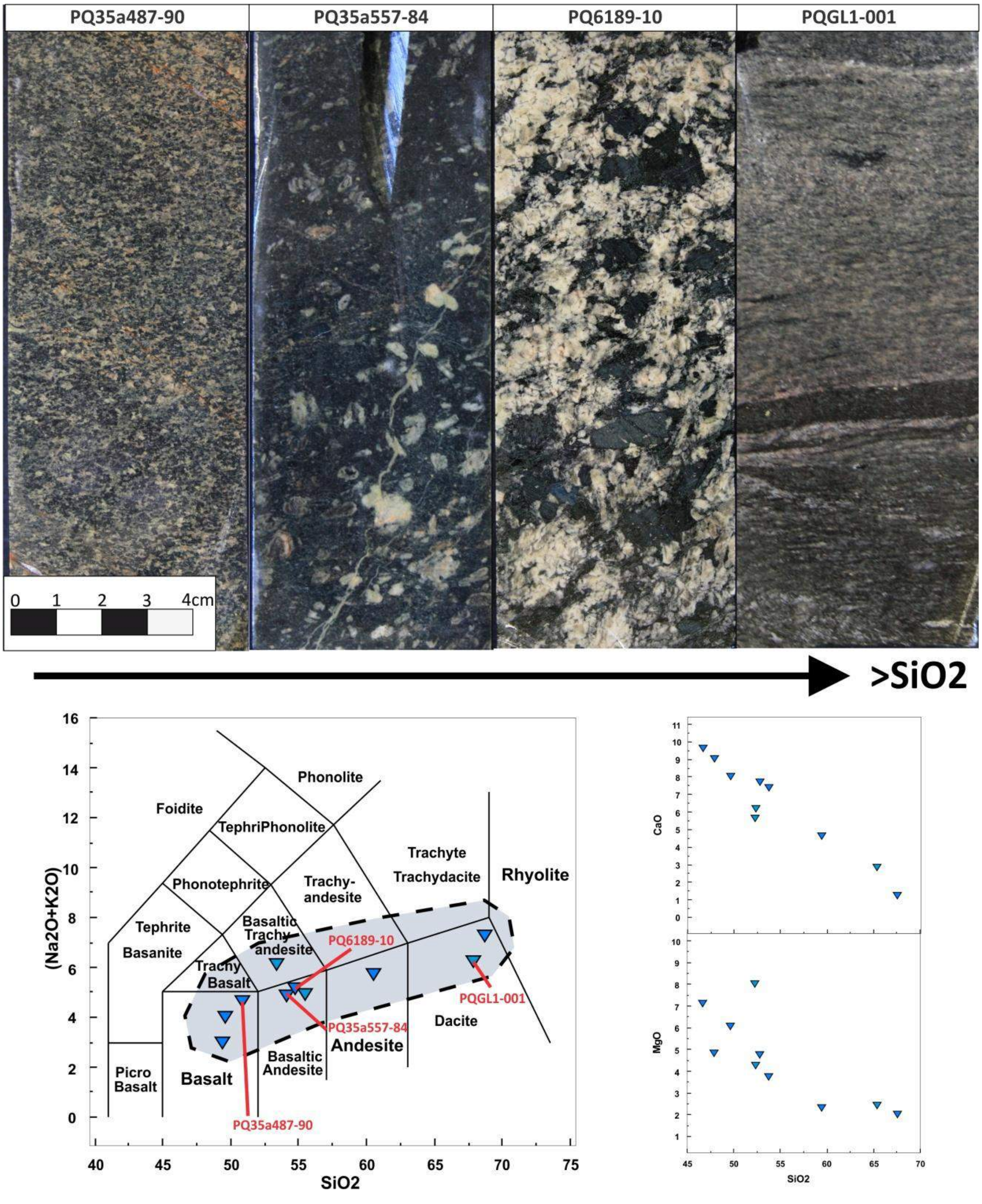

Figure 5.3-1: Textural and chemical variation of granitoids occurring in the basement of Pau-a-Pique basement.

Mafic igneous rocks, including basalts and mafic diorite has typical metamorphic assemblage that can be useful in defining the intensity of metamorphism within the metamorphic facies concept (Bucher and Grapes, 2011). According to Spear (1993) metamorphosed mafic rocks are particularly susceptible to changes in T and P. However despite of metamorphic facies concept being based on the metamorphism of mafic rocks the use of such rocks in determining the metamorphic conditions is less quantitative then that of pelite composition. According to the author the reasons are twofold, firstly basalts are chemically complex and require a large number of components to describe the chemical system. There are no rigorous projections that can be used as for pelites and therefore, the chemical system and phase relations are difficult to depict graphically. Secondly, a relative few minerals are encountered in metabasites, the most common one being amphibole, which can display a very wide range of chemical composition.

As mentioned above some of the metaigneous rocks occurring in the basement of Pau-a-Pique deposit include mafic diorite and andesite and such rocks seems to be useful on obtaining petrographic information about the metamorphic conditions. However most of examples on literature are based on metabasites and the exact metamorphic transformations in dioritic rocks has been neglected in most of text books. In spite of that some considerations can be made based on specific mineral transformations.

Plagioclase

According to Spear (1993) the characteristic assemblage of metabasites in the greenschist facies is Chl + Ab + Act + Qtz ± Cb (Cal, Dol, or Ank) ± Ttn and the characteristic assemblage in the amphibolite facies is Hbl + Pl (± Qtz ± Rt). The transition from greenschit to amphibolite facies therefore involves several important mineralogical changes. The plagioclase changes composition from albite to oligoclase, since the plagioclase displays a pronounced miscibility gap between albite and oligoclase which is called the peristerite gap. Because of this gap, plagioclase compositions do not change smoothly from greenchsit to amphibolite facies and its is not uncommon to find both albite and oligoclase existing in the same rock.

The calcification of plagioclase involves the dehydration of zoizite (Ep) into an anorthite component through the reaction: Zo + Qtz = An + H_2O (Spear 1993). The anorthite component dissolves into the existing plagioclase and the resultant feldspar is more calcic. The fisrt appearance of oligoclase is usually a good indicator of metamorphic grade and can be mapped as an isograde that defines the oligoclase zone (Spear 1993).

Obviously the presence of oligoclase in metabasalts is a clear evidence of metamorphism in the amphibolite facies since the original igneous plagioclase in such rocks is labradorite, therefore much more calcic. When, however, it involves rocks of dioritic composition, in which the typical plagioclase may vary from oligoclase to andesine, the presence of oligoclase must generate doubts about its metamorphic origin.

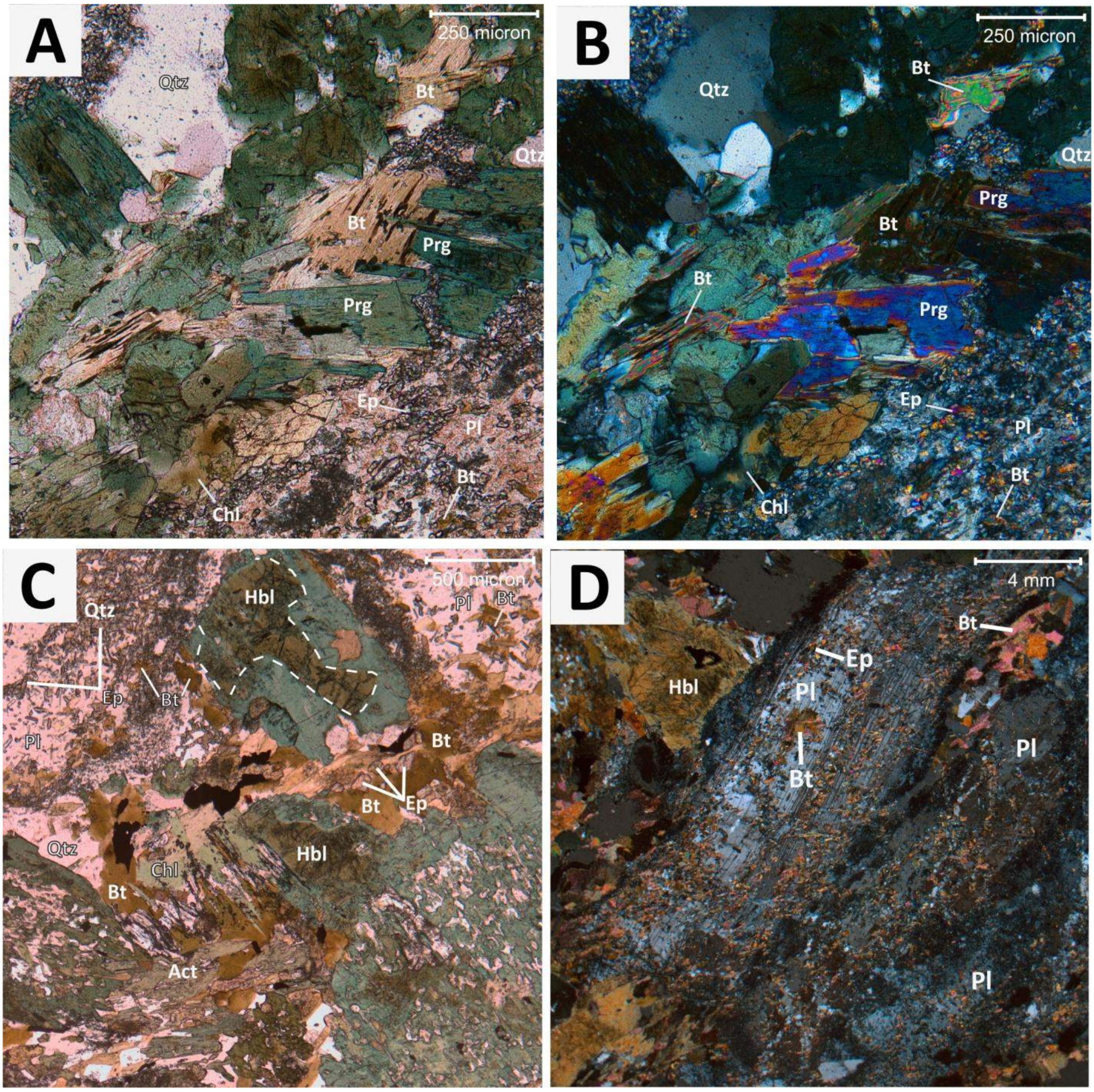

Figure 5.3-2: Petrographic aspects of diorites occurring in the basement of Pau-a-Pique. (A) and (B): textural aspects and mineral assemblage of fine-grained dioirte (PQ35a487-90), showing greenish blue pargasite associated with cholrite biotite; (C): Coarse grained diorite showing large crystals of amphibole with core of magmatic hornblende bordered by green amphibole of metamorphic origin; (D): Large deformed crystal of plagioclase showing in a texture that resembles magmatic; (E): Petrographic aspect of a fine grained diorite (on left), and detail of a large amphibole with texture of given by Mg-Hornblende in the core and pargasite in the rim as evidenced by the EDS spectra.

The composition of plagioclase in mafic diorites and andesites of the area vary from albite An_9 to oligoclase An_{20} as showed by microprobe analysis (PQ35a557-84) (Fig. 5.3-3). In many of the low deformed samples the original igneous texture is preserved and plagioclase maintained the characteristic phenocrystal texture and subhedral shape (Fig. 5.3-2d) however the innitial igneous compositions (typically andesine) have changed to a more Na composition (albite to oligoclase) as evidenced by microprobe analysis (Fig. 5.3-3) suggesting that recrystallization involved change of composition preserving the igneous texture in some cases. At the same time, the presence of oligaclase and albite can be interpreted as evidence of metamorphic condition on greenschist-amphibolite facies transition since such low Ca content (An<21) in oligoclase, not the expected for plagioclase occurring in mafic diorites, show a gap in composition suggestive of peristerite gap.

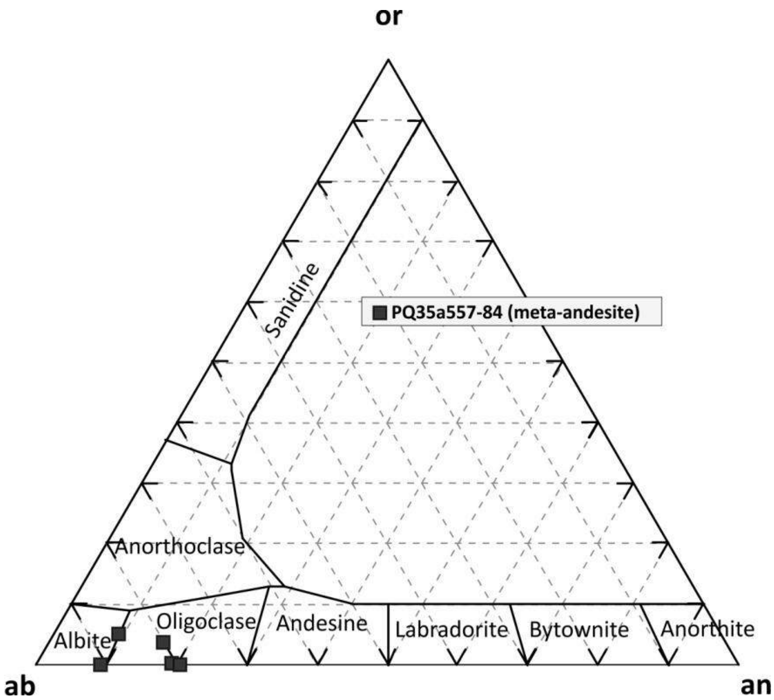

Figure 5.3-3: Diagram of plagioclase classification (Albite-Anorthite-orthoclase). It shows the composition of plagioclase of mafic diorite ranging from albite to oligoclase suggesting the presence of peristerite gap.

Biotite

A good indicative of metamorphic conditions of the uper greenschist to greenschist - amphibolite conditions is the presence of biotite. According to (Bucher and Grappes 2011) muscovite (K-white mica, sericite, phengite) is the most common K-bearing mineral in low grade metamafic rocks and this is also true for the lower greenschist facies, however, in the midle of greenchist facies (~400ºC), Bt appear for the first time replacing K-white mica. The biotite formation in metamafic rocks in the upper greenschist facies can be modeled by the following reactions:

$16Tr + 25Ms = 25Phl + 16Czo + 1Chl + 77 Qtz + 4 H_2O$ **(1)**

$4Tr + 6Chl + 25Cel = 25Phl + 4Czo + 63Qtz + 26H_2O$ **(2)**

$9Tr + 2Cal + 15Ms = 15Phl + 10Czo + 42Qtz + 2CO_2 + 4H_2O$ **(3)**

According to Bucher and Grapes (2011) the equilibrium of reaction (1) is close to 600ºC in pure KCMASH system and it is rather pressure insensitive however for real mineral composition of greenschist facies rocks, the formation of biotite from reaction (1) takes place around 400ºC. The color of the first biotite that appears during prograde metamorphism of mafic rocks is often green and it is indicative of high Fe^{3+} and low Ti content. Reaction consuming Celadonite component in K-white mica (2) is also possible for biotite-bearing metamafics, but it leaves behind a white-mica component that is closer to the Ms end-member composition. Other possible reaction involves carbonate (3) in which actinolite, carbonate and K-white mica reacts to form epidote and biote. In short, according to the authors, biotite forms in metamafics at about 400-450ºC and k-white micas is typically celadonitic (Phe, Ser) in low grade rocks and become more muscovitic (Ms) at the upper limit of the greenschist facies. The small amount of K_2O in mafic rocks is usually bound in K-white mica bellow 400ºC in Bt at temperatures above 400ºC, and there is little overlap of the two micas.

In the low deformed diorites of the area, biotite is the only K-bearing mica reported and is typically brown indicating its high level of Ti. There are no K-white micas over the plagioclase as commonly occurs in metamafics formed in greenschist facies, instead of it there is biotite which is indicative that K-white mica reacted to form biotite as modeled by the recation (1) and (3) at temperature above 400ºC.

Amphibole

Again most of the models involving metamorphism of metamafic rocks are based on metamorphic transformation occurring in basalts and gabbros. In such rocks the presence of actinolite and/or hornblende is a clear indicator of the metamorphic conditions. Because diorite is generally a hornblende-bearing igneous rock some care must be taken during petrographic studies to identify whether hornblende is a metamorphic product or an igneous relict.

In the greenchist amphibolite facies transition zone, the calcic amphibole change its composition from actinolite to hornblende. According to Spear (1993) most of the compositional variability of calcic amphiboles in medium grade metamorphic rocks takes place along an exchange that is part way between the pargasite exchange ($NaAl^{VI}Al^{IV}_2 = \square MgSi_2$) and the tschermaks exchange ($MgSi = Al^{IV}Al^{VI}$ or $FeSi = Al^{IV}Al^{VI}$), and increase in metamorphic grade from low grade (greenschist facies) transform the calcic amphiboles (actinolite) with only negligible Al and Na ($\square Ca_2Mg_5Si_8O_{22}(OH)_2$) into hornblende, which contains considerable Al and Na ($Na_{0.3}Ca_{1.8}Na_{0.2}(Fe,Mg)_{3.4}Al_{1.6}Si_{6.3}Al_{1.7}O_{22}(OH)_2$). According to the author during the change in amphibole composition a complicating factor is that amphiboles do not typically show a complete solid solution between actinolite and hornblende, but rather display a miscibility gap and because that these two minerals are often observed togheter in multual contact in rocks of amphibolite to greenschist facies trasition zones.

According to Deer et al. (1997), actinolite and Fe-pargasite may form pseudomorphs after clinopyroxene that, in some cases, are single crystals with actinolite and Fe-pargasite in optical continuity, in other polycrystilline felted intergrowth with sharp boundaries between the two domains. According to the author mass balance calculations show that the magmatic-Fe hornblende could break down almost isochemically to an iron-rich actinolite and Fe-pargasite, and the absence of actinolite is considered to be due to its stability in these bulk compositions.

The amphiboles present in the diorite and andesite of the area show a complex relationship. In coarse-grained diorites (e.g. PQ6189-10) some of largest crystals of amphibole often show a petrographic texture given by greenish brown to yellow core bordered by greenish yellow to greenish blue amphibole (Fig. 5.3-2c).

Since diorite is a hornblende-bearing igneous rock it was expected that these cores would represent magmatic hornblende being transformed into low Al amphibole (Actinolite) during greenschist metamophism. However a detailed petrographic study supported by Electron Microscope and EDS analysis hasn't shown a significant reduction on Al content from core to rim, instead of it, in most of the analyzed crystals, the Al content seems to be slightly higher in some portions of the rim, incompatible with the actinolite composition (Fig. 5.3-4).

Microprobe analysis of amphiboles present in a meta-andesite sample (PQ35a557-84) showed large range of composition with large variations on the content of Al, Si, Mg and Fe (Fig. 5.3-5). The results were treated and the structural formula were calculated based on recommended criteria adopted by IMA-2012 (Hawthorne et al., 2012). The calculations were made using an available spreadsheet developed by Locock (2014). The results supports the existence of three types of amphiboles occurring in the rock, an igneous Mg-hornblende and actinolite and pargasite.

The structural formula of one of each type of amphibole is presented bellow being **(1)**= Mg-hornblende; **(2)**= actinolite; **(3)**= pargasite. The ions are assigned to the general formula $\mathbf{AB_2C_2T_8O_{22}W_2}$, where the occupancy of the sites by cations and anions follow the priority given by A = □, Na, K, Ca, Pb, Li; B = Na, Ca, Mn^{2+}, Fe^{2+}, Mg, Li; C = Mg, Fe^{2+}, Mn^{2+}, Al, Fe^{3+}, Mn^{3+}, Ti^{4+}, Li; T = Si, Al, Ti^{4+}, Be; W = (OH), F, Cl, O^{2-}.

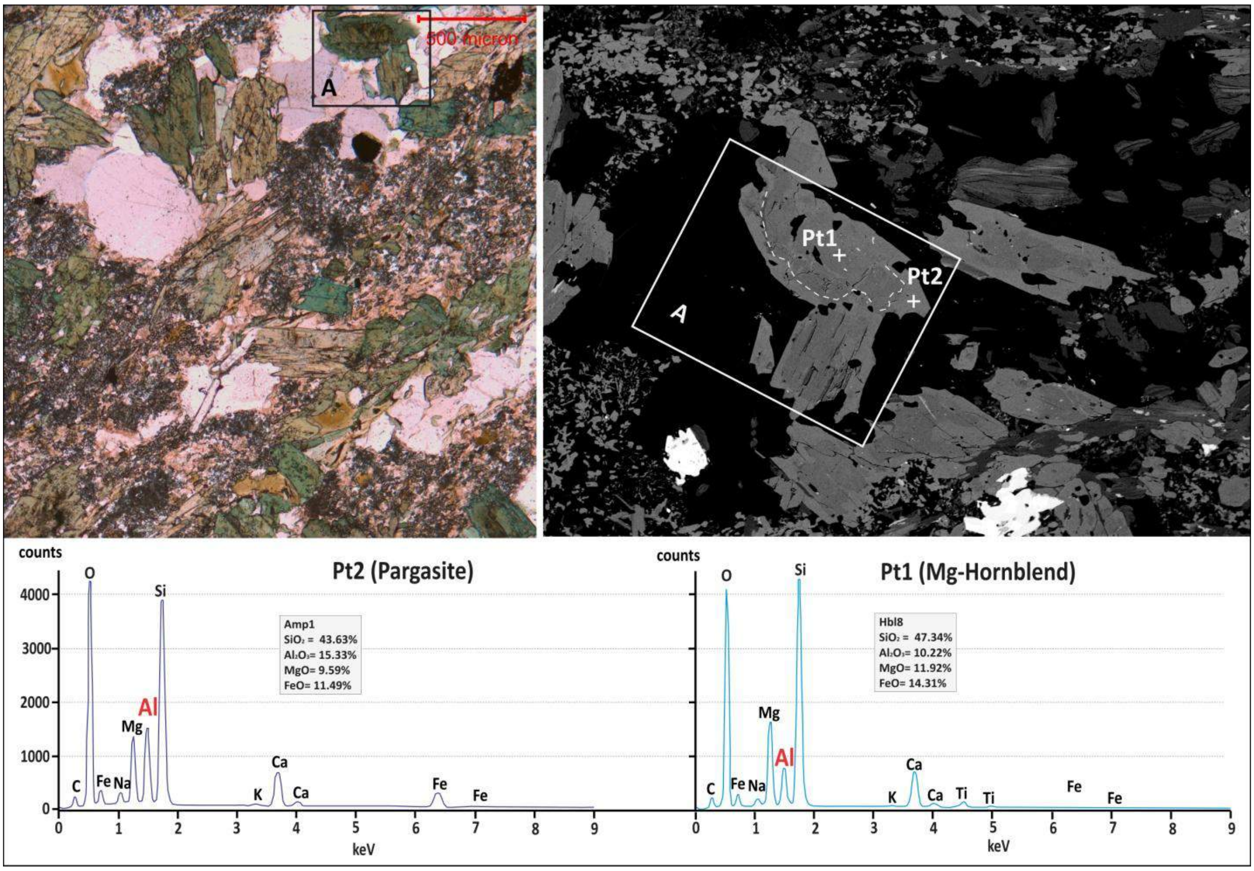

Figure 5.3-4: Petrographic aspect of a fine grained diorite (on left), and detail texture of a large amphibole crystal using electron microscope and EDS showing a texture given by Mg-Hornblende in the core and pargasite in the rim as evidenced by the EDS spectra on the bottom.

$$(Na_{0.36}K_{0.041})\ (Ca_{1.854}Mn_{0.076}Fe_{0.07})\ (Mg_{2.688}Fe^{2+}_{1.611}Al_{0.616}Fe^{3+}_{0.056}Ti_{0.029})\ (Si_{6.869}Al_{1.131})\ O_{22}\ (OH)_2\mathbf{(1)}$$

$$(Na_{0.115}K_{0.011})\ (Ca_{1.877}Mn_{0.066}Fe_{0.053}Na_{0.003})\ (Mg_{3.589}Fe^{2+}_{1.182}Al_{0.214}Ti_{0.015})\ (Si_{7.634}Al_{0.366})\ O_{22}\ (OH)_2\mathbf{(2)}$$

$$(Na_{0.466}K_{0.08})\ (Ca_{1.798}Fe_{0.097}Mn_{0.07}Na_{0.036})\ (Mg_{2.088}Fe^{2+}_{1.848}Al_{1.012}Ti_{0.053})\ (Si_{6.373}Al_{1.627})\ O_{22}\ (OH)_2\mathbf{(3)}$$

The chemical composition and structural formula of the analyzed amphiboles is detailed in the table 5.3-1.

Petrographic studies in the fine-grained mafic diorite (PQ35a487-90) supported by EDS analysis did not identify the presence of actinolite in these rocks, and most of amphiboles present with actinolite like textures (acicular shape) show pleocroism from greenish yellow to greenish blue and when analyzed by EDS it shows elevated Al content, suggesting of pargasitic composition. In fact actinolite is not easily found in the studied rocks but it is present as evidence by the microprobe analysis (PQ35a557-84). It is of difficult identification using only petrographic thecniques, because it probably is in optical continuity with Fe-pargasite or forming polycrystalline intergrowth as mentioned above.

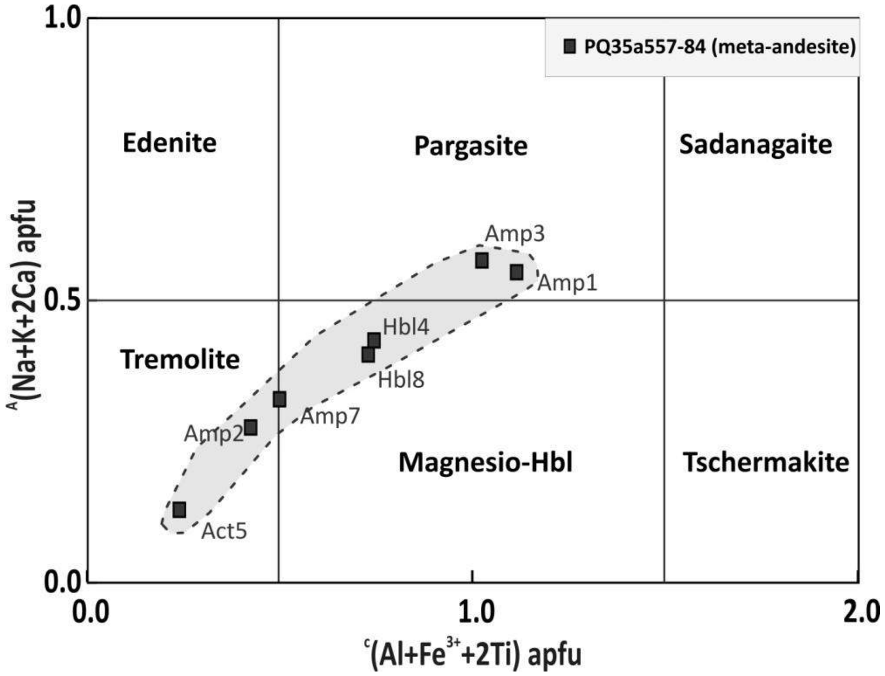

Figure 5.3-5: Diagram of amphibole classification (Hawthorne et al., 2012) showing the large variation in composition of amphiboles occurring in a sample of metandasite from the studied area.

From the petrographic aspects and chemical composition of amphiboles occurring in mafic diorites and andesites from Pau-a-Pique basement it is possible to suggest that the metamorphic conditions (P-T) has reached greenschist - amphibolite facies trasition, in which igneous amphibole (recorded in the core of some large crystals) reacted to form actinolite and Fe-pargasite and temperature in this case was above 400ºC.

It is supported by the fact that both, Low-Al amphibole and Al-rich amphibole are present in some of the samples. It is also coherent with the presence of oligoclase and albite and the presence of biotite.The absence of actinolite in the fine-grained rocks is suggestive that locally the bulk composition could have reached its stability.

Considering the assemblage given by actinolite-pargasite, epidote, bioitte, oligoclase-albite the temperature range for such rocks could be rougly estimated a range between 450 and 500ºC coincident with the greenschist amphibolite facies trasition (Fig. 5.3-6).

Table 5.3-1: Calculated structural formula for amphiboles from Pau-a-Pique basement (PQ35a557-84).

Sample	PQ35a557-84	PQ35a557-84	PQ35a557-84	PQ35a557-84	PQ35a557-84	PQ35a557-84	PQ35a557-84
Analyse	Hbl4	Hbl8	Amp2	Amp7	Act5	Amp1	Amp3
SiO2	47.01	47.34	50.77	50.43	53.74	43.63	43.35
TiO2	0.31	0.27	0.19	0.19	0.14	0.48	0.42
Al2O3	10.47	10.22	6.35	5.78	3.47	15.33	14.39
MnO	0.49	0.62	0.63	0.59	0.55	0.56	0.60
FeO	15.13	14.31	13.02	19.11	10.40	15.92	16.02
MgO	12.04	12.43	14.52	10.76	16.95	9.59	9.72
CaO	11.89	11.92	12.06	9.00	12.33	11.49	11.25
Na2O	1.35	1.28	0.89	2.01	0.43	1.77	1.81
K2O	0.27	0.22	0.15	0.18	0.06	0.43	0.39
F	0.00	0.00	0.00	0.00	0.00	0.00	0.00
Cl	0.00	0.00	0.00	0.00	0.00	0.00	0.00
Initial Total	98.95	98.61	98.57	98.05	98.06	99.19	97.94
T (ideally 8 apfu)							
Si	6.82	6.87	7.30	7.46	7.63	6.37	6.42
Al	1.18	1.13	0.70	0.55	0.37	1.63	1.58
T subtotal	8.00	8.00	8.00	8.00	8.00	8.00	8.00
C (ideally 5 apfu)							
Ti	0.03	0.03	0.02	0.02	0.02	0.05	0.05
Al	0.62	0.62	0.37	0.46	0.21	1.01	0.94
Fe3+	0.06	0.06	0.02	0.00	0.00	0.00	0.00
Fe2+	1.68	1.61	1.48	2.15	1.18	1.85	1.87
Mg	2.61	2.69	3.11	2.37	3.59	2.09	2.15
C subtotal	5.00	5.00	5.00	5.00	5.00	5.00	5.00
B (ideally 2 apfu)							
Mn2+	0.06	0.08	0.08	0.07	0.07	0.07	0.08
Fe2+	0.09	0.07	0.07	0.22	0.05	0.10	0.12
Ca	1.85	1.85	1.86	1.43	1.88	1.80	1.79
Na				0.28	0.00	0.04	0.02
B subtotal	2.00	2.00	2.00	2.00	2.00	2.00	2.00
A (from 0 to 1 apfu)							
Na	0.38	0.36	0.25	0.29	0.12	0.47	0.50
K	0.05	0.04	0.03	0.03	0.01	0.08	0.07
A subtotal	0.43	0.40	0.28	0.33	0.13	0.55	0.57
O	22.00	22.00	22.00	22.00	22.00	22.00	22.00
OH	2.00	2.00	2.00	2.00	2.00	2.00	2.00
Sum T,C,B,A	**15.43**	**15.40**	**15.28**	**15.32**	**15.13**	**15.55**	**15.57**
Mg/(Mg+Fe2+)	0.60	0.62	0.67	0.50	0.74	0.52	0.52
Tsi	6.82	6.87	7.30	7.46	7.63	6.37	6.42
Species	**magnesio-hornblende**	**magnesio-hornblende**	**actinolite**	**magnesio-hornblende**	**actinolite**	**pargasite**	**pargasite**

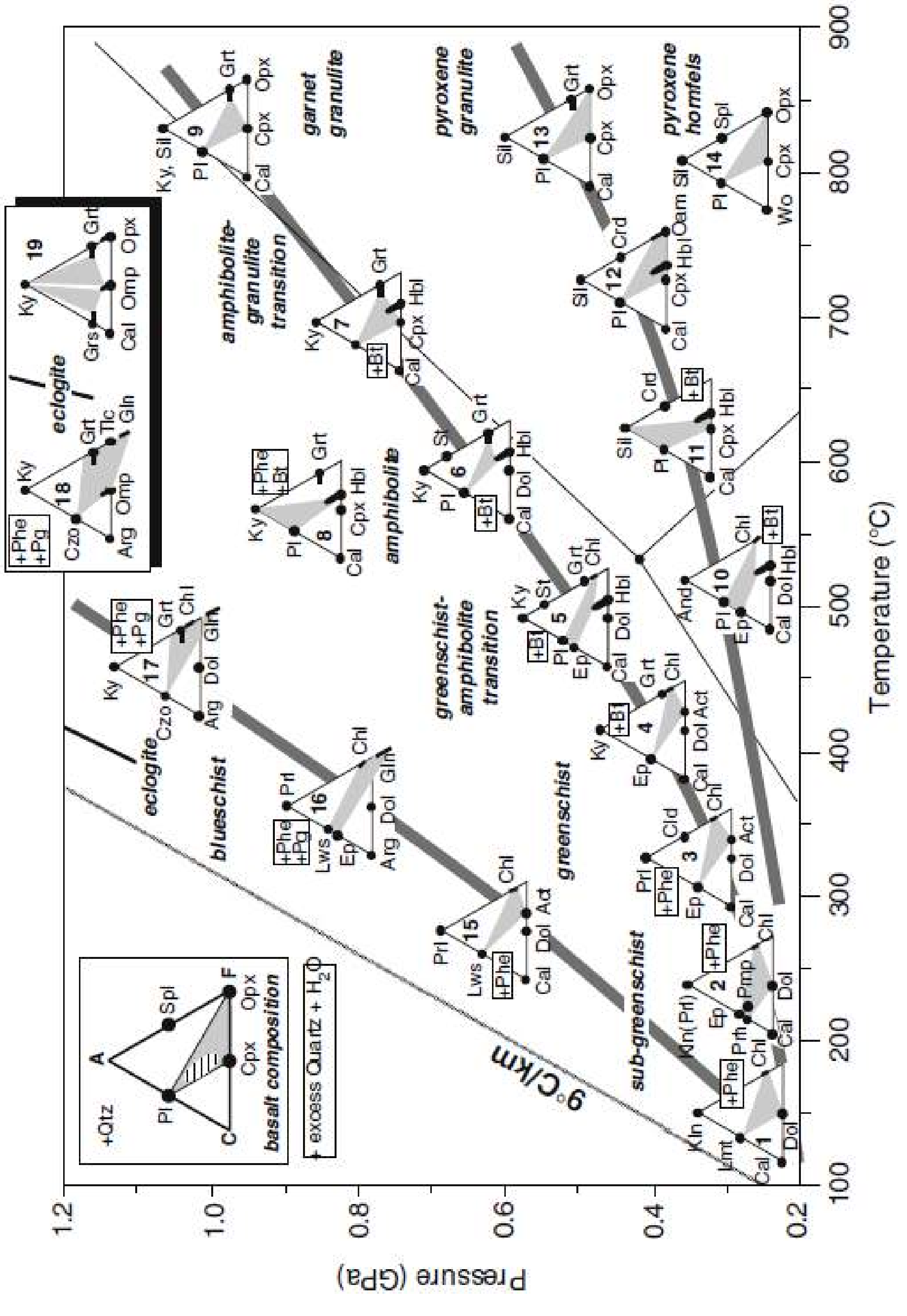

Figure 5.3-6: Metamorphism of mafic rocks (metabasalts) represented by ACF diagrams to ilustrate the phases transformation during metamorphism of mafic rocks (Extracted from Bucher and Grapes, 2011).

Tonalite and granodiorite

Non deformed tonalite and granodiorite seems to be less frequent, if compared to theo ccurrence of mafic diorite and andesite. Few examples of low deformed tonalite were observed in drill core samples from drill holes executed in the south portion of the deposit. However most of studied samples of tonalites and granodiorites is deformed by shearing and generally constitutes fine-grained gneiss of grey color. Compositional banding eventually occurs in zones where these rocks are deformed. These compositional banding are given by irregular layers of light-grey gneissintercalated with dark layers of biotite schist (Fig. 5.3-1).In fact, layers of biotite schist isa distinctive feature of the high deformed zones in Pau-a-Pique basement. However it is difficult to precise whether it is more common to a particular lithologic type (tonalite-granodiorite) or not, although the occurrence of such layers seems to be more frequent where felsic rocks are dominant.

The mineralogical composition of tonalites and granodiorites are given by Pl (oligoclase) + Qtz+ Bt + Ep + Rt ± Kfs ± Chl ± Amp ± Ttn ± Ms ± Mag ± Carb. The amount of Kfs vary from 0 (in tonalite) to 15% (in granodiorite). Amphibole is not always present, being biotite, the most frequent mafic mineral in non-deformed tonalite. When amphibole is present the amount rarely exceeds 5% of the modal composition. Chlorite is always associated with biotite and, like epidote, it seems to be more frequent in deformed rocks (Fig. 5.3-7c,d).

Muscovite was observed only in rocks that were subjected to medium to high deformation (PQGL1-001), in such rocks magnetite is also present and the Ti-rich mineral is rutile.

Quartz-feldspatic granitoids (granodiorite and tonalites) are helpless in metamorphic studies. The main constituent of these rocks - Qtz, Kfs, Pl, Bt, Ms, Hbl occurs over a wide range of P-T condition. These rocks enter the metamorphic realm in a predominantly dry state and thus like mafic rocks, in order for metamorphic reactions to begin, hydration, often significant amount, is necessary (Bucher and Grapes, 2011). Significant phase changes in such rocks will occurs only at high conditions of pressure and temperature. Generally under dry conditions and non-penetrative deformation granitiod rocks remain almost unchanged until the melting point is reached. In the absence of penetrative deformation primary igneous texture and structure are well preserved in metagranitoid rocks, even when subjected to UHP metamorphism (Bucher and Grapes, 2011).

In fact very small information about metamorphim can be obtained from the undeformed and low deformed felsic rocks. Some of the samples has more than 90% of its composition formed by plagioclase, quartz and biotite (Fig. 5.3-7a,b). The plagioclase is also helpless since oligoclase is the most common plagioclase in felsic rocks and thus do not support any precise inference about the metamorphic conditions. Considering that, no attempts were made to go further on analyzing the metamorphic conditions of low deformed tonalites and granodiorites.

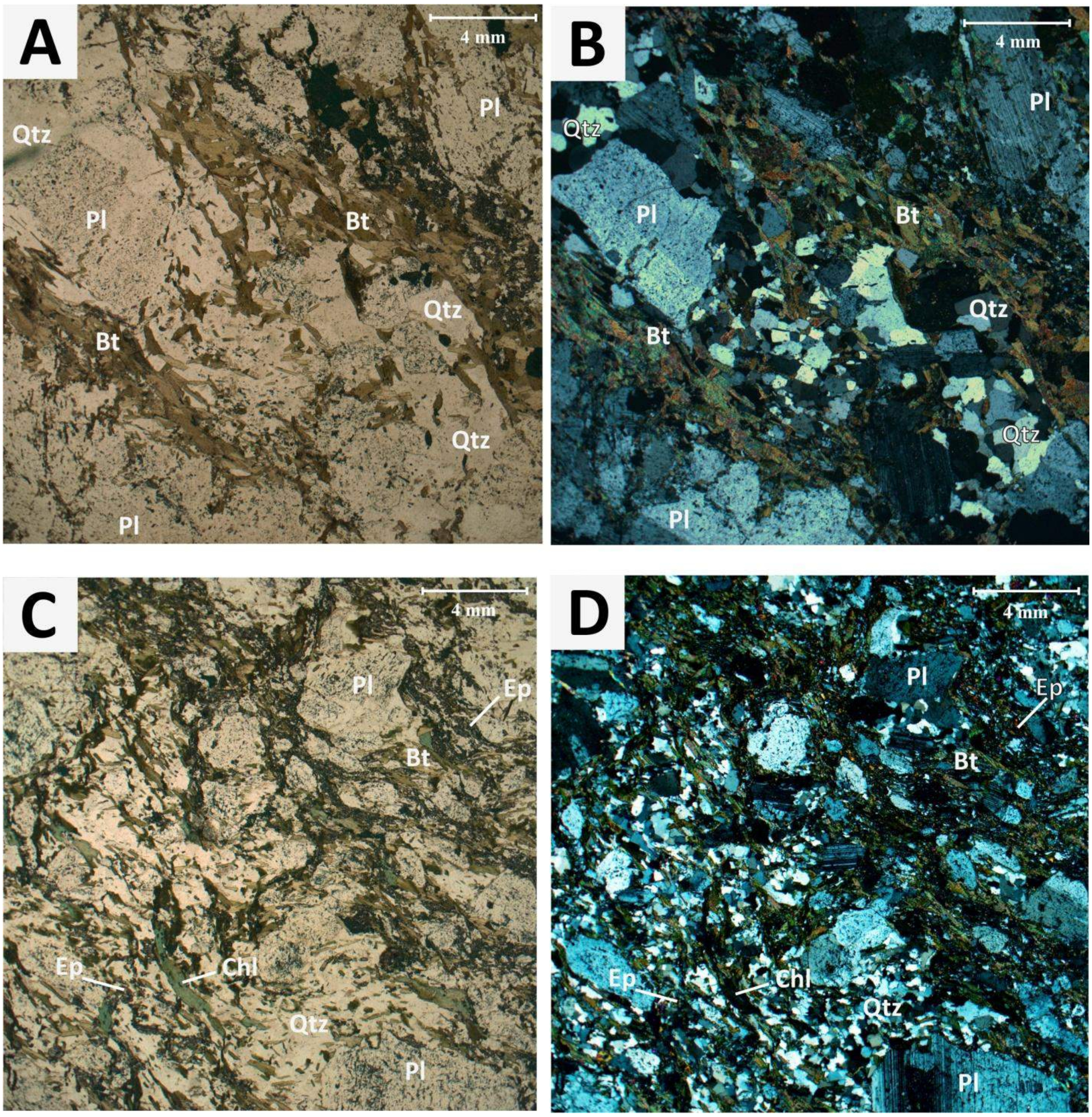

Figure 5.3-7: Petrographic aspects of low deformed tonalite. (A) and (B): textural aspects and mineral assemblage of coarse-grained tonalite composed by biotite quartz plagioclase, epidote and opaque minerals (B= same as in (A) but with crossed polarized ligth); (C) and (D): moderately deformed tonalite with higher concentration of epidote and presence of chlorite associated with biotite (D= same as in (C) but with crossed polarized light).

<u>Honblende-actinolite ''amphibolite'' (metamafic)</u>

Few occurrences of an exotic rock, named here hornblende-actinolite "amphibolite" were mapped to the northeast of Pau-a-Pique deposit (DOC128a- Fig. 5.1-2). It is estimated that these rocks has more than 95% of its modal composition formed by amphiboles (hornblende and actinolite) with chlorite also present. The chemical composition of these rocks reflects the mean composition of the rock-forming amphiboles: SiO_2= 51.1%; Al_2O_3= 5.1%; Fe_2O_3= 10.9;

MgO= 18.1, Cao= 10.4 and Na_2O= 0.4. It generally has a very limited area of occurrence (tens to hundreds of meters) being recognized on surface by its characteristic red argillaceous soil.

Petrographic study of these rocks show a coarse-grained rock formed by irregular relicts of hornblende crystals up to 9mm in length being surrounded by low Al amphibole (actinolite) (Fig 5.3-8). Hornblende seems to be a magmatic relict whereas actinolite is product of metamorphism over this rock.

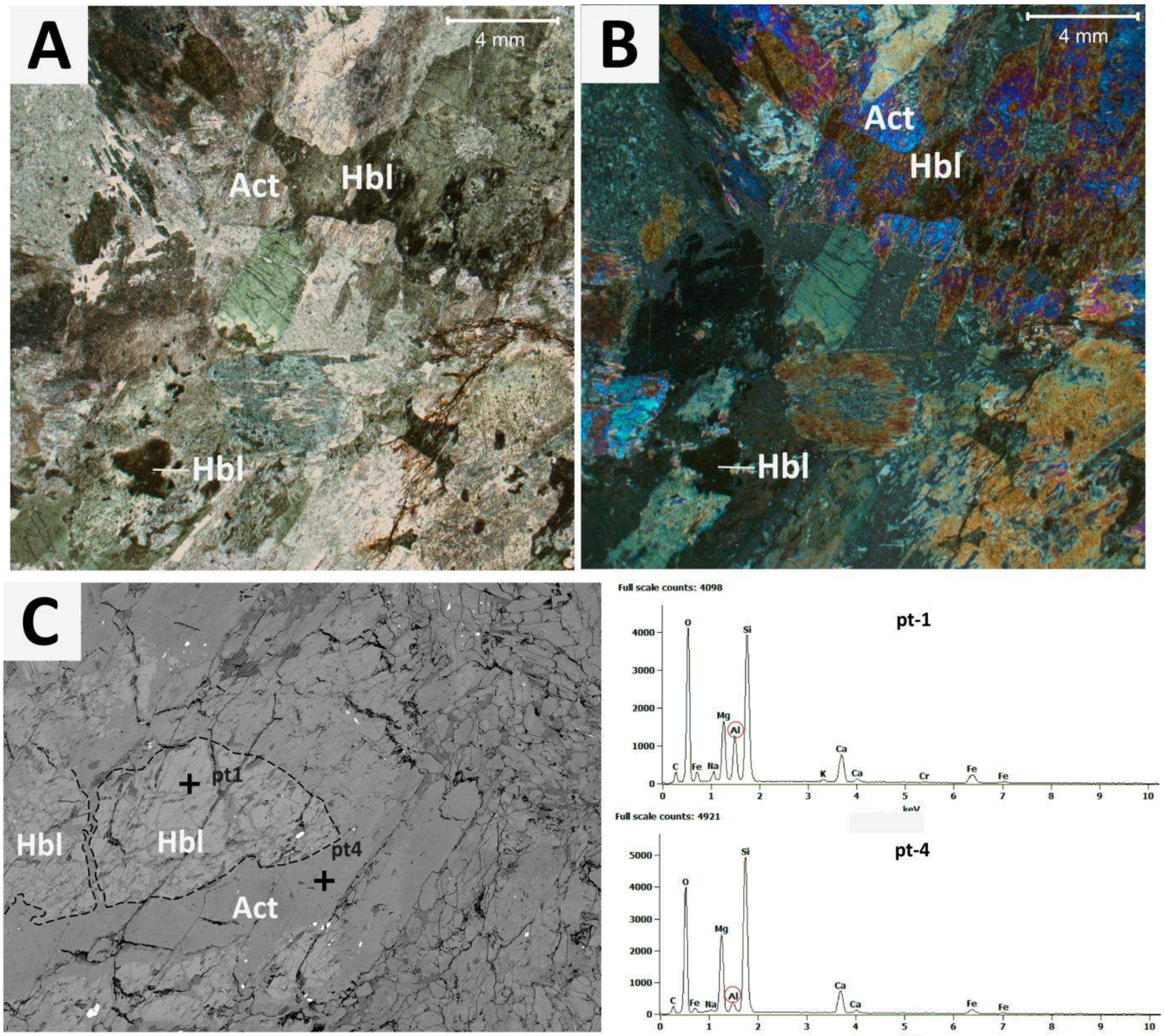

Figure 5.3-8: Textural aspect of hornblende-actinolite amphibolite. (A) and (B): photo of a thin section of these rocks showing cores of hornblende surrounded by actinolite (B: Cross polarized light). (C): Back-scattered image showing a more detailed image of the texture given by hornblende on the core and actonilite in the rim. (D): EDS spectra for the analyzed points (pt1 and pt4) in the back-scattered image showing the differences on Al content between the two zones given by different amphiboles.

The magmatic process of formation of hornblende cumulates is not matter of discussion in this research, however such rocks are not a rare feature in granitic suites. Occurrences of magmatic cumulates of hornblende associated with granitic suits has been reported in Joshua Tree National Park in California (Ianno and Paterson, 2014; Thompson and Garrison, 2014) as well as in Transverse ranges and Mojave Desert (Barth et al., 2008). Propose for formation of such cumulates includes crustal melting and fractional crystallization (Ianno and Paterson, 2014; Thompson and Garrison, 2014).

The precise composition of hornblende in these rocks is unknown since it wasn't chemically analyzed by microprobe, however the EDS spectra shows composition compatible with the cores of magmatic hornblende occurring in andesites and diorites of Pau-a-Pique basement. The transformation of hornblende into actinolite is very clear from petrographic studies and back-scattered imaging, and the difference between the two amphiboles is well marked on the EDS spectra given by a much lower counts of Al in actinolite (Fig. 5.3-8c.)

In all studied grains both, hornblende and actinolite has consistent compositionas shown by very low variation on EDS spectra's pattern. It is an evidence that magmatic hornblende has been transformed into actinolite and no other amphibole is present. The transformation of hornblende into actinolite with no presence of other metamorphic amphibole is, a prior, an evidence of metamorphism in greenschist facies.

The petrographic aspects is suggestive of lower metamorphic grade when compared to the mafic diorites of Pau-a-Pique basement. Nevertheless the petrographic aspect alone is too little to support it, when considering the complexity ofthe phase changes involving amphibole and the lack of chemical data to support it. On the other hand the geographic position of this sample must be accounted. These rocks are settled outside the Pau-a-Pique deposit area and consequently it is apparently outside of the high strain area (Corredor shear zone) and consequently it would mean lower conditions given by lower thermal gradients.

Metasedimentary rocks (Aguapeí group)

Quartz-feldspatic metasandstones and metaconglomerates are the dominant metasedimentary rocks cropping in the area. Well preserved fine-grained pelitic metasedimentary rocks are restricted to thin layers of phyllite occurring within thick sequences of metasandstones and metaconglomerates. In fact a thick sequence of pelite dominant sucession occurs in the internal portion of Caldeirão syncline (Vale da Promissão Formation), however the extensive weathering over the area favored the preservation of coarse-grained quartz feldspatic metasedimentary rocks rather than the pelitic ones, and when cropping out, it comprises deeply weathered, friable and saprolitize rock, useless for metamorphic studies.

Qtz-Fsp metasedimentary rocks

It is grouped here all coarse- to medium-grained siliciclastic rocks, with variable amount of feldsparincludingquartzite, metasandstone, and metaconglomerate from Aguapeí group.

Theses rocks show very simple mineralogical composition. Most rocks has more than 85% of its composition given by clasts of Qtz and Fsp, with Qtz, comprising more than 75%. In some samples the presence of Fsp wasn't even identified. The matrix is composed by Ser or Ms + Qtz + Mag ±Hem ±Rt ± Ilm± Tur. Metasandstones generally are subarcosean in composition.

Differences in both texture and mineralogy in quartz-feldspatic rocks can be observed along of the studied area and seems to be indicative of differences in metamorphic conditions. On southern, highly deformed metaconglomerates and metasandstones are characterized by stretched grains and pebbles of quartz and feldspar surrounded by crystals of muscovite of light green color (in hand samples) (Fig. 5.3-9a,b). In these rocks rutile and magnetite are the most common Ti-Fe oxides accessory, being ilmenite eventually present in minor amount. Deformed rocks with similar characteristics also occurs in the basal portions of Fortuna formation on northern area (Ernesto Mine area). The basal layers, near the contact between the Aguapeí group and the basement, show deformation characterized by stretching of sedimentary clasts and mineralogical association similar to that observed in Pau-a-Pique: Qtz + Ms + Rt + Mag + Ilm.

On central area the coarse-grained quartz- and quartz-feldspatic metasedimentary rocks were subjected to smaller rates of deformation. The original sedimentary texture is preserved on most of the samples. Fine-grained (20-30 microns) K-white mica (supposedly sericite) is the only phyllosilicate present in the matrix. Hematite and magnetite are the common oxide accessory, being rutile or ilmenite absent in these rocks.

The mineralogical differences on type of micas is also supported by difference in its chemical composition. The K-white micas occurring on central area show small amount of Fe (0.07 - 0.35 apfu) and Mg (0.09 - 0.26 apfu) whereas the Si content vary from 3 to 3.17 apfu. The muscovites from southern area has Si content of varying from 3.12 to 3.30 apfu , considerably higher Fe (0.26 - 0.43 apfu)and slightly smaller amount of Al. The larger content in Si is indicative of higher magnitude of phengitic component and may be indicative of higher pressure conditions. These differences will be explored below in the following sections.

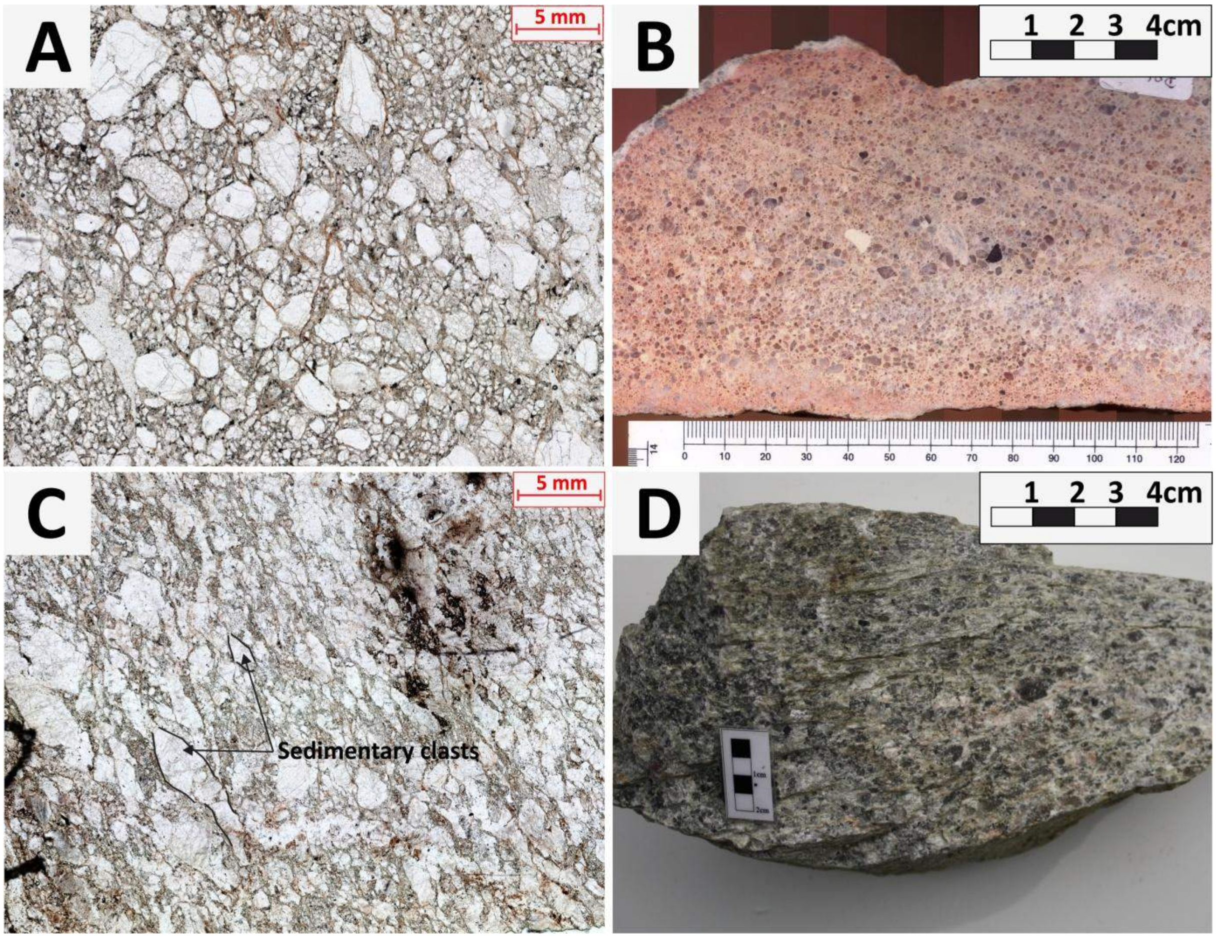

Figure 5.3-9: General aspects of coarse-grained quartz-feldspatic metasedimentary rocks ocurring in the Area. On top (A and B), the well preserved metasedimentary fabric of microconglomerate from central area, showing sub-rounded clasts with internal microcraks (A), and its general aspect on hand samples (B). On bottom (C and D), the deformed aspect of the correlative microconglomerate found on southern area, showing stretched as clasts (C) and its general aspect in hand samples (D).

At low grades (chl and Bt zones = greenschist facies) magnetite and rutile may coexist, yet hematite and ilmenite is restricted to solid solution although Ilm + Rt + Mag can be stable in reduced rocks. At intermediate grades (Grt, St, Ky zone = amphibolite facies) ilmenite + hematite replaces Mag + rutile (Spear, 1993). Hematite alone is a common accessory of low grade rocks and by conditions of Bt and garnet zones the hematite commonly gives way to magnetite (Spear 1993).

Metasandstones of subarcosean composition are, in general, useless for a well supported study of phase changes during prograde metamorphism specially those in areas under low grade conditions. Although the assemblage, Qtz-Ser in the matrix is indicative of greenschist facies it is not possible to specify which zone. The same is valid to Ms-Qtz assemblage.

The presence of Mag + Hem as accessory in Qtz-Ser assemblage rocks and Rt + Mag ± Ilm in Ms-Qtz assemblage reinforce the differences in both pressure and temperature but no further information can be extracted from it.

Plastic deformation microstructures in quartz

Crystals can deform internally without brittle fracturing by movement of lattice defects, during intracrystaline deformation (Paschier and Trow, 2005). At normal strain rates, most of minerals show temperature where crystalplastic deformation takes over from britlle deformation. This boundary is also the limit where, at sufficient strain, dynamic recrystallization starts at most as bulging (BLG) recrystallization (Paschier and Trow, 2005). At very low grade conditions (bellow 300ºC) brittle fracturing, pressure solution and solution transfer of material are the dominant deformation mechanism and the characteristic structures are fractures in grains, ondulose extinction and kink bands. BLG recrystallization may locally occurs in strongly deformed quartz (Paschier and Trow, 2005 and the references therein).

Dynamic recrystallization in quartz is consistently estimated as starting at ~250 - 300ºC (Stipp et al., 2002 and the references therein).

The textural analysis of quartz recrystallization mechanism can be an indicator of temperature (Stipp et al., 2002; Faleiros et al., 2010). BLG is the dominant mechanism of recrystallization between 280- 400ºC, sub-grain rotation (SGR) occurs between 400ºC and 500ºC and grain boundary migration, above 500ºC (Fig.5.3-10).

The optical microstrucuture present in coarse-grained metasedimentary rocks along the mapped area, define two zones of dynamic recrystalization: (A) a zone of bulging recristalization (BLG), mainly present in low deformed samples of conglomerates and metasandstones from the basal Fortuna formation on central studied area; (B) a zone of grain boundary migration (GBM) commonly observed in sediments affected by localized high deformation caused by shear zones. It is specially common in sheared sediments occurring near the mineralized zones of Pau-a-Pique mine, close to the contact between the basement and the metasedimentary rocks (transcurrent tectonic domain) and in rocks near the contact with the basement in Ernesto mine area (on northern area).

BLG zone:the coarse-grained metasedimentary rocks from BLG zone show rounded clasts of quartz with irregular shape and serrated boundaries. The contacts between the porphyroclasts are marked by pressure solution texture. Individually, the clasts show healed microcracks, ondulose extinction (with patchy texture in some cases) and deformation lamellae. Bulges of a few micrometer in diameter occurs in triple junction, in serrated grain boundaries (Fig. 5.3-11) and along of intergranular microcracks.

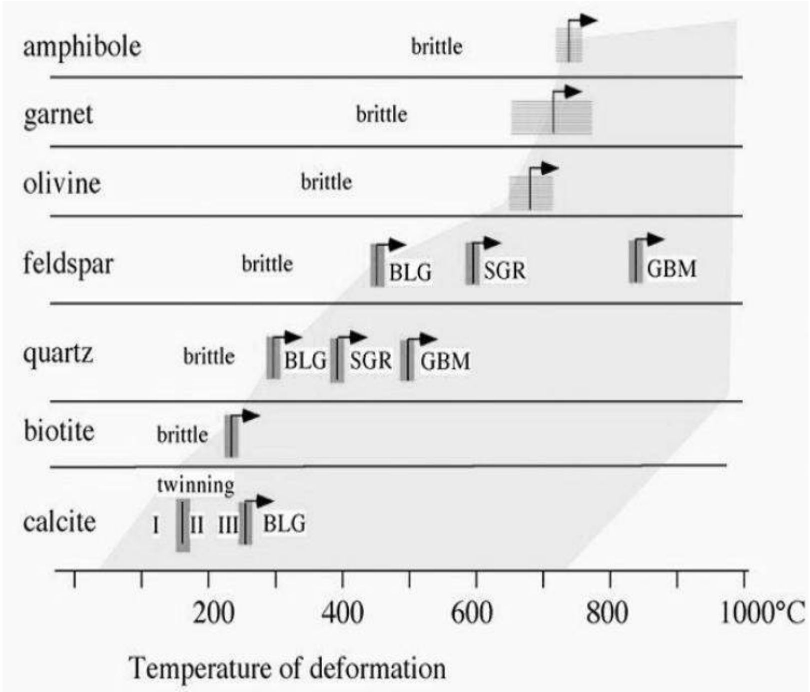

Figure 5.3-10: Temperature dependence of deformation mechanisms for different minerals. Bars indicate the transition zones. Arrows indicates the effect of strain rate. BLG, SGR, GM - main types of recrystallization (Paschier and Trow, 2005).

GBM zone: In such portion quartz has irregular shape, and are relatively coarse in size (100-500 um) although individual grain can be as small as 50 microns. The grains are slightly elongated and are characterized by lobated contact (Fig. 5.3-12). Most of grains shows very weak ondulose extinction. The earlier sedimentary porphyroclasts were completely recrystallized into aggregates ofquartz grains and ghosts of the sedimentary clasts are formed by aggregates of quartz surrounded by crystals of muscovite resembling the original sedimentary structure.

The group of texture observed in BLG zone is indicative of temperature ~300ºC (for sure between 280 and 400). Yet GBM dynamic recrystallization only occurs over ~500ºC at normal strain rates. Moreover GBM texture similar to the observed in the area are typical in temperature as high as 560ºC, as observed by Stipp et al. (2002) in low pressure metamorphism, or as high as 520ºC as described by Faleiros et al., (2010) in barrovian metamorphism, the last suggesting the neglectable effects of pressure on deformation mechnism of quartz.

Such difference in temperature between the two domain seems to be too high, especially considering the distance of occurrence between it. Besides that, when compared to the metamorphic phases present in the surrounding mafic rocks (andesites and diorites from Pau-a-Pique basement), even the bare minimum temperature necessary to GBM recrystallization be active at normal conditions (dry conditions), is slightly above the greenschist - amphibolite facies transition zone recognized in these rocks.

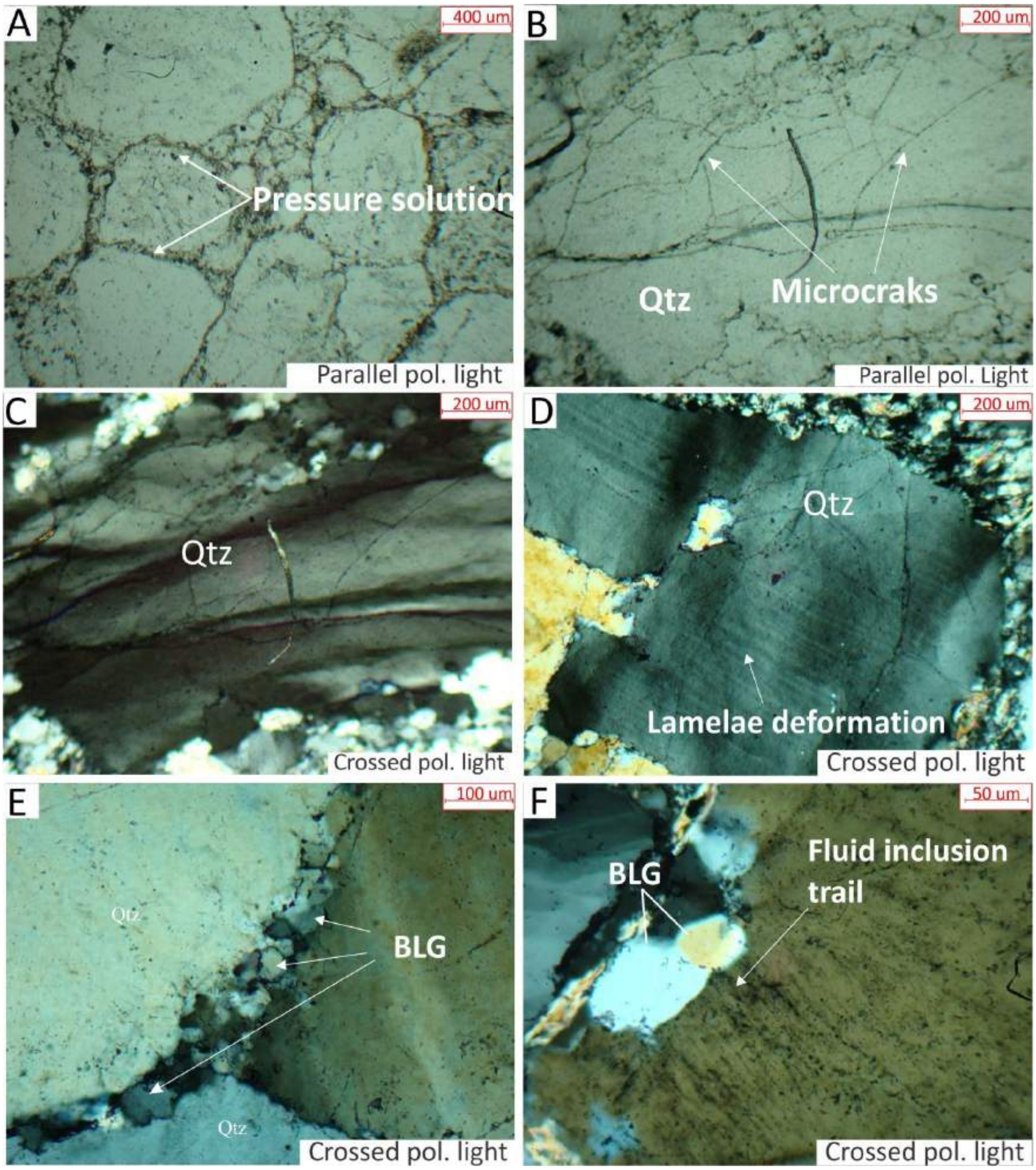

Figure 5.3-11: Textural aspects of quartz on BLG zone. (A): Pressure solution (developed during digenesis); (B): microcracksin sedimentary clast, developed under brittle conditions (before rock reach conditions for plastic deformation; (C): Ondulose extinction in the same sedimentary clast that shows microcracks; (D) Lamellae deformation in sedimentary clast of quartz; (E) Bulging recrystallization (BLG) occurring in triple junction of quartz grains; (F): Detail of bulging recrystallization (BLG) erasing fluid inclusion trails from the sedimentary grain.

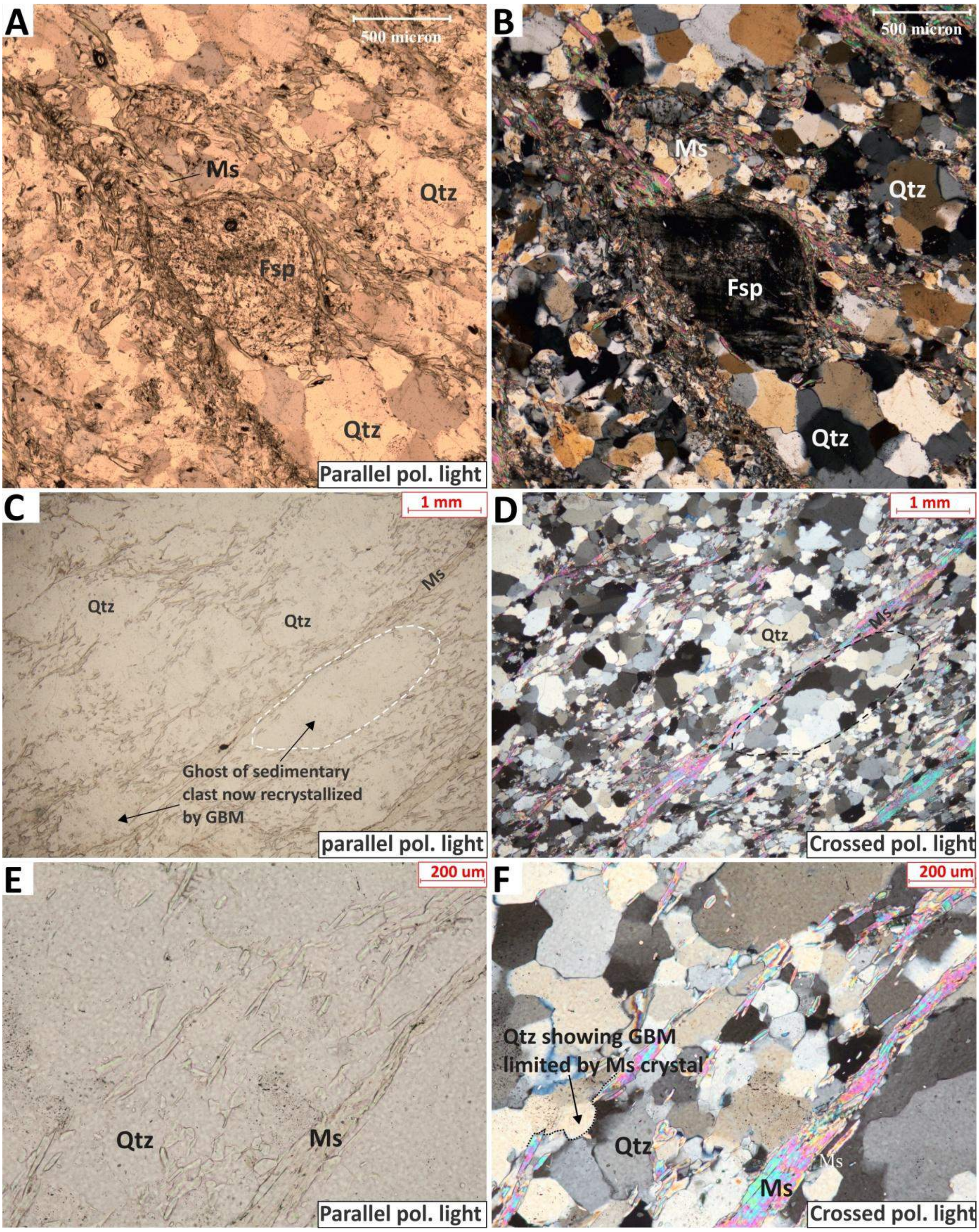

Figure 5.3-12: Textural aspects of quartz on GBM zone. A and B= quartz-feldspatic metaconglomerate showing a deformed crystal of feldspar on center; C and D= highly deformed metaconglomerate showing ghosts of sedimentary clasts grains that were totally recrystallized by GBM but still remain the sedimentary texture by being surrounded by muscovite layers. E and F: Detail of GBM texture in quartz showing lobulate contact, and the detail showing the direction of boundary migration in a window microstructure.

Indeed the deformation behavior of quartz is more complex when it involves water. The presence of water in the crystal lattice may have strong influence on dynamic recrystallization.

There are indications that with increasing water pressure in pore space, dislocation creep strength of quartz decreases probably through an increase in water fugacity in quartz grains (Paschier and Throw, 2005 and the references therein).

Some portions of the studied area show strong evidence for fluid-assisted deformation. The highly deformed zones on southern (Corredor shear zone) and along the contact between the metasediments and the basement on northern(Morro Solteiro shear zone) seems to be formed by fluid-assisted shearing in which the presence of water resultedin an important softening process during deformation.

The strain rate also seems to affect the temperature of occurrnece of a speciffic quartz recrystallization mechanisms. Dunlap et al., (1997) for example has estimated the transition SGR-GBM recrystallization in 330ºC for elevated strain rates.

Despite the doubts about the effects of strain rate and water active on dynamic recrystallization mechanism in quartz and the meaning of GBM occurring in the highly deformed rocks of the area, both the mineral assemblage and plastic deformation texture of coarse-grained quartz-feldspatic metasediments allows to propose that the metamorphic conditions in the area wasn't homogeneous. The conditions recorded in the highly deformed metasediments from Corredor shear zone (transcurrent domain) and Morro Solteiro shear zone is consistently higher than that recorded in metassediments from central area.

Pelitic rocks

Low weathered samples of pelitic and semi-peliticsediments were collected in few outcrops on central area. These rocks comprises fine grained phyllites and metasiltstone of dark-grey color. It occurs as thin layers of metric to centrimetric dimensions within thick packages of metasandstone and is more frequent on intermediate and superior strata of Fortuna formation, since the inferior portions are composed almost exclusively by metaconglomerate and metasandstone.

The philites are composed by very fine-grained flakes of mica (15 - 30 microns) in a preferred orientation. The recognized mineral phasesin these rocks are Ser (Ms) + Qtz + Chl + Hem± Tur. Sericite is the most abundantphase andgenerally comprises more than 60% of modal composition. Very small crystals of a dark-green mineral with low birefringence and irregular shape was identified as chlorite. It occurs associated with sericite and the crystal's limit with sericite isn't clear, having it, a transitional aspect.

Because of the small granulometry of quartz-like mineral in thin sections it wasn't possible to identify the presence of K-Fsp in these rocks.

The main difference between metagilites and metasiltstone is the amount of quartz, which in metasiltstone comprises around 50% of modal composition. Moreover the presence of chlorite wasn't identified in metasiltstone being sericite the only mica present.

The assemblage Ms + Chl + K-Fsp is typical of low-Al pelites formed at low to intermediate pressure in greenschist facies, in the zone of chlorite (Spear, 1993).

The presence of phyllites with chlorite and muscovite is a clear indication that the metamorphic conditions is in the chlorite zone and the temperature were below 400ºC, which is when biotite is crystallized by the reaction:

$\text{Chl+K-Fsp} = \text{Ms} + \text{Bt} + \text{Qtz} + H_2O$ (4)

Biotite is the first major isograd in prograde metamorphism of pelite. In fact the exact temperature of the first appearance of Bt+Ms is not well established but it is most likely to occurs in the pyrophylite field at $300< T < 400$ºC (Spear, 1993).

The temperature range of chlorite and muscovite stability (bellow 400ºC) is coherent with the temperature in which BLG of dynamic recrystallization is active, observed in coarse grained metassediementary rocks of the area. Based on that, it is possible to say that the temperature of metamorphism was bellow 400ºC and above 280ºC in the rocks of BLG zone. It is more likely to be somewhere in the interval between 300ºC and 400ºC.

The pressure limits however is more difficult to be established based only in petrographic aspects. The chemical composition of micas can give a comparative idea of pressure conditions based on Si and Al content in K-white micas whereby it is possible to calculate the size of *b*(Aº) parameter in these micas.

Variations in the *b* unit cell of K-white mica is widely used as a comparative geobarometer in low and very low-grade metapelitic rocks (Frey and Robinson, 1998). The *a* and *b* cell dimension of muscovite are affected by two substitution:

(1) $(\text{Mg, Fe}^{2+})^{vi} + \text{Si} = \text{Al}^{vi} + \text{Al}^{iv}$;
(2) $(\text{Fe}^{3+})^{vi} = \text{Al}^{vi}$

Substitution (1) is referred to variously as the "phengite", "celadonite" or "Tschermak" substitution, or (1) and (2) may be combined and called the celadonite substitution (Guidotti, 1984). Although both *a* and *b* dimension decrease with increasing Na/(Na+K) ratio, the effects of this ratio is not important when $\text{Na/(Na+K)} \leq 0.15$ (Frey and Robinson, 1999). In Na poor muscovite, the *b*-parameter varies linearly with the content of octahedral and tetrahedral sheet and the *b*-parameter can be calculated through the regression equations (Guidotti et al., 1989):

$$b\ (A^o) = 8.9931 + 0.0440\ \Sigma\ (Mg + Fe^{2+} + Fe^{3+}) \qquad (1)$$

$$b\ (A^o) = 9.1490 - 0.0258\ \Sigma\ (Al^{vi} + Al^{iv}) \qquad (2)$$

$$b\ (A^o) = 8.5966 + 0.0666\ Si \qquad (3)$$

Generally the *b* parameter of micas in low grade rocks is obtained by X-ray difractometer techniques using the dioctahedral mica (060) spacing and suitable internal standard. However, when it is possible to obtain high quality analytical data from analytical electron microscope (AEM), the regression equations above can be used to calculate the *b* dimension (Frey and Robison, 1998).

According to Frey and Robinson (1998), microanalysisof micas using AEM offer several advantages over X-ray diffraction techniques since it is possible avoid detrital micas being also possible to identify Na-rich micas and thus avoid it from calculations.

Microprobe analysis of micas occurring in both metapelites and in the matrix of coarse-grained quartz-feldspatic sediments were analyzed and the *b*parameter was calculated using the regression equations above.

Due to uncertainties associated with the calculations of Fe^{2+} and Fe^{3+} content in micas from Fe_2O_{3tot} (as given by microprobe analysis), only the equation (2) and (3) were used to calculate the *b*-parameter of micas. The calculated values for the rocks of the area vary from 8.997 to 9.014 (A°) using the equation (2) and from 8.992 to 9.007 (A°) using the equation (3). The results are shown graphically in Figure 5.3-13. The bars represent the difference in values obtained from the different equations.

According to the classification of pressure facies proposed by Guidotti and Sassi (1986) the *b* parameter of K-white micas suggest pressure condition on limit between low pressure and intermediate pressure with geothermal gradient of ~25°C/km.

The diagram of cumulative frequency (Fig. 5.3-14) curves of Sassi and Scolary (1974) is another way to obtain an easy comparative estimate of pressure based on *b*-parameter of K-white micas.

From samples of similar temperature but different pressure collected around the world the authors delimitate 6 pressure facies based on cumulative frequency of *b* cell parameter values of K-white micas. The facies range from low pressure metamorphism to glaucophanitic greenschist facies.

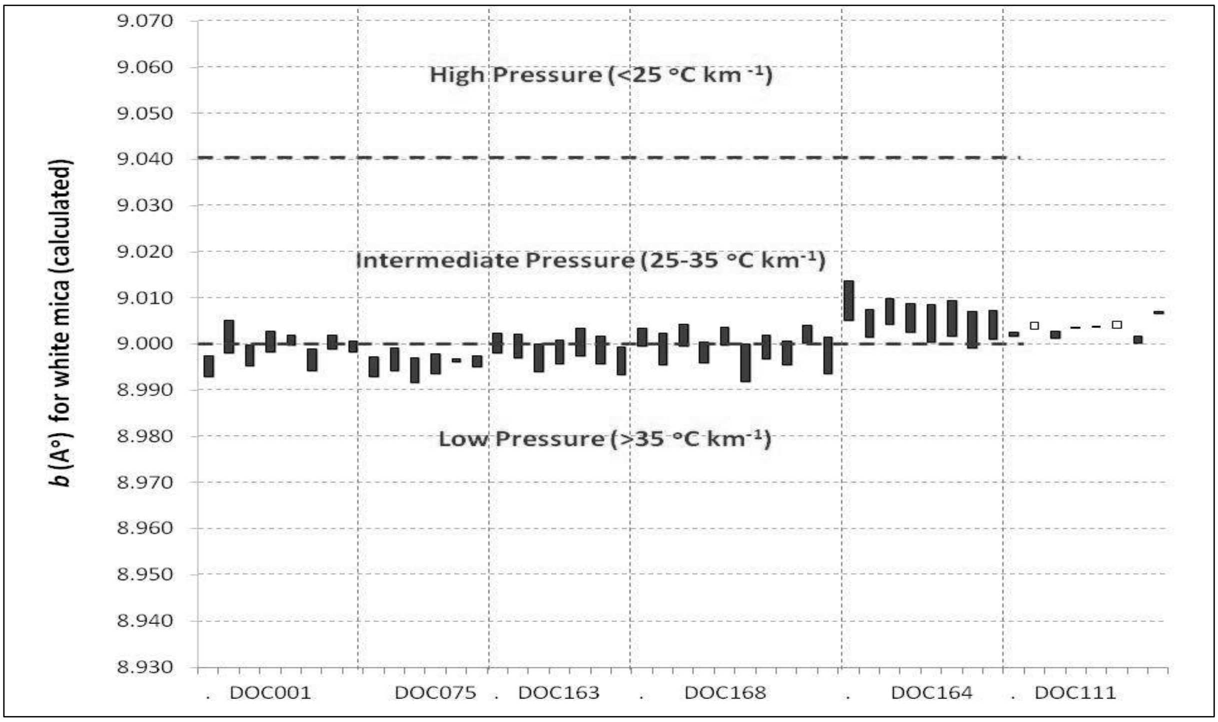

Figure 5.3-13: Results of calculatesb parameter of K-white micas from based on content of Al and Si. In the filled bars the top of the bar correspond to values obtained by equation (2) and the bottom by equation (3). In the empty bars is the opposite. Most of values are on the limit between low and intermediate pressure suggesting thermal gradient around 35ºC/km.

The values obtained through regression formula (2) and (3) from the studied samples, were plotted in the cumulative frequency diagram of Sassi and Scolary (1974). It suggest that the low deformed rocks from central and northern portion, records conditions compatible with low pressure areas. The plotted cumulative does not follow a tendency but is between facies (**2**): Low-pressure metamorphism (And+ Crd) with chlorite-zone (for ex.: Hereynian rectamorphism in Eastern Alps); and facies (**3**): Low-intermediate pressure metamorphism (And) with the Chl ~ Bt +Alm sequence in the greenschist facies (for ex. : New Hampshire) Fig. 5.3-14.

It is important to notice that most of the analyzed samples are not phyllites or quartz phyllites as recommended by the authors, whom argue that very quartz-rich rocks, rocks in which K-feldspar occurs as an essential component or chlorite-rich rocks should be avoided since in all these cases the *b* values turn out to be higher.

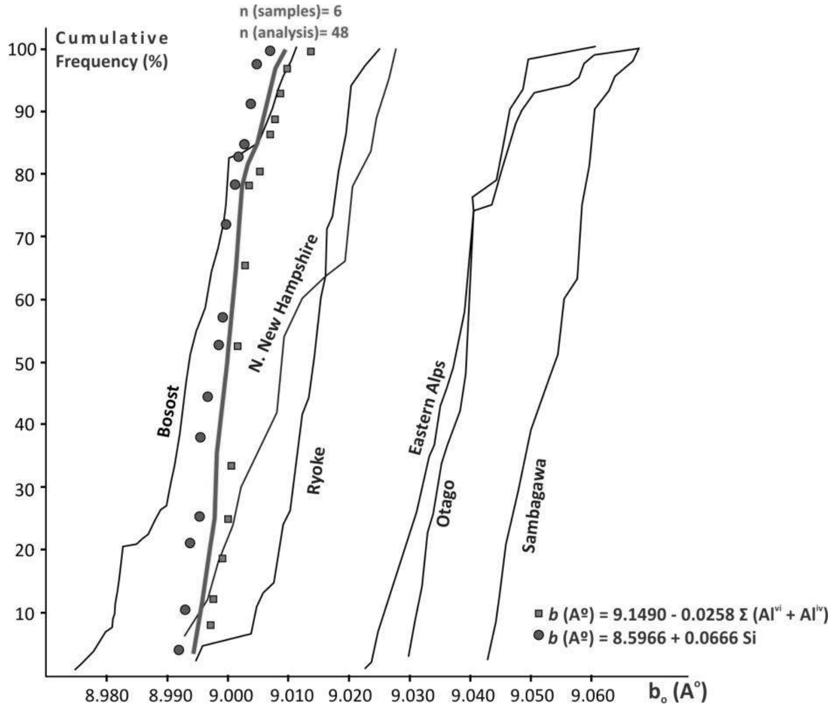

Fig. 5.3-14: Cumulative Frequency versus b-parameter in metassediments from LAC and comparison with other metamorphic terrain curves (Sassi and Scholari, 1974)

However analyzing the data obtained by the regression formulas (2) and (3) (Fig. 5.3-13), it is easy to notice that the main difference observed between the values of quartz feldspatic-coarse grained sediments and the phyllite sample (DOC00111) concerns the wider difference between the values obtained with the regression equation for each analysis. Working with the average values (obtained from subtraction of the value obtained by eq. (3) from the value obtained by eq. (2), represented by the central portion of each bar in Figure 5.3-13), the differences between the samples are not expressive and follow an general range between 8.993 and 9.010. Moreover the values for coarse-grained quartz feldspatic rocks are generally slight smaller then values of DOC0011 being thus the opposite of what would be expected for very quartz-rich samples.

Except for DOC00111, all the other samples are very coarse grained rocks with well preserved sedimentary texture. Apparently most of the coarse-grained clasts and pebbles did not take part into the metamorphic reactions occurred in the matrix since most of it show the original sedimentary fabric with internal plastic deformation of the clasts. Quartz recrystallization is generally restricted to thin zones occurring mainly in triple junction or microcracks. The metamorphic reactions in these particularly coarse-grained rocks must be limited to interactions between the minerals in the matrix which should not have been very quartz-rich portion considering the amount of K-white micas present.

Based on that, the calculated *b*-parameter from metamorphic K-white micas from matrix of very-coarse grained sediments seems usefulon studying pressure and the results suggest low pressure conditions for the studied rocks.

P-T projection based on *b*-parameter isopleths was proposed by Guidotti and Sassi, 1986 (Fig. 5.3-15). A range of pressure for the studied rocks was graphically estimated based on mean, maximum and minimum *b*-parameter values using a mean temperature of 350ºC. The mean temperature value comes from the interval of 300 and 400ºC determined by the occurrence of BLG recrystallization (estimated at 300ºC) and the maximum temperature where biotite is absent in pelitic rocks (400ºC).

From that it is possible to estimate a mean pressure around 2Kbar with a maximum of 3.2 Kbar and a minimum of 1.8 Kbar, which is coherent with the low grade (chlorite zone) phases present in studied rocks.

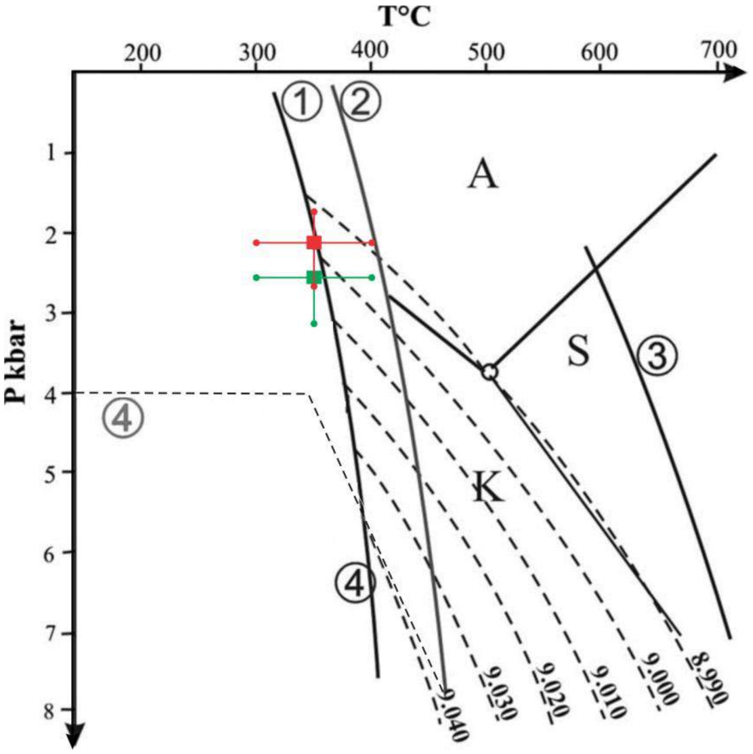

Fig. 5.3-1:. P–T graph with b-parameter isopleth (Guidotti and Sassi, 1986).Green square represents the b-parameter average value using regression equation (2) and red square represents the b-parameter average value using regression equation (3). The lines with dots represent the maximum and minimum values of both temperature and b-parameter value. Numbered circles indicate the reaction curves (thick lines): (1) kaolinite dehydration; (2) pyrophyllite dehydration; (3) St + Qz + Ms = Al–Si + Bt +H2O; and (4) glaucophane stability.

Shear Zones

As mentioned before the presence of mica schist is a common geological feature in the Corredor shear zone (CSZ) in Pau-a-Pique area. In fact the occurrence of these rocks are not restricted to the Pau-a-Pique area but it is common along most of the exposed contact between the basement and the sediments of Aguapeí group and a considerable number of gold deposits occurs associated with these shear zones.

In Ernesto Mine area, for example, the sub-horizontal contact between metasandstone of Fortuna formation and tonalitic rocks of basement is marked by a sub-horizontal shear zone (Morro Solteiro shear zone) characterized by a layer of muscovite schist of variable thickness (Fernandes et al., 2005a). This layer hosts the inferior level of Ernesto deposit (~300 Koz) charcterized by mineralized pyrite-bearing muscovite schist simillar in many ways to the mineralized zone of Pau a Pique. In Ernesto area there is at least 4 other gold deposits associated with these rocks.

This section however focuses on the geological meaning of mica schist occurring along shear zones in Pau-a-Pique area.

Characteristics and mineralogy

As previously described the southern portion of studied area is characterized by NNW-SSE sub-vertical shear zones dipping 60-85º SW. It is given by a complex system of minor anastomosed shear zones that affected both, the metasedimentary rocks and the basement rocks (Corredor shear zone - CSZ).

The central portion (the core) of CSZ is located in a vertical contact between the metasedimentary rocks and the basement where the main mineralized body of Pau-a-Pique deposit is located.

As result of differences in chemistry and rheology the shear zones show different characteristics and composition, depending on hosting rock. Shear zones formed over the metasedimentary rocks (quartz-feldspatic metaconglomerates), are more homogeneous and are characterized by metric to centimetric (in thickness) shear zones that roughly follow the general strata of the sedimentary rocks. It has concentrated the deformation within the shear planes which are sided by low deformed quartz-feldspatic rocks. These shear planes are composed by light-green quartz-muscovite schist (Fig 5.2-1), and the phases present are basically Ms + Qtz + Mag + Rt. These shear zones generally hosts quartz veins. It is characterized by milky quartz veins of cetimetric- to metric-scale which show evidence for syn-deformational emplacement due to its sigmoidal shape resulted from asymmetrical boudinage sub parallel to mylonitic foliation.

Shearing over the basement rocks has a more heterogeneous characteristic. Differently from most of shear zones occurring in the metasedimentary rocks, in those from the basement the strain is concentrated along wider shear zones (metric-scale) where is possible to see the evolution of deformation from non sheared protolith to mica schist that represents the most deformed portions (Fig. 5.3-16).

Due to the high weathering over the region, outcrops of basement rocks in Pau-a-Pique are absent. As result most of interpretation about structure and shape of shear zones over the basement rocks comes from drill core samples and a gallery mapping made during field work in the area.

The general foliation of basement rocks is locally associated with an array of meter-scale shear zones in an apparent anastomosed shape around lenses of low- to non-deformed granitoids. In drill core samples the shear zones appear as dark bands due to changes in mineralogy and grain size reduction. In most case the shear zones are marked by an increase in biotite content and in some cases it is also common an increase in the content of epidote.

The mineralogy is variable and seems to depend on both, the strain intensity and the initial composition of protolith. Mica schist formed by shearing of metaluminous protolith (tonalite and diorite) are composed by Ms+Bt+ Qtz + Cb + Chl+ Ap + Rt± Mag ± Py (Fig. 5.3-16 and Fig. 5.3-17). This composition may vary a little, and Bt + Cb can be more frequent in dioritic rocks whereas muscovite seems to be more frequent in tonalitic ones. In mica-schist formed by shearing of peraluminous protolith (granodiorite), Al-rich silicates (Kyanite) can be present and the typical assemblage is this rocks is given by Ms + Bt + Qtz + Tt + Ep + Cb + Chl ± Ky ± Mag ± Rt+ Ilm ± Ap ± Py (Fig. 5.3-16).

The sheared zones of the basement is generally associated with Albite-quartz veins. It is given by metric-scale veins of milky quartz, red albite, chlorite and carbonate (calcite). Other phases such as rutile, pyrite and apatite may be present in lesser amounts. Detailed descriprtion of these veins are given in section 5.4.2.

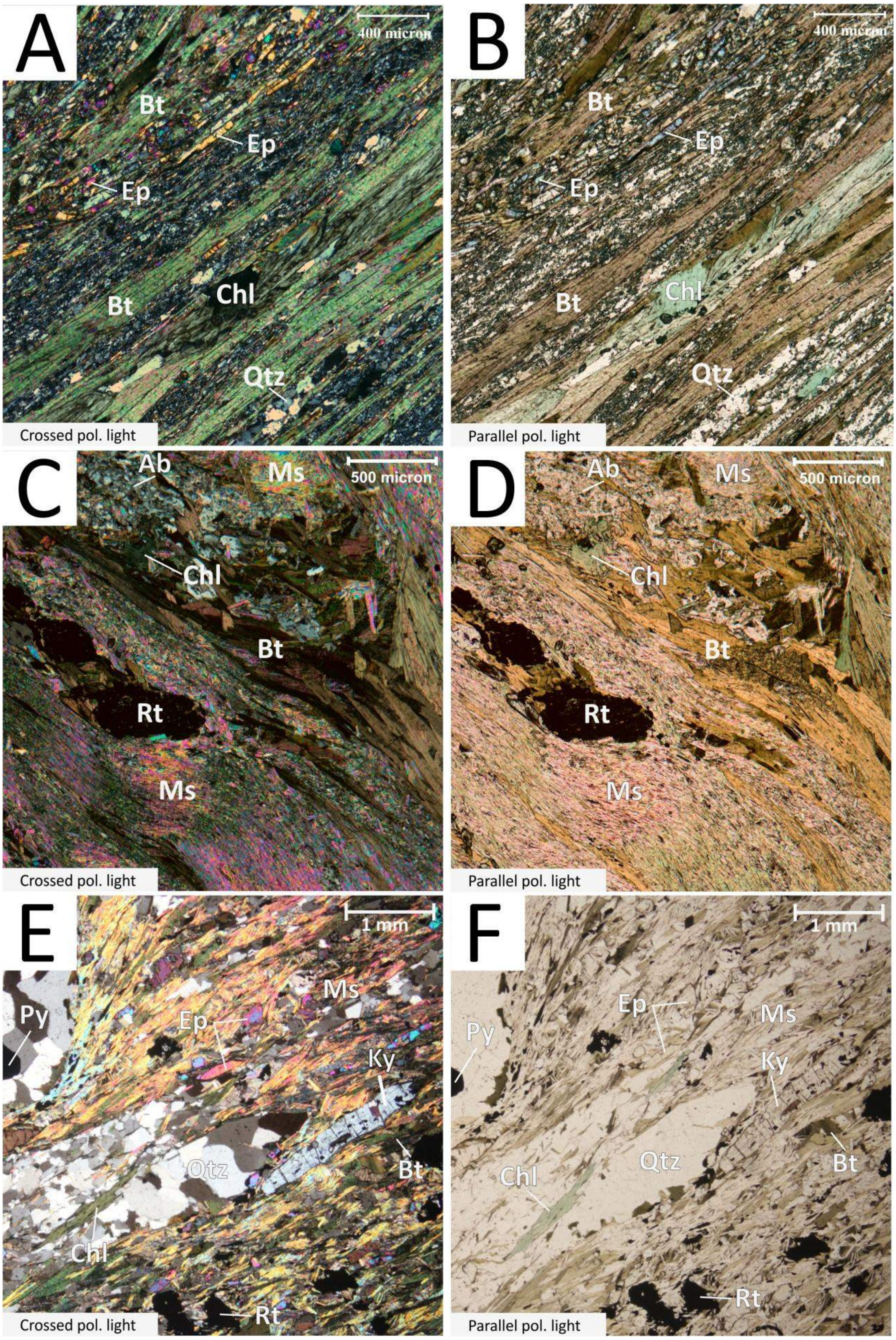

Fig. 5.3-16: Petrographic aspect of shear zones occurring in the basement. On top, (A and B), epidote biotite schist (PQ61101-13), interpreted as an intermediated level between protolith and the highest deformed zone. On middle (C and D), petrographic aspect of muscovite-biotite schist (PQ61108-90),interpreted as the highest level of shearing over dioritic protolith. On bottom (E and F) biotite-muscovite schist with syn-kinematic kyanite crystal, interpreted as highest level of fluid assisted shearing over granodiorites.

Important changes in both texture and mineralogy, occurs towards the contact with the sedimentary rocks. The main change lies on increase in frequency and dimension of the shear zones as closer to the contact. Furthermore muscovite become more frequent and biotite eventually disappear giving rise to a muscovite schist of grey color. In these rocks muscovite may represent up to 60% of modal composition and other phases present are, Qtz + Mag + Rt + Chl + Ilm + Ap ± Bt ± Py (Fig. 5.3-17).

Pyrite generally occur as porphyroblast and generally comprises less than 5% of the modal composition. It show evidence for syn- to late-tectonic growth given by the presence of pressure shadow and textural zoning characterized by porous core with curved inclusion pattern and massive rim. The inclusions in the porous zone is given by rutile, magnetite, ilmenite and muscovite suggest pyrite growth after these phases. Moreover the increase in pyrite content in these rocks is directly associated with increasing in gold grade.

The muscovite schist hosts another type of quartz veins. It is characterized by a swarm of centimetric quartz veins of sigmoidal shape formed by translucent quartz. It is evident that the quartz veins were subject of repeated britlle-ductile deformation as the veins system developed as well as after emplacement. At the microspope, repeated deformation is indicated by common ondulatory extinction deformation zones displaying various degrees of grain size reduction and growth of fibrous quartz in the pressure shadow of pyrite prophyroblasts.Free gold occurring within the quartz veins are not common being the gold occurring as small inclusion in phorphyroblasts of pyrite.

Chemical Variations

Because the igneous protolith occurring in Pau-a-Pique basement show variation in composition, analyzing chemical changes from protolith to shear zones formed over these rocks can be trick and the initial compositional differences must be accounted.

Whole-rock geochemical analyses made across some shear zones underline changes in chemical composition. Among the analyzed samples, three are undeformed metalumious protolith (Diorites, brown squares in the chemical diagrams), two are muscovite schist from the contact with metasedimentary rocks (red circle in the chemical diagrams) and the other samples are from different levels of deformation in shear zones occurring over metaluminous rocks (tonalite and diorite).

The protolith samples has composition compatible with igneous rocks in the Hughes's (1973) diagram (Fig. 5.3-18b). These are non-deformed samples of mafic diorite and andesite and shows metaluminous composition being considered to represent the most close composition to the magmatic protolith.

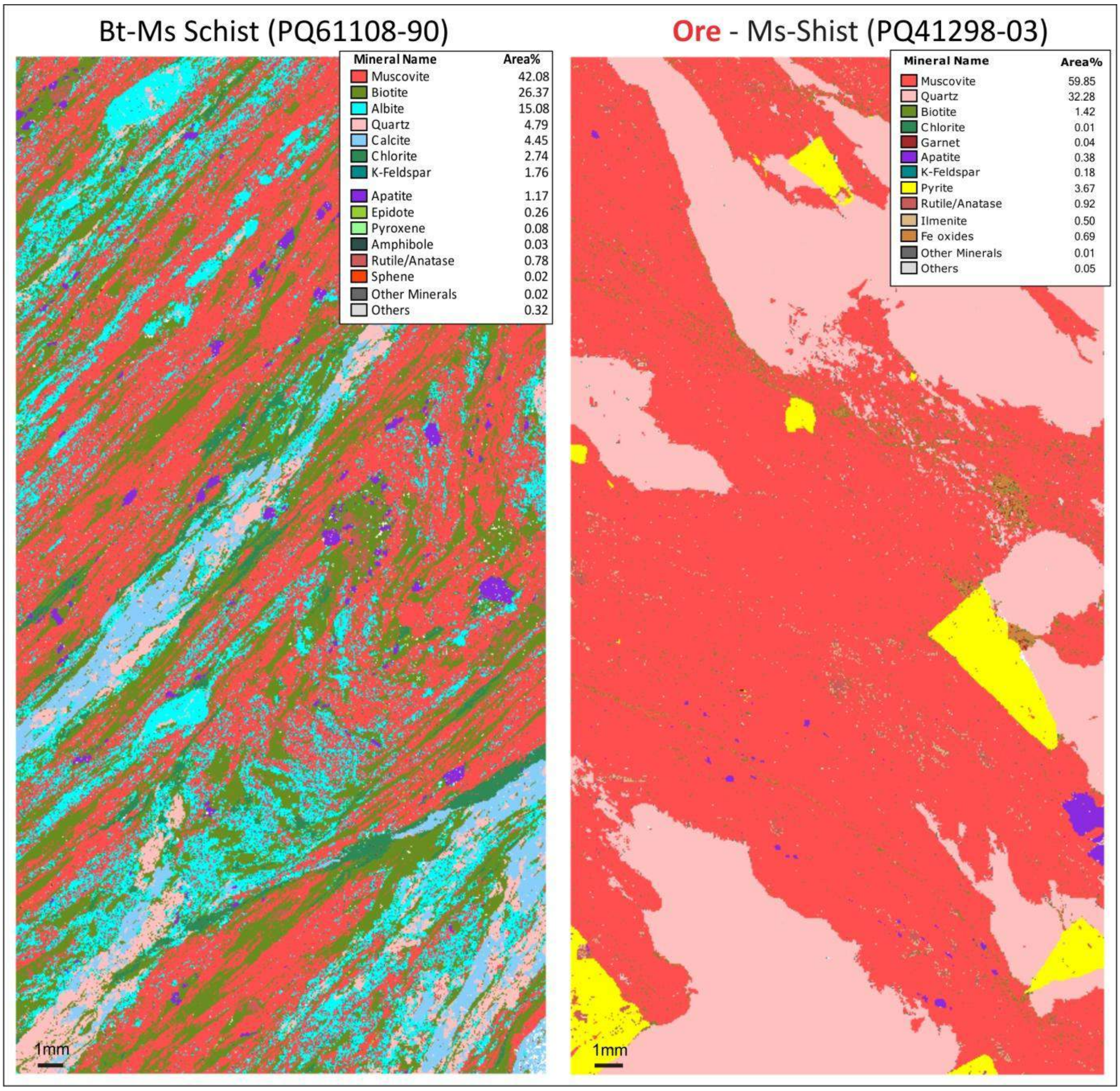

Fig. 5.3-17: Thin section QEMSCAN mapping of muscovite schist (PQ41298-03) and biotite-muscovite schist (PQ61108-90), showing the mineral phases present and its percentage (in area).

Both protolith and mica schists display the same pattern of REE with enrichment of LREE and low fractionation of HREE, typical from calc-alkaline magmas (Fig. 5.3-18a). In fact rocks from the shear zones show slightly small values of REE, when compared to the protolith.

In contrast some of the major elements of samples from shear zones display a well marked difference in composition related to protolith and most of the samples tend to lie outside the field of igneous rocks (Fig. 5.3-18b). The main differences are oserved on behavior of K_2O, Rb, SiO_2, CaO, Na_2O.(Fig. 5.3-18c,d,e and f).

Within Shear zones the LOI (mainly water content) is increased up to 7.9%, being the highest values associated with muscovite-rich schist from the contact. In Figure 5.3-19, negative variations of CaO, Na_2O with LOI suggest the mobility of these elements with increasing water content. Meanwhile the increase of K_2O and Al_2O_3 argues in favor of enrichment of K and Al with increase in water content.

These chemical and mineralogical changes in shear zones of Pau-a-Pique deposit attest for fluid-assisted shearing in which metasomatic process was responsible for transforming mylonite into mica schist by remobilization of major and minor elements.

Analyzing the chemical transformations recorded across a shear zone on a drill hole (PQ61), from non-deformed diorite (PQ6189-10) to its highly deformed correspondent (PQ61108-90) it is possible to identify major mineralogical transformations that attest for fluid-assisted shearing.

In low deformed diorites, plagioclase is still present (PQ61102-23) but the amount of epidote present suggest that part of Ca from amphiboles and some destroyed plagioclase was reallocated to Ca-rich minerals (carbonate, epidote and titanite). Part of Mg and Fe from amphiboles start to form biotite (Fig. 5.3-18). As the deformation progresses plagioclase is totally destroyed, epidote become a essential mineral and together with carbonate it accommodate the Ca from plagioclase (PQ61101-13). In these rocks amphibole is also totally destroyed and Fe and Mg will led to formation of an epidote-biotite schist but no muscovite is formed at these stage. In fact the variation in Al, K, Si and Ca at this stage of shearing is not that far from original protolith suggesting low remobilization of elements by hydrothermal fluids.

At the highly deformed correspondent (PQ61108-90) the content of Al_2O_3, K_2O, Na2O, CaO and SiO_2 suffer significant changes from its initial composition. At this stage the LOI is about 5%. Ms appears as an essential mineral and exceeds biotite, forming biotite-muscovite schist in which the micas represent more than 65% of modal compostion. Other important phases present include albite, calcite, epidote, chlorite and quartz. Calcite and quartz occur together as thin layers of quartz and calcite parallel to the foliation whereas albite occurs disperse in the rock.

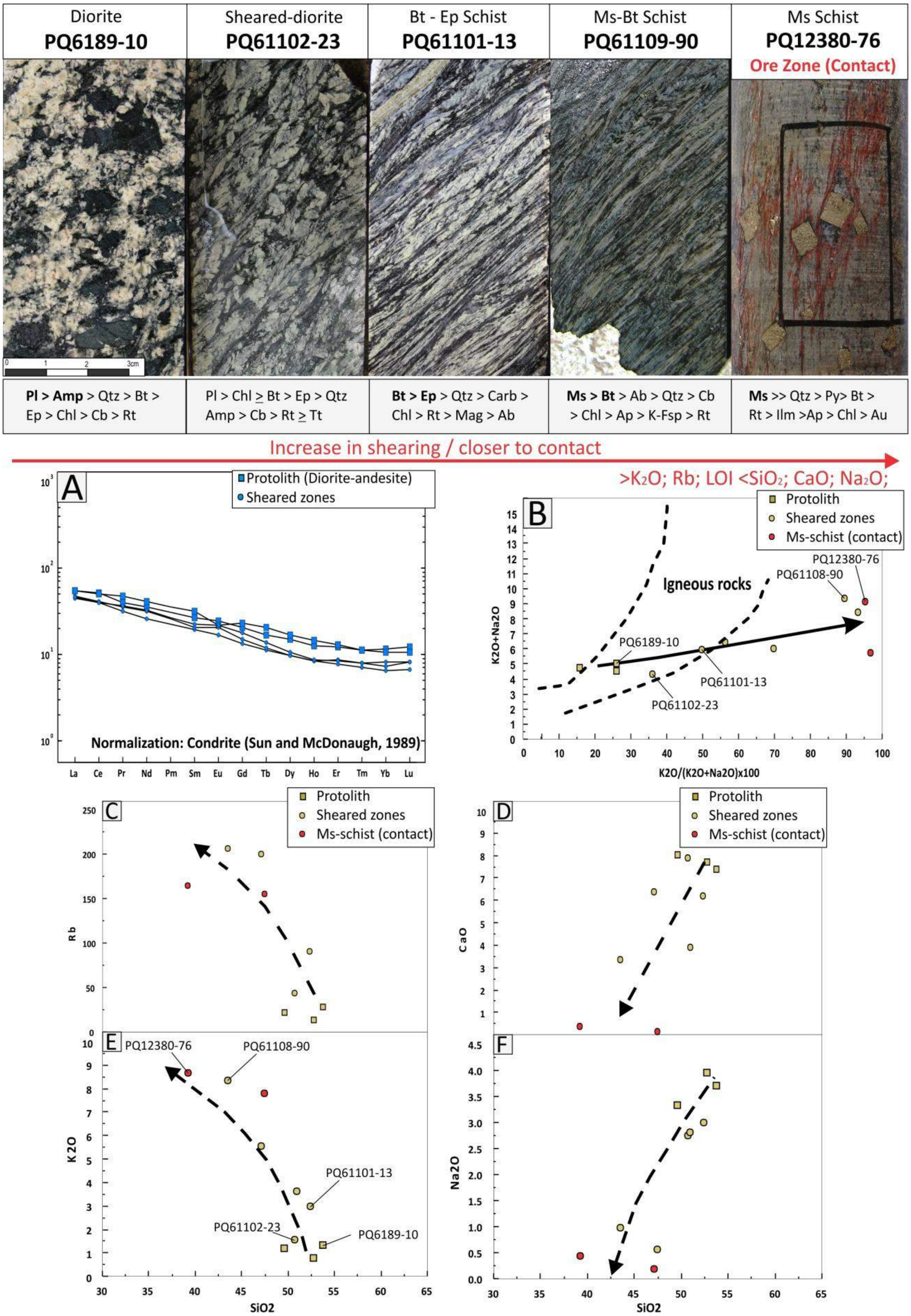

Fig. 5.3-18: On the top, textural and mineralogical aspects and differences from non-deformed protolith to the muscovite schist of the contact. Bellow chemical diagrams following the logical sequence observed on top. (A): ETR diagram normalized by condrite of Sun and Mcdonaugh (1989); (B): Whole-rock composition in (Na2O+K2O) versus K2O/(K2O+Na2O) (wt%) diagram (Hughes, 1973); (C, D E and F): Hacker diagrams of SiO2 versus Rb, CaO, K2O and Na2O**.**

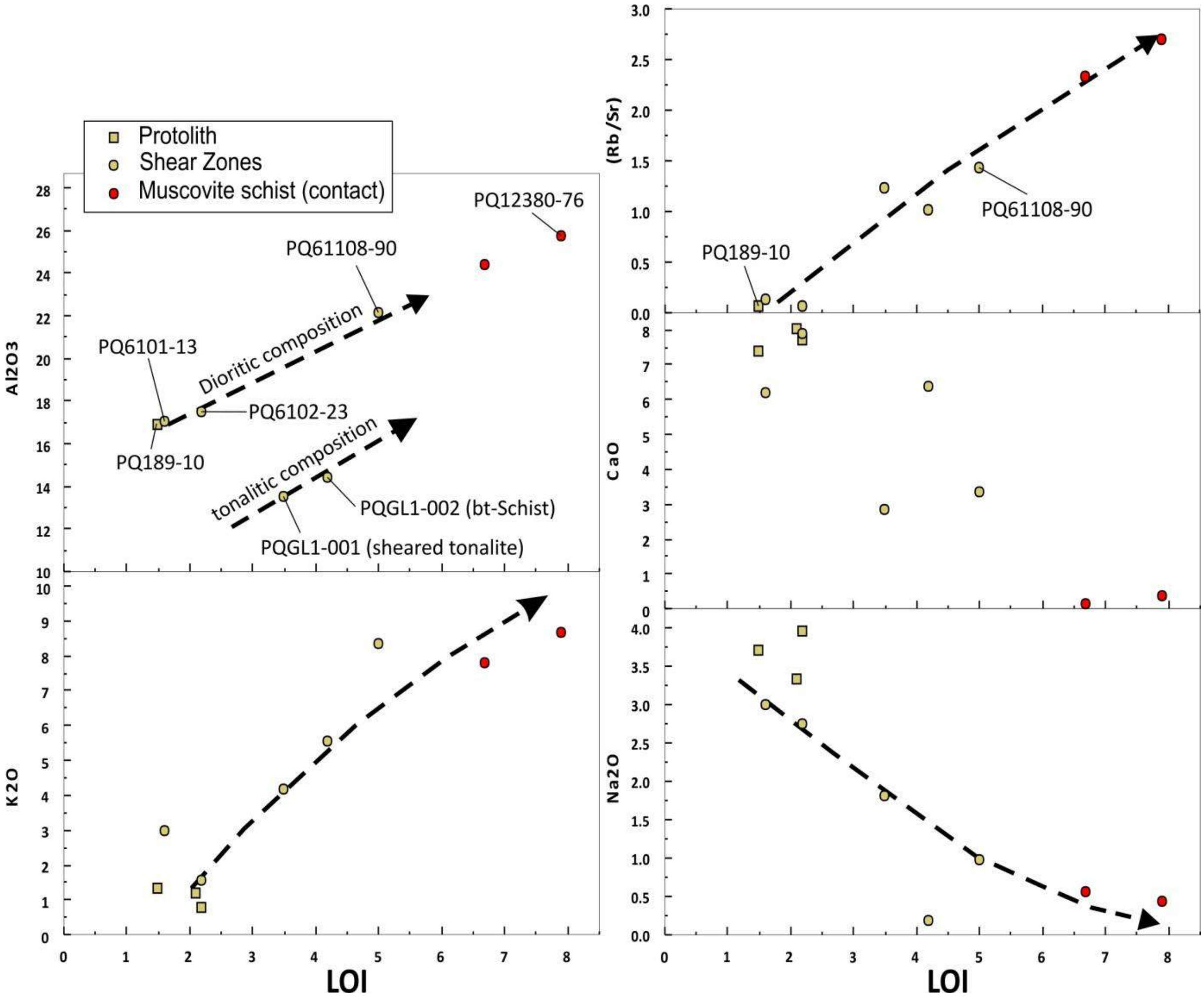

Fig. 5.3-19: Diagrams of water content (LOI) versus major and minor elements from non deformed protolith micas schist of shear zones, showing the behavior of elements during fluid assisted seharing.

Such changes in composition attest for mobility of Si, Na and Ca with water increase in which Ca and Na from the destroyed plagioclase is partially reallocated to calcite and Albite in these highly deformed zones. However the chemical difference from the initial composition suggest that part of these elements did not precipitate locally but was removed to outside of the rocks. A possibility is that part of Si, Na and in minor amount Ca, was reallocated to the quartz albite veins. At the same time the amount of muscovite and biotite seems to be incoherent with the initial content of K, since metaluminous diorite and tonalite doesn't have huge amounts of K-Fsp. In fact most of the K in these rocks are present in biotite and an input of K would be necessary to produce muscovite and biotite schist from an initial dioritic composition.

Probable sources of K are the metasedimentary rocks occurring nearby. The basal portion of Fortuna formation in Pau-a-Pique area is characterized by quartz-feldspatic metaconglomerates. Isn't clear how it proceeded, but a plausible hypothesis is that metasomatic fluids circulating through the pore of metasedimentary rocks may had been partially destroyed the K-Fsp and the released K was transported into the shear zones by channelization of fluids.

Aluminum is considered an immobile element, thus increases in its content is believed to be related to passive concentration. It is particularly important since kyanite was identified in one sample of biotite muscovite schist. Peraluminous protolith (granodiorite) is believed to be more suitable to evolve to kyanite bearing mica schist.The presence of Kyanite in fluid assisted shearzones formed over peraluminous orthogneiss is reported in Ille d'Yeu, France, by Sassier et al. (2006) and according to the authors, in peraluminous protolith the leaching of Ca, Sr and Na has formed biotite and muscovite and further leaching of other elements (K and Mg) can led to high concentration of Al leading the stability of kyanite in amphibolite facies conditions.Similar process must have occurred in some of peraluminous zones which would explain the occurrence of kyanite in some samples, however the metamorphic conditions reported by the authors seems to be higher than the observed in the studied area.

Positive variation in the LOI in less deformed samples can be attributed to the presence of Chlorite. However chlorite is here interpreted as a retrograde mineral since it is commonly associated with biotite in a substitution texture and may reflect latter hydrothermal process.

Some minor and trace elements such as Rb and Sr has similar behavior as K and Na respectively. The increase in K is roughly followed by the increase in Rb. In fact Rb and K tend to be together in rock-forming minerals and the increase up to four folds from the initial protolith composition seems to be related to input of Rb as example of K, however at the same time the passive concentration may have played an important role. Otherwise the Sr has a behavior similar to Na and in minor proportion to Ca. It may have behaved as a mobile element being leached from the highly deformed zones by hydrothermal fluids. The Rb/Sr ratio show an increases towards the highly deformed zones. In the protolith the amount of Rb is smaller than Sr, but it changes and Rb increase up to 9 folds from protolith to the mica schist meanwhile Sr is reduced up to three folds.

Discussion

According to Spear (1993), fluid infiltration may affect the bulk composition of a rock by mass transfer. However the amount of fluid required to cause significant shift in major element chemistry must be considerable.

Corredor shear zone is characterized by a strong strain localization, in most of cases, within outcrop-scale. Mica schist occurring along shear zones and the presence of abundant syn-deformational quartz and quartz-albite veins attest for channelized fluid flow during shearing.

Fluid assisted growth of phyllossilicates at the expenses of feldspar is a particularly efficient softening mechanism (Sassier, 2006 and the references therein) and may have played an important role on sharp strain localization.

During shearing extensive fluid channeling led to change in mineralogy and extremely modified rocks were formed by mass transfer. This process is recorded by gain in H_2O, K, Rb and losses in Si, Ca, Na and Sr, in the most deformed samples. Solubility of Na, Si and Ca and Sr, during fluid-assisted shearing explains the abundance of quartz-albite vein in the basement, since the process of destruction of plagioclase (oligoclase and albite) from granitoids rocks (especially those of felsic composition) may have released huge amounts of Na and Si in the system. Smaller amounts of Ca from amphiboles and plagioclase was also release into the system but part of the Ca were locally reallocated into Ca-rich minerals.

The syn-genetic aspects of metassomatic transformations indicate that shearing did not predate the hydrothermal event. It is supported by the presence of kyanite as product of metassomatic transformations. The presence of kyanite apparently resulted from channeled mass transfer and passive concentration of aluminum in shear zones over a peraluminous protolith (e.g. Sassier, 2006).

The general stability field of kyanite starts above 2Kbar and 370ºC, meanwhile the metamorphic conditions in non-deformed diorite suggests peak conditions on greenschist amphibolite facies transition (minimum temperature of 410ºC). These aspects suggest that fluid assisted shearing were active at temperature and pressure consistent with the peak conditions and account for being developed during prograde trajectory.

Rutile and magnetite and ilmentite are common accessory minerals being present in all studied samples of mica schist. Textural features and the ubiquity of these phases attest for a syn-genetic origin and in equilibrium with micas. Meanwhile the syn- to late-deformational aspect of pyrite porphyroblasts and the growth of it over ilmenite, rutile and magnetite (as evidence by the inclusions in the porous core of texturally zoned pyrite) is indicative of both, the syn-genetic character of Fe-Ti oxides and the late character of pyrite in relation to muscovite and biotite.

The zone of contact between a sedimentary basin and its basement seems to be a suitable place for beginning of shearing due differences in rheology. The deformation features recorded at the contact in Pau-a-Pique area suggest that the strain rate at the contact was higher than that recorded in shear zones in the basement and in the sedimentary sequence as well.

The dominance of muscovite rather than biotite in the shear zone of the contact suggest that shearing may have started preferentially over quartz-feldspatic conglomerates at contact surface, in which the water present in pore of the sediment may have played an important role on begging of shearing acting as weakening.

Further evolution of stress and strain rate may have had as consequence the spreading of strain localization to outside of the contact zone. At this point shear zones over the basement and the sedimentary sequence may have started being formed. It is particularly evident by differences in quartz vein stiles in each portion. The translucent quartz vein family hosted by muscovite schist of the contact is probably the first family of veins formed during the fluid-assisted shearing, as evidenced by its high deformed aspect. Thequartz-albite vein family, probably came later on strain pathsince it show less deformed aspect.

Considering that at least part of Na and Si of quartz-albite veins must had came from destruction of plagioclase by shearing of basement and its following transport by channelized fluids, the quartz albite vein is interpreted here as being formed during prograde conditions. Although the textural relationship between the two families may indicate a later genetic aspect of albite quartz veins in relation to the translucent quartz veins. However it does not comprises a late phase of veining during retrograde path.Besides that, the undeformed aspect eventually shown by quartz-albite seems to berelated to its presence in zones (cores) of low strain into the basement not meaning it was later on deformational history.

5.3.2 Geothermobarometry

Due to the lack of suitable rocks for conventional geothemobarometry based on equilibrium of paragenetic phases, independent thermometers and barometer based on chemistry of mineral phases and on oxygen isotopic equilibrium was applied in rocks from Pau-a-Pique area, on attempt to get the temperature of metamorphic peak in the area.

Ti-X_{Mg} in Biotite Thermometer

The empirical (X_{Mg} - Ti)- in- biotite thermometer of Henry et al. (2005) was tested to obtain the biotite formation temperature in biotite-muscovite schist and metandesite from Pau-a-Pique basement.

Henry's thermometer is an empirical thermometer based on relationship between Ti, temperature, and Mg/(Mg+Fe) values. It was calibrated using an extensive biotite dataset of natural samples of pelitic rocks in combination with the petrogenetic grid of Spear et al. (1999).

According to the author Ti concentration increases as a function of temperature in a non linear fashion, and for a given temperature Ti concentrations decrease with increase in Mg/(Mg+Fe).

The equation of dependence relation between Ti, X_{Mg} and temperature is expressed as follow:

$$\mathbf{T\ (^{o}C)} = \{[\ln(Ti_{apfu}) - a - c\,(X_{Mg})^{3}]/b\}^{0.333} \qquad (4)$$

Where T is in degree Celsius, Ti is the number of atoms per formula unit (apfu) normalized on the basis of 22 O atoms, XMg is Mg/(Mg+Fe), a= -2.3594, b=4.6482 x10^{-9} and c=-1.7283.

The calibration range for this expression is X_{Mg} = 0.275-1.000, Ti=0.04-0.060 apfu, and T= 480-800ºC, and the precision of the thermometer is $\pm$ 24ºC at lower temperature and $\pm$ 12 ºC at higher (Henry et al., 2005).

According to the authors, the mechanism of biotite substitution is primarily a response to misfit of octahedral and tetrahedral layers in magnesian biotite. Intermediate biotite (X_{Mg} <0.65), exhibit enhanced Ti concentration most consistent with the Ti deprotonation $TiO_2R_{-1}(OH)_{-2}$ exchange vector. Dominance of Ti-deprotonation substitution is largely a function of reduction of H_2O activity at higher metamorphic grades. The authors analyzed supplementary biotite data from metaluminous amphibolites and mafic granulites with variable H_2O activities. The data revealed that low Al biotite incorporates significantly higher concentration of Ti relative to peraluminous biotite as result of a combination of exchange vector $TiO_2R_{-1}(OH)_{-2}$ and $RSiAl_{-2}$ substituting in roughly, an 8:1 ratio.

The thermometer above was applied to analyzed biotite ofthree samples of biotite-bearing mica schist and one sample of undeformed mafic andesite (PQ35a557-84). The values obtained suggest a mean temperature of around 610ºC (Fig. 5.3-20).

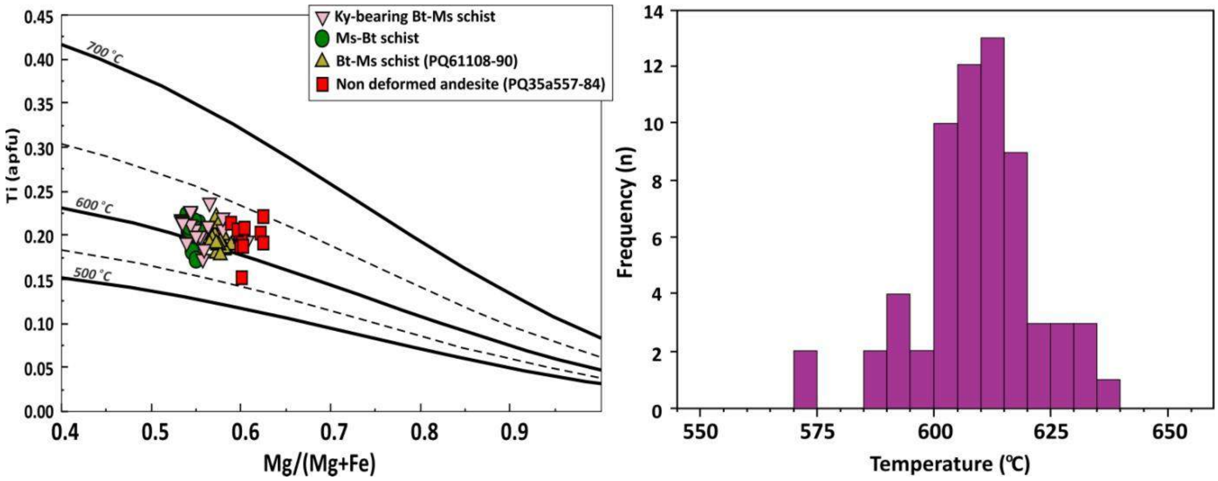

Fig. 5.3-20: On left concentration of Ti (apfu) and Mg mole fraction (XMg) in biotite plotted against isotherms defined by the Ti-Mg thermometer of Henry et al. (2005). On right, histogram of temperatures values obtained from Henry´s thermometer, showing peak in frequency between 600 and 620ºC**.**

Such temperatures seem too high, considering the petrographic aspect of the surrounding rocks.

Despite the presence of Kyanite in biotite-muscovite schist, which generally suggest amphibolite facies,most of petrographic aspects, of non-deformed protolith, suggest condition of greenschist-amphibolite facies transition (<550ºC).

At amphibolite facies(temperature ~610ºC), garnet would be expected in metaluminous mafic rocks (at least in the most normal composition) since at this temperature some of the epidote and chlorite consuming reactions produce garnet (Bucher and Grapes, 2011), given rise to the paragenesis Grt + And + Hbl.

Indeed the absence of garnet at high temperature in metamorphosed metaluminous mafic rocks is possible due to compositional variations and at low pressure(<4 Kbar). Considerind that at low pressure and 610ºC, Kyanite isn't stable and andalusite or sillimanite would be expected, considering kyanite in equilibrium with biotite.

In fact kyanite must not be exactly in equilibrium with biotite since the process that led kyanite crystallization involves removal of Mg and K from the system which probably affected the biotite composition. Anyways the field of stability between andalusite, sillimanite and kyanite is well established and at such high temperature the pressure necessary for stability of kyanite is above 6 Kbar which would be ideal for garnet crystallization in mafic rocks.

From the exposed above, it is possible to say that thermometer based on Ti in biotite has failed and showed temperatures above the metamorphic peak of the area. It can be explained by both, the nature of the analyzed rocks (metaluminous), and the high water activity in the studied rocks, contributing on increase in Ti concentration in biotite, driving the calculated values upward.

Phengite geobarometer

The pressure-temperature dependence of composition of K-white micas coexisting with K-Fsp is one of best known barometer in the literature. The magnitude of phengite component of mica is primarily a function of pressure (Frey and Robinson, 1998). This relation was firstly proposed by Velde (1965) who obtained relevant data to the following reaction:

Phengite = K-feldspar + Chlorite + Quartz + water (4)
Phengite= K-feldspar + Phlogopite + Quartz + water (5)

Experimental data for the latter reaction were provided by Massome and Schreyer (1987) who proposed a barometer based on Si content per formula unit (p.f.u.) of phengite, ideally $KAl_{2-x} Mg_x [Al_{1-x}Si_{3+}xO_{10}] (OH)_2$ with pressure, as well as a moderate decrease of Si (or x) with temperature. According to the authors the stability field of critical assemblage phengite + K-Fsp + Phl + Qtz ranges, in the presence of excess H_2O, from at least 350ºC to about 700ºC, but has an upper pressure limit in the range 16-22 Kbar, when Phl and K-Fsp react to form phengite and a K, Mg-rich siliceous fluid.

According to Essene (1999) the use of the above reaction to determine pressure depend critically on verification that in the rocks to which the barometer is applied, the buffering phases are present under equilibrium. As generally this is not the case, in the absence of K-Fsp, phengite barometry provides only minimum limits of pressure.

Massome and Schreyer (1987) present their calibration in graphical form using only the Si (apfu) content as function of P and T. Anderson (1996) calculated the Massome and Schereyer's graphical solution to the following equation:

$$P= -2.67Si^2 + 43.975Si + 0.01253\ T - 113.9995 \qquad (5)$$

According to the author the equation expresses Massome and Schereyer's data with high precision (r^2=0.999).

The barometer however has its limitations, as pointed out by Anderson (1996). It is sensitive, in which a $\pm$ 50ºC error correspond to an uncertainty of $\pm$ 0.6 Kbar, moreover it is strongly affected by analytical errors (± 0.05 atoms Si yields an additional error of ± 1.3 Kbar) leading to an overall of uncertainty of ± 2 Kbar.

The Phengite barometer of Massome and Schereyer (1987) was tested in analyzed muscovite from shear zones of Pau-a-Pique area, using the equation of Anderson (1996).

Mineral chemistry of analyzed Muscovites

The main mineralogical differences between mica schist formed in shear zones on basement and on metasedimentary rocks are related to the presence or absence of biotite. This difference regards on chemical composition of the protolith. Metasedimentary rocks are quartz rich rocks with feldspar in minor amounts, occurring as sedimentary clasts. Mg-bearing minerals are almost absent or in very low amounts whereas Fe is present in oxides occurring in the matrix.

During fluid-assisted shearing K-Fsp will provide great part of K and Al for the muscovite and part of iron in the matrix will recrystallize as iron oxide and part will occupy the spaces on the octahedral of muscovite structure. The characteristic light-green color of muscovite in sheared sediments seems to be related to the higher amount of iron in its structure when compared to grey color muscovite in the shear zone of the contact (Fig. 5.3-21).

The characteristic grey muscovite from the contact has larger amounts of Mg in its structure (Fig 5.3-21). The general absence of biotite in these rocks suggests that the main shear zone of the contact were preferentially formed over the sedimentary rocks with K-Fsp releasing K and Al to muscovite crystallization. Small amounts of Mg must have come from the neighbor basement and were allocated into the structure of muscovite. As consequence the muscovite in the contact has less amount of Fe and larger amount of Mg (Fig. Fig 5.3-21).

Differences in K and Na are also observed between the two types of mica, however the X_{Na} (Na/Na+K) in both group is lower than 0.15 (Fig. 5.3-21) which mean the presence of Na is not affecting the structure size (*b*-parameter) in a relevant proportion. The highest value of X_{Na} ratio in muscovite from the contact is another evidence of influence of basement on muscovite composition.

Despite the differences in Fe, Mg, Na and K content, between the two types of muscovite, the amount of Al and Si is very similar in both cases (Fig. 5.3-21). There is a trend in variation between Si and Al. The Si content increases with decreasing Al, suggesting that most of exchange between Al and Si was on tetrahedral.

A small group of analyzes show considerably higher values of Al and Si content. These analyses were discarded from barometry calculations since the barometer is very sensible to variation on Si content and, for not showing proportional differences in other elements it is likely to be more related to analytical errors rather than chemical substitution on muscovite structure.

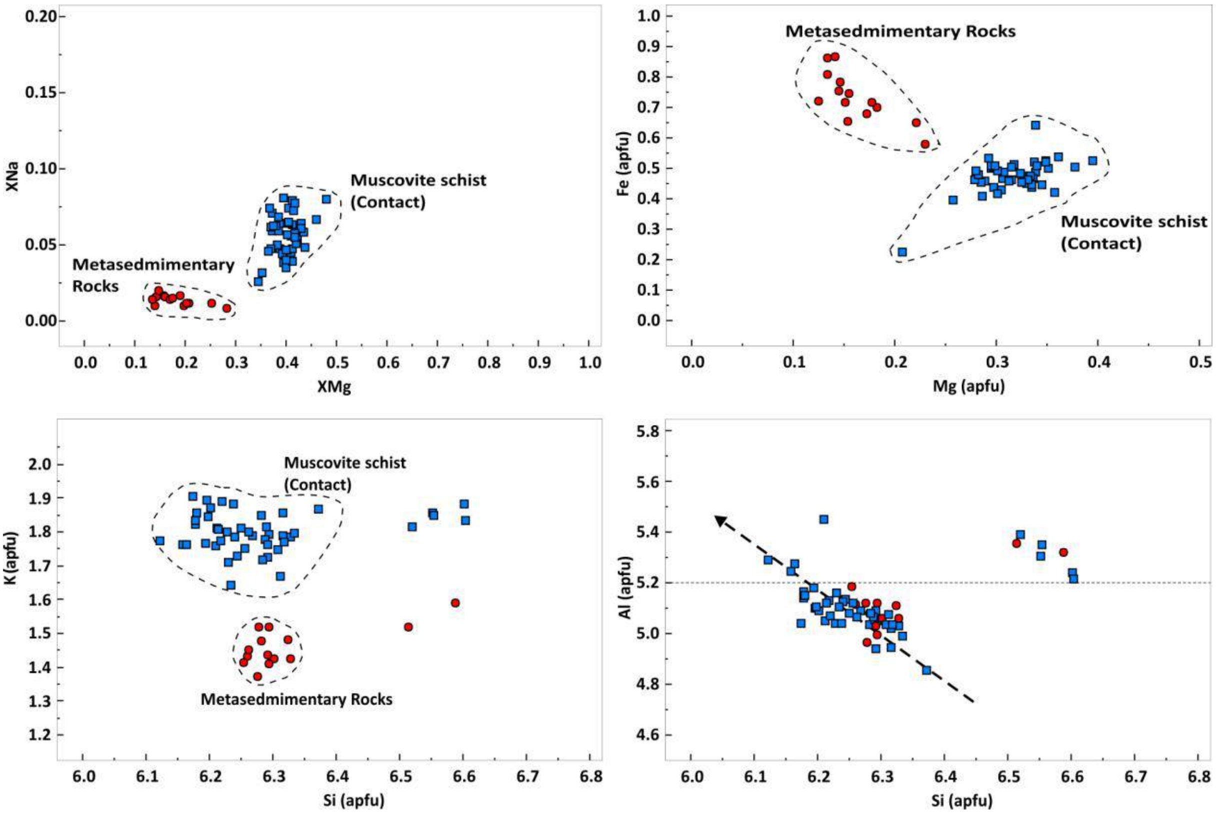

Figure 5.3-21: Chemical composition of muscovite. On top (left) diagram of Na/ (Na+K) versus Mg/ (Mg+Fe) and Fe versus Mg (on right). Both show chemical differences between muscovite from sheared sediments and from shear zone on contact. O bottom (left) K versus Si and (on right) Al versus Si.

Calculations using Si content in muscovitehas given pressure values between 0.9 and 4.3 Kbar and an average pressure of 2.9 Kbar. The estimated temperature used to pressure calculations was 445ºC, which is the mean temperature obtained using the Ti in quartz and $\delta^{18}O$ thermometers(see following sections). Moreover such temperature is in agreement whit the lower limit of greenschist-amphibolite facies transition. A Histogram of pressure interval versus frequency of occurrence is showed in (Fig. 5.3-22). From the histogram is possible to say that the most frequent calculated pressure values using phengite barometer is between 2.5 and 3.5 Kbar and the most representative value is 3.2 Kbar.

As mentioned above, on absence of K-feldspar in equilibrium with muscovite and phlogopite, the calculations using the phengite barometer of Massome and Schreyer (1987) gives only the minimum pressure. From that is possible to say that the minimum pressure for muscovite schist formed in shear zones of Pau-a-Pique area is ~**3.2 Kbar**.

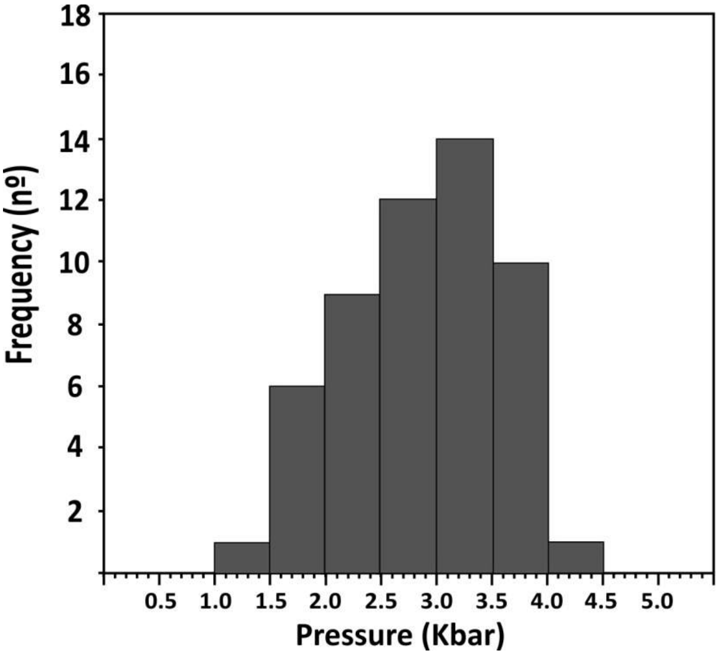

Fig. 5.3-22: Histogram of pressure values obtained from Massome and Schreyer (1987) using the equation of Anderson (1996) in an estimated temperature of 445ºC. The peak in frequency of pressure values occurs between 3.1 and 3.5 Kbar.

TitaniQ thermometry of Quartz veins

In order to estimate the temperature in whichquartz veins of Pau-a-Pique deposit were formed and the minimum temperature of mineralized quartz veins of Ernesto deposit, single mineral trace element thermometry of quartz was employed.

The variation of titanium in quartz as thermometer was firstly proposed by Wark and Watson (2006) and since then it has been considered a consistent thermometer for rocks in which rutile and quartz are in equilibrium. The substitution between Si^{4+} and Ti^{4+} occurs on four fold tetrahedral in quartz (Thomas et al., 2010), and the temperature dependence of that exchange can be used as geothermometer in either aqueous fluid or hydrous silicate melt at temperature ranging from 600 to 1000ºC at 1 GPa (Wark and Watson, 2006).

The degree to which Ti enter the structure of quartz is also dependent on the saturation of Ti in the growth environment. For that Ti-activity in the studied rocks is considered 1, since rutile is present and in equilibrium with the quartz.

According to Wark and Watson the Ti contents of quartz (in ppm by weight) from 13 experiment increases exponentially with reciprocal T and can be described by the equation:

$$\text{Log}\ (X_{Ti}^{Qtz}) = (5.69 \pm 0.02) - (3765 \pm 24) / T\ (K) \qquad (6)$$

Later works explored the pressure dependence on Ti solubility in quartz in presence of rutile (Thomas et al., 2010; Huang and Audétat, 2012). The effect of pressure on solubility of Ti in quartz is smaller than that of temperature but experimental data from the above authors demonstrated that it is not negligible as previously believed.

The dependence of Ti solubility on both pressure and temperature proposed by Thomas et al., (2010) can be expressed as:

$$RT \ln (X_{TiO2}^{Qtz}) = -60952 + 1.520.T\ (K) - 1741.P\ (Kbar) + RT \ln a_{TiO2} \tag{7}$$

where R is the gas constant 8.3145 J/K, T is the temperature in Kelvin, X_{TiO2}^{Qtz} is the mole fraction of TiO_2 in quartz and a_{TiO2} is the activity of TiO_2 in the system. According to Thomas et al., (2010), the *P-T* dependencies of Ti-in-quartz solubility can be used as thermobarometer when in combination with another thermobarometer in coexisting mineral, an independent *P* or *T* estimate of quartz crystallization, or well-constrained phase equilibrium. If temperature can be constrained within $\pm$ 25°C, pressure can be constrained to approximately$\pm$ 1.2 kbar. Alternatively if pressure can be constrained to within +1 Kbar, the temperature can be constrained to approximately $\pm$ 20°C. In order to obtain the temperature from a known pressure the above expression can be simplified to:

$$T(^{o}C) = [(a + c\ P) / (b - R \ln (X_{TiO2}^{Qtz}) + R \ln (a_{TiO2}))] -273.15 \tag{8}$$

where $a= 60952 \pm 3122; b= 1.520 \pm 0.04; c= 1741 \pm 63.$

The *P-T* dependence on Ti solubility of quartz, proposed by Thomas et al. (2010) was later re-evaluated by Huang and Audétat (2012). The authors found that the incorporation of Ti and other trace elements in hydrothermally grown quartz depends strongly on growth rate, with absolute concentration increasing rate of crystal growth. The Ti solubility observed during their study is about three times lower than those determined by Thomas et al. (2010). According to the authors the Ti solubility in the experiment of Thomas et al. (2010) may have been over estimated due to rapid crystal growth. As result Huang and Audétat (2012) proposed a new calibration:

$$\log Ti\ (ppm) = -0.27943\ 10^{4} / T - 660.53\ (P^{0.35} / T) + 5.6459 \tag{9}$$

where *T* is in Kelvin and *P* in kbar.

A limiting on application of TitaniQ thermobarometers regards on obtaining reliable values of Ti. In quartz formed at temperature above 600ºC, the Ti concentration can be determined by electron microprobe (EPMA) (Wark and Watson, 2006). However in quartz formed at temperature bellow 600ºC the Ti content has to be measured by equipments with lower detection limit than that of EMPA due the low concentrations in low temperature quartz. It includes the use of ionic microprobe (SIMS) and alternativelly, LA-ICP-MS.

Very few laboratories are equipped with SIMS, and those with the facility generally have long waiting list and expensive prices. The use of LA-ICP-MS has advantages on costs and time, since the analysis generally takes less than a minute. However a limiting on use of LA-ICP-MS on analysing quartz is the behavior of it during ablation, since it tends to broke into small pieces (chips) during ablation, affecting the quality of the results.

Concentration of Ti in quartz of quartz veins from Ernesto and Pau-a-Pique deposits were determined by LA-ICP-MS.The analyses were performed in one sample of pyrite-bearing quartz veins from the intermediate level of Ernesto deposit and in four samples of mineralized and barren quartz veins from Pau-a-Pique. The Ti concentration obtained in quartz from Ernesto deposit is between 2.67 and 4.38 ppm (uncertainty between 0.37 and 1.16ppm). Yet the Ti concentration in quartz veins from Pau-a-Piquedeposit is between 2.74 and 5.84 ppm (uncertainty between 0.25 and 0.85 ppm). The variation of Ti concentration between the samples is showed in (Fig. 5.3-23) where it is possible to notice little variations on Ti between the analyzed samples regardless the type of quartz veins or its spatial localization since most of values are between 2 and 6 ppm.

Values of temperature obtained from equations (8) and (9) are graphically shown in the histograms of Fig. 5.3-24. As both equations are pressure dependent, the calculations were perfomed using pressure of 3.2 Kbar for Pau-a-Pique samples (obtained from phengite barometer) and 0.01 Kbar for Ernesto samples.

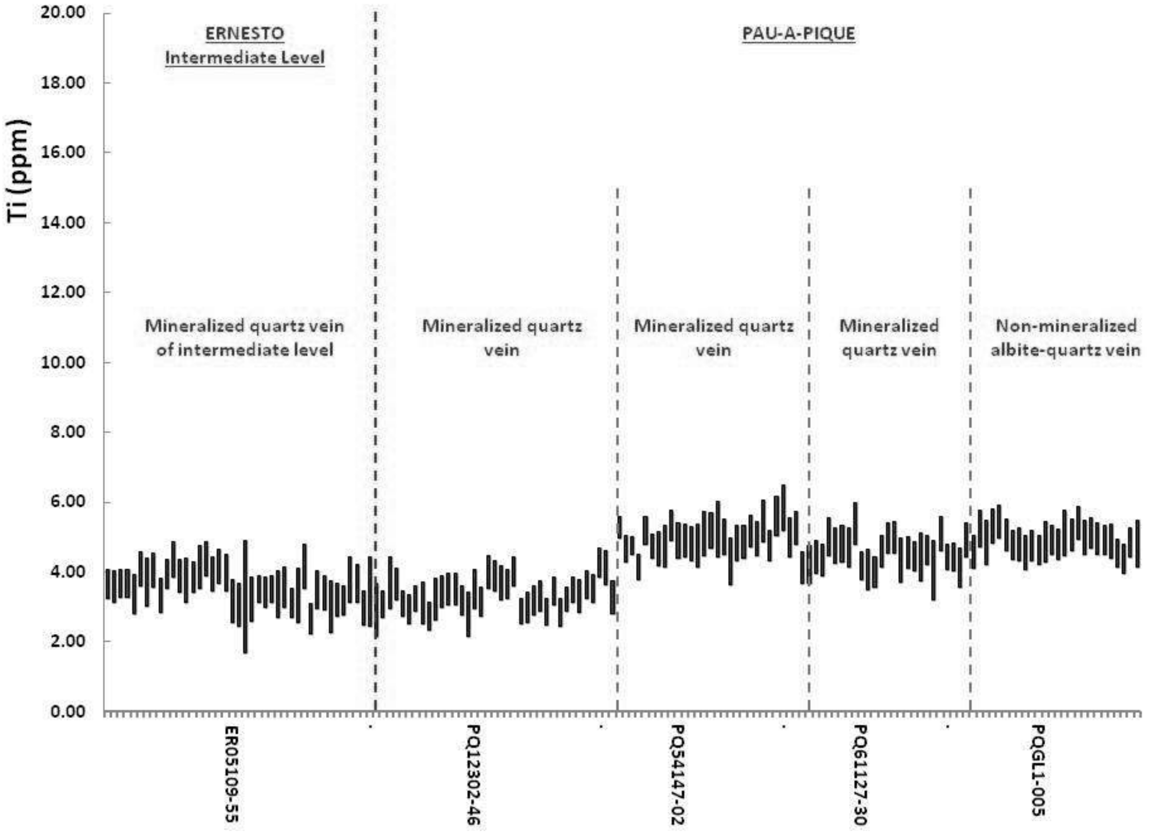

Fig. 5.3-23: Variation on Ti concentration in analyzed quartz veins Pau-a-Pique and Ernesto deposit. The bars represent the values with the uncertainty and the mean value (used in temperature calculations) is represented by the center of each bar.

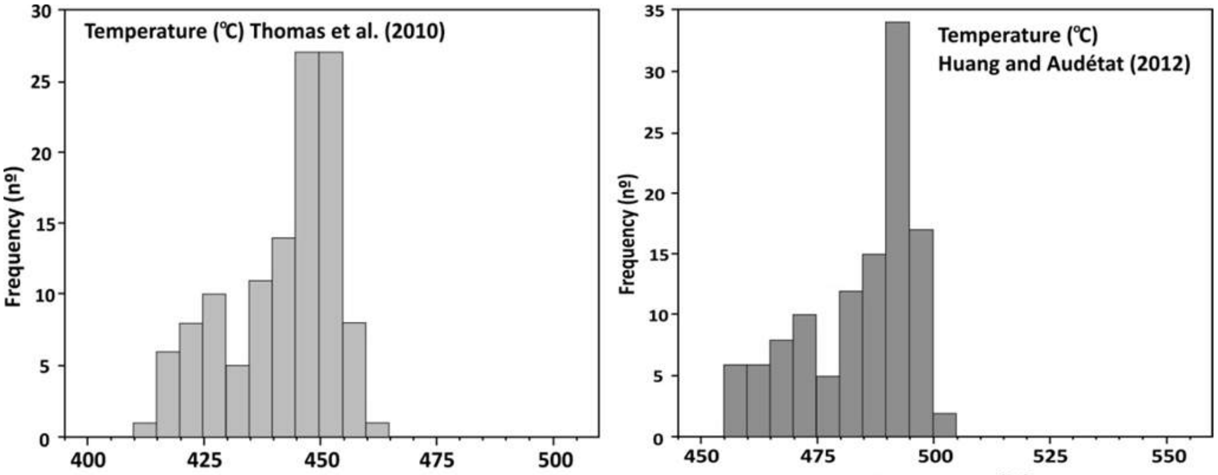

Fig. 5.3-24: Histograms of TitaniQ temperatures obtained using the calibrations of Thomas et al. (2010) (on left) and Huang and Audétat (2012) (on right) for Ti concentration of quartz vein and quartz albite veins from Pau-a-Pique deposit. Temperature estimations were made considering pressure= 3.2 kbar. The peak in frequency occurs between 485 and 499ºC using calibration of Huang and Audétat (2012), and between 445 and 454℃ using calibration of Thomas et al. (2010).

Since there is no pressure estimation for rocks from Ernesto area and considering that Pressure increases with temperature along the Ti isopleths in both calibrations, temperature estimations was mad using 3.2 Kbar (the minimum pressure found in shear zones of Pau a Pique area). Variations of 1Kbar gives variation of ~20ºC in both termometers which is not such a huge variations considering that pressure may have not variated more than 2Kbar in between the two areas.

The temperatures obtained from Pau-a-Pique samples using the calibration of Huang and Audétat (2012) are, in general, 42ºC higher than the obtained using the calibration of Thomas et al. (2010). The peak in frequency of temperature values occurs between 445 and 454ºC for calibration of Thomas et al. (2010) and between 485 and 499ºC for calibration of Huang and Audétat (2012).

The temperatures obtained from Ernesto sample, using calibration of Thomas et al. (2010), vary from 412 to 443ºC with peak of frequency between 426 and 430ºC (Fig. 5.3-25) and from 453 to 485ºC, with peak between 471 and 475ºC using calibration of Huang and Audétat (2012), suggesting the the temperature of cristalization of quartz veins in both areas were similar being however litlle bit lower in Enesto.

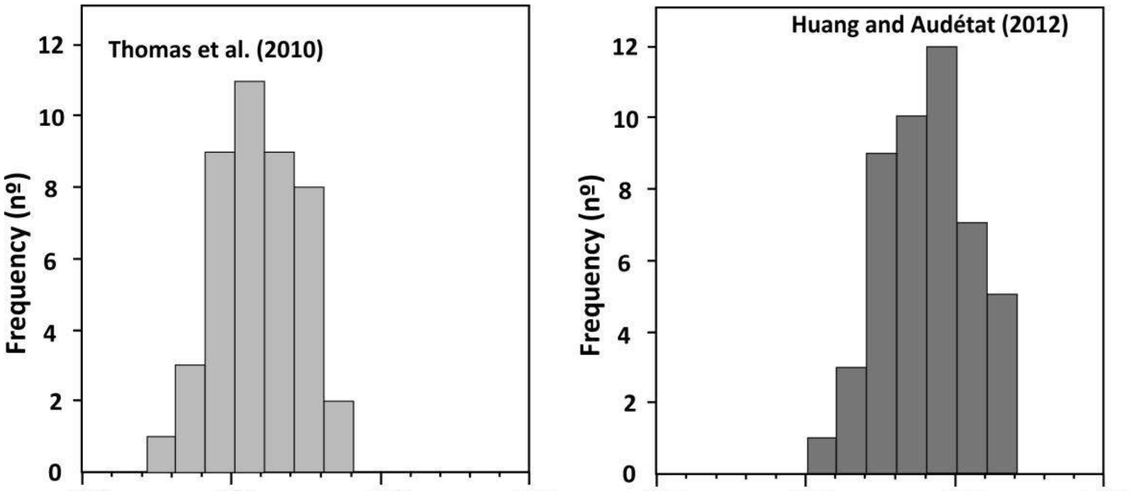

Fig. 5.3-25: Histograms of TitaniQ temperatures obtained using the calibrations of Thomas et al. (2010) and Huang and Audétat (2012) for Ti concentration of a sample of mineralized pyrite-bearing quartz vein from Ernesto deposit. Temperature estimations were made considering pressure= 0.01 kbar, to obtain the minimum temperature. The peak in frequency occurs between 295 and 304ºC using calibration of Huang and Audétat (2012), and between 365 and 379ºC using calibration of Thomas et al. (2010).

Cathodo-luminescence study of quartz veins

Quartz veins from Pau-a-Pique and Ernesto deposits were studied by SEM cathodo-luminescence (CL). Detection of CL-bright texture is particularly important when using TitaniQ thermometers. According to Rusk et al. (2008) Ti concentrations may act as CL activator in quartz formed at temperature above 400ºC.

Cathodo-luminescence imaging showed thatquartz veins of Pau-a-Pique and Ernesto may show CL-bright textures.

The texture observed in Pau-a-Pique tends to occurs at the less deformed portions of the veins where it doesn't show ondulatory extinction. Indeed it is a rare feature in Pau-a-Pique veins since most of quartz veins were subject to high deformation rates. Consequently most of studied samples showed CL-dark quartz.CL-bright textures are given by bright zones of irregular shape limited by the occurrence of fluid inclusions trailsin cores of clean quartz.

Some of the samples with CL-bright texture were analyzed by LA-ICP-MS in order to verify the influence of Ti concentrations in CL-bright zones. Apparently there is no correlation between Ti concentration and CL-bright texture, however the presence of Li above the detection limit were detected in bright zones being the Li content, higher in the core of CL-bright zones and, below the detection limit in CL-dark zones (Fig. 5.3-26 A, B).

The mineralized quartz veins of Ernesto deposit have growth zoning textures (Fig. 5.3-26 D). The presence of preserved growth zoning texture in quartz of mineralized veins suggests that the vein were subject to low rates of deformation. It is also observed by the petrographic aspects, such as absence of ondulatory extinction the rare presence of recrystallization textures.

Lithium is below the detection limit in all analysis and there is no apparent relationship between CL-bright zoning and Ti concentration. In fact in some portions Ti concentration seems to be higher as brighter the zone is, but in other portions of the same sample the opposite occurs, suggesting that there is no specific relationship between Ti and cathodo-luminescence activation of quartz at the studied sample (Fig. 5.3-26 E, F).

According to Rusk et al. (2008) other trace elements in quartz may be related to the occurrence CL activation such as Al, which correlates with CL fluctuations in low temperature quartz, but the detection limit of Al of used LA-ICP-MS doesn't allowed to analyze Al.

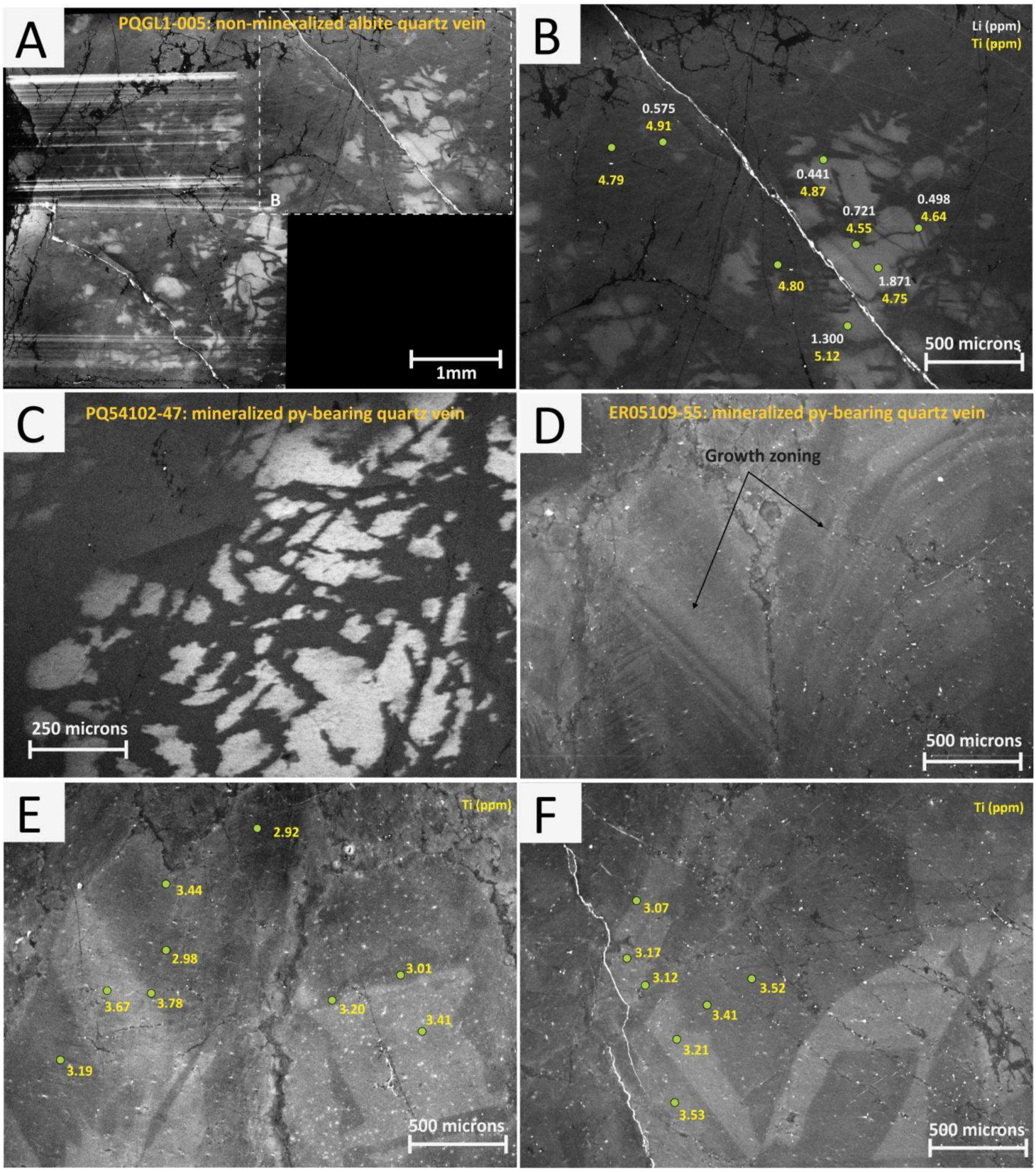

Fig. 5.3-26: Cathodo-luminescence texture of quartz vein from Ernesto and Pau-a-Pique deposits. (A) CL-bright texture occurring in non-mineralizedalbite quartz vein of Pau-a-Pique deposit; (B) variation on Ti and Li content in both CL-bright and CL-dark zones; (C) CL-bright texture occurring mineralized quartz vein of Pau-a-Pique deposit; (D) growth zoning texture in mineralized quartz vein of Ernesto deposit; (E and F) variation on Ti content in both CL-brighter and CL-darker zones.

Despite the presence of CL-bright texture, cathodo-luminescence imaging coupled with LA-ICP-MS analysis showed that the presence of CL-textures in both deposits has no apparent influence on Ti content and as consequence there are no issues regarding the application of TitaniQ thermobarometry at these rocks.

δ18O Thermometry

The isotopic fractionation of oxygen between any two phases is related to temperature of their formation. Stable isotope thermometry requires that the two phases are in isotopic equilibrium at the conditions of geological interest.

Based on the statements above, stable isotope thermometry using quartz-magnetite pair was tested in three samples of quartz veins hosted by muscovite schist occurring on contact between basements and sediments ofPau-a-Pique deposit. One of the samples was also tested using muscovite-magnetite pair.

The stable isotope data will be discussed in detail below. Here is shown only the temperature calculation.

Because the huge difference on fractionation between magnetite and quartz and between magnetite and muscovite, thermometry using these pairs are very sensitive to changes in temperature and are less influenced by contaminations.

As exposed before, the petrographic texture show evidences that quartz (in quartz veins), magnetite and muscovite were formed nearly peak conditions during fluid assisted shearing.

Two different calibrations was used for Qtz-Mag thermometry. Clayton and Kieffer (1991):

$$1000 \ln\sigma = A\,(10^{18})/T^6 + B\,(10^{12})/T^4 + C\,(10^{9})/T^3 + D\,(10^{16})/T^2 + E\,(10^{3})/T + F \qquad (10)$$

where 1000 lnσ is $\sim\delta^{18}O_{Qtz\text{-}Mag}$, A= 0.0120, B= -0.3320, C=0.000, D= 6.442, E= 0.000 and F= 0.000 and T is temperature in Kelvin, and Zheng and Simon (1991):

$$1000 \ln\sigma = D\,(10^{16})/T^2 + E\,(10^{3})/T + F \qquad (11)$$

where D= 1.120, E= 8.220 and F= -4.350. For the muscovite-magnetite pair was used the calibration of Valey (2003):

$$1000 \ln\sigma = D\,(10^{16})/T^2 + E\,(10^{3})/T + F \qquad (12)$$

where1000 lnσ= $\sim\delta^{18}O_{Ms\text{-}Mag}$, D= 4.920, E= 0.000 and F= 0.000.

The temperatures obtained using the above calibrations are between 373 and 518ºC (Fig. 5.3-27).

Calibration of Zheng and Simmon (1991) gave lower values of temperature (373 - 444ºC. It is approximately 75ºC lower than those of Cleyton and Kieffer (1991) in which temperature are between 446 and 518ºC. Thermometry using the pair Muscovite and magnetite (sample PQ31665-27) gave temperature of 418ºC using the calibration of Valey (2003) (Fig. 5.3-27), but Valey's thermometer was calibrated for temperatures above 600ºC and its validity for rocks formed in lower temperature is unknown.

The above calibrations are graphically expressed as curves in Figure 5.3-28. The mean value of temperature is around 448ºC (approximately the mean temperature obtained using TitaniQ thermometer of Thomas et al. (2010).

Zheng and Simon (1991) is a theoretical calibration and seem less consistent when compared to the experimental calibration of Cleyton and Kieffer (1991) (calibrated for temperature above 127ºC). The temperature obtained using Clayton and Keiffer's calibration gives a mean temperature of 490ºC consistent with temperatures obtained using Huang and Audétat (2012) calibration for TitaniQ thermometer.

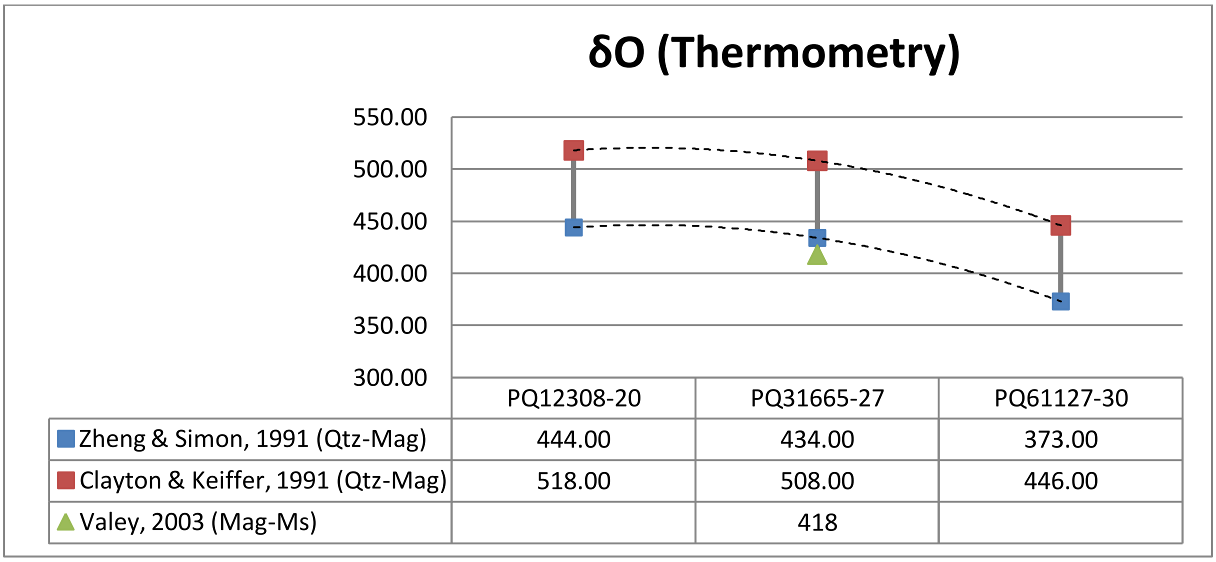

	PQ12308-20	PQ31665-27	PQ61127-30
🟦 Zheng & Simon, 1991 (Qtz-Mag)	444.00	434.00	373.00
🟥 Clayton & Keiffer, 1991 (Qtz-Mag)	518.00	508.00	446.00
▲ Valey, 2003 (Mag-Ms)		418	

Fig. 5.3-27: Results of δ18O thermometry using the pairs quartz-magnetite and muscovite-magnetite, using the calibration of Zheng and Simon (1991) and Clayton and Kieffer (1991) for quartz magnetite pairs and Valey (2003) from muscovite magnetite pair.

Considering that kyanite seems to be (petrographycally) in equilibrium with micas (biotite and muscovite), at ~500ºC the stability of kyanite would require a minimum pressure of ~4.2 Kbar or ~3.2 kbar at temperature of ~450ºC.

The pressure estimation using phengite content in absence of K-feldspar gives only the minimum pressure thus it is possible to conclude from geothermometric data that the metamorphic peak is somewhere between 445 and 518ºC and above 3.2 kbar.

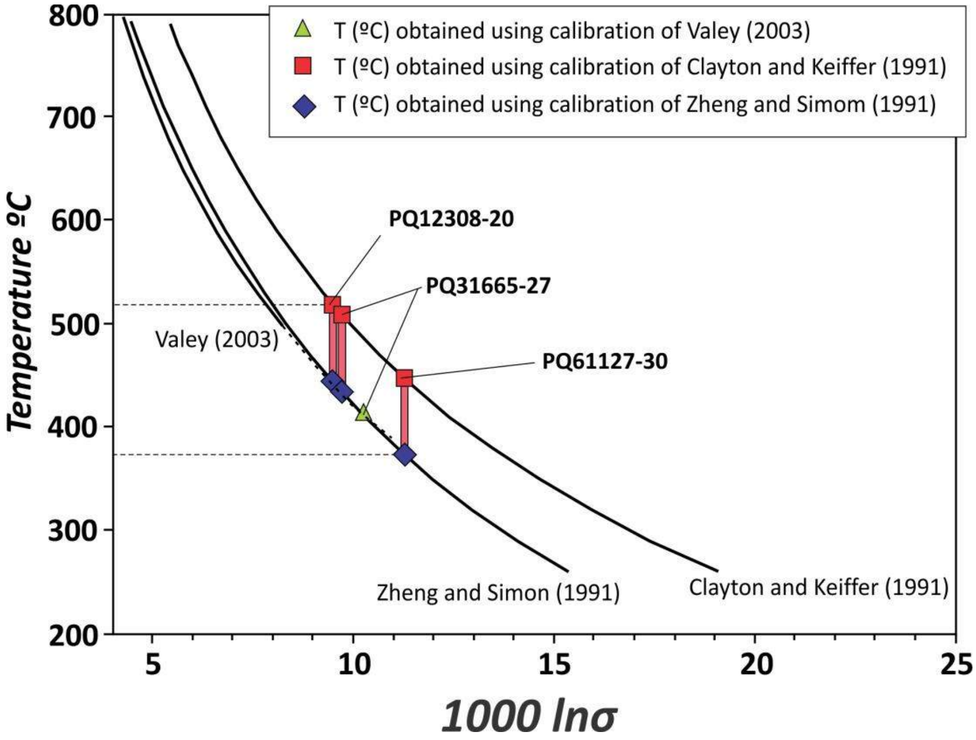

Fig. 5.3-28: Diagram of temperature versus 1000 lnσ (~δ18Ox-y). The curves represent the different calibrations and the symbols are the projection of δ18Ox-y on calibration curves. The red bars are the interval of temperature between the two calibrations.

Chlorite thermometry

Textural aspects

Chlorite is a common retrograde mineral in biotite-muscovite schist of Pau-a-Pique deposit, where it generally occurs as product of biotite alteration (Fig. 5.3-16a, b). It is also present is non-deformed diorites, generally associated with amphiboles and biotite.

It is an important mineral phase in the ore host rocks (muscovite schist and quartz albite vein with pyrite). In muscovite schist, chlorite occurs associated with pyrite. In some samples pyrite porphyroblasts are enclosed by thin layersof chlorite and in others it is forming the pressure shadows of pyriteporphyroblasts(Fig. 5.3-29). It generally occurs as pseudo-uniaxial plates arranged in rosette-shaped aggregates, associated with pyrite or filling fractures in veins (Fig. 5.3-29). A secondary form of occurrence is along later micro-cracks and micro-faults in quartz veins. In this case very fine-grained crystals of chlorite are filling micro-cracks that crosscut all kind of minerals in the sample, including earlier formed chlorites (Fig. 5.3-29).

The pyrite crystals occurring in albite- and albite-quartz veins tend to be massive not showing the typical textural zoning found in those of muscovite schist. However some of pyrite porphyroblasts occurring in samples of albite vein has fractures and mineral inclusions filled by chlorite in association with carbonate and galena (Fig. 5.3-30). Most of these porphyroblasts grown over a fracture, which is now, sealed by carbonate and chlorite. This texture, suggests that the mineral inclusions are syn-genetic to the porphyroblasts growth.

The retrograde aspect of chlorite in mica schist and its close relations with pyrite and carbonate suggest that these minerals are approximately syn-genetic to pyrite. The presence of chlorite in pressure shadows of pyrite attest for the syn-genetic aspect of it and its formations is related to at least, the later stages of pyrite crystallization. Thus, the temperature obtained for chlorite crystallization must be as closer as possible the temperature in which pyrite was precipitated.

Scanning-Electron microscope (SEM) study of chlorites occurring in pressure shadows of pyrite in muscovite schist, and in quartz-albite veins, revealed that some chlorites are characterized by oscillatory zoning. Electron microprobe micro-mapping showed that the oscillations correspond to chemical zoning with alternating iron-rich and magnesium-rich bands (Fig. 5.3-31).

Thermometry

The general structural formula of chlorite is $(Ru^{+2}\ Ry^{+3}\ Xz)^{iv}\ O10 + w(OH)8-$, where $u + y + z = 6$, $z = (y - w - x)/2$, $w = 0$, $R^{2+}$is generally given by Mg^{2+} or Fe^{2+}, R^{3+} generally given by Fe^{3+} or Al^{3+} and X = □ (De Caritat et al., 1993).

The wide compositional variety of chlorites occurs through the effect of three main substitutions Fe^{2+} = Mg, Tschermak $Al^{IV}Al^{VI}$ = Si (Mg, Fe^{2+}) and di/trioctahedral 3(Mg, Fe^{2+}) = □ + $2Al^{VI}$ and these substitution are known to be sensitive to pressure and temperature conditions of formation, to the bulk composition and the physico-chemical properties of the environment.

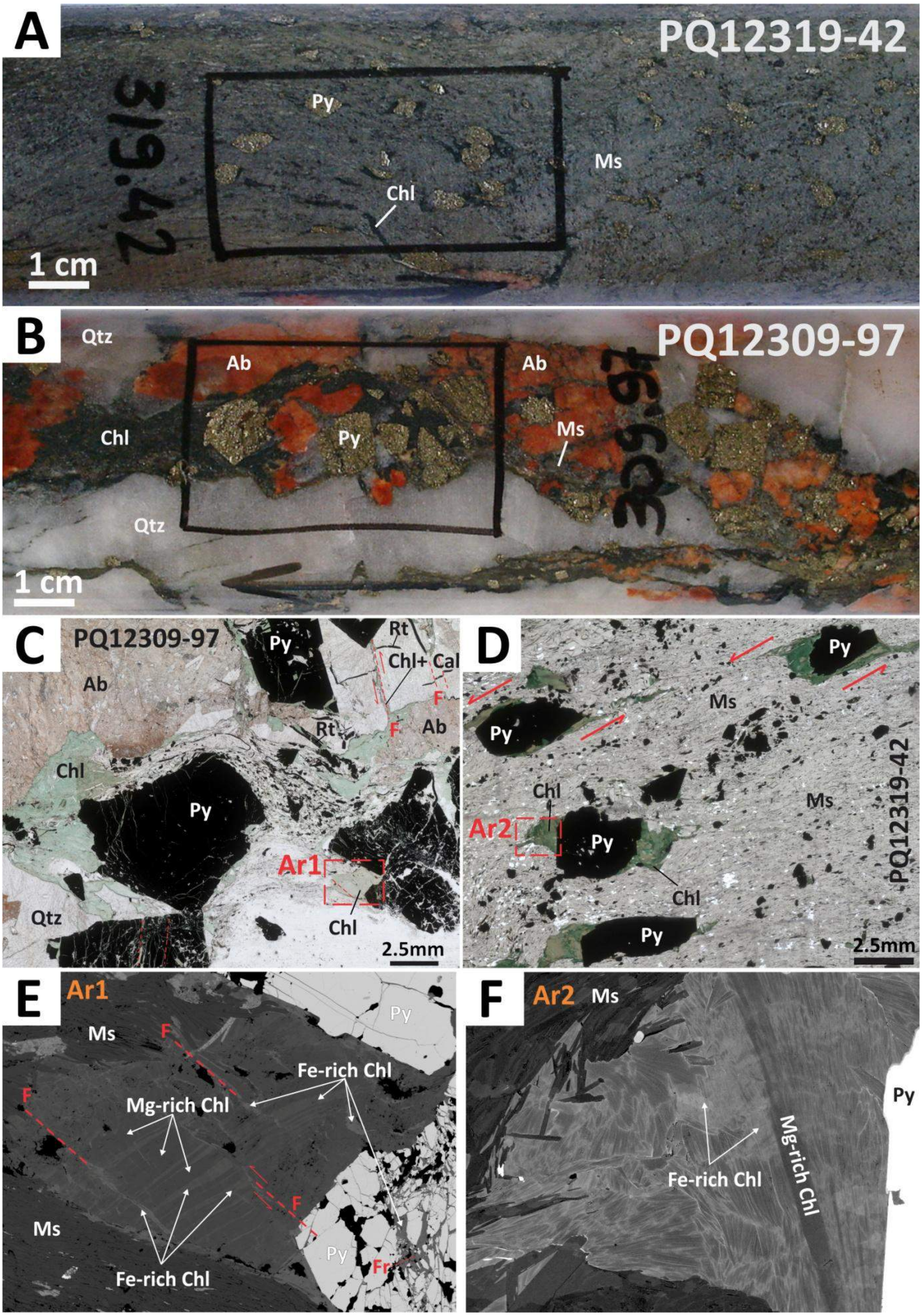

Figure 5.3-29: Textural aspects of chlorites occurring in pressure shadows and of pyrite porphyroblasts in muscovite schist and quartz veins, since hand scale to microscopic scale, showing structural features and the microprobe mapped areas of Figure 5.3-30**.**

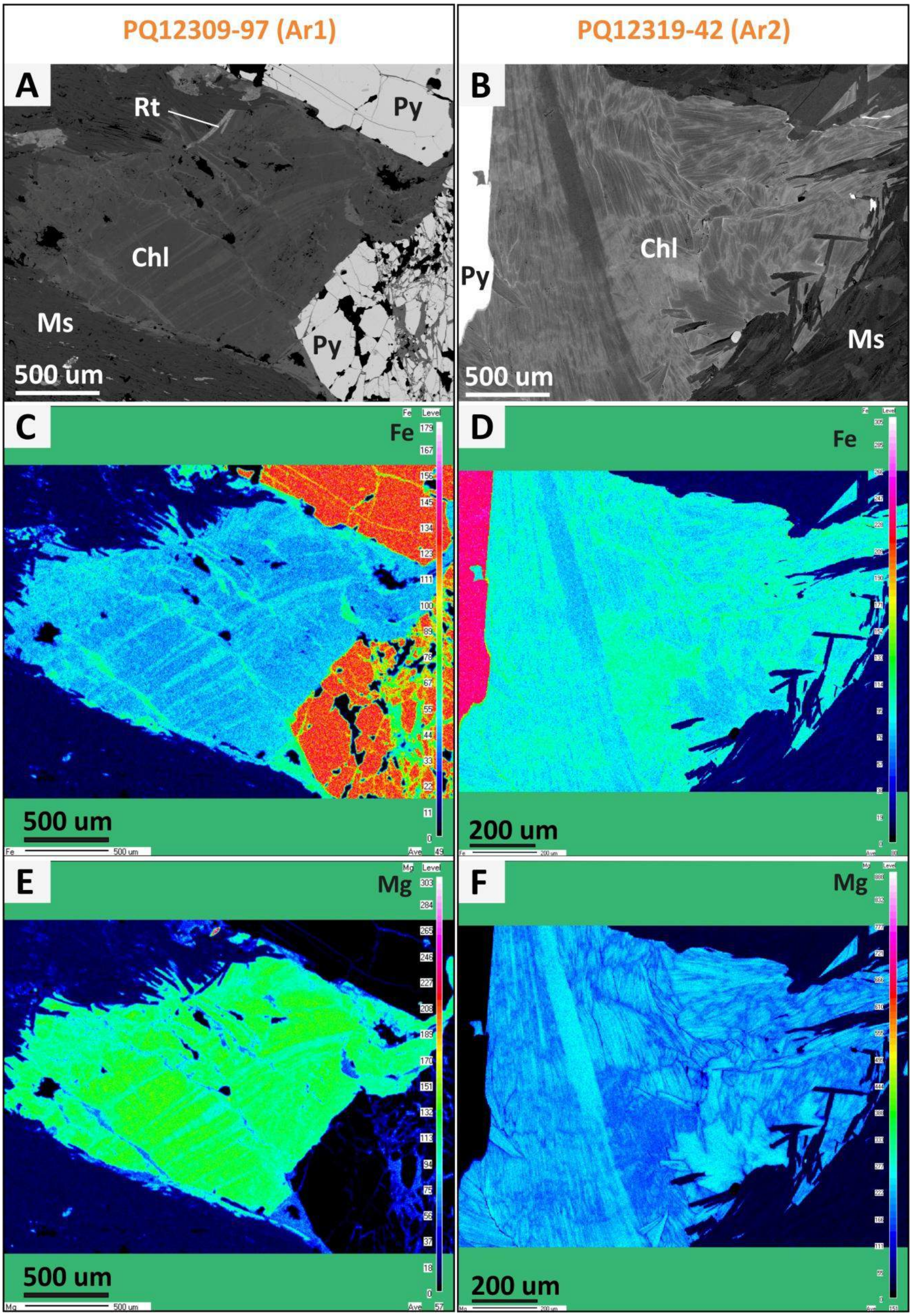

Figure 5.3-30: Microprobe X-ray (WDS) micro-mapping of chlorites showing oscillatory zoning. (A and B) SEM imaging of the mapped areas; (C and D):Microprobe mapping Fe; (E and F) Microprobe mapping Mg. In all compositional maps the colors are relative intensity and there is no direct correlation with concentration between the mapped areas.

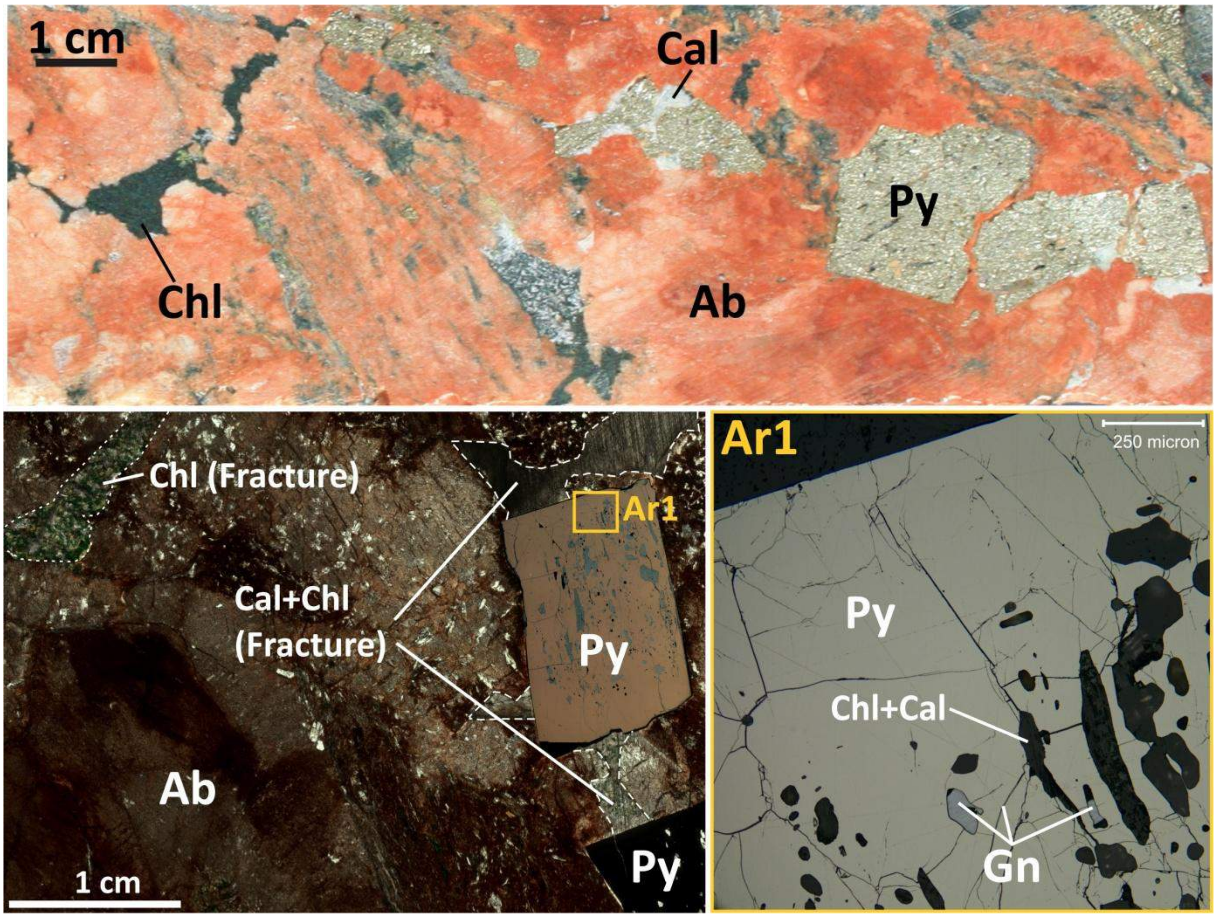

Figure 5.3-31: Textural association of pyrite, carbonate, chlorite and galena occurring in fractures of albite veins: On top, hand sample showing porphyroblasts of pyrite associate with carbonate. On bottom (left) micro scanning image showing porous pyrite formed along a fracture filled by carbonate and chlorite and. On right reflected light petrography showing galena occurring as inclusions and along fracture in pyrite and its association with chlorite and calcite.

There is a long discussion in the specialized literature about chlorite thermometry and despite the advances made in more than two decades since the first calibration of chlorite as thermometer, the huge compositional variability of chlorite is a limiting on its use.

Three different approaches to chlorite thermometry were developed through the past two decades, it comprises: the empirical thermometers based on amount of aluminumor/and octahedral vacancies (□) (e.g. Cathelineau and Nieva 1985; Kranidiotis and MacLean 1987; Cathelineau 1988; Hillier and Velde 1991; Jowett 1991; Zang and Fyfe 1995). The semi-empirical calibrations, based on relationship between temperature and equilibrium constant (K) of a reaction involving chlorite, end-members and, typically quartz and water (e.g. Walsh 1986; Inoue et al. 2009; Bourdelle et al. 2013); and the thermodynamic approach in which the mixing properties and activity composition relationship of chlorite are thermodynamically modeled (e.g. Lanari et al., 2014).

The main problem on using empirical calibration lies on influence of rock bulk composition and fO_2 in the chemical composition of chlorite and as consequence there isn't a single empirical thermometer that performs satisfactorily over a wide range of Al-content, Fe/(Fe+Mg) values, coexisting mineral assemblages, and temperatures (De Caritat et al., 1993). The thermodynamic approach circumvents this problem however the large range of compositional variation in chlorite was not properly handled by thermodynamic modeling.The semi-empirical approach proposed a new, better suited geothermometer that does not require the knowledge of the end-member thermodynamic properties, but in most of cases, it includes the effect of Fe^{3+} content on temperature estimations, requiring independent estimations of Fe^{3+} in chlorite (Bourdelle et al., 2013).

According to De Caritat et al. (1993) if the thermometer from empirical calibration is used to determine temperatures in chlorite from similar settings (bulk rock composition, fO_2, etc) satisfactory results may be obtained. It has two important advantage over the thermodynamic and semi-empirical calibrations, takes into account the compositional effects of multiple thermodynamic variables that do not need to be measured and is simple to be applied since it generally has form of a linear function. However, these empirical functions appear to be very sensitive to parameters other than temperature (e.g., coexisting mineral assemblage), and their use should not be extrapolated outside the calibration area/conditions without careful evaluation of the impact that these parameters may have upon chlorite composition.

Considering the problems that poses on semi-empirical and thermodynamic calibrations, for this study was applied the simple empirical calibration. Two calibrations was chosen for test, Cathelineau (1988) and Kranidiotis and MacLean (1987).

Kranidiotis and McLean (1987) thermometer was calibrated for hydrothermal chlorites of a volcanogenic massive sulfide deposit. The bulk rock comprises altered rhyodacite and rhyolite and the mineral phases present include quartz, albite, epidote, sericite, talc and stilpnomelane. The thermometer can be applied to conditions where chlorite is associated with other aluminous minerals:

$$T\ (^{\circ}C) = 106\ (Al^{IV} + 0.7(Fe/\ (Fe+Mg)) + 18 \qquad (15)$$

Cathelineau (1988) used the chlorite analyzes of Los Azufres, Mexico, by Cathelineau and Nieva (1985) and of Santon Sea by McDowell and Elders (1980). In Los Azufres, chlorite constitutes a major hydrothermal alteration product of an andesitic host rock. The mineral phases associated to chloriteinclude,Qtz, Ill, Ab,Py and Hem, in Los Azufres and Qtz, K-Fsp, Ank, Cal, Ab, Pl, Ill and Py in Salton Sea:

$$T\ (^{o}C) = -61.92 + 160.99(Al^{IV}) \qquad (14)$$

The structural formula of the studied chlorite was calculated using the program WinCac® (Yavuz et al., 2014). WinCac estimates H_2O (wt %), Fe_2O_3 (wt %) and FeO (wt %) amounts of chlorite analyses obtained from electron microprobe FeO_{tot} (wt %) contents according to the stoichiometric criteria (Yavuz et al., 2014). The amount of FeO_{tot} was calculated from Fe_2O_{3tot} (obtained from the microprobe analysis) by:

$$FeO_{tot} = Fe_2O_{3tot} \times 0.8998 \qquad (13)$$

in order to permit the entry of FeO_{tot} on program.

The program calculated the structural formula of chlorite based on 14 oxygen and also calculated the distribution of elements into the tetrahedral, octahedral and interlayer sites of the chlorite structure.

Five samples containing hydrothermal chlorite was used on obtaining chlorite temperature, three samples of muscovite schist and two samples of albite- and quartz-albite veins.

The temperatures obtained using the above calibrations are shown in the histogram of Figure (5.3-29). It ranges between 278 and 393ºC with the maximum between 370 and 375ºC using the calibration of Cathelineau (1988), and between 273 and 355 with maximum between 320 and 325ºC using the calibration of Kranidiotis and MacLean (1987).

Other seven calibrations based on Al^{IV} content of chlorite were tested using WinCac program none of then gave temperatures above 400ºCor below 200ºC.

In terms of bulk rock composition and geological setting, the calibration of Kranidiotis and MacLean (1987)seems to be more suitable to the composition of hydrothermal chlorites of Pau-a-Pique. From that it is possible to say that the mean temperature registered in chlorites of Pau-a-Pique deposit is about 325ºC.

The textural aspect of chlorites in association with thermometry can give additional information on understanding the wide range of temperature values obtained and process involved.

According to Trincal et al., (2015) oscillatory compositional zoning in Chlorites from Perinean Axial Zone (Spain) can be explained by alternation of cooling time and cyclical pulse of fluid hotter than the host rock. The author found differences in temperature from about 310 to 400ºC ± 50 applying the thermodynamic thermometer of Lanari et al. (2014).

Trincal et al. (2015) suggest that the input of hotter fluids could be related to fault valve process in which, high temperature fluid from deeper fault portions moved up by an abrupt increase in fracture permeability. According to the author temperature measurements in a fault after earthquake indicate a slightly positive anomaly (Trincal et al., 2015 and the references therein).

In a similar way, some of the studied samples shown huge variations of temperatures in zoned chlorites as result of alternate zoning. As observed by Trincal et al. (2015), the highest temperatures values are registered in the Mg-rich zones in contrast to the lower temperature found in Fe-rich zones. It suggests that a similar process was active during chlorite formation in some of the studied samples. Importantly, the authors used a totally different approach on obtaining temperature (the thermodynamic calibration of Lanari et al., 2014) but the same aspect of lower temperature in Fe-rich zones against the higher temperature in Mg-rich zones was observed.

If considering that the fluids responsible for chlorite crystallization was the same of sulfidations and mineralizations, the presence of alternating zoning in chlorite may indicates that alternating temperature may have played an important role on gold transporting and precipitation since variation in physical conditions of the fluid generally affects its solubility.

Independently, alternating zoning help to explain the large variations in temperature found aplying chlorite thermometry.Additionally the lowest temperature values were found in the extremely Fe-rich chlorites occurring along fractures and faults in the sample PQ12309-97 (Fig. 5.3-30a, c, e). The textural aspect of it indicates that this group of chlorite is later, since it occurs cross-cutting phases in the rock including the earlier formed chlorites (Fig. 5.3-29e). It can be interpreted as the later stages of fluid circulation and probably not related to pyrite crystallization (in which chlorites are characterized by alternating zoning).

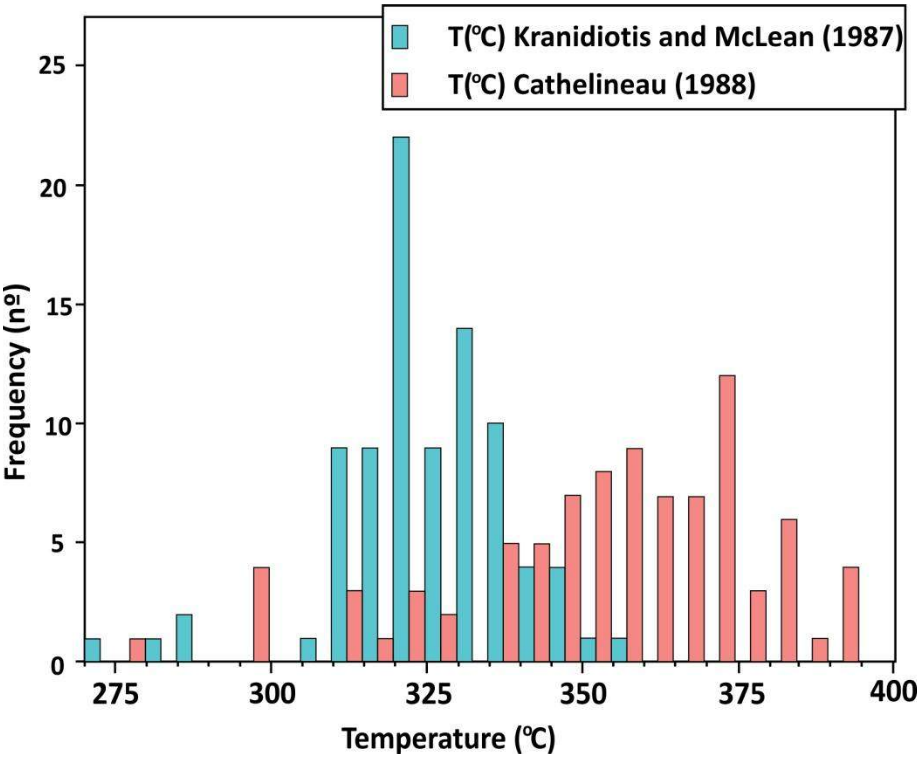

Figure 5.3-32: Histogram of temperature obtained from chlorite thermometry using calibrations of Cathelineau (1988) and Kranidiotis and McLean (1987).

5.3.3 Discussion

Most of the mapped area records conditions compatible with the chlorite zone of greenschist facies. It is particularly common on central area. In such portion the low grade conditions are evidenced by the presence of pelitic phyllites composed by sericite and chlorite where the temperature can be estimated as being above 280^{o}C (presence bulging recrystallization in quartz feldspatic rocks) and below400^{o}C(absence of biotite in pelitic rocks and absence of subgrain rotation-SGR). The *b*-parameter of K-white micas from metasedimentary rocks are coherent with low to intermediate pressure metamorphism (~25^{o}C/Km). Graphical estimation of pressure suggests mean value of 2.4 Kbar (between 1.8 and 3.1 Kbar).

In the shearing dominant areas (e.g.Corredor shear zone in the Transcurrent Domain) the association of phases and the geothermobaromeric data has pointed out to conditions above those recorded at the folded metasedimentary rocks on central area. These portions were subject to fluid-assisted shearing and strong strain localization. Mica schist occurring along the shear zones and the presence of abundant deformed quartz and quartz-albite veins attest for channelized fluid flow during shearing and confirm the role of mass transfer. This process is evidenced by gain in H_2O, K, Rb and losses in Si, Ca, Na and Sr, in the most deformed portions. The syn-genetic aspects of metasomatic transformations indicate that shearing did not predate the hydrothermal event. It is supported by the presence of syn-kinematic kyanite as product of metasomatic transformations in some extremely modified rocks.

The metamorphic phases present in non-deformed mafic diorites from Pau-a-Pique basement (Corredor shear zone) are coherent with greenschist-amphibolite facies transition. According to Bucher and Grappes (2008) reactions that characterizes the transition between greenschist and amphibolite occurs between 450 and 550^oC. Geothermometry of quartz veins using TitaniQ thermometer and oxygen isotope fractionation gave temperatures above 450^oC (~490^oC). Pressure estimations based on phengitic content of muscovite gave a minimum pressure of 3.2 Kbar.

Other important difference regards the quartz recrystallization mechanism. The typical high temperature GBM is predominant in most of recrystallized quartz in Pau-a-Pique as well as in the Morro Solteiro thrust shear zone on northern portion. It strongly contrasts with the typical low temperature BLG mechanism recorded in most of the metasedimentary rocks on central area and despite the doubts about the influence of fluid activity on mechanism of quartz recrystallization the temperature must have been higher in the shearing dominant areas.

From the exposed above it is possible to conclude that *P*-*T* conditions through the area wasn't uniform and considerable higher temperature is recordedin the Corredor shear zone in Pau-a-Pique deposit where the estimated temperature is at least 100^oC higher than that recorded in most of metasedimentary rocks on central area, and despite the low precision on pressure estimations the data suggest that difference can be higher than 1 Kbar.

The difference in rheology between the metasedimentary rocks and the granitoids of the basement is a suitable surface for strain concentration. It can explain, at least in part, why shearing is much more common along the exposed contact.

Similarities on deformation pattern between Pau-a-Pique deposit and the Inferior level of Ernesto mine on northern area indicates that fluid-assisted shearing was responsible for most deformation and rock transformations occurring along the trust shear zone that characterizes the contact between the Aguapeí Group and its tonalitic basement in the Ernesto area.

As mentioned in the section 5.2, the tectonic evolution of the area is believed to have started with folding in a P1 phase that evolved to shearing and thrusting (P2) with the progress of strain. As observed in many portions along Aguapeí belt the initial folding gave place to strike-slip shearing and trusting, as the strain increases.

From petrographic study and thermobarometric data it is possible to propose *P-T* path for the area the in which the pressure increases with temperature and the metamorphic peak is somewhere above 450°C and 3.2 Kbar of pressure (Fig. 5.3-33). Thermometry of chlorite suggests retrograde condition between around 325°C, during in which chlorite was crystallized. The retrograde reactions has transformed biotite into chlorite, and fracture of quartz albite veins were filled with chlorite and carbonate.

The textural association of chlorite and sulfide and the syn-to late-deformational aspect of the pyrite suggest that the sulfide was also formed during retrograde conditions and is more or less in equilibrium with chlorite and carbonate.

It is evident from the geological settings that Aguapeí belt has a more transcurrent behavior and has been considered as a minor episode of low grade intracratonic deformation occurred towards the end of Greenville interval (Tohver et al., 2004). Rizzoto et al. (2014) for example suggest that Aguapeí belt, together with Nova Brasilândiaand Sunsas belts would comprises the same geotectonic unit (Western Amazon belt) formed due the reactivation of crustal weakness that allowed the development of transcurrent zones. The weakness zone comprises a suture zone between Paraguá and Amazon Craton (represented by the volcano-sedimentary sequence of Rio Alegre terrain in the studied area) formed at the end of the docking of Paraguá Craton (Rizzoto et al., 2013).

Taking into account the widely accepted model in which Paraguá comprised a separated cratonic block, assembled to the Amazon between 1320 and 1340 Ma, and that during colisional event of Amazonia against Laurentia it was part of the of Amazon continental mass, the Aguapeí belt can be considered, from the point of view of reactivation of suture zone as an intraplate strike-slip deformation belt.

Some of the best-known examples of intra-plate strike-slip deformation belt include the High Atlas Mountains of North Africa. In these orogens, the exposed crustal levels typically experienced low-grade metamorphism (Buik et al., 2008). Other famous examples of intracratonic orogeny occur on central Australia. The Neoproterozoic-Cambrian Petermann and late Ordovician-Carboniferous Alice Springs Orogens are good examples of intraplate deformation occurred as reflex of deformation on plate margins. In all these cases the deformed belt occurs inside rigid plates along weakness zone in the crust.

The expected *P-T* path of a transcurrent intracratonic belt may be something similar to the obtained above, since there is no rapid exhumationand cooling may be accompanied by decompression.

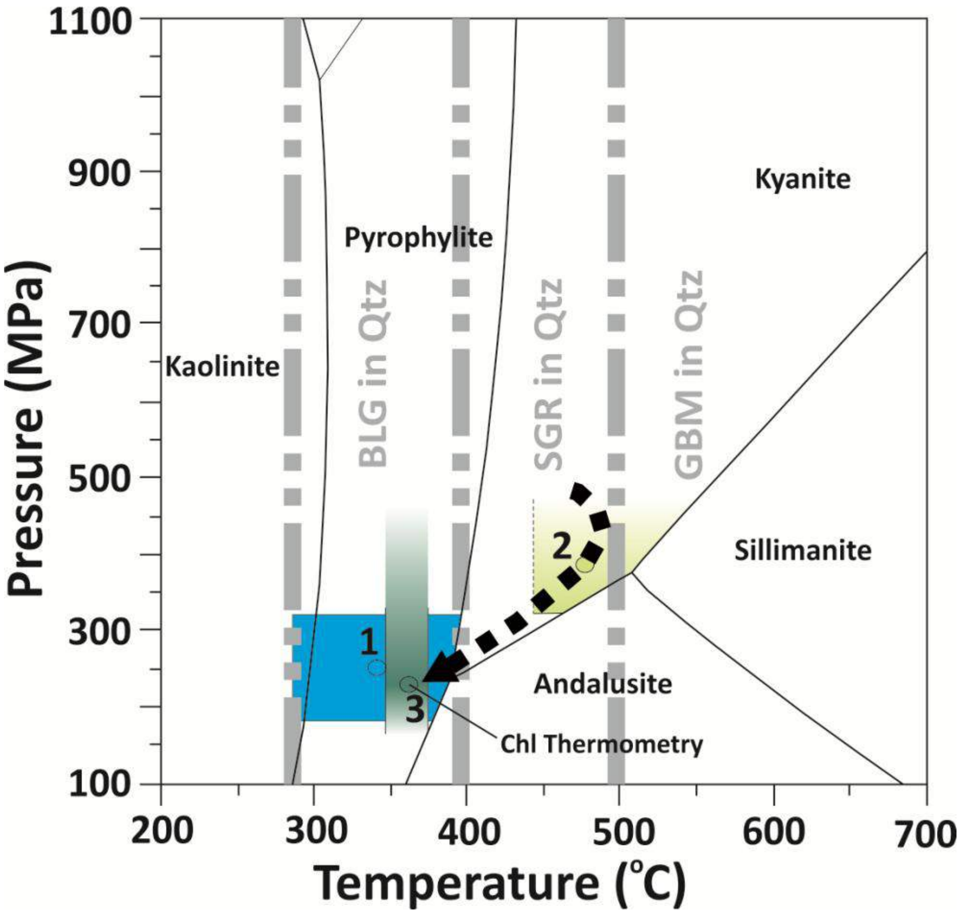

Figure 5.3-33: Proposed P-T path for the studied area. The blue polygon represents the interval of pressure and temperature recorded in the metasediments on central area. (1): Average conditions represented by the central point of the polygon. In the same way the light-green polygon is the interval of pressure and temperature recorded in shear zones (in Pau-a-Pique area) and represents the peak conditions. Its inferior limit is limited by the stability field of kyanite and the superior limit is opened, since pressure estimations gave only the minimum pressure and (2) represents the hypothetical average conditions. The dark-green polygon represents an interval of temperature during retrograde and is given by chlorite thermometry. In this case both, the top and the bottom are opened due to uncertainty about the pressure conditions.

However in this case the pressure is expected to be proportionally higher and despite the lack of well constrained pressure estimation, to explain the considerably high, temperature and the suggestive low pressure character of the P-T path without a magmatic event, an efficient heating process must had been active.

Cataclastic zones can produce heat, however its episodic and localized character doesn't seems an efficient mechanism of heat production and spreading. Meanwhile the widespread and uniform character of temperature verified along the contact zone requires a more effective heating process since heat produced by shearing (under anhydrous conditions) may be localized to the vicinity of faults and shear zones alone, doesn’t seems enough for such high differences on the general thermal gradients.

In contrasts circulating fluids are efficient on heat transport and distribution through the crust (Spear, 1993). The presence of extensive veining agues in favor, that huge amount of fluids were present during prograde conditions and the temperature recorded in quartz veins of Pau-a-Pique deposit are coherent with the metamorphic conditions recorded in cores of non-deformed diorites at the basement.

Such relation suggests that percolating fluids during metamorphism could be responsible for both, heat spreading and transport since hot fluids passing along the secondary porosity created by faulting has great potential to elevate the general temperature of an area. At the same time the percolation of hotter fluids coming from deeper portions of the crust can also help to explain the higher temperature reached by rocks along the shear zones when compared to the folded sediments on central area.

5.4 Mineralization

As mentioned above Alto Guaporé gold province (AGGP) (Fernandes et al., 2005a) comprises more than 30 gold occurrences and deposits and bellow is presented the geology and fluid characteristics of two of the gold deposits (Ernesto - Intermediate level and Pau-a-Pique) occurring in the central portion of AGGP.

5.4.1 Geology of Pau-a-Pique and Ernesto deposits

Ernesto and Pau-a-Pique gold deposits are located almost on central portion of Alto Guaporé Gold Province (AGGP). These two gold deposits are located more or less 40km in distance between each other and occurs in different tectonic settings.

The geological units in Pau-a-Pique depoist are structurated along a major sub-vertical anastomosed mylonitic belt called Corredor shear zone (Fernandes at al., 2006). The contact between the Aguapeí group and its basement is marked by a metric-scale layer of mica schist (phyllonite). The main ore body is hosted along a vertical sheared contact between the metasedimentary rocks and the basement. The hang-wall of Pau-a-Pique deposit is given by the basement of the Aguapeí group. At the deposit area, it is characterized by deformed and metamorphosed granitoids of predominant intermediate composition (diorite, tonalite and granodiorite), apparently associated with Pindaituba Intrusive suite (Ruiz, 2005). U/Pb zircon age of 1481 ± 07 Ma is reported by Geraldes et al. (2001) for tonalites of the basement.

The foot-wall of Pau-a-Pique deposit is given by metaconglomerates of Fortuna Formation and minor layers of coarse-grained metasandstone. In fact, most of metaconglomerates at the area display subtle transition to coarse-grained metasandstone with disperse gravels. Feldspar is generally present and occurs in the sandstone in the conglomerate matrix or in arkosic coarse-grained metasandstone layers. The gravels are relatively small and rarely reach 2cm in length. It is predominantly given by quartz but compositional variations are observed and include feldspar and lithic fragments. Preserved cross-bedding stratification in layers of metasandstone indicates stratigraphic up to SW. Other metasedimentary lithologic facies occurs to SW of Pau-a-Pique area and comprises (folded) fine-grained metasandstones, metasiltstone and phyllites (Fig.5.4-1).

As exposed before, most of the contact between the metaigneous basement and the metasedimentary rocks in Pau a Pique deposit is distinctly tectonic, marked by shearing that also affected the basement and the metasedimentary sequences on hang-wall and footwall of mineralized zone. Mica schist (phyllonite) formed by shearing of metaluminous protolith (tonalite and diorite) are composed by Ms + Bt + Qtz + Cb + Chl+ Ap + Rt + Mag. It may vary a little, and Bt + Carb can be more frequent to dioritic rocks whereas muscovite seems to be more frequent in tonalitic ones. In mica-schist formed by shearing of peraluminous protolith (granodiorite), kyanite can be present and the typical assemblage is given by Ms + Bt + Qtz + Tt + Ep + Cb + Chl + Mag + Rt + Ilm + Ap. Towards the contact with the metasedimentary rocks, there is an increase in frequency and dimension of the shear zones as closer as to the contact. Furthermore muscovite become more frequent and biotite eventually disappear giving rise to a muscovite schist of grey color (the most frequent host rock of the mineralization). In these rocks muscovite may represent up to 60% of modal composition and the other phases present include, Qtz + Mag + Rt + Chl + Ilm + Ap ± Bt.

Shear zones formed over quartz-feldspatic metaconglomerates are characterized by metric to centimetric shear planes that can be sided by low deformed metaconglomerate. It is composed by light-green quartz-muscovite schist, and the phases present are primarily Ms + Qtz + Mag + Rt.

The presence of mica schist derived from granitoids rocks, in shear zones indicates that during shearing, extensive fluid were present and led to change in mineralogy. Extremely modified rocks were formed by mass transfer during fluid-assisted shearing. Evidences for fluid percolation during shearing is given by the abundant presence of syn-deformational quartz veins associated with most of the mica schist occurring at the area.

A thick zone of quartz-filled breccias (silicified breccia) occurs to southwestern of the mineralized body. It apparently reflects a regional tectonic event under more brittle conditions and seems later to the mineralizing event since there is no record of positive gold results associated to it.

The early deformational stage at Ernesto area is given by nearly symmetrical folding of $S_{0,}$ subvertical NNW-SSE axial planar foliation (S_1) and slate cleavage on S_0 of folded fine grained-sediments. With the evolution of strain, the deformation mechanism has evolved to thrusting, marked by the SW to NE alloctony of the Aguapeí metasedimentary rockss over its basement (Fernandes et al., 2005a). It's created a major sub horizontal shear zones along the contact with the basement and minor sub-parallel shear zones in the basal layers of Fortuna Formation. The mylonitic foliation (S_2) is given by a schistosity along the sheared contact, and by asymmetrical folding and a low angle cleavage foliation (S_2) dipping 30-45^o on SW, in the fine-grained sedimentary layers towards the top portion of Fortuna formation.

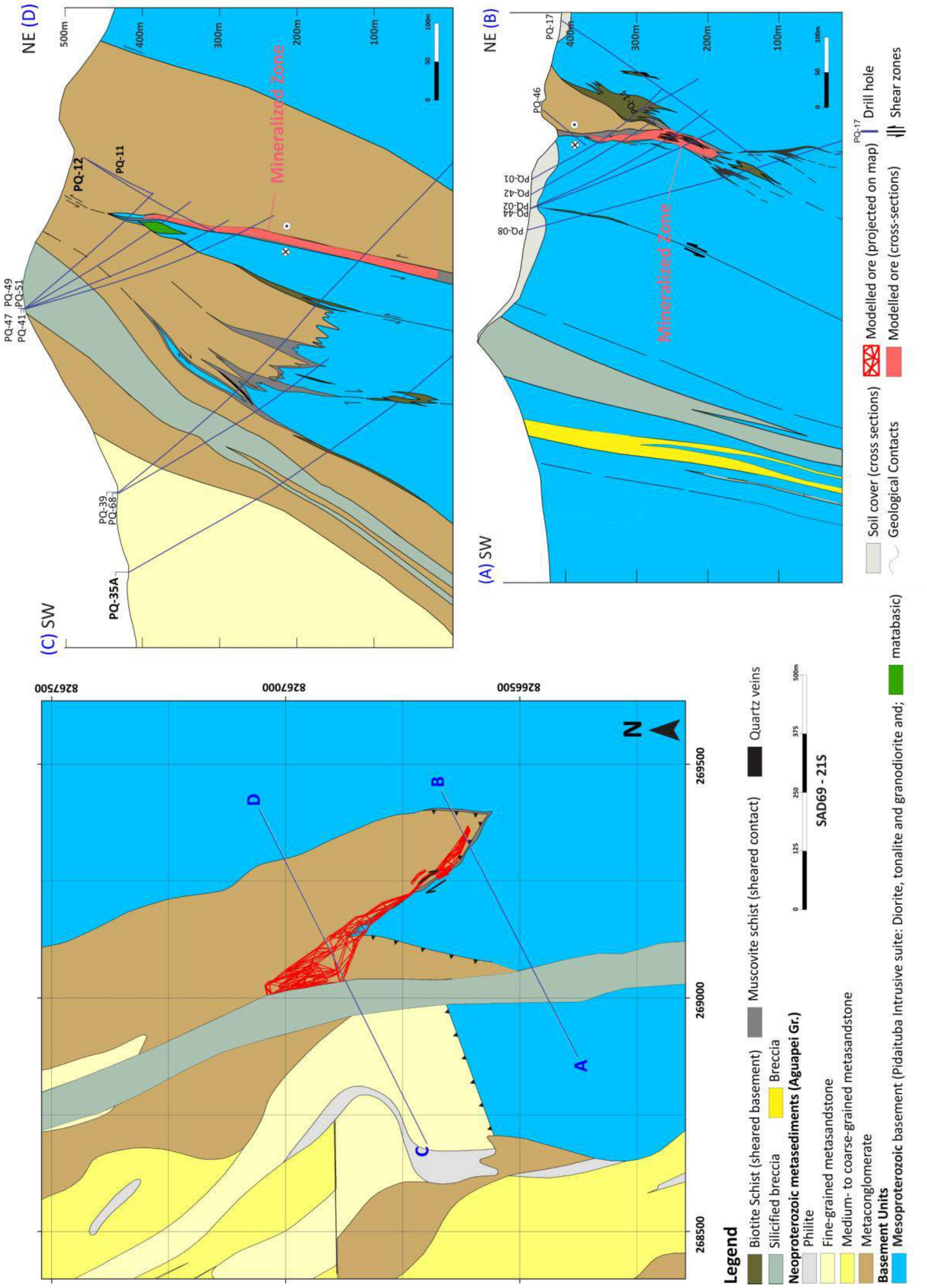

Figure 5.4-1: Detailed geological map and cross sections of Pau-a-Pique deposit

Similarly to Pau-a-Pique, the shear zones formed by thrusting show evidence of fluid-assisted shearing being characterized by green layers of magnetite-muscovite schist of variable width and deformed quartz veins with sigmoidal shape associated to it.

Most of the basement in Ernesto area is given by Mesoproterozoic granitoids of dominant tonalitic composition (Lavrinha Tonalite). It is composed by amphibole, biotite plagioclase and quartz (Fernandes et al., 2005a). U/Pb age of 1465 ± 04Ga is reported by Geraldes et al. (2001). It has a general dome-type shape and is partially covered by metasedimentary rocks of the Fortuna formation. The Paleoproteroic volcano-sedimentary sequence of the Alto Jauru Group (Jauru Terrane) comprises the basement on NW of the Ernesto area (Fig. 5.4-2).

A consistent layer of very coarse-grained arkosic metasandstone occurs at the basal portion, and a very regular layer of metaconglomerate with more or less 20 meter in width occurs interbeded with the predominant metasandstone and works as stratigraphic marker for the area. At the top a fine grained metasandstone show gradational contact with the medium- to coarse grained metasandstone occurring below and is succeeded by a thin layer of sericite schist, interpreted by some authors (e.g. Fernades et al., 2005a) as intensely deformed pelitic level.

Most of the covering metasedimentary rocks of Fortuna formation in the Ernesto area comprises medium- to coarse grained metasandstone with disperse gravels.

The major shear zone formed along the contact between the basement and the metasedimentary rocks (Morro Solteiro shear zone) hosts the inferior level of Ernesto deposit and also other smaller gold occurrences in the area (e.g. Nosde/Marinho, Pombinhas, Paulo, Nene). The mineralization is characterized by the disseminated porphyroblasts of pyrite associated with deformed quartz veins and muscovite schist. The superior Level is hosted by the layer of sericite schist. It is given by folded and boudinaged quartz veins and disseminated pyrite and magnetite in the host rock (Fernandes et al 2005a).

5.4.2 Quartz veintypes and aspects of the mineralized zones

Ernesto

The Intermediate Level of the Ernesto Mine comprises a low grade mineralization more or less restricted to a metric-scale layer of metaconglomerate. Two main families of quartz veins were identified. The first family (Type1) is emplaced along thin shear zones subparallel to the stratighaphic bedding (S_0).

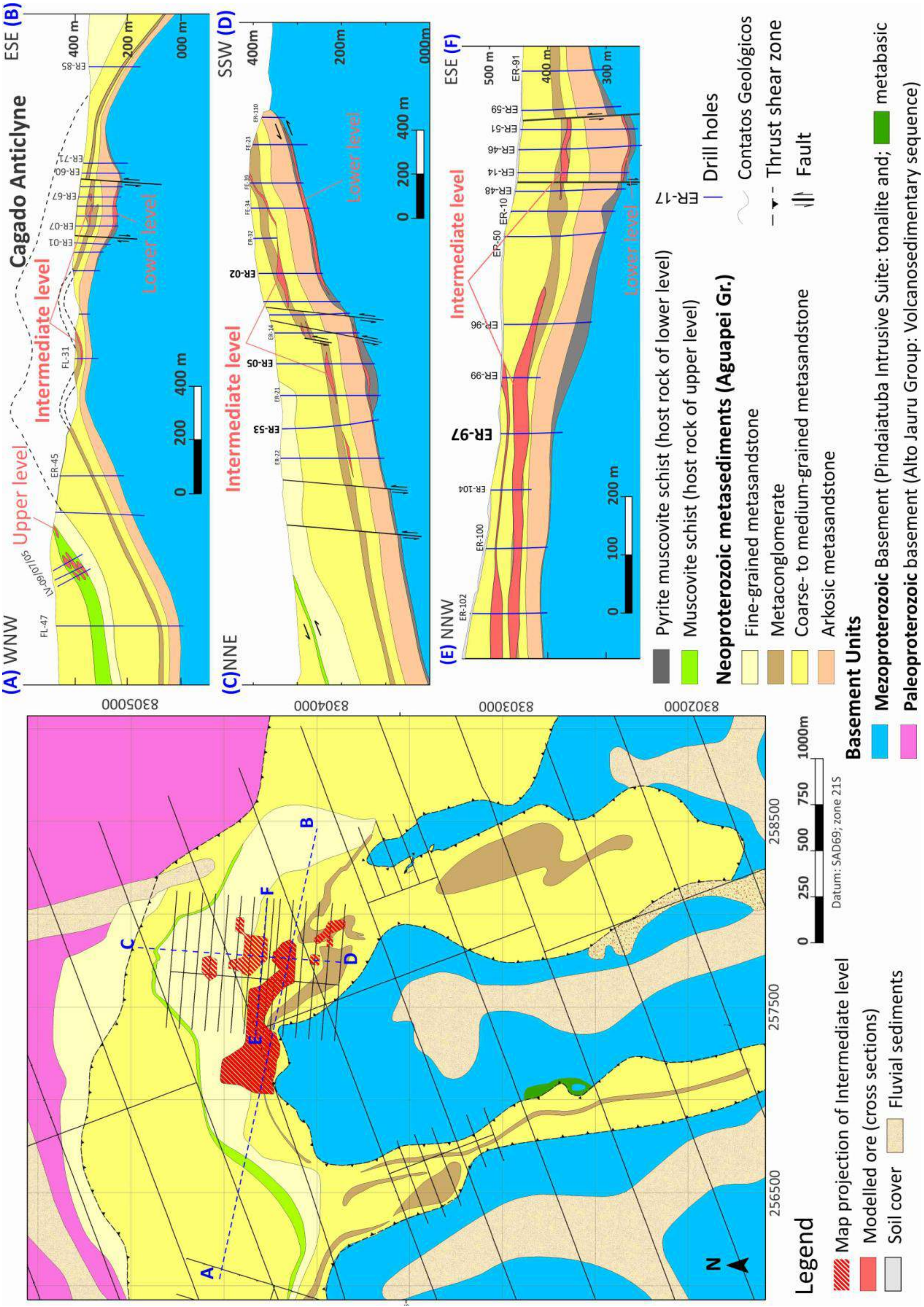

Figure 5.4-2: Detailed geological map and cross section of Ernesto deposit

It is hosted by a centimetric layer of light green muscovite schist and show an anastomosing pattern within the shear zone. A top sense (to NE) of shear is indicated by the internal geometry of the vein, since the veins comprises white boudins of quartz with sigmoidal shape surrounded by muscovite schist with magnetite (Fig. 5.4-3B).

Low deformed pyrite-bearing quartz veins (Type2) comprises the typical mineralized vein family in most of the intermediate level of Ernesto. It is given by milk quartz veins emplaced along a NW-SE fracture family, dipping at low angle (20-30º) to SW. Persistent to the metasandstone occurring above and below the conglomerate layer, as observed by face mapping of open pit mine (Fig. 5.4-3A), these veins are generally centimetric in width although locally it may form metric-scale pockets of diffuse quartz hosted by silicified wall-rock, where porphyroblasts of euhedral pyrite that can reach up to 10 cm in size. The wall-rock to the veins indicates that a pre-mineralizing hydrothermal event has occurred before sulfidation, since gold-bearing pyrites grown over hydrothermal magnetite, as evidenced by the presence of magnetite inclusions in the core of pyrite porphyroblasts.

Pau-a-Pique

The main mineralized zone of the Pau-a-Pique depoist is located in a sub-vertical shear zone formed along the contact between the metasedimentary rocks and metaigneous rocks of the basement (Fig. 5.4-4). The ore grade are mainly controlled by the presence of disseminated pyrite occurring in the mica schist of the contact and within quartz veins near the contact. The veins can be separated into three types according to form of occurrence, mineral phases and economic importance.

The higher ore grades in the Pau-a-Pique deposit are associated with deformed pyrite-bearing quartz veins (Type1). These veins are exclusively hosted by the mica schist of the contact and comprises a swarm of translucent, highly deformed quartz veins of centimetric dimension and sigmoidal shape. At the microscope, evidence of syn-deformational emplacement is given by repeated deformation, indicated by common ondulatory extinction, deformation zones displaying various degrees of grain size reduction and growth of fibrous quartz in the pressure shadow of pyrite grains.

During drill core descriptions it was observed that the occurrence of narrow non-mineralized zones in the muscovite schist of the contact is common. In these zones, quartz veins tend to be less deformed and milky and is associated with magnetic magnetite. These features contrast with the neighboring mineralized zone marked by more deformed (quartz boudins) and clear (translucent) quartz and disseminated pyrite occurring together with non-magnetic magnetite.

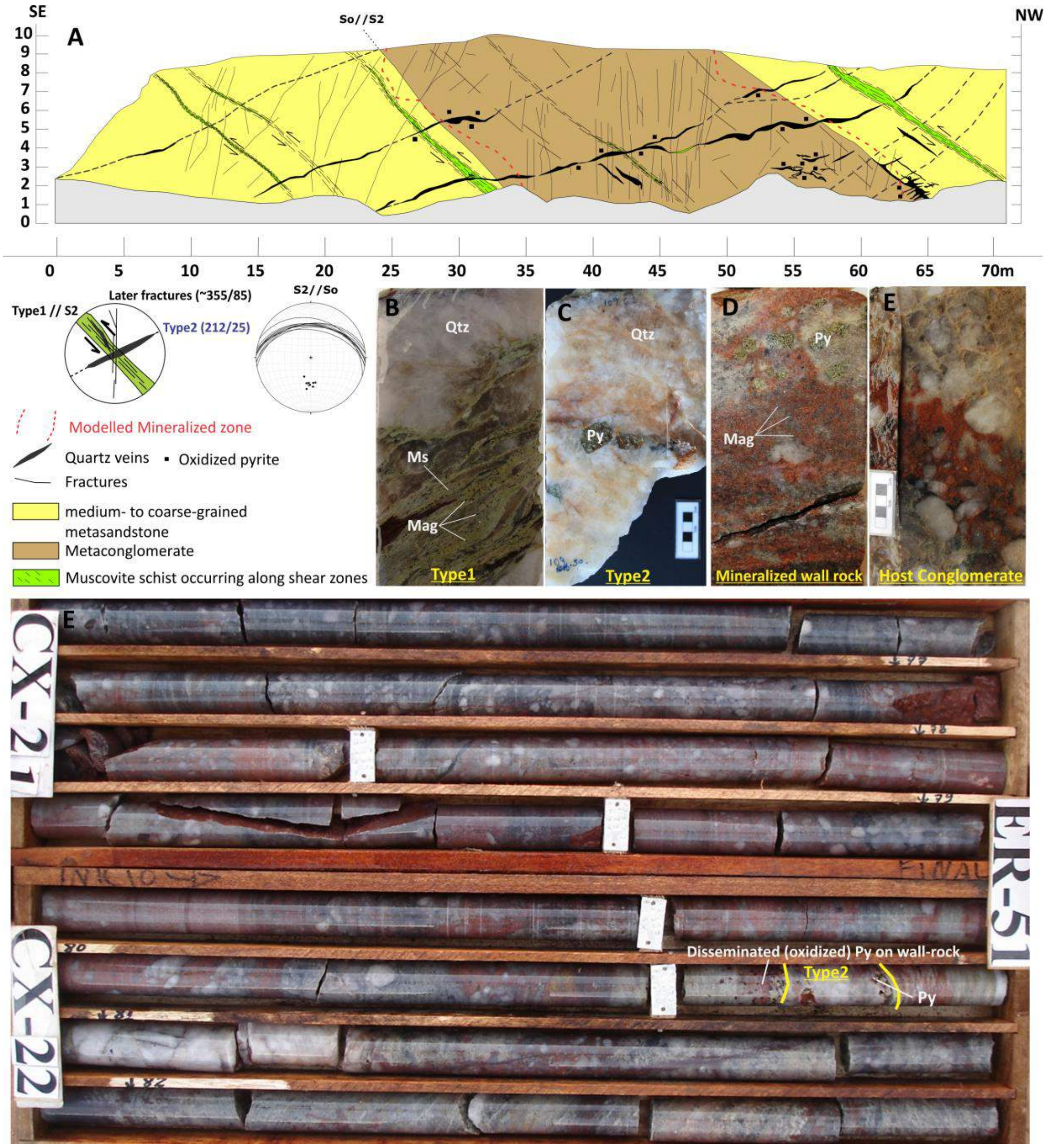

Figure 5.4-3: General aspect of mineralized zone of the intermediate level of Ernesto deposit. On top, a schematic face-mapping showing the tectonic relation between the two types of quartz veins. In the middle, pictures showing the textural aspect of mineralized and barren veins Type 1 and 2 (respectively) as well as barren and mineralized wall-rock. On bottom, photo of drill core samples showing the occurrence of mineralized quartz vein Type2 with disseminated pyrite in the metaconglomerate of wall-rock.

The second type of quartz vein is preferentially associated with the basement rocks (**Vqz2**). It comprises quartz-albite veins formed by white and milky quartz and red albite, with chlorite and carbonate (calcite) occurring as secondary phases (along fractures). Albite is the second more abundant phase and can suppress quartz in some portions, forming albite veins.

The size and frequency of the veins, as well as the presence of albite increases towards the contact with the sediments where it can reach metric size. Variable degrees of deformation is observed and it may appear folded or with sigmoidal shape, when hosted along shear zones in the basement (Fig. 5.4-4) or exhibits irregular shape and low deformed aspect when hosted by low deformed portions of the basement suggesting the degree of deformation is directly related to the level of deformation of its host rock. At the most deformed portions it shows evidence of repeated brittle-ductile deformation as the veins system developed as well as after emplacement. When close to the contact it may host the mineralization. In this case it is bearer of pyrite that generally occurs as porphyroblasts however, gold grades are generally lower than those found in translucent veins hosted by the muscovite schist on contact (Fig 5.4-4 A).

The third type of quartz vein is barren (**Type3**) and is exclusively hosted by sheared metasedimentary rocks (metaconglomerates and metasandstones) of the Aguapeí group. It comprises milky quartz veins of centimetric - to metric size and sigmoidal shape resulted from asymmetrical boudinage sub parallel to mylonitic foliation in the host rocks. The quartz sigmoids are involved by thin layers of green muscovite schist that gives an anastomosed shape to it.

A well established temporal relationship of veining for Pau-a-Pique deposit is difficult to be constructed due to the high deformed aspect of the quartz veins. Some characteristics (e.g. quartz color, shape and size) seems to be more related to the level of deformation in which the vein were subjected rather than the emplacement epoch. In portions where the two ore-bearing families are observed occurring together (e.g. albite-quartz family hosted by the muscovite schist of the contact), the albite-quartz family is discordant to the oriented boudins of translucent quartz and does show a more irregular shape that suggest a later genetic character of the albite-quartz family (Fig. 5.4-4 A, C). In spite of that it doesn't seems to represent a relevant separated events of veining formed by fluids of different origin, but later stages of emplacement within the same veining event, since there is no significant changes in the isotope signature between the families. The translucent vein family does represent early formed veins, during the initial stages of shearing and thus seems to had been subjected to a high level of deformation for being emplaced along a shear zone that show evidence of long-live reactivation during the evolutionary history. Differently the quartz-albite family seems to represent later veining stage on evolution of the regional Corredor shear zone. Most of Na for the albite veins must have come from destruction of plagioclase by shearing of granitoids of the basement which could explain, at least in part why the quartz-albite veins are restricted to the basement.

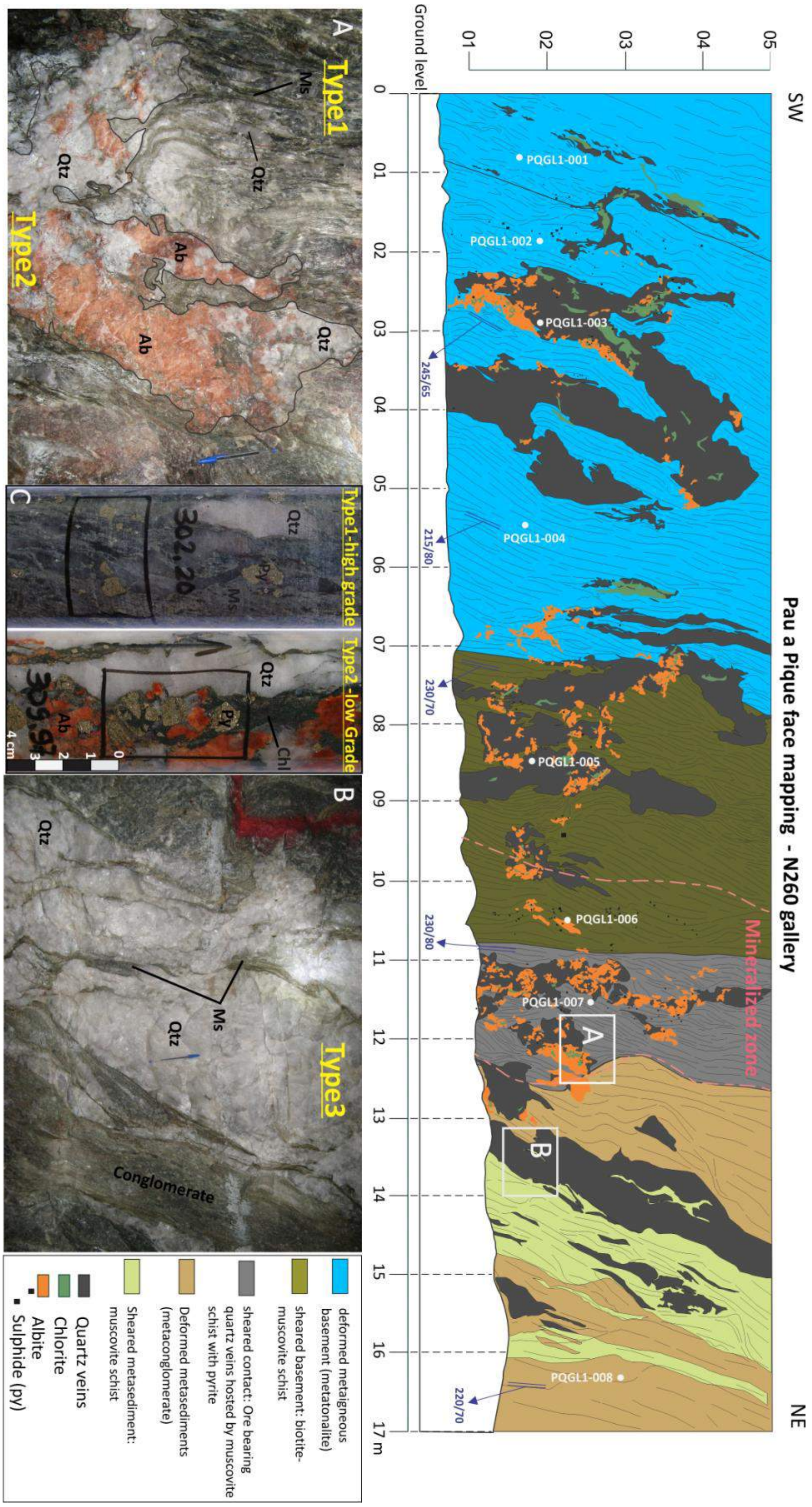

Figure 5.4-4: Face mapping of mineralized zone of Pau-a-Pique in the contact between the metaigeneous and the metasedimentary rocks. Photos showing the different types of quartz veins occurring at the mapped zone and detail of mineralized veins Type1 and 2.

5.4.3 Sulfidation

Ernesto

The only sulfide present in the studied samples of intermediate level of Ernesto is pyrite. It can be texturally divided into three types. The first type (Type1) occurs within mineralized quartz veins and comprises euhedral massive crystals with variable size. The second textural type (Type2) is restricted to the wall-rock of mineralized quartz veins. It is given by euhedral porous porphyroblasts grown over early-formed magnetite occurring in the conglomerate matrix. It is characterized by the presence of rounded inclusion of quartz (that has similar size to the matrix quartz grains) and partially destroyed magnetite occurring as inclusions at the core of porphyroblasts. The third textural type (Type3) was observed in deformed conglomerates occurring near inter-stratification shear zones. It comprises irregular shape aggregates of subhedral pyrite. The size of individual crystals can vary from 30 to 400 microns yet the aggregates can reach up to 2 cm in diameter.

There is no significant differences on concentration of trace elements between the textural types of pyrite and Co, As, Mo and Cu are the most common trace elements occurring above the detection limit of microprobe.

Gold is present as inclusions and may occurs associated with telluride, silver and bismuth in varied combinations of Au-Te, Bi-Te, Ag-Te and Au-Ag (Fig. 5.4-5).

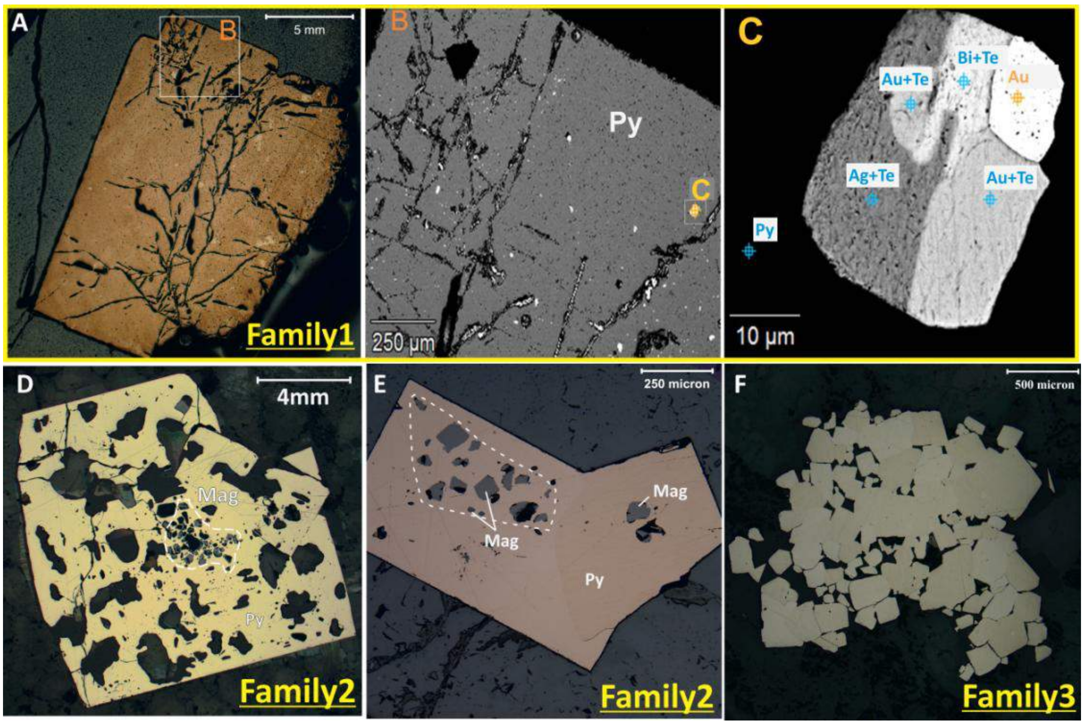

Figure 5.4-5: Textural types of sulfide occurring in Ernesto Deposit. A, B and C show massive euhedral massive pyrite with micron-scale inclusions of Gold. D and E show euhedral porous pyrite with magnetite in the core. F, photomicrograph of aggregates of subhedral pyrite (Type3)

Pau-a-Pique

The sulfidation associated to ore-related hydrothermal alteration of the Pau-a-Pique deposit is primarily given by disseminated pyrite and minor and localized occurrence of chalcopyrite and galena. Chalcopyrite is more frequent in the sheared portion of the basement or as micron-scale inclusions in pyrite porphyroblasts. Galena is the less frequent sulfide. Occurring as inclusions or along fractures in pyrite galena is generally associated with chlorite and carbonate. Although LA-ICP-MS analysis of pyrite indicates that galena is frequent as nano-inclusions in most of analyzed pyrites, it appears to be more frequent and bigger in pyrite occurring in albite-quartz veins, where it appear large enough to be studied by reflected light petrography.

Pyrite can be separated into two main textural types:

(1) the first type is more common to the translucent quartz vein family (type1) and its hosting muscovite schist. It comprises a family of texturally zoned pyrite which is characterized by an anhedral zone of porous pyrite, generally restricted to the core of porphyroblasts and by an euhedral massive rim (Fig. 5.4-6 A, B). In fact the textural zonation is more frequent and expressive in pyrite grown over muscovite schist associated with translucent veins (Type1), however it may show an incipient porosity when pyrite crystallized along fractures in the quartz veins. Ilmenite, magnetite and rutile comprises the most frequent phases at the porous core and suggest that pyrite has initially grown over of Ti-Fe oxides. Evidence for syn- to late-deformational crystallization is given by bending of aligned inclusions in the porous core, presence of fibrous quartz fringe in pressure shadows of porphyroblasts and massive euhedral rim in the same crystal (Fig. 5.4-6 B).

(2) The second textural type of pyrite is more common (but not restricted) to the albite- and quartz-albite vein family (Type2). It comprises euhedral massive crystals that can reach up to 5 cm in diameter and appear to have been crystallized along fracture in the albite-quartz veins where it generally occurs in association with calcite and chlorite.

SEM cathodo-luminescence (CL) study of pyrites didn't show contrasting CL textures in massive pyrites and between the zones in the texturally zoned pyrites. Meanwhile very small variations on trace elements between the families and between the textural zones were found by microprobe and LA-ICP-MS analysis. This indicates that most of differences concern only on textural aspects resulted from different deformation ratios of host rock and suggest a unique generations of pyrite in the studied samples.

Free gold was observed in the muscovite schist and along fractures in the translucent quartz vein family. However most of gold occurs as inclusions in pyrite (Fig. 5.4-6 D, F). It generally comprises anhedral or rounded inclusions of variable size and many of them are aligned along some plane or more or less following the boundary of porphyroblasts. Gold inclusions in pyrite are more common to the texturally zoned pyrites associated with muscovite schist and the translucent quartz vein family where it seems to be more frequent to the massive zone. In fact no visible gold inclusion where observed in pyrites occurring in albite-quartz-veins at the studied samples.

Other inclusion in pyrite includes telluride and silver inclusions that may be associated with gold in variable combination of Au-Te, Au-Ag or Ag-Te inclusions.

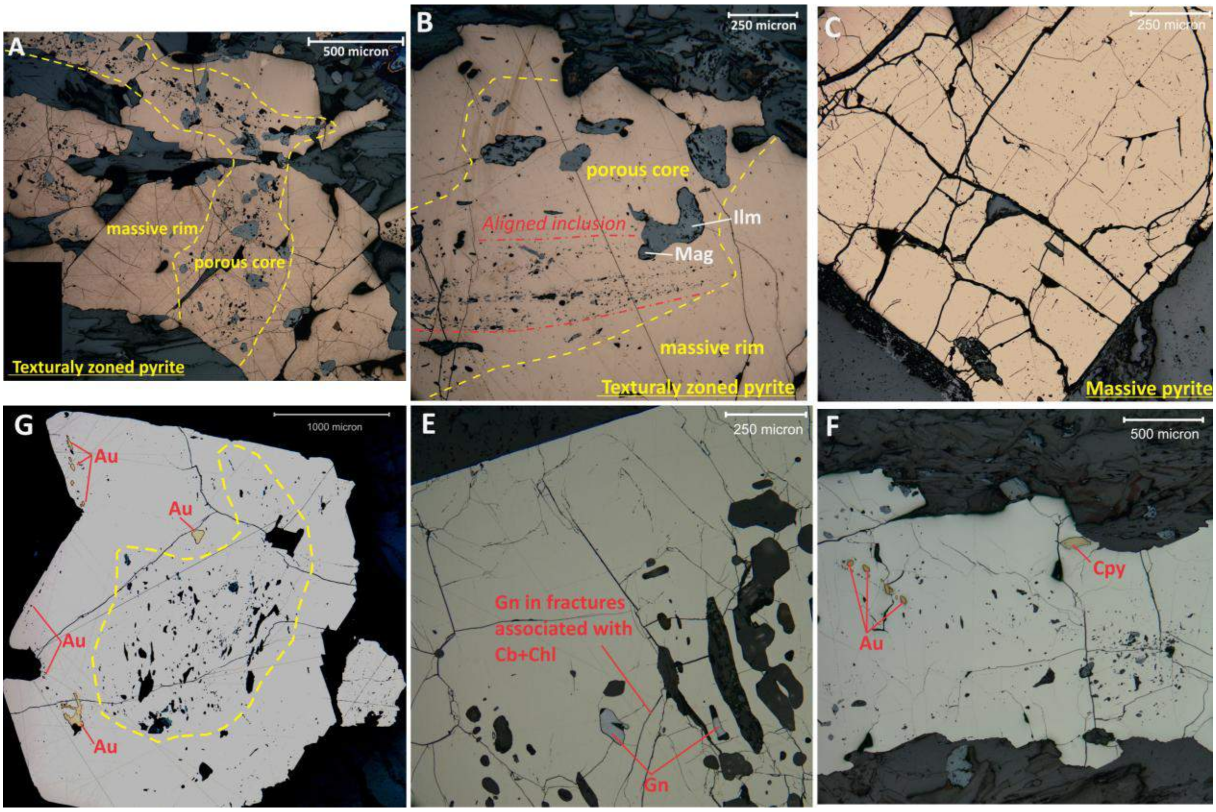

Figure 5.4-6: Photomicrograph of sulfides and pyrite textural types occurring in Pau-a-Pique deposit. A, B and C show texturally zoned pyrites with massive rime and porous core, more common to muscovite schist of the contact. C show part of a massive euhedral pyrite (Type2) generally occurring in quartz albite veins. D, texturally zoned pyrite with inclusions of gold within the massive rim, more or less following the shape of porphyroblasts. E, occurrence of galena along fractures and as inclusions in the pyrite porphyroblasts crystallized in veins of albite. Inclusions of gold and chalcopyrite in texturally zoned pyrite. It is important to notice that gold occurs along some plane within the pyrite.

5.4.4 Fluid inclusion petrography

The following description is based on observations made on ore-bearing quartz veins of the Pau-a-Pique and Ernesto deposits using reflected and transmitted light petrography assisted by SEM-cathodoluminescence imaging.

Pau-a-Pique

It is evident from both microscopic studies and field observations that ore-bearing quartz veins in Pau-a-Pique were subject to repeated events of deformation as the vein system developed as well as after emplacement. As mentioned above, common ondulatory extinction, recrystallization zones and the presence of fibrous quartz in the pressure shadow of pyrite grains are evidence of repeated brittle-ductile deformation at microscope-scale. The textural relationship between quartz and pyrite indicates that the sulfide precipitated within pre-existing quartz and where deformed during its initial stages of crystallization in some of the studied samples.

The most deformed family of quartz veins (translucent quartz family) also does carry the highest gold grades. Abundant fluid inclusions are found in samples from this family however the deformation of quartz has destroyed most of early formed inclusions which become aligned and have leaked and decrepitated.

Petrography and cathodoluminescence imaging showed trails of fluid inclusion within healed micro fractures across the boundaries of deformed quartz and persistent to zones of recrystallization (Fig. 5.4-7). Because of the repeated fracturing and recrystallization of quartz, domains with well preserved inclusions are restricted to cores of early formed quartz crystals. It was mapped and separated from recrystallization zone by the typical ondulose extinction of early formed quartz (Fig. 5.4-7).

Preserved primary fluid inclusions were not identified in any of the studied samples (following the classification proposed by Goldstein, 2003). In the same way CL-imaging of translucent quartz didn't show any primary grown texture in quartz, being, most of the early formed quartz, CL-dark. In fact CL-bright texture was observed only in some cores of clear quartz in albite quartz veins and in less deformed portions of translucent vein family. At these portions CL-bright zones has irregular shape and are limited by the occurrence of fluid inclusions trails (Fig. 5.4-8).

Previous study on mineralization and fluid inclusion of Ernesto and Pau-a-Pique deposits were made by Fernandes et al., (2005a) and Pulz et al., (2003) respectively.

For the Pau-a-Pique deposit, Pulz et al. (2003) identified four mineralization stages and 3 fluid inclusion populations. According to the authors the mineralization stages comprises an early (pyrrotite, chalcopyrite and galena) stage, an intermediate (pyrite I, native Au and Ag) stage, a late (pyrite II, native Au and AG) and weathered (hematite, magnetite and martite). Mineralizing fluids would be associated with biphasic, low salinity, aqueous (Type2) showing homogenization temperature between 160 and 180ºC. The authors also suggest that the gold deposition involved boiling. The other two fluid inclusions populations identified by the authors are an early, low salinity, triphasic aquo-carbonic inclusions (Type I) showing temperature between 190 and 230ºC and a late population of aqueous and vapor monophasic inclusions of diminute size (Type3).

Based on petrographic and thermometric studies it is possible to separate the inclusions occurring in Pau-a-Pique deposit into 6 main types according to their morphological characteristics occurrence form and composition. In terms of emplacement chronology it can be separated into 5 generations and are described bellow.

H_2O-CO_2 inclusions comprise the main family. It can be separated into two main types. The first type (Type1) comprises large inclusions (often >35um) commonly irregular shape. They contain variable proportions of an aqueous liquid (40-90 vol. %), two CO_2 phases (liquid and gas; 60-10 vol. %) and solid minerals phases (variable amount). The solid phase has a variable sizes and flaky rectangular or prismatic appearance (Fig. 5.4-9D). The second type (Type2) comprises smaller inclusions with more regular rounded or negative shape with almost constant proportions of aqueous liquid (88-92 vol. %) as well as the two-phase CO_2 (12-8 vol. %) and no solid phases is present. The last type occurs along trails in low deformed quartz and is more common to the translucent quartz family, but also occurs in the quartz albite veins (Fig. 5.4-9 A,B). In some of the studied sample the trails containing H2O-CO2 inclusions are passing through zones of high deformation. In such portions these inclusions are associated with empty (black) and necking down inclusions and those containing three phases may show variable proportions of aqueous liquid and two-CO2 phases suggesting that the inclusions had its initial composition modified due to quartz deformation that may have caused leaking.

The second family (Type3) comprises rounded to ellipsoidal inclusions or with negative shape and size up to 15um. They are generally smaller than Type 1 and 2 in the first family and consist of an aqueous liquid and a vapor phase. The latter typically occupies about 5 vol. percent of the inclusion's total volume (Fig.5.4-9E). They occur along trails within early formed quartz in translucent quartz veins and are rare to the albite quartz veins.

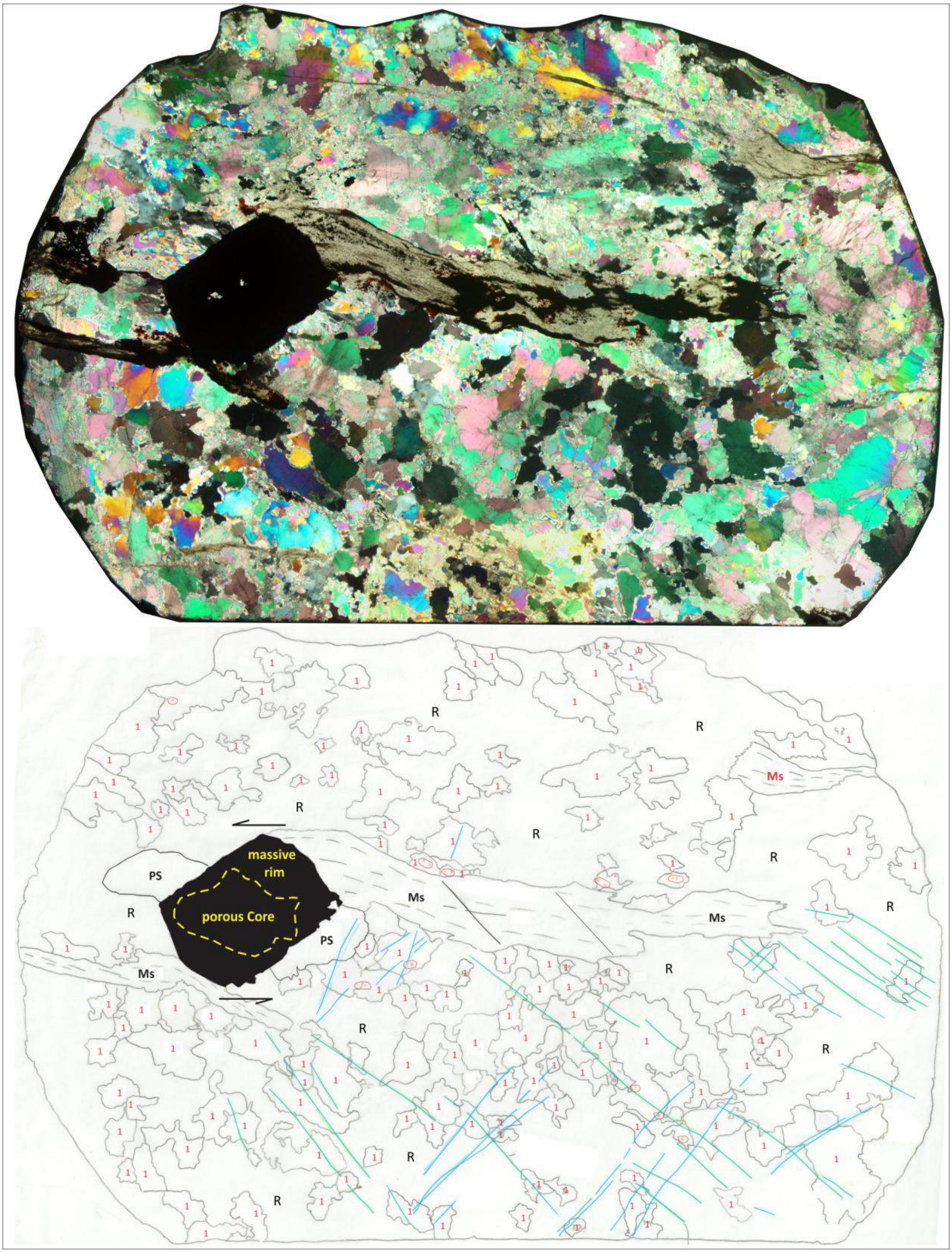

Figure.5.4-7: Thin section map of a high-grade (~20g/ton) sample of translucent quartz (sample PQ12302-46). R represents zones of quartz recrystallization; 1: are early formed quartz showing ondulose extinction; Ms: represents layers of muscovite schist; PS: is the pressure shadow of pyrite porphyroblasts (in black). Blue lines represent trails of fluid inclusion trapped along healed fractures. The small polygons (in red) are zone with isolated H2O-CO2 fluid inclusions.

The third family (Type4) comprises small rounded inclusions of variable size, although generally small (less than 5um) can reach up to 15um. They consist of monophasic or biphasic aqueous inclusions occurring along trails of healed quartz and are persistent through quartz crystals and recrystallization zones.

The fourth family (Type5) was observed only in one sample and comprises rounded inclusions occurring in healed fractures within cores of clean and low deformed quartz. They consist of aqueous inclusions that can be monophasic or biphasic. The vapor phase generally occupy about 5 vol. percent of the inclusion's total volume when biphasic. It is separated from Family3 due its contrasting high salinity on microthermometry. Moreover it is more homogeneous in size and shape (Fig. 5.4-9F).

The fifth family (Type6) comprises diminute (~1um) aqueous monophasic inclusion occurring along the latest fractures family. They generally consist of irregular shape inclusions and may show evidences of necking down and deformation (Fig.5.4-9 B and Fig. 5.4-8 D). Fractures where this family of inclusions is hosted show are CL-darkcontrasting with surrounding low CL-brightness quartz. It is the most common family of fluid inclusion and was observed in all studied samples.

Laser-Raman analysis in black inclusions occurring in translucent quartz veins of Pau-a-Pique has shown that they comprise empty or leaked inclusions. They occurs along trails in deformed quartz associated with monophasic or biphasic inclusion showing variable liquid-vapor ratio, suggesting it had its initial composition modified for later deformational events and thus wasn't considered in this study.

Ernesto

Fernandes et al. (2005a) did identify three families of fluid inclusions in deposits of Ernesto area. It comprises triphasic aqueous-carbonic inclusions (type1), biphasic aqueous carbonic inclusions (type2) and monophasic aqueous inclusions (Type3). According to the authors, monophasic inclusions have shown ice-melting above zero and were characterized as meta-stable aqueous inclusions. The authors also suggest that fluid circulation occurred at the end of Aguapeí deformation and classify these deposits as epigenetic.

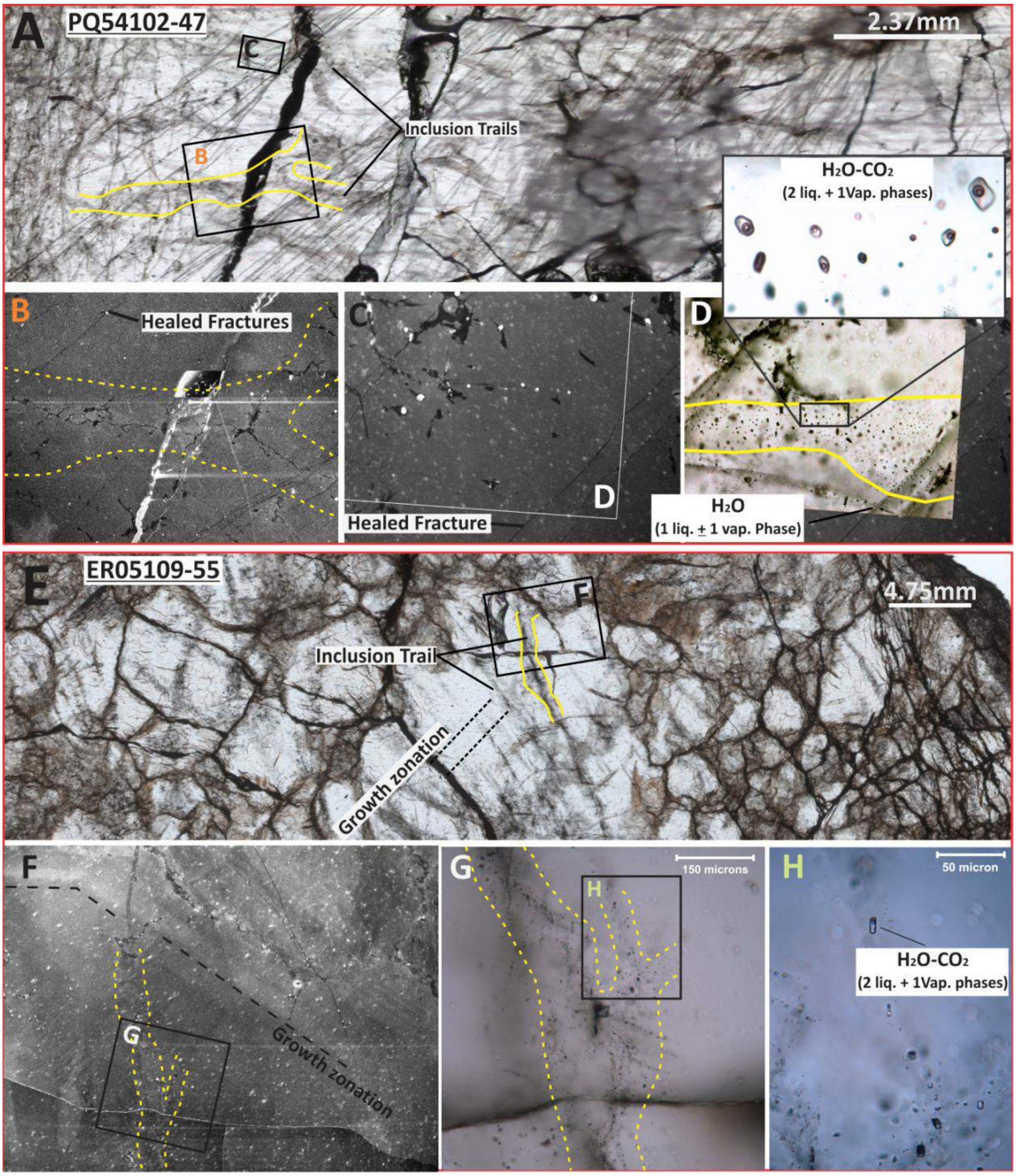

Figure 5.4-8: Cathodoluminescence-assisted petrography of fluid inclusion populations; A: Micro-scanning image of a double polished thin section from translucent quartz of Pau-a-Pique deposit. The lines in yellow outline a trail of secondary fluid inclusions which in turn is superimposed by a latter family of secondary inclusions occurring along fractures; B: SEM-CL image of an small area from the studied thin section showing the general CL-dark luminescence of quartz and non-luminescent patches (outlined by dashed yellow line) related to the trails of fluid inclusions outlined above. Non-luminescent straight lines are healed fractures; C: detailed SEM-CL image of another small area of the same thin section showing non-luminescent patches of CO2-H2O fluid inclusions (indicated in D) and healed fractures where latter aqueous monophasic inclusions are hosted; E: Micro-scanning image of a double polished thin section from mineralized vein of Ernesto (Type2). The yellow dashed lines are highlighting oriented trails of inclusions occurring within clear quartz; F: SEM-CL image of a small area from the above thin section showing growth zonation in quartz. In detail, the dashed yellow line is outlining trails of secondary fluid inclusions (showed in increasing detail in G and H).

The fluid inclusions found in mineralized veins of Ernesto deposit display a complex relationship. Petrographic studies assisted by cathodoluminescence imaging showed that the inclusions can be separated into three types. All types occurs along trails within early-formed quartz and cross-cut growth zoning (Fig. 5.4-8F, G and H), being secondary in origin, according to the classification of Goldstein (2003). No inclusions occurs parallel to growth zoning of quartz and most of it are along healed fracture that display contrasting CL-dark signature with the bright zoning quartz (Fig 5.4-8 F). Around porphyroblasts of pyrite the quartz doesn't show evidences of deformation and the inclusions are disperse in the quartz vein or occurring in trails (Fig.5.4-10). The quartz around pyrite porphyroblasts are CL-dark and contrasts with darker healed fractures and non-luminescent patches of irregular shape probably associated with process of zone-refining as described by Lambrecht and Diamond (2014).

The inclusions found in Ernesto were separated into three main types according to composition and form of occurrence.

The first type (Type1) comprises H_2O-CO_2 inclusions, are large, often >15um commonly with irregular shape. They occurs along trails on early formed quartz (quartz showing growth zoning - see Fig. 5.4-8 F, G, H) or as disperse inclusion in later quartz surrounding pyrite porphyroblasts. At room temperature (25ºC) they show different proportions of vapor-liquid phases (Fig. 5.4-10 C, D) and show evidence of heterogeneous entrapment, since the same family has inclusions with: only one phase (liquid CO2); two phases, with variable proportions of one aqueous liquid (10 - 90% vol. %) and one vapor (CO_2 - gas; 90-10 vol. %); and three phases with variable proportion of aqueous liquid (10-90 vol. %) and two CO_2 phases (liquid and gas; 10-100 vol. %). These features indicates sub-solvus conditions.

Type 2 inclusions (Fig. 5.4-10 D) are generally ellipsoidal and up to 30um in size. They consist of variable an aqueous liquid (~95 vol. %) and a vapor phase (~5%). They are the most common type in samples from Ernesto and as tend to occur in trails of secondary inclusions in early formed quartz and disperse in the later formed quartz (Fig. 5.4-10 B).

Type 3 inclusions comprise diminute rounded inclusions, generally less than 5um in diameter. They consist of predominantly homogeneous monophasic aqueous inclusion. When biphasic the vapor phase comprises less than 5% of inclusion's total volume. They are found occurring along healed fractures (Fig. 5.4-10 A) in both, early and newly formed quartz. In the later the CL-dark signature of surrounding quartz contrasts with the non luminescent quartz of healed fractures.

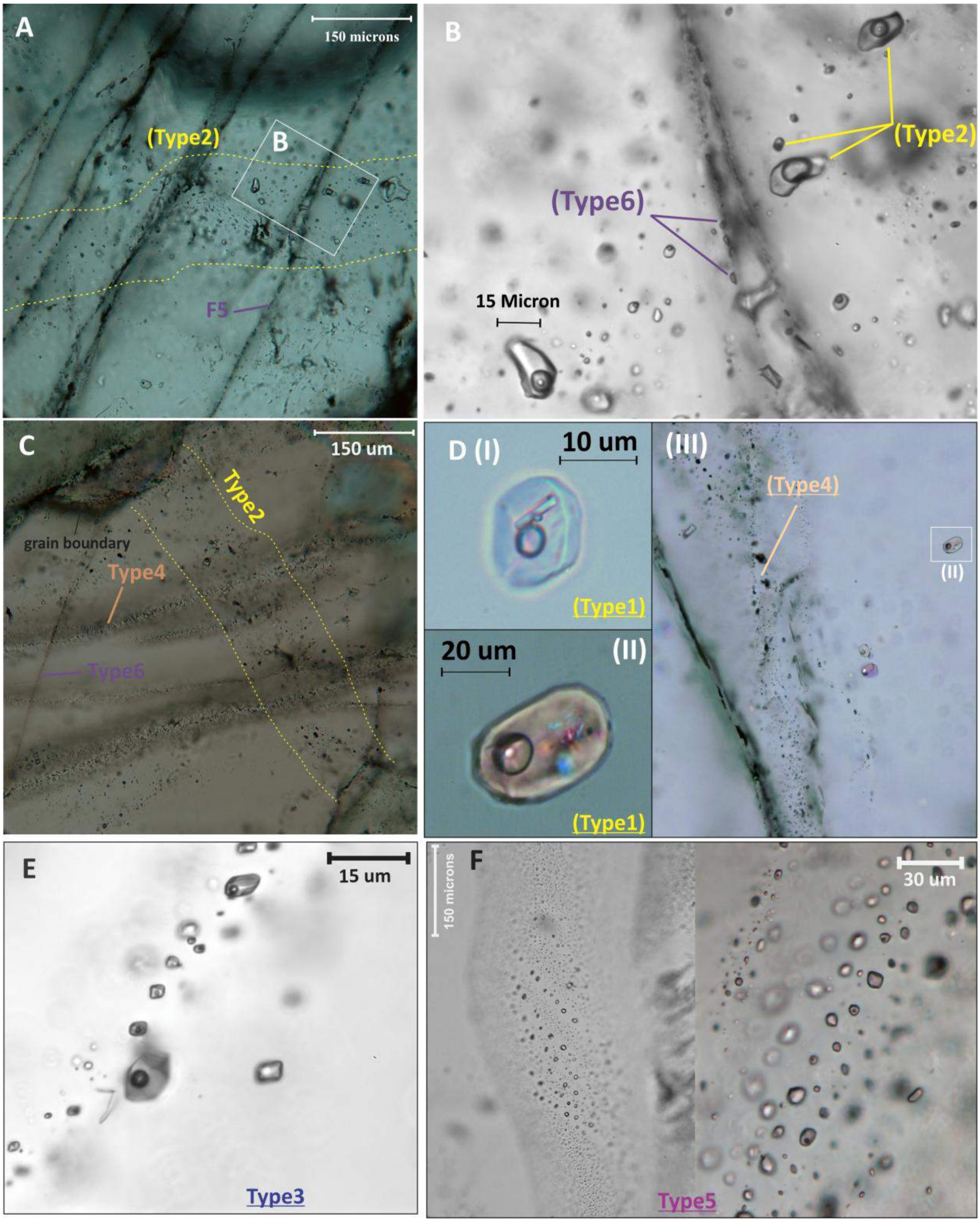

Figure 5.4-9: Photomicrographs of inclusions type occurring in quartz veins of Pau-a-Pique deposit. A: Relationship between Type2 and Type6. Type2 has a sprawled form of occurrence along trails meanwhile types 6 are trapped along healed fractures; (B): detail of inclusions Type2 from Photo A; (C): Three different types of fluid inclusion occurring in samples of translucent quartz. D (I and II) detail of polyphasic inclusion (Type1). The difference in shape and amounts of solid phases suggests they are accidental minerals trapped during fluid formation; D (III): The frequent isolated character of inclusions Type1 occurring within clear quartz with ondulose extinction; E: Biphasic aqueous fluid inclusions occurring in trails and; (F): Biphasic and monophasic high salinity inclusions (Type5). On left, the fracture in which these inclusions are trapped are oblique to the thin section, because of that they appear in a sprawled form however they occur along very thin factures. On right, the inclusions are showed in detail. All photographs was taken at a fix temperature of 25ºC.

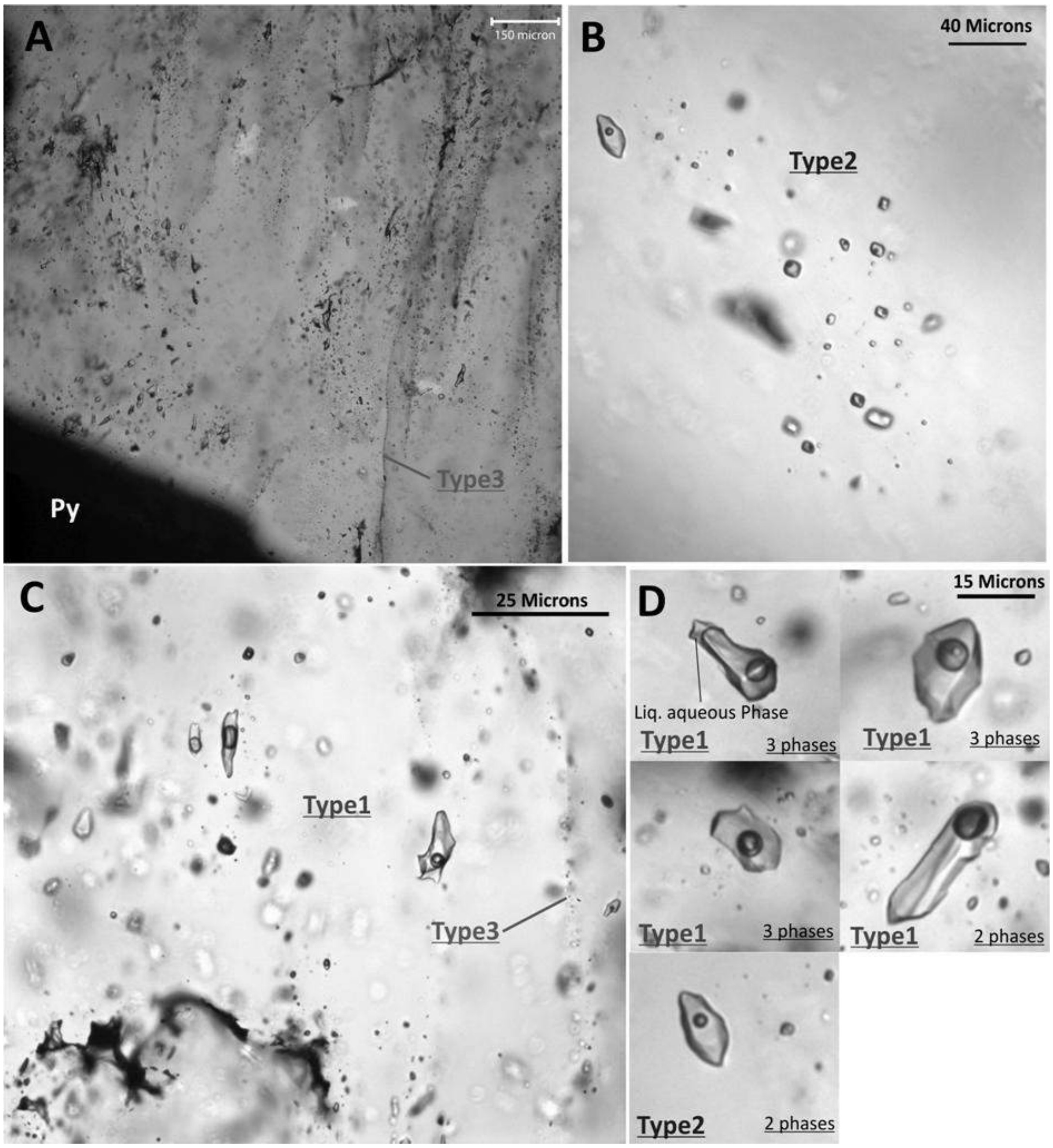

Fig.5.4.10: Fluid inclusions occurring in mineralized veins of Ernesto Intermediate Level. (A): Pattern of inclusions occurring in quartz around pyrite prophiroblstast. (B) Inclusions Type2; (C) Type1 and 3 occuring togheter; (D): Detail of variable liquid-gas ratio found in inclusions Type1 and detail of inclusion Type2. All photographs was taken at a fix temperature of 25ºC.

5.4.5 Fluid Inclusion Microthermometry and Laser Raman Spectroscopy

Microthermometric data are summarized in Table 5.4-1 and in Figure 5.4-12.

Pau-a-Pique

Type 1 and 2 inclusions have CO_2 melting between -56.6 and -57.5 ºC, and they have CO_2 homogenization to the liquid from 19.6 to 30.3. The microthermometric values suggest almost pure CO_2 which is also confirmed by laser Raman analysis (Fig. 5.4-11). During freezing gas-hydrates dissolves in the temperature range from 6.2 to 8.6 ºC, with most of measured temperatures between 7.1 and 8.0 ºC (Fig. 5.4-12). Considering the almost CO_2 pure composition of the gas phase, the dissociation temperature of gas hydrates (chlatrate temperature) correspond to a salinity ranging from 3.0 to 5.3 wt % NaCl equivalent. Estimations of relative volume proportion of aqueous fluid and gas phase was made by approximations based on relative area between the bubble and aqueous liquid phase at 25ºC and suggest variation of (12 -8 vol. % CO_2) for inclusions Type2. The CO_2 content is estimated between 12 and 32 mol%. Graphical estimations of molar volume (Vm) based on total homogenization temperature and partial homogenization of CO_2 indicates Vm around 25 and 30.5 cm^3/mol (Bakker and Diamond, 2000). On heating to total homogenization many of the inclusions has decrepitated before homogenize, as consequence only one inclusion from Type 1 and 55 from Type2 reached the total homogenization. Most of inclusions with size above 15 microns has decrepitated before homogenization and the smallest decrepitated inclusion has 7 microns in diameter and suggest minimum internal pressure of ~2kbars (Bodnar et al., 1989). Type1 and 2 inclusions generally homogenize into liquid between 211 and 282 ºC and few inclusions are likely to have critical behavior with gradual disappearance of meniscus. Eutectic ice melting was accurately measured only in five large inclusions. It ranges from -21.2 to -23.7 and suggest that the salts present in the liquid solution are primarily composed by NaCl, and may contain minor amounts of KCl, Na_2CO_3, $NaHCO_3$ and $NaSO_4$ (Shepherd et al., 1985).

Some of the Type 3 inclusions showed chlatrate formation during cooling experiments, suggesting the presence of CO_2. However, chlatrate formation was observed only in a few inclusions, most of Type3 inclusions only show ice melting temperature on cooling which in turn shows a consistent range of values ranging from -1.9 and -6.5 with most measurements between -2.5 and -3.0 ºC consistent with salinity of 4 - 4.6 wt% NaCl equiv.. Homogenization to the liquid occurred between 130 and 184 ºC.

Differently from Type 3, the Type 4 inclusions do not show a consistent vapor phase and those with a vapor bubble may show metastable behavior during homogenization. Gas-hydrate formation during cooling experiments indicates that small amounts of CO_2 were present, but not all inclusions did show chlatrate melting and those in which CO_2 is present show wide range of variation on chlatrate dissolution (from -4.8 to + 5.4 ºC). The presence of many empty inclusions was found along trails containing inclusions Type4 and suggest post entrapment changes.

Type 5 inclusions were found only in one sample. It has similar shape and occurrence form as Type 4 inclusions, however have a much higher salinity as evidence by ice melting temperature ranging from -14.2 to -9.6 which correspond to 13.1 - 17.3% wt NaCl equiv. As mentioned above, these inclusions can be monophasic or biphasic. During homogenization it may show a metastable behavior of vapor phase with homogenization occurring between 93 and 144 ºC.

Type 6 inclusions, were not studied during microthermometry because of their diminute size and frequent necking-down and deformed aspect suggesting it was subject to deformation after emplacement.

Table5.4-1:Sumary of the thermometric fluid Inclusion data from Pau-a-Pique and Ernesto deposits

Deposit	Type of Fluid Inclusion	Fluid System	Occurence	Tm_{CO2} (ºC)	Tfm (ºC)	Tm_{ICE} (ºC)	Tm_{CLA} (ºC)	Th_{CO2} (ºC)	Th_{TOT} (ºC)	n
Pau-a-Pique	Type1	$H_2O + CO_2 + NaCl$	isolated in clean quartz	-57.5 to -56.6	-21.8 to -20.6	-5.7 to -2.7	6.4 to 7.3	21.0 to 27.9	282 [a]	8
	Type2	$H_2O + CO_2 + NaCl$	cloudy trails	-57.9 to -56.5	-23.7 to -21.7 [b]	-7.5 to -4.2	6.2 to 8.6	19.6 to 30.3	211 to 281 [c]	126
	Type3	H2O + NaCl $\pm$ CO_2	trails	-	-	-3.1 to -1.9	-	-	130 to 184 [d]	37
	Type4	$H_2O + NaCl \pm CO_2$	trails	-	-	-	-4.8 to 5.4	-	98 to 157[f]	52
	Type5	$H_2O + NaCl$	trails	-	-	-14.2 to -9.6	-	-	93 to 144 [e]	24
Ernesto	Type1	$H_2O + CO_2 \pm NaCl \pm N_2$	trails	-58.0 to -56.6	-	-6.4 to -3.0	7.2 to 9.6	18.6 to 27.7	180 to 290	61
	Type2	H_2O-NaCl	Trails	-	-	-6.2 to -5.1	-	-	125 to 157	6

Tm_{CO2}, melting of the carbonic phase; Th_{CO2}, homogenization temperature of the carbonic phase to the liquid (L) or vapor state (V); Tfm, first melting of ice or eutetic melting temperature; Tm_{ICE}, ice melting temperature; Tm_{CLA}, gas hydrate melting temperature; Th_{TOT}, total homogenization temperature; n refers to number of individual fluid inclusions used for microthermometric analysis;

[a] Only one measument all other inclusions decripitated before homogenization

[b] Only three measuments

[c] 55 measurements of Th_{TOTAL} (others decripitated before homogenization)

[d] 29 measurements of Th_{TOTAL}

[e] 9 measurements of Th_{TOTAL}

[f] 16 measurements of Th_{TOTAL}

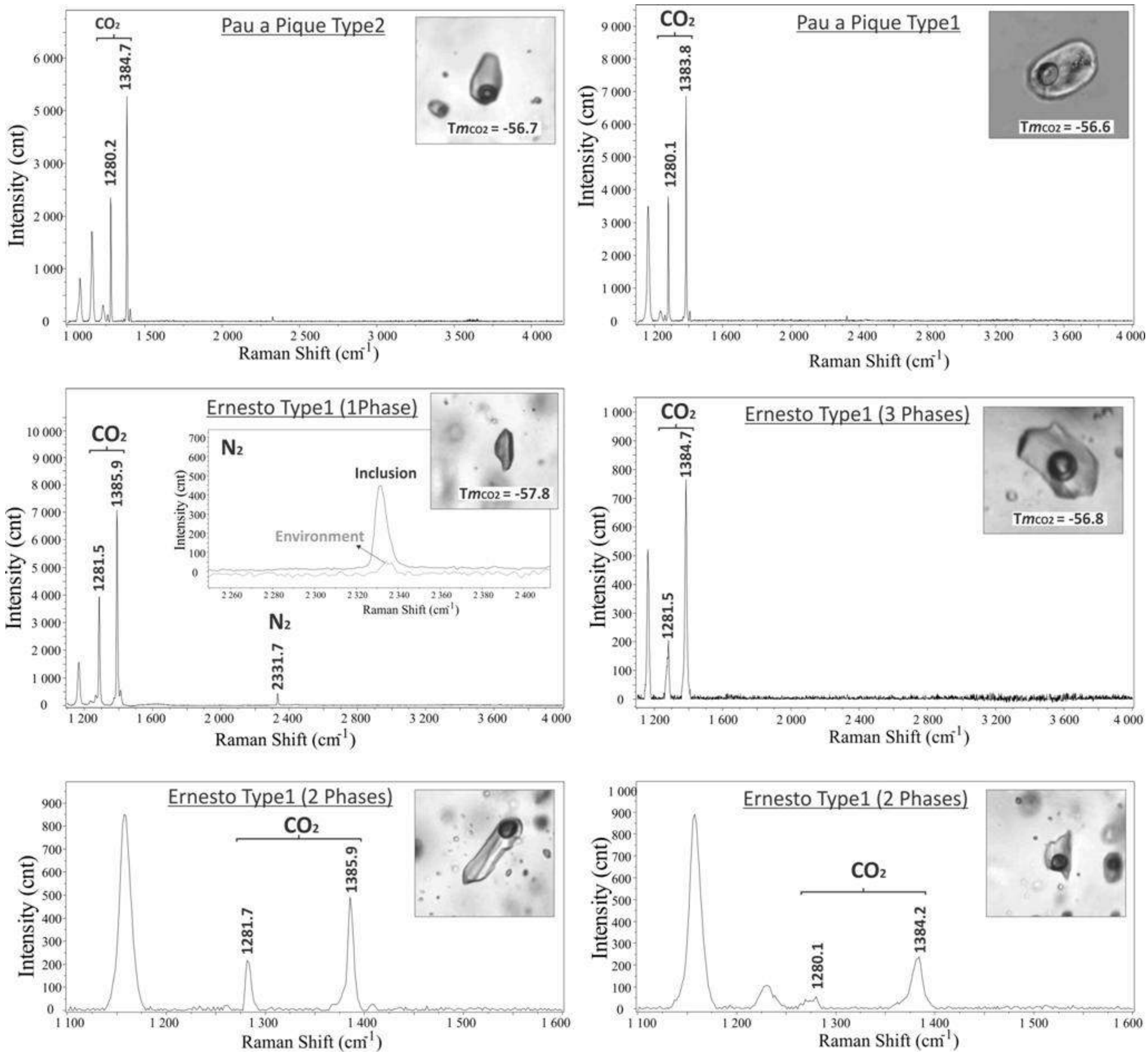

Figure 5.4-11: Raman spectrums of CO2-rich inclusion of Pau-a-Pique and Ernesto deposits. On top, inclusions Type 2 and 1 (on left and right respectively) of Pau-a-Pique deposit. The spectrums shows olny CO2 in the gás phase compatible with CO2 melting temperature of about -56.6ºC. In the midle (left) the spectra of monophasic gás inclusions composed by CO2 and small amounts of N2. In the same spectrum, the detail of N2 peak and its comparison to the peak given by N2 from the environment, in order to confirm the presence of N2. In the midle (right) spectrum of three phasic inclusions showing pure CO2 phase. On bottom detailed spectrum for biphasic inclusions in order to confirm the presence of CO2 in the bubble of biphasic inclusions of Ernesto deposit.

Ernesto

Type 1 inclusions show evidence of heterogeneous entrapment as observed by variable H_2O/CO_2 ratio. They vary from pure CO_2 (monophasic) inclusions until aqueous inclusions (biphasic) in which CO_2 occurs as gas bubble. They have CO_2 melting temperature between -56.6 and -58.0 ºC, and CO_2 homogenization to liquid between 18.6 and 27.7 ºC. Microthermometric data suggest an almost pure CO_2 although small amounts of N_2 were detected by Raman spectroscopy in monophasic CO_2 inclusions (Fig. 5.4-11). Calculations using Raman peaks (Burke, 2001) of analyzed inclusions containing N_2 suggest that the last may represent up to 8% of the gas phase, however the effects of environmental N_2 were not reduced from the total peak and the real amount of N2 is probably lower. No CH_4 were detected by Raman spectroscopy and variations on CO_2 melting temperature must be related exclusively to the presence of N_2. Total homogenization temperatures was obtained between 180 and 290ºC and most of it has occurred to liquid. No decriptation was noticed during heating experiments and suggest low pressure during inclusion entrapment (< 1Kbar) since the biggest inclusion measured has about 25 micrometer in diameter. Graphical estimations of molar volume were made in triphasic inclusions with volume fraction of CO_2 phase varying from 0.1 and 0.20 and the values ranging between 22 and 27 cm^3/mol were obtained. Chlatrate melting temperature ranges from 7.2 to 9.6 ºC with most values between 8.1 and 9.5ºC (Fig. 5.4-12) and correspond to salinity between 4 and 0.8 wt % NaCl equivalent.

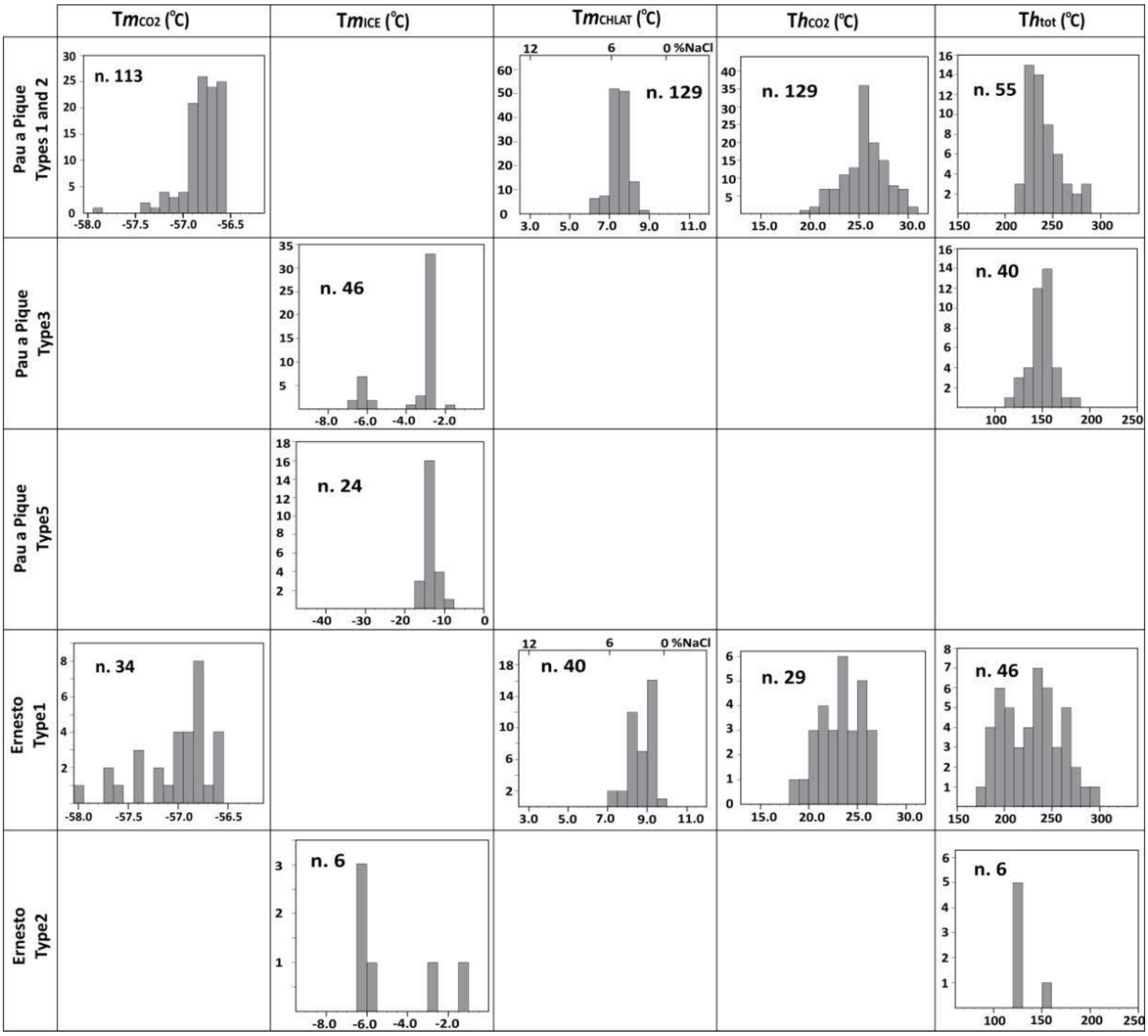

Figure 5.4-12: Histograms showing microthermometric data obtained on inclusions Type 1 and 2(grouped in the same histograms), 3 and 5 of Pau-a-Pique deposit and Type 1 and 2 of Ernesto deposit.

Although Type 2 inclusions have no separated CO_2 phase on petrography, gas hydrate formation in some of analyzed inclusions on cooling indicates that CO_2 is present. Total homogenization temperature to liquid occurred at temperatures around 125ºC for most of analyzed inclusions, however it is important to notice the low number of measured inclusions. Ice melting occurred between -5.1 and -6.2ºC and correspond to a salinity between 9 and 8.4 wt % NaCl equivalent.

Type 3 inclusions were not studied by microthermometry because of its diminute size which makes thermometric observations difficult.

5.4.6 LA-ICP-MS analysis of fluid inclusions

Three families of fluid inclusions (Types 2, 3 and 5) of the Pau-a-Pique deposit were individually analyzed by LA-ICP-MS in order to identify trace elements and metals dissolved in the fluid. A total of 26 individual analyses are shown in Table 5.4-2.

Table 5.4-2: LA-IC-MS analyses of fluid inclusion from the Pau-a-Pique deposit.

				Li			**As**			**Rb**			**Sr**			**Cs**		
Type	**Sample**	**Chip**	**Inc.**	**ppm**	(+/-)	LOD	**ppm**	(+/-)	LOD	**ppm**	(+/-)	LOD	**ppm**	(+/-)	LOD	**ppm**	(+/-)	LOD
2	PQ54	A13I	D	**149**	61	26	**640**	220	108	**153**	29	6	**71**	18	2	**2.6**	2.5	0.04
	PQ54	A13II	A	**70**	16	51	**880**	120	148				**4.4**	2.4	4	**0.42**	0.75	4
	PQ54	A13II	B				**1580**	630	148							**2.7**	6.1	4
	PQ54	A13II	F	**99**	85	51	**2340**	730	148				**19**	16	4			
	PQ54	A13II	G	**100**	60	51	**960**	260	148									
	PQ54	A13II	H	**205**	74	51	**1060**	260	148				**42**	18	4			
	PQ54	A4	B	**93**	51	53	**280**	220	204				**20**	12	4.1			
	PQ54	A4	C				**900**	230	204				**32**	9	4.1	**6**	3	4.5
	PQ54	A4	D	**137**	55	53	**2540**	660	204				**17**	10	4.1			
	PQ54	A4	G	**87**	88	53	**3700**	1200	204				**22**	15	4.1			
	PQ54	A4	J	**60**	31	53	**2090**	500	204				**20.8**	8.9	4.1			
	PQ61	D2	A1	**46**	41	26	**1190**	280	108							**0.8**	1.3	0.04
	PQ61	D2	A2	**81**	30	26	**430**	100	108									
	PQ61	D2	B				**440**	180	108							**0.14**	0.62	0.04
	PQ61	D2	C	**60**	30	26	**230**	100	108									
	PQ61	D2	F	**42**	46	26	**500**	190	108									
	PQ61	C1	A	**78**	50	31	**890**	280	87									
	PQ61	C1	G	**110**	38	31	**1660**	510	87	**4.7**	4.7	1.1	**17.1**	5.6	1.2	**3.1**	1.7	0.5
3	PQ12	8B	B+C*				**3500**	1900	204				**170**	91	4.1			
	PQ12	5A	I				**560**	240	147	**8**	12	11	**148**	29	7.8	**2**	3	2.2
	PQ12	5A	D				**1270**	360	147				**12**	7.5	7.8	**9**	5	2.2
	PQ12	5A	E				**770**	250	147				**121**	27	7.8	**21**	9	2.2
	PQ12	5A	G+H*				**1200**	700	147				**61**	29	7.8	**19**	18	2.2
	PQ12	11A	M				**480**	140	147				**44**	15	7.8	**3**	3	2.2
5	PQ61	D1	H	**479**	83	113				**37**	13	19	**2150**	290	15	**14**	5	1
	PQ61	D1	I	**320**	230	113				**61**	55	19	**2650**	300	15	**23**	20	1
	PQ61	D1	J										**2230**	340	15	**17**	14	1
	PQ61	D1	L	**260**	190	113				**60**	46	19	**2510**	220	15	**16**	10	1

* Bulk analysis (two inclusion at the same time)
LOD Limit of detection
(+/-) Uncertainty

The detected trace elements (above detection limit) comprise Li, As, Rb Sr and Cs.

Some differences can be observed between the families. Type 2 and 3 inclusions have consistent presence of Arsenic. The concentration ranges from 230ppm to 3700ppm in Type 2 inclusions, and from 480ppm to 3500ppm in Type 3 inclusions. Type 5 inclusions differ from Type 2 and 3 due to the absence of Arsenic, the constant concentration of Cs (with low uncertainty) and the high and constant concentration of Sr.

The main differences between the elements present in Type 2 and 3 inclusions regards the absence of Lithium and the constant presence of Sr in Type 3.

Lithium has been identified as luminescence-activator in some of studied quartz from the Pau-a-Pique deposit (Fig. 5.3-26). Quartz showing CL-bright texture was identified in some of translucent quartz veins and in albite-quartz veins of the Pau-a-Pique deposit. CL-bright cores of quartz are located in zones of clean quartz (without inclusion) and are limited by trails of secondary fluid inclusions. LA-ICP-MS analyses of the CL-bright quartz suggest that the brighter zones have higher concentration of Li in contrast with low concentrations of it in CL-dark zones.

The process of zone-refining in quartz proposed by Lambrecht and Diamond (2014) can explain the differences in Li content between the analysed inclusions and suggest that it is not related to the inclusion family but to the host sample. The authors suggested that secondary fluid inclusions containing solvent water can sequestrate trace elements (e.g. Ti, Li, Al and Na) from the early formed quartz in the walls of fluid inclusions forming non-luminescent quartz around it. This process can drive to an increment in concentration of trace elements of fluid inclusions and may led to formation of Ti and Al minerals.

In fact LA-ICP-MS analyzes of Types 2 and 5 inclusions were made in samples PQ54 (PQ54147-02) and PQ61 (PQ61127-30). The presence of CL-bright texture in zones of clean quartz was identified in both samples. In contrast, the sample PQ12 (PQ12302-46), in which the Type 3 inclusions were analyzed (also the most deformed sample between the studied quartz veins) doesn't show any CL-bright texture and LA-ICP-MS analyzes didn't identify the presence of Li as trace elements in quartz. Thus concentration of Li above the detection limit observed only in inclusions trapped in samples in which the quartz was previously enriched in Li account for post-entrapment modification and thus has no relation to the initial composition of fluid. The presence of Li in concentrations above the detection limit also confirms the secondary origin of inclusions Type2 in agreement with petrographic observations.

Pyrite is the only As-bearing sulfide present in the Pau-a-Pique deposit. Arsenic concentrations of pyrites from the Pau-a-Pique vary from 30 to 4700 ppm with a mean of 418 ppm as observed by microprobe analysis. Despite the huge variations in the Arsenic content in fluid inclusions, its constant presence in Type2 and 3 inclusions can be assumed as a link between these families of fluid inclusions and the fluid which has precipitated pyrite.

The absence of arsenic and the higher concentration of Sr is the main compositional difference between Type5 inclusions and the other two types. Their higher salinity the absence of Arsenic suggests that they represent latter fluids, not related to sulfide crystallization.

5.4.7 Stable Isotopes

Sulfur isotopes

Sulfur isotope data are presented in Table 5.4-3. A total of 16 pyritesamples from the Ernesto and Pau-a-Pique deposits were analyzed (6 from the Ernesto and 10 from the Pau-a-Pique). The pyrite from the intermediate level of Ernesto show values that are generally lower than that observed in the Pau-a-Pique. The six pyrite samples from Ernesto yielded δ^{34}S values in the range -1.2 to 2.6 per mil (mean 0.7). The ten pyrite samples from the Pau-a-Pique yielded δ^{34}S values between0.7 and 5.3 per mil (mean 3.2). As mentioned above other sulfides (galena and chalcopyrite) generally occurs as small inclusions in pyrite porphyroblasts and were not analyzed.

Table 5.4-3: Sulfur isotope data δ^{34}S (‰ vs. CDT)

Location Sample n.	δ^{34}S (per mil) in Pyrite	host rock
Ernesto (Intermediate level)		
ER97 29-71	1.0	quartz vein
ERFL02-007	0.7	quartz vein
ER02 99-48	-0.3	quartz vein
ER05 109-55	-0.4	quartz vein
ER05 118-75	2.6	min. metaconglomerate
ER97 33-31	-1.2	min. metasandstone
Pau-a-Pique		
PQ12 302-46	5.3	Qtz vein (T1)
PQ12 377-55	3.5	Qtz vein (T1)
PQ12 380-76	5.0	muscovite-schist
PQ12 424-26	1.4	Ab-Qtz vein (T2)
PQ12 435-61	3.2	Ab-Qtz vein (T2)
PQ41 298-03	5.0	muscovite schist
PQ61 154-02	0.7	muscovite schist
PQGL1-006	2.5	muscovite schist
PQPMFR360SE	4.7	ky-bearing Bt-Ms Schist

Oxygen isotopes

Table 5.4-4 shows oxygen isotope results for 16 samples of hydrothermal quartz and 7 samples of hydrothermal muscovite 2 samples of hydrothermal albite and 3 samples of hydrothermal magnetite from the mineralized zone of the studied deposits (Ernesto-intermediate level and Pau-a-Pique). It also show the results for 12 samples of quartz from other eight mineralized quartz veins from smaller gold occurrences at the central portion of Alto Guaporé Gold Belt (AGGP).

Table 5.4-4: Oxygen Isotope Data - $\delta^{18}O$ (‰ vs. SMOW)

Location			**Qtz**		**Ms**		**Ab**		**Mag**	
Sample n.	**Host rock**	**Nature of the samples**	$\delta^{18}O$	Yield	$\delta^{18}O$	Yield	$\delta^{18}O$	Yield	$\delta^{18}O$	Yield
Incra										
Incra I**	Volcanosed. Seq.	Mineralized qtz vein	8.4	99						
Corr. da Onca										
(1) Onça I**	Volcanosed. Seq.	Mineralized qtz vein	10.5	96						
Ernesto Area										
Marinho/Nosde										
(88)FN20**	sheared contact	Mineralized qtz vein	11.9	98						
(106)FN20**	metarenite	Mineralized qtz vein	12.5							
Lavrinha										
LV-Copacel**	metapelite	Mineralized qtz vein	13.1	99						
(32) LV05**	metapelite	Mineralized qtz vein	13.1	99						
Paulo										
(4) Paulo I**	Unknown	Mineralized qtz vein	11.3	98						
Nene										
10-S- Nenê I**	Unknown	Mineralized qtz vein	11.5	99						
Mineiros										
Mineiros I**	Unknown	Mineralized qtz vein	12.5	100						
Ernesto										
(64)ER64**	sheared contact	Miner. qtz vein (inf. Level)	10.9	99						
ER05109-55	metaconglomerate	Quartz vein (Type2)	11.3	105	10.0	105				
ER9729-71	metaconglomerate	Quartz vein (Type2)	12.0	92						
ER05108-25	metaconglomerate	Metaconglomerate	13.0	94						
ER05118-75	metaconglomerate	silicified wall rock	10.5	99						
ERFL2-007	metaconglomerate	Quartz vein (Type2)	15.3	128	11.0	105				
Pau-a-Pique										
Pau a Pique I**	sheared contact	Au qtz vein	11.3	99						
PQ31665-27	sheared contact	Transl. vein Family (T1)	11.5	94	12.0	104			1.75	96
PQGL1-007	sheared contact	Ab-Qtz Vein family (T2)	11.1	73						
PQ53163-58	sheared contact	Transl.vein Family (T1)	11.6	107	11.9	119				
PQ61127-30	sheared contact	Trans. vein Family (T1)	14.0	87					2.74	60
PQGL1-006b	sheared contact	Trans. vein Family (T1)	12.0	87	10.7	114				
PQ61154-02	sheared contact	Trans. vein Family (T1)	11.8	100	11.6	112				
PQGL1-005b	sheared contact	Ab-Qtz Vein family (T2)	11.1	100						
PQ12308-20	sheared contact	Trans. vein Family (T1)	12.2	93					2.74	58
PQ6184-76	sheared contact	Ab-Qtz Vein family (T2)	11.6	99			11.47	96		
PQ12435-61	Basement	Ab-Vein (T2)					11.55	153		
PQ55127-33	sheared contact	Trans. vein Family (T1)	13.2	62	8.9	110				
Maraboa I**	Granite	Mineralized qtz vein	9.9	96						

** Analyses made at Geological Survey of Canada, Ottawa, Canada. All other samples were analysed at United States Geological Survey, Denver, Colorado using samples collected during this research. T1: vein Type 1 of Pau a Pique; T2: VeinType 2 of Pau a Pique

The total range in $\delta^{18}O_{quartz}$ values of all studied samples is from 8.4 to 15.3 per mil. The $\delta^{18}O_{quartz}$ values range from 11.1 to 14.0 per mil for ore-bearing quartz veins of Pau-a-Pique deposit and from 10.5 to 15.2 per mil for Ernesto Deposit (intermediate level).

Similar values are found in hydrothermal muscovite. The $\delta^{18}O_{muscovite}$ values found in Ernesto deposit are 10.0 and 11.0 for Ernesto deposit and between 8.9 and 12.02 for Pau-a-Pique deposit.

The three lowest values (8.4, 9.9 and 10.5‰) for quartz were obtained for quartz veins emplaced in basement rocks (in volcano-sedimentary sequence of Alto Jauru and in Maraboa Granite). Veins hosted within shear zones formed along the contact between the sediments and the basement generally show values between 11.0 and 12.0, and veins hosted by metasediments show values between 10.5 and 15.3‰ with most values above 12‰. No significant differences on $\delta^{18}O_{quartz}$ were found between the quartz veins Type 1 and 2 (translucent and albite quartz vein respectively) of Pau-a-Pique deposit and suggest they were formed by the same fluid.

Hydrogen Isotopes

The hydrogen isotopes results are presented in Table 5.4-5. Hydrogen isotopes were analyzed in hydrous minerals (muscovite and Chlorite) and in fluid inclusions of mineralized quartz veins.

The total range in $\delta D_{muscovite}$values for muscovite is between -39.8 and -124.3‰ with most values ranging between -70 and -110‰. Similar range of values was obtained for chlorites ($\delta D_{chlorite}$) from Pau-Pique deposit (between -48.9 and -94.5‰).

In fluid inclusions the values tend to be higher and generally range from -36.6 to -102.1‰ with most values between -40 and -60‰.

5.4.8 Discussion

Evidences for mineralizing process and timing

Hydrothermal Alteration

The characteristics of fluids and hydrothermal alterations found in the Ernesto and Pau-a Pique deposits are similar to those found in orogenic gold deposits of Precambrian age (e.g. Groves et al., 1998; Goldfarb et al, 2005; Groves et al., 2003; Ridley and Diamond 2000).

Table 5.4-5: Hydrogen Isotope Data - δD (‰ vs. SMOW)

Location			**δD (o/oo; SMOW)**		
Sample	**Host Rock**	**Nature of the samples**	**F.I.**	**Ms**	**Chl**
Incra					
Incra I*	Volcanosed. Seq.	Au Qtz vein	-56.7		
Incra II*	Volcanosed. Seq.	sericitic wallrock to Incra I		-75.2	
Corr. da Onca					
(1) Onça I*	Volcanosed. Seq.	Au Qtz vein	-56.1		
29716-Onça II*	Volcanosed. Seq.	sericitic wallrock to Onça I		-107.6	
Ernesto Area					
Marinho/Nosde					
(85)FN20*	sheared contact	Au Qtz vein	-41.5		
(89)FN20*	sheared contact	sericitic wallrock to 85		-79.1	
(97)FN20*	sheared contact	altered tonalite (host)		-78.2	
(103)FN20*	sheared contact	tonalite (host)		-80.8	
(92)FN20*	sheared contact	sheared tonalite host to (88)		-99.1	
(88)FN20*	sheared contact	Au Qtz vein	-51.2		
(106)FN20*	metarenite	Au Qtz vein hosted by metarenite	-36.3		
Lavrinha					
LV-Copacel*	metapelite	Au Qtz vein	-40.3		
LV-29596*	metapelite	sericitic wallrock to Copacel		-78.6	
(33)LV05	metapelite	sericitic wallrock to (32)		-39.8	
Paulo					
(4) Paulo I*	Unknown	Au Qtz vein	-60.5		
29595-PauloII*	Unknown	sericitic wallrock to Paulo I		-76.6	
10-S- Nenê I*	Unknown	Au Qtz vein	-53.1		
29598-Nenê II*	Unknown	sericitic wallrock to Nenê I		-124.3	
Mineiros					
Mineiros II*	Unknown	sericitic wallrock to Mineiros I		-95.8	
Ernesto					
ER58-2*	sheared contact	sericitic wallrock		-77.2	
ER58-1*	sheared contact	Au Qtz vein	-37.9		
ER73*	sheared contact	sericitic wallrock		-83.1	
(61)ER61*	sheared contact	sericitic wallrock to 64		-72.5	
(64)ER64*	sheared contact	Au Qtz vein	-102.1		
ER05109-55	Metaconglomerate	Ms on wallrocks of Py bearing qtz vein		-53.9	
ERFL2-007	Metaconglomerate	Ms on wallrocks of Py bearing qtz vein		-49.6	
Pau-a-Pique					
Pau-a-Pique I*	sheared contact	Au Qtz vein	-63.8		
Pau-a-Pique II*	sheared contact	sericitic wallrock to Pau-a-Pique I		-114.4	
PQ31665-27	sheared contact	Non-mineralized Ms schist		-69.4	
PQ53163-58	sheared contact	Mineralized Py-bearing Ms schist		-76.9	
PQ61127-30	sheared contact	Qtz vein			-65.9
PQGL1-006b	sheared contact	Mineralized Py-bearing Ms schist		-91.2	
PQ61154-02	sheared contact	Mineralized Py-bearing Ms schist		-104.1	
PQ6184-76	sheared contact	Ab-Qtz vein			-48.9
PQ55127-33	sheared contact	Mineralized Py-bearing Qtz vein		-120.9	
PQ12435-61	sheared contact	Py-bearing Ab-Qtz vein			-94.5
PQ12380-76	sheared contact	Mineralized Py-bearing Ms schist		-80.4	
PQ12424-26	sheared contact	Py-bearing albite vein			-77.9

* Analyses executed by Geological Survey of Canada, Ottawa, Canada.
All other samples were analyzed at United States Geological Survey in Denver, Colorado using samples collected during this research. F.I.= Fluid inclusions; Ms = Muscovite; Chl = Chlorite.

In the Pau-a-Pique deposit, muscovite, magnetite, ilmenite, rutile and apatite are the main gangue phases associated with mineralized veins occurring along the contact between the metasedimentary rocks of Aguapeí group and the basement. These veins were subject to repeated brittle-ductile deformation as evidenced by recrystallization and plastic deformation of quartz.

During drill core descriptions it was observed that narrow zones of non-mineralized muscovite schist may occur within the mineralized body. These zones are marked by absence of pyrite moreover the quartz veins tend to be less deformed and milky and magnetite is magnetic. These features generally contrast with the neighboring mineralized zones marked deformed (boudins) and clear (translucent) quartz and the abundance of disseminated pyrite occurring together with martitized magnetite.

Quartz-albite veins are restricted to the basement rocks and their deformation is directly associated with the level of deformation of their host rock. When it is emplaced in low deformed portions of the basement they are less deformed, contrasting with the zones of high deformed basement (shear zones) where they are deformed showing differential boudinage and sigmoidal shape. The other phases associated with these veins are albite chlorite and carbonate. From petrography, it is clear that albite is contemporary to quartz and earlier to chlorite and carbonate that generally occurs in fractures in quartz and albite.

In the intermediate level of the Ernesto deposit, two types of quartz veins are common, the first type comprises barren quartz veins occurring along shear zones within the metasedimentary rocks, more or less parallel to the sedimentary stratification. The second type comprises low deformed, pyrite-bearing quartz veins of centimetric scale.

Magnetite and other oxides (rutile and ilmenite) are ubiquitous to all studied samples in both deposits. Ilmenite is the most frequent oxide associated with mica schist formed along shear zones in the Pau-a-Pique deposit being magnetite more frequent to Ernesto.

As exposed in section 5.3 fluid-assisted shearing during peak conditions is likely to be the process responsible for the formation of mica-schist in the Pau-a-Pique and is probably the process responsible for mica schist in the Ernesto. The syn-genetic character of the Fe-Ti oxides in relation to muscovite found in both deposits account for their hydrothermal origin.

Sulfidation of Fe-Ti oxides (mainly ilmenite in Pau-a-Pique and magnetite in Ernesto) as clearly observed by pyrite grown over magnetite on wall-rocks of quartz veins (Type2) in the Ernesto deposit and over Ilmenite rutile and magnetite in muscovite schist of Pau-a-Pique (inclusions in the core of texturally zoned pyrite) is a process associated with gold depositions in a number of ore deposits and has been experimentally tested in laboratory under varied conditions (e.g. Qian, 2010). Relevant studies of natural pyritization of magnetite and Fe-Ti oxides suggest that magnetite dissolution can be accompanied by extensive replacement by pyrite if magnetite were in contact with high concentration of H_2S. According to Qian et al. (2010) under reduced conditions the overall reaction of magnetite sulfidation can be written as:

$$Fe_3O4_{(mt)} + 3.74H_2S_{(aq)} + 2.26H^+ = 1.87FeS_{2(py)} +1.13Fe^{2+} + 4H_2O + 0.87H_{2(g)} \quad (14)$$

In both deposits the great majority gold occurs as inclusions in the sulfide (pyrite). In Pau-a-Pique the highest ore grades is associated with texturally zoned pyrite occurring in translucent quartz veins and in muscovite schist of the contact. In these pyrite, inclusions of gold tend to be more frequent in the massive rim of texturally zoned pyrite, where group of small inclusions of gold are often aligned along some plane or following the boundary of porphyroblasts. In Ernesto deposit inclusions of Au, Ag, Bi and Te are randomly distributed in euhedral crystals of pyrite in mineralized quartz veins.

These characteristics indicates that gold may have had precipitated contemporaneously with the growing pyrite in both deposits. As in the Pau-a-Pique the gold tend to be more frequent in the massive rim of texturally zoned pyrite, the precipitation may have occurred preferentially during the later stages of pyrite crystallization.

Chlorite only occurs in the Pau-a-Pique and it is always present in mineralized zones. It is also a common retrograde phase in mica schist, especially those biotite bearing, where chlorite occurs in a substitution texture. The close textural association with pyrite and its ubiquity in mineralized zones suggest that chlorite must be, at least in many of the studied samples, syn-genetic to pyrite. Minor amounts of chlorite are found within the crystals of muscovite in extremely rich portions of the deposits and reinforce its association with gold and sulfide. In quartz albite vein of the Pau-a-Pique, the pyrite generally does not show textural zonation and its crystallization seems too have occurred along fracture associated with carbonate, chlorite and galena. The last is found as inclusion in pyrite or along fractures (see Fig 5.3-3, section 5.3).

In fact the lower grades found in quartz albite veins would suggest another generation of pyrite, however the similar chemical composition observed among all studied samples as observed by microprobe and isotope analysis do not support such interpretation and the lower grades are likely to be related to lower amounts of pyrite found in those veins or to chemical conditions that not favored the gold precipitation. These conditions are discussed in detail bellow.

From the exposed above it is possible to say that gold is systematically associated with pyrite. Chlorite and carbonate are the guange minerals that show the closest relationship with pyrite among all other phases that are normally present in mineralized zones of the Pau-a-Pique. Quartz, albite, muscovite and Fe-Ti oxides seems to be earlier in relation to the sulfidation in most of examined samples.

Despite the proximity between pyrite and chlorite, as discussed in section 5.3.2 some Fe-rich chlorite occurring in quartz albite veins of the Pau-a- Pique are latter to pyrite and all other phases, including early-formed chlorite (see Fig. 5.3-30). These chlorites generally occur with carbonate along fractures and are chemically and texturally different from most chlorite believed to have crystallized in equilibrium with pyrite. They are finer in granulation and are also enriched in Fe and extremely poor in Mg. Temperature calculations suggest that they were formed at lower temperatures, attesting for their latter genetic interpretation. Thus not all chlorite and probably not all carbonate can be considered syn-genetic to pyrite.

Chlorite and carbonate does not occur in Ernesto and visual evidences of syn-genetic phases to pyrite are not recognized by petrography.

Interpretations about the mineralizing Fluid

The direct relationship between gold deposition and fluid type is difficult to be well established in the studied samples. In the Pau-a-Pique deposit the earliest preserved fluid in mineralized quartz veins are given by CO_2-rich fluids (Type 1 and 2) characterized by low salinity and almost pure CO_2 as volatile phase, with CO_2 content varying between 12 and 32 mol%. Type 2 inclusions are characterized by large amounts of arsenic dissolve in the fluid and are often observed in trails in clear quartz near sulfide crystals (Fig. 5.4-13). In the same way low salinity (<4 wt % of NaCl equiv.), CO_2-rich inclusions (Type1) is the main fluid inclusion family found in quartz surrounding gold-rich pyrite of mineralized veins of the Ernesto. These inclusions has variable CO_2/H_2O vol. ratio and petrographic studies indicates that monophasic CO_2 inclusions with minor amount (<8%) of N_2 are co-genetic to biphasic aqueous inclusions with minor CO_2 (almost pure) in the volatile phase (<10 mol %).

Low salinity (<6% NaCl equiv.), mixed aqueous-carbonic fluid with low to moderate CO_2 content (4-30 mol %) is recorded in the majority of orogenic gold deposits (Ridley and Diamond, 2000; Goldfarb et al., 2005). Most of these deposits were formed by H_2O-CO_2-H_2S+CH_4+N_2 fluids, in temperature about 200º and 500ºC, and between 1 and 4 Kbar of pressure (Goldfarb et al., 2005). In view of the ubiquity of CO2-rich fluids in lode gold deposits, the majority of authors have interpreted the low salinity, mixed aqueous-carbonic fluid to be the ore bearing fluid (Ridley and Diamond, 2000). The presence of CO2 on fluid transporting gold in most of only-gold deposits play a critical role during gold transport by buffering the fluid in a pH range where elevated gold concentration can be maintained by complexation with reduced sulphur (Phillip and Evans, 2004). In the world's major gold-only deposits these fluids have redox state more reducing than the hematite-magnetite buffer such that the sulphur is predominantly in the reduced state (Phillip and Evans, 2004; Phillips and Powell, 1993). For temperatures of 200-400ºC, pressure of 200 MPa and near neutral pH, Au $(HS)2^{-}$ is the dominant gold hydrosulfide complex (Benning and Seward, 1996; Phillip and Evans, 2004) and gold concentrations can be related to those sulfides species via:

$$Au(s) + H2S(aq) + HS^{-}(aq) = Au(HS)2^{-} + 1/2H2(aq)$$

Other compositional types of fluid inclusions, as commonly found in orogenic gold deposit, have been explained as: (1) end-member of phase separations that took place because of changing pressure or temperature conditions in the veins; (2) unrelated fluids that happened to be in the hydrothermal system at the time of mineralization, for instance fluids derived from nearby rocks or surface-derived fluids, (3) fluids infiltrated along fractures in the vein system at some time after the main vein-filling event, (4) inclusions of low salinity mixed aqueous-carbonic fluids that have been modified after entrapment (Ridley and Diamond, 2000 and the references therein).

Despite the physiochemical differences between CO2-rich inclusion of the Pau-a-Pique and Ernesto, its seems coherent to assume that in both cases CO2-rich inclusions was responsible for gold transporting and precipitation.

The presence of Magnetite and Fe-Ti oxides in the core of gold rich pyrites in both deposits can be explained by precipitation of pyrite and gold from low salinity, near neutral, CO2-rich reducing fluids (later and more reducing than magnetite) in agreement with the conditions of mineralizing CO_2-rich fluids observed in world's major gold-only deposits.

As mentioned above these fluids carry gold as hydrosulfide complex and thus meets the conditions necessary for Fe-Ti oxides pyritization. The constant presence of arsenic in CO_2-rich (Type2) inclusions in mineralized veins of Pau-a-Pique also favor the theory of precipitation of pyrite from CO2-rich fluids since pyrite is the only arsenic bearing phase present in both deposits. In addition it also account for the syn-genetic character of gold and pyrite as well.

The other fluid inclusion families may represent either later fluid infiltration along fractures, low salinity mixed aqueous-carbonic fluids that have been modified after entrapment and unrelated fluids that happened to be in the hydrothermal system. In the Pau-a-Pique Type 4 , 5 and 6 fluids are clearly later in relation to fluids Type 1 and 2 since they are entrapped along healed fractures. Type4 inclusions seems to have suffered post-entrapment modifications given their metastable behavior on microthermometry and by frequent necking-down. As consequence the complete interpretation about its origin turn out to be difficult and it is more likely to represent aqueous-rich infiltrations along fractures occurred during the latter stages of the mineralizing event since it have small amounts of CO_2 as evidenced by chlatrate formation during the cooling experiments. No microthermometric data was obtained from inclusion type 6 but it is clearly the later family among all other inclusions type, since they cross-cut all the other families of fluid inclusions. They may also represent later aqueous infiltration occurred after the mineralizing event. The type 5 inclusions have a contrasting higher salinity (13-17 wt% of NaCl equiv.) and may comprise unrelated fluids that happened to be in the hydrothermal system at the time of mineralization. It was found only in one sample and its constant and higher content of Sr found by LA-ICP-MS strongly differs from the other families of fluid inclusions present.

Inclusions Type3 (Biphasic aqueous inclusions) from Pau-a-Pique also has low salinity (4 - 4.6 wt% NaCl equiv) as evidenced by constant ice melting temperature between -1.9ºC and -3.1ºC. They occur in planar arrays and have relatively constant homogenization temperatures which suggest they didn't suffered post-entrapment modification. The presence of chlatrates on cooling (as observed in some of the inclusion) and the presence of arsenic as well, indicates that it may be related to the evolution of the original CO_2-rich to a water rich fluid or pulses of aqueous fluid during the main stage of fluid circulation. The differences observed on total homogenization temperature between the CO_2-rich family (Type 1 and 2) and aqueous family suggest that they are not co-genetic since large variation in pressure would be necessary for entrapment of low salinity aqueous fluid at temperature coherent with those found for the CO_2-rich family if considering phase separation. Moreover in samples of Pau-a-Pique most variations on water/gas ratio of fluid inclusions are related to post-entrapment modifications and non-modified CO_{2-} rich inclusions generally show a restricted range of CO_2 molar volume value. Thus infiltration of later aqueous fluids (e.g. meteoric water) seems to be more coherent as interpretation for these fluids.

Despite the constant presence of arsenic, the very low amounts of CO_2associated to the low salinity of these aqueous inclusions indicates that it has a lower potential to be the gold carrier in relation to the CO_2-rich inclusions. As consequence it can't be assumed as the main mineralizing fluid phase as previously proposed by Pulz et al. (2003). According to the authors the associations of native gold grains with biphasic aqueous inclusions suggest that gold deposition is related to percolation of aqueous solutions in the late stages of hydrothermal alteration in the Pau-a-Pique. They also suggested boiling as the process responsible for gold precipitation, based on variation of degree of fill (10-90%) along of the same array of fluid inclusions associated to similar total homogenization temperature for the inclusions with different degree of fill and the association between CO2-rich inclusions and aqueous inclusion in the same quartz grain.

In fact boiling has been invoked as responsible for gold precipitation in many deposits, however in orogenic gold deposits formed by CO_2-rich fluids, fluid-wall rock interaction is most commonly accepted as driving mineral precipitation where ordinaries are of disseminated and replacement style. The sulfidation of wall-rocks with high Fe/Fe+Mg ratios, including mafic igneous rocks will, destabilize gold as the sulfur bearing ligands are broken down into precipitated pyrite and thus gold grades may correlate with sulfide mineral abundance (Goldfarb et al., 2005). The fact that most of pyrite occurs in a replacement texture with Fe-Ti oxides in both deposits does support the theory of destabilization of gold and sulfur as the main responsible for gold precipitation rather than the boiling. Moreover most of quartz in Pau-a-Pique are highly deformed and recrystallized, and post-entrapment modifications could explain the variations on degree of fill in aqueous fluid inclusions if during petrography studies post-entrapment modifications wasn't taken into account.

The temperature for the mineralizing fluids of Pau-a-Pique can be extracted from the relationship between sulfide and chlorite. Crystallization temperature of chlorites were calculated in section 5.3 and the mean value (discarding the values obtained for latter Fe-rich chlorite) is around 325ºC and thus may represent the temperature in which the gold precipitated.

According to Ridley and Diamond (2000), carbonic fluids with small percentage of H_2O are predicted from experimental studies to be products of phase separation of a mixed low salinity aqueous-carbonic fluid within the range of pressure and temperature conditions implied for vein formation. The main family of fluid inclusions from Ernesto does show variations on CO_2/H_2O ratio. In zones of non-deformed quartz, around crystals of pyrite the inclusions does not show evidences of necking-down or leakage and huge variations on CO_2-H_2O ratio are observed.

Based on considerations of Phillip and Evans(2004) exposed above and considering that variations gas/liquid ratio found in inclusions in the Ernesto deposit are resulted from heterogeneous entrapment, the family Type1 was the responsible for gold mineralization of the Ernesto. As observed by Laser Raman spectroscopy the volatile phase is mainly composed by

CO_2 with minor amount of N_2 (up to 8% of the total of volatiles) and may be responsible for the variations found on CO_2 melting temperature.

Considering that these inclusions were formed by heterogeneous entrapment, the lowest homogenization temperature is approximately the trapping temperature for fluid at these conditions. The measurements of total homogenization temperature are between 180º and 280ºC with most of values 245ºC thus it is possible to propose that sulfidation and gold mineralization of intermediate level of Ernesto was formed at temperatures around 180 and 200ºC.

The aqueous fluid family (Type2) is similar to Type3 fluid inclusions of the Pau-a-Pique and similarly it seems to be later to the mineralizing fluid phase and may represent later infiltrations of lower temperature aqueous fluid.

Form the exposed above it is possible to conclude that the hydrothermal event responsible for mineralization is later in relation to most gangue minerals associated with pyrite in both deposits, specifically quartz in veins and micas in the wall-rock. Additionally the temperature in which gold precipitated in Ernesto is lower than those found in Pau-a-Pique using chlorite thermometer.

Stable isotopes as evidence of fluid source

The $\delta^{34}S_{pyrite}$ values obtained for Pau-a-Pique (0.7 to 5.3‰) are slightly higher than those found in Ernesto (-1.2 to 2.6‰). Despite the differences between the two deposits the range of values is coherent to many orogenic lode gold deposits in which $\delta^{34}S$ vary in a restricted range of -3 to +9 per mil (Ridley and Diamond, 2000 and the references therein).The more depleted values found in Ernesto can be related to some degree of oxidation by the interaction between the fluid and the sedimentary rocks fluid circulation.

From the $\delta D_{Chlorite}$ values obtained in this study, the hydrogen isotope composition of the fluid in equilibrium with the precipitating chlorite has been calculated by applying the quartz-water fractionation factors of Graham et al., (1984), extrapolated to lower temperatures. These calculations were performed at 325ºC (mean temperature obtained in chlorite thermometry). The Calculated δD values ranges from -15 to -60‰ and are more or less the expected for orogenic system in metamorphic belts.

The δD values for bulk analysis of fluid inclusions vary from -36 to -64‰ in the deposits of the central portion of AGGP (Table 5.4-5). The values indicates that these fluids has signature consistent with those found in orogenic systems as pointed out by Goldfarb et al. (2005).

The δD values obtained from muscovite vary from -39 to -124 per mil with most values between -70 and -110 per mil. Many of these values are out of the expected range of $\delta D_{muscovite}$ and such wide range of values seems to indicate some issue with fractionation equilibrium between the fluid and the mineral.

As exposed above the lighter of δD_{Fluid} measured directly in fluid inclusions is -64‰ thus calculations based on isotopic equilibrium between water and muscovite would give values heavier than -65‰, if considering that muscovite were crystallized in equilibrium with the mineralizing fluid. Calculation of the fractionation between muscovite and water at 325ºC gives fractionation values of -42.7 ($\delta_{muscovite\ -water}$) using calibration of Suzuoki and Epstein (1976). Applying this factor to all analyzed muscovite it will give calculated values of fluid between -82 and -6‰ with seven of the calculated values between the range of -35 and -65‰ (values found in the fluid inclusions). This correction factor works well for most of moderate $\delta D_{muscovite}$ but gives too heavy values for the fluid in some of calculated muscovite suggesting disequilibrium at 325ºC.

At the same time the petrographic aspects of muscovite suggest that it was formed earlier than the mineralizing event and as consequence it was not precipitated from fluids with temperatures of 325ºC, but probably at higher temperatures.

If considering that muscovite was in equilibrium with quartz and magnetite, the temperature in which magnetite has precipitated was about 490ºC as previously calculated using the fractionation temperature of quartz and magnetite. Using this temperature, and the same calibration for calculations of δD_{water} it will give a fractionation factor of -18.8 ($\delta_{muscovite\ -water}$) and the δD_{water} values obtained from these temperature are between -30.8 and -105.5 which satisfy the heavier values of muscovite.

The heavier value of muscovite from Pau-a-Pique deposit was obtained from the sample PQ31665-27. This sample comprises a non-mineralized sample of moderately deformed quartz vein with muscovite and magnetic magnetite in the walls of quartz. For having magnetic magnetite and for not being mineralized the sample does not show pyrite and thus it wasn't affected by mineralizing fluids and re-equilibration between muscovite (earlier formed) and the mineralizing fluid (CO2-rich, reducing fluids with temperature estimated around 325ºC) didn't happened.

The pair magnetite-quartz of this sample gave fractionation temperature of 508ºC. The δD_{water} of -52 is obtained applying this temperature to calculation of isotopic equilibrium between water and muscovite. The fractionation factor of oxygen between muscovite and water at 508ºC is 0, thus the $\delta^{18}O_{water}$ is ~12‰ (Table 5.4-4). This value fall almost in the central portions of the metamorphic field (Fig. 5.4-13) in the diagram of $\delta^{18}O_{H2O}$ versus δD_{H2O}.

For the lighter values (<-100‰) temperature lower than 325ºC would be necessary to give values coherent with those found in fluid inclusion, since lower values of temperature imply higher fractionation factor. Low values could represent later fluids passing through the most deformed zones of mineralization host rock.

Based on exposed above it is possible to suggest that the values of $\delta D_{muscovite}$ for the studied deposits may give values associated to multiple hydrothermal history which may complicate its interpretation if some is not considering the presence sulfide as later phase to muscovite.

A hypothesis for such wide range of values is that the heavier values may be recording equilibrium with fluids formed during fluid assisted shearing at peak conditions and the lighter values may be associated to fluid which passed through the rock in the later stages of hydrothermal evolution.

Other possibilities to such wide range of values would involve the infiltration of meteoric water. Very low δD values are found in meteoric waters in northern latitudes. The lowest values are found in Polar regions and suggest a geographic and climatic control on isotope fractionation of hydrogen during precipitation (Sheppard, 1986). Infiltration of meteoric waters has been used to explain low δD values in some of orogenic gold deposits.

This assumption presumes that the region where the deposit was located, was geographically positioned in extremely high altitudes if considering low latitudes, or in high latitudes if considering low altitudes. This assumption also presumes that the present day conditions of meteoric waters are applicable to the past.

In fact some paleogeographic reconstructions for the Amazon Craton suggest that its limiting contact with Laurentia was in latitude above 60ºS at about 1.0 Ga ago (Li et al., 2008). However the paleogeographic model for the Amazon Craton is not well constrained and the proposed model for its geographic position has low accuracy being constantly re-evaluated.

According to Goldfarb et al. (2005) rare outliners from -80 to -20‰ particularly from very low δD measurements are best interpreted as reflective of exchange effects of a very CH_4-rich reduced fluids. However in any of the studied inclusions was found trace of CH_4 and the lower values of Tm_{CO2} (~-58) are likely to be more related to the presence of N_2 rather than CH_4 as evidenced by Laser Raman analysis of some of Ernesto inclusions.

The $\delta^{18}O_{quartz}$ values for mineralized quartz veins of the central portions of AGGP vary from 8.4 and 15.3‰. The lowest values (8.4 to 10.5‰) were found in veins emplaced in igneous and metaigneous rocks of the basement (granite and volcanosedimentary sequences) meanwhile the highest values were found in veins emplaced in sedimentary rocks and are reflex of the interaction of the fluid with wall-rocks. Most values are between 11 and 12‰ and are observed in veins emplaced along shear zones formed in the contact between the sediments.

From the $\delta^{18}O$ values obtained from magnetite, quartz and albite, the oxygen isotope composition of the fluid in equilibrium with the precipitating quartz and albite has been calculated by applying the phase-water fractionation factors of Matsuhisa et al. (1979), yet the oxygen isotope composition of the fluid in equilibrium with magnetite was calculated by applying the magnetite-water fractionation factors of Cole et al. (2004). The runs were made at temperature of 490ºC, assuming that quartz, albite and magnetite are earlier to the mineralizing event and has suffered low effects of later fluid phases. The values obtained are between 6 and 12.9‰ at temperature of 490ºC and are coherent with metamorphic fluids.

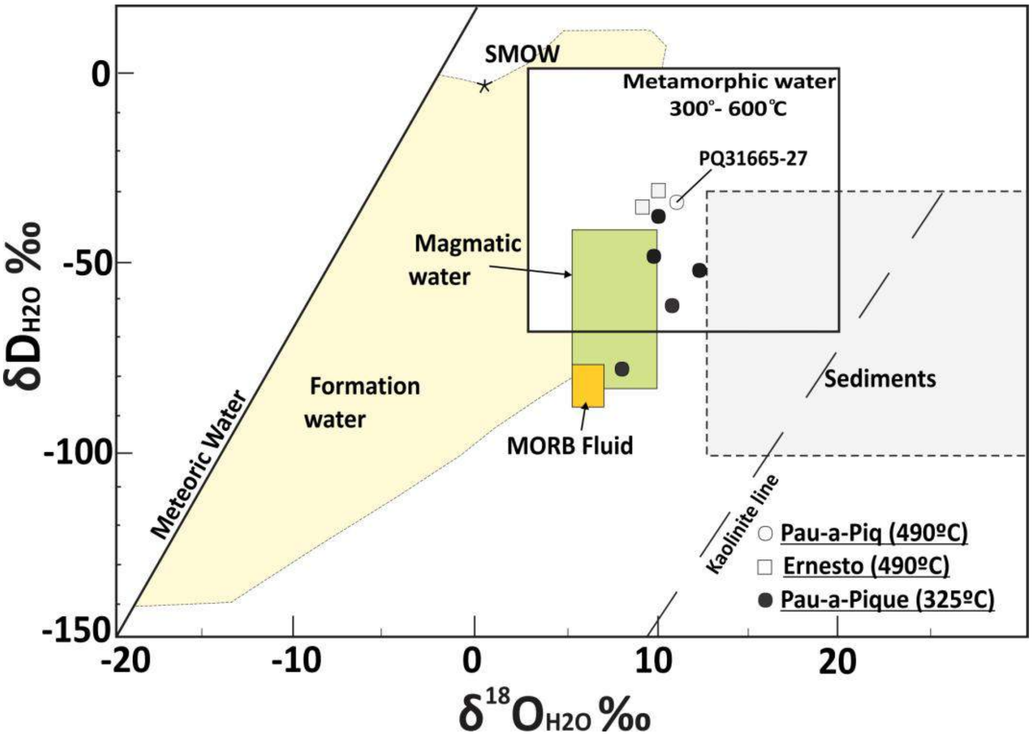

Figure 5.4-13: δ18OH2O versus δDH2O calculated from muscovite of Ernesto and Pau-a-Pique deposits. The metamorphic and sediments water field from Sheppard (1986); MORB and traditional magmatic water field from Taylor (1986).

At this temperature the $\delta^{18}O$ values of fluid obtained from, albite and magnetite are in the same range of values to those obtained from quartz. However when applying lower temperatures (325ºC) the calculated fluid does not meet the equilibrium between the precipitating quartz, magnetite and albite and are thus incoherent with the geologic observations.

It is possible to conclude that most of$\delta^{18}O$ and δD stable isotopes analysis failed on obtaining the source for fluid responsible for mineralization. Bulk analysis of fluid inclusions in this case gave the best indications for fluid signature and it is coherent with most of orogenic gold deposits hosted in metamorphic belt.

The better hypothesis for such failure is that some of the samples gangue mineral did not re-equilibrated completely preserving most of the original higher temperature.

6 Conclusions

The Aguapeí belt comprises a narrow thrust and folded belt formed in the latter stages of the collision between Amazonia and Laurentia during Rodínia Assembly.

In the most accepted model for the SW of Amazon Craton, the Paraguá Terrane comprises a separated cratonic block that assembled to Amazon between 1320 and 1340 Ma. The docking of Paraguá Craton formed a weakness zone along the contact with the Amazon Craton. The reactivation of this weakness zone as result of stress in the plate margin during the end of Mesoproterozoic has been argued by some author as the responsible for deformation and metamorphism of Aguapeí belt towards the end of Greenville interval.

From this point of view the Aguapeí belt may correspond to an intraplate strike-slip deformation belt in which deformation and metamorphism occurred as response to deformation occurring in the plate margins.

During the research, petrographic features consistent with greenschist metamorphism were observed in metasedimentary rocks of low deformed portions of the Aguapeí (mainly in domains where the deformation is characterized by folding). However along shear zones present in most of the contact between the metasedimentary rocks and the basement the conditions recorded are higher. Temperatures above 450ºC and pressures as higher as 3.2 kbar were obtained from some geothermobarometric calculations executed in samples from Corredor shear zone in Pau-a-Pique area.

Temperatures obtained using mineral phases formed along the shear zone are in agreement with the metamorphic features recorded in low-deformed mafic rocks proximal to these shear zones and suggest that peak conditions in the Corredor shear zones may have reached conditions coherent with greenschist-amphibolite facies transition.These conditions seem to be applicable to most of the exposed contact between the metasedimentary rocks and the basement in the central portion of AGGP.

At the same time the petrographic aspect and the chemical characteristics of the rocks occurring along the shear zones suggest that fluid were present during shearing and was responsible for most mineralogical transformations observed in these rocks. Extremely modified rocks were produced along the shear zones and chemical data showed that fluid percolation was responsible for such transformations. At the same time geothermometric studies based in trace elements in quartz from veins demonstrated that most of quartz veins precipitated from fluids of moderate temperature consistent with greenschist-amphibolite facies transition. The presence of abundant hydrous minerals and quartz veins indicates that huge amounts of fluid have circulated along the secondary porosity created by the shear zones.

The absence of syn-genetic magmatic intrusions nearby, and the fact that the quartz veins records temperature higher than those found in non-metassomatized metasedimentary rocks occurring around suggest that hot metamorphic fluids from deeper portions of the crust migrated along the contact and probably was responsible for the metassomatic transformations observed in the shear zones including quartz veining. Isotopic calculations of fluid in equilibrium with quartz, magnetite and albite give values of $\delta^{18}O$ coherent with metamorphic source.

Metalogenetic study of two gold deposits, one occurring along the shear zones of the contact, and one hosted by metasedimentary rocks, and located in different tectonic settings revealed that they show similar characteristics in terms of mineralizing timing and fluids. The study of fluid inclusions suggest that the mineralizing fluids in both cases comprises reduced, low salinity, CO_2-rich fluids and diverge from previous interpretation that proposed aqueous low salinity fluids as the gold carrier.

The petrographic aspects of the studied deposits suggest that the mineralizing fluids has precipitated pyrite and gold by destabilization of gold hydrosulfide complex due to interaction with the wall rock with high Fe/Fe+Mg rations. Thus the early formed Fe-Ti oxides played an important hole on mineralization since the higher gold grades tend to be associated with zones characterized by sulfidation of Fe-Ti oxides. At the same time the isotopic equilibrium between non-martitized magnetite and quartz (in quartz veins) and the textural aspect of the Fe-Ti oxides suggest that they are syn-genetic to quartz and thus are of metassomatic origin.

Considering the above, two contrasting hydrothermal events are recorded in the studied deposits, the first comprises most of veining observed in the area and is characterized by crystallization of muscovite and the formation of most of quartz veins and oxides present mainly along shear zones.The hydrothermal event responsible for the mineralization seems less expressive in terms amount of fluid. The characteristics of mineralization suggest that these fluids circulated preferentially through the evolving shearzoned during the later stages of deformation and most of fluid inclusions related to the mineralization event veins was trapped in deforming quartz veins which would justify their secondary aspect occurring along trails in early formed quartz.

The isotopic compositions of fluid inclusions as well as the composition of mineralizing fluid inclusions indicates that these deposits are similar to most of orogenic gold deposits occurring in metamorphic belt in which the origin of fluid has been attributed to metamorphic devolatilization.

The difference between the temperature obtained in mineralizing fluids (250º$_{\mathrm{Flinc}}$ 325ºC $_{\mathrm{chl}}$) and the temperature obtained from quartz using TitaniQ (~490º) indicates that the mineralization occurred during the retrograde path.

Explanation for the preservation of these deposits follow the line of thought proposed by Groves et al. (2005) in which most of deposits from this age were eroded during uplift caused by exhumation. Despite the lack of a well characterized tectonic architecture for the Aguapeí belt, in the studied area most of the structures suggest that the deformation evolved by predominant strike-slip movements due to reactivation of crustal scale structures. Considering that, it is expected low rate of exumation and for instance the preservation of the deposits hosted along shear zones occuring in greenschist facies terrane.

7 REFERENCES

ALM, E. et al. Fluid Characteristics and Genesis of Early Neoproterozoic Orogenic Gold-Quartz Veins in the Harnäs Area, Southwestern Sweden **Economic Geology,** v. 98, p. 1311-1328, 2003.

AMARAL, G. **Geologia Pré-Cambriana da Região Amazônica**. 1974. 212 (Livre Docência). Instituto de Geociências, Universidade de São Paulo, São Paulo.

ANDERSON, J. L. Status of Thermobarometry in granitic batholiths. **Transactions of the Royal Society of Edinburg: Earth Science,** v. 87, p. 14, 1996.

ARAUJO, L. M. B. **Evolução do Magmatismo Pós-Cinemático do Domínio Cachoeirinha: Suítes Intrusivas Rio Branco, Alvorada e Santa Cruz, SW do Cráton Amazônico, MT** 2008. (PhD). Univ. Estadual Paulista, Rio Claro. SP.

BAIA, F. H. **CARACTERIZAÇÃO LITOLÓGICA E ESTRUTURAL DA ÁREA "CAVA PRINCIPAL", ALVO AURÍFERO PAU-A-PIQUE, NA FAIXA AGUAPEÍ (PONTES E LACERDA, MT)** 2007. 62 (Bsc). Inst. de Geoc. e Ciencias Exatas, Univ. Estadual Paulista, Rio Claro - SP.

BAKKER, R. J.; DIAMOND, L. W. Determination of the composition and molar volume of H2O-CO2 fluid inclusions by microthermometry **Geochimica et Cosmochimica Acta,** v. 64, n. 10, p. 1753-1764, 2000.

BARTH, A. P. et al. **Magmatism and tectonics in a tilted crustal section through a continental arc, eastern Transverse Ranges and southern Mojave Desert**: The Geological Society of America. 11**:** 101-117 p. 2011.

BENNING, L. G.; SEWARD, T. M. Hydrosulfide complexing of Au(I) in hydrothermal solutions from 150-400 degrees C and 500-1500 bars. **Geochimica et Cosmochimica Acta,** v. 60, p. 1849-1871, 1996.

BETTENCOURT, J. et al. The Rondonian-San Ignacio Province in the SW Amazonian Craton: An overview. **Journal of South American Earth Sciences,** v. 29, n. 1, p. 28-46, FEB 2010 2010. ISSN 0895-9811.

BETTENCOURT, J. S. et al. Tectonic interpretation of ^{40}Ar/^{39}Ar ages on country rocks from the central sector of the Rio Negro-Juruena Province, southwest Amazonian Craton. **International Geology Reviews,** v. 38, p. 42-56, 1996.

BODNAR, R. J.; BINNS, P. R.; HALL, D. L. Quantitative evaluation of the decrepitation behaviour of fluid inclusions in quartz at one atmosphere confining pressure. **Journal of Metamorphic Geology,** v. 7, p. 229-242, 1989.

BOGER, S. et al. U-Pb age data from the Sunsas region of Eastern Bolivia, evidence for the allochthonous origin of the Paragua Block. **Precambrian Research,** v. 139, n. 3-4, p. 121-146, SEP 9 2005 2005. ISSN 0301-9268.

BOURDELLE, F. et al. A new chlorite geothermometer for diagenetic to low-grade metamorphic conditions. **Contrib Mineral Petrol,** v. 165, p. 723–735, 2013.

BUCHER, K.; GRAPES, R. **Petrogenesis of Metamorphic Rocks**. 8th. Springer, 2011. 428 ISBN 978-3-540-74168-8.

BUIK, I. S.; STORKEY, A. S.; WILLIAMS, I. S. Timing relationships between pegmatite emplacement, metamorphism and deformation during the intra-plate Alice Springs Orogeny, central Australia **J. metamorphic Geol.,** v. 26, p. 915-936, 2008.

BURKE. Raman microspectrometry of fluid inclusions. **Lithos,** v. 55 p. 139-158, 2001.

CATHELINEAU, M. Cation site occupancy in chlorites and illites as function of temperature **Clay Miner,** v. 23, p. 471-485, 1988.

CATHELINEAU, M.; NIEVA, D. A chlorite solid solution geothermometer The Los Azufres (Mexico) geothermal system **Contrib Mineral Petrol,** v. 91, p. 235-244, 1985.

CLAYTON, R. N.; KEIFFER, S. W. **Oxygen isotopic thermometer calibrations**. The Geochemical Society, 1991.

COLE, D. R. et al. An experimental and theoretical determination of oxygen isotope fractionation in the system magnetite-H2O from 300 to 800C. **Geochimica et Cosmochimica Acta,** v. 68, p. 3569-3585, 2004a.

______. An experimental and theoretical determination of oxygen isotope fractionation in the system magnetite-H2O from 300 to 800C. **Geochimica et Cosmochimica Acta,** v. 68, p. 3569-3585, 2004b.

CORDANI, U. G. et al. **Evolução Tectônica da Amazônia com base nos dados geocronológicos** II Congresso Geológico Chileno. Arica. Chile. Actas**:** 137-148 p. 1979.

______. The position of Amazonian Craton in supercontinents. **Gondwana Research,** v. 15, p. 396-407, 2009.

D'AGRELLA-FILHO, M. et al. Direct dating of paleomagnetic results from Precambrian sediments in the Amazon craton: Evidence for Grenvillian emplacement of exotic crust in SE Appalachians of North America. **Earth and Planetary Science Letters,** v. 267, n. 1-2, p. 188-199, MAR 1 2008 2008. ISSN 0012-821X.

DALZIEL, I. W. D. Pacific margins of Laurentia and East Antarctica-Australia as a conjugate rift pair: Evidence and implications for an Eocambrian supercontinent **Geology,** v. 19, p. 598-601, 1991.

DE CARITAT, P.; HUTCHEON, I.; WALSHE, J. L. CHLORITE GEOTHERMOMETRY: A REVIEW. **Clays and Clay Minerals,** v. 41, n. 2, p. 219-239, 1993.

DEER, W. A.; HOWIE, R. A.; ZUSSMAN, J. **Rock-Forming Minerals: Double-Chain Silicates**. Second. London: Geological Society, 1997. 747.

DUNLAP, W. J.; HIRTH, G.; TEYSSIER, C. Thermomechanical evolution of a ductile duplex. **Tectonics,** v. 16, n. 6, p. 983-1000, 1997.

ELMING, S. et al. A palaeomagnetic and Ar-40/Ar-39 study of late precambrian sills in the SW part of the Amazonian craton: Amazonia in the Rodinia reconstruction. **Geophysical Journal International,** v. 178, n. 1, p. 106-122, JUL 2009 2009. ISSN 0956-540X.

ESSENE, E. J. The current status of thermobarometry in metamorphic rocks. In: DALY, J. S.;CLIFF, R. A., *et al* (Ed.). **Evolution of Metamorphic belt**: Geological Society, v.PSpecial publication, 1989. p.45.

FALEIROS, F. M. et al. Quartz recrystallization regimes, c-axis texture transitions and fluid inclusion reequilibration in a prograde greenschist to amphibolite facies mylonite zone (Ribeira Shear Zone, SE Brazil) **Tectonophysics,** v. 485, p. 193-214, 2010.

FERNADES, C. J. et al. Geologia e Contrle Estrutural dos Depósitos de Ouro do Grupo Aguapeí - Região da Lavrinha, Sudoeste do Craton Amazônico. **Revista Brasileira de Geociências,** v. 35, n. 1, p. 10, 2005.

FERNANDES, C. J. et al. Geologia Estrutural e Idade ^{40}Ar/^{39}Ar do depósito Pau a Pique, Faixa Móvel Aguapeí, Sudoeste do estado de Mato Grosso. **Revista Brasileira de Geociências,** v. 36, n. 1, p. 13, 2006.

______. Compartimentação Tectônica da deformação na Faixa Móvel Aguapeí, Sudoeste do Cráton Amazônico, e as Mineralizações Auríferas Associadas. **Revista Brasileira de Geociências,** v. 35, n. 1, p. 12, 2005a.

FREY, M.; ROBINSON, D. **Low-grade metamorphism**. Oxford, England ; Malden, Mass.: Blackwell Science, 1998. x, 313 p. ISBN 0632047569.

GERALDES, M. C. **Geoquímica e Geocronologia do Plutonismo Granítico Mesoproterozóico do SW do Estado de Mato Grosso (SW do Cráton Amazônico)**. 2000. 193 (Doctorade). Inst. Geociencias, Univ. de São Paulo, São Paulo.

GERALDES, M. C. et al. Geochemistry and isotopic constraints on the origin of the Mesoproterozoic Rio Branco anorogenic" plutonic suite, SW of Amazonian Craton, Brazil: high heat flow and crustal extension behind the Santa Helena arc? **Journal of South American Earth Science,** v. 16, p. 1-14, 2004.

______. Middle Proterozoic Vein-Hosted Gold Deposits in the Pontes e Lacerda Region, Southwestern Amazonian Craton, Brazil **International Geology Review,** v. 39, p. 438-448, 1997.

______. **U/Pb constraints on Proterozoic magmatic arcs in SW Amazônia Cráton, Brazil.** . 2nd South American Symposium on Isotope Geology Córdoba, Argentina. Actas**:** 143 p. 1999.

______. U–Pb detrital zircon ages from the Aguapeí Group (Brazil):Implications for the geological evolution of the SW border of theAmazonian Craton. **Precambrian Research,** v. 244, p. 306-316, 2014.

______. Proterozoic geologic evolution of the SW part of the Amazonian Craton in Mato Grosso state, Brazil. **Precambrian Research,** v. 111, n. 1-4, p. 91-128, OCT 1 2001 2001. ISSN 0301-9268.

GOLDFARB, R. J. et al. Distribution, Character, and Genesis of Gold Deposits in Metamorphic Terranes. **Economic Geology,** v. 100th Anniversary volume, p. 407-450, 2005.

GOLDFARB, R. J.; GROVES, D. I.; GARDOLL, S. Orogenic gold and geologic time: a global synthesis. **Ore Geology Reviwes,** v. 18, p. 1-75, 2001.

GOLDSTEIN, R. H. Petrographic Analysis of Fluid Inclusions. In: SAMSON, I.;ANDERSON, A., *et al* (Ed.). **Fluid Inclusions Analysis and Intepretations**. Vancouver, British Columbia: Mineralogical Association of Canada, 2003. cap. 2, p.374. (Short Course).

GRAHAM, C. M.; ATKINSON, J.; HARMON, R. S. **Hydrogen isotope fractionation in the system chlorite-water**. p.139. 1984

GROVES, D. I. et al. Secular Changes in Global Tectonic Processes and Their Influence on the Temporal Distribution of Gold-Bearing Mineral Deposits **Economic geology,** v. 100th Anniversary Volume, p. 203-224, 2005.

______. Orogenic gold deposits: A proposed classification in the context of their crustal distribution and relationship to other gold deposit types **Ore Geology Reviews,** v. 13, p. 7-27, 1998.

______. Gold Deposits in Metamorphic Belts: Overview of Current Understanding, Outstanding Problems, Future Research, and Exploration Significance **Economic Geology,** v. 98, p. 1-29, 2003.

GUIDOTTI, C.; SASSI, F. Classification and correlation of metamorphic facies series by means of muscovite b0 data from Low-grademetapelites. **Neus Jahrbuch fur Mineralogie Abhandlungen,** v. 157, p. 363-380, 1986.

GUIDOTTI, C.; SASSI, F.; BLENCOE, J. Compositional controls on the a and b cell dimensions of 2M1 muscovite. **European Journal of Mineralogy,** v. 1, p. 71-84, 1989.

HAWTHORNE, F. C. et al. Nomenclature of the amphibole supergroup. **American Mineralogist,** v. 97, p. 2031-2048, 2012.

HENRY, D. J.; GUIDOTTI, C. V.; THOMSON, J. A. The Ti-saturation surface for low-to-medium pressure metapelitic biotites: Implications for geothermometry and Ti-substitution mechanisms **American Mineralogist,** v. 90, p. 316-328, 2005.

HILLIER, S.; VELDE, B. Octahedral occupancy and chemical composition of diagenetic (low-temperature) chlorites. . **Clay Miner** v. 26, p. 149-168, 1991.

HOFFMAN, P. E. Did the breakout of Laurentia turn Gondwanaland inside-out? **Science,** v. 252, p. 1409-1412, 1991.

HOLANDA, S. B. **História Geral da Civilização Brasileira:**. Brazil: Bertrand, 2003. 412.

HUANG, R.; AUDÉTAT, A. The titanium-in-quartz (TitaniQ) thermobarometer: A critical examination and re-calibration **Geochimica et Cosmochimica Acta,** v. 84, p. 75-89, 2012.

IANNO, A. J.; PATERSON, S. R. **Hornblende gabbros formed by crustal melting at Joshua Tree National Park, California** Goldschimidt. Sacramento-CA**:** 1 p. 2014

INOUE, A. et al. Application of chemical geothermometry to lowtemperature trioctahedral chlorites. **Clays Clay Miner,** v. 57, p. 371–382, 2009.

J, H. C. Spilites, keratophyres, and the igneous spectrum. **Geol Mag,** v. 109, n. 5, p. 513-527, 1973.

JOWETT, E. **Fitting iron and magnesium into the hydrothermal chlorite geothermometer** 1991.

KRANIDIOTIS, P.; MACLEAN, W. Systematics of chlorite alteration at the Phelps Dodge massive sulfide deposit, Matagami, Quebec. . **Economic Geology,** v. 82, p. 1898-1911, 1987.

LAMBRECHT, G.; DIAMOND, L. W. Morphological ripening of fluid inclusions and coupled zone-refining in quartz crystals revealed bt cthodoluminescence imaging: Implications for CL-petrography, fluid inclusion analysis and trace-lement geothermometry. **Geochimica et Comochimica Acta,** v. 141, p. 381-406, 2014.

LANARI, P.; WAGNER, T.; VIDAL, O. A thermodynamic model for di-trioctahedral chlorite from experimental and natural data in the system MgO–FeO–Al2O3–SiO2–H2O: applications to P–T sections and geothermometry **Contrib Mineral Petrol,** v. 167, n. 968, p. 2-19, 2014.

LEITE, J. A. D.; SAES, G. S. GEOLOGY OF THE SOUTHERN AMAZON CRATON IN SOUTHWESTERN MATO GROSSO, BRAZIL: A REVIEW **Revista Brasileira de Geociências,** v. 30, n. 1, p. 91-94, 2000.

LI, Z. X. et al. Assembly, configuration, and break-up history of Rodinia: A synthesis. **Precambrian Research,** v. 160, p. 179-210, 2008.

LITHERLAND, M. et al. THE PROTEROZOIC OF EASTERN BOLIVIA AND ITS RELATIONSHIP TO THE ANDEAN MOBILE BELT. **Precambrian Research,** v. 43, n. 3, p. 157-174, MAY 1989 1989. ISSN 0301-9268.

LITHERLAND, M.; BLOOMFIELD, K. THE PROTEROZOIC HISTORY OF EASTERN BOLIVIA. **Precambrian Research,** v. 15, n. 2, p. 157-&, 1981 1981. ISSN 0301-9268.

LITHERLAND, M. E. A. **The geology and mineral resources of the Bolivian Precambrian shield** Brit. Geological Survey, 1986.

LOCOCK, A. J. An Excel spreadsheet to classify chemical analyses of amphiboles following the IMA 2012 recommendations. **Computers & Geosciences,** v. 62, p. 11, 2014.

MASSOME, H.-J.; SCHREYER, W. Phengite geobarometry based on the limiting assemblage with K-feldspar, phlogopite, and quartz. **Contributions to Mineralogy and Petrology,** v. 96, p. 13, 1987.

MATOS, J. B. et al. Petrografia, Geoquímica e Geocronologia das Rochas do Orógeno Rio Alegre, Mato Grosso: Um Registro de Crosta Oceânica Mesoproterozóica no SW do Cráton Amazônico **Revista do Instituto de Geociências - USP,** v. 4, n. 1, p. 75-90, 2004.

MATSUHISA, Y.; GOLDSMITH, J. R.; CLAYTON, R. N. Oxygen isotopic fractionation in the system quartz-albite-anothite-water. **Geoch. Cosmochim. Acta** v. 43 p. 1131-1140, 1979.

MEIRELES, D. M. **Guardiões da Fronteira. Rio Guaporé, Século XVIII**. Petropoles-RJ: 1989.

MENEZES, R. G. et al. **Folha Pontes e Lacerda, SD.21-Y-C-II**. Brasilia: CPRM, 1993.

MONTEIRO, H. et al. **O 'Greenstone Belt' do Alto Jauru.** 34th Congresso Brasileiro de Geologia. Goiania - GO: Sociedade Brasileira de Geologia. Anais do 34th Congress. Bras. de Geologia**:** 630-647 p. 1986.

MORALES, N. **Modelo Estrutural da Mina São Francisco**. Pontes e Lacerda. 2007

PASCHIER, C. W.; TROW, A. J. **Microtectonics**. 2th. Springer, 2005.

PAULO, V. G. **Identificação dos eventos termotectônicos através do método 40Ar/39Ar nos terrenos Jauru, Pontes e Lacerda e Rio Alegre, SW do Cráton Amazônico**. 2005. 120 State University, Rio de Janeiro, Rio de Janeiro.

PHILLIPS, G. N.; EVANS, K. A. Role of CO_2 in the formation of gold deposits. **Nature,** v. 429, p. 860-863, 2004.

PHILLIPS, G. N.; POWELL, R. Link between gold provinces. **Economic Geology,** v. 88, p. 1084-1098, 1993.

PINHO, F. E. C.; FYFE, W. S.; PINHO, M. A. S. B. Early Proterozoic evolution of the Alto Jauru greenstone belt, southern Amazonian Craton, Brazil **International Geology Reviews,** v. 39, p. 220-229, 1997.

QIAN, G. et al. **Geochimica et Cosmochimica Acta,** v. 74, p. 5610-5630, 2010.

RIDLEY, J. R.; DIAMOND, L. W. **Fluid Chemistry of Orogenic Lode Gold Deposits and implications for Genetic Models**. Society of Economic Geologists, 2000.

RIZZOTTO, G. J. **Petrologia e Geotectônica do Grupo Nova Brasilândia, Rondônia** 1999. (Master). Federal University of Rio Grande do Sul Porto Alegre.

RIZZOTTO, G. J. et al. Tectonic evolution of the southern margin of the Amazonian craton in the late Mesoproterozoic based on field relationships and zircon U-Pb geochronology **Annals of the Brazilian Academy of Sciences,** v. 86, n. 1, p. 57-84, 2014.

RIZZOTTO, G. J.; LIMA, E. F.; CHEMALE JR, F. **Geologia do Grupo Nova Brasilândia, sudeste de Rondônia, acresção continental e implicações geotectônicas** Sociedade Brasileira de Geologia, 2001.

RIZZOTTO, G. J. et al. The Mesoproterozoic Guaporé suture in the SW Amazonian Craton: Geotectonic implications based on field geology, zircon geochronology and NdeSr isotope geochemistry **Journal of South American Earth Sciences,** v. 48, p. 271-295, 2013.

RUIZ, A. S. **EVOLUÇÃO GEOLÓGICA DO SUDOESTE DO CRÁTON AMAZÔNICO REGIÃO LIMÍTROFE BRASIL-BOLÍVIA – MATO GROSSO** 2005. 289 (Doctorade). Instituto de Geociências e Ciências Exatas, Universidade Estadual Paulista, Rio Claro - SP.

RUIZ, A. S. et al. **Cinturão Orogênico Aguapeí (1025 - 900): Um exemplo de Faixa Móvel Intracontinental no SW do Craton Amazônico**. Simpósio Nacional de Estudos Tectônico (SNET). Natal**:** 116-118 p. 2007.

RUSK, B. G.; LOWERS, H. A.; REED, M. H. Trace elements in hydrothermal quartz: Relationships to cathodoluminescent textures and insights into vein formation **Geology,** v. 36, n. 7, p. 547-550, 2008.

SADOWSKI, G.; BETTENCOURT, J. Mesoproterozoic tectonic correlations between eastern Laurentia and the western border of the Amazon Craton. **Precambrian Research,** v. 76, n. 3-4, p. 213-227, FEB 1996 1996. ISSN 0301-9268.

SAES, G. S. **Evolução tectônica e paleogeográfica do Aulacógeno Aguapeí (1.2–1.0 Ga) e dos terrenos do seu embasamento na porção sul do Craton Amazônico.** . 1999. 135 (Doctorade). Institute of Geociences, University of São Paulo, São Paulo.

SAES, G. S.; FRAGOSO CESAR, A. R. S. **Acresção de terrenos mesoproterozóicos no SW da Amazônia** 39º Congresso Brasileiro de Geologia. Salvador - BA: Sociedade Brasileira de Geologia (SBG). Boletim de Resumos Expandidos 1996.

SAES, G. S.; LEITE, J. A. D. EVOLUÇÃO TECTONO-SEDIMENTAR DO GRUPO AGUAPEÍ, PROTEROZÓICO MÉDIO NA PORÇÃO MERIDIONAL DO CRÁTON AMAZÔNICO: MATO GROSSO E ORIENTE BOLIVIANO **Revista Brasileira de Geociências,** v. 23, n. 1, p. 31-37, 1993.

SAES, G. S.; LEITE, J. A. D.; WESKA, R. K. **Geologia da Folha Jauru (SD.21.Y.C.III): uma síntese dos conhecimentos** 33rd Congresso Brasileiro de Geologia. Rio de Janeiro: Sociedade Brasileira de Geologia. Anais, vol. 5**:** 2193-2204 p. 1984.

SANTOS, J. et al. A new understanding of the provinces of the Amazon craton based on integration of field mapping and U-Pb and Sm-Nd geochronology. **Gondwana Research,** v. 3, n. 4, p. 453-488, OCT 2000 2000. ISSN 1342-937X.

______. Age and autochthonous evolution of the Sunsas Orogen in West Amazon Craton based on mapping and U-Pb geochronology. **Precambrian Research,** v. 165, n. 3-4, p. 120-152, SEP 20 2008 2008. ISSN 0301-9268.

SASSI, P. F.; SCOLARI, A. The bo Value of the Potassic White Micas as a Barometric Indicator in Low-Grade Metamorphism of Pelitic Schists **Contribution to Mineralogy and Petrology,** v. 45, p. 143-152, 1974.

SASSIER, C. et al. From granitoid to kyanite-bearing micaschist during fluid-assisted shearing (Ile d'Yeu, France) **Int J Earth Sci (Geol Rundsch),** v. 95, p. 2-18, 2006.

SCABORA, J. A.; DUARTE, C. L. A Jazida de Ouro de São Vicente - Município de Nova Lacerda - MT. **A Terra em Revista (CPRM),** v. 4, p. 11, 1998.

SHEPHERD, T. J.; RANKIN, A. H.; ALDERTON, D. H. M. **A Practical Guide to Fluid Inclusions Studies**. London UK: Blackie, 1985. 239.

SHEPPARD, S. M. F. **Characterization and Isotopic variations in Natural Waters**. Mineralogical Society of America, 1986. 570.

SOUZA, E. P.; HILDRED, P. R. **Contribuição ao estudo da geologia do Grupo Aguapeí, oeste de Mato Grosso** Congresso Brasileiro de Geologia. Camboriú: Sociedade Brasileira de Geologia. 2**:** 813-825 p. 1980.

SPEAR, F. S. **Metamorphic Phase Equilibria and Pressure-Temperature-Time Paths**. Washington, D.C.: Mineralogical Society of America, 1993. 799 ISBN 0-939950-34-0.

STIPP, M. et al. The eastern Tonale fault zone: a 'natural laboratory' for crystal plastic deformation of quartz over a temperature range from 250 to 700 ºC. **Journal of Structural Geology,** v. 24, p. 1861-1884, 2002.

SUZUOKI, T.; EPSTEIN, S. Hydrogen isotope fractionation between OH-bearing minerals and water. **Geochimica Cosmochimica Acta,** v. 40, p. 1229-1240, 1976.

TASSINARI, C.; MACAMBIRA, M. Geochronological provinces of the Amazonian Craton. **Episodes,** v. 22, n. 3, p. 174-182, SEP 1999 1999. ISSN 0705-3797.

TASSINARI, C. C. G. **O Mapa Geocronológico do Cráton Amazonico no Brasil: Revisão dos Dados Isotópicos**. 1996. (Doctorade). Instituto de Geociências, Universidade de São Paulo, São Paulo.

TEIXEIRA, W. et al. A review of the tectonic evolution of the Sunsas belt, SW Amazonian Craton. **Journal of South American Earth Sciences,** v. 29, n. 1, p. 47-60, FEB 2010 2010. ISSN 0895-9811.

______. Precise ID-TIMS U–Pb baddeleyite ages (1110–1112 Ma) for the Rincón del Tigre–Huanchaca large igneous province (LIP) of the Amazonian Craton: Implications for the Rodinia supercontinent **Precambrian Research,** v. In press, 2014.

______. A REVIEW OF THE GEOCHRONOLOGY OF THE AMAZONIAN CRATON - TECTONIC IMPLICATIONS. **Precambrian Research,** v. 42, n. 3-4, p. 213-227, MAR 1989 1989. ISSN 0301-9268.

THOMAS, J. B. et al. TitaniQ under pressure: the effect of pressure and temperature on the solubility of Ti in quartz **Contrib Mineral Petrol**, 2010.

THOMPSON, T.; GARRISON, J. **Petrology and Geochemistry of Hornblende Cumulates in Joshua tree National Park, California**. GSA Annual Meeting. Vancouver: GSA**:** 1 p. 2014.

THOVER, E. et al. Terrane transfer during the Grenville orogeny: tracing the Amazonian ancestry of southern Appalachian basement through Pb and Nd isotopes **Earth and Planetary Science Letters,** v. 228, p. 161-176, 2004.

TOHVER, E. et al. Restored transect across the exhumed Grenville orogen of Laurentia and Amazonia, with implications for crustal architecture. **Geology,** v. 34, n. 8, p. 669-672, AUG 2006 2006. ISSN 0091-7613.

______. Significance of the Nova Brasilandia metasedimentary belt in western Brazil: Redefining the Mesoproterozoic boundary of the Amazon craton. **Tectonics,** v. 23, n. 6, DEC 7 2004 2004a. ISSN 0278-7407.

______. Paleogeography of the Amazon craton at 1.2 Ga: early Grenvillian collision with the Llano segment of Laurentia. **Earth and Planetary Science Letters,** v. 199, n. 1-2, p. 185-200, MAY 30 2002 2002. ISSN 0012-821X.

TRINCAL, V. et al. Temperature micro-mapping in oscillatory-zoned chlorite: Application to study of a green-schist facies fault zone in the Pyrenean Axial Zone (Spain) **American Mineralogist,** v. 100, p. 2468-2483, 2015.

VALLEY, J. W. **Oxygen isotopes in zircon**. 2003.

VELDE, B. Phengite micas: Syntesis, stability, and natural occurrence. **American Journal of Science,** v. 263, p. 886-913, 1965.

WALSHE, J. L. A six-component chlorite solid solution model and the conditions of chlorite formation in hydrothermal and geothermal systems. **Econ Geol,** v. 81, p. 681-703, 1986.

WARK, D. A.; WATSON, E. B. TitaniQ: a titanium-in-quartz geothermometer. **Contributions to Mineralogy and Petrology,** v. 2006, p. 12, 2006.

ZANETTINI, P. et al. **Arqueologia e História – Vila Bela da Santíssima Trindade / MT: Relatório Final**. 2004

ZANG, W.; FYFE, W. Chloritization of the hydrothermally alteredbedrock at the Igarape Bahia gold deposit, Carajas, Brazil. **Mineral Deposita,** v. 30, p. 30-38, 1995.

ZHENG, Y. F.; SIMON, K. Oxygen isotope fractionation in hematite and magnetite: A theoretical calculation and application to geothermometry of metamorphic iron-formation. **European Journal of Mineralogy,** v. 3 p. 877-886, 1991.

Appendix I

(Table with geological points)

Tabela com os Pontos Geológicos executados:

Ponto	Coord. X	Coord. Y	Litologia	Cota	Descrição
DOCRPM000001	257044	8293447	Solo argiloso Branco com manchas	293	Aflor de solo argiloso aparentemente trata se da zona maclada de um perfil lateritico As condicoes de alt não permitem afirmar com firmeza o protolito mas parcece se tratar de um granito
DOCRPM000002	256464	8293130	Laterita	311	Afloramento de crosta lateritica ferruginosa dificil reonhecimento da rocha que esta ocorrendo no local
DOCRPM000003	256037	8293351	Float de qtz (predominante)	298	Afloramento de float de quartzo no chao da estrada de acesso a serra Qtz Bco leito com oxido de fe nas fraturas
DOCRPM000004	255790	8293397	Metassedimento (blocos)	285	Afloramento de blocos de metarenito granulacao media a fina cor amarela
DOCRPM000005	255513	8293343	Metaconglomerado	275	Metacongl intercal c metarenito grosso a medio presenca de estratific cruzada preservada Seixos c cerca de 1 cm pobremente arredondados
DOCRPM000006	255487	8293315	Metarenito Grosso	287	Metarenito medio a grosso estratific cruzada preserv A lito muda de metacong para metarenito do ultimo ponto para esse
DOCRPM000007	255444	8293248	Metarenito Fino/Metapelito (intercalação)	289	Metarenito fino- quartzito intercal c finas camadas de metapelito Estratif cruz preserv metapelito cor cinza escuro sem alt hidrotermal
DOCRPM000008	255322	8292479	Metarenito	288	Aflor de corte de estrada Rocha fortemente alterada aparentemente metarenito grosso bco alterado com muito caolim talvez metaren feldspatico
DOCRPM000009	255276	8292883	Metarenito Fino	274	Aflor de metarenito fino dobrado aparentemente na zona de charneira Em algumas porcoes o metarenito parece estar silicifcado
DOCRPM000010	255340	8293008	Metarenito Grosso	280	Metarenito grosso aflorando na beia de uma drenagem
DOCRPM000011	255363	8293085	Metarenito Fino/Metapelito (intercalação)	285	Aflor de metarentio fino intercalado com metapelito Ocorre um mineral q a principio parece ser mica que apresenta cor roxa Afloramento no chao da estrada
DOCRPM000012	260438	8295311	Float de qtz (predominante)	307	Aflor de float de qtz encaixado em um material saprolitico totalmente desestruturado mas que aparentemente parece alt de granito
DOCRPM000013	260459	8295365	Granito	306	Afloramento de granito leucocratico branco de granulacao fina equigranular com FK biotita epidoto plag e qutz
DOCRPM000014	262533	8295785	Solo avermelhado argiloso	289	Solo vermelho argiloso aparentemente trata-se da alteração d uma rocha granitica Ainda embasamento
DOCRPM000015	262933	8295968	Coluvio (solo com blocos de rochas)	367	Material de coluvio Blocos de quartzo associado a solo organico cinza Local de mudanca na vegetacao
DOCRPM000016	262972	8296000	Metarenito Médio	395	Afloramento de Blocos de metarenito cor amarelo claro aparentemente não estão in situ. Metarenito fino a Medio
DOCRPM000017	263020	8296007	Metarenito Médio	416	Afloramento de metarenito fino a medio foliado Em alguns Locais chega a ser microconglomeratico Rocha bco amarelada presenca de oxido de Fe
DOCRPM000018	263070	8296019	Metaconglomerado	436	Aflor de microconglomerado metarenito grosso no topo da serra Seixo com até 0,7 de compr rocha fortemente fol c qtz e sericita verde Pacere ocorrem uma sericitizacao no topo da serra
DOCRPM000019	263099	8296031	Metarenito Grosso	417	Aflor de metarenito grosso microconglomerado cor branco amarelado Presenca de ser verde em algumas porcoes q parece indicar q o topo da serra é marcada por um silicificao sericitizacao
DOCRPM000020	263141	8296032	Metaconglomerado	399	Afloramento de metaconglomerado na forma de gde blocos seixos com ate 3 cm de comprimento pouco arredondados
DOCRPM000021	263175	8296023	Metaconglomerado	381	Aflor de blocos de metacong apesar de não estar in situ parece ser a lito aflor no local
DOCRPM000022	263600	8296112	xisto avermelhado (saprolitizado)	345	Blocos de xisto fortemente intemp cor vermelha Aparentemente trata se do xisto pontes e lacerda
DOCRPM000023	262660	8295294	xisto avermelhado (saprolitizado)	325	Aflor de corte de estrada rocha totalmente saprolitizada no entantanto pelas feições é possivel reconhecer a estrutura e que se trata de algo semelhante a um xisto
DOCRPM000024	264726	8296838	Sericita qtz xisto	356	Ocorrencia de blocos na beira da estrada não há certeza se são blocos do local Trata se de blocos de um ser qtz xisto cor verde granulacao fina
DOCRPM000025	265692	8296677	granito grosso avermelhado	368	Aflor de granito no chao da estrada Granito foliado fortemente intemp equigranular granulacao grossa levemente avermelhado
DOCRPM000026	265839	8296919	Float de qtz (predominante)	380	Afloramento de float de quartzo associado a biotita xisto
DOCRPM000027	265963	8297126	xisto avermelhado (saprolitizado)	390	Aflor de xisto no chao da estrada rocha xistosa fortemente intemp aparentemente trata se de um biotita muscovita xisto Presenca de blocos de qtz associado
DOCRPM000028	266015	8297209	Biotita xisto	390	Continua ocorr de xistos. Intercal de biotita xisto cor prta com com outro tipo mais intemperizado de dificil reconhecimento Bandamento composicional Gde qte de float de qtz assoc
DOCRPM000029	266241	8297570	Saprolito	373	rocha semelhante a um granito cor branca equigranular fino fortemente epidotizado Rocha fortemente intemperizada. Pode ser tb uma porcao mais quartzosa dentro de uma sequ sed
DOCRPM000030	266386	8297800	xisto avermelhado (saprolitizado)	370	Aflor de xisto Bandamento comp Em algumas partes o mat e menos estrutrado com aspecto granitico no entanto e fortemente quartzoso c sericita assoc
DOCRPM000031	251191	8290156	Metassedimento (blocos)	268	Ocorrencia de blocos de metassedimento no sopé da encosta trata se de um metarenito silicificado Presenca de blocos de metapelito alguns metros acima Material de coluvio
DOCRPM000032	251353	8290239	Metarenito Fino	311	Afloramento de blocos de metarenito fino fortemente silicificado apesar de não estarem in situ q trata se da rocha que ocorre no local
DOCRPM000033	251448	8290301	Metarenito Médio	367	Afloramento de metarenito fino silicificado presenca de venulas brancas com qtz em varias direcoes

DOCRPM000034	251506	8290331	Metarenito Fino	407	Metarenito médio a grosso Há uma mudanca na granulometria do metarenito aparentemente mais no sope ocorre intercalacao de metarenito metapelito intercal passando p granul mais grossa no topo
DOCRPM000035	251527	8290365	Metarenito Fino	412	Continua ocorrendo blocos de metarenito fino no topo da serra
DOCRPM000036	251631	8290439	Metarenito Fino	380	Afloramento de metarenito medio a fino blocos aparentemente i situ na encosta da serra
DOCRPM000037	251913	8290396	Solo avermelhado argiloso	348	Solo marrom avermelhado argiloso semelhante a solo de alt de granito ou alguma rocha pelitica Não como reconhecer a rocha protolito
DOCRPM000038	251961	8290573	Metarenito Fino	345	Ocorrencia de blocos de metassedimento na encosta da serra Rocha silicificada Metarenito fino geralmente cor branca em alguns blocos observa se vestigios de silicificacao
DOCRPM000039	252013	8290622	Metarenito Fino	377	Afloramento de metarenito fino no topo da serra a rocha aflora na forma de blocos Observa se q existe uma silicificacao bem forte na rocha e em alguns blocos Silicific associada a stockwork
DOCRPM000040	251896	8290808	Metarenito Fino	360	Afloramento de metarenito fino silicificado Stockwork Brecha silicificada
DOCRPM000041	251915	8291146	Metarenito Médio	390	Afloramento proximo ao topo da serra blocos de metarenito medio
DOCRPM000042	252064	8291162	Metarenito Grosso	374	Afloramento de metarenito grosso na encosta da serra aparentemente material in situ
DOCRPM000043	252189	8291200	Metarenito Fino	335	Afloramento de metarenito proximo ao sope da encosta Metarenito fino a medio predominando graulacao fina
DOCRPM000044	266068	8290595	Solo Marrom avermelhado argilo arenoso	395	Solo avermelhado proximo ao contato mudanca na cor do solo não há como saber se esse solo é resultado de pura laterizacao ou se e decorrente de alt do embasamento 20 m E mundanca na cor
DOCRPM000045	265953	8290585	Metassedimento (blocos)	418	Metaconglomerado cor branca amarelada formada por seixos de mais de 1cm de comprimento presenca de laterita e qtz no chao
DOCRPM000046	265917	8290590	Metarenito Médio	420	Afloramento de metarenito medio a microconglomerado no chao da estrada Rocha fortemente foliada Granulometria muda do ultimo ponto para este
DOCRPM000047	265850	8290441	Laterita	402	Afloramento de laterita crosta ferruginsa no chao da estrada que vai para a sede da fazenda
DOCRPM000048	265806	8290416	Metarenito Grosso	400	Afloramento de metarenito grosso a microconglomerado semelhante ao ultimo ponto. Rocha apresenta estratificacao cruzada preservada Mudanca na direcao do mergulho
DOCRPM000049	265765	8290379	Metaconglomerado	390	Aflor de metaconglomerado grosso igual ao do ponto 0045 Seixos gdes com ate 3 cm de compr Trata se de clastos suportados pouca matrix
DOCRPM000050	265714	8290375	Metarenito Médio	380	Aflor de metarenito medio a fino aparentemente há novamente uma mudanca na foliacao que fica vertical Há poucas porcoes com microconglomerado
DOCRPM000051	265661	8290340	Metarenito Fino	382	Aflor de metarenito fino a medio aparentemente dobrado onde o eixo da dobra mergulha para SE No entanto há duvidas se não poderia ser uma feicao sedimentar
DOCRPM000052	265524	8290273	Metarenito	365	aflor de blocos de metarenito e metaconglomerado no sope da encosta Aparentemente trata se de material de coluvio mas em alguns locais observa se q o mat parece estar in situ
DOCRPM000053	265455	8290275	Solo lateritico	362	Mudanca na cor do solo vermelho com gde qte de laterita Material um pouco mais argiloso aparentemente zona de ocorr do embasamento
DOCRPM000054	265455	8290236	Saprolito	360	Aflor de material saprolitico vermelho muito alt imtemp Material bem friavel observa se que a textura remete a uma rocha ignea de granulacao fina semelhante a um diorito Presenca de grao de qtz
DOCRPM000055	265011	8289533	Granito	344	Rocha saprolitizada branca com estrutura de material granitico Presenca de graos de qtz ainda preservados o q indica ocorrencia de granito de granulacao grossa
DOCRPM000056	264731	8289289	Granito	314	Blocos de granito branco equigranular ocorrencia de blocos na estrada
DOCRPM000057	263436	8288760	Solo Marrom avermelhado argilo arenoso	322	Solo marron avermelhado ponto de controle ausencia de alfor
DOCRPM000058	262591	8288536	Solo Marrom avermelhado argilo arenoso	347	Solo marrom claro c gde qte de laterita solo bem evoluido no perfil não há mais evidencias do protolito pela cor infere se estar ainda no embasamento
DOCRPM000059	261280	8289845	Saprolito	340	Vossoroca onde ocorre um perfil profundo de um saprolito q parece ser alteracao do granito Observa se que a textura remete a um granito granulacao grossa presenca de vqz ainda preserv
DOCRPM000060	257595	8286707	Metarenito Fino/Metapelito (intercalação)	296	Aflor de corte de estrada rocha fortemente intemp dada por bandamento comp intecal de camadas amarelo esbranq e avermelhada A granulometria varia de silte a areia fina
DOCRPM000061	258170	8287181	Metapelito	294	Blocos de metapelito cor vermelho Intercal ritmica entre camadas claras e avermelhadas Presenca de oxido de Fe entre as camadas So dobrado
DOCRPM000062	258236	8287241	Metapelito	307	Aflor de metapelito bco intercal com metapelito roxo na forma de finas camadas q apresentam se dobradas Alt hidrot dada pela presenca de ser e py oxidada Proximo ocorre vqz bco leitoso
DOCRPM000063	258741	8287778	Coluvio (solo com blocos de rochas)	329	Solo cinza escuro Ponto controle Solo cinza escuro com gde qte de blocos de qtz Aparentemente material de coluvio
DOCRPM000064	258789	8287839	Metarenito Fino	352	Blocos de metarenito fino na encosta da serra Alguns blocos apresentam se silicificados Aparentemente não foram muito transportados
DOCRPM000065	258841	8287887	Metarenito Fino/ Metassiltito (intercalaçao)	384	Aflor de metarenito fino Rocha cor cinza esbranquicada fortemente foliada A foliacao principal Sn e marcada pela presenca de finas camadas de sericita verde
DOCRPM000066	258892	8287924	Microconglomerado	412	Aflor intercal de microconglomerado e metarenito grosso Rocha cinza esbranquicada com seixos de quartzo de varios tamanhos Algumas porcoes parece estar silicificada
DOCRPM000067	258921	8287980	Metarenito Grosso	433	Aflor de blocos de metarenito medio a grosso Alguns talvez silicificados topo da serra

DOCRPM000068	258971	8288003	Microconglomerado	431	Aflor de blocos de metarenito grosso e microconglomeratico na descida da serra Rocha cor amarelada graos de seixos mal selecionados
DOCRPM000069	258991	8288019	Metaconglomerado	413	Aflor na descida da serra Observa se q a rocha predominate no local é um metarenito grosso a microconglomerado no entanto Ocorre uma rocha formada por uma matriz de hematita c grao de qtz
DOCRPM000070	259082	8288085	Coluvio (solo com blocos de rochas)	407	Blocos de metassed fino intercal c metapelito cor vermelha no entanto eles ocorrem numa peq elevacao e não há como saber se são mat de coluvio da serra a leste ou proprio do vale
DOCRPM000071	259099	8288110	Metarenito Fino	417	Aflor de metarenito fino bco amarelado
DOCRPM000072	259226	8288225	Metarenito Médio	489	Blcos de metarenito medio a fino na encosta Talvez mat de coluvio não há como saber
DOCRPM000073	259266	8288248	Metarenito Fino/Metapelito (intercalação)	505	Aflor de metarenito fino intercal c metapelito cor preta aparentemente trata se de metapelito mas as camadas são escarcas e as vezes se assemelha muito a hematita
DOCRPM000074	259426	8288368	Microconglomerado	592	Aflor de microconglomerado Rocha cor bca c peq seixos de menos de 0,7 cm de compr em gde parte dos casos O metapelito desaparece a uns 70 mts entre o ultimo ponte e este
DOCRPM000075	259475	8288403	Metaconglomerado	586	Aflor de metaconglomerado Seixos c mais de 3 cm de compr clastos suportados por uma matriz dada por metarenito grosso
DOCRPM000076	259536	8288466	Metarenito Médio	537	Aflor de metarenito medio cor amarelo averm a granulometria varia de fina a media
DOCRPM000077	269469	8291996	Microconglomerado	436	Aflor de blocos de metassedimento fortemente hidrotermalizado silicif associada a stockwork gde qte de venulas de qtz Em aguns casos a rocha perde sua textura. Microconglomerado
DOCRPM000078	269458	8291896	Metassedimento (blocos)	404	Blocos de metassed silicific Presenca de stockwork no sope da encosta provavelmente rolados da serra. Gde qte de venulas q mascara a textura da rocha.
DOCRPM000079	269368	8291977	Calciossilicatada	409	Blocos d uma rocha esverdeada no chão da estrada A rocha apresenta granulação fina com min de cor verde igual a epidoto Rocha muito semelhante a calciosilicatada Alt intemp vermelha
DOCRPM000080	269779	8291897	Granito Médio avermelhado	402	Aflor granito roseo foliado gnaissific formado por qz fk plag biotita e hbl Ocorrencia na forma de matacoes na beira da estrada
DOCRPM000081	270202	8291845	Granito Médio avermelhado	448	Aflor de matacoes de granito granulac fina a media foliado gnaissificado composto por fk bt hbl plag e qtz
DOCRPM000082	270400	8291874	Float de qtz (predominante)	438	Float de qtz no chao da estrada presenca de qyz cinza claro a bco com gde qte de turmalina e presenca de oxido de Fe em algumas porcoes
DOCRPM000083	270633	8291864	Granito Médio avermelhado	434	Aflor de granito gnaissificado granulacao fina a media cor vermelha presenca de vqz cor cinza clara semitranslucido orienatdos na direcao do granito
DOCRPM000084	271000	8292593	Granito Médio avermelhado	400	Aflor de blocos e matacoes de granito fino a medio gnaissificado cor vermelha semelhante ao dos pontos anteriores
DOCRPM000085	253028	8288304	Metarenito Fino	434	Aflor de metarenito fino cor bca na encosta da serra
DOCRPM000086	253072	8288310	Metarenito Fino/Metapelito (intercalação)	423	Aflor de metarenito fino intercalado c finas camadas de metassilitio metapelito de ate 1 cm de espessura presenca de estratific cruzada
DOCRPM000087	253084	8288331	Metarenito Fino	409	Metarenito fino cor branca rocha foliada Ponto de controle continua a ocorrencia de metarenito fino
DOCRPM000088	253106	8288348	Contato	405	Inicio da ocorrencia de uma brecha formada por clastos de metarenito silicificado angulosos sustentados por uma matriz de cor marrom avermelhado fina Talvez seja a fonte de ouro do bananal
DOCRPM000089	253088	8288414	Contato	372	Fim da ocorrencia da brecha incio da ocorrencia de metarenito fino intercalado com metassiltito cor vermelho Os clastos da brecha são de metarenito fino e metapelito
DOCRPM000090	253176	8288505	Metarenito Médio	350	Metarenito fino a medio aparentemente feldspatico Rocha alterada pelo intemperismo A rocha apresenta se mais friavel e homegeno do q se observa se no fortuna q sempre tem intercalacoes
DOCRPM000091	253194	8288533	Contato	360	Aflor do contato entre metarenito bco e metapelito cor vermelha q ocorre a leste Contato gradual intercalacao de bandas ritmicas entre metarenito e metassiltito no contato
DOCRPM000092	253229	8288635	Metarenito Fino/ Metassiltito (intercalaçao)	351	Aflor de metarenito fino metapelito cor levemente arroxeada Depois da camada de metapelito q aparece no contato do ponto anterior q persiste por uns 50m volta a ocorrer metarenito fino intercal por meatassiltito
DOCRPM000093	253368	8288808	Metarenito Fino/ Metassiltito (intercalaçao)	316	Aflor de metarenito fino cinza arroxeado em uma drenagem Aparentemente trata se de material da Fm vale da promissao Presenca de finas camada de metassiltito em algumas partes
DOCRPM000094	254162	8289588	Metarenito Fino	312	Aflor de metarenito fino no chao de uma estr Rocha amar averm a granul pred é areia no entanto em algumas porcoes a rocha passa para silte ou mais raramente argila Venulas com silicif em algumas partes
DOCRPM000095	255897	8288865	Laterita	315	Blcos de ganga lateritica ferruginosa q indica forte laterizacai e dificuldade de encontrar afloramentos de rocha na area Espessa corbertura lateritica
DOCRPM000096	256612	8287470	Metarenito Fino	312	Aflor de metarenito fino a medio cor brco avermelhado no chao da estrada Rocha fortemente intemp
DOCRPM000097	256760	8287203	Metarenito Fino	312	Aflor de metarenito fino a medio cor verde amarelado a roxo Forte fraturamento q e semelhante a uma foliacao
DOCRPM000098	258503	8285786	Metassiltito	305	Aflor de metarenito fino cor rosa na beira da estrada A granulometria varia de fino a silte e talvez a rocha se classifique melhor como metassiltito porem a rocha esta fortemente intemp
DOCRPM000099	259435	8284944	Metassiltito	315	Metassiltito cor roxa a bca avermelhado Aflor na beira da estrada Rocha fortemente intemperizada

DOCRPM000100	260185	8284179	Metarenito Médio	340	Metarenito fino a medio fortemente silicific q torna dificil o reconhecimento da granulometria Presenca de venulas de qtz bco leitoso Matriz da rocha esta silicifado
DOCRPM000101	262706	8282555	Metarenito Médio	387	Aflor de metarenito fino a medio Rocha fortemente intemp corte de estrada
DOCRPM000102	263186	8282269	Metapelito	403	Metapelito roxo finamente acamadado com camadas de metarenito cor bca Aflor na forma de ocorrencias de blocos in situ
DOCRPM000103	264403	8283658	Solo lateritico	358	Solo lateritico na estrada Não há afloramento pois o solo deve ser espesso O solo tem cor avermelhada
DOCRPM000104	264642	8286604	Solo cinza escuro organico	337	Ponto de controle ocorrencia de um solo organico cinza topografia plana ausencia de afloramentos
DOCRPM000105	266449	8287501	Saprolito	330	Aflor de corte de estrada Material fortemente intemp A textura lembra uma rocha granitica intemperizada de granulacao grossa
DOCRPM000106	266763	8287633	Metarenito Médio	338	Arenito granulacao media Aflor de corte de estrada Rocha bca Sericita marca os planos de foliacao Inicio da ocorrencia de aguapei A 10 m a E do pt anterior ocorre metapelito
DOCRPM000107	266802	8287619	Metarenito Fino	343	Aflor de metarenito fino fortemente foliado presenca de sericita nos plan de foliacao
DOCRPM000108	266930	8287614	Metarenito Fino	347	Aflor de metarenito fino no chao da estrada Rocha já bastante intemperizada até esse ponto ainda é aguapei
DOCRPM000109	266999	8287657	Saprolito	345	Aflor de rocha intemp na beira da estrada O material tem um aspecto xistoso e parece já ser mat do embasamento no entanto não há como ter certeza se não se trata de um metapelito intemp
DOCRPM000110	267052	8287739	Metarenito Fino/Metapelito (intercalação)	354	Aflor de corte de estrada Rocha fortemente intemp Intercal de metarenito fino com metapelito Ao que td indica ainda é aguapei e o ponto anterior não é embasamento como especulado
DOCRPM000111	267087	8287789	Metapelito	360	Aflor de corte de estr Ocorrencia de metapelito cor cinza azulado predominante no ponto No entanto há um bandamento comp bem marcado com metassiltito. Ainda e Aguapei
DOCRPM000112	267461	8288554	Metarenito Fino	340	Aflor de corte de estrada Rocha muito semelhante a um metarenito fino do gr Aguapei Rocha fortemente intemp no entanto seu aspecto e muito semelhante a arenitos do Vale da promissao
DOCRPM000113	270250	8282380	Solo cinza escuro organico	343	Solo Organico cinza sem afloramento ponto de controle
DOCRPM000114	270258	8282426	Muscovita xisto	342	Aflor no chao da estrada trata-se de um muscobvita xisto Presenca um mineral arredondado que parece ser granada ou cloritoide Granulacao grossa Abundancia de float de qtz na estrada
DOCRPM000115	270446	8282792	Saprolito	337	Aflor corte de estrada rocha intensamente saprolitizada Trata se de um granito gnaissificado os minerais já estao extremamente alterados textura granitica ainda preservada
DOCRPM000116	270760	8283523	Saprolito	354	Aflor de corte de estrada rocha fortemente alterada intempericamente Trata se de um granito milonitizada Não e possivel reconhecer a mineralogia
DOCRPM000117	270985	8284073	Granito Santa Helena	380	Aflor no chao da estrada trata se de granito com estrutura gnaissica fortemente foliado pouco intemperizado A foliacao e marcada pela orientacao de minerais como biotita e muscovita
DOCRPM000118	271561	8284947	Granito Santa Helena	420	Aflor no chao da estrada Granito gnaissificado rosa fortemente foliaco foliacao gnaissica
DOCRPM000119	273557	8285315	Granito Santa Helena	414	Aflor no chao da estrada laje de granito foliado com estrutra gnaissica muito semelhante ao ponto anterior
DOCRPM000120	274728	8285240	Muscovita xisto	452	Aflor de muscovita xisto foretemente alterado em meio a um saprolito ou solo fortemente evoluido aparentemente alteracao do granito assim o musc xisto parece ser uma ZC dentor do granito
DOCRPM000121	276211	8285796	Granito Santa Helena	418	Aflor de granito granulação grossa foliado Foliacao dada pela orientacao dos minerais na rocha Cor roseo claro a branco
DOCRPM000122	267265	8272466	Solo Marrom arenoso	405	Ponto de controle inicio do perfil limite com a propriedade serra azul. Solo arenoso marrom
DOCRPM000123	267151	8272466	Metarenito Grosso	421	Aflor de blocos in situ Metarenito grosso com estratificação cruzada
DOCRPM000124	267049	8272412	Metarenito Fino/Metapelito (intercalação)	404	Aflor em drenagem intercalação de metapelito c metarenito fino predominio de metarenito fino A drenagem parece estar encaixada na zona de ocorrencia do metapelito
DOCRPM000125	266873	8272135	Metarenito Grosso		Aflor de metarenito grosso no chão. Blocos
DOCRPM000126	266893	8271627	Metarenito	536	Afloramento de metarenito granulometria média blocos proximo ao topo da serra
DOCRPM000127	267007	8271350	Metarenito Fino	532	Afloramento em uma cachoeira seca intercalação de metarenito fino e quartzito ou metarenito muito fino O bandamento parece formar uma dobra porem não há como saber se se trata de dobra ou estratificação
DOCRPM000128	268505	8271765	Metagabro	372	Afloramento no chao da estrada Rocha composta por gde qte de clorita e actinolita textura grossa gabrioca Trata-se de um metagabro que ocorre dentro do dominio do granito Sta Helena Rocha cor verde escura.
DOCRPM000129	268837	8271829	Solo Marrom avermelhado argilo arenoso	393	Ponto de controle solo vermelho argiloso preso em raizes de arvores caidas idicando ainda a presença de rochas básicas no local
DOCRPM000130	269054	8271762	Solo Marrom arenoso	405	Ponto de controle Solo arenoso cor marrom típico de alteração de metassedimentos
DOCRPM000131	269186	8271573	Metarenito Fino		Afloramento de metarenito com granulometria variando de fina a média. E em algumas porções observa se metarenito
DOCRPM000132	270175	8270840	Saprolito	453	Aflor de corte de estrada material saprolítico alteração de granito Textura ainda preservada onde é possivel observa cristais de minerais aparementemente FK com cerca de 1 cm alterados para caolim
DOCRPM000155	255338	8292491	Metarenito Fino/Metapelito (intercalação)	285	Aflor de metasedimento do aguapei inrtacalação entre meta-argilitos e metarenitos medio a grosso. Aparentemente ainda trata se da fm Fortuna.

DOCRPM000156	254648	8291520	Metapelito	296	Aflor de metasedimento fino friável cor branco avermelhado. Aparentememente trata-se de metasiltito intercalado com meta-argilito. Presença de pintas escruras semelhates a Py. Rochas da Fm Vale da Promissão
DOCRPM000157	270248	8275170	xisto avermelhado (saprolitizado)	435	Aflor com Gde variedade de rochas A rocha predominante é um xisto no entanto o estado de alt imtemp deixa duvidas sobre a possível genese presença de uma rocha que se parece muito com um granito todo deformado como se o xisto fosse produto da alteração de
DOCRPM000158	269588	8270436	Metaconglomerado	436	Aflro de metassedimentos com forte xitosidade dada pela presença de uma mica cor verde clara. A textura da rocha parece indicar que se trata de um metaconglomerado com seixos deformados
DOCRPM000159	269622	8270532	Metaconglomerado	439	Aflor de uma rocha fortemente micacea com foliação bem marcada. A mica é uma muscovita de cor verde Observa-se que entre as micas há a presença de agregados de quartzo que parecem ser seixos deformados em forma de sigmoides. Aparentemente se trata de meta
DOCRPM000160	269843	8270748	Granito Porfirítico	445	Aflor de granito pofirítico com fenocristais de FK cor rosa. Esse granito e muito parecido com o que ocorre na porção norte do pau a pique na embasamento nas proximidades da linha 600 Fenocristais com tamanho em torno de 1 a 5 cm
DOCRPM000161	267021	8270408	Metarenito Fino/Metapelito (intercalação)	435	Aflor de metarenito fino interacalado com finas camadas de metapelito de cor cinza escura
DOCRPM000162	255692	8293222	Metaconglomerado	367	Metaconglomerado de tamanho variado presença de seixos de até 1 1/2 cm de comprimento matriz metarenitica
DOCRPM000163	255834	8293095	Metaconglomerado	416	Aflor de metaconglomerado rocha com intercalação de metarenito grosso e metaconglomerado os seixos chegam a ter mais de 3 cm de comprimento
DOCRPM000164	256282	8292496	Metaconglomerado	469	Aflor de metaconglomerado com seixos de tamanho médio grão com tamanho médio de cerca de 0.4 cm de comprimento
DOCRPM000165	256331	8292416	Metaconglomerado	463	Aflor de metaconglomerado rocha cor cinza esverdeada com seixos de até 0,5 cm de comprimento afloramento de blocos
DOCRPM000166	265553	8290309	Metarenito Fino/Metapelito (intercalação)	368	Afloramento de intercalação entre metarenito fino e meta-argilito O metarenito apresenta cor creme enquanto que o meta-argilito apresenta cor cinza escuro O afloramento é domindado por metarenito sendo as camada de meta-argilitos bem finas entre o metarenito
DOCRPM000167	265546	8290288	Metarenito Fino/Metapelito (intercalação)	375	Mesmo aflor do ponto anterior coleta de amostra para difração. Intercalação de metarenito fino e metapelito
DOCRPM000168	258193	8290421	Metaconglomerado	418	Aflor de metaconglomerado. Rocha cor cinza com intercalações de metarenito grosso e metaconglomerado
DOCRPM000169	258290	8290091	Metarenito Fino/Metapelito (intercalação)	465	Aflor de blocos intercalaçãode meta-argilito e metarenito fino A rocha prodominate é o metarenito já o meta-argilito ocorre como finas camadas no arenito e tem cor cinza escuro
DOCRPM000170	258302	8290001	Metaconglomerado	487	Aflor de metaconglomerado intercalado com metarenito grosso Aparentemente apresenta um leve silicificação
DOCRPM000171	251023	8279875	Metachert	256	Blocos de metachert e blocos de metadiabásio Não observa-se a presença de afloramento na área apenas crostas lateríticas ferruginosas A rocha apresenta cor preta a cinza e estrutura compacta
DOCRPM000172	251289	8269913	xisto avermelhado (saprolitizado)	310	Afloramente de xisto saprolitizado avermelhado composto aparentemente por muscovita. O estado de alteração não permite determinar exatamente qual é a rocha e sua mineralogia no entanto pode-se dizer que se trata de um mica xisto
DOCRPM000173	252509	8274525	Metachert	280	Blocos na beira da estrada. Presena de blocos de metachert proximo a uma drenagem e foi observado a presença de um bloco de metabasalto > todos são blocos com forma arredondada indicando talvez um pouco de transporte
DOCRPM000174	249173	8277638	Granito branco fino	280	Aflor de uma rocha cor avermelhada saprolitizada A rocha é muito semelhante a um granito fino branco onde observa-se a presenca de um material que esta sendo caolinizado
DOCRPM000175	263189	8282685	Metarenito Médio	449	Afloramento de metarenito no chao Variação na granulometria do metarenito a rocha apresenta-se fortemente dobrada
DOCRPM000176	263115	8282827	Metaconglomerado	446	Aflor de blocos de metaconglomerado com tamanho medio dos seixos em torno de 0.5cm
DOCRPM000177	263086	8282920	Metaconglomerado	430	Aflor de blocos de metaconglomerado Rocha cor cinza formada por micas e quartzo Parcialmente intemperizada O seixos chegam a ter cerca de 1.5 cm de comprimento
DOCRPM000178	262904	8283399	Metaconglomerado	434	Blocos de metaconglomerado A rocha parece não estar in situ Rocha foliada com seixos de 1 cm de comprimento
DOCRPM000179	257104	8304433	Metapelito	408	Meta-argilito cinza escuro coletado na Bancada da mina para análise de difração de RX
DOCRPM000180	257105	8304442	Metapelito	408	Meta-argilito cinza escuro coletado na Bancada da mina para análise de difração de RX
DOCRPM000181	257113	8304447	Metapelito	408	Meta-argilito cinza escuro coletado na Bancada da mina para análise de difração de RX
DOCRPM000182	257118	8304457	Metapelito	408	Meta-argilito cinza escuro coletado na Bancada da mina para análise de difração de RX
DOCRPM000183	257126	8304469	Metapelito	408	Meta-argilito cinza escuro coletado na Bancada da mina para análise de difração de RX
DOCRPM000184	257134	8304470	Metapelito	408	Meta-argilito cinza escuro coletado na Bancada da mina para análise de difração de RX
DOCRPM000185	257160	8304487	Metapelito	408	Meta-argilito cinza escuro coletado na Bancada da mina para análise de difração de RX
DOCRPM000186	257178	8304501	Metapelito	408	Meta-argilito cinza escuro coletado na Bancada da mina para análise de difração de RX

DOCRPM000134	271408	8271533	Metapelito		Afloramento no chão da estada de acesso ao Pau a Pique Rocha filito de várias cores predominando a cor cinza. Rocha fortemente alterada presença de minerais que são muito semelhantes a Cloritoide
DOCRPM00133A	271184	8271341	Contato		Aflor de corte de estrada Contato entre metarenito grosso e quartzito Passagem gradual de uma litologia para outra com aumento da frequencia de camadas de metarenito grosso até o predomínio do mesmo.
DOCRPM00133B	271176	8271336	Contato		Afllor de corte de estrada Contato entre filito ou metapelito e quartzito ou metarenito fino. O metapelito ou filito apresnta-se alterado com cor vermelha c min arredondados q lembram cloritoide a passagem é gradual com aumento da freq de quartzito
DOCRPM000135	271723	8271686	Metarenito	421	Aflor no leito de estrada metarenito medio cor verde clara presenca de zonas de cis com veio de qtz presenca de fraturas que parecem ter sido preenchidas durante hidrotermalismo gerando estrutura xistosa
DOCRPM000136	271834	8272174	Granito Santa Helena	426	Aflor no chao da estrada Granito roseo foliado tipico do santa helena com granulação media anisotropico com granualçao media composto por biotita e muscovita com secundarios
DOCRPM000137	272049	8272978	Granito	408	Afor de corte de estrada Rocha fortemente cisalhada com granulação fina. Presnça de biotita quartzo muscovita e feldspato. Grau de intemperismo moderado A rocha se assemelha a um granito deformado fortemente cisalhado
DOCRPM000138	273106	8273281	Granito Santa Helena	483	Aflor no chao da estrada Granito roseo com granulacao fina fortemente alterado com biotita muscovita com acessorios Rocha foliada com uma foliação gnaissica
DOCRPM000139	275579	8274028	Granito Santa Helena	468	Aflor de matacoes de granito com granulação media cor rosa anisotropico foliado com folicao gnaissica cor roseo com biotita e muscovita
DOCRPM000140	277551	8276185	Granito Santa Helena	365	Aflor de granito foliado roseo com biotita e muscovita Continua o granito tipico do Santa helena foliado com biotita e muscovita. Desde o ultimo ponto ve-se frenquentemente esses matacoes de granito
DOCRPM000141	277933	8280687	Granito Santa Helena	394	Aflor de granito fino a medio foliado roseo tipico Santa helena
DOCRPM000142	252516	8278718	Laterita	269	Inico perfil no Rio Alegre Solo Argiloso vermelho com gde qte de lateriats na forma de seixos
DOCRPM000143	251389	8279593	Laterita		Afloramento de crosta lateritica associado a um solo vermelho escuro
DOCRPM000144	249852	8280770	Laterita	249	Aflor de crosta lateritica em meio a solo vermleho ponto de controle
DOCRPM000145	249044	8281434	Laterita	267	Aflor de crosta lateritica
DOCRPM000146	247277	8282816	xisto avermelhado (saprolitizado)	270	Aflor de material xistoso fortemente intemperizado cor vermelho amarelado nçao há como saber que tipo de xisto mas parece algum tipo de filito grafitoso
DOCRPM000147	246370	8283531	Saprolito	244	Aflor de material saprolitico cor amarelo esbranquicado com textura semelhante a uma rocha granitoide
DOCRPM000150	255472	8293255	Metarenito Fino/Metapelito (intercalação)		Afloramento de metapelito intercalado com metarenito. O meta-argilito apresenta cor cinza escuro e granulacao finae ocorem em bandas de menos de 1 cm de espessura Aflor dentro da faixa de metapelito mapeada
DOCRPM000151	268409	8286551	Quartzito		Aflor de quartzitodobrado cor brca granulacao fina presenca de camadas de muscovita entre as camadas de qtzito a muscovita tem cor verde e apresenta bem cristalizada. Fora das camadas de muscovita ocorre umas camadas de um xisto alterado
DOCRPM000152	269920	8286382	Granito Santa Helena		Granito Roseo granulacao fina fortemente foliado Rocha homogenea anisotropico a foliacao Sn é dada pela orientacao planar de cristais de biotita e muscovita
DOCRPM000153	270328	8277572	Sericita qtz xisto		Aflor de rocha xistosa com bastante muscovita cor verde, foliacao bem forte e presenca de gde qte de veios e venul de qtz Aparentmente trata de uma zona de cisalhamento dentro do granito ou no contato do memso
DOCRPM000154	270277	8276276	Sericita qtz xisto		Aflor de rocha xistosa fortemente alterada com niveis de material qtzo feldspatico muito semelhante a material arcoseano O xisto apresenta pequenos buracos deixados por minerais arredondados q esta alterado para um min amarelo semelhante a granada
DOCRPM000148	251547	8288144	Metabasalto		Afloramento de Blocos de metabasica unidade Rio Alegre. Rocha cor verde granulaçao media. Uma textura mais tendendo a metadiabásio e outra semelhante a metabasalto

Appendix II

(Geochemical Data- Whole Rock)

Samples	PQGL1-001	PQGL1-002	PQGL1-006	PQGL1-008	PQ61101-13	PQ6189-10	PQ61102-23	PQ61108-90	PQ12380-76
Location	Pau-a-Pique	Pau-a-Pique	Pau-a-Pique	Pau-a-Pique	Pau-a-Pique	Pau-a-Pique	Pau-a-Pique	Pau-a-Pique	Pau-a-Pique
Rock	Shear. dior.	Bt Sch	Ms Sch	Conglom.	Sheared dior.	Dior.	Shear. dior.	Bt Sch	Ms Sch
SiO2 (%)	65.39	47.17	47.54	85.75	52.41	53.82	50.71	43.56	39.24
Al2O3 (%)	13.48	14.39	24.37	7.73	17.03	16.87	17.48	22.11	25.72
TiO2 (%)	0.51	2.6	1.41	0.35	1.63	1.54	1.89	1.57	1.82
Fe2O3 (%)	5.35	13.67	10.11	1.8	10.11	9.51	10.47	8.87	14.04
CaO (%)	2.81	6.35	0.11	0.09	6.18	7.36	7.89	3.32	0.34
K2O (%)	4.16	5.54	7.8	2.39	2.96	1.31	1.55	8.33	8.66
Na2O (%)	1.8	0.18	0.56	0.63	2.98	3.69	2.75	0.97	0.43
MgO (%)	2.4	3.99	0.96	0.17	4.25	3.71	4.19	5.22	1.31
MnO (%)	0.24	0.4	0.02	0.02	0.15	0.12	0.14	0.21	0.04
P2O5 (%)	0.11	1.17	0.02	0.06	0.3	0.35	0.37	0.46	0.17
Cr2O3 (%)	0.003	0.004	0.031	<0.002	0.005	0.003	0.004	0.008	0.012
Ba (ppm)	1021	1201	2360	403	1036	535	655	1975	1537
Be (ppm)	6	2	2	1	<1	1	<1	1	4
Cd (ppm)	<0.1	<0.1	<0.1	<0.1	<0.1	<0.1	<0.1	<0.1	<0.1
Ce (ppm)	21.4	41.1	27.3	67.5	24.4	30.9	24.2	25.2	22.1
Co (ppm)	13.6	30.7	28.7	4.3	27.8	29.1	27.6	19.9	50.8
Cs (ppm)	6.4	15.1	3.2	1.4	8.2	1.7	3.9	10.9	3.6
Cu (ppm)	0.5	54	38.1	4.5	47.8	49.4	57.8	0.6	3.5
Dy (ppm)	2.8	5.11	4.8	2.99	2.49	4.3	2.71	2.5	2.22
Er (ppm)	1.52	2.69	2.85	1.79	1.28	2.15	1.4	1.44	1.07
Eu (ppm)	0.83	2.15	1.31	0.74	0.97	1.25	1.25	1.19	1.01
Ga (ppm)	12.5	18.3	29.5	8.2	17.2	16.1	17.2	21.4	28.9
Gd (ppm)	2.94	6.26	5.1	3.71	2.75	4.78	3.65	3.09	3.11
Hf (ppm)	2.4	1.9	5.1	3	1.3	3	1.1	1.1	1.6
Ho (ppm)	0.5	1.02	1.01	0.57	0.47	0.83	0.49	0.47	0.38
La (ppm)	10.3	20	12.9	29.9	10.7	13.1	10.8	11.2	11.1
Lu (ppm)	0.27	0.39	0.56	0.26	0.17	0.27	0.21	0.21	0.15
Mo (ppm)	0.2	0.1	0.3	0.2	0.1	1	1	<0.1	<0.1
Nb (ppm)	3.9	3.4	6.1	8.8	1.4	3.5	2	7.2	3.9
Nd (ppm)	11	23.4	15.3	27	12	19	15	14.8	13.7
Ni (ppm)	<20	<20	40	<20	30	27	25	25	51
Pb (ppm)	6.7	12.4	7.5	1.3	2.5	0.8	2	3.5	18.9
Pr (ppm)	2.77	5.47	3.86	7.59	3.03	4.46	3.42	3.34	3.28
Rb (ppm)	121.6	199	155	75.5	89.7	27.9	43.6	205.7	164.1
Sc (ppm)	10	28	22	3	24	24	24	22	34
Sm (ppm)	2.42	5.94	4.08	4.75	2.94	4.87	3.45	3.18	3
Sn (ppm)	<1	1	2	<1	<1	<1	<1	1	3
Sr (ppm)	99.9	198.2	66.5	27.1	742	447.5	832	144	60.8
Ta (ppm)	0.5	0.3	0.7	1.4	0.2	0.3	0.2	0.5	0.6
Tb (ppm)	0.46	0.94	0.85	0.53	0.42	0.76	0.51	0.44	0.4
Th (ppm)	2.5	0.8	3.4	11.7	2.2	1.6	1	1.5	1.5
Tm (ppm)	0.22	0.39	0.49	0.27	0.18	0.29	0.2	0.2	0.17
U (ppm)	0.9	1.4	8.9	2.6	1.2	0.4	0.7	0.6	1.5
V (ppm)	79	191	203	27	355	315	369	243	324
W (ppm)	1.6	4.7	12.3	0.9	1.1	<0.5	1.8	15.9	28.8
Y (ppm)	14.7	31.2	29	16.4	12.1	22.2	15.6	12.7	12.7
Yb (ppm)	1.55	2.61	3.59	1.7	1.1	1.81	1.4	1.25	0.97
Zr (ppm)	78.7	70.6	180.7	102.5	33.4	112.2	34.6	30.5	56.9
Ag (ppm)	<0.1	0.2	2.7	<0.1	<0.1	<0.1	<0.1	<0.1	1.3
As (ppm)	2.2	3.6	10.6	<0.5	0.8	3.4	1.6	2.6	25.3
Au (ppb)	<0.5	11.6	4196.2	48.9	27.5	1.2	11.8	5.9	35489.6
Bi (ppm)	<0.1	5	3.8	<0.1	<0.1	<0.1	<0.1	<0.1	5.3
Hg (ppm)	<0.01	<0.01	<0.01	<0.01	<0.01	<0.01	<0.01	<0.01	<0.01
Ni (ppm)	13.5	14.6	33	0.9	26.5	23	23.5	21.7	30.1
Sb (ppm)	<0.1	<0.1	<0.1	<0.1	<0.1	<0.1	<0.1	<0.1	<0.1
Se (ppm)	<0.5	1.1	1.9	<0.5	<0.5	<0.5	<0.5	<0.5	2.5
Tl (ppm)	0.4	1.3	0.1	<0.1	0.5	0.1	0.3	1.1	0.2
Zn (ppm)	42	99	5	<1	75	62	69	110	20
LOI	3.5	4.2	6.7	1	1.6	1.5	2.2	5	7.9
Sum	99.81	99.7	99.63	99.94	99.65	99.74	99.68	99.62	99.72
TOT/C	0.62	0.85	<0.02	<0.02	<0.02	<0.02	<0.02	0.57	<0.02
TOT/S	<0.02	1.41	4.35	<0.02	0.04	0.13	0.14	<0.02	6.63
Fe/(Fe+Mg)	0.721	0.799	0.924	0.925	0.734	0.748	0.743	0.663	0.926

Samples	PQ35A557-89	PQ35A487-90	DOC 00081	DOC 00128A	DOC 00148A	DOC 00152	DOC 00160	DOC 00173	ER63210-89
Location	Pau-a-Pique	Pau-a-Pique	Regional	Pau-a-Pique	Regional	Regional	Regional	Regional	Ernesto
Rock	Dior.	Dior.	Grt S Helena	Mafic	Mafic R. Alegre	Grt S Helena	Grt Pindaituba	Mafic R. Alegre	Diorito (ER)
SiO2 (%)	52.79	49.66	77.29	51.09	50.36	77.48	72.2	49.53	69.52
Al2O3 (%)	16.68	16.63	11.51	5.11	13.59	11.64	13.99	16.24	14.33
TiO2 (%)	1.17	1.55	0.13	0.2	1.84	0.14	0.29	0.39	0.32
Fe2O3 (%)	9.37	10.8	1.65	10.94	13.72	1.64	2.52	12.76	2.61
CaO (%)	7.68	8.01	0.43	10.39	7.06	0.62	1.17	11.22	2.23
K2O (%)	0.75	1.18	4.94	0.07	0.03	4.75	4.59	0.27	3.81
Na2O (%)	3.94	3.32	3.05	0.35	3.24	3.02	3.31	1.04	3.15
MgO (%)	4.72	6.03	0.05	18.08	4.46	0.13	0.64	6.06	0.95
MnO (%)	0.15	0.14	0.03	0.16	0.2	0.03	0.05	0.24	0.05
P2O5 (%)	0.29	0.32	0.01	0.03	0.17	0.01	0.05	<0.01	0.11
Cr2O3 (%)	0.018	0.02	<0.002	0.082	0.003	<0.002	<0.002	0.008	<0.002
Ba (ppm)	305	639	156	26	93	83	911	71	1446
Be (ppm)	2	1	5	<1	2	3	4	<1	1
Cd (ppm)	<0.1	<0.1	<0.1	<0.1	<0.1	<0.1	<0.1	<0.1	<0.1
Ce (ppm)	31.2	14.7	134.5	11.6	22.6	149.7	70.3	4.1	42.3
Co (ppm)	24.8	33.7	0.2	96.2	39.4	1.2	3.3	42	3
Cs (ppm)	0.6	0.7	2	<0.1	<0.1	3.7	1.5	<0.1	4.4
Cu (ppm)	22.8	30.7	0.6	6.4	70.1	1.7	1.6	97.1	4
Dy (ppm)	3.81	2.4	13.18	1.5	5.8	8.58	5.23	1.22	2.31
Er (ppm)	2.03	1.31	9.21	0.75	3.44	6.4	3.56	0.9	1.13
Eu (ppm)	1.41	1.15	0.35	0.53	1.49	0.19	0.75	0.36	0.74
Ga (ppm)	16.3	13.8	17.5	4.8	18.7	16.3	15.3	12	13.7
Gd (ppm)	4.21	2.81	11.39	2.13	5.16	7.67	4.77	1.02	2.58
Hf (ppm)	3.1	1.4	7.5	0.5	3.3	5.3	4.5	0.4	3.5
Ho (ppm)	0.71	0.49	3.06	0.28	1.19	2.01	1.12	0.3	0.38
La (ppm)	12.8	6.2	57.2	13.2	10	75.3	35.7	2.2	20.4
Lu (ppm)	0.31	0.19	1.44	0.09	0.5	1.15	0.65	0.16	0.18
Mo (ppm)	0.9	1	0.9	<0.1	0.3	0.9	0.4	1.1	0.2
Nb (ppm)	2.7	1.5	19.3	0.4	3.5	16.3	8.2	0.4	4.1
Nd (ppm)	16.7	8.7	53.4	12.2	15.6	48.5	31.1	2.4	17
Ni (ppm)	28	55	<20	267	<20	<20	<20	<20	<20
Pb (ppm)	1.1	0.6	2.5	0.4	3.2	4	5.9	0.1	4.4
Pr (ppm)	3.82	1.99	14.07	2.83	3.29	15.57	8.45	0.54	4.73
Rb (ppm)	13.5	21.4	209.7	0.6	0.6	306.3	139	5.8	83.9
Sc (ppm)	24	27	2	37	38	1	5	49	4
Sm (ppm)	4.02	2.48	11.26	2.16	4.55	8.29	5.59	0.74	2.84
Sn (ppm)	<1	<1	5	<1	<1	17	2	<1	<1
Sr (ppm)	416.8	332.6	18.9	48.8	518	18.3	201	141.3	196.6
Ta (ppm)	0.2	0.1	1.1	<0.1	0.2	1.5	0.5	<0.1	0.4
Tb (ppm)	0.62	0.43	2.09	0.28	0.9	1.36	0.82	0.19	0.39
Th (ppm)	1.8	0.6	15.5	<0.2	0.8	30.2	7	<0.2	2.8
Tm (ppm)	0.29	0.18	1.48	0.1	0.47	1.07	0.58	0.15	0.15
U (ppm)	0.9	0.3	6.4	<0.1	0.3	6.4	3	<0.1	2.1
V (ppm)	176	242	<8	80	413	<8	37	301	24
W (ppm)	0.7	0.7	0.8	<0.5	<0.5	2.1	<0.5	<0.5	<0.5
Y (ppm)	19.3	12.7	87.6	8.2	33.3	61	27.1	7.3	10.4
Yb (ppm)	1.95	1.2	9.41	0.55	3.27	7.22	4.04	0.92	1.15
Zr (ppm)	125.8	50.9	192.9	14.2	108.2	135.8	149.4	14	113.8
Ag (ppm)	<0.1	<0.1	<0.1	<0.1	<0.1	<0.1	<0.1	<0.1	<0.1
As (ppm)	<0.5	0.6	0.5	<0.5	6.1	<0.5	<0.5	0.5	0.8
Au (ppb)	1.7	70.5	1	<0.5	<0.5	<0.5	<0.5	2.1	<0.5
Bi (ppm)	<0.1	<0.1	<0.1	<0.1	<0.1	0.5	<0.1	<0.1	<0.1
Hg (ppm)	<0.01	<0.01	<0.01	<0.01	<0.01	<0.01	<0.01	<0.01	<0.01
Ni (ppm)	17.1	32.4	1.4	90.7	19.2	1	2.3	11.4	1.7
Sb (ppm)	<0.1	<0.1	<0.1	<0.1	1.4	<0.1	<0.1	<0.1	<0.1
Se (ppm)	<0.5	0.6	<0.5	<0.5	<0.5	<0.5	<0.5	<0.5	<0.5
Tl (ppm)	<0.1	<0.1	<0.1	<0.1	<0.1	0.5	0.5	<0.1	<0.1
Zn (ppm)	48	49	35	19	95	32	43	52	7
LOI	2.2	2.1	0.8	3.1	5.1	0.5	1	2.1	2.7
Sum	99.78	99.74	99.91	99.67	99.75	99.93	99.82	99.81	99.79
TOT/C	0.06	0.03	<0.02	<0.02	0.65	<0.02	<0.02	0.03	0.38
TOT/S	0.03	0.14	<0.02	<0.02	0.05	<0.02	<0.02	0.08	<0.02
Fe/(Fe+Mg)	0.697	0.675	0.975	0.412	0.781	0.936	0.820	0.709	0.761

Appendix III

(Strcutural formula and microprobe data - Muscovite)

Samples	DOC075	DOC075	DOC075	DOC075	DOC075	DOC075
Analysis	3	12	4	13	6	7
SiO2	46.057	45.867	46.055	45.983	46.317	45.642
TiO2	0.103	0.142	0.097	0.124	0.076	0.103
Al2O3	38.281	37.534	38.442	37.990	38.249	37.673
FeO	2.893	3.189	2.822	3.038	2.574	2.897
MnO	0.000	0.011	0.016	0.007	0.013	0.005
MgO	0.199	0.306	0.235	0.261	0.241	0.201
CaO	0.004	0.034	0.018	0.014	0.019	0.009
Na2O	0.349	0.365	0.399	0.387	0.354	0.395
K2O	8.948	8.863	9.142	8.692	7.813	7.960
SrO	0.000	0.000	0.000	0.000	0.000	0.000
BaO	0.000	0.000	0.000	0.000	0.000	0.000
Rb2O	0.000	0.000	0.000	0.000	0.000	0.000
Cs2O	0.000	0.000	0.000	0.000	0.000	0.000
Ga2O3	0.000	0.000	0.000	0.000	0.000	0.000
F	0.000	0.000	0.000	0.000	0.000	0.000
Cl	0.003	0.001	0.002	0.013	0.004	0.018
Cr2O3	0.029	0.014	0.023	0.000	0.019	0.013
NiO	0.000	0.000	0.000	0.000	0.000	0.000
CuO	0.000	0.000	0.000	0.000	0.000	0.000
Li2O	0.000	0.000	0.000	0.000	0.000	0.000
H2O	4.599	4.565	4.612	4.581	4.585	4.527
Subtotal	101.465	100.890	101.862	101.090	100.263	99.443
O=F,Cl	0.001	0.000	0.000	0.003	0.001	0.004
Total	101.464	100.890	101.862	101.087	100.262	99.439
Si	6.004	6.024	5.988	6.015	6.056	6.040
Al iv	1.996	1.976	2.012	1.985	1.944	1.960
Al vi	3.887	3.835	3.879	3.872	3.950	3.915
Ti	0.010	0.014	0.010	0.012	0.007	0.010
Cr	0.003	0.001	0.002	0.000	0.002	0.001
Fe	0.315	0.350	0.307	0.332	0.281	0.321
Mn	0.000	0.001	0.002	0.001	0.001	0.001
Mg	0.039	0.060	0.045	0.051	0.047	0.040
Zn	0.000	0.000	0.000	0.000	0.000	0.000
Sn	0.000	0.000	0.000	0.000	0.000	0.000
Ga	0.000	0.000	0.000	0.000	0.000	0.000
Ni	0.000	0.000	0.000	0.000	0.000	0.000
Cu	0.000	0.000	0.000	0.000	0.000	0.000
Li*	0.000	0.000	0.000	0.000	0.000	0.000
Ca	0.001	0.005	0.003	0.002	0.003	0.001
Na	0.088	0.093	0.100	0.098	0.090	0.101
K	1.488	1.485	1.516	1.450	1.303	1.344
Sr	0.000	0.000	0.000	0.000	0.000	0.000
Ba	0.000	0.000	0.000	0.000	0.000	0.000
Rb	0.000	0.000	0.000	0.000	0.000	0.000
Cs	0.000	0.000	0.000	0.000	0.000	0.000
OH*	3.999	4.000	4.000	3.997	3.999	3.996
F	0.000	0.000	0.000	0.000	0.000	0.000
Cl	0.001	0.000	0.000	0.003	0.001	0.004
TOTAL	17.831	17.844	17.864	17.818	17.685	17.734
Fe/Fe+Mg	0.891	0.854	0.871	0.867	0.857	0.890

Samples	DOC168	DOC168	DOC168	DOC168	DOC168	DOC168	DOC168	DOC168	DOC168	DOC168
Analysis	1	2	11	4	6	7	10	8	9	12
SiO2	46.688	44.814	45.827	46.322	46.427	45.092	45.841	45.662	45.655	44.810
TiO2	0.106	0.150	0.236	0.266	0.226	0.156	0.151	0.124	0.188	0.196
Al2O3	36.582	35.741	35.704	37.367	36.310	36.873	36.555	36.858	35.594	36.119
FeO	3.644	3.780	3.982	3.693	4.072	4.419	3.772	3.405	3.934	4.274
MnO	0.051	0.014	0.050	0.048	0.063	0.008	0.063	0.045	0.033	0.025
MgO	0.475	0.430	0.408	0.415	0.527	0.233	0.448	0.437	0.444	0.332
CaO	0.015	0.003	0.009	0.000	0.008	0.005	0.013	0.003	0.038	0.007
Na2O	0.252	0.275	0.245	0.233	0.223	0.240	0.199	0.224	0.254	0.232
K2O	9.312	9.375	8.994	8.324	8.314	8.900	8.829	8.984	8.474	8.994
SrO	0.000	0.000	0.000	0.000	0.000	0.000	0.000	0.000	0.000	0.000
BaO	0.000	0.000	0.000	0.000	0.000	0.000	0.000	0.000	0.000	0.000
Rb2O	0.000	0.000	0.000	0.000	0.000	0.000	0.000	0.000	0.000	0.000
Cs2O	0.000	0.000	0.000	0.000	0.000	0.000	0.000	0.000	0.000	0.000
Ga2O3	0.000	0.000	0.000	0.000	0.000	0.000	0.000	0.000	0.000	0.000
F	0.000	0.000	0.000	0.000	0.000	0.000	0.000	0.000	0.000	0.000
Cl	0.009	0.048	0.028	0.005	0.009	0.000	0.000	0.006	0.019	0.008
Cr2O3	0.000	0.006	0.008	0.000	0.012	0.010	0.009	0.004	0.042	0.030
NiO	0.000	0.000	0.000	0.000	0.000	0.000	0.000	0.000	0.000	0.000
CuO	0.000	0.000	0.000	0.000	0.000	0.000	0.000	0.000	0.000	0.000
Li2O	0.000	0.000	0.000	0.000	0.000	0.000	0.000	0.000	0.000	0.000
H2O	4.583	4.434	4.493	4.589	4.554	4.513	4.532	4.528	4.472	4.464
Subtotal	101.716	99.068	99.983	101.261	100.746	100.449	100.413	100.278	99.146	99.490
O=F,Cl	0.002	0.011	0.006	0.001	0.002	0.000	0.000	0.001	0.004	0.002
Total	101.714	99.057	99.976	101.260	100.744	100.449	100.413	100.277	99.142	99.489
Si	6.106	6.044	6.106	6.052	6.110	5.991	6.066	6.046	6.115	6.016
Al iv	1.894	1.956	1.894	1.948	1.890	2.009	1.934	1.954	1.885	1.984
Al vi	3.746	3.726	3.714	3.806	3.742	3.765	3.767	3.797	3.735	3.732
Ti	0.010	0.015	0.024	0.026	0.022	0.016	0.015	0.012	0.019	0.020
Cr	0.000	0.001	0.001	0.000	0.001	0.001	0.001	0.000	0.004	0.003
Fe	0.399	0.426	0.444	0.404	0.448	0.491	0.417	0.377	0.441	0.480
Mn	0.006	0.002	0.006	0.005	0.007	0.001	0.007	0.005	0.004	0.003
Mg	0.093	0.087	0.081	0.081	0.103	0.046	0.088	0.086	0.089	0.066
Zn	0.000	0.000	0.000	0.000	0.000	0.000	0.000	0.000	0.000	0.000
Sn	0.000	0.000	0.000	0.000	0.000	0.000	0.000	0.000	0.000	0.000
Ga	0.000	0.000	0.000	0.000	0.000	0.000	0.000	0.000	0.000	0.000
Ni	0.000	0.000	0.000	0.000	0.000	0.000	0.000	0.000	0.000	0.000
Cu	0.000	0.000	0.000	0.000	0.000	0.000	0.000	0.000	0.000	0.000
Li*	0.000	0.000	0.000	0.000	0.000	0.000	0.000	0.000	0.000	0.000
Ca	0.002	0.000	0.001	0.000	0.001	0.001	0.002	0.000	0.005	0.001
Na	0.064	0.072	0.063	0.059	0.057	0.062	0.051	0.057	0.066	0.060
K	1.553	1.613	1.529	1.387	1.396	1.508	1.490	1.517	1.448	1.540
Sr	0.000	0.000	0.000	0.000	0.000	0.000	0.000	0.000	0.000	0.000
Ba	0.000	0.000	0.000	0.000	0.000	0.000	0.000	0.000	0.000	0.000
Rb	0.000	0.000	0.000	0.000	0.000	0.000	0.000	0.000	0.000	0.000
Cs	0.000	0.000	0.000	0.000	0.000	0.000	0.000	0.000	0.000	0.000
OH*	3.998	3.989	3.994	3.999	3.998	4.000	4.000	3.999	3.996	3.998
F	0.000	0.000	0.000	0.000	0.000	0.000	0.000	0.000	0.000	0.000
Cl	0.002	0.011	0.006	0.001	0.002	0.000	0.000	0.001	0.004	0.002
TOTAL	17.872	17.942	17.862	17.768	17.778	17.891	17.839	17.853	17.811	17.905
Fe/Fe+Mg	0.811	0.831	0.846	0.833	0.813	0.914	0.825	0.814	0.832	0.878

Samples	PQ35A	PQ35A	PQ35A	PQ35A	PQ35A	PQ35A	PQ35A	PQ35A	PQ35A	PQ35A	PQ35A	PQ35A	PQ35A
Analysis	2	3	4	5	6	7	9	10	8	13	14	17	12
SiO2	46.364	46.120	48.077	47.447	47.120	46.861	46.714	46.450	47.338	46.825	47.141	46.705	46.799
TiO2	0.983	1.044	0.597	0.376	0.831	0.846	1.035	0.966	0.745	0.845	1.233	1.121	1.122
Al2O3	31.423	30.912	32.926	32.704	32.289	31.883	32.573	31.233	32.085	32.049	32.608	32.336	32.100
FeO	6.875	7.580	5.263	6.288	6.402	6.677	6.896	7.594	5.809	5.750	5.856	6.401	6.656
MnO	0.058	0.065	0.112	0.053	0.054	0.053	0.051	0.075	0.085	0.059	0.055	0.024	0.080
MgO	0.728	0.702	1.173	0.927	0.893	0.724	0.645	0.666	1.114	0.827	0.780	0.627	0.778
CaO	0.012	0.021	0.010	0.017	0.032	0.059	0.004	0.012	0.020	0.011	0.035	0.020	0.000
Na2O	0.141	0.088	0.063	0.098	0.081	0.128	0.135	0.119	0.093	0.093	0.133	0.167	0.121
K2O	8.279	8.741	8.808	8.951	8.669	8.292	8.533	8.136	8.350	8.854	8.064	8.366	8.483
SrO	0.000	0.000	0.000	0.000	0.000	0.000	0.000	0.000	0.000	0.000	0.000	0.000	0.000
BaO	0.000	0.000	0.000	0.000	0.000	0.000	0.000	0.000	0.000	0.000	0.000	0.000	0.000
Rb2O	0.000	0.000	0.000	0.000	0.000	0.000	0.000	0.000	0.000	0.000	0.000	0.000	0.000
Cs2O	0.000	0.000	0.000	0.000	0.000	0.000	0.000	0.000	0.000	0.000	0.000	0.000	0.000
Ga2O3	0.000	0.000	0.000	0.000	0.000	0.000	0.000	0.000	0.000	0.000	0.000	0.000	0.000
F	0.000	0.000	0.000	0.000	0.000	0.000	0.000	0.000	0.000	0.031	0.000	0.000	0.000
Cl	0.028	0.008	0.002	0.005	0.009	0.011	0.006	0.005	0.006	0.008	0.011	0.004	0.005
Cr2O3	0.021	0.000	0.008	0.008	0.000	0.002	0.018	0.007	0.012	0.015	0.037	0.001	0.005
NiO	0.000	0.000	0.000	0.000	0.000	0.000	0.000	0.000	0.000	0.000	0.000	0.000	0.000
CuO	0.000	0.000	0.000	0.000	0.000	0.000	0.000	0.000	0.000	0.000	0.000	0.000	0.000
Li2O	0.000	0.000	0.000	0.000	0.000	0.000	0.000	0.000	0.000	0.000	0.000	0.000	0.000
H2O	4.411	4.402	4.557	4.518	4.494	4.455	4.494	4.423	4.484	4.438	4.501	4.471	4.479
Subtotal	99.324	99.684	101.597	101.390	100.874	99.992	101.103	99.685	100.142	99.804	100.453	100.242	100.627
O=F,Cl	0.006	0.002	0.000	0.001	0.002	0.002	0.001	0.001	0.001	0.015	0.002	0.001	0.001
Total	99.317	99.682	101.597	101.389	100.872	99.990	101.102	99.684	100.141	99.790	100.450	100.241	100.626
Si	6.292	6.279	6.325	6.296	6.285	6.303	6.231	6.296	6.328	6.303	6.276	6.262	6.264
Al iv	1.708	1.721	1.675	1.704	1.715	1.697	1.769	1.704	1.672	1.697	1.724	1.738	1.736
Al vi	3.319	3.240	3.432	3.411	3.361	3.359	3.351	3.286	3.384	3.388	3.393	3.372	3.328
Ti	0.100	0.107	0.059	0.037	0.083	0.086	0.104	0.098	0.075	0.086	0.123	0.113	0.113
Cr	0.002	0.000	0.001	0.001	0.000	0.000	0.002	0.001	0.001	0.002	0.004	0.000	0.001
Fe	0.780	0.863	0.579	0.698	0.714	0.751	0.769	0.861	0.649	0.647	0.652	0.718	0.745
Mn	0.007	0.007	0.013	0.006	0.006	0.006	0.006	0.009	0.010	0.007	0.006	0.003	0.009
Mg	0.147	0.142	0.230	0.183	0.178	0.145	0.128	0.134	0.222	0.166	0.155	0.125	0.155
Zn	0.000	0.000	0.000	0.000	0.000	0.000	0.000	0.000	0.000	0.000	0.000	0.000	0.000
Sn	0.000	0.000	0.000	0.000	0.000	0.000	0.000	0.000	0.000	0.000	0.000	0.000	0.000
Ga	0.000	0.000	0.000	0.000	0.000	0.000	0.000	0.000	0.000	0.000	0.000	0.000	0.000
Ni	0.000	0.000	0.000	0.000	0.000	0.000	0.000	0.000	0.000	0.000	0.000	0.000	0.000
Cu	0.000	0.000	0.000	0.000	0.000	0.000	0.000	0.000	0.000	0.000	0.000	0.000	0.000
Li*	0.000	0.000	0.000	0.000	0.000	0.000	0.000	0.000	0.000	0.000	0.000	0.000	0.000
Ca	0.002	0.003	0.001	0.002	0.005	0.008	0.001	0.002	0.003	0.002	0.005	0.003	0.000
Na	0.037	0.023	0.016	0.025	0.021	0.033	0.035	0.031	0.024	0.024	0.034	0.043	0.031
K	1.433	1.518	1.478	1.515	1.475	1.423	1.452	1.407	1.424	1.520	1.369	1.431	1.448
Sr	0.000	0.000	0.000	0.000	0.000	0.000	0.000	0.000	0.000	0.000	0.000	0.000	0.000
Ba	0.000	0.000	0.000	0.000	0.000	0.000	0.000	0.000	0.000	0.000	0.000	0.000	0.000
Rb	0.000	0.000	0.000	0.000	0.000	0.000	0.000	0.000	0.000	0.000	0.000	0.000	0.000
Cs	0.000	0.000	0.000	0.000	0.000	0.000	0.000	0.000	0.000	0.000	0.000	0.000	0.000
OH*	3.993	3.998	4.000	3.999	3.998	3.998	3.999	3.999	3.999	3.985	3.998	3.999	3.999
F	0.000	0.000	0.000	0.000	0.000	0.000	0.000	0.000	0.000	0.013	0.000	0.000	0.000
Cl	0.007	0.002	0.000	0.001	0.002	0.002	0.001	0.001	0.001	0.002	0.002	0.001	0.001
TOTAL	17.828	17.904	17.809	17.879	17.842	17.811	17.848	17.829	17.792	17.841	17.742	17.807	17.831
Fe/Fe+Mg	0.841	0.858	0.716	0.792	0.801	0.838	0.857	0.865	0.745	0.796	0.808	0.851	0.828

Samples	DOC001	DOC001	DOC001	DOC001	DOC001	DOC001	DOC001	DOC001	PQ35A
Analysis	1	2	3	5	6	7	8	10	16
SiO2	46.063	45.714	45.834	45.898	46.451	46.281	46.729	46.036	47.052
TiO2	0.070	0.121	0.107	0.154	0.158	0.133	0.113	0.091	0.574
Al2O3	38.206	35.509	37.214	36.258	36.738	37.892	37.069	36.887	33.067
FeO	2.717	5.212	3.183	4.011	3.329	3.411	3.707	3.245	6.417
MnO	0.000	0.143	0.010	0.021	0.029	0.024	0.036	0.007	0.084
MgO	0.360	0.392	0.351	0.355	0.342	0.374	0.415	0.257	0.768
CaO	0.012	0.001	0.021	0.007	0.013	0.007	0.001	0.018	0.036
Na2O	0.411	0.129	0.302	0.241	0.326	0.299	0.257	0.341	0.123
K2O	8.932	8.965	9.048	8.833	8.641	8.600	8.520	8.620	8.329
SrO	0.000	0.000	0.000	0.000	0.000	0.000	0.000	0.000	0.000
BaO	0.000	0.000	0.000	0.000	0.000	0.000	0.000	0.000	0.000
Rb2O	0.000	0.000	0.000	0.000	0.000	0.000	0.000	0.000	0.000
Cs2O	0.000	0.000	0.000	0.000	0.000	0.000	0.000	0.000	0.000
Ga2O3	0.000	0.000	0.000	0.000	0.000	0.000	0.000	0.000	0.000
F	0.000	0.000	0.000	0.000	0.000	0.000	0.000	0.000	0.000
Cl	0.008	0.006	0.016	0.015	0.009	0.000	0.000	0.026	0.001
Cr2O3	0.019	0.001	0.011	0.000	0.025	0.001	0.000	0.000	0.005
NiO	0.000	0.000	0.000	0.000	0.000	0.000	0.000	0.000	0.000
CuO	0.000	0.000	0.000	0.000	0.000	0.000	0.000	0.000	0.000
Li2O	0.000	0.000	0.000	0.000	0.000	0.000	0.000	0.000	0.000
H2O	4.597	4.504	4.546	4.518	4.557	4.606	4.595	4.528	4.510
Subtotal	101.395	100.696	100.641	100.312	100.618	101.628	101.441	100.057	100.966
O=F,Cl	0.002	0.001	0.004	0.003	0.002	0.000	0.000	0.006	0.000
Total	101.394	100.695	100.638	100.308	100.616	101.628	101.441	100.052	100.966
Si	6.006	6.084	6.041	6.086	6.109	6.026	6.097	6.087	6.255
Al iv	1.994	1.916	1.959	1.914	1.891	1.974	1.903	1.913	1.745
Al vi	3.878	3.655	3.822	3.753	3.804	3.841	3.799	3.836	3.436
Ti	0.007	0.012	0.011	0.015	0.016	0.013	0.011	0.009	0.057
Cr	0.002	0.000	0.001	0.000	0.003	0.000	0.000	0.000	0.001
Fe	0.296	0.580	0.351	0.445	0.366	0.371	0.405	0.359	0.713
Mn	0.000	0.016	0.001	0.002	0.003	0.003	0.004	0.001	0.009
Mg	0.070	0.078	0.069	0.070	0.067	0.073	0.081	0.051	0.152
Zn	0.000	0.000	0.000	0.000	0.000	0.000	0.000	0.000	0.000
Sn	0.000	0.000	0.000	0.000	0.000	0.000	0.000	0.000	0.000
Ga	0.000	0.000	0.000	0.000	0.000	0.000	0.000	0.000	0.000
Ni	0.000	0.000	0.000	0.000	0.000	0.000	0.000	0.000	0.000
Cu	0.000	0.000	0.000	0.000	0.000	0.000	0.000	0.000	0.000
Li*	0.000	0.000	0.000	0.000	0.000	0.000	0.000	0.000	0.000
Ca	0.002	0.000	0.003	0.001	0.002	0.001	0.000	0.003	0.005
Na	0.104	0.033	0.077	0.062	0.083	0.076	0.065	0.088	0.032
K	1.486	1.522	1.521	1.494	1.450	1.428	1.418	1.454	1.412
Sr	0.000	0.000	0.000	0.000	0.000	0.000	0.000	0.000	0.000
Ba	0.000	0.000	0.000	0.000	0.000	0.000	0.000	0.000	0.000
Rb	0.000	0.000	0.000	0.000	0.000	0.000	0.000	0.000	0.000
Cs	0.000	0.000	0.000	0.000	0.000	0.000	0.000	0.000	0.000
OH*	3.998	3.999	3.997	3.997	3.998	4.000	4.000	3.994	4.000
F	0.000	0.000	0.000	0.000	0.000	0.000	0.000	0.000	0.000
Cl	0.002	0.001	0.003	0.003	0.002	0.000	0.000	0.006	0.000
TOTAL	17.845	17.896	17.856	17.843	17.793	17.806	17.782	17.800	17.819
Fe/Fe+Mg	0.809	0.882	0.836	0.864	0.845	0.837	0.834	0.876	0.824

Samples	DOC111	DOC111	DOC111	DOC111	DOC111	DOC111	DOC111	DOC111
Analysis	1	3	5	8	10	11	12	13
SiO2	46.710	47.014	47.094	47.579	46.437	46.837	46.972	47.080
TiO2	0.296	0.298	0.192	0.329	0.273	0.317	0.317	0.246
Al2O3	36.614	36.427	36.905	36.930	35.972	36.220	37.160	35.329
FeO	1.258	1.194	1.385	1.388	1.286	1.255	1.364	1.466
MnO	0.005	0.004	0.000	0.023	0.008	0.000	0.010	0.011
MgO	0.752	0.897	0.929	0.851	0.847	0.809	0.780	0.948
CaO	0.015	0.006	0.020	0.005	0.022	0.039	0.026	0.028
Na2O	0.607	0.519	0.513	0.522	0.505	0.546	0.541	0.654
K2O	9.394	8.665	9.603	9.082	9.076	8.635	9.325	9.960
SrO	0.000	0.000	0.000	0.000	0.000	0.000	0.000	0.000
BaO	0.000	0.000	0.000	0.000	0.000	0.000	0.000	0.000
Rb2O	0.000	0.000	0.000	0.000	0.000	0.000	0.000	0.000
Cs2O	0.000	0.000	0.000	0.000	0.000	0.000	0.000	0.000
Ga2O3	0.000	0.000	0.000	0.000	0.000	0.000	0.000	0.000
F	0.091	0.091	0.042	0.146	0.212	0.166	0.083	0.219
Cl	0.000	0.000	0.000	0.001	0.005	0.003	0.000	0.000
Cr2O3	0.033	0.033	0.007	0.004	0.009	0.017	0.026	0.026
NiO	0.000	0.000	0.000	0.000	0.000	0.000	0.000	0.000
CuO	0.000	0.000	0.000	0.000	0.000	0.000	0.000	0.000
Li2O	0.000	0.000	0.000	0.000	0.000	0.000	0.000	0.000
H2O	4.520	4.517	4.584	4.556	4.410	4.460	4.566	4.440
Subtotal	100.296	99.666	101.274	101.416	99.063	99.304	101.170	100.405
O=F,Cl	0.038	0.038	0.018	0.062	0.091	0.070	0.035	0.092
Total	100.258	99.628	101.256	101.354	98.972	99.233	101.135	100.313
Si	6.138	6.183	6.133	6.168	6.171	6.187	6.116	6.214
Al iv	1.862	1.817	1.867	1.832	1.829	1.813	1.884	1.786
Al vi	3.809	3.829	3.799	3.811	3.806	3.827	3.819	3.710
Ti	0.029	0.029	0.019	0.032	0.027	0.031	0.031	0.024
Cr	0.003	0.003	0.001	0.000	0.001	0.002	0.003	0.003
Fe	0.138	0.131	0.151	0.151	0.143	0.139	0.149	0.162
Mn	0.001	0.000	0.000	0.002	0.001	0.000	0.001	0.001
Mg	0.147	0.176	0.180	0.164	0.168	0.159	0.151	0.187
Zn	0.000	0.000	0.000	0.000	0.000	0.000	0.000	0.000
Sn	0.000	0.000	0.000	0.000	0.000	0.000	0.000	0.000
Ga	0.000	0.000	0.000	0.000	0.000	0.000	0.000	0.000
Ni	0.000	0.000	0.000	0.000	0.000	0.000	0.000	0.000
Cu	0.000	0.000	0.000	0.000	0.000	0.000	0.000	0.000
Li*	0.000	0.000	0.000	0.000	0.000	0.000	0.000	0.000
Ca	0.002	0.001	0.003	0.001	0.003	0.006	0.004	0.004
Na	0.155	0.132	0.130	0.131	0.130	0.140	0.137	0.167
K	1.575	1.453	1.595	1.502	1.539	1.455	1.549	1.677
Sr	0.000	0.000	0.000	0.000	0.000	0.000	0.000	0.000
Ba	0.000	0.000	0.000	0.000	0.000	0.000	0.000	0.000
Rb	0.000	0.000	0.000	0.000	0.000	0.000	0.000	0.000
Cs	0.000	0.000	0.000	0.000	0.000	0.000	0.000	0.000
OH*	3.962	3.962	3.983	3.940	3.910	3.930	3.966	3.909
F	0.038	0.038	0.017	0.060	0.089	0.069	0.034	0.091
Cl	0.000	0.000	0.000	0.000	0.001	0.001	0.000	0.000
TOTAL	17.860	17.756	17.877	17.795	17.818	17.758	17.843	17.935
Fe/Fe+Mg	0.484	0.427	0.455	0.478	0.460	0.465	0.495	0.464

Samples	DOC065	DOC065	DOC065	DOC065	DOC065	DOC065	DOC065	DOC065	DOC065	DOC065	DOC065	DOC065
Analysis	1	3	4	5	6	7	9	10	11	12	13	14
SiO2	47.283	46.904	47.792	48.349	48.315	47.628	47.152	47.206	48.027	48.040	47.659	48.462
TiO2	0.762	0.557	0.687	0.782	0.484	0.778	0.462	0.798	0.565	0.614	0.637	0.421
Al2O3	28.335	28.587	29.420	28.699	28.916	28.780	28.882	28.465	28.891	28.611	28.853	28.665
FeO	5.793	5.706	5.787	5.640	5.434	5.693	5.673	5.868	5.597	5.543	5.927	5.545
MnO	0.096	0.188	0.060	0.151	0.180	0.074	0.054	0.087	0.040	0.162	0.078	0.203
MgO	2.171	2.370	2.160	2.471	2.395	2.371	2.301	2.147	2.307	2.475	2.389	2.584
CaO	0.020	0.035	0.022	0.000	0.001	0.000	0.034	0.000	0.022	0.000	0.003	0.013
Na2O	0.131	0.133	0.165	0.154	0.118	0.092	0.110	0.133	0.112	0.128	0.112	0.099
K2O	10.632	10.083	10.610	10.531	10.353	10.615	10.608	10.809	10.340	10.884	10.875	10.939
SrO	0.000	0.000	0.000	0.000	0.000	0.000	0.000	0.000	0.000	0.000	0.000	0.000
BaO	0.000	0.000	0.000	0.000	0.000	0.000	0.000	0.000	0.000	0.000	0.000	0.000
Rb2O	0.000	0.000	0.000	0.000	0.000	0.000	0.000	0.000	0.000	0.000	0.000	0.000
Cs2O	0.000	0.000	0.000	0.000	0.000	0.000	0.000	0.000	0.000	0.000	0.000	0.000
Ga2O3	0.000	0.000	0.000	0.000	0.000	0.000	0.000	0.000	0.000	0.000	0.000	0.000
F	0.000	0.000	0.000	0.000	0.000	0.000	0.000	0.000	0.019	0.000	0.000	0.000
Cl	0.019	0.008	0.009	0.003	0.000	0.003	0.001	0.000	0.021	0.001	0.008	0.003
Cr2O3	0.021	0.013	0.000	0.055	0.010	0.018	0.025	0.023	0.000	0.009	0.013	0.010
NiO	0.000	0.000	0.000	0.000	0.000	0.000	0.000	0.000	0.000	0.000	0.000	0.000
CuO	0.000	0.000	0.000	0.000	0.000	0.000	0.000	0.000	0.000	0.000	0.000	0.000
Li2O	0.000	0.000	0.000	0.000	0.000	0.000	0.000	0.000	0.000	0.000	0.000	0.000
H2O	4.381	4.366	4.459	4.471	4.456	4.430	4.394	4.393	4.425	4.446	4.439	4.469
Subtotal	99.644	98.950	101.171	101.305	100.662	100.480	99.696	99.930	100.363	100.914	100.992	101.414
O=F,Cl	0.004	0.002	0.002	0.001	0.000	0.001	0.000	0.000	0.013	0.000	0.002	0.001
Total	99.639	98.948	101.169	101.305	100.662	100.480	99.695	99.930	100.350	100.913	100.990	101.413
Si	6.464	6.439	6.423	6.483	6.502	6.446	6.434	6.444	6.488	6.479	6.435	6.501
Al iv	1.536	1.561	1.577	1.517	1.498	1.554	1.566	1.556	1.512	1.521	1.565	1.499
Al vi	3.030	3.064	3.084	3.019	3.089	3.038	3.080	3.023	3.088	3.027	3.027	3.034
Ti	0.078	0.057	0.069	0.079	0.049	0.079	0.047	0.082	0.057	0.062	0.065	0.042
Cr	0.002	0.001	0.000	0.006	0.001	0.002	0.003	0.002	0.000	0.001	0.001	0.001
Fe	0.662	0.655	0.651	0.632	0.612	0.644	0.647	0.670	0.632	0.625	0.669	0.622
Mn	0.011	0.022	0.007	0.017	0.021	0.008	0.006	0.010	0.005	0.019	0.009	0.023
Mg	0.442	0.485	0.433	0.494	0.480	0.478	0.468	0.437	0.464	0.498	0.481	0.517
Zn	0.000	0.000	0.000	0.000	0.000	0.000	0.000	0.000	0.000	0.000	0.000	0.000
Sn	0.000	0.000	0.000	0.000	0.000	0.000	0.000	0.000	0.000	0.000	0.000	0.000
Ga	0.000	0.000	0.000	0.000	0.000	0.000	0.000	0.000	0.000	0.000	0.000	0.000
Ni	0.000	0.000	0.000	0.000	0.000	0.000	0.000	0.000	0.000	0.000	0.000	0.000
Cu	0.000	0.000	0.000	0.000	0.000	0.000	0.000	0.000	0.000	0.000	0.000	0.000
Li*	0.000	0.000	0.000	0.000	0.000	0.000	0.000	0.000	0.000	0.000	0.000	0.000
Ca	0.003	0.005	0.003	0.000	0.000	0.000	0.005	0.000	0.003	0.000	0.000	0.002
Na	0.035	0.035	0.043	0.040	0.031	0.024	0.029	0.035	0.029	0.033	0.029	0.026
K	1.854	1.765	1.819	1.801	1.777	1.833	1.846	1.882	1.782	1.872	1.873	1.872
Sr	0.000	0.000	0.000	0.000	0.000	0.000	0.000	0.000	0.000	0.000	0.000	0.000
Ba	0.000	0.000	0.000	0.000	0.000	0.000	0.000	0.000	0.000	0.000	0.000	0.000
Rb	0.000	0.000	0.000	0.000	0.000	0.000	0.000	0.000	0.000	0.000	0.000	0.000
Cs	0.000	0.000	0.000	0.000	0.000	0.000	0.000	0.000	0.000	0.000	0.000	0.000
OH*	3.996	3.998	3.998	3.999	4.000	3.999	4.000	4.000	3.987	4.000	3.998	3.999
F	0.000	0.000	0.000	0.000	0.000	0.000	0.000	0.000	0.008	0.000	0.000	0.000
Cl	0.004	0.002	0.002	0.001	0.000	0.001	0.000	0.000	0.005	0.000	0.002	0.001
TOTAL	18.118	18.091	18.108	18.088	18.059	18.106	18.132	18.142	18.060	18.137	18.155	18.138
Fe/Fe+Mg	0.600	0.575	0.600	0.561	0.560	0.574	0.580	0.605	0.577	0.557	0.582	0.546

Samples	DOC164	DOC164	DOC164	DOC164	DOC164	DOC164	DOC164	DOC164	DOC163	DOC163	DOC163	DOC065
Analysis	10	8	9	7	6	4	3	1	10	2	1	15
SiO2	46.044	46.309	45.773	45.984	45.877	45.158	45.792	46.304	45.578	45.682	45.563	48.212
TiO2	0.294	0.161	0.254	0.293	0.240	0.276	0.152	0.167	0.019	0.074	0.075	0.345
Al2O3	33.112	35.097	33.881	34.479	34.637	33.741	35.045	35.201	36.099	36.370	37.048	29.083
FeO	5.169	4.084	4.009	4.168	4.244	4.350	3.953	3.828	2.677	2.725	2.483	5.491
MnO	0.060	0.052	0.047	0.051	0.061	0.032	0.067	0.025	0.009	0.011	0.007	0.059
MgO	0.816	0.617	0.583	0.572	0.655	0.561	0.608	0.615	0.268	0.252	0.259	2.420
CaO	0.000	0.006	0.017	0.000	0.003	0.000	0.000	0.000	0.015	0.002	0.030	0.032
Na2O	0.215	0.293	0.237	0.270	0.274	0.263	0.290	0.335	0.448	0.446	0.552	0.123
K2O	10.640	10.187	10.414	10.125	10.599	10.454	10.629	10.427	10.548	10.651	10.441	10.765
SrO	0.000	0.000	0.000	0.000	0.000	0.000	0.000	0.000	0.000	0.000	0.000	0.000
BaO	0.000	0.000	0.000	0.000	0.000	0.000	0.000	0.000	0.000	0.000	0.000	0.000
Rb2O	0.000	0.000	0.000	0.000	0.000	0.000	0.000	0.000	0.000	0.000	0.000	0.000
Cs2O	0.000	0.000	0.000	0.000	0.000	0.000	0.000	0.000	0.000	0.000	0.000	0.000
Ga2O3	0.000	0.000	0.000	0.000	0.000	0.000	0.000	0.000	0.000	0.000	0.000	0.000
F	0.000	0.000	0.000	0.000	0.000	0.000	0.000	0.000	0.000	0.000	0.000	0.000
Cl	0.001	0.008	0.059	0.008	0.000	0.041	0.017	0.002	0.006	0.026	0.003	0.000
Cr2O3	0.003	0.000	0.026	0.013	0.010	0.007	0.010	0.008	0.014	0.000	0.017	0.013
NiO	0.000	0.000	0.000	0.000	0.000	0.000	0.000	0.000	0.000	0.000	0.000	0.000
CuO	0.000	0.000	0.000	0.000	0.000	0.000	0.000	0.000	0.000	0.000	0.000	0.000
Li2O	0.000	0.000	0.000	0.000	0.000	0.000	0.000	0.000	0.000	0.000	0.000	0.000
H2O	4.461	4.525	4.428	4.481	4.496	4.400	4.496	4.530	4.492	4.509	4.536	4.460
Subtotal	100.815	101.338	99.728	100.443	101.096	99.283	101.059	101.442	100.173	100.747	101.014	101.004
O=F,Cl	0.000	0.002	0.013	0.002	0.000	0.009	0.004	0.000	0.001	0.006	0.001	0.000
Total	100.814	101.336	99.714	100.442	101.096	99.274	101.055	101.441	100.172	100.741	101.014	101.004
Si	6.189	6.134	6.177	6.150	6.118	6.139	6.101	6.129	6.083	6.066	6.022	6.481
Al iv	1.811	1.866	1.823	1.850	1.882	1.861	1.899	1.871	1.917	1.934	1.978	1.519
Al vi	3.436	3.614	3.567	3.586	3.562	3.546	3.605	3.620	3.761	3.759	3.793	3.090
Ti	0.030	0.016	0.026	0.029	0.024	0.028	0.015	0.017	0.002	0.007	0.007	0.035
Cr	0.000	0.000	0.003	0.001	0.001	0.001	0.001	0.001	0.002	0.000	0.002	0.001
Fe	0.581	0.452	0.452	0.466	0.473	0.495	0.440	0.424	0.299	0.303	0.275	0.617
Mn	0.007	0.006	0.005	0.006	0.007	0.004	0.008	0.003	0.001	0.001	0.001	0.007
Mg	0.164	0.122	0.117	0.114	0.130	0.114	0.121	0.121	0.053	0.050	0.051	0.485
Zn	0.000	0.000	0.000	0.000	0.000	0.000	0.000	0.000	0.000	0.000	0.000	0.000
Sn	0.000	0.000	0.000	0.000	0.000	0.000	0.000	0.000	0.000	0.000	0.000	0.000
Ga	0.000	0.000	0.000	0.000	0.000	0.000	0.000	0.000	0.000	0.000	0.000	0.000
Ni	0.000	0.000	0.000	0.000	0.000	0.000	0.000	0.000	0.000	0.000	0.000	0.000
Cu	0.000	0.000	0.000	0.000	0.000	0.000	0.000	0.000	0.000	0.000	0.000	0.000
Li*	0.000	0.000	0.000	0.000	0.000	0.000	0.000	0.000	0.000	0.000	0.000	0.000
Ca	0.000	0.001	0.002	0.000	0.000	0.000	0.000	0.000	0.002	0.000	0.004	0.005
Na	0.056	0.075	0.062	0.070	0.071	0.069	0.075	0.086	0.116	0.115	0.141	0.032
K	1.824	1.721	1.793	1.727	1.803	1.813	1.806	1.760	1.796	1.804	1.760	1.846
Sr	0.000	0.000	0.000	0.000	0.000	0.000	0.000	0.000	0.000	0.000	0.000	0.000
Ba	0.000	0.000	0.000	0.000	0.000	0.000	0.000	0.000	0.000	0.000	0.000	0.000
Rb	0.000	0.000	0.000	0.000	0.000	0.000	0.000	0.000	0.000	0.000	0.000	0.000
Cs	0.000	0.000	0.000	0.000	0.000	0.000	0.000	0.000	0.000	0.000	0.000	0.000
OH*	4.000	3.998	3.987	3.998	4.000	3.991	3.996	4.000	3.999	3.994	3.999	4.000
F	0.000	0.000	0.000	0.000	0.000	0.000	0.000	0.000	0.000	0.000	0.000	0.000
Cl	0.000	0.002	0.013	0.002	0.000	0.009	0.004	0.000	0.001	0.006	0.001	0.000
TOTAL	18.098	18.008	18.028	18.000	18.072	18.070	18.072	18.032	18.031	18.039	18.035	18.118
Fe/Fe+Mg	0.780	0.788	0.794	0.804	0.784	0.813	0.785	0.777	0.849	0.858	0.843	0.560

Samples	DOC163	DOC163	DOC163	DOC163
Analysis	5	6	7	8
SiO2	45.521	45.192	45.864	45.491
TiO2	0.034	0.062	0.041	0.009
Al2O3	36.632	35.590	36.753	37.220
FeO	2.748	3.316	3.158	2.682
MnO	0.012	0.019	0.022	0.008
MgO	0.216	0.370	0.285	0.233
CaO	0.000	0.002	0.004	0.003
Na2O	0.451	0.335	0.417	0.427
K2O	10.432	10.425	10.362	10.417
SrO	0.000	0.000	0.000	0.000
BaO	0.000	0.000	0.000	0.000
Rb2O	0.000	0.000	0.000	0.000
Cs2O	0.000	0.000	0.000	0.000
Ga2O3	0.000	0.000	0.000	0.000
F	0.000	0.000	0.000	0.000
Cl	0.005	0.000	0.000	0.000
Cr2O3	0.001	0.007	0.000	0.000
NiO	0.000	0.000	0.000	0.000
CuO	0.000	0.000	0.000	0.000
Li2O	0.000	0.000	0.000	0.000
H2O	4.512	4.463	4.548	4.537
Subtotal	100.562	99.782	101.455	101.027
O=F,Cl	0.001	0.000	0.000	0.000
Total	100.560	99.782	101.455	101.027
Si	6.048	6.072	6.047	6.012
Al iv	1.952	1.928	1.953	1.988
Al vi	3.785	3.709	3.758	3.810
Ti	0.003	0.006	0.004	0.001
Cr	0.000	0.001	0.000	0.000
Fe	0.305	0.373	0.348	0.296
Mn	0.001	0.002	0.002	0.001
Mg	0.043	0.074	0.056	0.046
Zn	0.000	0.000	0.000	0.000
Sn	0.000	0.000	0.000	0.000
Ga	0.000	0.000	0.000	0.000
Ni	0.000	0.000	0.000	0.000
Cu	0.000	0.000	0.000	0.000
Li*	0.000	0.000	0.000	0.000
Ca	0.000	0.000	0.001	0.000
Na	0.116	0.087	0.107	0.109
K	1.768	1.787	1.742	1.756
Sr	0.000	0.000	0.000	0.000
Ba	0.000	0.000	0.000	0.000
Rb	0.000	0.000	0.000	0.000
Cs	0.000	0.000	0.000	0.000
OH*	3.999	4.000	4.000	4.000
F	0.000	0.000	0.000	0.000
Cl	0.001	0.000	0.000	0.000
TOTAL	18.022	18.040	18.018	18.021
Fe/Fe+Mg	0.877	0.834	0.861	0.866

Sample	PQ12309	PQ12309	PQ12309	PQ12309	PQ12309	PQ12309	PQ12309	PQ12309	PQ12309
Analysis	1	2	3	4	5	6	7	8	9
SiO2	45.33	46.59	44.13	45.29	45.92	46.15	47.37	44.74	47.13
TiO2	0.64	0.42	0.57	0.54	0.55	0.50	0.03	0.65	0.54
Al2O3	32.14	31.68	30.78	32.11	31.51	31.79	35.24	32.30	31.71
Cr2O3	0.01	0.01	0.07	0.03	0.02	0.01	0.00	0.06	0.00
FeO	3.82	3.71	4.01	4.36	4.43	4.63	2.05	3.53	4.15
MnO	0.01	0.02	0.02	0.02	0.01	0.03	0.00	0.00	0.01
MgO	1.46	1.78	1.59	1.46	1.87	1.97	1.07	1.40	1.63
CaO	0.00	0.00	0.00	0.02	0.06	0.00	0.03	0.03	0.02
Na2O	0.66	0.60	0.58	0.55	0.57	0.61	0.68	0.70	0.40
K2O	10.12	10.39	10.57	10.46	10.39	10.53	10.51	10.03	10.52
ZnO	0.00	0.00	0.00	0.00	0.00	0.00	0.00	0.00	0.00
Cl	0.00	0.00	0.01	0.00	0.00	0.00	0.01	0.01	0.00
F	0.00	0.00	0.00	0.00	0.00	0.00	0.00	0.00	0.00
Sub-Total	94.20	95.20	92.32	94.84	95.33	96.21	96.97	93.45	96.12
-O equiv. Cl	0.00	0.00	0.00	0.00	0.00	0.00	0.00	0.00	0.00
-O equiv. F	0.00	0.00	0.00	0.00	0.00	0.00	0.00	0.00	0.00
Total	94.20	95.20	92.32	94.84	95.33	96.21	96.97	93.45	96.12
num ox	22.00	22.00	22.00	22.00	22.00	22.00	22.00	22.00	23.00
Si	6.20	6.30	6.20	6.18	6.23	6.21	6.21	6.16	6.60
Ti	0.07	0.04	0.06	0.06	0.06	0.05	0.00	0.07	0.06
Al	5.18	5.05	5.10	5.16	5.04	5.05	5.45	5.24	5.24
Cr	0.00	0.00	0.01	0.00	0.00	0.00	0.00	0.01	0.00
Fe	0.44	0.42	0.47	0.50	0.50	0.52	0.22	0.41	0.49
Mn	0.00	0.00	0.00	0.00	0.00	0.00	0.00	0.00	0.00
Mg	0.30	0.36	0.33	0.30	0.38	0.40	0.21	0.29	0.34
Ca	0.00	0.00	0.00	0.00	0.01	0.00	0.00	0.00	0.00
Na	0.18	0.16	0.16	0.14	0.15	0.16	0.17	0.19	0.11
K	1.77	1.79	1.89	1.82	1.80	1.81	1.76	1.76	1.88
Zn	0.00	0.00	0.00	0.00	0.00	0.00	0.00	0.00	0.00
Cl	0.00	0.00	0.00	0.00	0.00	0.00	0.00	0.00	0.00
F	0.00	0.00	0.00	0.00	0.00	0.00	0.00	0.00	0.00
Total	14.12	14.11	14.22	14.17	14.17	14.20	14.03	14.12	14.72
XFe	0.18	0.18	0.19	0.20	0.20	0.21	0.10	0.17	0.20
XNa	0.07	0.07	0.06	0.06	0.06	0.06	0.08	0.08	0.04
XK	0.74	0.76	0.75	0.74	0.73	0.73	0.82	0.75	0.76

Sample	PQ12309	PQ12309	PQ12309	PQ12309	PQ12309	PQ12309	PQ12309	PQ12309
Analysis	10	12	13	14	15	16	17	18
SiO2	45.31	46.65	47.01	46.05	43.96	46.89	46.17	46.63
TiO2	0.64	0.64	0.73	0.74	0.78	0.61	0.68	0.63
Al2O3	32.88	31.68	31.46	32.20	30.40	31.94	32.18	32.45
Cr2O3	0.01	0.05	0.04	0.08	0.11	0.03	0.01	0.05
FeO	3.45	4.13	4.14	3.79	4.55	4.07	3.68	4.03
MnO	0.00	0.01	0.01	0.01	0.00	0.01	0.01	0.00
MgO	1.27	1.53	1.62	1.52	1.73	1.45	1.50	1.43
CaO	0.00	0.03	0.00	0.00	0.01	0.00	0.00	0.02
Na2O	0.71	0.35	0.50	0.65	0.43	0.44	0.68	0.54
K2O	10.14	10.76	10.23	10.28	10.62	10.59	10.00	10.44
ZnO	0.00	0.00	0.00	0.00	0.00	0.00	0.00	0.00
Cl	0.00	0.00	0.00	0.00	0.00	0.00	0.00	0.00
F	0.00	0.02	0.00	0.00	0.03	0.00	0.00	0.00
Sub-Total	94.42	95.82	95.73	95.32	92.59	96.02	94.92	96.21
-O equiv. Cl	0.00	0.00	0.00	0.00	0.00	0.00	0.00	0.00
-O equiv. F	0.00	0.01	0.00	0.00	0.01	0.00	0.00	0.00
Total	94.42	95.83	95.73	95.32	92.60	96.02	94.92	96.21
num ox	22.00	22.00	23.00	22.00	22.00	22.00	22.00	22.00
Si	6.17	6.28	6.60	6.22	6.18	6.29	6.24	6.24
Ti	0.07	0.06	0.08	0.07	0.08	0.06	0.07	0.06
Al	5.27	5.03	5.21	5.13	5.04	5.05	5.13	5.12
Cr	0.00	0.01	0.00	0.01	0.01	0.00	0.00	0.00
Fe	0.39	0.47	0.49	0.43	0.53	0.46	0.42	0.45
Mn	0.00	0.00	0.00	0.00	0.00	0.00	0.00	0.00
Mg	0.26	0.31	0.34	0.31	0.36	0.29	0.30	0.29
Ca	0.00	0.00	0.00	0.00	0.00	0.00	0.00	0.00
Na	0.19	0.09	0.14	0.17	0.12	0.11	0.18	0.14
K	1.76	1.85	1.83	1.77	1.90	1.81	1.73	1.78
Zn	0.00	0.00	0.00	0.00	0.00	0.00	0.00	0.00
Cl	0.00	0.00	0.00	0.00	0.00	0.00	0.00	0.00
F	0.00	0.00	0.00	0.00	0.00	0.00	0.00	0.00
Total	14.11	14.10	14.69	14.11	14.23	14.08	14.07	14.09
XFe	0.17	0.19	0.20	0.18	0.21	0.19	0.18	0.19
XNa	0.08	0.04	0.06	0.07	0.05	0.05	0.08	0.06
XK	0.75	0.77	0.75	0.75	0.74	0.76	0.74	0.75

Sample	PQ12280	PQ12280	PQ12280	PQ12280	PQ12280	PQ12280	PQ12280	PQ12280	PQ12280	PQ12280	PQ12280
Analysis	1	2	3	5	4	6	7	8	9	10	11
SiO2	46.99	44.79	46.49	43.84	44.58	44.29	44.33	44.01	45.63	46.47	44.50
TiO2	0.56	0.52	0.57	0.59	0.57	0.55	0.50	0.54	0.37	0.54	0.48
Al2O3	30.34	31.30	31.92	30.90	30.79	31.28	30.36	30.63	31.44	30.86	31.07
Cr2O3	0.02	0.02	0.00	0.02	0.02	0.02	0.01	0.03	0.02	0.01	0.03
FeO	4.62	4.18	4.25	4.29	4.36	4.18	4.41	4.27	4.43	4.37	4.33
MnO	0.01	0.00	0.02	0.00	0.00	0.01	0.02	0.00	0.01	0.03	0.00
MgO	1.73	1.49	1.42	1.40	1.53	1.45	1.61	1.50	1.47	1.73	1.64
CaO	0.04	0.02	0.00	0.00	0.00	0.01	0.01	0.00	0.00	0.00	0.03
Na2O	0.33	0.58	0.65	0.68	0.46	0.57	0.41	0.63	0.57	0.44	0.52
K2O	10.79	10.20	10.31	10.19	10.61	10.42	10.46	10.39	10.36	10.70	10.37
ZnO	0.00	0.00	0.00	0.00	0.00	0.00	0.00	0.00	0.00	0.00	0.00
Cl	0.01	0.01	0.00	0.00	0.00	0.00	0.00	0.01	0.00	0.00	0.01
F	0.01	0.02	0.02	0.00	0.02	0.00	0.00	0.00	0.06	0.00	0.00
Sub-Total	95.43	93.09	95.63	91.91	92.91	92.80	92.11	92.00	94.29	95.16	92.97
-O equiv. Cl	0.00	0.00	0.00	0.00	0.00	0.00	0.00	0.00	0.00	0.00	0.00
-O equiv. F	0.00	0.01	0.01	0.00	0.01	0.00	0.00	0.00	0.02	0.00	0.00
Total	95.43	93.10	95.64	91.91	92.92	92.80	92.11	92.00	94.32	95.16	92.97
num ox	22.00	22.00	23.00	22.00	22.00	22.00	22.00	22.00	22.00	22.00	22.00
Si	6.37	6.21	6.55	6.18	6.22	6.18	6.24	6.20	6.25	6.32	6.20
Ti	0.06	0.05	0.06	0.06	0.06	0.06	0.05	0.06	0.04	0.06	0.05
Al	4.85	5.12	5.30	5.14	5.07	5.15	5.04	5.09	5.08	4.94	5.10
Cr	0.00	0.00	0.00	0.00	0.00	0.00	0.00	0.00	0.00	0.00	0.00
Fe	0.52	0.49	0.50	0.51	0.51	0.49	0.52	0.50	0.51	0.50	0.50
Mn	0.00	0.00	0.00	0.00	0.00	0.00	0.00	0.00	0.00	0.00	0.00
Mg	0.35	0.31	0.30	0.30	0.32	0.30	0.34	0.32	0.30	0.35	0.34
Ca	0.01	0.00	0.00	0.00	0.00	0.00	0.00	0.00	0.00	0.00	0.00
Na	0.09	0.16	0.18	0.19	0.12	0.16	0.11	0.17	0.15	0.12	0.14
K	1.87	1.81	1.85	1.83	1.89	1.86	1.88	1.87	1.81	1.86	1.84
Zn	0.00	0.00	0.00	0.00	0.00	0.00	0.00	0.00	0.00	0.00	0.00
Cl	0.00	0.00	0.00	0.00	0.00	0.00	0.00	0.00	0.00	0.00	0.00
F	0.00	0.00	0.00	0.00	0.00	0.00	0.00	0.00	0.01	0.00	0.00
Total	14.12	14.15	14.75	14.20	14.19	14.19	14.18	14.21	14.15	14.14	14.19
XFe	0.21	0.20	0.20	0.20	0.20	0.20	0.21	0.20	0.21	0.20	0.20
XNa	0.03	0.06	0.07	0.07	0.05	0.06	0.04	0.07	0.06	0.05	0.06
XK	0.75	0.74	0.73	0.73	0.75	0.74	0.75	0.73	0.73	0.75	0.74

Sample	PQ12302	PQ12302	PQ12302	PQ12302	PQ12302	PQ12302	PQ12302
Analysis	1	2	3	4	5	6	8
SiO2	47.35	47.09	47.32	47.23	46.73	46.59	44.07
TiO2	0.37	0.52	0.43	0.41	0.44	0.53	0.54
Al2O3	32.45	33.01	32.26	31.83	31.92	32.34	32.29
Cr2O3	0.06	0.03	0.00	0.02	0.00	0.02	0.00
FeO	3.92	3.96	4.02	4.15	4.18	4.26	4.20
MnO	0.01	0.02	0.00	0.00	0.00	0.03	0.01
MgO	1.70	1.53	1.67	1.69	1.66	1.41	1.36
CaO	0.00	0.00	0.00	0.00	0.00	0.00	0.00
Na2O	0.51	0.58	0.46	0.47	0.35	0.42	0.40
K2O	10.15	10.26	9.80	10.48	10.33	10.22	10.00
ZnO	0.00	0.00	0.00	0.00	0.00	0.00	0.00
Cl	0.01	0.01	0.00	0.00	0.01	0.00	0.00
F	0.00	0.00	0.00	0.00	0.00	0.00	0.00
Sub-Total	96.52	97.00	95.96	96.26	95.62	95.83	92.86
-O equiv. Cl	0.00	0.00	0.00	0.00	0.00	0.00	0.00
-O equiv. F	0.00	0.00	0.00	0.00	0.00	0.00	0.00
Total	96.52	97.00	95.96	96.26	95.62	95.83	92.86
num ox	22.00	23.00	22.00	22.00	22.00	22.00	22.00
Si	6.29	6.52	6.31	6.32	6.29	6.26	6.12
Ti	0.04	0.05	0.04	0.04	0.04	0.05	0.06
Al	5.09	5.39	5.07	5.02	5.06	5.12	5.29
Cr	0.01	0.00	0.00	0.00	0.00	0.00	0.00
Fe	0.44	0.46	0.45	0.46	0.47	0.48	0.49
Mn	0.00	0.00	0.00	0.00	0.00	0.00	0.00
Mg	0.34	0.32	0.33	0.34	0.33	0.28	0.28
Ca	0.00	0.00	0.00	0.00	0.00	0.00	0.00
Na	0.13	0.15	0.12	0.12	0.09	0.11	0.11
K	1.72	1.81	1.67	1.79	1.77	1.75	1.77
Zn	0.00	0.00	0.00	0.00	0.00	0.00	0.00
Cl	0.00	0.00	0.00	0.00	0.00	0.00	0.00
F	0.00	0.00	0.00	0.00	0.00	0.00	0.00
Total	14.05	14.71	14.00	14.09	14.07	14.06	14.12
XFe	0.19	0.19	0.20	0.20	0.20	0.20	0.21
XNa	0.06	0.06	0.05	0.05	0.04	0.05	0.05
XK	0.75	0.75	0.75	0.75	0.76	0.75	0.75

Sample	PQ12302	PQ12302	PQ12302	PQ12302	PQ12302	PQ12302	PQ12302	PQ12302
Analysis	7	9	11	10	12	13	14	15
SiO2	46.66	47.26	47.65	47.89	46.89	46.63	46.84	47.19
TiO2	0.58	0.50	0.39	0.49	0.56	0.52	0.39	0.52
Al2O3	31.05	31.96	32.18	31.99	32.15	32.73	32.40	32.34
Cr2O3	0.00	0.01	0.00	0.01	0.02	0.00	0.00	0.05
FeO	5.67	4.32	4.01	4.00	4.77	4.07	3.95	4.06
MnO	0.00	0.00	0.00	0.01	0.00	0.02	0.00	0.01
MgO	1.69	1.63	1.70	1.76	1.47	1.57	1.59	1.64
CaO	0.00	0.00	0.00	0.00	0.00	0.00	0.00	0.00
Na2O	0.24	0.41	0.55	0.44	0.29	0.58	0.52	0.49
K2O	10.23	10.25	10.46	10.64	10.55	10.01	10.35	10.11
ZnO	0.00	0.00	0.00	0.00	0.00	0.00	0.00	0.00
Cl	0.01	0.00	0.00	0.01	0.00	0.00	0.00	0.00
F	0.00	0.00	0.00	0.05	0.00	0.00	0.00	0.00
Sub-Total	96.12	96.35	96.94	97.22	96.71	96.13	96.05	96.40
-O equiv. Cl	0.00	0.00	0.00	0.00	0.00	0.00	0.00	0.00
-O equiv. F	0.00	0.00	0.00	0.02	0.00	0.00	0.00	0.00
Total	96.13	96.35	96.94	97.24	96.71	96.13	96.05	96.40
num ox	22.00	22.00	22.00	22.00	22.00	22.00	23.00	22.00
Si	6.29	6.31	6.32	6.33	6.26	6.23	6.56	6.29
Ti	0.06	0.05	0.04	0.05	0.06	0.05	0.04	0.05
Al	4.94	5.03	5.03	4.99	5.06	5.16	5.35	5.08
Cr	0.00	0.00	0.00	0.00	0.00	0.00	0.00	0.01
Fe	0.64	0.48	0.44	0.44	0.53	0.46	0.46	0.45
Mn	0.00	0.00	0.00	0.00	0.00	0.00	0.00	0.00
Mg	0.34	0.32	0.34	0.35	0.29	0.31	0.33	0.33
Ca	0.00	0.00	0.00	0.00	0.00	0.00	0.00	0.00
Na	0.06	0.11	0.14	0.11	0.08	0.15	0.14	0.13
K	1.76	1.75	1.77	1.80	1.80	1.71	1.85	1.72
Zn	0.00	0.00	0.00	0.00	0.00	0.00	0.00	0.00
Cl	0.00	0.00	0.00	0.00	0.00	0.00	0.00	0.00
F	0.00	0.00	0.00	0.01	0.00	0.00	0.00	0.00
Total	14.09	14.05	14.08	14.08	14.08	14.07	14.73	14.04
XFe	0.26	0.21	0.19	0.19	0.22	0.20	0.19	0.20
XNa	0.03	0.05	0.06	0.05	0.03	0.06	0.06	0.05
XK	0.71	0.75	0.75	0.76	0.75	0.74	0.75	0.75

Sample	ERFL2	ERFL2	ERFL2	ERFL2	ERFL2	ERFL2	ERFL2	ERFL2	ERFL2	ERFL2	ERFL2
Analysis	1	2	3	4	5	6	7	8	9	10	11
SiO2	45.17	46.14	46.67	44.05	45.60	45.97	44.67	46.18	46.39	44.96	44.55
TiO2	0.26	0.17	0.37	0.16	0.14	0.26	0.23	0.17	0.45	0.48	0.33
Al2O3	34.49	36.34	34.27	34.02	36.14	35.31	35.48	36.57	34.57	34.20	34.57
Cr2O3	0.02	0.02	0.00	0.00	0.00	0.02	0.01	0.02	0.02	0.01	0.00
FeO	4.29	3.42	4.19	3.83	3.15	4.00	3.79	3.37	4.67	4.94	4.52
MnO	0.00	0.00	0.01	0.00	0.00	0.02	0.00	0.00	0.02	0.02	0.01
MgO	0.44	0.14	0.60	0.37	0.32	0.28	0.46	0.25	0.50	0.48	0.45
CaO	0.03	0.09	0.03	0.05	0.04	0.01	0.04	0.03	0.01	0.03	0.03
Na2O	0.29	0.36	0.33	0.33	0.37	0.33	0.32	0.39	0.35	0.32	0.31
K2O	9.77	9.67	9.44	10.43	9.86	10.56	9.08	9.99	10.36	10.01	9.63
ZnO	0.00	0.00	0.00	0.00	0.00	0.00	0.00	0.00	0.00	0.00	0.00
Cl	0.02	0.01	0.02	0.01	0.03	0.00	0.01	0.02	0.00	0.00	0.00
F	0.00	0.00	0.06	0.04	0.00	0.00	0.00	0.00	0.00	0.00	0.00
Sub-Total	94.78	96.35	95.91	93.24	95.63	96.78	94.08	96.95	97.36	95.46	94.41
-O equiv. Cl	0.01	0.00	0.01	0.00	0.01	0.00	0.00	0.01	0.00	0.00	0.00
-O equiv. F	0.00	0.00	0.02	0.02	0.00	0.00	0.00	0.00	0.00	0.00	0.00
Total	94.78	96.35	95.94	93.26	95.64	96.78	94.09	96.96	97.36	95.46	94.41
num ox	23.00	22.00	22.00	22.00	22.00	22.00	22.00	22.00	22.00	22.00	22.00
Si	6.39	6.10	6.21	6.08	6.07	6.11	6.05	6.07	6.14	6.08	6.06
Ti	0.03	0.02	0.04	0.02	0.01	0.03	0.02	0.02	0.04	0.05	0.03
Al	5.75	5.66	5.37	5.54	5.68	5.53	5.66	5.67	5.39	5.45	5.55
Cr	0.00	0.00	0.00	0.00	0.00	0.00	0.00	0.00	0.00	0.00	0.00
Fe	0.51	0.38	0.47	0.44	0.35	0.44	0.43	0.37	0.52	0.56	0.51
Mn	0.00	0.00	0.00	0.00	0.00	0.00	0.00	0.00	0.00	0.00	0.00
Mg	0.09	0.03	0.12	0.08	0.06	0.06	0.09	0.05	0.10	0.10	0.09
Ca	0.00	0.01	0.00	0.01	0.01	0.00	0.01	0.00	0.00	0.00	0.00
Na	0.08	0.09	0.09	0.09	0.10	0.08	0.08	0.10	0.09	0.08	0.08
K	1.76	1.63	1.60	1.84	1.68	1.79	1.57	1.68	1.75	1.73	1.67
Zn	0.00	0.00	0.00	0.00	0.00	0.00	0.00	0.00	0.00	0.00	0.00
Cl	0.00	0.00	0.00	0.00	0.00	0.00	0.00	0.00	0.00	0.00	0.00
F	0.00	0.00	0.01	0.01	0.00	0.00	0.00	0.00	0.00	0.00	0.00
Total	14.63	13.92	13.91	14.10	13.96	14.04	13.92	13.96	14.04	14.05	14.01
XFe	0.22	0.18	0.22	0.19	0.17	0.19	0.21	0.17	0.22	0.24	0.23
XNa	0.03	0.04	0.04	0.04	0.05	0.04	0.04	0.05	0.04	0.04	0.04
XK	0.75	0.78	0.74	0.78	0.79	0.77	0.75	0.78	0.74	0.73	0.74

Sample	PQ12424	PQ12280	PQ12280
Analysis	25	120	130
SiO2	46.38	47.52	46.63
TiO2	0.64	0.30	0.57
Al2O3	32.19	32.01	32.09
Cr2O3	0.02	0.00	0.00
FeO	4.62	4.05	4.11
MnO	0.02	0.01	0.00
MgO	1.74	1.66	1.40
CaO	0.10	0.00	0.00
Na2O	0.34	0.53	0.57
K2O	9.56	10.50	10.42
ZnO	0.00	0.00	0.00
Cl	0.01	0.01	0.00
F	0.00	0.00	0.05
Sub-Total	95.60	96.57	95.79
-O equiv. Cl	0.00	0.00	0.00
-O equiv. F	0.00	0.00	0.02
Total	95.61	96.57	95.82
num ox	23.00	22.00	22.00
Si	6.52	6.33	6.27
Ti	0.07	0.03	0.06
Al	5.33	5.03	5.09
Cr	0.00	0.00	0.00
Fe	0.54	0.45	0.46
Mn	0.00	0.00	0.00
Mg	0.36	0.33	0.28
Ca	0.02	0.00	0.00
Na	0.09	0.14	0.15
K	1.71	1.78	1.79
Zn	0.00	0.00	0.00
Cl	0.00	0.00	0.00
F	0.00	0.00	0.01
Total	14.65	14.09	14.10
XFe	0.23	0.19	0.19
XNa	0.04	0.06	0.06
XK	0.73	0.75	0.75

Appendix IV

(Structural formula and Microprobe data - Biotite)

Sample	PQ12308-20	PQ12308-20	PQ12308-20	PQ12308-20	PQ12308-20	PQ12308-20	PQ12308-20
Analysis	15	5	6	7	10	12	13
SiO2	36.44	37.46	37.46	37.77	37.05	37.87	37.75
TiO2	1.78	1.71	1.79	1.63	1.82	1.81	1.81
Al2O3	16.69	16.69	17.26	16.99	16.92	16.69	16.69
FeO	18.56	18.26	18.22	18.37	18.31	18.45	18.43
MnO	0.20	0.18	0.18	0.19	0.19	0.18	0.19
MgO	12.29	12.38	12.26	12.43	12.47	12.30	12.42
CaO	0.00	0.04	0.00	0.00	0.00	0.00	0.00
Na2O	0.09	0.11	0.11	0.12	0.12	0.09	0.10
K2O	10.05	9.91	9.87	10.00	9.34	9.99	10.02
SrO	0.00	0.00	0.00	0.00	0.00	0.00	0.00
BaO	0.00	0.00	0.00	0.00	0.00	0.00	0.00
Rb2O	0.00	0.00	0.00	0.00	0.00	0.00	0.00
ZnO	0.00	0.00	0.00	0.00	0.00	0.00	0.00
F	0.21	0.32	0.33	0.42	0.42	0.40	0.32
Cl	0.01	0.00	0.01	0.00	0.01	0.01	0.00
Cr2O3	0.00	0.00	0.00	0.00	0.00	0.00	0.00
NiO	0.00	0.00	0.00	0.00	0.00	0.00	0.00
CuO	0.00	0.00	0.00	0.00	0.00	0.00	0.00
Li2O*	0.00	0.00	0.00	0.00	0.00	0.00	0.00
H2O*	3.87	3.86	3.88	3.85	3.80	3.85	3.89
Subtotal	100.19	100.94	101.37	101.78	100.46	101.65	101.62
O=F,Cl	0.09	0.14	0.14	0.18	0.18	0.17	0.14
Total	100.10	100.80	101.23	101.61	100.28	101.48	101.48
Si	5.51	5.59	5.56	5.59	5.55	5.62	5.60
Al iv	2.49	2.41	2.44	2.41	2.45	2.38	2.40
Al vi	0.48	0.53	0.58	0.56	0.54	0.53	0.52
Ti	0.20	0.19	0.20	0.18	0.20	0.20	0.20
Cr	0.00	0.00	0.00	0.00	0.00	0.00	0.00
Fe	2.35	2.28	2.26	2.27	2.29	2.29	2.29
Mn	0.03	0.02	0.02	0.02	0.02	0.02	0.02
Mg	2.77	2.76	2.71	2.74	2.78	2.72	2.75
Zn	0.00	0.00	0.00	0.00	0.00	0.00	0.00
Sn	0.00	0.00	0.00	0.00	0.00	0.00	0.00
Ga	0.00	0.00	0.00	0.00	0.00	0.00	0.00
Ni	0.00	0.00	0.00	0.00	0.00	0.00	0.00
Cu	0.00	0.00	0.00	0.00	0.00	0.00	0.00
Li*	0.00	0.00	0.00	0.00	0.00	0.00	0.00
Ca	0.00	0.01	0.00	0.00	0.00	0.00	0.00
Na	0.03	0.03	0.03	0.04	0.03	0.03	0.03
K	1.94	1.89	1.87	1.89	1.79	1.89	1.90
Sr	0.00	0.00	0.00	0.00	0.00	0.00	0.00
Ba	0.00	0.00	0.00	0.00	0.00	0.00	0.00
Rb	0.00	0.00	0.00	0.00	0.00	0.00	0.00
Cs	0.00	0.00	0.00	0.00	0.00	0.00	0.00
OH*	3.90	3.85	3.84	3.80	3.80	3.81	3.85
F	0.10	0.15	0.15	0.19	0.20	0.19	0.15
Cl	0.00	0.00	0.00	0.00	0.00	0.00	0.00
TOTAL	19.79	19.71	19.68	19.71	19.66	19.68	19.70

Sample	PQ12308-20	PQ12308-20	PQ12308-20	PQ12308-20	PQ12308-20	PQ12308-20	PQ12308-20
Analysis	15	16	21	22	23	24	25
SiO2	38.14	37.42	38.19	37.05	37.19	35.61	36.95
TiO2	1.86	1.86	1.83	1.88	1.91	1.50	1.82
Al2O3	16.94	16.62	16.70	16.48	16.58	16.82	16.77
FeO	18.56	18.35	17.70	17.92	18.28	19.73	18.45
MnO	0.18	0.17	0.15	0.18	0.15	0.18	0.18
MgO	12.38	12.24	12.60	12.49	12.47	13.56	12.88
CaO	0.00	0.00	0.00	0.00	0.00	0.00	0.00
Na2O	0.09	0.09	0.11	0.08	0.05	0.05	0.07
K2O	9.86	10.17	9.84	9.50	9.21	7.67	9.01
SrO	0.00	0.00	0.00	0.00	0.00	0.00	0.00
BaO	0.00	0.00	0.00	0.00	0.00	0.00	0.00
Rb2O	0.00	0.00	0.00	0.00	0.00	0.00	0.00
ZnO	0.00	0.00	0.00	0.00	0.00	0.00	0.00
F	0.37	0.35	0.35	0.38	0.53	0.27	0.27
Cl	0.02	0.01	0.00	0.01	0.00	0.00	0.00
Cr2O3	0.00	0.00	0.00	0.00	0.00	0.00	0.00
NiO	0.00	0.00	0.00	0.00	0.00	0.00	0.00
CuO	0.00	0.00	0.00	0.00	0.00	0.00	0.00
Li2O*	0.00	0.00	0.00	0.00	0.00	0.00	0.00
H2O*	3.90	3.84	3.89	3.80	3.74	3.82	3.87
Subtotal	102.30	101.13	101.35	99.76	100.10	99.22	100.28
O=F,Cl	0.16	0.15	0.15	0.16	0.22	0.11	0.11
Total	102.14	100.98	101.20	99.60	99.88	99.11	100.17
Si	5.61	5.59	5.65	5.59	5.59	5.40	5.53
Al iv	2.39	2.41	2.35	2.41	2.41	2.60	2.47
Al vi	0.55	0.51	0.56	0.51	0.52	0.41	0.49
Ti	0.21	0.21	0.20	0.21	0.22	0.17	0.21
Cr	0.00	0.00	0.00	0.00	0.00	0.00	0.00
Fe	2.28	2.29	2.19	2.26	2.30	2.50	2.31
Mn	0.02	0.02	0.02	0.02	0.02	0.02	0.02
Mg	2.72	2.72	2.78	2.81	2.79	3.07	2.87
Zn	0.00	0.00	0.00	0.00	0.00	0.00	0.00
Sn	0.00	0.00	.	0.00	0.00	0.00	0.00
Ga	0.00	0.00	0.00	0.00	0.00	0.00	0.00
Ni	0.00	0.00	0.00	0.00	0.00	0.00	0.00
Cu	0.00	0.00	0.00	0.00	0.00	0.00	0.00
Li*	0.00	0.00	0.00	0.00	0.00	0.00	0.00
Ca	0.00	0.00	0.00	0.00	0.00	0.00	0.00
Na	0.03	0.03	0.03	0.02	0.01	0.02	0.02
K	1.85	1.94	1.86	1.83	1.76	1.48	1.72
Sr	0.00	0.00	0.00	0.00	0.00	0.00	0.00
Ba	0.00	0.00	0.00	0.00	0.00	0.00	0.00
Rb	0.00	0.00	0.00	0.00	0.00	0.00	0.00
Cs	0.00	0.00	0.00	0.00	0.00	0.00	0.00
OH*	3.82	3.83	3.84	3.82	3.75	3.87	3.87
F	0.17	0.17	0.16	0.18	0.25	0.13	0.13
Cl	0.00	0.00	0.00	0.00	0.00	0.00	0.00
TOTAL	19.65	19.72	19.64	19.66	19.62	19.67	19.65

Sample	PQ35a557-89	PQ35a557-90	PQ35a557-91	PQ35a557-92	PQ35a557-93
Analysis	A1	A2	B1	B2	B3
SiO2	37.36	37.09	36.99	37.61	37.70
TiO2	1.76	1.66	1.81	1.72	1.99
Al2O3	16.49	16.59	17.39	17.08	17.15
FeO	16.57	16.90	16.17	15.81	15.41
MnO	0.13	0.15	0.18	0.16	0.15
MgO	13.85	14.22	15.01	14.85	14.45
CaO	0.07	0.07	0.05	0.02	0.02
Na2O	0.14	0.14	0.11	0.13	0.12
K2O	9.15	8.67	7.68	8.70	9.16
SrO	0.00	0.00	0.00	0.00	0.00
BaO	0.00	0.00	0.00	0.00	0.00
Rb2O	0.00	0.00	0.00	0.00	0.00
ZnO	0.00	0.00	0.00	0.00	0.00
F	0.20	0.20	0.08	0.10	0.19
Cl	0.01	0.01	0.00	0.01	0.00
Cr2O3	0.00	0.00	0.00	0.00	0.00
NiO	0.00	0.00	0.00	0.00	0.00
CuO	0.00	0.00	0.00	0.00	0.00
Li2O*	0.00	0.00	0.00	0.00	0.00
H2O*	3.91	3.91	4.01	4.02	3.98
Subtotal	99.64	99.63	99.46	100.20	100.31
O=F,Cl	0.09	0.09	0.03	0.04	0.08
Total	99.56	99.54	99.43	100.15	100.23
Si	5.58	5.54	5.48	5.55	5.56
Al iv	2.42	2.46	2.52	2.45	2.44
Al vi	0.49	0.47	0.51	0.51	0.54
Ti	0.20	0.19	0.20	0.19	0.22
Cr	0.00	0.00	0.00	0.00	0.00
Fe	2.07	2.11	2.00	1.95	1.90
Mn	0.02	0.02	0.02	0.02	0.02
Mg	3.09	3.17	3.31	3.27	3.18
Zn	0.00	0.00	0.00	0.00	0.00
Sn	0.00	0.00	0.00	0.00	0.00
Ga	0.00	0.00	0.00	0.00	0.00
Ni	0.00	0.00	0.00	0.00	0.00
Cu	0.00	0.00	0.00	0.00	0.00
Li*	0.00	0.00	0.00	0.00	0.00
Ca	0.01	0.01	0.01	0.00	0.00
Na	0.04	0.04	0.03	0.04	0.04
K	1.74	1.65	1.45	1.64	1.72
Sr	0.00	0.00	0.00	0.00	0.00
Ba	0.00	0.00	0.00	0.00	0.00
Rb	0.00	0.00	0.00	0.00	0.00
Cs	0.00	0.00	0.00	0.00	0.00
OH*	3.90	3.90	3.96	3.95	3.91
F	0.09	0.10	0.04	0.05	0.09
Cl	0.00	0.00	0.00	0.00	0.00
TOTAL	19.66	19.66	19.54	19.61	19.61

Sample	PQ35a557-94	PQ35a557-95	PQ35a557-96	PQ35a557-97	PQ35a557-98	PQ35a557-100
Analysis	E1	F1	G1	G2	H1	B1
SiO2	37.78	37.76	38.04	37.78	37.30	34.83
TiO2	1.81	1.67	1.92	1.84	1.86	1.33
Al2O3	16.89	16.64	16.37	16.74	16.70	17.19
FeO	16.50	16.45	16.92	16.58	16.53	18.75
MnO	0.14	0.14	0.16	0.15	0.13	0.20
MgO	13.96	14.07	13.66	13.76	14.18	15.88
CaO	0.01	0.04	0.00	0.00	0.10	0.04
Na2O	0.12	0.11	0.13	0.11	0.12	0.07
K2O	9.74	9.68	9.78	9.74	9.27	5.51
SrO	0.00	0.00	0.00	0.00	0.00	0.00
BaO	0.00	0.00	0.00	0.00	0.00	0.00
Rb2O	0.00	0.00	0.00	0.00	0.00	0.00
ZnO	0.00	0.00	0.00	0.00	0.00	0.00
F	0.13	0.15	0.14	0.07	0.14	0.00
Cl	0.00	0.01	0.00	0.00	0.01	0.02
Cr2O3	0.00	0.00	0.00	0.00	0.00	0.00
NiO	0.00	0.00	0.00	0.00	0.00	0.00
CuO	0.00	0.00	0.00	0.00	0.00	0.00
Li2O*	0.00	0.00	0.00	0.00	0.00	0.00
H2O*	4.00	3.98	3.99	4.02	3.97	3.95
Subtotal	101.09	100.69	101.12	100.78	100.30	97.78
O=F,Cl	0.06	0.07	0.06	0.03	0.06	0.00
Total	101.03	100.63	101.06	100.75	100.25	97.78
Si	5.57	5.59	5.62	5.59	5.54	5.28
Al iv	2.43	2.41	2.38	2.41	2.46	2.72
Al vi	0.50	0.49	0.47	0.51	0.46	0.35
Ti	0.20	0.19	0.21	0.20	0.21	0.15
Cr	0.00	0.00	0.00	0.00	0.00	0.00
Fe	2.04	2.04	2.09	2.05	2.05	2.38
Mn	0.02	0.02	0.02	0.02	0.02	0.03
Mg	3.07	3.10	3.01	3.03	3.14	3.59
Zn	0.00	0.00	0.00	0.00	0.00	0.00
Sn	0.00	0.00	0.00	0.00	0.00	0.00
Ga	0.00	0.00	0.00	0.00	0.00	0.00
Ni	0.00	0.00	0.00	0.00	0.00	0.00
Cu	0.00	0.00	0.00	0.00	0.00	0.00
Li*	0.00	0.00	0.00	0.00	0.00	0.00
Ca	0.00	0.01	0.00	0.00	0.02	0.01
Na	0.04	0.03	0.04	0.03	0.03	0.02
K	1.83	1.83	1.84	1.84	1.76	1.06
Sr	0.00	0.00	0.00	0.00	0.00	0.00
Ba	0.00	0.00	0.00	0.00	0.00	0.00
Rb	0.00	0.00	0.00	0.00	0.00	0.00
Cs	0.00	0.00	0.00	0.00	0.00	0.00
OH*	3.94	3.93	3.93	3.97	3.93	4.00
F	0.06	0.07	0.06	0.03	0.06	0.00
Cl	0.00	0.00	0.00	0.00	0.00	0.00
TOTAL	19.70	19.70	19.68	19.68	19.69	19.58

Sample	PQ61108-90	PQ61108-90	PQ61108-90	PQ61108-90	PQ61108-90	PQ61108-90	PQ61108-90
Analysis	1	2	4	5	6	7	8
SiO2	37.13	37.24	37.04	37.25	37.28	36.96	37.09
TiO2	1.71	1.70	1.80	1.69	1.68	1.80	1.84
Al2O3	15.95	16.24	16.57	16.67	16.59	16.13	16.26
FeO	17.25	17.48	16.92	16.93	17.00	17.12	17.34
MnO	0.28	0.26	0.27	0.27	0.28	0.28	0.26
MgO	13.30	13.11	13.02	12.72	12.99	13.01	13.04
CaO	0.01	0.02	0.00	0.01	0.00	0.03	0.00
Na2O	0.05	0.08	0.10	0.16	0.08	0.06	0.09
K2O	9.76	9.84	9.81	9.68	9.80	9.78	9.82
SrO	0.00	0.00	0.00	0.00	0.00	0.00	0.00
BaO	0.00	0.00	0.00	0.00	0.00	0.00	0.00
Rb2O	0.00	0.00	0.00	0.00	0.00	0.00	0.00
ZnO	0.00	0.00	0.00	0.00	0.00	0.00	0.00
F	0.10	0.15	0.15	0.04	0.12	0.19	0.12
Cl	0.00	0.03	0.01	0.00	0.01	0.02	0.01
Cr2O3	0.00	0.00	0.01	0.00	0.00	0.02	0.02
NiO	0.00	0.00	0.00	0.00	0.00	0.00	0.00
CuO	0.00	0.00	0.00	0.00	0.00	0.00	0.00
Li2O*	0.00	0.00	0.00	0.00	0.00	0.00	0.00
H2O*	3.93	3.91	3.91	3.97	3.93	3.87	3.92
Subtotal	99.47	100.08	99.61	99.39	99.78	99.27	99.82
O=F,Cl	0.04	0.07	0.06	0.02	0.05	0.09	0.05
Total	99.43	100.01	99.54	99.37	99.73	99.18	99.77
Si	5.60	5.59	5.57	5.60	5.60	5.59	5.58
Al iv	2.40	2.41	2.43	2.40	2.40	2.41	2.42
Al vi	0.44	0.47	0.51	0.56	0.53	0.47	0.46
Ti	0.19	0.19	0.20	0.19	0.19	0.21	0.21
Cr	0.00	0.00	0.00	0.00	0.00	0.00	0.00
Fe	2.18	2.20	2.13	2.13	2.13	2.17	2.18
Mn	0.04	0.03	0.03	0.03	0.04	0.04	0.03
Mg	2.99	2.93	2.92	2.85	2.91	2.93	2.93
Zn	0.00	0.00	0.00	0.00	0.00	0.00	0.00
Sn	0.00	0.00	0.00	0.00	0.00	0.00	0.00
Ga	0.00	0.00	0.00	0.00	0.00	0.00	0.00
Ni	0.00	0.00	0.00	0.00	0.00	0.00	0.00
Cu	0.00	0.00	0.00	0.00	0.00	0.00	0.00
Li*	0.00	0.00	0.00	0.00	0.00	0.00	0.00
Ca	0.00	0.00	0.00	0.00	0.00	0.00	0.00
Na	0.02	0.02	0.03	0.05	0.02	0.02	0.03
K	1.88	1.88	1.88	1.86	1.88	1.89	1.88
Sr	0.00	0.00	0.00	0.00	0.00	0.00	0.00
Ba	0.00	0.00	0.00	0.00	0.00	0.00	0.00
Rb	0.00	0.00	0.00	0.00	0.00	0.00	0.00
Cs	0.00	0.00	0.00	0.00	0.00	0.00	0.00
OH*	3.95	3.92	3.93	3.98	3.94	3.90	3.94
F	0.05	0.07	0.07	0.02	0.06	0.09	0.06
Cl	0.00	0.01	0.00	0.00	0.00	0.00	0.00
TOTAL	19.73	19.73	19.71	19.68	19.70	19.72	19.72

Sample	PQ61108-90	PQ61108-90	PQ61108-90	PQ61108-90	PQ61108-90	PQ61108-90	PQ61108-90
Analysis	11	12	13	14	15	16	17
SiO2	36.83	36.13	36.61	35.61	36.35	36.56	37.14
TiO2	1.68	1.90	1.63	1.77	1.94	1.67	1.77
Al2O3	16.01	15.80	16.62	16.45	16.08	16.23	16.30
FeO	16.75	17.51	16.88	17.00	17.34	17.05	16.68
MnO	0.28	0.30	0.29	0.26	0.31	0.28	0.29
MgO	13.49	13.17	13.21	13.14	13.05	13.07	12.96
CaO	0.00	0.00	0.00	0.01	0.01	0.00	0.00
Na2O	0.08	0.05	0.12	0.16	0.07	0.04	0.10
K2O	9.69	9.80	9.66	9.56	9.95	9.86	9.74
SrO	0.00	0.00	0.00	0.00	0.00	0.00	0.00
BaO	0.00	0.00	0.00	0.00	0.00	0.00	0.00
Rb2O	0.00	0.00	0.00	0.00	0.00	0.00	0.00
ZnO	0.00	0.00	0.00	0.00	0.00	0.00	0.00
F	0.16	0.20	0.19	0.14	0.18	0.11	0.12
Cl	0.02	0.00	0.00	0.00	0.01	0.00	0.01
Cr2O3	0.00	0.01	0.01	0.03	0.01	0.00	0.00
NiO	0.00	0.00	0.00	0.00	0.00	0.00	0.00
CuO	0.00	0.00	0.00	0.00	0.00	0.00	0.00
Li2O*	0.00	0.00	0.00	0.00	0.00	0.00	0.00
H2O*	3.87	3.83	3.87	3.84	3.86	3.89	3.91
Subtotal	98.85	98.70	99.08	97.98	99.14	98.76	99.01
O=F,Cl	0.07	0.09	0.08	0.06	0.08	0.05	0.05
Total	98.78	98.62	99.00	97.92	99.07	98.71	98.96
Si	5.58	5.52	5.54	5.47	5.53	5.56	5.61
Al iv	2.42	2.48	2.46	2.53	2.47	2.44	2.39
Al vi	0.45	0.37	0.50	0.44	0.41	0.47	0.52
Ti	0.19	0.22	0.19	0.20	0.22	0.19	0.20
Cr	0.00	0.00	0.00	0.00	0.00	0.00	0.00
Fe	2.12	2.24	2.14	2.18	2.20	2.17	2.11
Mn	0.04	0.04	0.04	0.03	0.04	0.04	0.04
Mg	3.05	3.00	2.98	3.01	2.96	2.96	2.92
Zn	0.00	0.00	0.00	0.00	0.00	0.00	0.00
Sn	0.00	0.00	0.00	0.00	0.00	0.00	0.00
Ga	0.00	0.00	0.00	0.00	0.00	0.00	0.00
Ni	0.00	0.00	0.00	0.00	0.00	0.00	0.00
Cu	0.00	0.00	0.00	0.00	0.00	0.00	0.00
Li*	0.00	0.00	0.00	0.00	0.00	0.00	0.00
Ca	0.00	0.00	0.00	0.00	0.00	0.00	0.00
Na	0.02	0.02	0.03	0.05	0.02	0.01	0.03
K	1.87	1.91	1.86	1.87	1.93	1.91	1.88
Sr	0.00	0.00	0.00	0.00	0.00	0.00	0.00
Ba	0.00	0.00	0.00	0.00	0.00	0.00	0.00
Rb	0.00	0.00	0.00	0.00	0.00	0.00	0.00
Cs	0.00	0.00	0.00	0.00	0.00	0.00	0.00
OH*	3.92	3.90	3.91	3.93	3.91	3.95	3.94
F	0.08	0.10	0.09	0.07	0.09	0.05	0.06
Cl	0.00	0.00	0.00	0.00	0.00	0.00	0.00

TOTAL	19.74	19.80	19.74	19.80	19.79	19.76	19.69
Sample	PQ61108-90	PQ61108-90	PQ61108-90	PQ61108-90	PQ61108-90	PQ61108-90	PQ61108-90
Analysis	19	20	21	22	23	24	25
SiO2	36.89	36.89	37.36	37.06	37.25	37.15	37.05
TiO2	1.77	1.89	1.67	1.58	1.65	1.75	1.70
Al2O3	16.10	16.21	16.44	16.65	16.49	16.57	16.00
FeO	17.24	17.34	16.74	16.68	16.85	17.08	17.57
MnO	0.33	0.31	0.28	0.29	0.28	0.30	0.31
MgO	12.93	13.22	12.86	12.76	13.16	12.65	12.84
CaO	0.03	0.00	0.02	0.00	0.00	0.00	0.02
Na2O	0.09	0.06	0.10	0.11	0.11	0.07	0.04
K2O	9.72	9.81	9.75	9.56	9.60	9.78	9.63
SrO	0.00	0.00	0.00	0.00	0.00	0.00	0.00
BaO	0.00	0.00	0.00	0.00	0.00	0.00	0.00
Rb2O	0.00	0.00	0.00	0.00	0.00	0.00	0.00
ZnO	0.00	0.00	0.00	0.00	0.00	0.00	0.00
F	0.17	0.11	0.20	0.20	0.16	0.14	0.15
Cl	0.02	0.02	0.00	0.00	0.01	0.00	0.03
Cr2O3	0.01	0.00	0.00	0.02	0.01	0.01	0.05
NiO	0.00	0.00	0.00	0.00	0.00	0.00	0.00
CuO	0.00	0.00	0.00	0.00	0.00	0.00	0.00
Li2O*	0.00	0.00	0.00	0.00	0.00	0.00	0.00
H2O*	3.87	3.92	3.89	3.87	3.91	3.91	3.88
Subtotal	99.17	99.80	99.29	98.80	99.49	99.44	99.27
O=F,Cl	0.07	0.05	0.08	0.08	0.07	0.06	0.07
Total	99.09	99.75	99.20	98.72	99.42	99.37	99.19
Si	5.59	5.56	5.63	5.61	5.60	5.60	5.61
Al iv	2.41	2.44	2.37	2.39	2.40	2.40	2.39
Al vi	0.46	0.43	0.55	0.58	0.52	0.54	0.46
Ti	0.20	0.21	0.19	0.18	0.19	0.20	0.19
Cr	0.00	0.00	0.00	0.00	0.00	0.00	0.01
Fe	2.18	2.18	2.11	2.11	2.12	2.15	2.23
Mn	0.04	0.04	0.04	0.04	0.04	0.04	0.04
Mg	2.92	2.97	2.89	2.88	2.95	2.84	2.90
Zn	0.00	0.00	0.00	0.00	0.00	0.00	0.00
Sn	0.00	0.00	0.00	0.00	0.00	0.00	0.00
Ga	0.00	0.00	0.00	0.00	0.00	0.00	0.00
Ni	0.00	0.00	0.00	0.00	0.00	0.00	0.00
Cu	0.00	0.00	0.00	0.00	0.00	0.00	0.00
Li*	0.00	0.00	0.00	0.00	0.00	0.00	0.00
Ca	0.00	0.00	0.00	0.00	0.00	0.00	0.00
Na	0.03	0.02	0.03	0.03	0.03	0.02	0.01
K	1.88	1.88	1.87	1.85	1.84	1.88	1.86
Sr	0.00	0.00	0.00	0.00	0.00	0.00	0.00
Ba	0.00	0.00	0.00	0.00	0.00	0.00	0.00
Rb	0.00	0.00	0.00	0.00	0.00	0.00	0.00
Cs	0.00	0.00	0.00	0.00	0.00	0.00	0.00
OH*	3.92	3.94	3.91	3.90	3.92	3.93	3.92
F	0.08	0.05	0.09	0.10	0.07	0.07	0.07
Cl	0.00	0.00	0.00	0.00	0.00	0.00	0.01
TOTAL	19.72	19.74	19.67	19.67	19.69	19.68	19.70

Sample	PQ61108-90	PQ61108-90	PQ61108-90	PQ61108-90	PQ61108-90	PQ61108-90
Analysis	26	27	28	29	30	31
SiO2	36.72	37.18	36.91	36.85	36.99	36.88
TiO2	1.71	1.59	1.66	1.67	1.57	1.68
Al2O3	16.72	16.11	16.46	16.42	16.53	15.98
FeO	16.88	17.06	16.78	16.78	16.84	17.45
MnO	0.28	0.30	0.29	0.31	0.30	0.30
MgO	12.95	12.87	12.71	12.81	12.90	13.19
CaO	0.02	0.00	0.00	0.03	0.03	0.00
Na2O	0.15	0.07	0.13	0.11	0.10	0.08
K2O	9.57	9.75	9.42	9.70	9.60	9.89
SrO	0.00	0.00	0.00	0.00	0.00	0.00
BaO	0.00	0.00	0.00	0.00	0.00	0.00
Rb2O	0.00	0.00	0.00	0.00	0.00	0.00
ZnO	0.00	0.00	0.00	0.00	0.00	0.00
F	0.13	0.23	0.21	0.17	0.18	0.18
Cl	0.00	0.02	0.01	0.02	0.00	0.00
Cr2O3	0.01	0.00	0.01	0.00	0.00	0.01
NiO	0.00	0.00	0.00	0.00	0.00	0.00
CuO	0.00	0.00	0.00	0.00	0.00	0.00
Li2O*	0.00	0.00	0.00	0.00	0.00	0.00
H2O*	3.90	3.84	3.84	3.86	3.88	3.88
Subtotal	99.05	99.02	98.42	98.73	98.92	99.54
O=F,Cl	0.06	0.10	0.09	0.08	0.08	0.08
Total	98.99	98.92	98.33	98.65	98.85	99.46
Si	5.55	5.63	5.61	5.59	5.60	5.58
Al iv	2.45	2.37	2.39	2.41	2.40	2.42
Al vi	0.53	0.51	0.56	0.53	0.55	0.43
Ti	0.19	0.18	0.19	0.19	0.18	0.19
Cr	0.00	0.00	0.00	0.00	0.00	0.00
Fe	2.13	2.16	2.13	2.13	2.13	2.21
Mn	0.04	0.04	0.04	0.04	0.04	0.04
Mg	2.92	2.91	2.88	2.90	2.91	2.97
Zn	0.00	0.00	0.00	0.00	0.00	0.00
Sn	0.00	0.00	0.00	0.00	0.00	0.00
Ga	0.00	0.00	0.00	0.00	0.00	0.00
Ni	0.00	0.00	0.00	0.00	0.00	0.00
Cu	0.00	0.00	0.00	0.00	0.00	0.00
Li*	0.00	0.00	0.00	0.00	0.00	0.00
Ca	0.00	0.00	0.00	0.00	0.00	0.00
Na	0.04	0.02	0.04	0.03	0.03	0.02
K	1.85	1.88	1.83	1.88	1.85	1.91
Sr	0.00	0.00	0.00	0.00	0.00	0.00
Ba	0.00	0.00	0.00	0.00	0.00	0.00
Rb	0.00	0.00	0.00	0.00	0.00	0.00
Cs	0.00	0.00	0.00	0.00	0.00	0.00
OH*	3.94	3.88	3.90	3.91	3.91	3.91
F	0.06	0.11	0.10	0.08	0.08	0.09
Cl	0.00	0.00	0.00	0.01	0.00	0.00
TOTAL	19.71	19.70	19.66	19.70	19.69	19.77

Sample	PQGL1002	PQGL1002	PQGL1002	PQGL1002	PQGL1002	PQGL1002	PQGL1002	PQGL1002	PQGL1002
Analysis	1	2	3	4	5	6	7	8	9
SiO2	34.42	34.27	35.22	35.00	35.13	35.56	35.50	34.42	35.61
TiO2	1.69	1.65	1.70	1.61	1.39	1.81	1.57	1.91	1.50
Al2O3	15.73	16.18	15.65	15.38	15.43	15.49	15.35	15.31	15.43
FeO	15.69	14.82	16.85	16.47	16.23	17.41	17.08	15.85	16.25
MnO	0.20	0.18	0.18	0.18	0.18	0.19	0.18	0.18	0.19
MgO	11.37	11.55	11.55	11.63	11.49	11.23	11.24	11.58	11.56
CaO	0.03	0.03	0.02	0.00	0.01	0.07	0.00	0.01	0.03
Na2O	0.07	0.08	0.06	0.06	0.05	0.06	0.08	0.06	0.09
K2O	8.82	8.49	9.11	8.91	9.03	9.27	9.14	8.43	8.98
SrO	0.00	0.00	0.00	0.00	0.00	0.00	0.00	0.00	0.00
BaO	0.00	0.00	0.00	0.00	0.00	0.00	0.00	0.00	0.00
Rb2O	0.00	0.00	0.00	0.00	0.00	0.00	0.00	0.00	0.00
ZnO	0.00	0.00	0.00	0.00	0.00	0.00	0.00	0.00	0.00
F	0.11	0.09	0.15	0.21	0.19	0.14	0.06	0.08	0.06
Cl	0.00	0.01	0.00	0.00	0.01	0.00	0.02	0.00	0.00
Cr2O3	0.00	0.01	0.03	0.00	0.00	0.00	0.00	0.01	0.00
NiO	0.00	0.00	0.00	0.00	0.00	0.00	0.00	0.00	0.00
CuO	0.00	0.00	0.00	0.00	0.00	0.00	0.00	0.00	0.00
Li2O*	0.00	0.00	0.00	0.00	0.00	0.00	0.00	0.00	0.00
H2O*	3.63	3.63	3.69	3.62	3.62	3.71	3.72	3.64	3.72
Subtotal	91.75	90.98	94.20	93.07	92.77	94.94	93.93	91.46	93.42
O=F,Cl	0.04	0.04	0.06	0.09	0.08	0.06	0.03	0.04	0.03
Total	91.71	90.94	94.14	92.98	92.68	94.88	93.90	91.43	93.39
Si	5.60	5.59	5.61	5.64	5.67	5.64	5.68	5.61	5.69
Al iv	2.40	2.41	2.39	2.36	2.33	2.36	2.32	2.39	2.31
Al vi	0.62	0.70	0.55	0.56	0.61	0.53	0.57	0.56	0.60
Ti	0.21	0.20	0.20	0.19	0.17	0.22	0.19	0.23	0.18
Cr	0.00	0.00	0.00	0.00	0.00	0.00	0.00	0.00	0.00
Fe	2.14	2.02	2.25	2.22	2.19	2.31	2.28	2.16	2.17
Mn	0.03	0.02	0.02	0.02	0.02	0.03	0.02	0.02	0.03
Mg	2.76	2.81	2.74	2.79	2.77	2.66	2.68	2.82	2.76
Zn	0.00	0.00	0.00	0.00	0.00	0.00	0.00	0.00	0.00
Sn	0.00	0.00	0.00	0.00	0.00	0.00	0.00	0.00	0.00
Ga	0.00	0.00	0.00	0.00	0.00	0.00	0.00	0.00	0.00
Ni	0.00	0.00	0.00	0.00	0.00	0.00	0.00	0.00	0.00
Cu	0.00	0.00	0.00	0.00	0.00	0.00	0.00	0.00	0.00
Li*	0.00	0.00	0.00	0.00	0.00	0.00	0.00	0.00	0.00
Ca	0.01	0.01	0.00	0.00	0.00	0.01	0.00	0.00	0.00
Na	0.02	0.03	0.02	0.02	0.02	0.02	0.03	0.02	0.03
K	1.83	1.77	1.85	1.83	1.86	1.87	1.86	1.75	1.83
Sr	0.00	0.00	0.00	0.00	0.00	0.00	0.00	0.00	0.00
Ba	0.00	0.00	0.00	0.00	0.00	0.00	0.00	0.00	0.00
Rb	0.00	0.00	0.00	0.00	0.00	0.00	0.00	0.00	0.00
Cs	0.00	0.00	0.00	0.00	0.00	0.00	0.00	0.00	0.00
OH*	3.95	3.95	3.92	3.89	3.90	3.93	3.96	3.96	3.97
F	0.05	0.05	0.08	0.11	0.10	0.07	0.03	0.04	0.03
Cl	0.00	0.00	0.00	0.00	0.00	0.00	0.01	0.00	0.00
TOTAL	19.61	19.55	19.65	19.63	19.63	19.65	19.63	19.57	19.60

Sample	PQGL1002	PQGL1002	PQGL1002	PQGL1002	PQGL1002	PQGL1002	PQGL1002	PQGL1002	PQGL1002
Analysis	11	12	13	14	16	17	18	19	10
SiO2	34.48	32.46	32.46	34.73	35.39	35.73	35.93	35.89	34.82
TiO2	1.61	1.59	1.44	1.86	1.77	1.66	1.81	1.78	1.83
Al2O3	15.39	12.76	14.58	15.63	15.88	16.00	15.45	15.86	15.28
FeO	16.26	12.95	13.16	17.24	17.76	17.11	18.28	17.49	16.89
MnO	0.16	0.13	0.15	0.18	0.17	0.20	0.21	0.20	0.18
MgO	11.40	10.08	11.42	11.56	11.90	11.77	11.77	11.33	11.33
CaO	0.00	0.05	0.01	0.01	0.05	0.00	0.00	0.02	0.00
Na2O	0.08	0.02	0.06	0.07	0.05	0.07	0.02	0.07	0.04
K2O	8.71	7.95	7.88	9.01	9.15	9.39	9.43	9.28	9.10
SrO	0.00	0.00	0.00	0.00	0.00	0.00	0.00	0.00	0.00
BaO	0.00	0.00	0.00	0.00	0.00	0.00	0.00	0.00	0.00
Rb2O	0.00	0.00	0.00	0.00	0.00	0.00	0.00	0.00	0.00
ZnO	0.00	0.00	0.00	0.00	0.00	0.00	0.00	0.00	0.00
F	0.17	0.24	0.10	0.16	0.08	0.11	0.23	0.06	0.26
Cl	0.00	0.00	0.01	0.00	0.01	0.00	0.01	0.02	0.00
Cr2O3	0.02	0.01	0.00	0.02	0.00	0.00	0.01	0.01	0.00
NiO	0.00	0.00	0.00	0.00	0.00	0.00	0.00	0.00	0.00
CuO	0.00	0.00	0.00	0.00	0.00	0.00	0.00	0.00	0.00
Li2O*	0.00	0.00	0.00	0.00	0.00	0.00	0.00	0.00	0.00
H2O*	3.60	3.19	3.39	3.67	3.78	3.77	3.73	3.79	3.59
Subtotal	91.88	81.41	84.66	94.13	95.99	95.81	96.88	95.79	93.33
O=F,Cl	0.07	0.10	0.04	0.07	0.04	0.05	0.10	0.03	0.11
Total	91.81	81.31	84.62	94.06	95.96	95.76	96.78	95.76	93.22
Si	5.62	5.90	5.66	5.56	5.55	5.60	5.61	5.63	5.62
Al iv	2.38	2.10	2.34	2.44	2.45	2.40	2.39	2.37	2.38
Al vi	0.58	0.64	0.66	0.50	0.49	0.56	0.45	0.57	0.52
Ti	0.20	0.22	0.19	0.22	0.21	0.20	0.21	0.21	0.22
Cr	0.00	0.00	0.00	0.00	0.00	0.00	0.00	0.00	0.00
Fe	2.22	1.97	1.92	2.31	2.33	2.24	2.39	2.30	2.28
Mn	0.02	0.02	0.02	0.02	0.02	0.03	0.03	0.03	0.02
Mg	2.77	2.73	2.97	2.76	2.78	2.75	2.74	2.65	2.72
Zn	0.00	0.00	0.00	0.00	0.00	0.00	0.00	0.00	0.00
Sn	0.00	0.00	0.00	0.00	0.00	0.00	0.00	0.00	0.00
Ga	0.00	0.00	0.00	0.00	0.00	0.00	0.00	0.00	0.00
Ni	0.00	0.00	0.00	0.00	0.00	0.00	0.00	0.00	0.00
Cu	0.00	0.00	0.00	0.00	0.00	0.00	0.00	0.00	0.00
Li*	0.00	0.00	0.00	0.00	0.00	0.00	0.00	0.00	0.00
Ca	0.00	0.01	0.00	0.00	0.01	0.00	0.00	0.00	0.00
Na	0.03	0.01	0.02	0.02	0.01	0.02	0.01	0.02	0.01
K	1.81	1.84	1.75	1.84	1.83	1.88	1.88	1.86	1.87
Sr	0.00	0.00	0.00	0.00	0.00	0.00	0.00	0.00	0.00
Ba	0.00	0.00	0.00	0.00	0.00	0.00	0.00	0.00	0.00
Rb	0.00	0.00	0.00	0.00	0.00	0.00	0.00	0.00	0.00
Cs	0.00	0.00	0.00	0.00	0.00	0.00	0.00	0.00	0.00
OH*	3.91	3.86	3.94	3.92	3.96	3.95	3.88	3.96	3.87
F	0.09	0.14	0.06	0.08	0.04	0.05	0.11	0.03	0.13
Cl	0.00	0.00	0.00	0.00	0.00	0.00	0.00	0.01	0.00
TOTAL	19.62	19.44	19.54	19.68	19.69	19.67	19.70	19.63	19.65

Appendix V

(Structural formula and Microprobe data - Chlorite)

Sample	PQ12309-97	PQ12309-97	PQ12309-97	PQ12309-97	PQ12309-97	PQ12309-97	PQ12309-97	PQ12309-97	PQ12309-97
Analysis	1.00	2.00	3.00	4.00	5.00	6.00	7.00	8.00	9.00
SiO2	25.77	25.57	25.07	25.23	25.49	25.05	26.04	25.95	23.59
TiO2	0.07	0.04	0.03	0.05	0.05	0.02	0.01	0.04	0.05
Al2O3	20.69	19.56	17.54	18.09	21.06	18.72	18.13	20.29	19.94
V2O3	0.00	0.00	0.00	0.00	0.00	0.00	0.00	0.00	0.00
Cr2O3	0.02	0.01	0.00	0.00	0.00	0.01	0.01	0.01	0.00
Mn2O3	0.00	0.00	0.00	0.00	0.00	0.00	0.00	0.00	0.00
Fe2O3	24.44	31.99	37.42	36.56	24.46	37.33	39.61	26.70	29.12
FeO	0.00	0.00	0.00	0.00	0.00	0.00	0.00	0.00	0.00
MnO	0.26	0.27	0.54	0.49	0.30	0.51	0.35	0.26	0.28
MgO	18.12	13.26	9.13	9.44	17.92	9.04	8.13	16.70	14.67
CaO	0.01	0.00	0.03	0.05	0.00	0.01	0.05	0.01	0.01
BaO	0.00	0.00	0.00	0.00	0.00	0.00	0.00	0.00	0.00
Na2O	0.01	0.03	0.01	0.02	0.00	0.00	0.00	0.00	0.01
K2O	0.00	0.01	0.00	0.00	0.00	0.00	0.01	0.00	0.00
F	0.00	0.02	0.00	0.00	0.00	0.00	0.00	0.00	0.00
Cl	0.00	0.01	0.01	0.00	0.00	0.01	0.00	0.00	0.00
H2O	10.61	9.22	10.22	10.07	10.72	9.32	7.66	10.04	12.33
Total	100.00	100.00	100.00	100.00	100.00	100.00	100.00	100.00	100.00
Si	2.52	2.52	2.55	2.55	2.50	2.52	2.58	2.54	2.40
Ti	0.01	0.00	0.00	0.00	0.00	0.00	0.00	0.00	0.00
Al	2.39	2.27	2.10	2.16	2.43	2.22	2.12	2.34	2.39
Mn(3+)	0.00	0.00	0.00	0.00	0.00	0.00	0.00	0.00	0.00
Fe(3+)	1.80	2.37	2.87	2.78	1.80	2.82	2.95	1.97	2.23
Fe(2+)	0.00	0.00	0.00	0.00	0.00	0.00	0.00	0.00	0.00
Mn	0.02	0.02	0.05	0.04	0.02	0.04	0.03	0.02	0.02
Mg	2.64	1.95	1.39	1.42	2.62	1.35	1.20	2.44	2.23
Ca	0.00	0.00	0.00	0.01	0.00	0.00	0.01	0.00	0.00
Ba	0.00	0.00	0.00	0.00	0.00	0.00	0.00	0.00	0.00
Na	0.00	0.01	0.00	0.00	0.00	0.00	0.00	0.00	0.00
K	0.00	0.00	0.00	0.00	0.00	0.00	0.00	0.00	0.00
Rb	0.00	0.00	0.00	0.00	0.00	0.00	0.00	0.00	0.00
Cs	0.00	0.00	0.00	0.00	0.00	0.00	0.00	0.00	0.00
Li	0.00	0.00	0.00	0.00	0.00	0.00	0.00	0.00	0.00
F	0.00	0.01	0.00	0.00	0.00	0.00	0.00	0.00	0.00
Cl	0.00	0.00	0.00	0.00	0.00	0.00	0.00	0.00	0.00
OH	8.00	7.99	8.00	8.00	8.00	8.00	8.00	8.00	8.00
Si	2.52	2.52	2.55	2.55	2.50	2.52	2.58	2.54	2.40
Al(IV)	1.48	1.48	1.45	1.45	1.50	1.48	1.42	1.46	1.60
Total (Tet)	4.00	4.00	4.00	4.00	4.00	4.00	4.00	4.00	4.00
Al(VI)	0.91	0.80	0.66	0.71	0.93	0.74	0.70	0.88	0.80
Ti	0.01	0.00	0.00	0.00	0.00	0.00	0.00	0.00	0.00
V	0.00	0.00	0.00	0.00	0.00	0.00	0.00	0.00	0.00
Cr	0.00	0.00	0.00	0.00	0.00	0.00	0.00	0.00	0.00
Mn3+	0.00	0.00	0.00	0.00	0.00	0.00	0.00	0.00	0.00
Fe3+	1.80	2.37	2.87	2.78	1.80	2.82	2.95	1.97	2.23
Fe2+	0.00	0.00	0.00	0.00	0.00	0.00	0.00	0.00	0.00
Mn	0.02	0.02	0.05	0.04	0.02	0.04	0.03	0.02	0.02
Mg	2.64	1.95	1.39	1.42	2.62	1.35	1.20	2.44	2.23
Total (Oct)	5.38	5.15	4.96	4.96	5.38	4.96	4.88	5.30	5.28
[Octahedral vacant]	0.62	0.85	1.04	1.04	0.62	1.04	1.12	0.70	0.72
Ca	0.00	0.00	0.00	0.01	0.00	0.00	0.01	0.00	0.00
Na	0.00	0.01	0.00	0.00	0.00	0.00	0.00	0.00	0.00
K	0.00	0.00	0.00	0.00	0.00	0.00	0.00	0.00	0.00
Total	0.00	0.01	0.00	0.01	0.00	0.00	0.01	0.00	0.00
OH	8.00	7.99	8.00	8.00	8.00	8.00	8.00	8.00	8.00
Total]	8.00	8.00	8.00	8.00	8.00	8.00	8.00	8.00	8.00

Sample	PQ12309-97	PQ12309-97	PQ12309-97	PQ12309-97	PQ12309-97	PQ12309-97	PQ12309-97	PQ12309-97	PQ12309-97
Analysis	10.00	11.00	12.00	13.00	14.00	15.00	18.00	19.00	20.00
SiO2	23.79	23.82	25.33	24.01	24.50	25.31	24.66	25.10	24.71
TiO2	0.01	0.04	0.22	0.08	0.07	0.03	0.02	0.05	0.03
Al2O3	17.57	19.53	20.55	19.43	20.54	20.42	16.99	17.76	17.41
V2O3	0.00	0.00	0.00	0.00	0.00	0.00	0.00	0.00	0.00
Cr2O3	0.02	0.00	0.04	0.02	0.00	0.02	0.00	0.00	0.00
Mn2O3	0.00	0.00	0.00	0.00	0.00	0.00	0.00	0.00	0.00
Fe2O3	38.70	29.02	26.78	26.96	26.76	27.81	39.85	38.15	41.71
FeO	0.00	0.00	0.00	0.00	0.00	0.00	0.00	0.00	0.00
MnO	0.45	0.30	0.26	0.27	0.27	0.28	0.44	0.50	0.40
MgO	8.18	15.24	16.42	16.27	16.38	16.15	8.88	9.42	7.54
CaO	0.03	0.01	0.02	0.02	0.04	0.01	0.00	0.02	0.02
BaO	0.00	0.00	0.00	0.00	0.00	0.00	0.00	0.00	0.00
Na2O	0.03	0.00	0.02	0.02	0.01	0.00	0.00	0.02	0.00
K2O	0.00	0.01	0.00	0.01	0.00	0.00	0.00	0.00	0.01
F	0.00	0.00	0.00	0.00	0.00	0.00	0.00	0.00	0.00
Cl	0.00	0.01	0.01	0.00	0.01	0.00	0.00	0.01	0.00
H2O	11.23	12.03	10.36	12.93	11.42	9.97	9.15	8.97	8.17
Total	100.00	100.00	100.00	100.00	100.00	100.00	100.00	100.00	100.00
Si	2.47	2.42	2.49	2.45	2.44	2.49	2.50	2.52	2.49
Ti	0.00	0.00	0.02	0.01	0.01	0.00	0.00	0.00	0.00
Al	2.15	2.34	2.38	2.33	2.41	2.36	2.03	2.10	2.07
Mn(3+)	0.00	0.00	0.00	0.00	0.00	0.00	0.00	0.00	0.00
Fe(3+)	3.02	2.22	1.98	2.07	2.01	2.06	3.04	2.89	3.16
Fe(2+)	0.00	0.00	0.00	0.00	0.00	0.00	0.00	0.00	0.00
Mn	0.04	0.03	0.02	0.02	0.02	0.02	0.04	0.04	0.03
Mg	1.26	2.31	2.41	2.47	2.44	2.37	1.34	1.41	1.13
Ca	0.00	0.00	0.00	0.00	0.00	0.00	0.00	0.00	0.00
Ba	0.00	0.00	0.00	0.00	0.00	0.00	0.00	0.00	0.00
Na	0.01	0.00	0.00	0.00	0.00	0.00	0.00	0.00	0.00
K	0.00	0.00	0.00	0.00	0.00	0.00	0.00	0.00	0.00
Rb	0.00	0.00	0.00	0.00	0.00	0.00	0.00	0.00	0.00
Cs	0.00	0.00	0.00	0.00	0.00	0.00	0.00	0.00	0.00
Li	0.00	0.00	0.00	0.00	0.00	0.00	0.00	0.00	0.00
F	0.00	0.00	0.00	0.00	0.00	0.00	0.00	0.00	0.00
Cl	0.00	0.00	0.00	0.00	0.00	0.00	0.00	0.00	0.00
OH	8.00	8.00	8.00	8.00	8.00	8.00	8.00	8.00	8.00
Si	2.47	2.42	2.49	2.45	2.44	2.49	2.50	2.52	2.49
Al(IV)	1.53	1.58	1.51	1.55	1.56	1.51	1.50	1.48	1.51
Total (Tet)	4.00	4.00	4.00	4.00	4.00	4.00	4.00	4.00	4.00
Al(VI)	0.62	0.75	0.87	0.78	0.86	0.85	0.53	0.63	0.56
Ti	0.00	0.00	0.02	0.01	0.01	0.00	0.00	0.00	0.00
V	0.00	0.00	0.00	0.00	0.00	0.00	0.00	0.00	0.00
Cr	0.00	0.00	0.00	0.00	0.00	0.00	0.00	0.00	0.00
Mn3+	0.00	0.00	0.00	0.00	0.00	0.00	0.00	0.00	0.00
Fe3+	3.02	2.22	1.98	2.07	2.01	2.06	3.04	2.89	3.16
Fe2+	0.00	0.00	0.00	0.00	0.00	0.00	0.00	0.00	0.00
Mn	0.04	0.03	0.02	0.02	0.02	0.02	0.04	0.04	0.03
Mg	1.26	2.31	2.41	2.47	2.44	2.37	1.34	1.41	1.13
Total (Oct)	4.94	5.30	5.30	5.34	5.33	5.30	4.96	4.97	4.89
[Octahedral vacant]	1.06	0.70	0.70	0.66	0.67	0.70	1.04	1.03	1.11
Ca	0.00	0.00	0.00	0.00	0.00	0.00	0.00	0.00	0.00
Na	0.01	0.00	0.00	0.00	0.00	0.00	0.00	0.00	0.00
K	0.00	0.00	0.00	0.00	0.00	0.00	0.00	0.00	0.00
Total	0.01	0.00	0.01	0.01	0.01	0.00	0.00	0.01	0.00
OH	8.00	8.00	8.00	8.00	8.00	8.00	8.00	8.00	8.00
Total]	8.00	8.00	8.00	8.00	8.00	8.00	8.00	8.00	8.00

Sample	PQ12309-97	PQ12309-97	PQ12309-97	PQ12309-97	PQ12309-97	PQ12309-97	PQ12309-97	PQ12309-97	PQ12309-97
Analysis	21.00	22.00	23.00	24.00	25.00	26.00	27.00	28.00	29.00
SiO2	24.48	24.52	24.85	25.28	25.66	25.48	24.91	24.80	26.07
TiO2	0.05	0.02	0.06	0.02	0.05	0.07	0.06	0.06	0.05
Al2O3	20.27	17.59	19.92	17.50	21.34	21.67	20.48	20.47	18.61
V2O3	0.00	0.00	0.00	0.00	0.00	0.00	0.00	0.00	0.00
Cr2O3	0.01	0.00	0.00	0.00	0.01	0.03	0.00	0.00	0.03
Mn2O3	0.00	0.00	0.00	0.00	0.00	0.00	0.00	0.00	0.00
Fe2O3	24.76	41.12	27.87	41.49	24.40	24.45	29.08	24.92	36.36
FeO	0.00	0.00	0.00	0.00	0.00	0.00	0.00	0.00	0.00
MnO	0.26	0.32	0.28	0.39	0.28	0.26	0.30	0.28	0.37
MgO	18.02	7.55	16.32	7.57	18.09	17.90	15.31	17.78	10.78
CaO	0.02	0.00	0.01	0.01	0.00	0.00	0.00	0.01	0.03
BaO	0.00	0.00	0.00	0.00	0.00	0.00	0.00	0.00	0.00
Na2O	0.00	0.02	0.00	0.01	0.01	0.00	0.00	0.01	0.00
K2O	0.01	0.01	0.00	0.00	0.00	0.00	0.00	0.00	0.00
F	0.00	0.00	0.00	0.00	0.00	0.00	0.00	0.00	0.00
Cl	0.00	0.00	0.00	0.01	0.00	0.00	0.00	0.00	0.00
H2O	12.13	8.86	10.69	7.72	10.16	10.15	9.87	11.68	7.68
Total	100.00	100.00	100.00	100.00	100.00	100.00	100.00	100.00	100.00
Si	2.45	2.49	2.47	2.53	2.50	2.48	2.46	2.47	2.56
Ti	0.00	0.00	0.00	0.00	0.00	0.01	0.00	0.00	0.00
Al	2.39	2.10	2.33	2.06	2.45	2.48	2.38	2.40	2.15
Mn(3+)	0.00	0.00	0.00	0.00	0.00	0.00	0.00	0.00	0.00
Fe(3+)	1.86	3.14	2.08	3.12	1.79	1.79	2.16	1.87	2.69
Fe(2+)	0.00	0.00	0.00	0.00	0.00	0.00	0.00	0.00	0.00
Mn	0.02	0.03	0.02	0.03	0.02	0.02	0.03	0.02	0.03
Mg	2.69	1.14	2.41	1.13	2.62	2.60	2.25	2.64	1.58
Ca	0.00	0.00	0.00	0.00	0.00	0.00	0.00	0.00	0.00
Ba	0.00	0.00	0.00	0.00	0.00	0.00	0.00	0.00	0.00
Na	0.00	0.00	0.00	0.00	0.00	0.00	0.00	0.00	0.00
K	0.00	0.00	0.00	0.00	0.00	0.00	0.00	0.00	0.00
Rb	0.00	0.00	0.00	0.00	0.00	0.00	0.00	0.00	0.00
Cs	0.00	0.00	0.00	0.00	0.00	0.00	0.00	0.00	0.00
Li	0.00	0.00	0.00	0.00	0.00	0.00	0.00	0.00	0.00
F	0.00	0.00	0.00	0.00	0.00	0.00	0.00	0.00	0.00
Cl	0.00	0.00	0.00	0.00	0.00	0.00	0.00	0.00	0.00
OH	8.00	8.00	8.00	8.00	8.00	8.00	8.00	8.00	8.00
Si	2.45	2.49	2.47	2.53	2.50	2.48	2.46	2.47	2.56
Al(IV)	1.55	1.52	1.53	1.47	1.50	1.52	1.54	1.53	1.44
Total (Tet)	4.00	4.00	4.00	4.00	4.00	4.00	4.00	4.00	4.00
Al(VI)	0.84	0.59	0.80	0.59	0.94	0.96	0.83	0.87	0.71
Ti	0.00	0.00	0.00	0.00	0.00	0.01	0.00	0.00	0.00
V	0.00	0.00	0.00	0.00	0.00	0.00	0.00	0.00	0.00
Cr	0.00	0.00	0.00	0.00	0.00	0.00	0.00	0.00	0.00
Mn3+	0.00	0.00	0.00	0.00	0.00	0.00	0.00	0.00	0.00
Fe3+	1.86	3.14	2.08	3.12	1.79	1.79	2.16	1.87	2.69
Fe2+	0.00	0.00	0.00	0.00	0.00	0.00	0.00	0.00	0.00
Mn	0.02	0.03	0.02	0.03	0.02	0.02	0.03	0.02	0.03
Mg	2.69	1.14	2.41	1.13	2.62	2.60	2.25	2.64	1.58
Total (Oct)	5.42	4.89	5.32	4.88	5.38	5.38	5.27	5.40	5.01
[Octahedral vacant]	0.58	1.11	0.68	1.12	0.62	0.62	0.73	0.60	0.99
Ca	0.00	0.00	0.00	0.00	0.00	0.00	0.00	0.00	0.00
Na	0.00	0.00	0.00	0.00	0.00	0.00	0.00	0.00	0.00
K	0.00	0.00	0.00	0.00	0.00	0.00	0.00	0.00	0.00
Total	0.00	0.00	0.00	0.00	0.00	0.00	0.00	0.00	0.00
OH	8.00	8.00	8.00	8.00	8.00	8.00	8.00	8.00	8.00
Total]	8.00	8.00	8.00	8.00	8.00	8.00	8.00	8.00	8.00

Sample	PQ12280-73	PQ12280-73	PQ12280-73	PQ12280-73	PQ12280-73	PQ12280-73
Analysis	1.00	2.00	3.00	4.00	5.00	6.00
SiO2	26.13	25.97	24.79	24.86	25.85	26.18
TiO2	0.06	0.07	0.08	0.06	0.07	0.07
Al2O3	19.74	20.84	20.35	20.29	20.92	20.73
V2O3	0.00	0.00	0.00	0.00	0.00	0.00
Cr2O3	0.01	0.01	0.00	0.01	0.01	0.00
Mn2O3	0.00	0.00	0.00	0.00	0.00	0.00
Fe2O3	24.99	24.46	24.42	24.82	24.26	24.52
FeO	0.00	0.00	0.00	0.00	0.00	0.00
MnO	0.26	0.27	0.27	0.26	0.28	0.27
MgO	18.09	18.07	18.05	17.81	18.31	18.31
CaO	0.01	0.00	0.00	0.00	0.02	0.00
BaO	0.00	0.00	0.00	0.00	0.00	0.00
Na2O	0.02	0.03	0.02	0.00	0.01	0.00
K2O	0.01	0.00	0.01	0.00	0.00	0.00
F	0.02	0.04	0.01	0.01	0.04	0.00
Cl	0.01	0.00	0.00	0.00	0.01	0.00
H2O	10.66	10.26	12.01	11.86	10.25	9.90
Total	100.00	100.00	100.00	100.00	100.00	100.00
Si	2.56	2.53	2.47	2.48	2.52	2.54
Ti	0.00	0.01	0.01	0.00	0.01	0.01
Al	2.28	2.39	2.39	2.38	2.40	2.37
Mn(3+)	0.00	0.00	0.00	0.00	0.00	0.00
Fe(3+)	1.85	1.79	1.83	1.86	1.78	1.79
Fe(2+)	0.00	0.00	0.00	0.00	0.00	0.00
Mn	0.02	0.02	0.02	0.02	0.02	0.02
Mg	2.65	2.62	2.68	2.65	2.66	2.65
Ca	0.00	0.00	0.00	0.00	0.00	0.00
Ba	0.00	0.00	0.00	0.00	0.00	0.00
Na	0.00	0.01	0.00	0.00	0.00	0.00
K	0.00	0.00	0.00	0.00	0.00	0.00
Rb	0.00	0.00	0.00	0.00	0.00	0.00
Cs	0.00	0.00	0.00	0.00	0.00	0.00
Li	0.00	0.00	0.00	0.00	0.00	0.00
F	0.01	0.01	0.00	0.00	0.01	0.00
Cl	0.00	0.00	0.00	0.00	0.00	0.00
OH	7.99	7.99	8.00	8.00	7.99	8.00
Si	2.56	2.53	2.47	2.48	2.52	2.54
Al(IV)	1.44	1.47	1.53	1.52	1.48	1.46
Total (Tet)	4.00	4.00	4.00	4.00	4.00	4.00
Al(VI)	0.85	0.92	0.86	0.86	0.92	0.91
Ti	0.00	0.01	0.01	0.00	0.01	0.01
V	0.00	0.00	0.00	0.00	0.00	0.00
Cr	0.00	0.00	0.00	0.00	0.00	0.00
Mn3+	0.00	0.00	0.00	0.00	0.00	0.00
Fe3+	1.85	1.79	1.83	1.86	1.78	1.79
Fe2+	0.00	0.00	0.00	0.00	0.00	0.00
Mn	0.02	0.02	0.02	0.02	0.02	0.02
Mg	2.65	2.62	2.68	2.65	2.66	2.65
Total (Oct)	5.36	5.37	5.41	5.40	5.38	5.37
[Octahedral vacant]	0.64	0.63	0.59	0.61	0.62	0.63
Ca	0.00	0.00	0.00	0.00	0.00	0.00
Na	0.00	0.01	0.00	0.00	0.00	0.00
K	0.00	0.00	0.00	0.00	0.00	0.00
Total	0.01	0.01	0.01	0.00	0.00	0.00
OH	7.99	7.99	8.00	8.00	7.99	8.00
Total]	8.00	8.00	8.00	8.00	8.00	8.00

Sample	PQ12280-73	PQ12280-73	PQ12280-73	PQ12280-73	PQ12280-73	PQ12280-73	PQ12280-73
Analysis	7.00	8.00	9.00	10.00	11.00	12.00	13.00
SiO2	24.65	24.74	24.85	25.98	25.23	26.46	26.29
TiO2	0.07	0.06	0.08	0.06	0.06	0.05	0.06
Al2O3	19.42	19.92	19.32	20.97	19.65	19.63	20.83
V2O3	0.00	0.00	0.00	0.00	0.00	0.00	0.00
Cr2O3	0.00	0.01	0.00	0.01	0.01	0.01	0.02
Mn2O3	0.00	0.00	0.00	0.00	0.00	0.00	0.00
Fe2O3	25.49	25.29	26.43	23.65	24.83	26.44	25.17
FeO	0.00	0.00	0.00	0.00	0.00	0.00	0.00
MnO	0.27	0.24	0.26	0.25	0.22	0.27	0.27
MgO	17.55	17.36	17.04	18.45	17.58	17.47	17.87
CaO	0.02	0.03	0.00	0.00	0.00	0.01	0.00
BaO	0.00	0.00	0.00	0.00	0.00	0.00	0.00
Na2O	0.00	0.02	0.02	0.00	0.02	0.00	0.02
K2O	0.01	0.00	0.01	0.00	0.00	0.00	0.00
F	0.00	0.00	0.11	0.08	0.09	0.05	0.00
Cl	0.00	0.02	0.00	0.01	0.00	0.01	0.00
H2O	12.50	12.31	11.93	10.58	12.34	9.63	9.48
Total	100.00	100.00	100.00	100.00	100.00	100.00	100.00
Si	2.48	2.48	2.49	2.53	2.53	2.58	2.54
Ti	0.01	0.00	0.01	0.00	0.00	0.00	0.00
Al	2.31	2.36	2.29	2.41	2.32	2.25	2.37
Mn(3+)	0.00	0.00	0.00	0.00	0.00	0.00	0.00
Fe(3+)	1.93	1.91	2.00	1.74	1.87	1.94	1.83
Fe(2+)	0.00	0.00	0.00	0.00	0.00	0.00	0.00
Mn	0.02	0.02	0.02	0.02	0.02	0.02	0.02
Mg	2.64	2.60	2.55	2.68	2.63	2.53	2.58
Ca	0.00	0.00	0.00	0.00	0.00	0.00	0.00
Ba	0.00	0.00	0.00	0.00	0.00	0.00	0.00
Na	0.00	0.00	0.00	0.00	0.00	0.00	0.00
K	0.00	0.00	0.00	0.00	0.00	0.00	0.00
Rb	0.00	0.00	0.00	0.00	0.00	0.00	0.00
Cs	0.00	0.00	0.00	0.00	0.00	0.00	0.00
Li	0.00	0.00	0.00	0.00	0.00	0.00	0.00
F	0.00	0.00	0.04	0.03	0.03	0.02	0.00
Cl	0.00	0.00	0.00	0.00	0.00	0.00	0.00
OH	8.00	8.00	7.96	7.97	7.97	7.98	8.00
Si	2.48	2.48	2.49	2.53	2.53	2.58	2.54
Al(IV)	1.52	1.52	1.51	1.47	1.47	1.42	1.46
Total (Tet)	4.00	4.00	4.00	4.00	4.00	4.00	4.00
Al(VI)	0.79	0.84	0.78	0.94	0.85	0.83	0.92
Ti	0.01	0.00	0.01	0.00	0.00	0.00	0.00
V	0.00	0.00	0.00	0.00	0.00	0.00	0.00
Cr	0.00	0.00	0.00	0.00	0.00	0.00	0.00
Mn3+	0.00	0.00	0.00	0.00	0.00	0.00	0.00
Fe3+	1.93	1.91	2.00	1.74	1.87	1.94	1.83
Fe2+	0.00	0.00	0.00	0.00	0.00	0.00	0.00
Mn	0.02	0.02	0.02	0.02	0.02	0.02	0.02
Mg	2.64	2.60	2.55	2.68	2.63	2.53	2.58
Total (Oct)	5.39	5.37	5.36	5.39	5.37	5.33	5.35
[Octahedral vacant]	0.61	0.63	0.64	0.61	0.63	0.68	0.65
Ca	0.00	0.00	0.00	0.00	0.00	0.00	0.00
Na	0.00	0.00	0.00	0.00	0.00	0.00	0.00
K	0.00	0.00	0.00	0.00	0.00	0.00	0.00
Total	0.00	0.01	0.01	0.00	0.00	0.00	0.00
OH	8.00	8.00	7.96	7.97	7.97	7.98	8.00
Total]	8.00	8.00	8.00	8.00	8.00	8.00	8.00

Sample	PQ12442-26	PQ12442-26	PQ12442-26	PQ12442-26	PQ12442-26	PQ12442-26	PQ12442-26	PQ12442-26	PQ12442-26
Analysis	1.00	2.00	6.00	7.00	8.00	10.00	11.00	12.00	13.00
SiO2	25.20	25.92	26.51	27.57	27.31	25.47	25.50	25.60	25.48
TiO2	0.04	0.03	0.07	0.03	0.03	0.06	0.06	0.06	0.08
Al2O3	19.86	19.99	20.46	17.86	18.18	21.33	21.08	21.57	21.29
V2O3	0.00	0.00	0.00	0.00	0.00	0.00	0.00	0.00	0.00
Cr2O3	0.01	0.00	0.01	0.00	0.00	0.00	0.02	0.02	0.02
Mn2O3	0.00	0.00	0.00	0.00	0.00	0.00	0.00	0.00	0.00
Fe2O3	24.87	25.28	23.74	26.35	27.82	23.31	23.25	24.14	24.57
FeO	0.00	0.00	0.00	0.00	0.00	0.00	0.00	0.00	0.00
MnO	0.28	0.31	0.27	0.32	0.43	0.22	0.23	0.29	0.30
MgO	18.21	18.11	19.12	17.96	16.40	18.62	18.60	18.26	17.81
CaO	0.03	0.09	0.04	0.03	0.06	0.33	0.25	0.12	0.18
BaO	0.00	0.00	0.00	0.00	0.00	0.00	0.00	0.00	0.00
Na2O	0.00	0.01	0.01	0.00	0.00	0.00	0.04	0.03	0.01
K2O	0.00	0.00	0.00	0.02	0.00	0.00	0.01	0.01	0.01
F	0.00	0.00	0.00	0.00	0.00	0.00	0.00	0.00	0.03
Cl	0.00	0.00	0.00	0.01	0.02	0.01	0.02	0.01	0.01
H2O	11.51	10.24	9.77	9.85	9.77	10.65	10.94	9.87	10.24
Total	100.00	100.00	100.00	100.00	100.00	100.00	100.00	100.00	100.00
Si	2.50	2.54	2.56	2.69	2.67	2.49	2.50	2.48	2.49
Ti	0.00	0.00	0.01	0.00	0.00	0.00	0.00	0.00	0.01
Al	2.32	2.30	2.33	2.05	2.10	2.45	2.43	2.47	2.45
Mn(3+)	0.00	0.00	0.00	0.00	0.00	0.00	0.00	0.00	0.00
Fe(3+)	1.86	1.86	1.73	1.93	2.05	1.71	1.71	1.76	1.80
Fe(2+)	0.00	0.00	0.00	0.00	0.00	0.00	0.00	0.00	0.00
Mn	0.02	0.03	0.02	0.03	0.04	0.02	0.02	0.02	0.02
Mg	2.69	2.64	2.75	2.61	2.39	2.71	2.72	2.64	2.59
Ca	0.00	0.01	0.00	0.00	0.01	0.03	0.03	0.01	0.02
Ba	0.00	0.00	0.00	0.00	0.00	0.00	0.00	0.00	0.00
Na	0.00	0.00	0.00	0.00	0.00	0.00	0.01	0.01	0.00
K	0.00	0.00	0.00	0.00	0.00	0.00	0.00	0.00	0.00
Rb	0.00	0.00	0.00	0.00	0.00	0.00	0.00	0.00	0.00
Cs	0.00	0.00	0.00	0.00	0.00	0.00	0.00	0.00	0.00
Li	0.00	0.00	0.00	0.00	0.00	0.00	0.00	0.00	0.00
F	0.00	0.00	0.00	0.00	0.00	0.00	0.00	0.00	0.01
Cl	0.00	0.00	0.00	0.00	0.00	0.00	0.00	0.00	0.00
OH	8.00	8.00	8.00	8.00	8.00	8.00	8.00	8.00	7.99
Si	2.50	2.54	2.56	2.69	2.67	2.49	2.50	2.48	2.49
Al(IV)	1.50	1.46	1.44	1.31	1.33	1.51	1.50	1.52	1.51
Total (Tet)	4.00	4.00	4.00	4.00	4.00	4.00	4.00	4.00	4.00
Al(VI)	0.82	0.84	0.89	0.74	0.77	0.94	0.93	0.95	0.93
Ti	0.00	0.00	0.01	0.00	0.00	0.00	0.00	0.00	0.01
V	0.00	0.00	0.00	0.00	0.00	0.00	0.00	0.00	0.00
Cr	0.00	0.00	0.00	0.00	0.00	0.00	0.00	0.00	0.00
Mn3+	0.00	0.00	0.00	0.00	0.00	0.00	0.00	0.00	0.00
Fe3+	1.86	1.86	1.73	1.93	2.05	1.71	1.71	1.76	1.80
Fe2+	0.00	0.00	0.00	0.00	0.00	0.00	0.00	0.00	0.00
Mn	0.02	0.03	0.02	0.03	0.04	0.02	0.02	0.02	0.02
Mg	2.69	2.64	2.75	2.61	2.39	2.71	2.72	2.64	2.59
Total (Oct)	5.40	5.37	5.40	5.31	5.25	5.39	5.39	5.38	5.36
[Octahedral vacant]	0.60	0.63	0.60	0.69	0.75	0.61	0.61	0.62	0.64
Ca	0.00	0.01	0.00	0.00	0.01	0.03	0.03	0.01	0.02
Na	0.00	0.00	0.00	0.00	0.00	0.00	0.01	0.01	0.00
K	0.00	0.00	0.00	0.00	0.00	0.00	0.00	0.00	0.00
Total	0.00	0.01	0.01	0.01	0.01	0.04	0.04	0.02	0.02
OH	8.00	8.00	8.00	8.00	8.00	8.00	8.00	8.00	7.99
Total]	8.00	8.00	8.00	8.00	8.00	8.00	8.00	8.00	8.00

Sample	PQ12442-26	PQ12442-26	PQ12442-26	PQ12442-26	PQ12442-26	PQ12442-26	PQ12442-26	PQ12442-26	PQ12442-26
Analysis	15.00	16.00	17.00	18.00	19.00	20.00	21.00	22.00	23.00
SiO2	26.42	26.14	24.91	25.07	25.59	25.74	25.73	25.89	25.54
TiO2	0.08	0.06	0.06	0.08	0.05	0.08	0.07	0.05	0.06
Al2O3	19.86	20.83	20.34	20.83	21.59	21.44	21.61	21.44	21.54
V2O3	0.00	0.00	0.00	0.00	0.00	0.00	0.00	0.00	0.00
Cr2O3	0.02	0.01	0.00	0.02	0.03	0.03	0.02	0.01	0.00
Mn2O3	0.00	0.00	0.00	0.00	0.00	0.00	0.00	0.00	0.00
Fe2O3	24.67	23.46	24.21	24.08	23.94	23.76	23.89	24.31	23.82
FeO	0.00	0.00	0.00	0.00	0.00	0.00	0.00	0.00	0.00
MnO	0.29	0.29	0.30	0.26	0.28	0.28	0.28	0.27	0.28
MgO	18.69	19.06	18.46	18.61	18.47	18.59	18.39	18.47	18.40
CaO	0.00	0.00	0.01	0.00	0.00	0.00	0.02	0.00	0.00
BaO	0.00	0.00	0.00	0.00	0.00	0.00	0.00	0.00	0.00
Na2O	0.01	0.01	0.00	0.01	0.01	0.01	0.04	0.00	0.00
K2O	0.01	0.00	0.00	0.00	0.00	0.01	0.03	0.00	0.00
F	0.00	0.01	0.02	0.00	0.02	0.03	0.00	0.00	0.00
Cl	0.01	0.00	0.00	0.00	0.00	0.01	0.02	0.00	0.00
H2O	9.96	10.12	11.70	11.04	10.03	10.04	9.91	9.55	10.36
Total	100.00	100.00	100.00	100.00	100.00	100.00	100.00	100.00	100.00
Si	2.57	2.53	2.47	2.47	2.48	2.50	2.49	2.50	2.49
Ti	0.01	0.00	0.00	0.01	0.00	0.01	0.01	0.00	0.00
Al	2.27	2.38	2.38	2.42	2.47	2.45	2.47	2.44	2.47
Mn(3+)	0.00	0.00	0.00	0.00	0.00	0.00	0.00	0.00	0.00
Fe(3+)	1.80	1.71	1.81	1.78	1.75	1.73	1.74	1.77	1.74
Fe(2+)	0.00	0.00	0.00	0.00	0.00	0.00	0.00	0.00	0.00
Mn	0.02	0.02	0.03	0.02	0.02	0.02	0.02	0.02	0.02
Mg	2.71	2.76	2.73	2.73	2.67	2.69	2.66	2.66	2.67
Ca	0.00	0.00	0.00	0.00	0.00	0.00	0.00	0.00	0.00
Ba	0.00	0.00	0.00	0.00	0.00	0.00	0.00	0.00	0.00
Na	0.00	0.00	0.00	0.00	0.00	0.00	0.01	0.00	0.00
K	0.00	0.00	0.00	0.00	0.00	0.00	0.00	0.00	0.00
Rb	0.00	0.00	0.00	0.00	0.00	0.00	0.00	0.00	0.00
Cs	0.00	0.00	0.00	0.00	0.00	0.00	0.00	0.00	0.00
Li	0.00	0.00	0.00	0.00	0.00	0.00	0.00	0.00	0.00
F	0.00	0.00	0.01	0.00	0.01	0.01	0.00	0.00	0.00
Cl	0.00	0.00	0.00	0.00	0.00	0.00	0.00	0.00	0.00
OH	8.00	7.99	7.99	8.00	7.99	7.99	8.00	8.00	8.00
Si	2.57	2.53	2.47	2.47	2.48	2.50	2.49	2.50	2.49
Al(IV)	1.43	1.47	1.53	1.53	1.52	1.50	1.51	1.50	1.51
Total (Tet)	4.00	4.00	4.00	4.00	4.00	4.00	4.00	4.00	4.00
Al(VI)	0.84	0.92	0.85	0.88	0.95	0.95	0.96	0.94	0.96
Ti	0.01	0.00	0.00	0.01	0.00	0.01	0.01	0.00	0.00
V	0.00	0.00	0.00	0.00	0.00	0.00	0.00	0.00	0.00
Cr	0.00	0.00	0.00	0.00	0.00	0.00	0.00	0.00	0.00
Mn3+	0.00	0.00	0.00	0.00	0.00	0.00	0.00	0.00	0.00
Fe3+	1.80	1.71	1.81	1.78	1.75	1.73	1.74	1.77	1.74
Fe2+	0.00	0.00	0.00	0.00	0.00	0.00	0.00	0.00	0.00
Mn	0.02	0.02	0.03	0.02	0.02	0.02	0.02	0.02	0.02
Mg	2.71	2.76	2.73	2.73	2.67	2.69	2.66	2.66	2.67
Total (Oct)	5.39	5.41	5.43	5.43	5.40	5.40	5.39	5.39	5.40
[Octahedral vacant]	0.61	0.59	0.57	0.57	0.60	0.60	0.61	0.61	0.60
Ca	0.00	0.00	0.00	0.00	0.00	0.00	0.00	0.00	0.00
Na	0.00	0.00	0.00	0.00	0.00	0.00	0.01	0.00	0.00
K	0.00	0.00	0.00	0.00	0.00	0.00	0.00	0.00	0.00
Total	0.00	0.00	0.00	0.00	0.00	0.00	0.01	0.00	0.00
OH	8.00	7.99	7.99	8.00	7.99	7.99	8.00	8.00	8.00
Total]	8.00	8.00	8.00	8.00	8.00	8.00	8.00	8.00	8.00

Sample	PQ12442-26	PQ12442-26	PQ12442-26
Analysis	24.00	26.00	27.00
SiO2	24.66	25.80	24.10
TiO2	0.09	0.06	0.07
Al2O3	21.41	21.67	20.53
V2O3	0.00	0.00	0.00
Cr2O3	0.02	0.02	0.00
Mn2O3	0.00	0.00	0.00
Fe2O3	23.94	23.94	23.97
FeO	0.00	0.00	0.00
MnO	0.30	0.33	0.31
MgO	18.20	18.42	17.58
CaO	0.01	0.06	0.11
BaO	0.00	0.00	0.00
Na2O	0.01	0.00	0.02
K2O	0.03	0.02	0.04
F	0.02	0.00	0.00
Cl	0.01	0.00	0.01
H2O	11.32	9.68	13.27
Total	100.00	100.00	100.00
Si	2.44	2.49	2.44
Ti	0.01	0.00	0.01
Al	2.49	2.47	2.45
Mn(3+)	0.00	0.00	0.00
Fe(3+)	1.78	1.74	1.83
Fe(2+)	0.00	0.00	0.00
Mn	0.03	0.03	0.03
Mg	2.68	2.65	2.65
Ca	0.00	0.01	0.01
Ba	0.00	0.00	0.00
Na	0.00	0.00	0.00
K	0.00	0.00	0.01
Rb	0.00	0.00	0.00
Cs	0.00	0.00	0.00
Li	0.00	0.00	0.00
F	0.01	0.00	0.00
Cl	0.00	0.00	0.00
OH	7.99	8.00	8.00
Si	2.44	2.49	2.44
Al(IV)	1.56	1.51	1.56
Total (Tet)	4.00	4.00	4.00
Al(VI)	0.93	0.96	0.89
Ti	0.01	0.00	0.01
V	0.00	0.00	0.00
Cr	0.00	0.00	0.00
Mn3+	0.00	0.00	0.00
Fe3+	1.78	1.74	1.83
Fe2+	0.00	0.00	0.00
Mn	0.03	0.03	0.03
Mg	2.68	2.65	2.65
Total (Oct)	5.42	5.39	5.40
[Octahedral vacant]	0.58	0.61	0.60
Ca	0.00	0.01	0.01
Na	0.00	0.00	0.00
K	0.00	0.00	0.01
Total	0.01	0.01	0.02
OH	7.99	8.00	8.00
Total]	8.00	8.00	8.00

Sample	PQ35a557	PQ35a557	PQ35a557	PQ35a557	PQ35a557	PQ35a557	PQ35a557	PQ35a557	PQ35a557	PQ35a557
Analysis	1.00	2.00	3.00	4.00	5.00	6.00	7.00	8.00	9.00	10.00
SiO2	26.83	27.02	26.39	26.08	26.38	26.36	26.16	28.33	26.64	25.94
TiO2	0.05	0.06	0.09	0.07	0.03	0.03	0.07	0.01	0.06	0.05
Al2O3	20.43	20.41	21.77	21.40	21.33	16.46	21.12	17.37	20.50	20.32
V2O3	0.00	0.00	0.00	0.00	0.00	0.00	0.00	0.00	0.00	0.00
Cr2O3	0.05	0.02	0.00	0.05	0.06	0.03	0.03	0.02	0.08	0.08
Mn2O3	0.00	0.00	0.00	0.00	0.00	0.00	0.00	0.00	0.00	0.00
Fe2O3	22.48	22.46	21.70	21.76	21.93	23.84	21.08	26.19	22.33	21.46
FeO	0.00	0.00	0.00	0.00	0.00	0.00	0.00	0.00	0.00	0.00
MnO	0.21	0.23	0.25	0.19	0.24	0.25	0.23	0.28	0.23	0.19
MgO	20.02	20.15	20.24	19.57	20.19	18.41	20.23	18.30	19.76	19.41
CaO	0.00	0.00	0.01	0.02	0.00	0.05	0.00	0.02	0.01	0.00
BaO	0.00	0.00	0.00	0.00	0.00	0.00	0.00	0.00	0.00	0.00
Na2O	0.01	0.00	0.00	0.03	0.01	0.00	0.00	0.00	0.00	0.00
K2O	0.00	0.00	0.00	0.04	0.00	0.01	0.00	0.00	0.01	0.00
F	0.00	0.00	0.02	0.02	0.00	0.00	0.00	0.04	0.00	0.00
Cl	0.00	0.01	0.00	0.02	0.00	0.00	0.00	0.00	0.00	0.01
H2O	9.91	9.63	9.54	10.76	9.82	14.57	11.08	9.45	10.38	12.54
Total	100.00	100.00	100.00	100.00	100.00	100.00	100.00	100.00	100.00	100.00
Si	2.58	2.59	2.53	2.53	2.54	2.70	2.54	2.74	2.58	2.57
Ti	0.00	0.00	0.01	0.01	0.00	0.00	0.01	0.00	0.00	0.00
Al	2.32	2.31	2.46	2.45	2.42	1.99	2.42	1.98	2.34	2.37
Mn(3+)	0.00	0.00	0.00	0.00	0.00	0.00	0.00	0.00	0.00	0.00
Fe(3+)	1.63	1.62	1.56	1.59	1.59	1.84	1.54	1.91	1.63	1.60
Fe(2+)	0.00	0.00	0.00	0.00	0.00	0.00	0.00	0.00	0.00	0.00
Mn	0.02	0.02	0.02	0.02	0.02	0.02	0.02	0.02	0.02	0.02
Mg	2.88	2.88	2.89	2.83	2.89	2.81	2.93	2.64	2.85	2.87
Ca	0.00	0.00	0.00	0.00	0.00	0.01	0.00	0.00	0.00	0.00
Ba	0.00	0.00	0.00	0.00	0.00	0.00	0.00	0.00	0.00	0.00
Na	0.00	0.00	0.00	0.01	0.00	0.00	0.00	0.00	0.00	0.00
K	0.00	0.00	0.00	0.00	0.00	0.00	0.00	0.00	0.00	0.00
Rb	0.00	0.00	0.00	0.00	0.00	0.00	0.00	0.00	0.00	0.00
Cs	0.00	0.00	0.00	0.00	0.00	0.00	0.00	0.00	0.00	0.00
Li	0.00	0.00	0.00	0.00	0.00	0.00	0.00	0.00	0.00	0.00
F	0.00	0.00	0.01	0.01	0.00	0.00	0.00	0.01	0.00	0.00
Cl	0.00	0.00	0.00	0.00	0.00	0.00	0.00	0.00	0.00	0.00
OH	8.00	8.00	7.99	7.99	8.00	8.00	8.00	7.99	8.00	8.00
Si	2.58	2.59	2.53	2.53	2.54	2.70	2.54	2.74	2.58	2.57
Al(IV)	1.42	1.41	1.47	1.47	1.46	1.30	1.46	1.26	1.42	1.43
Total (Tet)	4.00	4.00	4.00	4.00	4.00	4.00	4.00	4.00	4.00	4.00
Al(VI)	0.90	0.90	0.98	0.98	0.95	0.69	0.96	0.73	0.92	0.94
Ti	0.00	0.00	0.01	0.01	0.00	0.00	0.01	0.00	0.00	0.00
V	0.00	0.00	0.00	0.00	0.00	0.00	0.00	0.00	0.00	0.00
Cr	0.00	0.00	0.00	0.00	0.00	0.00	0.00	0.00	0.01	0.01
Mn3+	0.00	0.00	0.00	0.00	0.00	0.00	0.00	0.00	0.00	0.00
Fe3+	1.63	1.62	1.56	1.59	1.59	1.84	1.54	1.91	1.63	1.60
Fe2+	0.00	0.00	0.00	0.00	0.00	0.00	0.00	0.00	0.00	0.00
Mn	0.02	0.02	0.02	0.02	0.02	0.02	0.02	0.02	0.02	0.02
Mg	2.88	2.88	2.89	2.83	2.89	2.81	2.93	2.64	2.85	2.87
Total (Oct)	5.43	5.43	5.46	5.43	5.46	5.37	5.47	5.31	5.43	5.44
[Octahedral vacant]	0.57	0.57	0.54	0.57	0.54	0.63	0.53	0.69	0.57	0.56
Ca	0.00	0.00	0.00	0.00	0.00	0.01	0.00	0.00	0.00	0.00
Na	0.00	0.00	0.00	0.01	0.00	0.00	0.00	0.00	0.00	0.00
K	0.00	0.00	0.00	0.00	0.00	0.00	0.00	0.00	0.00	0.00
Total	0.00	0.00	0.00	0.01	0.00	0.01	0.00	0.00	0.00	0.00
OH	8.00	8.00	7.99	7.99	8.00	8.00	8.00	7.99	8.00	8.00
Total]	8.00	8.00	8.00	8.00	8.00	8.00	8.00	8.00	8.00	8.00

Sample	PQ41298-03	PQ41298-03	PQ41298-03	PQ41298-03	PQ41298-03	PQ41298-03	PQ41298-03	PQ41298-03	PQ41298-03
Analysis	1.00	2.00	3.00	4.00	5.00	6.00	7.00	8.00	9.00
SiO2	25.03	24.88	25.53	24.91	25.11	25.83	25.71	24.82	25.40
TiO2	0.08	0.08	0.07	0.10	0.08	0.09	0.08	0.07	0.12
Al2O3	20.45	19.52	20.59	20.72	20.65	20.97	20.90	20.98	19.92
V2O3	0.00	0.00	0.00	0.00	0.00	0.00	0.00	0.00	0.00
Cr2O3	0.00	0.00	0.00	0.00	0.00	0.00	0.00	0.00	0.00
Mn2O3	0.00	0.00	0.00	0.00	0.00	0.00	0.00	0.00	0.00
Fe2O3	23.81	25.80	23.71	22.24	23.27	21.98	23.56	22.92	24.22
FeO	0.00	0.00	0.00	0.00	0.00	0.00	0.00	0.00	0.00
MnO	0.23	0.18	0.19	0.21	0.22	0.22	0.21	0.23	0.19
MgO	17.03	15.07	16.87	16.80	16.58	17.70	16.70	16.91	16.06
CaO	0.00	0.00	0.00	0.06	0.00	0.00	0.00	0.00	0.00
BaO	0.00	0.00	0.00	0.00	0.00	0.00	0.00	0.00	0.00
Na2O	0.00	0.01	0.00	0.03	0.01	0.00	0.01	0.00	0.04
K2O	0.01	0.04	0.04	0.02	0.01	0.00	0.02	0.01	0.02
F	0.00	0.00	0.05	0.02	0.04	0.04	0.08	0.06	0.06
Cl	0.02	0.02	0.00	0.01	0.02	0.00	0.01	0.00	0.01
H2O	13.18	14.28	12.78	14.00	13.98	13.02	12.76	13.81	13.74
Total	99.84	99.87	99.81	99.10	99.95	99.83	99.99	99.78	99.75
Si	2.52	2.56	2.56	2.55	2.55	2.58	2.57	2.52	2.58
Ti	0.01	0.01	0.01	0.01	0.01	0.01	0.01	0.01	0.01
Al	2.43	2.37	2.43	2.49	2.47	2.47	2.46	2.51	2.39
Mn(3+)	0.00	0.00	0.00	0.00	0.00	0.00	0.00	0.00	0.00
Fe(3+)	1.81	2.00	1.79	1.71	1.78	1.65	1.77	1.75	1.85
Fe(2+)	0.00	0.00	0.00	0.00	0.00	0.00	0.00	0.00	0.00
Mn	0.02	0.02	0.02	0.02	0.02	0.02	0.02	0.02	0.02
Mg	2.56	2.31	2.52	2.56	2.51	2.63	2.49	2.56	2.43
Ca	0.00	0.00	0.00	0.01	0.00	0.00	0.00	0.00	0.00
Ba	0.00	0.00	0.00	0.00	0.00	0.00	0.00	0.00	0.00
Na	0.00	0.00	0.00	0.01	0.00	0.00	0.00	0.00	0.01
K	0.00	0.00	0.00	0.00	0.00	0.00	0.00	0.00	0.00
Rb	0.00	0.00	0.00	0.00	0.00	0.00	0.00	0.00	0.00
Cs	0.00	0.00	0.00	0.00	0.00	0.00	0.00	0.00	0.00
Li	0.00	0.00	0.00	0.00	0.00	0.00	0.00	0.00	0.00
F	0.00	0.00	0.02	0.01	0.01	0.01	0.03	0.02	0.02
Cl	0.00	0.00	0.00	0.00	0.00	0.00	0.00	0.00	0.00
OH	8.00	8.00	7.98	7.99	7.98	7.99	7.97	7.98	7.98
Si	2.52	2.56	2.56	2.55	2.55	2.58	2.57	2.52	2.58
Al(IV)	1.48	1.44	1.44	1.45	1.45	1.42	1.43	1.48	1.42
Total (Tet)	4.00	4.00	4.00	4.00	4.00	4.00	4.00	4.00	4.00
Al(VI)	0.96	0.92	0.99	1.04	1.02	1.05	1.03	1.02	0.97
Ti	0.01	0.01	0.01	0.01	0.01	0.01	0.01	0.01	0.01
V	0.00	0.00	0.00	0.00	0.00	0.00	0.00	0.00	0.00
Cr	0.00	0.00	0.00	0.00	0.00	0.00	0.00	0.00	0.00
Mn3+	0.00	0.00	0.00	0.00	0.00	0.00	0.00	0.00	0.00
Fe3+	1.81	2.00	1.79	1.71	1.78	1.65	1.77	1.75	1.85
Fe2+	0.00	0.00	0.00	0.00	0.00	0.00	0.00	0.00	0.00
Mn	0.02	0.02	0.02	0.02	0.02	0.02	0.02	0.02	0.02
Mg	2.56	2.31	2.52	2.56	2.51	2.63	2.49	2.56	2.43
Total (Oct)	5.35	5.25	5.32	5.33	5.32	5.36	5.31	5.35	5.28
[Octahedral vacant]	0.65	0.75	0.68	0.67	0.68	0.64	0.69	0.65	0.72
Ca	0.00	0.00	0.00	0.01	0.00	0.00	0.00	0.00	0.00
Na	0.00	0.00	0.00	0.01	0.00	0.00	0.00	0.00	0.01
K	0.00	0.00	0.00	0.00	0.00	0.00	0.00	0.00	0.00
Total	0.00	0.01	0.00	0.01	0.00	0.00	0.00	0.00	0.01
OH	8.00	8.00	7.98	7.99	7.98	7.99	7.97	7.98	7.98
Total]	8.00	8.00	8.00	8.00	8.00	8.00	8.00	8.00	8.00

Sample	PQ41298-03	PQ41298-03	PQ41298-03	PQ41298-03	PQ41298-03	PQ41298-03	PQ41298-03	PQ41298-03
Analysis	10.00	11.00	12.00	13.00	14.00	16.00	15.00	17.00
SiO2	25.39	25.04	25.44	25.46	25.19	25.45	25.06	25.21
TiO2	0.08	0.08	0.06	0.07	0.12	0.08	0.09	0.08
Al2O3	21.05	20.46	20.96	20.96	21.14	21.27	20.75	20.60
V2O3	0.00	0.00	0.00	0.00	0.00	0.00	0.00	0.00
Cr2O3	0.01	0.00	0.00	0.01	0.00	0.00	0.00	0.00
Mn2O3	0.00	0.00	0.00	0.00	0.00	0.00	0.00	0.00
Fe2O3	22.73	23.23	24.33	23.15	22.54	23.23	22.45	23.13
FeO	0.00	0.00	0.00	0.00	0.00	0.00	0.00	0.00
MnO	0.24	0.23	0.22	0.22	0.24	0.22	0.24	0.23
MgO	17.11	16.64	16.31	16.74	17.36	17.25	17.13	17.03
CaO	0.00	0.00	0.00	0.00	0.00	0.00	0.02	0.00
BaO	0.00	0.00	0.00	0.00	0.00	0.00	0.00	0.00
Na2O	0.01	0.01	0.00	0.00	0.02	0.01	0.03	0.02
K2O	0.01	0.02	0.01	0.01	0.01	0.02	0.01	0.01
F	0.00	0.02	0.03	0.02	0.00	0.11	0.01	0.03
Cl	0.00	0.00	0.00	0.00	0.00	0.00	0.00	0.00
H2O	13.09	14.18	12.63	13.29	13.15	12.23	13.50	13.53
Total	99.73	99.91	99.99	99.93	99.78	99.82	99.29	99.85
Si	2.55	2.55	2.54	2.56	2.53	2.53	2.54	2.55
Ti	0.01	0.01	0.00	0.01	0.01	0.01	0.01	0.01
Al	2.49	2.45	2.47	2.48	2.50	2.49	2.48	2.45
Mn(3+)	0.00	0.00	0.00	0.00	0.00	0.00	0.00	0.00
Fe(3+)	1.72	1.78	1.83	1.75	1.70	1.74	1.71	1.76
Fe(2+)	0.00	0.00	0.00	0.00	0.00	0.00	0.00	0.00
Mn	0.02	0.02	0.02	0.02	0.02	0.02	0.02	0.02
Mg	2.56	2.52	2.43	2.51	2.60	2.56	2.59	2.56
Ca	0.00	0.00	0.00	0.00	0.00	0.00	0.00	0.00
Ba	0.00	0.00	0.00	0.00	0.00	0.00	0.00	0.00
Na	0.00	0.00	0.00	0.00	0.00	0.00	0.01	0.00
K	0.00	0.00	0.00	0.00	0.00	0.00	0.00	0.00
Rb	0.00	0.00	0.00	0.00	0.00	0.00	0.00	0.00
Cs	0.00	0.00	0.00	0.00	0.00	0.00	0.00	0.00
Li	0.00	0.00	0.00	0.00	0.00	0.00	0.00	0.00
F	0.00	0.01	0.01	0.01	0.00	0.04	0.00	0.01
Cl	0.00	0.00	0.00	0.00	0.00	0.00	0.00	0.00
OH	8.00	7.99	7.99	7.99	8.00	7.96	8.00	7.99
Si	2.55	2.55	2.54	2.56	2.53	2.53	2.54	2.55
Al(IV)	1.45	1.45	1.46	1.44	1.47	1.47	1.46	1.45
Total (Tet)	4.00	4.00	4.00	4.00	4.00	4.00	4.00	4.00
Al(VI)	1.04	1.00	1.01	1.04	1.03	1.02	1.02	1.00
Ti	0.01	0.01	0.00	0.01	0.01	0.01	0.01	0.01
V	0.00	0.00	0.00	0.00	0.00	0.00	0.00	0.00
Cr	0.00	0.00	0.00	0.00	0.00	0.00	0.00	0.00
Mn3+	0.00	0.00	0.00	0.00	0.00	0.00	0.00	0.00
Fe3+	1.72	1.78	1.83	1.75	1.70	1.74	1.71	1.76
Fe2+	0.00	0.00	0.00	0.00	0.00	0.00	0.00	0.00
Mn	0.02	0.02	0.02	0.02	0.02	0.02	0.02	0.02
Mg	2.56	2.52	2.43	2.51	2.60	2.56	2.59	2.56
Total (Oct)	5.34	5.33	5.30	5.32	5.36	5.35	5.35	5.34
[Octahedral vacant]	0.66	0.67	0.70	0.68	0.64	0.65	0.65	0.66
Ca	0.00	0.00	0.00	0.00	0.00	0.00	0.00	0.00
Na	0.00	0.00	0.00	0.00	0.00	0.00	0.01	0.00
K	0.00	0.00	0.00	0.00	0.00	0.00	0.00	0.00
Total	0.00	0.00	0.00	0.00	0.00	0.00	0.01	0.00
OH	8.00	7.99	7.99	7.99	8.00	7.96	8.00	7.99
Total]	8.00	8.00	8.00	8.00	8.00	8.00	8.00	8.00

Sample	PQ12308-20	PQ12308-20	PQ12308-20	PQ12308-20	PQ12308-20	PQ12308-20	PQ12308-20	PQ12308-20	PQ12308-20
Analysis	1.00	3.00	9.00	17.00	18.00	19.00	20.00	1.00	2.00
SiO2	28.07	26.31	26.56	28.71	28.30	29.35	29.72	29.48	26.89
TiO2	0.04	0.09	0.06	0.04	0.02	0.02	0.09	0.03	0.07
Al2O3	17.63	20.76	19.77	16.59	16.91	16.47	16.02	16.92	20.96
V2O3	0.00	0.00	0.00	0.00	0.00	0.00	0.00	0.00	0.00
Cr2O3	0.00	0.00	0.00	0.00	0.00	0.00	0.00	0.00	0.00
Mn2O3	0.00	0.00	0.00	0.00	0.00	0.00	0.00	0.00	0.00
Fe2O3	26.14	22.58	23.13	25.29	25.70	24.89	24.61	21.84	18.83
FeO	0.00	0.00	0.00	0.00	0.00	0.00	0.00	0.00	0.00
MnO	0.29	0.34	0.29	0.27	0.27	0.26	0.22	0.22	0.22
MgO	17.07	18.54	18.19	17.78	17.43	18.05	18.17	20.10	20.64
CaO	0.00	0.00	0.00	0.00	0.00	0.00	0.00	0.07	0.05
BaO	0.00	0.00	0.00	0.00	0.00	0.00	0.00	0.00	0.00
Na2O	0.03	0.01	0.00	0.01	0.00	0.00	0.01	0.00	0.01
K2O	0.03	0.00	0.00	0.01	0.02	0.02	0.13	0.04	0.00
F	0.02	0.08	0.05	0.05	0.06	0.08	0.05	0.04	0.00
Cl	0.00	0.01	0.00	0.01	0.00	0.01	0.02	0.00	0.00
H2O	10.64	11.30	11.84	11.27	11.04	10.78	10.98	10.48	10.83
Total	99.96	99.97	99.87	100.00	99.72	99.89	99.99	99.21	98.49
Si	2.76	2.58	2.63	2.83	2.80	2.87	2.91	2.87	2.63
Ti	0.00	0.01	0.00	0.00	0.00	0.00	0.01	0.00	0.01
Al	2.04	2.40	2.30	1.93	1.97	1.90	1.85	1.94	2.41
Mn(3+)	0.00	0.00	0.00	0.00	0.00	0.00	0.00	0.00	0.00
Fe(3+)	1.93	1.67	1.72	1.88	1.91	1.83	1.81	1.60	1.39
Fe(2+)	0.00	0.00	0.00	0.00	0.00	0.00	0.00	0.00	0.00
Mn	0.02	0.03	0.02	0.02	0.02	0.02	0.02	0.02	0.02
Mg	2.50	2.71	2.68	2.61	2.57	2.63	2.65	2.92	3.01
Ca	0.00	0.00	0.00	0.00	0.00	0.00	0.00	0.01	0.00
Ba	0.00	0.00	0.00	0.00	0.00	0.00	0.00	0.00	0.00
Na	0.01	0.00	0.00	0.00	0.00	0.00	0.00	0.00	0.00
K	0.00	0.00	0.00	0.00	0.00	0.00	0.02	0.00	0.00
Rb	0.00	0.00	0.00	0.00	0.00	0.00	0.00	0.00	0.00
Cs	0.00	0.00	0.00	0.00	0.00	0.00	0.00	0.00	0.00
Li	0.00	0.00	0.00	0.00	0.00	0.00	0.00	0.00	0.00
F	0.01	0.03	0.02	0.02	0.02	0.03	0.02	0.01	0.00
Cl	0.00	0.00	0.00	0.00	0.00	0.00	0.00	0.00	0.00
OH	7.99	7.97	7.98	7.98	7.98	7.97	7.98	7.99	8.00
Si	2.76	2.58	2.63	2.83	2.80	2.87	2.91	2.87	2.63
Al(IV)	1.24	1.42	1.37	1.17	1.20	1.13	1.09	1.13	1.37
Total (Tet)	4.00	4.00	4.00	4.00	4.00	4.00	4.00	4.00	4.00
Al(VI)	0.79	0.98	0.93	0.76	0.76	0.77	0.76	0.81	1.04
Ti	0.00	0.01	0.00	0.00	0.00	0.00	0.01	0.00	0.01
V	0.00	0.00	0.00	0.00	0.00	0.00	0.00	0.00	0.00
Cr	0.00	0.00	0.00	0.00	0.00	0.00	0.00	0.00	0.00
Mn3+	0.00	0.00	0.00	0.00	0.00	0.00	0.00	0.00	0.00
Fe3+	1.93	1.67	1.72	1.88	1.91	1.83	1.81	1.60	1.39
Fe2+	0.00	0.00	0.00	0.00	0.00	0.00	0.00	0.00	0.00
Mn	0.02	0.03	0.02	0.02	0.02	0.02	0.02	0.02	0.02
Mg	2.50	2.71	2.68	2.61	2.57	2.63	2.65	2.92	3.01
Total (Oct)	5.25	5.38	5.36	5.27	5.26	5.26	5.25	5.35	5.46
[Octahedral vacant]	0.75	0.62	0.64	0.73	0.74	0.74	0.75	0.65	0.54
Ca	0.00	0.00	0.00	0.00	0.00	0.00	0.00	0.01	0.00
Na	0.01	0.00	0.00	0.00	0.00	0.00	0.00	0.00	0.00
K	0.00	0.00	0.00	0.00	0.00	0.00	0.02	0.00	0.00
Total	0.01	0.00	0.00	0.00	0.00	0.00	0.02	0.01	0.01
OH	7.99	7.97	7.98	7.98	7.98	7.97	7.98	7.99	8.00
Total]	8.00	8.00	8.00	8.00	8.00	8.00	8.00	8.00	8.00

Sample	PQ12308-20	PQ12308-20	PQ12308-20
Analysis	3.00	4.00	2.00
SiO2	29.80	29.82	26.58
TiO2	0.15	0.03	0.06
Al2O3	16.97	16.60	21.36
V2O3	0.00	0.00	0.00
Cr2O3	0.00	0.00	0.02
Mn2O3	0.00	0.00	0.00
Fe2O3	21.25	21.41	18.99
FeO	0.00	0.00	0.00
MnO	0.17	0.18	0.26
MgO	19.92	20.30	20.66
CaO	0.10	0.09	0.01
BaO	0.00	0.00	0.00
Na2O	0.01	0.01	0.00
K2O	0.08	0.02	0.00
F	0.00	0.00	0.00
Cl	0.01	0.00	0.01
H2O	11.53	11.52	12.05
Total	99.98	99.99	100.00
Si	2.90	2.90	2.59
Ti	0.01	0.00	0.00
Al	1.95	1.91	2.46
Mn(3+)	0.00	0.00	0.00
Fe(3+)	1.56	1.57	1.39
Fe(2+)	0.00	0.00	0.00
Mn	0.01	0.01	0.02
Mg	2.89	2.95	3.00
Ca	0.01	0.01	0.00
Ba	0.00	0.00	0.00
Na	0.00	0.00	0.00
K	0.01	0.00	0.00
Rb	0.00	0.00	0.00
Cs	0.00	0.00	0.00
Li	0.00	0.00	0.00
F	0.00	0.00	0.00
Cl	0.00	0.00	0.00
OH	8.00	8.00	8.00
Si	2.90	2.90	2.59
Al(IV)	1.10	1.10	1.41
Total (Tet)	4.00	4.00	4.00
Al(VI)	0.85	0.81	1.05
Ti	0.01	0.00	0.00
V	0.00	0.00	0.00
Cr	0.00	0.00	0.00
Mn3+	0.00	0.00	0.00
Fe3+	1.56	1.57	1.39
Fe2+	0.00	0.00	0.00
Mn	0.01	0.01	0.02
Mg	2.89	2.95	3.00
Total (Oct)	5.32	5.34	5.48
[Octahedral vacant]	0.68	0.66	0.52
Ca	0.01	0.01	0.00
Na	0.00	0.00	0.00
K	0.01	0.00	0.00
Total	0.02	0.01	0.00
OH	8.00	8.00	8.00
Total]	8.00	8.00	8.00

Appendix VI

(Microprobe data - Sulfide)

SAMPLE	Analysis	Sb%	S%	Fe%	As%	Cu%	Ag%	Ni%	Co%	Te%	Pb%	Sn%	V%	Mn%	Zn%	Mo%	Cd%	TOTAL
PQ12302-20	Py1_01	0.00	53.03	47.05	0.023	0.013	0.00	0.00	0.92	0.00	0.00	0.00	0.00	0.00	0.01	0.045	0.00	101.09
PQ12302-20	Py1_10	0.00	53.37	44.07	0.452	0.032	0.00	0.00	5.29	0.00	0.00	0.00	0.00	0.00	0.00	0.034	0.00	103.25
PQ12302-20	Py1_11	0.00	53.37	46.89	0.051	0.003	0.00	0.00	1.07	0.00	0.00	0.00	0.00	0.00	0.00	0.057	0.00	101.45
PQ12302-20	Py1_02	0.00	54.47	44.17	0.310	0.001	0.00	0.00	4.70	0.00	0.00	0.01	0.00	0.00	0.01	0.011	0.00	103.68
PQ12302-20	Py1_03	0.00	53.91	47.25	0.037	0.000	0.00	0.00	0.66	0.00	0.00	0.00	0.00	0.00	0.00	0.046	0.00	101.90
PQ12302-20	Py1_04	0.00	52.80	45.29	0.386	0.000	0.00	0.00	3.69	0.00	0.00	0.00	0.00	0.00	0.01	0.038	0.00	102.22
PQ12302-20	Py1_05	0.00	52.74	47.08	0.003	0.019	0.00	0.00	1.05	0.00	0.00	0.00	0.00	0.00	0.01	0.053	0.00	100.96
PQ12302-20	Py1_06	0.00	52.90	44.19	0.473	0.013	0.00	0.00	5.36	0.00	0.00	0.00	0.00	0.00	0.01	0.026	0.00	102.96
PQ12302-20	Py1_07	0.00	53.71	47.01	0.022	0.000	0.00	0.00	0.83	0.00	0.02	0.00	0.00	0.00	0.00	0.023	0.00	101.62
PQ12302-20	Py1_08	0.00	52.76	46.92	0.000	0.017	0.00	0.00	1.04	0.00	0.00	0.01	0.00	0.00	0.00	0.028	0.00	100.77
PQ12302-20	Py1_09	0.00	53.20	46.76	0.073	0.001	0.00	0.01	0.60	0.00	0.00	0.01	0.00	0.00	0.01	0.039	0.02	100.73
PQ12302-20	Py2_01	0.00	52.72	46.87	0.023	0.008	0.00	0.00	0.87	0.00	0.00	0.00	0.00	0.00	0.01	0.048	0.00	100.56
PQ12302-20	Py2_02	0.00	52.61	46.69	0.045	0.000	0.00	0.00	1.08	0.00	0.00	0.00	0.00	0.00	0.00	0.032	0.00	100.47
PQ12302-20	Py2_03	0.00	52.33	46.56	0.077	0.005	0.00	0.00	1.14	0.00	0.00	0.00	0.00	0.00	0.00	0.037	0.00	100.15
PQ12302-20	Py2_04	0.00	53.04	46.90	0.000	0.018	0.01	0.00	0.87	0.00	0.00	0.00	0.00	0.00	0.00	0.030	0.02	100.88
PQ12302-46	Py1_01	0.00	51.60	46.66	0.071	0.015	0.00	0.00	0.95	0.00	0.00	0.00	0.00	0.00	0.01	0.044	0.00	99.35
PQ12302-46	Py1_02	0.00	51.73	46.69	0.043	0.009	0.00	0.00	0.97	0.00	0.00	0.00	0.00	0.00	0.01	0.052	0.00	99.49
PQ12302-46	Py1_03	0.00	51.46	46.57	0.013	0.032	0.00	0.00	1.03	0.00	0.00	0.00	0.00	0.00	0.01	0.044	0.00	99.16
PQ12302-46	Py1_04	0.00	52.10	46.63	0.001	0.006	0.00	0.00	0.74	0.00	0.00	0.00	0.00	0.00	0.00	0.047	0.00	99.52
PQ12302-46	Py1_05	0.00	51.66	46.67	0.049	0.006	0.00	0.00	0.93	0.00	0.00	0.00	0.00	0.00	0.00	0.054	0.00	99.38
PQ12302-46	Py1_06	0.00	51.25	46.65	0.012	0.028	0.00	0.00	0.76	0.00	0.00	0.01	0.00	0.00	0.00	0.055	0.00	98.77
PQ12302-46	Py1_07	0.00	52.22	46.49	0.109	0.024	0.00	0.01	1.07	0.00	0.00	0.00	0.00	0.00	0.00	0.056	0.00	99.98
PQ12302-46	Py1_08	0.00	51.12	46.71	0.012	0.000	0.00	0.00	0.80	0.00	0.01	0.00	0.00	0.00	0.00	0.048	0.00	98.71
PQ12302-46	Py1_09	0.00	50.78	46.61	0.009	0.007	0.00	0.00	1.21	0.00	0.00	0.00	0.00	0.00	0.00	0.055	0.00	98.67
PQ12302-46	Py1_10	0.00	52.07	46.36	0.001	0.022	0.00	0.00	1.05	0.00	0.00	0.00	0.00	0.00	0.00	0.040	0.00	99.55
PQ12302-46	Py1_11	0.00	51.17	46.45	0.000	0.010	0.00	0.00	0.80	0.00	0.00	0.00	0.00	0.00	0.00	0.041	0.01	98.48
PQ12302-46	Py1_12	0.00	51.13	46.67	0.019	0.017	0.00	0.00	0.51	0.00	0.00	0.01	0.00	0.00	0.00	0.032	0.00	98.38
PQ12302-46	Py1_13	0.00	50.98	46.46	0.025	0.000	0.00	0.00	0.86	0.00	0.00	0.02	0.00	0.00	0.01	0.042	0.00	98.40
PQ12302-46	Py1_14	0.00	50.95	46.38	0.026	0.020	0.00	0.00	0.74	0.00	0.00	0.01	0.00	0.00	0.00	0.038	0.00	98.16
PQ12302-46	Py2_01	0.00	51.76	46.41	0.022	0.000	0.00	0.00	0.57	0.00	0.00	0.00	0.00	0.00	0.01	0.025	0.00	98.79
PQ12302-46	Py2_02	0.00	52.76	46.64	0.031	0.031	0.00	0.00	0.76	0.00	0.00	0.00	0.00	0.00	0.01	0.045	0.00	100.28
PQ12302-46	Py2_03	0.00	51.92	46.52	0.037	0.008	0.00	0.00	1.29	0.00	0.00	0.00	0.00	0.00	0.00	0.055	0.00	99.84
PQ12302-46	Py2_04	0.00	52.11	46.68	0.045	0.000	0.00	0.00	0.83	0.00	0.00	0.00	0.00	0.00	0.00	0.058	0.00	99.72
PQ12302-46	Py2_05	0.00	50.85	46.31	0.019	0.002	0.00	0.00	0.68	0.00	0.00	0.00	0.00	0.00	0.00	0.037	0.00	97.90

SAMPLE	Analysis	Sb%	S%	Fe %	As %	Cu %	Ag %	Ni %	Co %	Te %	Pb %	Sn %	V %	Mn %	Zn %	Mo %	Cd %	TOTAL
PQ12302-46	Py2_06	0.00	52.83	46.45	0.022	0.017	0.00	0.00	0.93	0.00	0.00	0.01	0.00	0.00	0.01	0.038	0.00	100.30
PQ12302-46	Py2_07	0.00	52.49	45.53	0.166	0.012	0.01	0.00	2.83	0.00	0.01	0.02	0.00	0.00	0.00	0.040	0.00	101.10
PQ12302-46	Py3_01	0.00	52.05	46.51	0.026	0.027	0.00	0.00	0.94	0.00	0.01	0.00	0.00	0.00	0.00	0.050	0.00	99.61
PQ12302-46	Py3_02	0.00	52.20	46.53	0.004	0.000	0.00	0.00	0.80	0.00	0.00	0.00	0.00	0.00	0.00	0.036	0.00	99.58
PQ12302-46	Py3_03	0.00	51.81	46.29	0.052	0.000	0.00	0.03	1.04	0.00	0.00	0.00	0.00	0.00	0.00	0.049	0.01	99.29
PQ12309-97	Py1_01	0.00	53.13	46.85	0.000	0.000	0.00	0.00	0.73	0.00	0.00	0.00	0.00	0.00	0.00	0.046	0.00	100.77
PQ12309-97	Py1_02	0.00	52.40	46.75	0.000	0.028	0.00	0.00	1.09	0.00	0.01	0.00	0.00	0.00	0.00	0.050	0.00	100.33
PQ12309-97	Py1_03	0.00	51.81	46.70	0.015	0.001	0.00	0.00	1.48	0.00	0.00	0.00	0.00	0.00	0.00	0.041	0.00	100.05
PQ12309-97	Py2a_01	0.00	51.58	46.86	0.039	0.000	0.00	0.00	1.04	0.00	0.00	0.00	0.00	0.00	0.00	0.026	0.00	99.55
PQ12309-97	Py2a_02	0.00	51.49	46.90	0.000	0.006	0.00	0.00	0.94	0.00	0.00	0.00	0.00	0.00	0.00	0.049	0.00	99.39
PQ12309-97	Py2a_03	0.00	50.20	45.85	0.000	0.022	0.00	0.00	0.46	0.00	0.00	0.00	0.00	0.00	0.01	0.041	0.00	96.58
PQ12309-97	Py2b_01	0.00	50.59	46.12	0.043	0.000	0.00	0.00	0.89	0.00	0.00	0.01	0.00	0.00	0.00	0.049	0.00	97.69
PQ12309-97	Py2b_02	0.00	51.48	45.98	0.035	0.012	0.00	0.00	0.73	0.00	0.00	0.00	0.00	0.00	0.01	0.042	0.00	98.28
PQ12309-97	Py2b_03	0.00	50.68	46.07	0.001	0.011	0.00	0.00	0.84	0.00	0.00	0.00	0.00	0.00	0.01	0.050	0.00	97.66
PQ12309-97	Py2c_01	0.00	51.10	46.47	0.000	0.000	0.00	0.00	1.03	0.00	0.01	0.00	0.00	0.00	0.00	0.052	0.00	98.67
PQ12309-97	Py2d_01	0.00	51.71	46.45	0.039	0.001	0.00	0.00	0.59	0.00	0.00	0.00	0.00	0.00	0.00	0.050	0.00	98.84
PQ12309-97	Py2d_02	0.00	50.41	46.28	0.030	0.000	0.00	0.00	0.62	0.00	0.00	0.00	0.00	0.00	0.01	0.032	0.00	97.37
PQ12309-97	Py2d_03	0.00	49.05	45.89	0.000	0.000	0.00	0.00	0.90	0.00	0.00	0.00	0.00	0.00	0.01	0.033	0.00	95.88
PQ12309-97	Py2e_01	0.00	50.36	46.38	0.000	0.013	0.00	0.00	0.75	0.00	0.00	0.00	0.00	0.00	0.00	0.028	0.03	97.57
PQ12309-97	Py2e_02	0.00	50.66	46.37	0.000	0.018	0.00	0.00	0.51	0.00	0.01	0.00	0.00	0.00	0.00	0.041	0.00	97.62
PQ12309-97	Py2e_03	0.00	50.37	46.39	0.038	0.006	0.00	0.00	0.75	0.00	0.00	0.00	0.00	0.00	0.00	0.054	0.00	97.62
PQ12309-97	Py2e_04	0.00	51.57	46.34	0.032	0.001	0.00	0.00	0.71	0.00	0.00	0.00	0.00	0.00	0.00	0.048	0.00	98.70
PQ12309-97	Py2e_05	0.00	50.99	46.42	0.056	0.010	0.00	0.00	0.55	0.00	0.00	0.00	0.00	0.00	0.00	0.065	0.00	98.09
PQ12309-97	Py3_01	0.00	52.55	46.74	0.000	0.000	0.00	0.00	0.83	0.00	0.00	0.00	0.00	0.00	0.00	0.043	0.00	100.16
PQ12309-97	Py3_02	0.00	51.71	46.43	0.008	0.022	0.00	0.00	0.96	0.00	0.00	0.00	0.00	0.00	0.00	0.024	0.00	99.16
PQ12309-97	Py3_03	0.00	51.13	46.33	0.037	0.000	0.00	0.00	0.86	0.00	0.00	0.00	0.00	0.00	0.00	0.042	0.00	98.40
PQ12319-42	Py1_01	0.00	53.97	46.81	0.038	0.002	0.00	0.00	1.15	0.00	0.00	0.00	0.00	0.00	0.01	0.013	0.00	101.99
PQ12319-42	Py1_02	0.00	54.70	46.99	0.043	0.000	0.00	0.10	1.39	0.00	0.00	0.00	0.00	0.00	0.00	0.014	0.00	103.25
PQ12319-42	Py1_03	0.00	54.65	47.06	0.000	0.006	0.00	0.00	1.20	0.00	0.00	0.00	0.00	0.00	0.01	0.026	0.08	103.03
PQ12319-42	Py1_04	0.00	53.00	46.78	0.025	0.001	0.00	0.00	1.25	0.00	0.00	0.00	0.00	0.00	0.00	0.002	0.00	101.06
PQ12319-42	Py1_05	0.00	54.64	47.04	0.069	0.020	0.01	0.00	1.30	0.00	0.00	0.00	0.00	0.00	0.00	0.009	0.00	103.09
PQ12319-42	Py1_06	0.00	54.45	47.18	0.022	0.011	0.00	0.00	1.33	0.00	0.00	0.00	0.00	0.00	0.00	0.004	0.00	103.00
PQ12319-42	Py1_07	0.00	54.11	46.93	0.000	0.023	0.00	0.01	1.24	0.00	0.00	0.01	0.00	0.00	0.00	0.015	0.02	102.36
PQ12319-42	Py1_08	0.00	54.41	47.07	0.000	0.012	0.00	0.00	1.27	0.00	0.00	0.00	0.00	0.00	0.00	0.028	0.00	102.80

SAMPLE	Analysis	Sb%	S%	Fe %	As %	Cu %	Ag %	Ni %	Co %	Te %	Pb %	Sn %	V %	Mn %	Zn %	Mo %	Cd %	TOTAL
PQ12319-42	Py2_10	0.00	54.72	46.24	0.021	0.000	0.00	0.00	1.34	0.00	0.00	0.00	0.00	0.00	0.00	0.007	0.01	102.34
PQ12319-42	Py2_11	0.00	54.39	46.43	0.000	0.016	0.00	0.00	1.28	0.00	0.00	0.00	0.00	0.00	0.01	0.000	0.00	102.12
PQ12319-42	Py2_12	0.00	49.90	45.55	0.024	0.024	0.00	0.00	1.14	0.00	0.00	0.00	0.03	0.04	0.01	0.000	0.00	96.72
PQ12319-42	Py2_13	0.00	54.75	46.60	0.000	0.000	0.00	0.00	1.55	0.00	0.00	0.00	0.00	0.00	0.01	0.002	0.00	102.91
PQ12319-42	Py2_14	0.00	55.01	46.87	0.059	0.000	0.00	0.00	1.51	0.00	0.00	0.00	0.00	0.00	0.01	0.024	0.00	103.48
PQ12319-42	Py2_15	0.00	54.91	46.57	0.013	0.004	0.00	0.00	1.21	0.00	0.00	0.01	0.00	0.00	0.01	0.028	0.00	102.75
PQ12319-42	Py2_01r	0.00	55.04	46.25	0.002	0.014	0.00	0.00	1.19	0.00	0.01	0.00	0.00	0.00	0.00	0.028	0.00	102.54
PQ12319-42	Py2_02r	0.00	54.64	45.71	0.000	0.013	0.00	0.00	1.68	0.00	0.01	0.00	0.00	0.00	0.00	0.031	0.02	102.10
PQ12319-42	Py2_03	0.00	54.81	45.57	0.066	0.000	0.00	0.00	1.74	0.00	0.00	0.00	0.00	0.00	0.00	0.029	0.00	102.23
PQ12319-42	Py2_04	0.00	54.34	45.71	0.054	0.025	0.00	0.00	1.27	0.00	0.00	0.01	0.00	0.00	0.00	0.017	0.00	101.42
PQ12319-42	Py2_05	0.00	54.35	45.45	0.037	0.000	0.00	0.00	1.87	0.00	0.00	0.00	0.00	0.00	0.00	0.016	0.00	101.73
PQ12319-42	Py2_06	0.00	54.64	46.20	0.000	0.004	0.00	0.00	1.35	0.00	0.00	0.00	0.00	0.00	0.01	0.030	0.00	102.23
PQ12319-42	Py2_07	0.00	54.64	46.16	0.039	0.008	0.01	0.00	1.32	0.00	0.00	0.00	0.00	0.00	0.01	0.019	0.00	102.20
PQ12319-42	Py2_08	0.00	54.11	45.83	0.000	0.020	0.00	0.00	1.34	0.00	0.01	0.02	0.00	0.00	0.01	0.006	0.00	101.35
PQ12319-42	Py2_09	0.00	54.42	46.30	0.004	0.004	0.00	0.00	1.15	0.00	0.00	0.01	0.00	0.00	0.00	0.007	0.04	101.94
PQ12319-42	Py3_01	0.00	54.03	46.90	0.064	0.017	0.00	0.00	1.14	0.00	0.00	0.00	0.00	0.00	0.01	0.024	0.00	102.18
PQ12319-42	Py3_02	0.00	54.45	46.98	0.000	0.006	0.00	0.00	1.24	0.00	0.00	0.00	0.00	0.00	0.00	0.026	0.00	102.69
PQ12319-42	Py3_03	0.00	54.57	46.67	0.007	0.000	0.00	0.00	1.17	0.00	0.00	0.00	0.00	0.00	0.00	0.030	0.01	102.46
PQ12319-42	Py3_04	0.00	54.38	46.84	0.009	0.000	0.00	0.00	1.14	0.00	0.00	0.00	0.00	0.00	0.01	0.027	0.06	102.47
PQ12328-85	Py1_01	0.00	53.43	46.95	0.027	0.028	0.00	0.00	1.18	0.00	0.00	0.00	0.00	0.00	0.01	0.023	0.00	101.64
PQ12328-85	Py1_02	0.00	52.91	46.97	0.058	0.000	0.00	0.00	0.89	0.00	0.01	0.00	0.00	0.00	0.00	0.030	0.00	100.88
PQ12328-85	Py1_03	0.00	53.86	46.91	0.016	0.033	0.00	0.00	0.58	0.02	0.00	0.01	0.00	0.00	0.01	0.032	0.00	101.46
PQ12328-85	Py1_04	0.00	52.46	46.83	0.081	0.025	0.00	0.00	1.00	0.00	0.00	0.00	0.00	0.00	0.01	0.036	0.00	100.45
PQ12328-85	Py1_05	0.00	53.73	46.91	0.000	0.003	0.00	0.00	0.93	0.00	0.00	0.00	0.00	0.00	0.01	0.019	0.00	101.61
PQ12328-85	Py2_01	0.00	53.62	46.51	0.016	0.000	0.00	0.04	1.63	0.00	0.00	0.01	0.00	0.00	0.00	0.037	0.00	101.87
PQ12328-85	Py2_02	0.00	52.99	46.94	0.047	0.000	0.00	0.00	1.14	0.00	0.00	0.00	0.00	0.00	0.01	0.046	0.00	101.18
PQ12328-85	Py2_03	0.00	52.84	47.02	0.029	0.000	0.00	0.00	0.92	0.00	0.00	0.00	0.00	0.00	0.01	0.043	0.00	100.86
PQ12328-85	Py2_04	0.00	53.56	46.76	0.000	0.000	0.00	0.00	1.29	0.00	0.00	0.00	0.00	0.00	0.00	0.050	0.00	101.66
PQ12328-85	Py2_05	0.00	52.04	46.83	0.046	0.000	0.00	0.00	1.16	0.00	0.00	0.00	0.00	0.00	0.01	0.047	0.00	100.13
PQ12328-85	Py2_06	0.00	52.23	46.68	0.008	0.000	0.00	0.00	1.27	0.00	0.00	0.00	0.00	0.00	0.00	0.042	0.00	100.22
PQ12328-85	Py2_07	0.00	51.88	45.68	0.019	0.007	0.00	0.00	0.74	0.01	0.00	0.00	0.00	0.00	0.01	0.012	0.00	98.35
PQ12328-85	Py2_08	0.00	53.15	46.38	0.000	0.000	0.00	0.05	1.07	0.00	0.00	0.01	0.00	0.00	0.01	0.032	0.00	100.70
PQ12328-85	Py2_09	0.00	53.62	47.03	0.013	0.014	0.00	0.00	1.16	0.00	0.00	0.00	0.00	0.00	0.00	0.039	0.00	101.88
PQ12328-85	Py2_10	0.00	53.07	47.07	0.000	0.009	0.00	0.00	1.14	0.00	0.00	0.00	0.00	0.00	0.01	0.017	0.00	101.32

SAMPLE	Analysis	Sb%	S%	Fe %	As %	Cu %	Ag %	Ni %	Co %	Te %	Pb %	Sn %	V %	Mn %	Zn %	Mo %	Cd %	TOTAL
PQ12328-85	Py2_11	0.00	53.52	47.00	0.039	0.000	0.00	0.00	1.03	0.00	0.00	0.00	0.00	0.00	0.01	0.042	0.00	101.64
PQ12328-85	Py4_01	0.00	53.82	46.64	0.000	0.000	0.00	0.04	1.61	0.00	0.00	0.01	0.00	0.00	0.00	0.025	0.00	102.14
PQ12328-85	Py4_02	0.00	53.38	46.82	0.010	0.000	0.00	0.00	1.02	0.00	0.00	0.00	0.00	0.00	0.01	0.017	0.00	101.26
PQ12328-85	Py4_03	0.00	52.93	46.44	0.012	0.000	0.00	0.01	0.94	0.00	0.00	0.00	0.00	0.00	0.01	0.037	0.00	100.39
PQ12328-85	Py4_04	0.00	53.06	46.70	0.000	0.011	0.00	0.00	1.01	0.00	0.00	0.00	0.00	0.00	0.01	0.018	0.00	100.82
PQ12328-85	Py4_05	0.00	54.07	46.88	0.000	0.000	0.00	0.00	0.97	0.00	0.00	0.00	0.00	0.00	0.01	0.026	0.00	101.96
PQ12328-85	Py4_06	0.00	52.45	46.81	0.000	0.000	0.00	0.00	0.99	0.00	0.00	0.01	0.00	0.00	0.01	0.019	0.00	100.30
PQ12328-85	Py4_07	0.00	53.73	47.14	0.000	0.000	0.00	0.00	1.04	0.00	0.00	0.00	0.00	0.00	0.00	0.015	0.00	101.92
PQ12328-85	Py4_08	0.00	52.11	46.23	0.047	0.000	0.00	0.00	1.00	0.03	0.00	0.00	0.00	0.01	0.02	0.029	0.00	99.47
PQ12328-85	Py4_09	0.00	53.97	47.26	0.040	0.000	0.00	0.00	0.97	0.00	0.00	0.00	0.00	0.00	0.01	0.000	0.01	102.26
PQ12328-85	Py4_10	0.00	54.26	46.97	0.010	0.005	0.00	0.00	1.10	0.00	0.00	0.01	0.00	0.00	0.01	0.022	0.00	102.39
PQ12328-85	Py4_11	0.00	54.08	47.18	0.008	0.000	0.00	0.00	1.06	0.00	0.00	0.00	0.00	0.00	0.00	0.003	0.00	102.33
PQ12328-85	Py4_12	0.00	53.34	46.91	0.045	0.000	0.00	0.00	0.71	0.00	0.00	0.00	0.00	0.00	0.01	0.028	0.00	101.03
PQ12328-85	Py4_13	0.00	54.65	47.10	0.074	0.034	0.00	0.00	0.85	0.00	0.00	0.00	0.00	0.00	0.01	0.030	0.00	102.74
PQ12328-85	Py4_14	0.00	54.55	47.01	0.003	0.003	0.00	0.00	1.51	0.00	0.00	0.01	0.00	0.00	0.00	0.013	0.00	103.10
PQ12328-85	Py4_15	0.00	53.48	47.14	0.030	0.011	0.00	0.00	0.96	0.00	0.01	0.00	0.00	0.00	0.01	0.023	0.00	101.67
PQ12328-85	Py4_16	0.00	53.99	46.97	0.036	0.009	0.00	0.00	0.96	0.00	0.00	0.00	0.00	0.00	0.01	0.043	0.03	102.05
PQ12328-85	Py4_17	0.00	54.45	46.93	0.002	0.000	0.00	0.00	1.07	0.00	0.02	0.00	0.00	0.00	0.00	0.031	0.00	102.50
PQ12328-85	Py5_01	0.00	54.00	46.99	0.000	0.000	0.00	0.00	1.22	0.00	0.00	0.00	0.00	0.00	0.00	0.012	0.03	102.26
PQ12328-85	Py5_02	0.00	53.62	47.07	0.000	0.000	0.00	0.00	1.44	0.00	0.00	0.00	0.00	0.00	0.00	0.017	0.00	102.15
PQ12328-85	Py5_03	0.00	54.43	46.83	0.019	0.014	0.00	0.04	1.23	0.00	0.00	0.00	0.00	0.00	0.00	0.023	0.00	102.58
PQ12328-85	Py5_04	0.00	54.39	47.09	0.035	0.000	0.00	0.00	1.25	0.00	0.00	0.00	0.00	0.00	0.01	0.028	0.00	102.80
PQ12328-85	Py5_05	0.00	53.61	47.09	0.046	0.000	0.00	0.00	0.84	0.00	0.00	0.00	0.00	0.00	0.00	0.027	0.00	101.61
PQ12328-85	Py5_06	0.00	53.81	47.18	0.001	0.017	0.00	0.00	1.04	0.00	0.00	0.00	0.00	0.00	0.01	0.037	0.00	102.10
PQ12328-85	Py5_07	0.00	52.76	47.15	0.000	0.000	0.00	0.00	0.75	0.00	0.00	0.00	0.00	0.00	0.00	0.045	0.00	100.71
PQ12328-85	Py5_08	0.00	52.72	46.97	0.042	0.000	0.00	0.00	0.98	0.00	0.00	0.00	0.00	0.00	0.00	0.045	0.00	100.76
PQ12328-85	Py5_09	0.00	53.59	47.01	0.019	0.000	0.00	0.00	1.41	0.00	0.00	0.00	0.00	0.00	0.00	0.040	0.00	102.09
PQ12328-85	Py5_10	0.00	53.74	47.06	0.016	0.000	0.00	0.00	0.55	0.00	0.00	0.00	0.00	0.00	0.00	0.032	0.00	101.40
PQ12328-85	Py5_11	0.00	53.13	47.17	0.049	0.000	0.00	0.00	1.01	0.00	0.00	0.00	0.00	0.00	0.01	0.055	0.00	101.42
PQ12328-85	Py5_12	0.00	52.83	46.74	0.051	0.000	0.00	0.00	1.00	0.00	0.00	0.00	0.00	0.00	0.00	0.032	0.00	100.67
PQ12328-85	Py5_13	0.00	52.92	47.01	0.000	0.000	0.00	0.00	1.07	0.00	0.00	0.00	0.01	0.00	0.01	0.039	0.00	101.05
PQ12328-85	Py5_14	0.00	52.96	47.01	0.000	0.018	0.00	0.00	0.85	0.00	0.00	0.00	0.00	0.00	0.01	0.026	0.00	100.89
PQ12424-26	Py1_01	0.00	52.81	46.42	0.000	0.003	0.00	0.00	0.83	0.00	0.00	0.01	0.00	0.00	0.01	0.037	0.00	100.12
PQ12424-26	Py1_02	0.00	52.04	46.27	0.031	0.031	0.00	0.00	1.14	0.00	0.00	0.00	0.00	0.00	0.01	0.046	0.00	99.56

SAMPLE	Analysis	Sb%	S%	Fe %	As %	Cu %	Ag %	Ni %	Co %	Te %	Pb %	Sn %	V %	Mn %	Zn %	Mo %	Cd %	TOTAL
PQ12424-26	Py1_03	0.00	52.87	46.53	0.052	0.000	0.00	0.00	1.13	0.00	0.00	0.01	0.01	0.00	0.00	0.043	0.00	100.64
PQ12424-26	Py1_04	0.00	52.90	46.56	0.026	0.006	0.00	0.00	0.60	0.00	0.00	0.00	0.00	0.00	0.00	0.038	0.00	100.14
PQ12424-26	Py1_05	0.00	52.89	46.57	0.000	0.032	0.00	0.00	1.13	0.00	0.02	0.01	0.00	0.00	0.00	0.030	0.00	100.69
PQ12424-26	Py1_06	0.00	52.53	46.54	0.000	0.008	0.00	0.00	0.72	0.00	0.00	0.00	0.00	0.00	0.00	0.033	0.00	99.84
PQ12424-26	Py1_07	0.00	53.30	46.62	0.056	0.000	0.00	0.00	1.16	0.00	0.00	0.00	0.00	0.00	0.00	0.018	0.00	101.17
PQ12424-26	Py1_08	0.00	52.73	46.26	0.052	0.016	0.00	0.00	1.45	0.00	0.00	0.00	0.00	0.00	0.00	0.041	0.00	100.55
PQ12424-26	Py1_09	0.00	53.17	46.76	0.016	0.013	0.00	0.00	0.63	0.00	0.00	0.02	0.00	0.00	0.01	0.030	0.00	100.65
PQ12424-26	Py2_01	0.00	53.39	46.93	0.000	0.030	0.00	0.00	0.74	0.00	0.00	0.00	0.00	0.00	0.01	0.025	0.00	101.14
PQ12424-26	Py2_02	0.00	52.89	45.83	0.000	0.016	0.00	0.00	2.01	0.00	0.00	0.00	0.00	0.00	0.00	0.051	0.04	100.84
PQ12424-26	Py2_03	0.00	53.18	46.79	0.000	0.005	0.00	0.00	1.34	0.00	0.00	0.00	0.00	0.00	0.01	0.025	0.00	101.35
PQ12424-26	Py2_04	0.00	53.27	46.76	0.000	0.008	0.00	0.00	1.29	0.00	0.00	0.00	0.00	0.00	0.00	0.031	0.03	101.40
PQ12424-26	Py2_05	0.00	52.42	46.86	0.000	0.000	0.00	0.00	1.16	0.00	0.00	0.00	0.00	0.00	0.00	0.040	0.00	100.48
PQ12424-26	Py3_01	0.00	52.66	46.71	0.012	0.024	0.00	0.00	0.57	0.00	0.00	0.00	0.00	0.00	0.01	0.040	0.00	100.03
PQ12424-26	Py3_02	0.00	52.59	46.74	0.021	0.001	0.00	0.00	1.15	0.00	0.00	0.00	0.00	0.00	0.01	0.022	0.00	100.54
PQ12424-26	Py3_03	0.00	52.94	46.84	0.019	0.007	0.00	0.00	1.17	0.00	0.00	0.00	0.00	0.00	0.00	0.027	0.00	101.00
PQ12424-26	Py3_04	0.00	53.61	46.92	0.045	0.000	0.00	0.00	1.09	0.00	0.00	0.00	0.00	0.00	0.00	0.032	0.00	101.70
PQ35a447-84	Py1a_01	0.00	53.01	46.98	0.000	0.000	0.00	0.00	0.97	0.00	0.00	0.00	0.00	0.00	0.01	0.036	0.00	101.00
PQ35a447-84	Py1a_02	0.00	51.52	46.33	0.053	0.020	0.00	0.00	1.22	0.00	0.00	0.00	0.00	0.00	0.01	0.026	0.00	99.19
PQ35a447-84	Py1a_03	0.00	52.74	46.41	0.055	0.016	0.00	0.00	1.56	0.00	0.00	0.00	0.00	0.00	0.00	0.027	0.00	100.82
PQ35a447-84	Py1b_01	0.00	53.14	46.45	0.019	0.018	0.00	0.00	2.15	0.00	0.01	0.00	0.00	0.00	0.01	0.025	0.00	101.82
PQ35a447-84	Py1b_02	0.00	52.24	46.92	0.006	0.019	0.00	0.00	0.92	0.00	0.02	0.00	0.00	0.00	0.01	0.035	0.00	100.15
PQ35a447-84	Py1b_03	0.00	52.91	46.84	0.044	0.027	0.00	0.00	0.85	0.00	0.00	0.00	0.00	0.00	0.00	0.030	0.00	100.69
PQ35a447-84	Py1c_01	0.00	53.55	46.60	0.038	0.018	0.00	0.00	1.87	0.00	0.00	0.00	0.00	0.00	0.00	0.036	0.00	102.12
PQ35a447-84	Py1c_02	0.00	52.81	46.70	0.050	0.010	0.00	0.00	1.49	0.00	0.01	0.01	0.00	0.00	0.00	0.023	0.00	101.12
PQ35a447-84	Py1c_03	0.00	52.86	46.78	0.065	0.037	0.00	0.00	0.94	0.00	0.00	0.00	0.00	0.00	0.00	0.040	0.00	100.73
PQ35a447-84	Py1c_04	0.00	53.07	46.86	0.070	0.023	0.00	0.00	1.22	0.00	0.00	0.00	0.00	0.00	0.01	0.034	0.00	101.30
PQ35a447-84	Py1d_01	0.00	53.74	46.69	0.005	0.021	0.00	0.00	1.32	0.00	0.00	0.01	0.00	0.00	0.00	0.015	0.00	101.80
PQ35a447-84	Py1d_02	0.00	52.12	47.18	0.011	0.000	0.00	0.00	0.89	0.00	0.01	0.01	0.00	0.00	0.00	0.048	0.00	100.27
PQ35a447-84	Py1d_03	0.00	52.16	47.02	0.055	0.006	0.00	0.00	1.06	0.00	0.00	0.00	0.00	0.00	0.00	0.025	0.00	100.32
PQ35a447-84	Py2_01	0.00	52.98	44.80	0.024	0.135	0.00	0.00	4.19	0.00	0.00	0.00	0.00	0.00	0.01	0.024	0.00	102.16
PQ35a447-84	Py4_01c	0.00	53.16	46.67	0.029	0.014	0.00	0.00	1.64	0.00	0.00	0.00	0.00	0.00	0.00	0.034	0.00	101.55
PQ35a447-84	Py4_02r	0.00	53.26	46.46	0.024	0.014	0.00	0.00	1.70	0.00	0.01	0.00	0.00	0.00	0.00	0.034	0.00	101.51
PQ35a447-84	Py5_02r	0.00	53.18	46.48	0.046	0.000	0.00	0.00	1.42	0.00	0.00	0.00	0.00	0.00	0.00	0.034	0.00	101.16
PQ35a447-84	Py6_01c	0.00	53.33	46.54	0.000	0.006	0.00	0.00	1.71	0.00	0.00	0.00	0.00	0.00	0.00	0.029	0.00	101.62

SAMPLE	Analysis	Sb%	S%	Fe %	As %	Cu %	Ag %	Ni %	Co %	Te %	Pb %	Sn %	V %	Mn %	Zn %	Mo %	Cd %	TOTAL
PQ35a447-84	Py6_02 r	0.00	53.31	46.85	0.000	0.000	0.00	0.00	1.25	0.00	0.04	0.00	0.00	0.00	0.01	0.026	0.00	101.49
PQ35a447-84	Py5_01 c	0.00	53.24	46.40	0.051	0.010	0.00	0.00	1.97	0.00	0.00	0.00	0.00	0.00	0.01	0.028	0.00	101.72
PQGL1-0002	Py1_1	0.00	51.29	42.67	0.000	0.002	0.00	0.00	1.20	0.00	0.00	0.01	0.00	0.00	0.00	0.010	0.00	95.18
PQGL1-0002	Py1_2	0.00	50.39	42.48	0.022	0.011	0.00	0.00	0.94	0.00	0.00	0.00	0.00	0.00	0.01	0.002	0.00	93.84
PQGL1-0002	Py1_3	0.00	50.65	42.41	0.024	0.012	0.00	0.00	0.95	0.00	0.00	0.00	0.00	0.00	0.00	0.006	0.00	94.05
PQGL1-0002	Py1_4	0.00	51.12	42.74	0.050	0.022	0.00	0.00	0.80	0.00	0.00	0.00	0.00	0.00	0.01	0.000	0.00	94.74
PQGL1-0002	Py1_5	0.00	49.67	42.27	0.001	0.025	0.00	0.00	1.00	0.00	0.00	0.00	0.00	0.00	0.01	0.029	0.00	93.01
PQGL1-0002	Py2_1	0.00	50.82	42.77	0.004	0.000	0.00	0.00	1.18	0.00	0.00	0.01	0.00	0.00	0.02	0.029	0.00	94.84
PQGL1-0002	Py2_2	0.00	50.20	43.03	0.017	0.019	0.00	0.00	0.91	0.00	0.00	0.00	0.00	0.00	0.00	0.019	0.00	94.20
PQGL1-0002	Py2_3	0.00	51.17	43.17	0.000	0.007	0.00	0.00	0.75	0.00	0.00	0.01	0.00	0.00	0.00	0.020	0.00	95.14
PQGL1-0002	Py2_4	0.00	51.11	43.03	0.000	0.003	0.00	0.00	1.21	0.00	0.00	0.00	0.00	0.00	0.01	0.006	0.00	95.38
PQGL1-0002	Py2_5	0.00	51.01	42.86	0.000	0.018	0.00	0.00	1.56	0.00	0.00	0.00	0.00	0.00	0.01	0.005	0.00	95.45
PQGL1-0002	Py3_1	0.00	51.21	42.96	0.014	0.033	0.00	0.00	1.00	0.00	0.00	0.00	0.00	0.00	0.00	0.010	0.00	95.22
PQGL1-0002	Py3_2	0.00	50.08	42.64	0.028	0.000	0.00	0.00	0.92	0.00	0.00	0.00	0.00	0.00	0.01	0.000	0.00	93.68
PQGL1-0002	Py3_3	0.00	51.01	42.90	0.001	0.019	0.00	0.00	1.17	0.00	0.00	0.00	0.00	0.00	0.00	0.011	0.00	95.12
PQGL1-0002	Py3_4	0.00	51.47	43.01	0.009	0.012	0.00	0.00	0.97	0.00	0.00	0.00	0.00	0.00	0.01	0.002	0.00	95.48
PQGL1-0002	Py3_5	0.00	50.62	42.62	0.062	0.018	0.00	0.00	0.66	0.00	0.00	0.00	0.00	0.00	0.00	0.000	0.03	94.01
ER02 97-90	Py1a_01	0.00	52.10	47.32	0.040	0.009	0.00	0.00	0.88	0.00	0.00	0.00	0.00	0.00	0.01	0.048	0.00	100.41
ER02 97-90	Py1a_02	0.00	52.22	47.20	0.038	0.023	0.00	0.00	0.91	0.00	0.00	0.01	0.00	0.00	0.00	0.034	0.00	100.44
ER02 97-90	Py1a_03	0.00	52.11	47.26	0.000	0.029	0.00	0.00	0.83	0.00	0.00	0.00	0.00	0.00	0.01	0.035	0.00	100.28
ER02 97-90	Py1a_04	0.00	51.12	47.15	0.050	0.032	0.00	0.00	0.88	0.00	0.00	0.01	0.00	0.00	0.00	0.037	0.00	99.29
ER02 97-90	Py1a_05	0.00	51.41	47.09	0.000	0.024	0.00	0.00	0.63	0.00	0.00	0.00	0.00	0.00	0.01	0.047	0.00	99.21
ER02 97-90	Py1a_06	0.00	52.80	46.91	0.003	0.016	0.00	0.00	0.95	0.00	0.00	0.00	0.00	0.00	0.01	0.048	0.00	100.73
ER02 97-90	Py1b_01	0.00	52.05	47.00	0.009	0.010	0.00	0.00	0.78	0.00	0.00	0.00	0.00	0.00	0.01	0.029	0.00	99.89
ER02 97-90	Py1b_02	0.00	52.03	47.03	0.000	0.013	0.00	0.00	0.59	0.00	0.01	0.00	0.00	0.00	0.00	0.033	0.00	99.70
ER02 97-90	Py1b_03	0.00	52.60	47.18	0.000	0.009	0.00	0.00	0.92	0.00	0.00	0.01	0.00	0.00	0.01	0.024	0.00	100.75
ER02 97-90	Py1b_04	0.00	52.10	47.10	0.000	0.008	0.00	0.00	0.89	0.00	0.00	0.00	0.00	0.00	0.00	0.036	0.00	100.13
ER02 97-90	Py1b_05	0.00	53.32	47.30	0.018	0.000	0.00	0.00	1.06	0.00	0.00	0.01	0.00	0.00	0.00	0.019	0.00	101.72
ER02 97-90	Py1b_06	0.00	53.97	47.39	0.000	0.014	0.00	0.00	0.76	0.00	0.00	0.00	0.00	0.00	0.00	0.051	0.03	102.21
ER05109-55	Py1_01	0.00	54.36	47.19	0.021	0.017	0.00	0.00	0.96	0.00	0.00	0.00	0.00	0.00	0.00	0.039	0.00	102.59
ER05109-55	Py1_02	0.00	53.64	47.09	0.025	0.036	0.00	0.00	1.02	0.00	0.00	0.00	0.00	0.00	0.00	0.027	0.01	101.85
ER05109-55	Py1_03	0.00	54.16	47.27	0.062	0.028	0.00	0.00	1.06	0.00	0.00	0.00	0.00	0.00	0.01	0.034	0.00	102.63
ER05109-55	Py1_04	0.00	54.07	47.18	0.000	0.026	0.00	0.00	1.17	0.00	0.00	0.00	0.00	0.00	0.00	0.032	0.00	102.49
ER05109-55	Py1_05	0.00	53.78	47.32	0.029	0.025	0.00	0.00	0.74	0.00	0.00	0.00	0.00	0.00	0.00	0.031	0.06	101.98
SAMPLE	Analysis	Sb%	S%	Fe %	As %	Cu %	Ag %	Ni %	Co %	Te %	Pb %	Sn %	V %	Mn %	Zn %	Mo %	Cd %	TOTAL
ER05 118-75	Py1_01	0.00	50.62	46.46	0.000	0.016	0.00	0.00	0.75	0.00	0.00	0.00	0.00	0.00	0.00	0.038	0.01	97.90

ER05 118-75	Py1_02	0.00	52.19	46.46	0.000	0.013	0.00	0.00	0.47	0.00	0.00	0.01	0.00	0.00	0.00	0.057	0.00	99.19
ER05 118-75	Py1_03	0.00	51.63	46.61	0.003	0.000	0.00	0.00	0.61	0.00	0.00	0.00	0.00	0.00	0.00	0.049	0.01	98.91
ER05 118-75	Py1_04	0.00	52.38	46.82	0.004	0.061	0.00	0.00	0.72	0.00	0.00	0.01	0.00	0.00	0.01	0.053	0.00	100.05
ER05 118-75	Py1_05	0.00	51.97	46.68	0.021	0.011	0.00	0.00	0.86	0.00	0.00	0.00	0.00	0.00	0.00	0.045	0.00	99.60
ER05 118-75	Py1_06	0.00	50.92	46.57	0.000	0.059	0.00	0.00	0.70	0.00	0.00	0.00	0.00	0.00	0.00	0.050	0.00	98.30
ER05 118-75	Py1_07	0.00	52.30	46.84	0.032	0.018	0.00	0.00	0.52	0.00	0.00	0.00	0.00	0.00	0.01	0.022	0.00	99.75
ER05 118-75	Py1_08	0.00	51.74	46.68	0.072	0.026	0.00	0.00	0.61	0.00	0.00	0.00	0.00	0.00	0.00	0.035	0.00	99.18
ER05 118-75	Py1_09	0.00	51.51	47.12	0.057	0.014	0.00	0.00	0.96	0.00	0.00	0.00	0.00	0.00	0.00	0.044	0.00	99.71
ER05 118-75	Py1_10	0.00	52.21	47.03	0.051	0.023	0.00	0.00	0.79	0.00	0.00	0.00	0.00	0.00	0.01	0.034	0.00	100.14
ER05 118-75	Py1_11	0.00	54.04	47.33	0.000	0.056	0.00	0.00	0.71	0.00	0.00	0.00	0.00	0.00	0.00	0.044	0.00	102.19
ER05 118-75	Py1_12	0.00	53.78	47.28	0.043	0.047	0.00	0.00	1.01	0.00	0.00	0.00	0.00	0.00	0.00	0.030	0.00	102.19
ER05 118-75	Py1_13	0.00	52.11	47.22	0.042	0.015	0.00	0.00	0.73	0.00	0.00	0.00	0.00	0.00	0.00	0.051	0.00	100.17
ER05 118-75	Py1_14	0.00	51.81	47.43	0.038	0.023	0.01	0.00	0.94	0.00	0.00	0.00	0.00	0.00	0.01	0.028	0.00	100.28
ER05 118-75	Py2_01	0.00	51.07	46.84	0.042	0.000	0.00	0.00	0.81	0.00	0.00	0.01	0.00	0.00	0.00	0.037	0.01	98.82
ER05 118-75	Py2_02	0.00	51.41	47.03	0.069	0.008	0.00	0.00	0.93	0.00	0.00	0.01	0.00	0.00	0.01	0.029	0.00	99.49
ER05 118-75	Py2_03	0.00	52.07	47.08	0.054	0.000	0.00	0.00	0.57	0.00	0.00	0.00	0.00	0.00	0.00	0.041	0.00	99.81
ER05 118-75	Py2_04	0.00	52.88	47.10	0.057	0.000	0.00	0.00	0.53	0.00	0.00	0.00	0.00	0.00	0.00	0.041	0.00	100.61
ER97 33-31	Py1_01	0.00	52.96	47.32	0.020	0.010	0.00	0.00	0.60	0.00	0.00	0.00	0.00	0.00	0.01	0.050	0.00	100.96
ER97 33-31	Py1_02	0.00	53.02	47.37	0.087	0.000	0.00	0.00	1.25	0.00	0.00	0.00	0.00	0.00	0.00	0.039	0.00	101.77
ER97 33-31	Py1_03	0.00	52.85	47.27	0.036	0.020	0.00	0.00	0.93	0.00	0.00	0.00	0.00	0.00	0.00	0.049	0.00	101.16
ER97 33-31	Py1_04	0.00	52.02	47.27	0.001	0.041	0.00	0.00	0.80	0.00	0.00	0.01	0.00	0.00	0.01	0.040	0.00	100.20
ER97 33-31	Py1_05	0.00	52.63	47.23	0.036	0.014	0.00	0.00	0.90	0.00	0.02	0.00	0.00	0.00	0.00	0.046	0.00	100.87
ER97 33-31	Py1_06	0.00	52.74	47.16	0.030	0.000	0.01	0.00	1.11	0.00	0.00	0.00	0.00	0.00	0.01	0.039	0.00	101.08
ER97 33-31	Py1_07	0.00	52.85	47.05	0.069	0.003	0.00	0.00	0.88	0.00	0.00	0.00	0.00	0.00	0.00	0.048	0.00	100.90
ER97 33-31	Py1_08	0.00	52.56	47.22	0.009	0.027	0.00	0.00	0.47	0.00	0.00	0.00	0.00	0.00	0.01	0.041	0.00	100.34
ER97 33-31	Py1_09	0.00	52.70	47.26	0.035	0.003	0.00	0.00	1.04	0.00	0.00	0.00	0.00	0.00	0.00	0.034	0.00	101.08
ER97 33-31	Py1_10	0.00	53.16	47.19	0.076	0.023	0.00	0.00	0.62	0.00	0.00	0.00	0.00	0.00	0.00	0.035	0.00	101.11
ER97 33-31	Py1_11	0.00	52.53	47.13	0.033	0.021	0.00	0.00	0.78	0.00	0.02	0.00	0.00	0.00	0.01	0.023	0.00	100.53
ER97 33-31	Py1_12	0.00	53.01	47.24	0.000	0.021	0.00	0.00	0.69	0.00	0.01	0.00	0.00	0.00	0.00	0.033	0.00	101.01
ER97 33-31	Py1_14	0.00	51.86	46.47	0.805	0.022	0.00	0.00	0.65	0.00	0.00	0.00	0.00	0.00	0.00	0.024	0.00	99.84
ER97 33-31	Py1_15	0.00	52.62	46.33	0.434	0.015	0.00	0.00	0.93	0.00	0.00	0.00	0.00	0.00	0.00	0.016	0.00	100.35
ER97 33-31	Py1_16	0.00	51.82	46.71	0.597	0.017	0.00	0.00	0.94	0.00	0.00	0.00	0.00	0.00	0.00	0.025	0.00	100.12
ER97 33-31	Py1_17	0.00	52.81	46.88	0.023	0.002	0.00	0.00	0.87	0.00	0.00	0.00	0.00	0.00	0.00	0.024	0.00	100.61
SAMPLE	Analysis	Sb%	S%	Fe %	As %	Cu %	Ag %	Ni %	Co %	Te %	Pb %	Sn %	V %	Mn %	Zn %	Mo %	Cd %	TOTAL

ER97 33-31	Py1c_01	0.00	53.89	47.17	0.000	0.030	0.00	0.00	1.01	0.00	0.00	0.00	0.00	0.00	0.01	0.041	0.03	102.19
ER97 33-31	Py1c_02	0.00	53.49	47.18	0.018	0.013	0.00	0.00	0.80	0.00	0.00	0.00	0.00	0.00	0.00	0.034	0.00	101.54
ER97 33-31	Py1c_03	0.00	52.84	47.25	0.060	0.021	0.00	0.00	0.77	0.00	0.00	0.00	0.00	0.00	0.01	0.039	0.00	101.00
ER97 33-31	Py1c_04	0.00	52.34	46.97	0.378	0.010	0.00	0.00	0.83	0.00	0.00	0.00	0.00	0.00	0.00	0.033	0.00	100.56
ER97 33-31	Py1c_05	0.00	52.32	46.98	0.172	0.021	0.00	0.00	0.78	0.00	0.02	0.00	0.00	0.00	0.00	0.037	0.00	100.33
ER97 33-31	Py1c_06	0.00	53.58	47.07	0.023	0.032	0.00	0.00	0.98	0.00	0.01	0.00	0.00	0.00	0.00	0.026	0.00	101.73
ER97 33-31	Py1c_07	0.00	53.44	47.19	0.000	0.013	0.00	0.00	0.71	0.00	0.00	0.00	0.00	0.00	0.01	0.041	0.00	101.41
ER97 33-31	Py1c_08	0.00	52.31	46.89	0.000	0.027	0.00	0.00	0.89	0.00	0.00	0.00	0.00	0.00	0.00	0.039	0.00	100.16
ER97 33-31	Py2_01	0.00	54.46	47.22	0.000	0.020	0.00	0.00	1.00	0.00	0.00	0.00	0.00	0.00	0.00	0.044	0.00	102.75
ER97 33-31	Py2_02	0.00	54.04	47.28	0.035	0.000	0.00	0.00	1.19	0.00	0.00	0.01	0.00	0.00	0.00	0.011	0.00	102.56
ER97 33-31	Py2_03	0.00	54.04	47.20	0.063	0.002	0.00	0.02	0.89	0.00	0.00	0.00	0.00	0.00	0.01	0.015	0.05	102.29
ER97 33-31	Py2_04	0.00	54.36	47.26	0.015	0.039	0.00	0.00	0.83	0.00	0.00	0.00	0.00	0.00	0.00	0.020	0.00	102.53
ER97 33-31	Py2_05	0.00	53.90	47.06	0.019	0.033	0.00	0.00	0.88	0.00	0.00	0.02	0.00	0.00	0.01	0.031	0.00	101.96
ER97 33-31	Py2_06	0.00	53.68	47.24	0.005	0.018	0.00	0.00	1.14	0.00	0.00	0.01	0.00	0.00	0.01	0.035	0.02	102.14
ER97 33-31	Py2_07	0.00	54.12	47.36	0.014	0.014	0.00	0.00	0.98	0.00	0.00	0.00	0.00	0.00	0.01	0.024	0.00	102.52
ER97 33-31	Py2_08	0.00	53.37	47.42	0.023	0.000	0.00	0.00	0.88	0.00	0.01	0.00	0.00	0.00	0.00	0.033	0.00	101.75
ER97 33-31	Py2_09	0.00	54.01	47.24	0.088	0.032	0.00	0.00	1.32	0.01	0.00	0.00	0.00	0.00	0.00	0.027	0.00	102.73
ER97 33-31	Py2_10	0.00	53.75	47.35	0.000	0.000	0.00	0.00	0.92	0.00	0.00	0.00	0.00	0.00	0.01	0.010	0.00	102.04
ER97 33-31	Py2_11	0.00	53.87	47.30	0.015	0.009	0.00	0.00	0.99	0.00	0.00	0.00	0.00	0.00	0.00	0.029	0.00	102.21
ER97 33-31	Py2_12	0.00	53.93	46.95	0.020	0.024	0.00	0.00	1.25	0.00	0.00	0.00	0.00	0.00	0.00	0.030	0.00	102.20
ER97 33-31	Py2_13	0.00	53.41	47.32	0.013	0.015	0.00	0.00	1.16	0.00	0.01	0.00	0.00	0.00	0.01	0.029	0.00	101.97
ER97 33-31	Py2_14	0.00	53.39	47.16	0.000	0.041	0.00	0.00	1.16	0.00	0.00	0.01	0.00	0.00	0.00	0.027	0.00	101.79
ER97 33-31	Py2_15	0.00	53.84	47.15	0.002	0.001	0.00	0.00	1.08	0.00	0.00	0.00	0.00	0.00	0.01	0.030	0.00	102.11
ER97 33-31	Py2_16	0.00	53.13	47.08	0.000	0.005	0.00	0.00	1.26	0.00	0.01	0.00	0.00	0.00	0.00	0.037	0.02	101.54
ER97 33-31	Py2_17	0.00	53.62	47.35	0.000	0.028	0.00	0.00	0.96	0.00	0.01	0.00	0.00	0.00	0.01	0.036	0.00	102.01
ER97 33-31	Py3b_01	0.00	53.17	46.89	0.000	0.017	0.00	0.00	1.02	0.00	0.02	0.00	0.00	0.00	0.01	0.015	0.00	101.14
ER97 33-31	Py3b_02	0.00	54.02	47.01	0.054	0.028	0.00	0.00	0.81	0.00	0.00	0.00	0.00	0.00	0.01	0.020	0.00	101.94
ER97 33-31	Py3b_03	0.00	54.20	47.00	0.000	0.036	0.00	0.14	0.81	0.00	0.00	0.00	0.00	0.00	0.01	0.048	0.00	102.25
ER97 33-31	Py4_01	0.00	53.21	47.14	0.043	0.021	0.00	0.00	1.10	0.00	0.00	0.00	0.00	0.00	0.01	0.024	0.00	101.55
ER97 33-31	Py4_02	0.00	53.54	46.93	0.014	0.040	0.00	0.00	1.08	0.00	0.00	0.01	0.00	0.00	0.01	0.017	0.00	101.64
ER97 33-31	Py4_03	0.00	53.76	46.91	0.003	0.028	0.00	0.00	0.62	0.00	0.00	0.00	0.00	0.00	0.01	0.027	0.00	101.35
ER97 33-31	Py4_04	0.00	53.78	47.06	0.000	0.061	0.00	0.00	0.81	0.00	0.00	0.00	0.00	0.00	0.00	0.025	0.00	101.74
ER97 33-31	Py4_05	0.00	54.70	47.22	0.000	0.045	0.00	0.00	0.91	0.00	0.00	0.00	0.00	0.00	0.00	0.029	0.00	102.90
ER97 33-31	Py4_06	0.00	54.25	47.26	0.031	0.017	0.00	0.00	0.88	0.00	0.00	0.01	0.00	0.00	0.01	0.018	0.00	102.48

SAMPLE	Analysis	Sb%	S%	Fe %	As %	Cu %	Ag %	Ni %	Co %	Te %	Pb %	Sn %	V %	Mn %	Zn %	Mo %	Cd %	TOTAL
ER97 33-31	Py4_07	0.00	54.35	47.35	0.073	0.026	0.00	0.00	1.32	0.00	0.00	0.00	0.00	0.00	0.01	0.020	0.00	103.13
ER97 33-31	Py4_08	0.00	53.95	47.28	0.000	0.023	0.00	0.03	1.10	0.00	0.00	0.00	0.00	0.00	0.00	0.039	0.01	102.44
ER97 33-31	Py4_09	0.00	54.02	47.10	0.019	0.046	0.00	0.00	1.20	0.00	0.01	0.00	0.00	0.00	0.01	0.022	0.00	102.43
ER97 33-31	Py4_10	0.00	53.39	47.25	0.092	0.028	0.00	0.00	1.03	0.00	0.00	0.00	0.00	0.00	0.02	0.026	0.00	101.84
PQGL1-0002	Cpy1	0.00	32.57	27.08	0.055	29.985	0.00	0.00	0.41	0.00	0.00	0.00	0.00	0.00	0.03	0.000	0.00	90.12
PQGL1-0002	Cpy2	0.00	33.17	27.07	0.018	29.744	0.00	0.00	0.21	0.00	0.00	0.01	0.00	0.00	0.02	0.000	0.00	90.25
PQGL1-0002	Cpy3	0.00	33.05	26.23	0.000	29.177	0.00	0.00	0.25	0.00	0.00	0.00	0.00	0.00	0.03	0.000	0.00	88.74
PQGL1-0002	Cpy4	0.00	32.89	25.70	0.034	25.714	0.00	0.00	0.49	0.00	0.00	0.00	0.00	0.00	0.02	0.000	0.00	84.85
PQ35a447-84	Cpy1	0.00	34.31	30.37	0.017	33.689	0.00	0.00	0.21	0.00	0.00	0.00	0.00	0.00	0.03	0.000	0.00	98.63
PQ35a447-84	Cpy2	0.00	33.60	30.25	0.000	33.993	0.00	0.00	0.14	0.00	0.00	0.00	0.00	0.00	0.03	0.000	0.00	98.03
PQ12328-85	Cpy3	0.00	33.11	30.64	0.000	33.470	0.00	0.00	0.02	0.00	0.00	0.00	0.00	0.00	0.05	0.000	0.00	97.28
PQ12328-85	Cpy4	0.00	34.51	30.28	0.005	33.871	0.00	0.00	0.29	0.00	0.00	0.01	0.00	0.00	0.03	0.000	0.00	99.00
PQ12319-42	Cpy1	0.00	35.35	30.58	0.047	32.690	0.00	0.00	0.41	0.00	0.00	0.00	0.00	0.00	0.03	0.000	0.00	99.11
PQ12424-26	Gn1	0.00	14.46	0.14	0.018	0.013	0.07	0.00	0.00	0.02	87.54	0.00	0.00	0.00	0.00	0.000	0.00	102.26
PQ12424-26	Gn2	0.00	14.45	0.42	0.017	0.022	0.00	0.00	0.16	0.03	87.96	0.00	0.00	0.00	0.00	0.000	0.00	103.05

Appendix VII

(LA-ICP-MS data - Quartz)

Date	Sample	Chip	Sample spot	**Li (ppm) m7**	Min. uncertainty (+/-)	**Ti (ppm) m47**	Min. uncertainty (+/-)
6/9/2015	ER05109-55	B4	qtz1			**3.660**	0.430
6/9/2015	ER05109-55	B4	qtz2			**3.580**	0.440
6/9/2015	ER05109-55	B4	qtz3			**3.690**	0.400
6/9/2015	ER05109-55	B4	qtz4			**3.670**	0.390
6/9/2015	ER05109-55	B4	qtz5			**3.370**	0.550
6/9/2015	ER05109-55	C1	qtz1			**4.090**	0.500
6/9/2015	ER05109-55	C1	qtz2			**3.720**	0.680
6/9/2015	ER05109-55	C1	qtz3			**4.050**	0.500
6/9/2015	ER05109-55	C1	qtz4			**3.330**	0.500
6/9/2015	ER05109-55	C1	qtz5			**3.940**	0.410
6/10/2015	ER05109-55	D1	qtz1	-	-	**4.360**	0.500
6/10/2015	ER05109-55	D1	qtz2	-	-	**3.880**	0.470
6/10/2015	ER05109-55	D1	qtz3	-	-	**3.750**	0.630
6/10/2015	ER05109-55	D1	qtz4	-	-	**3.850**	0.440
6/10/2015	ER05109-55	D1	qtz5	-	-	**4.140**	0.620
6/10/2015	ER05109-55	D1	qtz6	-	-	**4.380**	0.470
6/10/2015	ER05109-55	D1	qtz7	-	-	**3.950**	0.480
6/10/2015	ER05109-55	D1	qtz8	-	-	**4.150**	0.490
6/10/2015	ER05109-55	D1	qtz9	-	-	**3.990**	0.520
6/11/2015	PQ12302-46	9A	9A_1	-	0.037	**3.700**	0.730
6/11/2015	PQ12302-46	9A	9A_2	**0.158**	0.030	**3.670**	0.450
6/11/2015	PQ12302-46	9A	9A_3	**0.073**	0.029	**3.100**	0.370
6/11/2015	PQ12302-46	9A	9A_4	-	-	**2.930**	0.420
6/11/2015	PQ12302-46	9A	9A_5	-	-	**3.240**	0.370
6/11/2015	PQ12302-46	9A	9A_6	**0.113**	0.051	**3.120**	0.600
6/12/2015	PQ12302-46	6A1	6A1_1			**2.740**	0.400
6/12/2015	PQ12302-46	6A1	6A1_2			**3.230**	0.600
6/12/2015	PQ12302-46	6A1	6A1_3			**3.440**	0.440
6/12/2015	PQ12302-46	6A1	6A1_4			**3.530**	0.450
6/12/2015	PQ12302-46	8B	8B_1			**3.510**	0.460
6/12/2015	PQ12302-46	8B	8B_2			**3.190**	0.430
6/12/2015	PQ12302-46	8B	8B_3			**2.780**	0.630
6/12/2015	PQ12302-46	8B	8B_4			**3.530**	0.560
6/12/2015	PQ12302-46	12A	12A_1			**3.150**	0.410
6/12/2015	PQ12302-46	12A	12A_2			**4.000**	0.460
6/12/2015	PQ12302-46	12A	12A_3			**3.890**	0.420
6/12/2015	PQ12302-46	12A	12A_4			**3.690**	0.490
6/12/2015	PQ12302-46	12A	12A_5			**3.660**	0.410
6/12/2015	PQ12302-46	12A	12A_6			**4.030**	0.410
6/12/2015	PQ12302-46	11A	11A_1			**2.880**	0.360
6/12/2015	PQ12302-46	11A	11A_2			**2.990**	0.430
6/12/2015	PQ12302-46	11A	11A_3			**3.200**	0.410
6/12/2015	PQ12302-46	11A	11A_4			**3.310**	0.440
6/12/2015	PQ12302-46	5D	5D_1			**2.850**	0.380
6/12/2015	PQ12302-46	5D	5D_2			**3.460**	0.390
6/12/2015	PQ12302-46	5D	5D_3			**2.850**	0.400
6/12/2015	PQ12302-46	5D	5D_4			**3.210**	0.340
6/12/2015	PQ12302-46	5D	5D_5			**3.490**	0.360
6/12/2015	PQ12302-46	5A	5A_1			**3.320**	0.460

Date	Sample	Chip	Sample spot	**Li (ppm) m7**	Min. uncertainty (+/-)	**Ti (ppm) m47**	Min. uncertainty (+/-)
6/12/2015	PQ12302-46	5A	5A_2			**3.630**	0.400
6/12/2015	PQ12302-46	5A	5A_3			**3.530**	0.410
6/12/2015	PQ12302-46	5A	5A_4			**4.270**	0.420
6/12/2015	PQ12302-46	5A	5A_5			**4.130**	0.490
6/12/2015	PQ12302-46	5A	5A-6			**3.290**	0.470
6/11/2015	PQ54147-02	A13I	qtz2	-	-	**5.280**	0.321
6/11/2015	PQ54147-02	A13I	qtz3	-	-	**4.670**	0.363
6/11/2015	PQ54147-02	A13I	qtz4	-	-	**4.750**	0.255
6/11/2015	PQ54147-02	A13I	qtz5	-	-	**4.150**	0.365
6/11/2015	PQ54147-02	A13I	qtz6	**0.078**	0.031	**5.190**	0.397
6/11/2015	PQ54147-02	A13I	qtz7	**0.179**	0.030	**4.740**	0.349
6/11/2015	PQ54147-02	A8	A8_1	-	-	**4.670**	0.480
6/11/2015	PQ54147-02	A8	A8_2	**0.058**	0.030	**4.740**	0.590
6/11/2015	PQ54147-02	A8	A8_3	-	-	**5.330**	0.440
6/11/2015	PQ54147-02	A8	A8_4	-	-	**4.910**	0.510
6/11/2015	PQ54147-02	A8	A8_5	-	-	**4.890**	0.470
6/11/2015	PQ54147-02	A8	A8_6	**0.072**	0.031	**4.820**	0.480
6/11/2015	PQ54147-02	A8	A8_7	-	0.031	**4.770**	0.610
6/11/2015	PQ54147-02	A8	A8_8	**0.090**	0.040	**5.100**	0.630
6/12/2015	PQ54147-02	A4	A4_1			**5.190**	0.490
6/12/2015	PQ54147-02	A4	A4_2			**5.240**	0.790
6/12/2015	PQ54147-02	A4	A4_3			**5.010**	0.500
6/12/2015	PQ54147-02	A4	A4_4			**4.310**	0.660
6/15/2015	PQ54147-02	E1	E1_1	**0.541**	0.074	**4.820**	0.500
6/15/2015	PQ54147-02	E1	E1_2	**1.372**	0.071	**4.880**	0.470
6/15/2015	PQ54147-02	E1	E1_3	**1.302**	0.069	**5.170**	0.460
6/15/2015	PQ54147-02	E1	E1_4	**0.634**	0.083	**4.950**	0.480
6/15/2015	PQ54147-02	E1	E1_5	**1.410**	0.100	**5.460**	0.590
6/15/2015	PQ54147-02	E1	E1_6	**1.621**	0.078	**4.770**	0.430
6/15/2015	PQ54147-02	E1	E1_7	**0.482**	0.048	**5.620**	0.560
6/15/2015	PQ54147-02	E1	E1_8	**0.687**	0.099	**5.840**	0.660
6/15/2015	PQ54147-02	E1	E1_9	**1.820**	0.110	**5.000**	0.570
6/15/2015	PQ54147-02	E1	E1_10	**0.286**	0.042	**5.260**	0.460
6/10/2015	PQ61127-30	PQLT	qtz1	**1.289**	0.082	**4.130**	0.460
6/10/2015	PQ61127-30	PQLT	qtz2	**0.903**	0.069	**4.230**	0.540
6/10/2015	PQ61127-30	PQLT	qtz3	**0.583**	0.071	**4.440**	0.480
6/10/2015	PQ61127-30	PQLT	qtz4	**1.392**	0.072	**4.340**	0.450
6/10/2015	PQ61127-30	PQLT	qtz5	**1.378**	0.075	**5.000**	0.540
6/10/2015	PQ61127-30	PQLT	qtz6	**1.395**	0.062	**4.760**	0.510
6/10/2015	PQ61127-30	PQLT	qtz7	**1.066**	0.077	**4.810**	0.530
6/10/2015	PQ61127-30	PQLT	qtz8	-	0.023	**4.710**	0.570
6/11/2015	PQ61127-30	C1	C1-1	**0.128**	0.030	**5.390**	0.580
6/11/2015	PQ61127-30	C1	C1-2	-	-	**4.190**	0.390
6/11/2015	PQ61127-30	C1	C1-3	-	-	**4.070**	0.570
6/11/2015	PQ61127-30	C1	C1-4	-	-	**3.990**	0.440
6/15/2015	PQ61127-30	H	30_H_2	-	-	**4.600**	0.450
6/15/2015	PQ61127-30	H	30_H_3	**1.685**	0.099	**4.990**	0.430
6/15/2015	PQ61127-30	H	30_H_4	**0.113**	0.036	**5.010**	0.450

Date	Sample	Chip	Sample spot	**Li (ppm) m7**	Min. uncertainty (+/-)	**Ti (ppm) m47**	Min. uncertainty (+/-)
6/15/2015	PQ61127-30	H	30_H_5	-	-	**4.340**	0.630
6/15/2015	PQ61127-30	H	30_H_6	**0.080**	0.036	**4.560**	0.460
6/15/2015	PQ61127-30	H	30_H_7	-	-	**4.440**	0.410
6/15/2015	PQ61127-30	H	30_H_8	**1.540**	0.110	**4.440**	0.680
6/15/2015	PQ61127-30	H	30_H_9	**0.090**	0.030	**4.630**	0.430
6/15/2015	PQ61127-30	H	30_H_10	-	-	**4.040**	0.850
6/15/2015	PQ61127-30	H	30_H_11	-	-	**5.110**	0.480
6/15/2015	PQ61127-30	H	30_H_12	-	-	**4.440**	0.360
6/15/2015	PQ61127-30	H	30_H_13	**1.329**	0.092	**4.440**	0.400
6/15/2015	PQ61127-30	H	30_H_14	**1.120**	0.120	**4.120**	0.570
6/15/2015	PQGL1-005	Ar1	Ar1_qtz1	**0.520**	0.380	**4.910**	0.490
6/15/2015	PQGL1-005	Ar1	Ar1_qtz2	**0.734**	0.470	**4.580**	0.460
6/15/2015	PQGL1-005	Ar1	Ar1_qtz3	**0.061**	0.360	**5.250**	0.520
6/15/2015	PQGL1-005	Ar1	Ar1_qtz4	**0.398**	0.460	**4.850**	0.620
6/15/2015	PQGL1-005	Ar1	Ar1_qtz5	**0.597**	0.360	**5.330**	0.490
6/15/2015	PQGL1-005	Ar1	Ar1_qtz6	**1.228**	0.400	**5.440**	0.480
6/15/2015	PQGL1-005	Ar1	Ar1_qtz7	-	-	**5.070**	0.450
6/15/2015	PQGL1-005	Ar1	Ar1_qtz8	**1.522**	0.360	**4.780**	0.410
6/15/2015	PQGL1-005	Ar1	Ar1_qtz9	-	-	**4.800**	0.470
6/15/2015	PQGL1-005	Ar1	Ar1_qtz10	**0.721**	0.700	**4.550**	0.480
6/15/2015	PQGL1-005	Ar1	Ar1_qtz11	**1.871**	0.370	**4.750**	0.430
6/15/2015	PQGL1-005	Ar1	Ar1_qtz12	**0.498**	0.320	**4.640**	0.420
6/15/2015	PQGL1-005	Ar1	Ar1_qtz13	**0.441**	0.400	**4.870**	0.580
6/15/2015	PQGL1-005	Ar1	Ar1_qtz14	**0.575**	0.330	**4.910**	0.420
6/15/2015	PQGL1-005	Ar1	Ar1_qtz15	-	-	**4.790**	0.440
6/15/2015	PQGL1-005	Ar1	Ar1_qtz16	**1.300**	0.440	**5.120**	0.660
6/15/2015	PQGL1-005	Ar2	Ar2_qtz1	-	-	**5.050**	0.450
6/15/2015	PQGL1-005	Ar2	Ar2_qtz2	-	-	**5.400**	0.470
6/15/2015	PQGL1-005	Ar2	Ar2_qtz_3	-	-	**4.990**	0.480
6/15/2015	PQGL1-005	Ar2	Ar2_qtz_4	-	-	**5.130**	0.440
6/15/2015	PQGL1-005	Ar2	Ar2_qtz_5	-	-	**4.950**	0.460
6/15/2015	PQGL1-005	Ar2	Ar2_qtz_6	-	-	**4.910**	0.410
6/15/2015	PQGL1-005	Ar2	Ar2_qtz_7	-	-	**4.890**	0.480
6/15/2015	PQGL1-005	Ar2	Ar2_qtz_8	-	-	**4.540**	0.410
6/15/2015	PQGL1-005	Ar2	Ar2_qtz_9	-	-	**4.370**	0.420
6/15/2015	PQGL1-005	Ar2	Ar2_qtz_10	-	-	**4.850**	0.420
6/15/2015	PQGL1-005	Ar2	Ar2_qtz_11	-	-	**4.810**	0.680

Appendix VIII

(Fluid Inclusion Microthermometry)

Pau-a-Pique

Sample	Chip	Map	Incl.	Type	Masurements								Homog. Observ.	Area	
					TmCO2	Tfm	Tmice	Tm Chlat	ThCO2	Mode	Th	Mode		% Liq	%Gas
PQ12302-46	5-F	10	A	1	-56.4	-21.2	-3.7	7.2	27.9	L			Decript. in 315.1	88.8	11.2
PQ12302-46	5-F	10	E	4				0.1							
PQ12302-46	5-F	10	F	4				-0.1							
PQ12302-46	5-F	10	M	4				-0.1							
PQ12302-46	5-A	11	A	3		-35.8	-2.9				160.4	L		92.7	7.3
PQ12302-46	5-A	11	B	3			-2.8				142.1	L			
PQ12302-46	5-A	11	D	3			-2.8				147.1	L			
PQ12302-46	5-A	11	E	3			-1.9				148.2	L			
PQ12302-46	5-A	11	F	3			-2.7				141.8	L			
PQ12302-46	5-A	11	G	3				-0.2							
PQ12302-46	5-A	11	H	3				-0.2			145.1	L			
PQ12302-46	5-D	2	B	4				-0.4							
PQ12302-46	5-D	2	F	4				0.0							
PQ12302-46	5-D	2	I	4		-22.3		0.2							
PQ12302-46	5-D	2	H	4		-22.3		0.2							
PQ12302-46	5-D	2	G	4				0.0							
PQ12302-46	5-D	2	J	4		-33.3		-0.1							
PQ12302-46	5-D	2	K	3				0.0							
PQ12302-46	5-D	2	L	3				0.0							
PQ12302-46	5-D	2		3				0.0							
PQ12302-46	5-D	2		3				0.0							
PQ12302-46	5-D	2		3				5.4							
PQ12302-46	5E	16	A	2	-56.6	-22.8			22.7	L					
PQ12302-46	5E	16	B	2	-56.7			6.8	23.1	L	281.3	L-M(?)			
PQ12302-46	5E	16	C	2	-56.8			7.1	24.9	L-M (?)			Decripit. in 250.4	79.3	20.7
PQ12302-46	5E	16	D	2	-56.6			6.6	26.5	L-M (?)	314.7	L	on cooling bubble was bigger than before heating		
PQ12302-46	5E	16	E	2	-56.8			6.7	25.7	L	258.0	L	on cooling the buble didn´t reappeared		
PQ12302-46	5E	16	F	2	-56.8			6.7	25.1	L	281.4	L	on heating buble appeared again		
PQ12302-46	5E	14	A	2	-56.5	-21.7	-6.5	6.5	27.2	V				85.4	14.6
PQ12302-46	5E	14	I	2	-56.6			6.2	25.2	L					
PQ12302-46	5E	14	J	2	-56.7			6.2	24.8	V-M(?)				47.1	52.9
PQ12302-46	5G	18	A	5			-0.4								
PQ12302-46	5G	18	B	5			-0.2								
PQ12302-46	5G	18	C	5			-0.1								

PQ12302-46	5G	18	D	5			-0.2								
PQ12302-46	5G	18	E	5			-0.4								
PQ12302-46	5G	18	F	5			-0.4								
PQ12302-46	5G	18	G	5			-0.3								
PQ12302-46	5F	5	B	1			-2.7								
PQ12302-46	5F	5	G	3			-2.7							92.4	7.6
PQ12302-46	5F	5	D	3			-2.7							91.7	8.3
PQ12302-46	5F	5	E	3			-2.8							87.8	12.2
PQ12302-46	5F	5	H	3		-35.5	-2.7								
PQ12302-46	5F	5	I	3			-2.7								
PQ12302-46	6A1	1	C	1	-56.5	-21.8	-5.9	7.2	22.9	L					
PQ12302-46	6A1	1	G	2	-56.4			6.6	28.3	L			on heating buble become bigger after 250.0		
PQ12302-46	6A1	1	A	1	-56.5	-20.6		6.4	25.9	L	282.2	L			
PQ12302-46	6A1	1	H	1	-56.5			7.1	25.3	L			Holding temp in 205.7 inclusion homogenize, moreover a fracture was observed close to the inclusion		
PQ12302-46	6A1	1	L	5			-3.3				144.2	L			
PQ12302-46	6A1	1	I	5			-2.2								
PQ12302-46	6A	1	K	5			-3.1								
PQ12302-46	6A1	1	M	5			2.2				157.3	L			
PQ12302-46	6A2	1	A	1	-56.7			7.3	27.8	L				91.5	8.5
PQ12302-46	6A2	1	B	2	-57.7	-23.7	-6.7	7.2	25.5	L	255.8	L		77.7	22.3
PQ12302-46	6A2	1	F	2	-57.0			7.2	23.6	L					
PQ12302-46	6A2	1	G	2	-57.1		-6.5	7.1	25.2	L					
PQ12302-46	6A2	1	H	2	-57.0			7.1	-26.3	L	272.6	L			
PQ12302-46	6A2	1	D	1	-57.3			6.4	21.0	L					
PQ12302-46	6A2	1	E	2	-57.0			7.2	25.8	L					
PQ12302-46	11a	1	A	1	-56.5			6.6	25.8	L				82.4	17.6
PQ12302-46	11a	1	D	3				0.0			148.5	L			
PQ12302-46	11a	1	N	3				0.1					Th > 165		
PQ12302-46	11a	1	O	3				0.1					Th > 166		
PQ12302-46	11a	1	E	3			-2.6				151.7	L			
PQ12302-46	11a	1	F	3			-2.7				153.4	L		89.2	10.8
PQ12302-46	11a	1	I	3			-2.7				149.4	L		93.6	6.4
PQ12302-46	11a	1	J	3			-2.6				149.8	L			
PQ12302-46	11a	1	K	3			-2.7				145.4	L			
PQ12302-46	11a	1	L	3			-2.7				144.9	L			

PQ12302-46	11a	1	M	3		-2.8								
PQ12302-46	8b	1	A	3		-3.0				155.7	L		90.0	10.0
PQ12302-46	8b	1	B	3		-2.7				148.2	L			
PQ12302-46	8b	1	C	3		-2.9				158.2	L			
PQ12302-46	8b	1	D	3		-3.1				160.2	L			
PQ12302-46	8b	1	E	3		-3.1				158.2	L			
PQ12302-46	8b	1	F	3		-2.8						heated above 220.0 and no homogenization observed		
PQ12302-46	8b	1	G	3		-2.7						heated above 220.0 and no homogenization observed		
PQ12302-46	8b	1	H	3		-2.8				184.0	L			
PQ12302-46	8b	1	I	3		-2.9				160.2	L			
PQ12302-46	8b	1	J	3		-2.9				149.5	L			
PQ12302-46	8b	1	K	3		-2.9				130.1	L			
PQ12302-46	8b	1	L	3		-2.8				147.4	L			
PQ12302-46	9b	1	A	3		-2.7				154.3	L			
PQ12302-46	9b	1	B	3		-2.8				167.4	L			
PQ12302-46	9b	1	C	3		-2.7				157.2	L		86.4	13.6
PQ12302-46	9b	1	D	3		-2.5				156.8	L			
PQ12302-46	9b	1	E	3		-2.8				153.1	L			
PQ12302-46	9b	1	F	3		-2.5				161.9	L			
PQ12302-46	9b	1	G	3		-2.8				163.0	M	Gradual desappearing of men.		
PQ12302-46	9b	1	H	3		-2.6				171.2	L		89.5	10.5
PQ12302-46	9a		A	2	-56.4	-7.5	6.8	27.3	L					
PQ12302-46	9a		B	2	-56.4		7.3	28.4	L					
PQ12302-46	9c	2	A	2	-56.6		7.4	27.4	M	decrip		Decrip. in 232.7		
PQ12302-46	9c	2	B	2	-56.4		7.1	28.1	M	decrip		Decrip. in 270.0		
PQ12302-46	9c	2	C	2	-56.6		7.1	28.0	M	decrip				
PQ12302-46	9c	2	D	2	-56.6			25.4	M	decrip				
PQ12302-46	9c	2	F	2	-56.6		7.2	28.0	M	decrip				
PQ12302-46	9c	2	J	2			7.6	24.6	L	243.0	L			
PQ12302-46	9c	2	L	2	-56.8		7.4	23.1	L	decrip				
PQ54102-47	C7	1	F	2	-56.4		7.4	28.6				Decrip.iIn 210.0		
PQ54102-47	C7	1	C	2	-56.4		7.4	30.1		271.9	L		73.7	26.3
PQ54102-47	C7	1	D	2	-56.4		7.4	28.3				Decrip. in 252.3 (almost homogenized)	73.0	27.0
PQ54102-	C7	1	A	2	-56.5		7.3	30.0		214.5	L		85.	14.7

47													3	
PQ54102-47	C7	1	B	2	-56.5		7.3	29.2		210.5	L		74.0	26.0
PQ54102-47	C7	1	M	2	-56.5		7.8	27.6						
PQ54102-47	C7	1	O	2	-56.4		7.2	29.1						
PQ54102-47	C7	1	P	2	-56.5		7.5	29.3		266.8	L			
PQ54102-47	C7	1	I	4		-3.4				135.1	L			
PQ54102-47	C7	1	L	4		-1.2				120.7	L			
PQ54102-47	C7	1	K	4		-1.9				148.3	L			
PQ54102-47	C7	1	R	4		0.8				115.7	L			
PQ54102-47	C7	1	S	4		-0.3				104.3	L			
PQ54102-47	C7	1	T	4		-1.1				107.1	L			
PQ54102-47	C6II	1	Y	4		3.7				124.8	L			
PQ54102-47	C6II	1	Z	4		0.0				134.7	L			
PQ54102-47	C6II	1	C	2	-56.7		7.5	20.8	L			Decrip. in 213.5		
PQ54102-47	C6II	1	O	2	-56.8	-5.1	7.7	22.3	L			Decrip. in 207.0	75.9	24.1
PQ54102-47	C6II	1	D	2	-56.7	-4.9	7.6	23.3	L			Decrip. in 221.0	76.9	23.1
PQ54102-47	C6II	1	J	2	-56.7	-4.9	7.6	23.7	L	245.6	L		82.6	17.4
PQ54102-47	C6II	1	P	2	-56.7		7.7	23.6	L			Decrip. in 205.5		
PQ54102-47	C6II	1	I	2	-56.6		7.3	25.0	L			Decrip. in 239		
PQ54102-47	C6II	1	L	2	-56.6		7.6	26.3	L	241.6	L			
PQ54102-47	C6II	1	M	2	-56.6		7.6	26.6	L	249.7	L			
PQ54102-47	C6II	1	E	2			7.6	23.2	L	241.3	L			
PQ54102-47	C6II	1	F	2	-56.6		7.6	23.2	L	241.4	L			
PQ54102-47	C6II	2	G	2						256.5	L			
PQ54102-47	C6II	1	Q	2	-56.6		7.6	26.5	L	217.5	L			
PQ54102-47	C6II	1	R	2	-56.6		7.6	21.6	L					
PQ54102-47	C6II	1	S	2	-56.6		7.6	22.6	L					
PQ54102-47	C6II	1	A	2	-56.5		7.6	26.8	L					
PQ54102-47	C6II	1	X	2	-56.7		7.6	24.8	L					
PQ54102-47	C6II	1	V	2	-56.7	-4.4	7.7	24.2	L			Decrip. in 226.3		
PQ54102-47	C6II	1	T	2	-56.7		7.5	19.6	L					
PQ54102-47	C6II	1	U	2	-56.7		7.6	25.6	L			Decrip. in 205.3		
PQ54102-47	C4	1	A	2	-56.6		7.2	25.2	L	241.7	L			
PQ54102-47	C4	1	B	2			7.2	26.4	L	254.4	L			
PQ54102-47	C4	1	C	2	-56.5		7.2	24.7	L			Decrip. in 225.8		
PQ54102-47	C4	1	D	2	-56.5		7.4	25.6	L	236.2	L			
PQ54102-47	C4	1	E	2	-56.6		7.3	28.2	L	255.9	L			
PQ54102-47	C4	1	F	2	-56.6		7.3	27.2	L	261.5	L			
PQ54102-47	C4	1	G	2			7.3	28.0	L	254.3	L			
PQ54102-47	C4	1	H	2	-56.5			26.6	L					
PQ54102-47	C4	1	I	2			7.5	25.2	L	239.5	L			

PQ54102-47	C4	1	J	2	-56.5		7.2	25.3	L	234.7	L			
PQ54102-47	C4	1	K	2			7.3	23.8	L	241.8	L			
PQ54102-47	C4	1	L	2			7.3	25.2	L	241.8	L			
PQ54102-47	C4	1	R	2			7.3	23.7	L	261.5	L			
PQ54102-47	C4	1	M	4		0.3				110.1	L			
PQ54102-47	C4	1	N	4		1.9				98.4	L			
PQ54102-47	C4	1	P	4		4.7								
PQ54102-47	C4	1	Q	4		-3.8				116.9	L			
PQ54102-47	C4	1	S	4		0.0				110.1	L			
PQ54102-47	A8	1	A	2	-56.6		8.0	26.3	L					
PQ54102-47	A8	1	B	2	-56.6		7.9	27.4	L	233.0	L			
PQ54102-47	A8	1	C	2	-56.7		7.9	25.6	L	229.0	L			
PQ54102-47	A8	1	D	2	-56.7		7.8	25.7	L			Decrip. in 228.5 (almost homogenized)		
PQ54102-47	A8	1	E	2	-56.7		7.8	26.6	L	232.8	L			
PQ54102-47	A8	1	F	2	-56.7		7.9	26.6	L	232.8	L			
PQ54102-47	A8	1	G	2	-56.8		8.1	25.6	L	226.0	L			
PQ54102-47	A8	1	H	2	-56.7	-4.8	8.1	25.7	L			Decrip. in 230.5	81.5	18.5
PQ54102-47	A8	1	I	2	-56.7		8.1	25.7	L	223.5	L		77.0	23.0
PQ54102-47	A8	1	J	2	-56.6		8.0	26.3	L	226.3	L		79.5	20.5
PQ54102-47	A8	1	K	2	-56.8	-4.9	8.1	24.4	L	228.2	L			
PQ54102-47	A8	1	L	2	-56.7		8.1	25.5	L	223.5	L			
PQ54102-47	A8	1	M	2	-56.6	-4.7	8.1	24.6	L	223.5	L			
PQ54102-47	A8	1	N	2	-56.5	-4.3	8.2	29.1	L			Fracture appeared in 208.0, bubble stayed stable until 230 and when it decriptated	81.3	18.7
PQ54102-47	A8	1	O	2	-56.7		8.1	26.1	L					
PQ54102-47	A8	1	P	2	-56.7		8.1	25.1	L					
PQ54102-47	A8	1	Q	2	-56.7		7.8	26.0	L	225.3	L			
PQ54102-47	A8	1	R	2	-56.7		7.9	26.0	L	221.4	L		64.8	35.2
PQ54102-47	A8	1	T	2	-56.6		7.9	27.1	L	235.1	L			
PQ54102-47	A8	1	U	2	-56.7		7.9	27.1	L	222.0	L			
PQ54102-47	A8	1	V	2	-56.7		8.1	25.9	L	231.0	L			
PQ54102-47	A4	1	A	2	-56.4	-4.8	8.4	23.9	L					
PQ54102-47	A7	1	A	2	-56.7	-4.7	8.1	22.8	L			Decrip.in 205.0		
PQ54102-47	A7	1	B	2	-56.6		7.8	25.8	L	229.7	L			
PQ54102-47	A7	1	C	2	-56.7	-4.9	7.9	24.6	L	226.5	L			
PQ54102-47	A7	1	D	2	-56.6		7.7	27.2	L	237.3	L			
PQ54102-47	A7	1	E	2	-56.6		7.6	25.8	L			Decrip.in 214.6		
PQ54102-47	A7	1	F	2	-56.5		7.9	25.4	L					

PQ54102-47	A7	1	G	2	-56.7		7.6	25.4	L	233.6	L	
PQ54102-47	A7	1	H	2	-56.6	-4.8	7.9	26.0	L			
PQ54102-47	A7	1	I	2	-56.6	-5.0	7.6	26.2	L	238.5	L	
PQ54102-47	A7	1	J	2	-56.5		7.7	26.9	L			Decrip. in 223.0
PQ54102-47	A7	1	K	2	-56.6		7.6	26.6	L	232.2	L	
PQ54102-47	A7	1	L	2	-56.6		8.0	25.4	L			Decrip in 229.0
PQ54102-47	A7	1	M	2	56.7		7.8	24.1	L			
PQ54102-47	A7	1	N	2	-56.6		7.9	25.5	L	229.7	L	
PQ54102-47	A7	1	O	2	-56.6		8.0	25.6	L	226.5	L	
PQ54102-47	A7	1	P	2	-56.8		7.9	25.9	L	224.0	L	
PQ54102-47	A7	1	Q	2	-56.6		7.4	26.8	L			
PQ54102-47	A7	1	R	2	-56.6		7.9	26.4	L	233.2	L	
PQ54102-47	A7	1	S	2	-56.4		7.7	24.9	L			
PQ54102-47	A13 I		A	2	-56.6	-5.1	7.5	24.8	L			
PQ54102-47	A13 II		B	2		-4.2	8.6					
PQ54102-47	A13 III		C	2	-57.3	-5.1	8.2	22.6	L			
PQ61127-30	A	1	A	3		4.4						
PQ61127-30	A	1	B	3		4.4				112.4		
PQ61127-30	A	1	C	3		-2.5				136.7		
PQ61127-30	A	1	D	3		4.5				110.8		
PQ61127-30	A	1	E	3		1.5						
PQ61127-30	A	1	F	3		4.0				106.0		
PQ61127-30	A	1	G	3		0.2				169.0		
PQ61127-30	A	1	H	3		4.4						
PQ61127-30	A	1	I	3						108.8		
PQ61127-30	A	1	J	3		-0.5				175.1		
PQ61127-30	A	1	K	3		0.5						
PQ61127-30	A	1	L	3		0.3						
PQ61127-30	A	1	M	3		4.1						
PQ61127-30	A	1	N	3		2.0						
PQ61127-30	A	1	O	2	-57.2		6.5	25.7	L			
PQ61127-30	A	1	P	2	-57.2		7.8	27.2	M	231.8	L	
PQ61127-30	A	1	Q	2	-57.0		7.8	26.2	L			
PQ61127-30	A	1	R	3			0.1			115.3		
PQ61127-30	A	1	S	3								
PQ61127-30	A	1	T	3						237.8	L	
PQ61127-30	B	1	A	3		-6.4				139.9	L	
PQ61127-30	B	1	B	3		-5.6				148.4	L	
PQ61127-30	B	1	C	3		-6.1				152.8	L	
PQ61127-	B	1	D	3		-6.1				129.7	L	

30														
PQ61127-30	B	1	E	3		-6.5				117.1	L			
PQ61127-30	B	1	F	3		-6.5				156.4	L			
PQ61127-30	B	1	G	3		-5.6				-				
PQ61127-30	B	1	H	3		-3.6				-				
PQ61127-30	B	1	I	3		-6.1				130.4	L			
PQ61127-30	B	1	J	3		-6.2				133.9	L			
PQ61127-30	B	1	K	3		-6.1				130.6	L			
PQ61127-30	B	1	L	3		-6.4				134.9	L			
PQ61127-30	B	1	M	3			2.1			-				
PQ61127-30	B	1	N	3		-				160.6	L			
PQ61127-30	C	1	A	2	-56.3	-4.7	7.6	30.3	L				82.8	17.2
PQ61127-30	C	1	B	2	-56.4		7.5	29.8	L					
PQ61127-30	C	1	C	2	-56.4		7.6	29.2	L					
PQ61127-30	C	1	D	2	-56.4		7.6	28.5	L					
PQ61127-30	C	1	E	2	-56.4		7.6	27.0	L					
PQ61127-30	C	2	F	2			7.2	21.2	L			Decrip. in 218.0		
PQ61127-30	C	2	G	2			7.4	21.5	L			Decrip. in 259.6		
PQ61127-30	C	2	H	2			7.1	21.1	L					
PQ61127-30	C	2	I	2			7.1	21.5	L					
PQ61127-30	C	2	J	2			7.3	21.4	M					
PQ61127-30	C	2	K	2			7.2	22.3	L					
PQ61127-30	C	2	L	2			7.3							
PQ61127-30	C	2	M	2			7.2							
PQ61127-30	C	2	N	2			7.4							
PQ61127-30	C	2	O	2			7.4	21.3	L					
PQ61127-30	D1	2	A	6		-13.6				112.2	L			
PQ61127-30	D1	2	B	6		-14.3								
PQ61127-30	D1	2	C	6		-15.4								
PQ61127-30	D1	2	D	6		-13.7				109.6	L			
PQ61127-30	D1	2	E	6		-10.8								
PQ61127-30	D1	2	F	6		-14.5				165.5 (?)	L			
PQ61127-30	D1	2	G	6		-14.0				102.8	L			
PQ61127-30	D1	2	H	6		-10.8								
PQ61127-30	D1	2	I	6		-11.2								
PQ61127-30	D1	2	J	6		-14.5								
PQ61127-30	D1	2	K	6		-15.4				144.2	L			
PQ61127-30	D1	2	L	6		-15.9				116.0	L			
PQ61127-30	D1	2	M	6		-14.7				131.2	L			
PQ61127-30	D1	2	N	6		-14.5				93.0	L			
PQ61127-	D1	2	O	6		-11.2								

30										
PQ61127-30	D1	2	P	6		-14.2		103.9	L	
PQ61127-30	D1	2	Q	6		-9.6				
PQ61127-30	D1	1	A	6		-13.4				
PQ61127-30	D1	1	B	6		-13.4				
PQ61127-30	D1	1	C	6		-13.3				
PQ61127-30	D1	1	D	6		-13.3				
PQ61127-30	D1	1	E	6		-13.1				
PQ61127-30	D1	1	F	6		-13.3				
PQ61127-30	D1	1	G	6		-13.3				
PQ61127-30	H1	1	B	6			0.9			
PQ61127-30	H1	1	C	6			0.2			
PQ61127-30	H1	1	H	5			4.0			
PQ61127-30	H1	1	I	5			1.5			
PQ61127-30	H1	1	J	5		-3.7	4.7			
PQ61127-30	H1	1	K	5			4.0			
PQ61127-30	H1	1	L	5			-0.5			
PQ61127-30	H1	1	M	5			-0.6			
PQ61127-30	H1	1	N	5			2.1			
PQ61127-30	H1	1	O	5			0.4			
PQ61127-30	D2		A	5	-56.5	-4.7	-28.0		L	

Ernesto

Sample	Chip	Map	Incl.	Type	Masurements								Homog. Observ.	Area	
					TmCO2	Tfm	Tmice	Tm Chlat	ThCO2	Mode	Th	Mode		% Liq	%Gas
ER05109-55	B6	1	A	1	-57.7			8.6	21.5	L	204.8	L	Static bubble desapear gradually. Easy to see the Homog. T		
ER05109-55	B6	1	B	1				8.5			195.6	L	Static bubble desapear gradually. Easy to see the Homog. T		
ER05109-55	B6	1	C	1	-56.8			9.5	26.4	L	244.3	L	Moving bubble easy sure about T of Homogeniz.		
ER05109-55	B6	1	E	1	-57				20.7	L					
ER05109-55	B6	1	F	1	-57				21.9	L					
ER05109-55	B6	1	G	1							196.8	L	Static bubble desapear gradually. Difficult to be sure of exact Homogen T		
ER05109-55	B6	1	H	1							185.4	L	Moving bubble easy sure about T of Homogeniz.		
ER05109-55	B6	1	I	1				9.2			269.2	L	Static bubble but sure about T of Homog.		
ER05109-55	B6	1	J	1	-56.9			9.5	19.5	L	230	L	Static bubble but sure about T of Homog.		
ER05109-55	B6	1	K	1				9.1	18.6	L	207.2	L	Static bubble desapear gradually. Difficult to be sure of exact Homogen T		
ER05109-55	B6	1	L	1	-56.8			9.4	24.1	L	218.3	L	Static bubble desapear gradually. Difficult to be sure of exact Homogen T		
ER05109-55	B6	1	M	1				8.8			182.8	L	Moving bubble easy sure about T of Homogeniz.		
ER05109-55	B6	1	N	1				9.3			189.9	L	Static bubble desapear gradually. Difficult to be sure of exact Homogen T		

ER05109-55	B6	1	O	1	-56.7		9.5	25.5	L	242.9	L	Moving bubble easy sure about T of Homogeniz.
ER05109-55	B6	1	P	1	-56.8		7.5			235.3	L	Moving bubble easy sure about T of Homogeniz.
ER05109-55	B6	1	Q	1	-56.8		9.5	24.7	L	230.2		Static bubble desapear gradually. Difficult to be sure of exact Homogen T
ER05109-55	B7	1	AA			-1.1						
ER05109-55	B7	1	A							322.9	L	Moving bubble easy sure about T of Homogeniz.
ER05109-55	B7	1	B	1			8.2			242.4	L	
ER05109-55	B7	1	C	1						245.1	L	
ER05109-55	B7	1	D	1		-5.1				271.7	L	Static bubble desapear gradually. Easy to see the Homog. T
ER05109-55	B7	1	E	1		-6.4	7.2			258.2	L	
ER05109-55	B7	1	F	1		-4.5				280.7	L	
ER05109-55	B7	1	G	1		-4.9	8.6			239.5	L	
ER05109-55	B7	1	H	1		-4.3				237.1	L	
ER05109-55	B7	1	I	1		-4.5	8.2			225.6	L	
ER05109-55	B7	1	J	1		-4.9	8.1			261.1	L	
ER05109-55	B7	1	K	1		-4.6	8.3			262.7	L	
ER05109-55	B7	1	L	1	-57.4	-5.3	8.5	20.6	L	221.5	L	
ER05109-55	B7	1	M	1		-4.2	8.4			180.1	L	
ER05109-55	B7	1	N	1		-4.2	8.8			190.9	L	
ER05109-55	B7	1	O	1		-4	9	26.5	L	235.6	L	
ER05109-55	B7	1	P	1						262.3	L	Static bubble desapear gradually. Easy to see the Homog. T
ER05109-55	B7	1	Q	2		-2.9				156.7	L	Static bubble desapear gradually. Easy to see the Homog. T
ER05109-55	B7	1	R			-3.5						
ER05109-55	B7	1	S			-3.3						
ER05109-55	B7	1	T			-3.2						
ER05109-55	B7	1	U	1						248.8	L	
ER05109-55	B7	1	V	1	-57.8	-4.4	8.6	23.3	desap. Menisc	190.9	L	
ER05109-55	B7	1	W			0						
ER05109-55	B7	1	Z	1	-57.6			4.2	L			
ER05109-55	B7	1	ZZ									
ER05109-55	B7	1	YY									
ER05109-55	B7	1	XX	1	-57.1	-4.3	9.5	20.5	L			
ER05109-55	B7	1	WW			-8						
ER05109-55	B7	1	HH				1.6					
ER05109-55	B7	1	BB				1.6					

ER05109-55	B7	1	CC				1.6					
ER05109-55	B4	1	A	1	-56.8	8.9		25.7	desap. Menisc			
ER05109-55	B4	1	B	1	-56.8			22.8	L			
ER05109-55	B8	1	A	2		-6.2				125.2	L	
ER05109-55	B8	1	B	2		-6.1				126.6	L	
ER05109-55	B8	1	C									
ER05109-55	B8	1	D	2						126.3	L	
ER05109-55	B8	1	E									
ER05109-55	B8	1	F	2						127.1	L	
ER05109-55	B8	1	G									
ER05109-55	B8	1	H	2		-6.1						
ER05109-55	B8	1	I	2		-5.7				126.6	L	
ER05109-55	B8	1	J									
ER05109-55	B8	1	K									
ER05109-55	B8	1	L									
ER05109-55	B8	1	M	1	-56.6					249.9	L	static bubble
ER05109-55	B8	1	N	1		-4.6	8.2	27.7	L	185.5	L	static bubble
ER05109-55	B8	1	O									
ER05109-55	B8	1	P				9			237.7	L	moving bubble
ER05109-55	B8	1	Q				8.1			221.5	L	moving bubble
ER05109-55	B8	1	R	1	-56.9					234.9	L	static bubble
ER05109-55	B8	1	S			-2.6	9.3	24.8	L	173.3	L	
ER05109-55	B8	1	T	1	-56.8		9.3	24.7	L	271.6	L	moving bubble
ER05109-55	B8	1	U	1	-57.2		7.6	21.3	L			
ER05109-55	B8	1	V	1	-58		8.4	18.8				
ER05109-55	B8	1	W									
ER05109-55	B8	1	Y									
ER05109-55	G1	1	A	1	-57.8	-3.9	8.5	23.2	L	201.1	L	Moving Bubble
ER05109-55	G1	1	B	1	-56.8	-3.3	9.4			237.7	L	static buble
ER05109-55	G1	1	C	1	-57.4		9.6	23.8	L	200.2	L	static buble
ER05109-55	G1	1	D	1	-57	-3.1	9.4	25.2	L	214.3	L	static buble
ER05109-55	G1	1	E	1	-56.9	-3.6	9.2	25.8	desp. Men	232.5	L	static buble
ER05109-55	G1	1	F			-5.4				325.2	L	Moving Bubble
ER05109-55	G1	1	H	1	-57.4	-3.2	9.5	22.2		197.7	L	Moving Bubble
ER05109-55	G1	1	I	1		-3.9				261.8	L	static buble
ER05109-55	G1	1	K	1	-56.6							
ER05109-55	G1	1	L	1	-56.6							
ER05109-55	G1	1	N	1			9.2			290.8	L	Moving Bubble
ER05109-55	G1	1	O	1	-56.9	-3	9.4	25.4	L	213.2	L	static buble
ER05109-55	G1	1	P	1	-57			23.4	L			
ER05109-55	G1	1	Q	1	-57.8	-4.6	8.2	22.8	L	204.6	L	static buble
ER05109-55	G1	1	R	1	-57.7	-4.4	8.3	23.2	L	202.9	L	static buble
ER05109-55	C1		A	1	-57.2		8	23.8	L			
ER05109-55	D1		A			-5.2	7.7					
ER05109-55	D1		B	1	-56.6							
ER05109-55	D1		C	1		-4.4						
ER05109-55	B11		A	1		-5.1						

Appendix IX

(Portrait of Mesoproterozoic evolution of SW of Amazon Craton)

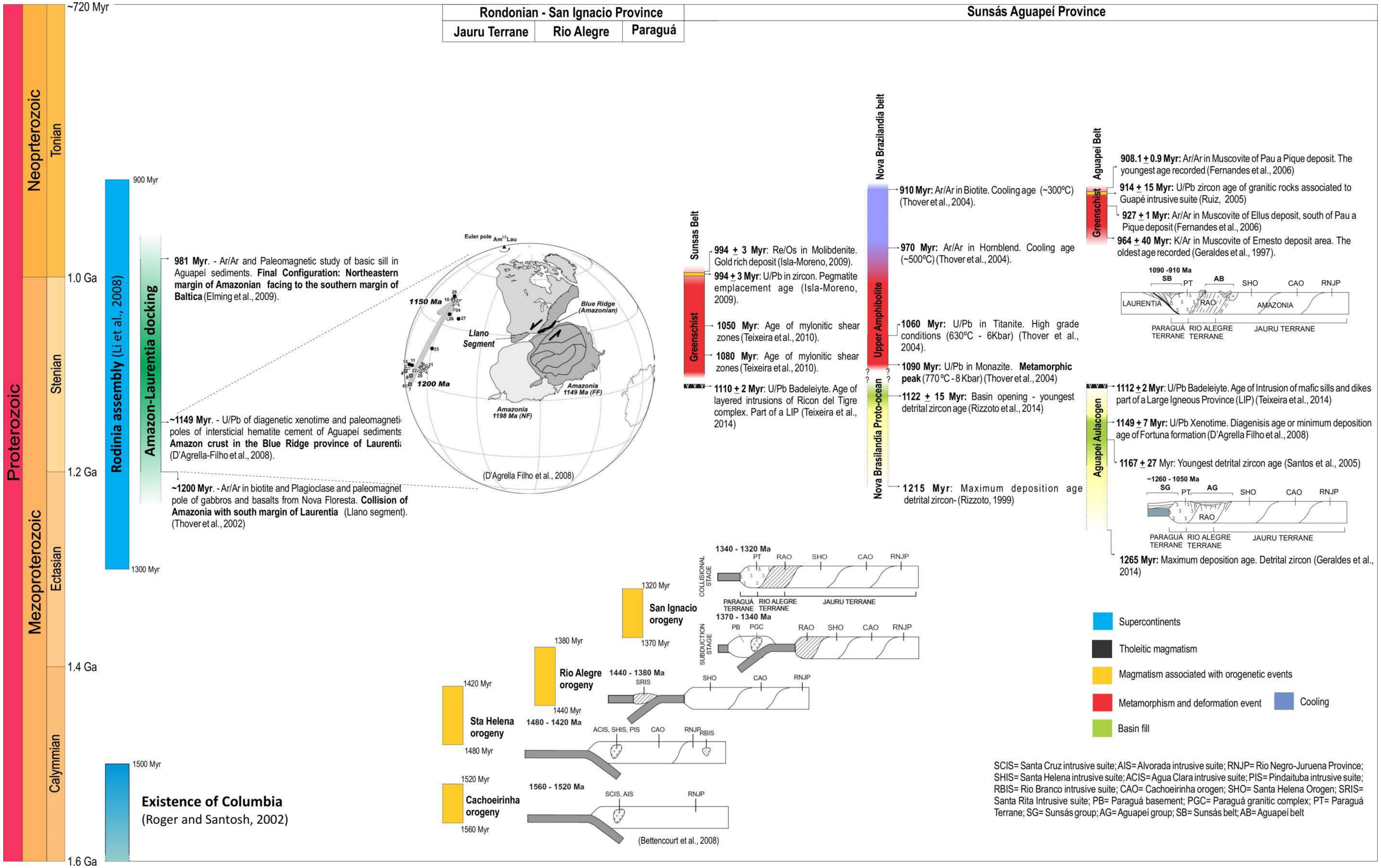

981 Myr. - Ar/Ar and Paleomagnetic study of basic sill in Aguapeí sediments. **Final Configuration: Northeastern margin of Amazonian facing to the southern margin of Baltica** (Elming et al., 2009).

~1149 Myr. - U/Pb of diagenetic xenotime and paleomagneti poles of intersticial hematite cement of Aguapeí sediments **Amazon crust in the Blue Ridge province of Laurenti** (D'Agrella-Filho et al., 2008).

~1200 Myr. - Ar/Ar in biotite and Plagioclase and paleomagnet pole of gabbros and basalts from Nova Floresta. **Collision of Amazonia with south margin of Laurentia** (Llano segment). (Thover et al., 2002)

994 + 3 Myr: Re/Os in Molibdenite. Gold rich deposit (Isla-Moreno, 2009).

994 + 3 Myr: U/Pb in zircon. Pegmatite emplacement age (Isla-Moreno, 2009).

1050 Myr: Age of mylonitic shear zones (Teixeira et al., 2010).

1080 Myr: Age of mylonitic shear zones (Teixeira et al., 2010).

1110 + 2 Myr: U/Pb Badeleiyte. Age of layered intrusions of Ricon del Tigre complex. Part of a LIP (Teixeira et al., 2014)

910 Myr: Ar/Ar in Biotite. Cooling age (~300ºC) (Thover et al., 2004).

970 Myr: Ar/Ar in Hornblend. Cooling age (~500ºC) (Thover et al., 2004).

1060 Myr: U/Pb in Titanite. High grade conditions (630ºC - 6Kbar) (Thover et al., 2004).

1090 Myr: U/Pb in Monazite. **Metamorphic peak** (770 ºC - 8 Kbar) (Thover et al., 2004)

1122 + 15 Myr: Basin opening - youngest detrital zircon age (Rizzoto et al., 2014)

1215 Myr: Maximum deposition age detrital zircon- (Rizzoto, 1999)

908.1 + 0.9 Myr: Ar/Ar in Muscovite of Pau a Pique deposit. The youngest age recorded (Fernandes et al., 2006)

914 + 15 Myr: U/Pb zircon age of granitic rocks associated to Guapé intrusive suite (Ruiz, 2005)

927 + 1 Myr: Ar/Ar in Muscovite of Ellus deposit, south of Pau a Pique deposit (Fernandes et al., 2006)

964 + 40 Myr: K/Ar in Muscovite of Ernesto deposit area. The oldest age recorded (Geraldes et al., 1997).

1112 + 2 Myr: U/Pb Badeleiyte. Age of Intrusion of mafic sills and dikes part of a Large Igneous Province (LIP) (Teixeira et al., 2014)

1149 + 7 Myr: U/Pb Xenotime. Diagenisis age or minimum deposition age of Fortuna formation (D'Agrella Filho et al., 2008)

1167 + 27 Myr: Youngest detrital zircon age (Santos et al., 2005)

1265 Myr: Maximum deposition age. Detrital zircon (Geraldes et al., 2014)

SCIS= Santa Cruz intrusive suite; AIS= Alvorada intrusive suite; RNJP= Rio Negro-Juruena Province; SHIS= Santa Helena intrusive suite; ACIS= Agua Clara intrusive suite; PIS= Pindaituba intrusive suite; RBIS= Rio Branco intrusive suite; CAO= Cachoeirinha orogen; SHO= Santa Helena Orogen; SRIS= Santa Rita Intrusive suite; PB= Paraguá basement; PGC= Paraguá granitic complex; PT= Paraguá Terrane; SG= Sunsás group; AG= Aguapeí group; SB= Sunsás belt; AB= Aguapeí belt

Appendix X

(Detailed geological Map of Studied Area)

Geological Map of the Research Area

Scale 1:50,000

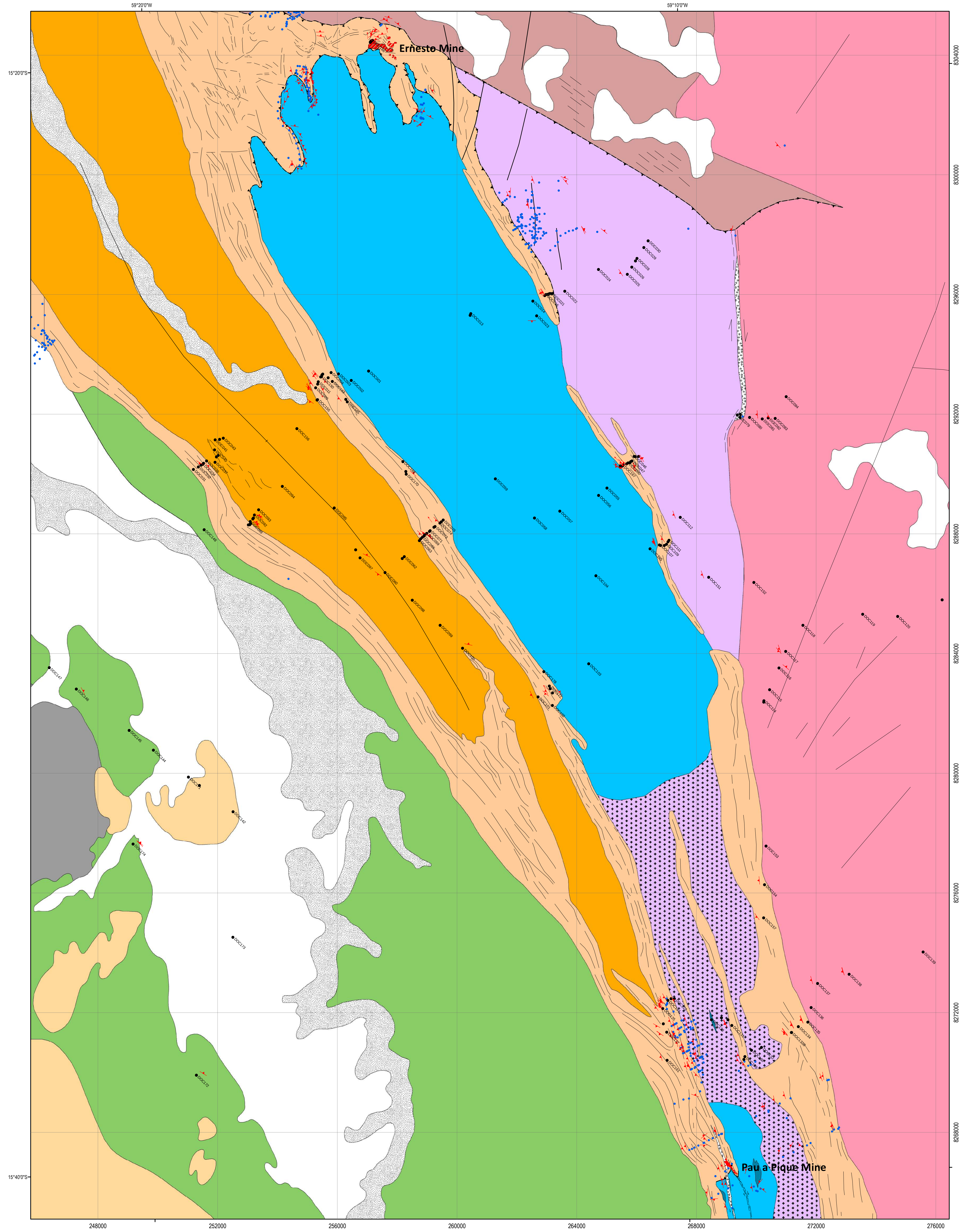

Geological Units

PHANEROZOIC

- ☐ Recent cover (lateritic crusts)
- ▒ Fluvial sediments

PROTEROZOIC

NEOPROTEROZOIC

- ▨ Breccia

Sunsás Aguapeí Province

Aguapeí Group (siliciclastic metassediments deposited in an aulacogen basin): 0.964 - 0.908 Ga (metamorphism)

- 🟧 Vale da Promissão Formation (metarenite and metapelite associated to subamrine fans and related tuibidite system)
- 🟨 Fortuna Formation (metarenite and metaconglomerate associated to alluvial fans and braided channels).

MESO- and PALEOPROTEROZOIC

Rondonian-San Ignacio Province

Rio Alegre Terrain

Vocano sedimentary sequence - Rio Alegre: 1.49 - 1.51 Ga

- ⬛ São Fabiano Formation (metassedimentary rocks)
- 🟩 Minouro Formation (volcanic rocks of basic to ultrabasic composition associated to cherts and BIF)

Jauru Terrain

Santa Helena Intrusive Suite: 1.48 - 1.42 Ga

- 🟥 Hornblend-biotite granite (foliated)

Pindaituba Intrusive Suit: 1.48-1.42 Ga

- 🟪 biotite granite (Maraboa)
- ▨ Porphyritic biotite monzogranite (foliated)
- 🟦 Mafic rocks (amphibolite)
- 🟦 Metadiorite, metagranodiorite and metatonalite (foliated)

Paleoproterozoic Basemment (Alto Jauru Group): 1.76-1.72 Ga

- 🟫 Pontes e Lacerda volcano sedimentary sequence (great variety of rocks including: quartzites, pelitic schist and metavolcanics (metabasalts, metandesites, acid-tuffs)

Legeng of simbols

- Thrust Fault
- Structural lineaments
- Sincline fold axis
- Foliation (Sn)
- Fold Axis (En)
- ● Geologic points (excuted during the research)
- ● Geologic points (Executed by the Yamana exploration team)
- Pau a Pique ore projection
- ▨ Ernesto ore projection

N

0 1,250 2,500 5,000 7,500 10,000 m

South American 1969
Zona 21 S

Satelite Image of the studied area

Map of first vertical derivative of the total magnetic field (from CPRM)

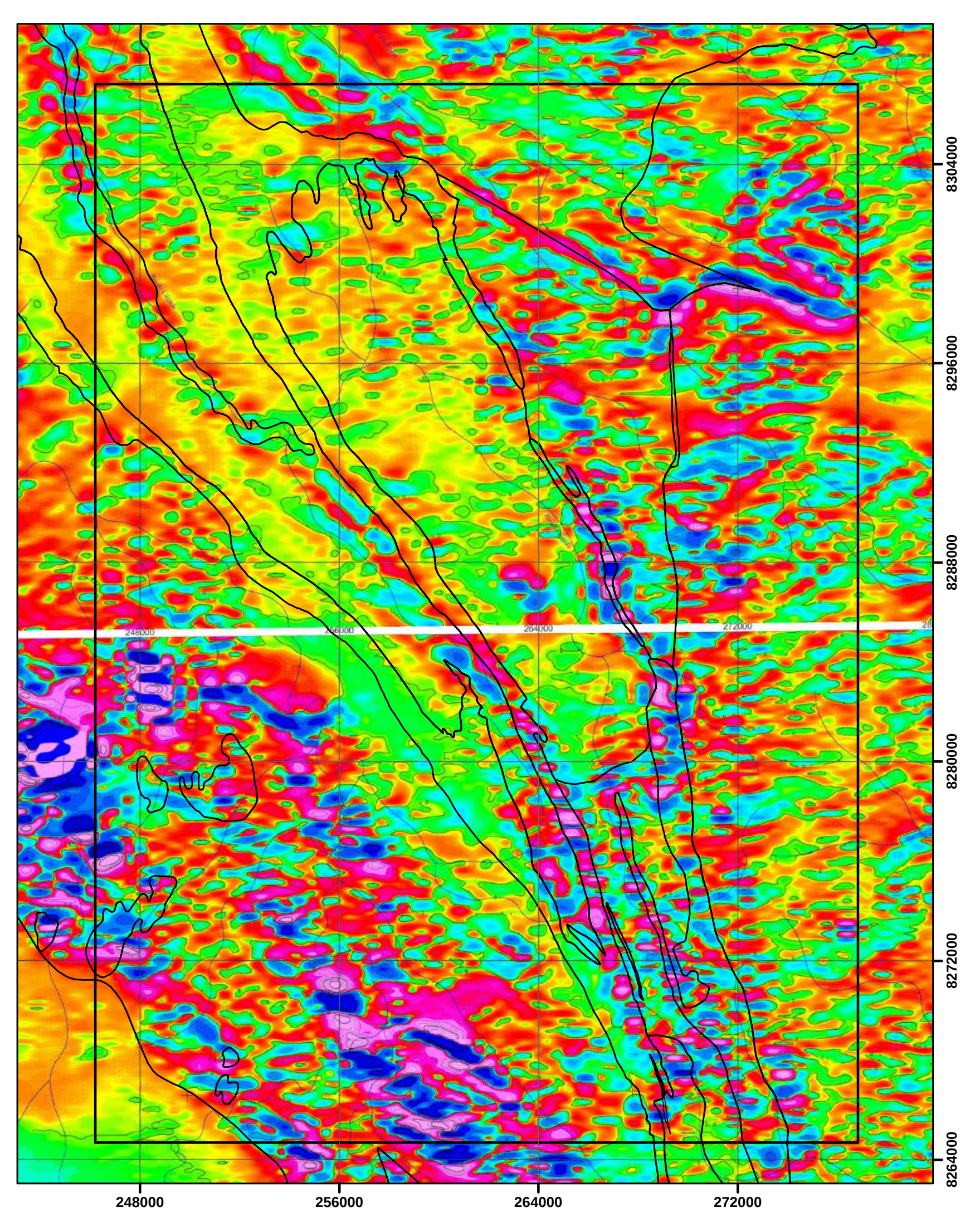

Map of analytic signal of total magnetic field (from CPRM)

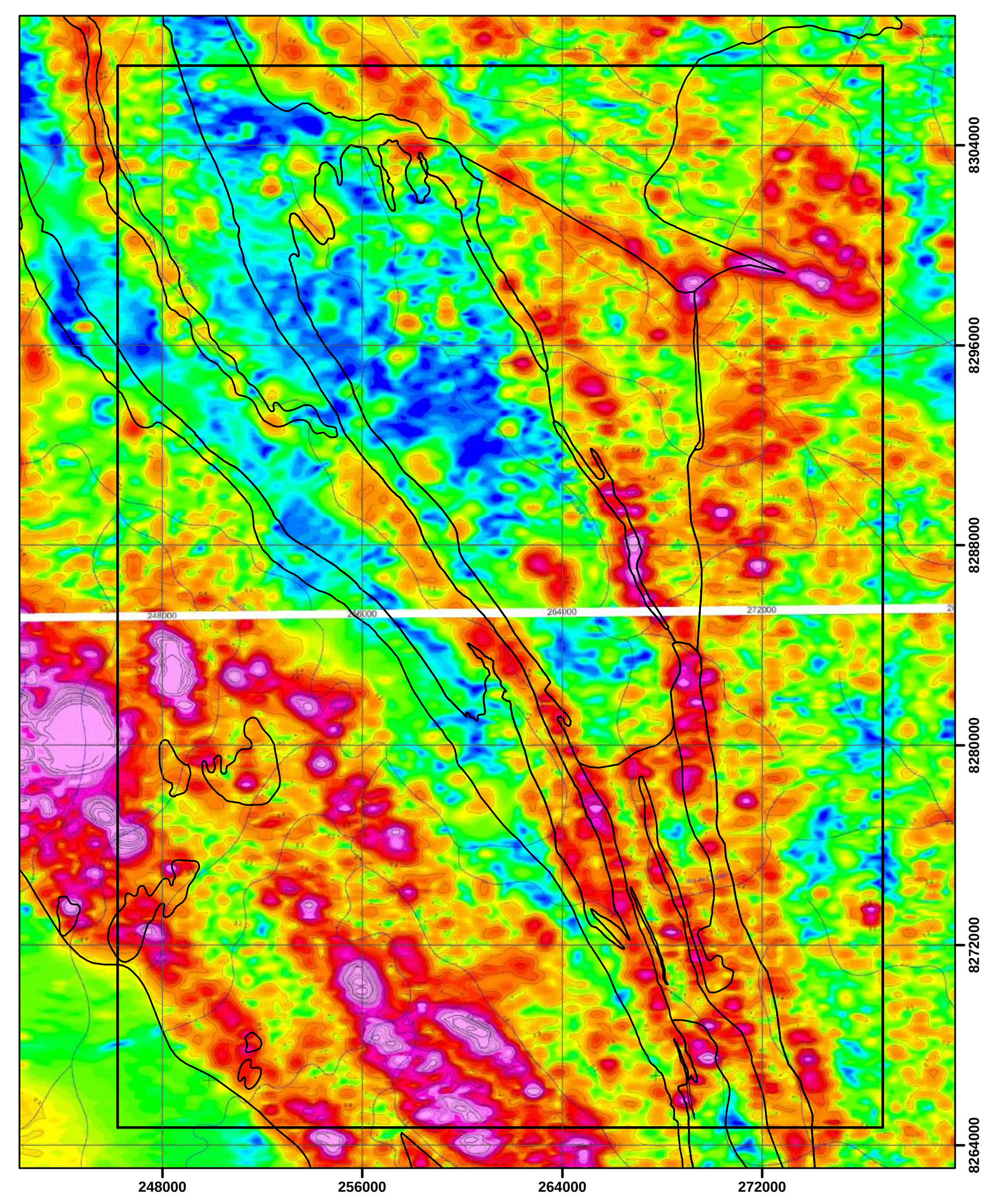

K concentration Map (in %) (from CPRM)

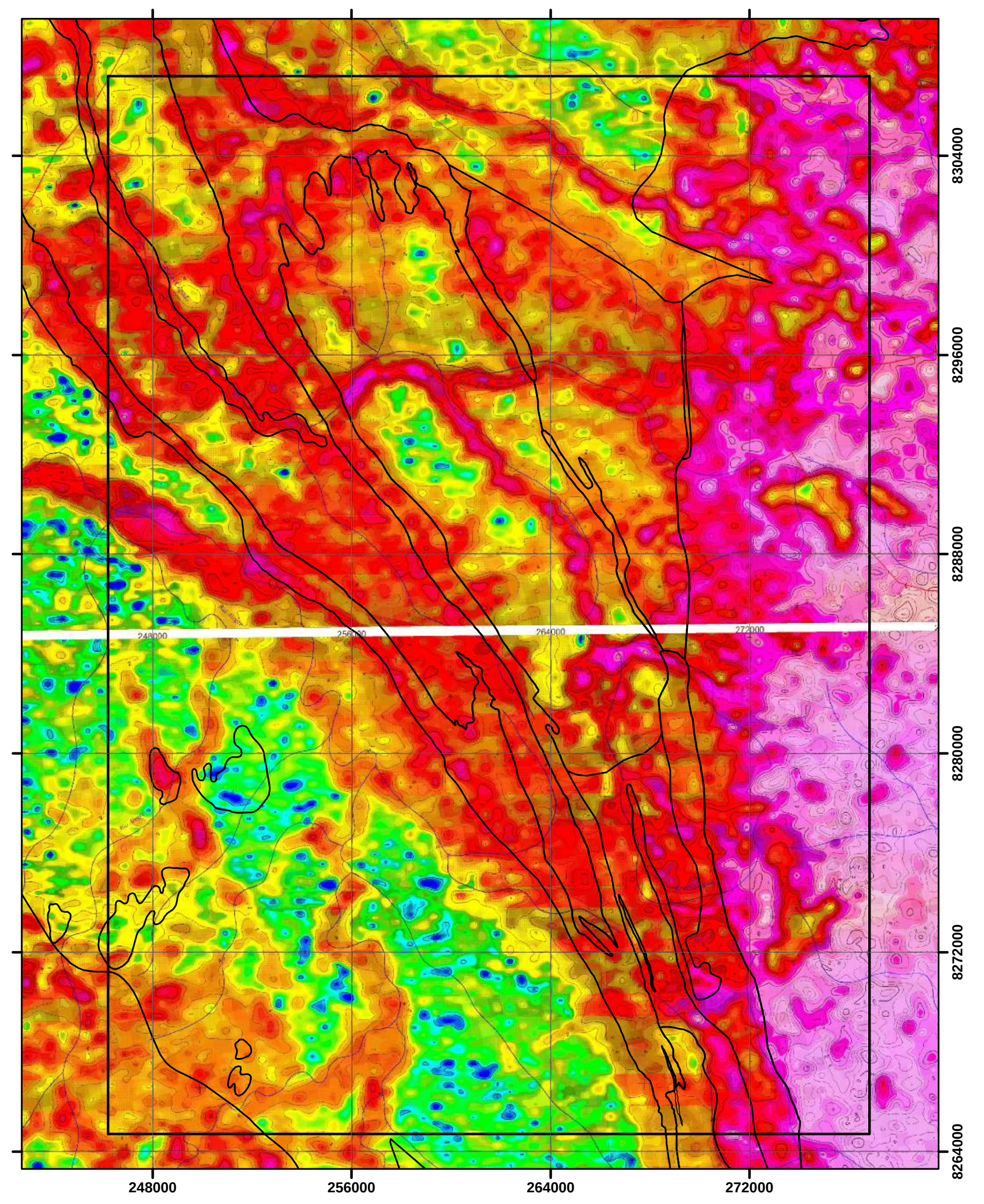

IMPORTANT NOTICE: All geophyscical pictures exposed above comprises part of the geophysical charts SD.21-Y-C-V and SD.21-Y-C-II, resulted from Sudoeste de Rondonia (RO/MT) Project, made by the Brazilian Geological Survey (CPRM). It comprises 1:100.000 geophysical maps in PDF format bought by Serra da Borda Mineração e Metalurgia S/A (a former company of Yamana Gold Inc. group). It was georeferenced and organized as image layer in a GIS platform by the Yamana exploration team and was used in this research to support the mapping of the studied area. It is present here only as illustrative pictures and all copyrights are reserved to the owner of authorship.